

Science

Science  
Advances

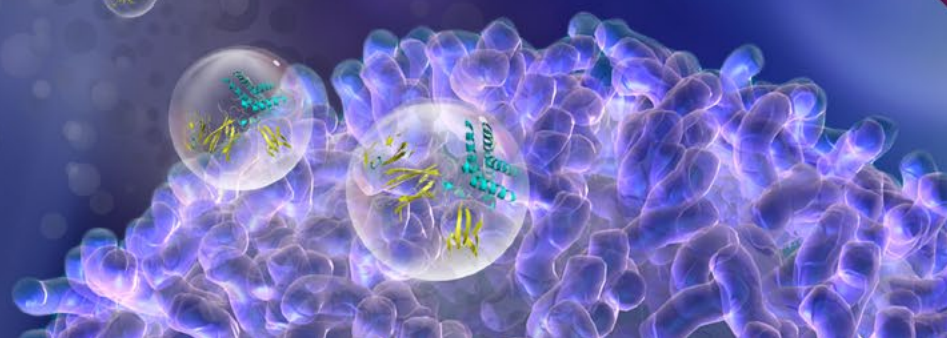
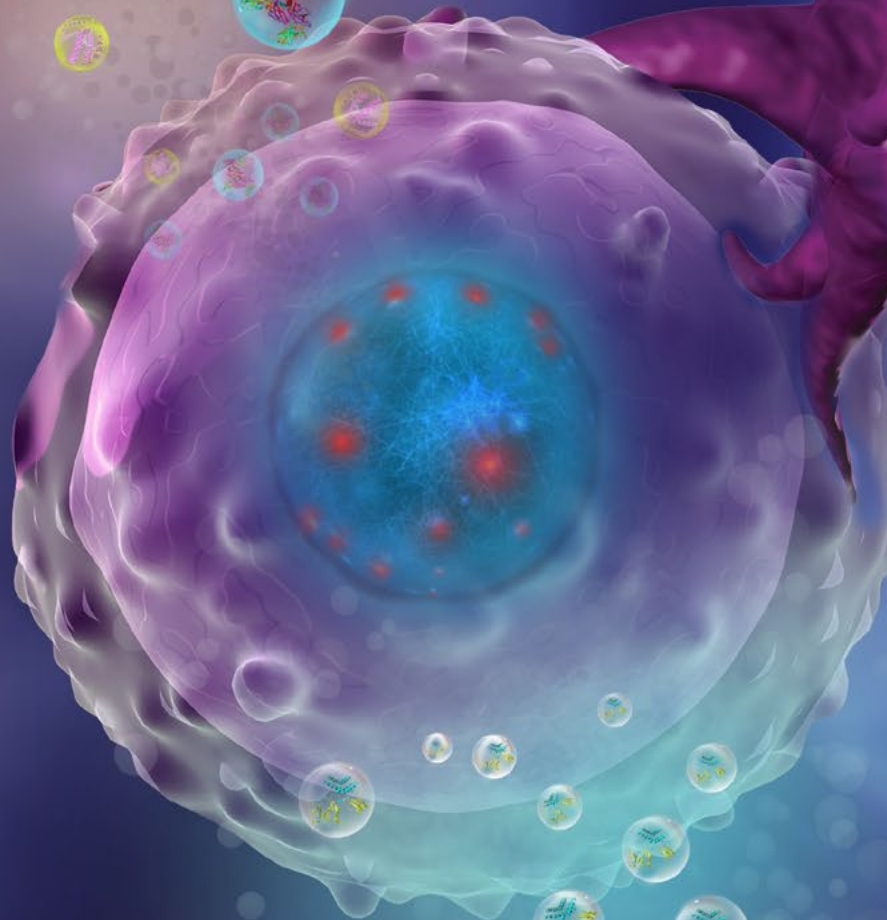
Science  
Immunology

Science  
Signaling

Science  
Translational  
Medicine

SPECIAL  
EDITION

# IMMUNOLOGY



 AAAS

[aaas.org/science-journals](http://aaas.org/science-journals)



## Publish your research in the *Science* family of journals

The *Science* family of journals (*Science*, *Science Advances*, *Science Immunology*, *Science Robotics*, *Science Signaling*, and *Science Translational Medicine*) are among the most highly-regarded journals in the world for quality and selectivity. Our peer-reviewed journals are committed to publishing cutting-edge research, incisive scientific commentary, and insights on what's important to the scientific world at the highest standards.

**Submit your research today!**

Learn more at [ScienceMag.org/journals](https://www.sciencemag.org/journals)

**Science**  
JOURNALS AAAS

## SPECIAL EDITION: Immunology

Select research published in *Science*, *Science Advances*, *Science Immunology*, *Science Signaling*, and *Science Translational Medicine*



This collection of articles from the *Science* family of journals highlights the latest research on immune engineering, neuroimmunology, immunotherapy of infectious diseases with neutralizing antibodies, immunodeficiency diseases, tissue-resident memory T cells, circadian clock effects on inflammation, signaling by chimeric antigen receptor (CAR) T cells, and autoimmunity.

Image: Madeleine Flynn, Graphic Support Officer, Qimr Berghofer Medical Research Institute.



### Editor-in-Chief

Jeremy Berg, Ph.D.  
*Science* family of journals  
AAAS, Washington, DC

## Science | AAAS

*Science* is a leading outlet for scientific news, commentary, and cutting-edge research. The journal publishes original peer-reviewed research across the sciences, with articles that consistently rank among the most cited in the world.

### Editors

Lisa D. Chong, Ph.D.  
Valda J. Vinson, Ph.D.  
Jake S. Yeston, Ph.D.

### Immunology Editors

Priscilla N. Kelly  
Seth T. Scanlon, Ph.D.

## Science Advances | AAAS OPEN ACCESS

*Science Advances* is the digital, open access expansion of *Science* magazine. The journal publishes significant, innovative original research that advances the frontiers of science across a broad range of disciplines, from bioscience and medicine to neuroscience, physics, ecology, and material sciences.

### Managing Editor

Philippa J. Benson, Ph.D.

### Editor

Ali Shalatifard, Ph.D.

### Deputy Editors

Lynden Archer, Ph.D.  
Julia Chan, Ph.D.  
Aaron Clauset, Ph.D.  
Juan de Pablo, Ph.D.  
Dale Dorset, Ph.D.  
Sarah Fortune, M.D.  
Karen Gleason, Ph.D.  
Kip Hodges, Ph.D.  
Jeremy Jackson, Ph.D.

Jonathan Katz, Ph.D.  
Kevin LaBar, Ph.D.  
Shahid Naeem, Ph.D.  
Nicholas Peppas, Ph.D.  
John Rogers, Ph.D.  
Leslie Vosshall, Ph.D.  
Philip Yeagle, Ph.D.  
Warren Warren, Ph.D.

## Science Immunology | AAAS

*Science Immunology* publishes original, peer-reviewed, science-based research articles that report critical advances in all areas of immunological research, including important new tools and techniques.

### Chief Scientific Advisors

Abul K. Abbas, M.D.  
*University of California,  
San Francisco*

### Editor

Ifor Williams, M.D., Ph.D.

### Editorial Team

Anand Balasubramani, Ph.D.

Federica Sallusto, Ph.D.

*Università della Svizzera Italiana*

## Science Signaling | AAAS

*Science Signaling* publishes peer-reviewed, original research investigating cell signaling that underlies physiology and disease, on the molecular, cellular, intercellular and organismal levels.

### Chief Scientific Advisor and Academic Editor

Michael B. Yaffe, M.D., Ph.D.  
*Massachusetts Institute  
of Technology*

### Editor

John F. Foley, Ph.D.

### Deputy Editor

Wei Wong, Ph.D.

### Editorial Team

Leslie K. Ferrarelli, Ph.D.  
Annalisa M. VanHook, Ph.D.  
Erin R. Williams, Ph.D.

## Science Translational Medicine | AAAS

*Science Translational Medicine* is an interdisciplinary journal that publishes translational research with impact for human health that fills the knowledge gaps between preclinical studies and clinical applications.

### Chief Scientific Advisors

Elazer R. Edelman, M.D., Ph.D.  
*Massachusetts Institute  
of Technology*

### Editor

Orla M. Smith, Ph.D.

Garret FitzGerald, M.D.

*University of Pennsylvania*

### Editorial Team

Catherine A. Charneski, Ph.D.  
Caitlin A. Czajka, Ph.D.  
Mattia Maroso, Ph.D.  
Yevgeniya Nusinovich, M.D., Ph.D.  
Lindsey Pujanandez, Ph.D.

Learn more and submit your research today: [aaas.org/science-journals](https://www.aaas.org/science-journals)

## IN THIS BOOKLET

### Science

- 5** **REPORT**  
**Selective targeting of engineered T cells using orthogonal IL-2 cytokine-receptor complexes**  
Jonathan T. Sockolosky *et al.* (K. Christopher Garcia)
- 11** **REPORT**  
**Choline acetyltransferase-expressing T cells are required to control chronic viral infection**  
Maureen A. Cox *et al.* (Tak W. Mak)

### Science Advances

- 16** **RESEARCH ARTICLE**  
**Chimeric camel/human heavy-chain antibodies protect against MERS-CoV infection**  
V. Stalin Raj *et al.* (Bart L. Haagmans)
- 26** **RESEARCH ARTICLE**  
**Genetic and structural insights into broad neutralization of hepatitis C virus by human V<sub>H</sub>1-69 antibodies**  
Netanel Tzarum *et al.* (Mansun Law)

### Science Immunology

- 37** **RESEARCH ARTICLE**  
**Tuberculosis and impaired IL-23-dependent IFN- $\gamma$  immunity in humans homozygous for a common TYK2 missense variant**  
Stéphanie Boisson-Dupuis *et al.* (Jean-Laurent Casanova)
- 56** **RESEARCH ARTICLE**  
**Generation and persistence of human tissue-resident memory T cells in lung transplantation**  
Mark E. Snyder *et al.* (Donna L. Farber)



### Science Signaling

- 73** **RESEARCH ARTICLE**  
**Desynchronization of the molecular clock contributes to the heterogeneity of the inflammatory response**  
Nancy C. Allen *et al.* (Ruslan Medzhitov)
- 83** **RESEARCH ARTICLE**  
**Phosphoproteomic analysis of chimeric antigen receptor signaling reveals kinetic and quantitative differences that affect cell function**  
Alexander I. Salter *et al.* (Stanley R. Riddell)

### Science Translational Medicine

- 100** **RESEARCH ARTICLE**  
**Recurrent group A *Streptococcus* tonsillitis is an immunosusceptibility disease involving antibody deficiency and aberrant T<sub>FH</sub> cells**  
Jennifer M. Dan *et al.* (Shane Crotty)
- 110** **RESEARCH ARTICLE**  
**Sustained B cell depletion by CD19-targeted CART cells is a highly effective treatment for murine lupus**  
Rita Kansal *et al.* (Marko Radic)



Publisher / Science family of journals: **Bill Moran**  
AD/ Business Development: **Justin Sawyers**  
Marketing Manager: **Shawana Arnold**  
Layout/Design: **Kim Huynh**

#### Sponsorship Opportunities:

Laurie Faraday, *Science*  
lfaraday@aaas.org | +1.508.747.9395  
1200 New York Ave NW, Washington DC 20005

Learn more and submit your research today: [aaas.org/science-journals](http://aaas.org/science-journals)

## IMMUNE ENGINEERING

Copyright © 2018 The Authors, some rights reserved\*

# Selective targeting of engineered T cells using orthogonal IL-2 cytokine-receptor complexes

Jonathan T. Sockolosky,<sup>1,2</sup> Eleonora Trotta,<sup>3\*</sup> Giulia Parisi,<sup>4\*</sup> Lora Picton,<sup>1</sup> Leon L. Su,<sup>1</sup> Alan C. Le,<sup>5</sup> Akanksha Chhabra,<sup>5</sup> Stephanie L. Silveria,<sup>3</sup> Benson M. George,<sup>2,5,6</sup> Indigo C. King,<sup>7</sup> Matthew R. Tiffany,<sup>8</sup> Kevin Jude,<sup>1</sup> Leah V. Sibener,<sup>1,9</sup> David Baker,<sup>7</sup> Judith A. Shizuru,<sup>5</sup> Antoni Ribas,<sup>4,10</sup> Jeffrey A. Bluestone,<sup>3,10</sup> K. Christopher Garcia<sup>1,2,10,11†</sup>

Interleukin-2 (IL-2) is a cytokine required for effector T cell expansion, survival, and function, especially for engineered T cells in adoptive cell immunotherapy, but its pleiotropy leads to simultaneous stimulation and suppression of immune responses as well as systemic toxicity, limiting its therapeutic use. We engineered IL-2 cytokine-receptor orthogonal (*ortho*) pairs that interact with one another, transmitting native IL-2 signals, but do not interact with their natural cytokine and receptor counterparts. Introduction of *orthoIL-2Rβ* into T cells enabled the selective cellular targeting of *orthoIL-2* to engineered CD4<sup>+</sup> and CD8<sup>+</sup> T cells in vitro and in vivo, with limited off-target effects and negligible toxicity. *OrthoIL-2* pairs were efficacious in a preclinical mouse cancer model of adoptive cell therapy and may therefore represent a synthetic approach to achieving selective potentiation of engineered cells.

**A**doptive transfer of tumor-reactive T cells has evolved into a clinically useful therapy capable of inducing antitumor immunity in patients (1, 2). However, the broad application of adoptive T cell transfer (ACT) therapies to treat cancer has several limitations, including the production of sufficient quantities of cells for infusion and the failure of transferred T cells to persist and remain functional in vivo. In the clinic, the concomitant administration of the T cell growth factor interleukin-2 (IL-2) improves the survival, function, and antitumor activity of transplanted T cells (3, 4). However, the use of IL-2 to potentiate ACT is complicated by the pleiotropic nature of IL-2, which induces both

immune stimulatory and suppressive T cell responses as well as potentially severe toxicities (5). This is governed by the interaction between IL-2 and the IL-2 receptor (IL-2R), which consists of  $\alpha$ ,  $\beta$ , and  $\gamma$  subunits (6). IL-2R $\beta$  and the common  $\gamma$ -chain (IL-2R $\gamma$ ) together form the signaling dimer and bind IL-2 with moderate affinity, whereas IL-2R $\alpha$  (CD25) does not signal but increases the affinity of IL-2 for the binary ( $\beta\gamma$ ) IL-2 receptor to sensitize T cells to low concentrations of IL-2.

The activity of IL-2 as an adjuvant to ACT is dependent on the balance between activation of transplanted and endogenous T cell subsets bearing natural IL-2 receptors, as well as host responses that cause dose-limiting toxicities. Strategies to overcome these limitations could improve T cell immunotherapy (7, 8). Recognizing the need for new approaches that afford precise targeting of IL-2-dependent functions to a specific cell type of interest, we devised a strategy to redirect the specificity of IL-2 toward adoptively transferred T cells. This method, based on receptor-ligand orthogonalization, uses a mutant IL-2 cytokine and mutant IL-2 receptor that bind specifically to one another but not to their wild-type counterparts (Fig. 1A).

We focused on the murine IL-2/IL-2R $\beta$  interaction to enable in vivo characterization in syngeneic mouse models. The IL-2R $\beta$  chain was chosen as the mutant receptor because the  $\beta$  chain is required for signal transduction and can bind IL-2 independently. We devised a two-step approach to engineer orthogonal IL-2/IL-2R $\beta$  pairs informed by the crystal structure of the IL-2 high-affinity receptor complex (6) (Fig. 1B). First, point mutations of the IL-2R $\beta$  chain were identified from inspection of the interface between IL-2 and IL-2R $\beta$  that abrogated binding

to wild-type IL-2 (Fig. 1, C to E). The IL-2R $\beta$  hot-spot residues His<sup>134</sup> and Tyr<sup>135</sup> make numerous contacts with IL-2 that contribute a majority of the binding free energy between IL-2 and IL-2R $\beta$  (6) (Fig. 1E). A double mutant IL-2R $\beta$  [His<sup>134</sup> → Asp (H134D) and Tyr<sup>135</sup> → Phe (Y135F)], referred to herein as *orthoIL-2Rβ*, lacked detectable binding to IL-2 (Fig. 1D), even in the presence of CD25 (fig. S1) (7, 9).

Next, we used yeast display-based evolution to mutate, and thus remodel, the wild-type IL-2 interface region that was opposing (or facing the site of) the IL-2R $\beta$  mutations in the crystal structure, in order to create a molecule that bound to *orthoIL-2Rβ* but not to wild-type IL-2R $\beta$ . IL-2 residues in proximity to the *orthoIL-2Rβ* binding interface were randomly mutated and were chosen on the basis of a homology model of the mouse IL-2/IL-2R $\beta$  complex (Fig. 1E) derived from the crystal structure of the human IL-2 receptor complex (6). A library of ~10<sup>8</sup> unique IL-2 mutants was displayed on the surface of yeast (fig. S2) and subjected to multiple rounds of both positive (against *orthoIL-2Rβ*) and negative (against IL-2R $\beta$ ) selection (figs. S2 and S3). This collection of yeast-displayed IL-2 mutants bound the *orthoIL-2Rβ*, but not wild-type IL-2R $\beta$ , and retained CD25 binding (Fig. 1D). Sequencing of yeast clones from the evolved IL-2 libraries revealed a consensus set of mutations at IL-2 positions in close structural proximity to the *orthoIL-2Rβ* mutations (fig. S4). Interestingly, a Gln<sup>30</sup> → Asn (Q30N) mutation was highly conserved across three independent mutant IL-2 yeast libraries, whereas all other IL-2 positions used a restricted but not specific mutational signature. We found that IL-2 mutations Q30N, Met<sup>33</sup> → Val (M33V), and Asp<sup>34</sup> → Leu or Met (D34L/M) appear to form a small nonpolar pocket to compensate for the IL-2R $\beta$  Y135F mutation, whereas Gln<sup>36</sup> → Thr, Ser, Lys, or Glu (Q36T/S/K/E) and Glu<sup>37</sup> → Tyr or His (E37Y/H) mutations present a polar or charged surface to compensate for the IL-2R $\beta$  H134D mutation (Fig. 1F).

Because of the affinity-enhancing effects of CD25 expression on the interaction of IL-2 with the binary ( $\beta\gamma$ ) IL-2 receptor (10), IL-2 mutants with negligible binding to IL-2R $\beta$  alone may still form a functional signaling complex on cells that also express CD25 (8). Therefore, we used a yeast-based functional screen to further triage IL-2 mutants that bound specifically to the *orthoIL-2Rβ* and signaled selectively on T cells that express the *orthoIL-2Rβ* (Fig. 1G and fig. S5), and produced recombinant forms of select IL-2 mutants (*orthoIL-2*) for characterization (figs. S6 to S8).

We focused our efforts on two *orthoIL-2* mutants, 1G12 and 3A10. *OrthoIL-2* 1G12 and 3A10 share the consensus Q30N, M33V, and D34L mutations but differ at positions Glu<sup>29</sup>, Gln<sup>36</sup>, Glu<sup>37</sup>, and Arg<sup>41</sup> (Fig. 1I). *OrthoIL-2* 1G12 and 3A10 bound the *orthoIL-2Rβ* with an affinity comparable to that of the wild-type IL-2/IL-2R $\beta$  interaction and displayed little to no detectable binding to wild-type IL-2R $\beta$  (Fig. 1H and figs. S7 and S8) but differed in their ability to activate IL-2R $\beta$  signaling in CD25-positive wild-type

<sup>1</sup>Departments of Molecular and Cellular Physiology and Structural Biology, Stanford University School of Medicine, Stanford, CA 94305, USA. <sup>2</sup>Stanford Cancer Institute, Stanford University School of Medicine, Stanford, CA 94305, USA. <sup>3</sup>Diabetes Center and Department of Medicine, University of California, San Francisco, CA 94143, USA. <sup>4</sup>Division of Hematology-Oncology, Department of Medicine, David Geffen School of Medicine, and Jonsson Comprehensive Cancer Center, University of California, Los Angeles, CA 90095, USA. <sup>5</sup>Department of Blood and Marrow Transplantation, Institute for Stem Cell Biology and Regenerative Medicine, and Ludwig Center for Cancer Stem Cell Research and Medicine, Stanford University School of Medicine, Stanford, CA 94305, USA. <sup>6</sup>Stanford Medical Scientist Training Program, Stanford University, Stanford, CA 94305, USA. <sup>7</sup>Department of Biochemistry, Howard Hughes Medical Institute, and Institute for Protein Design, University of Washington, Seattle, WA 98195, USA. <sup>8</sup>Department of Pediatrics and Genetics, Stanford University School of Medicine, Stanford, CA 94305, USA. <sup>9</sup>Immunology Graduate Program, Stanford University School of Medicine, Stanford, CA 94305, USA. <sup>10</sup>Parker Institute for Cancer Immunotherapy, 1 Letterman Drive, Suite D3500, San Francisco, CA 94129, USA. <sup>11</sup>Howard Hughes Medical Institute, Stanford University School of Medicine, Stanford, CA 94305, USA.

\*These authors contributed equally to this work.

†Corresponding author. Email: kgarcia@stanford.edu

and *orthoIL-2Rβ* T cells. Stimulation of *orthoIL-2Rβ* T cells (fig. S5B) with *orthoIL-2* 1G12 resulted in dose-dependent phosphorylation of STAT5 (pSTAT5), a hallmark of IL-2R signaling, with potency similar to that of wild-type IL-2, but also induced pSTAT5 on wild-type T cells, albeit with significantly reduced potency relative to IL-2 (Fig. 1, G and I, and fig. S6). By comparison, *orthoIL-2* 3A10 was specific for *orthoIL-2Rβ* T cells, but with a weaker potency relative to IL-2 (Fig. 1, G and I, and fig. S6). We speculated that *orthoIL-2* 1G12 activity on wild-type T cells is a consequence of weak residual binding to wild-type IL-2Rβ (fig. S7). Low-affinity interactions with IL-2Rβ alone are enhanced in the presence of CD25 (8). Indeed, *orthoIL-2* 1G12 exhibited binding to wild-type IL-2Rβ when first captured by CD25, with limited binding in the absence of CD25 (figs. S1 and S8). *OrthoIL-2* 3A10 did not bind appreciably to IL-2Rβ even in the presence of CD25, in agreement with its negligible biological activity on CD25-positive T cells. Interaction of *orthoIL-2* 1G12 and 3A10 with *orthoIL-2Rβ* was significantly enhanced in the presence of CD25, with apparent binding affinities of the ternary CD25/*orthoIL-2Rβ*/*orthoIL-2* complex that correlate with their respective potency on *orthoIL-2Rβ* T cells (fig. S1).

In clinical ACT regimens, patient-derived T cells for ACT are expanded in IL-2 before re-infusion in order to obtain sufficient numbers of therapeutic cells with the desired genotype/phenotype (2). We explored the in vitro activity of *orthoIL-2* on activated primary mouse CD8<sup>+</sup> T cells engineered to express the *orthoIL-2Rβ* and a yellow fluorescent protein (YFP) to distinguish modified (YFP<sup>+</sup>) and unmodified (YFP<sup>-</sup>) cells (Fig. 2A). The transcription factor STAT5 is phosphorylated upon IL-2 engagement with the IL-2R and translocates to the nucleus, where it promotes the proliferation and cell cycle progression of T cells (11). Wild-type IL-2 induced the phosphorylation of STAT5 (pSTAT5) in both wild-type and *orthoIL-2Rβ* CD8<sup>+</sup> T cells with similar potency and signaling amplitude, indicating functional signal transduction through the wild-type receptor but not *orthoIL-2Rβ* (Fig. 2B). By comparison, *orthoIL-2* 1G12 potently activated STAT5 on *orthoIL-2Rβ*-transduced T cells, with a potency increase by a factor of ~5 relative to wild-type T cells. *OrthoIL-2* 3A10 induced somewhat weaker, albeit selective pSTAT5 on *orthoIL-2Rβ*-expressing but not wild-type T cells (Fig. 2, B, D, and E). These results were consistent with the biased binding of the *orthoIL-2*s to the *orthoIL-2Rβ*, which translated into the selective or specific expansion of *orthoIL-2Rβ* T cells cultured ex vivo in *orthoIL-2* 1G12 or 3A10, respectively (Fig. 2, C and D). The *orthoIL-2Rβ*-transduced T cells cultured in saturating concentrations of *orthoIL-2* 3A10 became enriched to near homogeneity after 3 to 5 days (Fig. 2F).

IL-2 is indispensable for the development and function of regulatory T cells (T<sub>regs</sub>) (12), which are sensitive to IL-2 as a result of constitutive expression of CD25 and require IL-2Rβ-dependent activation of STAT5 signaling for survival and function (13). Both *orthoIL-2* 1G12 and 3A10 re-

tained specificity for T<sub>regs</sub> modified to express the *orthoIL-2Rβ*, with potency similar to that on CD8<sup>+</sup> T cells (Fig. 2G and fig. S9, A and B). In addition to cells that naturally respond to IL-2, activation of *orthoIL-2Rβ* signaling pathways with *orthoIL-2*

could, in principle, be achieved in any cell type that also expresses the IL-2Rγ. Activated mouse B cells expressed the IL-2Rγ but lacked appreciable levels of IL-2Rβ (14, 15) and were relatively insensitive to IL-2-dependent STAT5 activation

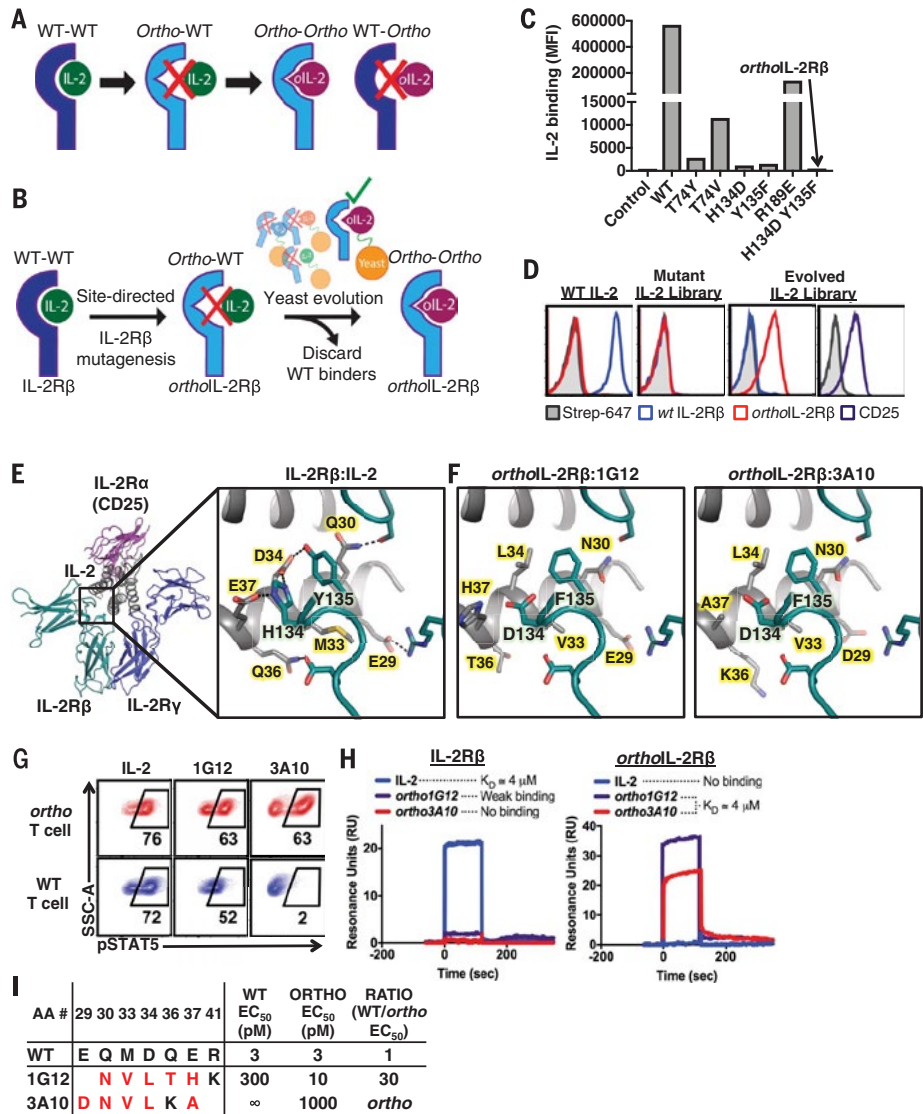
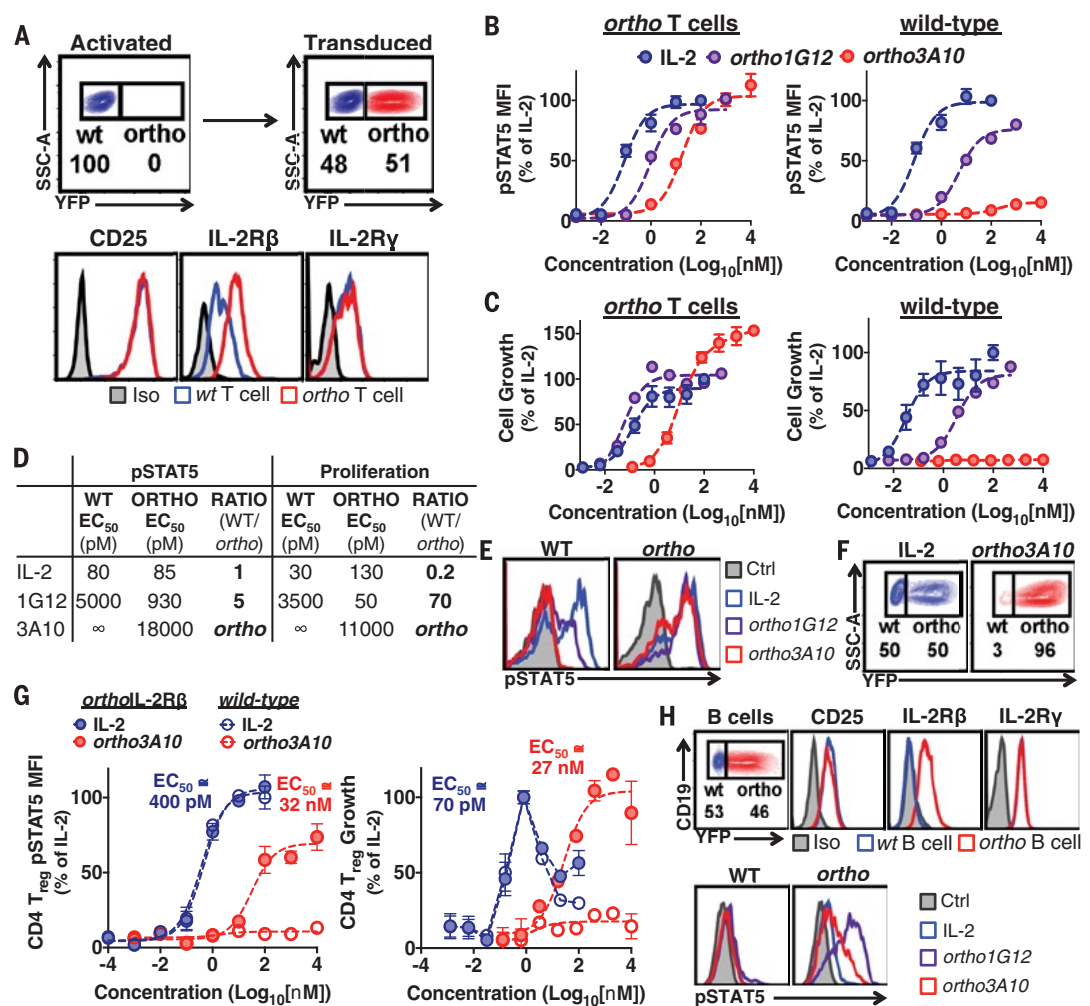


**Fig. 1. Engineering and characterization of orthogonal IL-2 and IL-2R pairs.** (A) Schematic overview of orthogonal IL-2/IL-2R pairs, consisting of a mutant IL-2 cytokine and mutant IL-2R that interact specifically with each other but do not cross-react with their wild-type counterparts. (B) Strategy used to engineer orthogonal IL-2/IL-2Rβ pairs. (C) Wild-type and mutant IL-2Rβ tetramer binding to wild-type IL-2 displayed on yeast by fluorescence-activated cell sorting. MFI, mean fluorescence intensity. Data are representative of two independent experiments. (D) Histograms of wild-type IL-2Rβ (blue), *orthoIL-2Rβ* (red), or CD25 (purple) binding to yeast-displayed wild-type IL-2, the naive mutant IL-2 yeast library, or mutant IL-2 yeast clones after in vitro evolution. In vitro evolution of three independent mutant IL-2 yeast libraries (fig. S4) yielded similar results. (E) Homology model of the mouse IL-2/IL-2Rβ structure and the site I interface of IL-2 (gray) and contacts with IL-2Rβ His<sup>134</sup> and Tyr<sup>135</sup> (teal). Dashed lines indicate potential polar contacts. (F) Model of the *orthoIL-2*/*orthoIL-2Rβ* interactions. (G) Off-yeast pSTAT5 functional screen of IL-2 mutant activity on wild-type and *orthoIL-2Rβ* CTLL-2 T cells. (H) Representative surface plasmon resonance (SPR) sensograms of wild-type and *orthoIL-2* binding to wild-type IL-2Rβ or *orthoIL-2Rβ*. Data are representative of two independent experiments. K<sub>D</sub>, dissociation constant. (I) Sequences of wild-type (WT) IL-2, *orthoIL-2* 1G12, and *orthoIL-2* 3A10 and corresponding in vitro bioactivity (pSTAT5 EC<sub>50</sub>) on wild-type and *orthoIL-2Rβ* CTLL-2 T cells. Amino acid codes: A, Ala; D, Asp; E, Glu; F, Phe; H, His; K, Lys; L, Leu; M, Met; N, Asn; Q, Gln; T, Thr; V, Val; Y, Tyr.

**Fig. 2. OrthoIL-2 signals through the orthoIL-2R expressed in primary mouse lymphocyte subsets, resulting in specific expansion of CD4 and CD8 T cells in vitro.** (A) Flow cytometry data of mouse T cells transduced with the orthoIL-2Rβ and a YFP reporter (top panels) and associated cell surface levels of CD25, IL-2Rβ, and IL-2Rγ. (B to F) Dose-response curves of (B) STAT5 phosphorylation after 20 min of stimulation and (C) proliferation of wild-type (open circles) and orthoIL-2Rβ (solid circles) CD8<sup>+</sup> T cells cultured for 4 days in IL-2 or orthoIL-2; (D) table of respective pSTAT5 and proliferation EC<sub>50</sub> from data in (B) and (C). Representative histograms of (E) STAT5 phosphorylation and (F) scatterplots of CD8<sup>+</sup> wild-type (YFP<sup>-</sup>) and orthoIL-2Rβ (YFP<sup>+</sup>) T cells expanded in IL-2.



(A) Flow cytometry data of mouse T cells transduced with the orthoIL-2Rβ and a YFP reporter (top panels) and associated cell surface levels of CD25, IL-2Rβ, and IL-2Rγ. (B to F) Dose-response curves of (B) STAT5 phosphorylation after 20 min of stimulation and (C) proliferation of wild-type (open circles) and orthoIL-2Rβ (solid circles) CD8<sup>+</sup> T cells cultured for 4 days in IL-2 or orthoIL-2; (D) table of respective pSTAT5 and proliferation EC<sub>50</sub> from data in (B) and (C). Representative histograms of (E) STAT5 phosphorylation and (F) scatterplots of CD8<sup>+</sup> wild-type (YFP<sup>-</sup>) and orthoIL-2Rβ (YFP<sup>+</sup>) T cells expanded in IL-2. Data are means ± SD (n = 3 biological replicates). Dashed lines represent curves fit to a log (agonist) versus response (three parameters) model in Prism. (G) Dose-response curves of STAT5 phosphorylation (left) and proliferation (right) of wild-type and orthoIL-2Rβ CD4<sup>+</sup> T<sub>reg</sub>s cultured in IL-2 or orthoIL-2. Data are means ± SD (n = 3 biological replicates). (H) Representative histograms of primary mouse B cells transduced with the orthoIL-2Rβ and stimulated with the indicated cytokines for quantification of intracellular pSTAT5 as in fig. S9.

(Fig. 2H and fig. S9, E and F). Transduction of the orthoIL-2Rβ into activated B cells rendered them responsive to orthoIL-2 (Fig. 2H and fig. S9, E and F), but with reduced potency and increased specificity relative to T cells. Specificity was due to the lack of appreciable wild-type IL-2Rβ on B cells (fig. S9E).

In a host with an intact immune system, adoptively transferred T cells must compete with host cells for survival signals such as IL-2 (16). However, unlike wild-type IL-2, there should be minimal competition from endogenous cells for orthoIL-2 consumption. Thus, we determined the in vivo activity of orthoIL-2 and orthoIL-2Rβ T cells in mice with intact immune systems. A mixture of wild-type and orthoIL-2Rβ CD8<sup>+</sup> T cells was adoptively transferred into wild-type mice, and the impact of IL-2 and orthoIL-2 administration on transplanted T cells and the host immune system was quantified (Fig. 3A). OrthoIL-2 1G12 significantly expanded CD8<sup>+</sup> T cells transduced with the orthoIL-2Rβ at doses equivalent to or lower than wild-type IL-2, which acted through the endogenous IL-2Rβ expressed in both wild-type and orthoIL-2Rβ T cells (Fig. 3B and fig. S10).

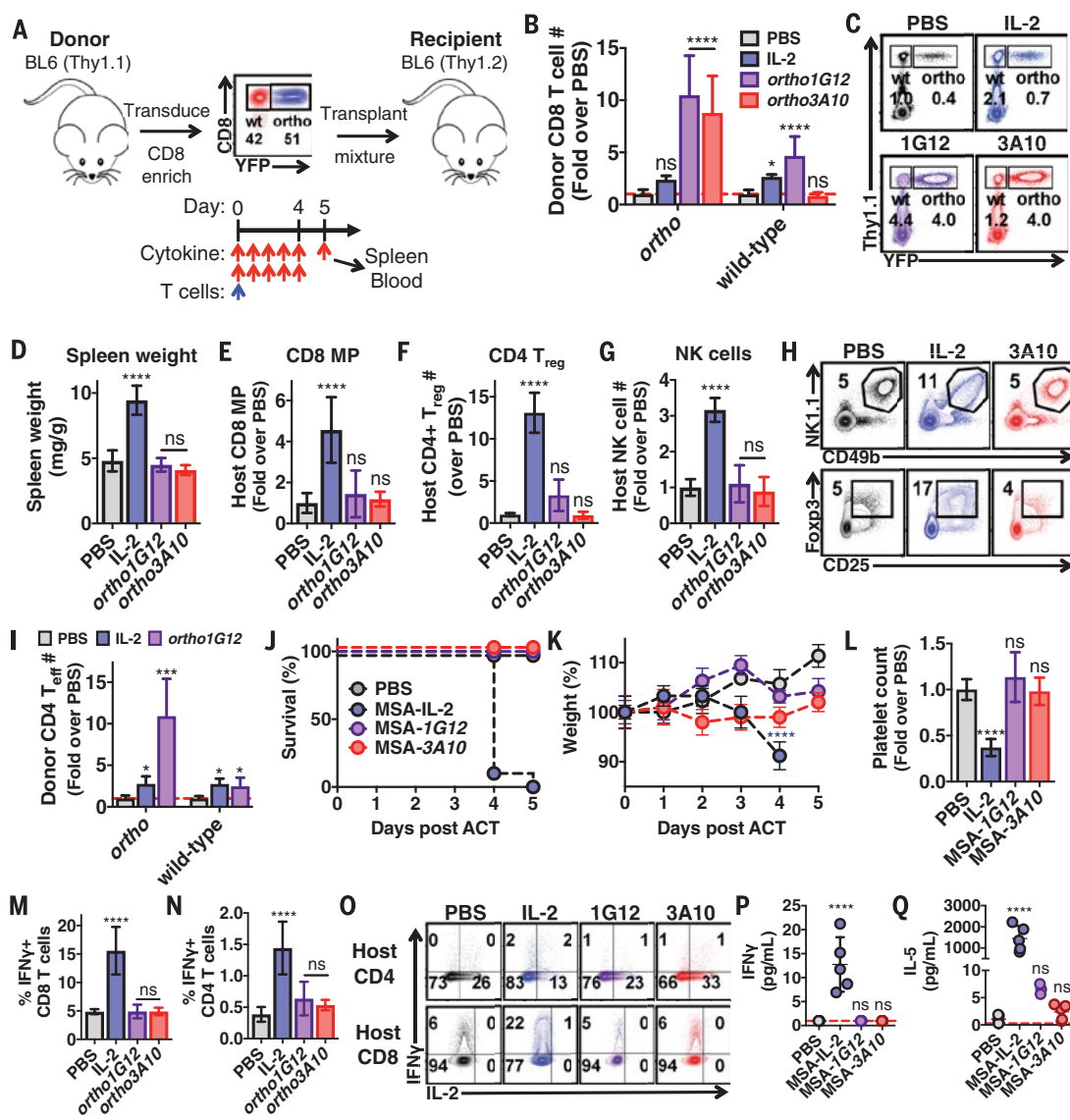
The selectivity of orthoIL-2 1G12 for orthoIL-2Rβ T cells was dose-dependent, with increased activity on wild-type cells at increased dose amounts and/or frequency of treatment (Fig. 3, B and C, and figs. S10 to S12). These results were consistent with the in vitro selectivity of orthoIL-2 1G12 signaling through the orthoIL-2Rβ could trigger endogenous IL-2 production by the orthoIL-2Rβ T cells, leading to indirect signaling through the wild-type IL-2R in cis or trans.

At high doses and twice-daily administration, orthoIL-2 3A10 resulted in the substantial expansion of orthoIL-2Rβ T cells with high specificity and no wild-type T cell expansion (Fig. 3, B and C, and figs. S11 and S12). This finding suggests that the effects of high-dose orthoIL-2 1G12 treatment were due not to induction of endogenous IL-2 by orthoIL-2Rβ CD8<sup>+</sup> T cells, but rather to low-level cross-reactivity with the wild-type IL-2Rβ by this molecule. The orthoIL-2 variants also promoted the in vivo expansion of orthoIL-2Rβ CD4<sup>+</sup> effector T cell (T<sub>eff</sub>) (Fig. 3I and fig. S12) and orthoIL-2Rβ CD4<sup>+</sup> T<sub>reg</sub> (fig. S9, C and D) cell subsets with specificity similar to that in CD8<sup>+</sup> T cells.

The two different orthoIL-2 variants exhibited specificities in vivo that mirrored their relative specificities in vitro. Despite its ability to activate wild-type IL-2Rβ signaling, albeit with about one order of magnitude less potency than orthoIL-2Rβ signaling, orthoIL-2 1G12 administration was relatively specific for orthoIL-2Rβ T cells in vivo (Fig. 3, B to H, and figs. S10 to S12). In mice treated twice daily with orthoIL-2 1G12 only, CD4<sup>+</sup> T<sub>reg</sub>s were elevated to a substantially lower degree than observed in IL-2-treated mice (Fig. 3F). However, the orthoIL-2 3A10 variant, consistent with the lack of wild-type IL-2Rβ signaling, had no detectable activity on host cell subset numbers (fig. S11) or expression of CD25, PD-1, and TIM-3, which are up-regulated by early or late IL-2R signaling (fig. S13).

To improve in vivo half-life and enable more convenient dosing, we fused IL-2 and orthoIL-2 to mouse serum albumin (17) (MSA), which has been shown to extend the half-life of mouse IL-2 from 5 hours to 50 hours (18). Fusion to MSA had little to no impact on IL-2- or orthoIL-2-dependent T cell proliferation in vitro (fig. S14); however, the in vivo activity was greatly enhanced. Fusion of

**Fig. 3. *OrthoIL-2* promotes the specific expansion of *orthoIL-2Rβ*-modified T cells in mice with negligible toxicity.** (A) Schematic of the adoptive CD8<sup>+</sup> T cell transplant mouse model. (B) Quantification of donor wild-type and *ortho* CD8<sup>+</sup> T cells in the spleen of recipient mice treated twice daily with phosphate-buffered saline (PBS), IL-2 (250,000 IU/dose), *orthoIL-2* 1G12 (250,000 IU/dose), or *orthoIL-2* 3A10 (2,500,000 IU/dose). (C) Representative flow cytometry data quantified in (B) depicting donor (Thy1.1<sup>+</sup>) wild-type (YFP<sup>-</sup>) and *orthoIL-2Rβ* (YFP<sup>+</sup>) CD8<sup>+</sup> T cells in the spleen of recipient mice. (D) Spleen weight of mice treated in (B) normalized to total body weight on day of killing. (E to G) Quantification of exogenous cytokine administration on host (E) CD8<sup>+</sup> memory phenotype T cell (MP, CD44<sup>+</sup>CD62L<sup>+</sup>), (F) CD4<sup>+</sup> T<sub>reg</sub> (CD25<sup>+</sup>Foxp3<sup>+</sup>), and (G) natural killer (NK) cell (CD3-NK1.1<sup>+</sup>CD49b<sup>+</sup>) numbers in the spleen of mice treated in (A). (H) Representative flow cytometry data as quantified in (F) and (G). Data in (B) to (H) are means ± SD (*n* = 5 mice per group). \**P* < 0.05, \*\*\*\**P* < 0.0001 [analysis of variance (ANOVA)]; ns, not significant. (I) Quantification of donor wild-type and *orthoIL-2Rβ* CD4<sup>+</sup> T<sub>eff</sub> in the spleen of recipient mice treated once daily with PBS, IL-2 (250,000 IU/dose), or *orthoIL-2* 1G12 (1,000,000 IU/dose). Data are means ± SD and are representative of two independent experiments (*n* = 4 mice per group). \**P* < 0.05, \*\*\**P* < 0.001 (ANOVA). (J) Survival of mice that received a mixture of wild-type and *orthoIL-2Rβ* CD8<sup>+</sup> T cells followed by daily administration of IL-2 or *orthoIL-2* fused to MSA. All mice received a total of 250,000 IU/day of the respective MSA fusion protein on an IL-2 basis for 5 days. (K) Mouse body weight over time normalized to the group average on day 0 as treated in (J). (L) Platelet counts in peripheral blood on day 4 as treated in (J). Data in (J) to (L) are means ± SD (*n* = 5 mice per group). \*\*\*\**P* < 0.0001 (ANOVA). (M to O) Quantification of cytokine administration on host (M) CD8<sup>+</sup> and (N) CD4<sup>+</sup> T cell production of IFN-γ upon ex vivo restimulation with phorbol 12-myristate 13-acetate (PMA) and ionomycin. (O) Representative flow cytometry data as quantified in (M) and (N). (P and Q) Serum (P) IFN-γ and (Q) IL-5 concentrations on day 7 in mice treated daily with PBS or with MSA-IL-2, MSA-1G12, or MSA-3A10 (each 25,000 IU/dose) for 7 days. Data are means ± SD (*n* = 5 mice per group). \*\*\*\**P* < 0.0001 (ANOVA).



*orthoIL-2* 1G12 to MSA substantially increased its activity on cells that express the wild-type IL-2R relative to native *orthoIL-2* 1G12, leading to increased off-target effects and toxicity (fig. S15). However, the MSA-*orthoIL-2* 3A10 fusion protein retained exquisite specificity for *orthoIL-2Rβ* T cells (fig. S16).

One of the major limitations of IL-2 in the clinic is that IL-2 toxicity limits the use of high-dose IL-2 therapy for metastatic cancer and as an adjuvant to adoptive T cell therapy (12). IL-2

administered as a MSA fusion resulted in a number of dose-dependent and dose-accumulating toxicities that led to weight loss, restricted mobility, hypothermia, ruffled fur, hunched posture, splenomegaly, lymphomegaly, and death (Fig. 3, J to L, and figs. S15 to S18). In contrast, MSA-*orthoIL-2* 3A10 was nontoxic at all doses evaluated. MSA-*orthoIL-2* 3A10 activity was negligible on all IL-2-responsive host cell subsets evaluated.

In addition to its role as a proliferative cytokine, IL-2 is a potent effector cytokine capable of

activating cytotoxic T cell functions and T cell inflammatory pathways (19). We determined the capacity of adoptively transferred *orthoIL-2Rβ* CD8<sup>+</sup> T cells to produce interferon-γ (IFN-γ) and cell surface levels of the immune inhibitory receptors PD-1 and TIM-3 after expansion in vivo with *orthoIL-2*. TIM-3 expression correlates with a highly dysfunctional CD8<sup>+</sup> T cell state, whereas PD-1 expression is associated with both T cell activation and exhaustion (20). *OrthoIL-2Rβ* T cells expanded in *orthoIL-2* produced significantly more

**Fig. 4. OrthoIL-2-expanded T cells retain effector function and promote an antitumor response against syngeneic B16-F10 tumors in mice.**

(A) Quantification of total number of IFN- $\gamma$ -positive wild-type or *ortho*IL-2R $\beta$  CD8<sup>+</sup> T cells recovered from the spleen as treated in Fig. 3 (left) and representative flow cytometry data (right).

(B) Cell surface expression levels of PD-1 (left) and TIM-3 (right) on wild-type and *ortho*IL-2R $\beta$  CD8<sup>+</sup> T cells in the spleen after administration of the indicated cytokines. Data are means  $\pm$  SD ( $n = 5$  mice per group). \* $P < 0.05$ , \*\*\*\* $P < 0.0001$  (ANOVA).

(C) gp100 pMHC tetramer staining of *ortho*IL-2R $\beta$ -transduced pmel-1 transgenic CD8<sup>+</sup> T cells. (D) In vitro cytotoxicity of *ortho*IL-2R $\beta$  pmel-1 transgenic T cells against antigen-positive (B16-F10) but not antigen-negative (MC38) tumor cells at a 20:1 (E:T) ratio. Data are means  $\pm$  SD ( $n = 3$  biological replicates). \*\* $P < 0.01$  (Student  $t$  test).

(E and F) Tumor growth (E) and survival (F) of C57BL/6J mice bearing subcutaneous B16-F10 tumors treated with wild-type (wt T) or *ortho*IL-2R $\beta$  pmel-1 transgenic CD8<sup>+</sup> T cells (*ortho* T) and IL-2 or *ortho*IL-2 1G12. Data are means  $\pm$  SEM ( $n = 5$  mice per group). \*\*\*\* $P < 0.0001$  (two-way ANOVA) (E); \*\* $P < 0.01$  (log-rank test) (F).

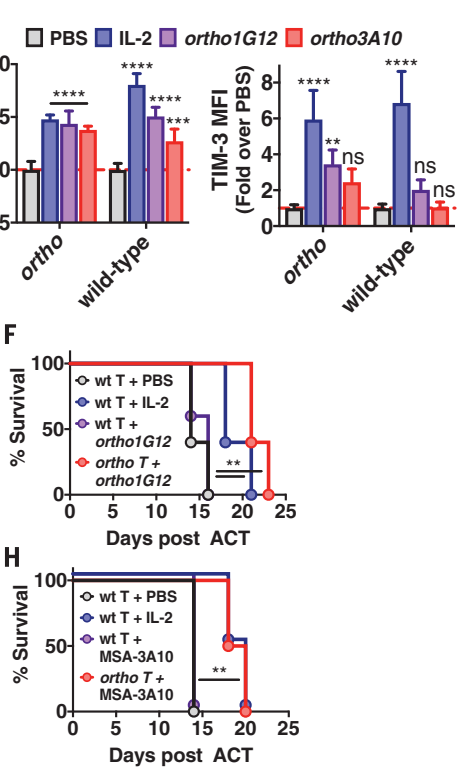
IFN- $\gamma$  than IL-2-expanded cells (Fig. 4A). PD-1 levels were similar on *ortho*IL-2R $\beta$  T cells from both IL-2- and *ortho*IL-2-treated mice (Fig. 4B). Interestingly, TIM-3 levels were significantly lower on *ortho*IL-2R $\beta$  T cells from mice treated with *ortho*IL-2 relative to those treated with IL-2 (Fig. 4B).

The differential activity of *ortho*IL-2 on both T cell expansion and function may be due to increased bioavailability of *ortho*IL-2 for *ortho*IL-2R $\beta$  T cells as the result of a reduced antigen sink or alternative host factors influenced by IL-2 but not *ortho*IL-2, which in turn may influence the function of transplanted T cells. For instance, IL-2 but not *ortho*IL-2 treatment increased host CD4<sup>+</sup> and CD8<sup>+</sup> T cell IFN- $\gamma$  production upon ex vivo restimulation (Fig. 3, M to O) and increased the serum concentration of numerous inflammatory cytokines, including IFN- $\gamma$ , IL-4, IL-5, IL-6, and IL-13 (Fig. 3, P and Q, and fig. S17). The ability to decouple direct IL-2 activity on transplanted T cells from indirect host bystander effects using *ortho*IL-2/IL-2R pairs may have important therapeutic implications.

To investigate prospective clinical applications of orthogonal IL-2/IL-2R pairs, we determined the efficacy of tumor-specific *ortho*IL-2R $\beta$  T cells in the B16-F10 mouse model of melanoma. Transgenic pmel-1 T cell receptor (TCR) cells (pmel-1 T cells) express a high-affinity TCR that recognizes

the B16-F10 specific ortholog of human gp100 (19), a self antigen overexpressed in human melanoma (Fig. 4, C and D). Adoptive transfer of pmel-1 T cells in combination with lymphocyte depletion and IL-2 administration can model ACT approaches to treat human cancer. Adoptive transfer of pmel-1 T cells accompanied by five daily injections of IL-2 significantly delayed tumor growth in mice and increased survival relative to mice treated only with T cells and saline (Fig. 4, E to G). Transfer of *ortho*IL-2R $\beta$  pmel-1 T cells followed by treatment with native *ortho*IL-2 1G12 at a dose that had minimal activity on wild-type IL-2R cells (fig. S10) produced a significant tumor growth delay and survival advantage that mirrored the IL-2 treatment group (Fig. 4, E and F). Similar antitumor responses were observed in mice treated with *ortho*IL-2R $\beta$  pmel-1 T cells and MSA-*ortho*IL-2 3A10 (Fig. 4, G and H). There was no therapeutic benefit of *ortho*IL-2 in mice that received wild-type pmel-1 T cells, indicating that *ortho*IL-2 activity is dependent on expression of the *ortho*IL-2R $\beta$  in pmel-1 T cells.

Our results constitute an approach to redirect the specificity of IL-2 toward engineered T cells using orthogonal IL-2 cytokine-receptor pairs, which enables the selective expansion of desired T cell subsets in settings of adoptive cell therapy, but with limited off-target activity and



(H) of C57BL/6J mice bearing subcutaneous B16-F10 tumors treated with wild-type (wt T) or *ortho*IL-2R $\beta$  pmel-1 transgenic CD8<sup>+</sup> T cells (*ortho* T) and IL-2 or *ortho*IL-2 3A10 fused to MSA. Data are means  $\pm$  SEM ( $n = 4$  mice per group). \*\*\*\* $P < 0.0001$  (two-way ANOVA) (G); \*\* $P < 0.01$  (log-rank test) (H).

negligible toxicity. Engineering orthogonal molecular recognition at a protein-small molecule or protein-protein interface has resulted in synthetic enzymes, kinases, transcription factors, and receptors with controllable biological functions, but here we apply this concept to protein interactions with cell surface receptors to control signaling specificity and downstream cellular functions (21–28). Orthogonal IL-2/IL-2R pairs may be useful not only as a research tool but in the clinic to specifically enrich transduced T cells that express a target gene of interest, such as a CAR or engineered TCR, when coupled with expression of the *ortho*IL-2R $\beta$ . Our approach, and variations of this orthogonalization strategy, may be applicable to other cytokines, growth factors, hormones, and ligand-receptor interactions to decipher and manipulate otherwise complex biological systems.

REFERENCES AND NOTES

1. M. Kalos, C. H. June, *Immunity* **39**, 49–60 (2013).
2. S. A. Rosenberg, N. P. Restifo, *Science* **348**, 62–68 (2015).
3. C. Yee et al., *Proc. Natl. Acad. Sci. U.S.A.* **99**, 16168–16173 (2002).
4. R. Andersen et al., *Clin. Cancer Res.* **22**, 3734–3745 (2016).
5. S. A. Rosenberg, *J. Immunol.* **192**, 5451–5458 (2014).
6. X. Wang, M. Rickert, K. C. Garcia, *Science* **310**, 1159–1163 (2005).
7. A. M. Levin et al., *Nature* **484**, 529–533 (2012).

8. A. B. Shanafelt *et al.*, *Nat. Biotechnol.* **18**, 1197–1202 (2000).
9. M. Rickert, M. J. Boulanger, N. Goriatcheva, K. C. Garcia, *J. Mol. Biol.* **339**, 1115–1128 (2004).
10. E. Roessler *et al.*, *Proc. Natl. Acad. Sci. U.S.A.* **91**, 3344–3347 (1994).
11. R. Moriggi *et al.*, *Immunity* **10**, 249–259 (1999).
12. T. R. Malek, *Annu. Rev. Immunol.* **26**, 453–479 (2008).
13. D. Klatzmann, A. K. Abbas, *Nat. Rev. Immunol.* **15**, 283–294 (2015).
14. S. Amu, I. Gjerdtsson, A. Tarkowski, M. Brisslert, *Scand. J. Immunol.* **64**, 482–492 (2006).
15. O. Boyman, J. Sprent, *Nat. Rev. Immunol.* **12**, 180–190 (2012).
16. L. Gattinoni *et al.*, *J. Exp. Med.* **202**, 907–912 (2005).
17. J. T. Sockolosky, F. C. Szoka, *Adv. Drug Deliv. Rev.* **91**, 109–124 (2015).
18. E. F. F. Zhu *et al.*, *Cancer Cell* **27**, 489–501 (2015).
19. W. W. Overwijk *et al.*, *J. Exp. Med.* **198**, 569–580 (2003).
20. K. Sakuishi *et al.*, *J. Exp. Med.* **207**, 2187–2194 (2010).
21. M. G. J. Baud *et al.*, *Science* **346**, 638–641 (2014).

22. S. Atwell, M. Ultsch, A. M. De Vos, J. A. Wells, *Science* **278**, 1125–1128 (1997).
23. D. M. Spencer, T. J. Wandless, S. L. Schreiber, G. R. Crabtree, *Science* **262**, 1019–1024 (1993).
24. D. J. Mandell, T. Kortemme, *Nat. Chem. Biol.* **5**, 797–807 (2009).
25. G. T. Kapp *et al.*, *Proc. Natl. Acad. Sci. U.S.A.* **109**, 5277–5282 (2012).
26. J. S. Park *et al.*, *Proc. Natl. Acad. Sci. U.S.A.* **111**, 5896–5901 (2014).
27. S. M. Lewis *et al.*, *Nat. Biotechnol.* **32**, 191–198 (2014).
28. C. Y. Wu, K. T. Roybal, E. M. Puchner, J. Onuffer, W. A. Lim, *Science* **350**, aab4077 (2015).

#### ACKNOWLEDGMENTS

We thank M. McCracken for expertise in T cell immunotherapy; N. Saligrama, A. Cravens, M. Hollander, F. Zhao, Y. Rosenberg-Hasson, and the Stanford Human Immune Monitoring Core (HIMC) for technical assistance; and R. Fernandes for helpful discussion. The data presented in this paper are tabulated in the main text and supplementary materials. Supported by NIH grants R37 AI051321 and HHMI (K.C.G.); a 2016 Stanford Cancer Institute translational

research grant (J.T.S., A.R., and K.C.G.); NIH grant R35 CA197633, the Ressler Family Fund, and the Parker Institute for Cancer Immunotherapy (G.P. and A.R.); the Sean N. Parker Autoimmunity Research Laboratory (J.A.B.); and fellowship support from Stanford Molecular and Cellular Immunobiology NIH training grant 5T32 AI072905 and a PhRMA Foundation Translational Medicine and Therapeutics postdoctoral award (J.T.S.). J.A.B. and A.R. are members of the Parker Institute for Cancer Immunotherapy. K.C.G., J.T.S., I.C.K., and D.B. are inventors on patent applications 62/217,364 and 62/375,089 submitted by Stanford University that cover the use of orthogonal cytokine-receptor pairs for use in cellular immunotherapy.

#### SUPPLEMENTARY MATERIALS

[www.sciencemag.org/content/359/6379/1037/suppl/DC1](http://www.sciencemag.org/content/359/6379/1037/suppl/DC1)  
Materials and Methods  
Figs. S1 to S18  
References (29–35)

30 October 2017; accepted 11 January 2018  
10.1126/science.aar3246

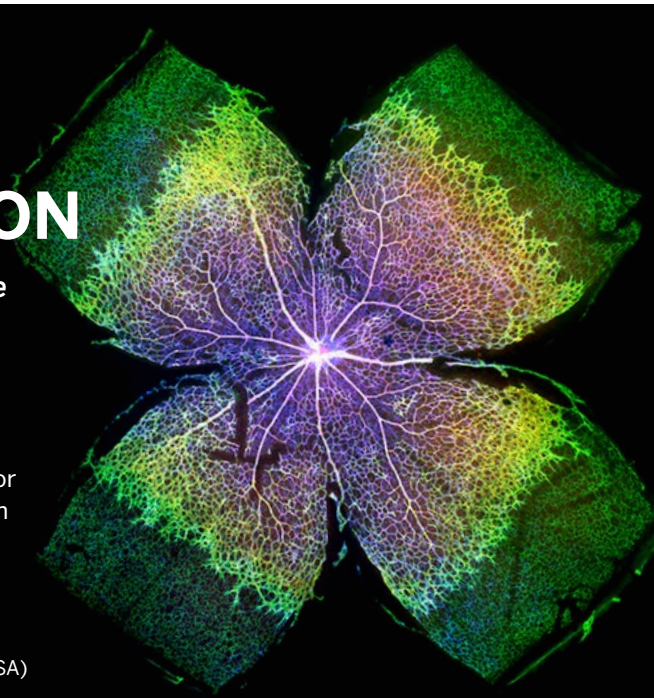
# THIS IS NOT SCIENCE FICTION

This is captivating, impactful *Science*

Contact us today to discuss pricing options for adding any of these journals to your collection of *Science* resources.

#### Institutional Licensing

[ScienceMag.org/request](http://ScienceMag.org/request) | [scienceonline@aaaas.org](mailto:scienceonline@aaaas.org)  
1-866-265-4152 (USA) | +1-202-326-6730 (outside USA)



**Science**  
AAAS

**Science  
Advances**

**Science  
Immunology**

**Science  
Robotics**

**Science  
Signaling**

**Science  
Translational  
Medicine**

## NEUROIMMUNOLOGY

Copyright © 2018 The Authors, some rights reserved\*

# Choline acetyltransferase-expressing T cells are required to control chronic viral infection

Maureen A. Cox<sup>1</sup>, Gordon S. Duncan<sup>1</sup>, Gloria H. Y. Lin<sup>1\*</sup>, Benjamin E. Steinberg<sup>1,2,†</sup>, Lisa X. Yu<sup>3</sup>, Dirk Brenner<sup>1,4,5</sup>, Luke N. Buckler<sup>1</sup>, Andrew J. Elia<sup>1</sup>, Andrew C. Wakeham<sup>1</sup>, Brian Nieman<sup>3,6</sup>, Carmen Dominguez-Brauer<sup>1</sup>, Alisha R. Elford<sup>1</sup>, Kyle T. Gill<sup>1</sup>, Shawn P. Kubli<sup>1</sup>, Jillian Haight<sup>1</sup>, Thorsten Berger<sup>1</sup>, Pamela S. Ohashi<sup>1,7</sup>, Kevin J. Tracey<sup>8</sup>, Peder S. Olofsson<sup>8,9</sup>, Tak W. Mak<sup>1,6,7,10,‡</sup>

Although widely studied as a neurotransmitter, T cell–derived acetylcholine (ACh) has recently been reported to play an important role in regulating immunity. However, the role of lymphocyte-derived ACh in viral infection is unknown. Here, we show that the enzyme choline acetyltransferase (ChAT), which catalyzes the rate-limiting step of ACh production, is robustly induced in both CD4<sup>+</sup> and CD8<sup>+</sup> T cells during lymphocytic choriomeningitis virus (LCMV) infection in an IL-21–dependent manner. Deletion of *Chat* within the T cell compartment in mice ablated vasodilation in response to infection, impaired the migration of antiviral T cells into infected tissues, and ultimately compromised the control of chronic LCMV clone 13 infection. Our results reveal a genetic proof of function for ChAT in T cells during viral infection and identify a pathway of T cell migration that sustains antiviral immunity.

The prototypic neurotransmitter acetylcholine (ACh) was the first neurotransmitter identified (1, 2). ACh has numerous physiological roles, including mediating skeletal and smooth muscle contraction, communication between neurons, and induction of vasodilation (1–3). In addition to neurons, a population of CD4<sup>+</sup> T cells and B cells express the enzyme choline acetyltransferase (ChAT) (4, 5), which catalyzes the rate-limiting step of ACh production. Although these ChAT-expressing T cells have a demonstrated impact on blood pressure (6) and the release of inflammatory cytokines (4), the biological role of immune-derived ACh during infection has not been elucidated. In this study, we have determined

that *Chat* is induced by IL-21 in T cells during infection to facilitate T cell entry into infected tissues, thereby genetically identifying the function of T cell–derived ACh during an immune response.

*Chat*<sup>+</sup> CD4<sup>+</sup> T cells uniformly exhibit an “antigen-experienced” phenotype (4). Yet, the signals that drive *Chat* expression in T cells are undefined. We infected *Chat*-green fluorescent protein (GFP) reporter mice (7) with the rapidly cleared Armstrong strain of lymphocytic choriomeningitis virus (LCMV-Arm). There was a massive increase in *Chat*-GFP expression in both CD4<sup>+</sup> and CD8<sup>+</sup> T cells 8 days postinfection (Fig. 1A). In splenic virus-specific T cells, expression rapidly declined after LCMV-Arm clearance (Fig. 1B), yet *Chat*-GFP expression was retained in both virus-specific CD4<sup>+</sup> and CD8<sup>+</sup> T cells from mice chronically infected with LCMV clone 13 (LCMV-Cl13) (Fig. 1B). GFP expression correlated with *Chat* mRNA in T cells (Fig. 1C). In CD4<sup>+</sup> T cells, *Chat*-GFP was expressed by all subsets; however, expression was highest in T follicular helper (T<sub>FH</sub>) cells (fig. S1, A to D). In CD8<sup>+</sup> T cells, there was no correlation with either memory precursor or short-lived effector phenotypes (fig. S1E). Furthermore, *Chat*-GFP was induced in germinal center (GC) B cells in the spleen, although *Chat* expression was not retained in this population during persistent infection (fig. S1, F and G). *Chat*-GFP was also induced in both CD4<sup>+</sup> and CD8<sup>+</sup> T cells after vesicular stomatitis virus infection (fig. S1H).

The kinetics of *Chat*-GFP expression during acute and chronic infection implicates viral signals in driving *Chat* induction in T cells. Viral infection induces numerous cytokines that influence T cells, including type I interfer-

ons (IFN-I), interleukin-2 (IL-2), IL-6, IL-7, IL-10, IL-15, and IL-21 (8). We activated *Chat*-GFP P14 T cell receptor (TCR) transgenic T cells in vitro with the GP33 peptide in the presence or absence of these cytokines. The only condition that resulted in *Chat* induction in P14 cells in vitro was IL-21 with peptide stimulation (Fig. 1D and fig. S2A). We evaluated the contribution of IL-21 signaling to *Chat* induction in vivo by infecting IL-21 receptor–deficient (*Il21r*<sup>−/−</sup>) mice (9) expressing the *Chat*-GFP reporter with LCMV-Cl13. We observed a decrease in the fraction of both CD4<sup>+</sup> and CD8<sup>+</sup> T cells expressing *Chat*-GFP in *Il21r*<sup>−/−</sup> mice (Fig. 1E). Mice heterozygous for *Il21r* (*Il21r*<sup>+/-</sup>) showed a mixed phenotype. The expression of *Chat*-GFP in B cell populations was not reduced in *Il21r*<sup>−/−</sup> animals (Fig. 1E). *Chat*-GFP<sup>+</sup> cells in *Il21r*<sup>−/−</sup> mice also demonstrated a lower mean fluorescence intensity (MFI) for the reporter molecule, suggesting reduced expression (Fig. 1F and fig. S2B).

IL-21 is critical for antiviral immunity (10–12). Thus, we investigated the role of IL-21–induced *Chat* in T cells (*T-Chat*) by using *Chat*<sup>fllox</sup> mice (13) crossed with CD4-cre mice (14) to generate *Chat*<sup>fllox/fllox</sup> CD4-cre<sup>−</sup> (*Chat*<sup>MVT</sup>) and *Chat*<sup>fllox/fllox</sup> CD4-cre<sup>+</sup> (*T-Chat*<sup>KO</sup>) animals. Cre-driven recombination occurs at the double-positive stage in the thymus (14), resulting in deletion of *Chat* in both CD4<sup>+</sup> and CD8<sup>+</sup> T cells (fig. S3A) and a subsequent failure to produce ACh (fig. S3B). Notably, the loss of *Chat* specifically within T cells resulted in a failure to control LCMV-Cl13 in a subset of the animals (Fig. 2A), revealing that *Chat* expression in T cells is required during chronic infection. This failure to control LCMV-Cl13 corresponded with the attrition of virus-specific CD8<sup>+</sup> T cells over time (Fig. 2B), poor cytokine production (Fig. 2C), and increased expression of inhibitory receptors (Fig. 2, D and E). There was no difference in the number of antiviral T cells in LCMV-Arm-infected *T-Chat*<sup>KO</sup> mice (fig. S4), which has also been reported for *Il21*<sup>−/−</sup> animals (15). Although we observed high *Chat* expression in T<sub>FH</sub> and GC B cells (fig. S1), there were no deficits in either antiviral CD4<sup>+</sup> T cell numbers or in the anti-LCMV antibody response in *T-Chat*<sup>KO</sup> mice (fig. S5).

Loss of IL-21 signaling results in decreased T cell infiltration of tissues in bone marrow chimeras (16, 17). Thus, we evaluated tissue infiltration by *Il21r*<sup>−/−</sup> T cells during LCMV-Cl13 infection using intravascular staining (18). We found a reduction in virus-specific T cells that had migrated into infected livers of *Il21r*<sup>−/−</sup> mice (Fig. 3A). *Chat*-expressing T cells reduce blood pressure by producing ACh (3, 6), which may facilitate T cell entry into tissues by slowing blood flow. Consequently, we also found a reduction in virus-specific CD8<sup>+</sup> T cells in both the liver and salivary gland of *T-Chat*<sup>KO</sup> mice after LCMV-Cl13 infection (Fig. 3, B and C). No difference in the number of circulating virus-specific cells was found in either *Il21r*<sup>−/−</sup> or *T-Chat*<sup>KO</sup> mice (fig. S6, A to C). We observed a similar trend in the liver for virus-specific CD4<sup>+</sup> T cells (fig. S6D). Poor migration into tissues

<sup>1</sup>The Campbell Family Institute for Breast Cancer Research, Princess Margaret Cancer Centre, University Health Network, Toronto, ON M5G 2M9, Canada. <sup>2</sup>Department of Anesthesia, University of Toronto, Toronto, ON M5G 1E2, Canada. <sup>3</sup>Mouse Imaging Centre, The Hospital for Sick Children, Toronto, ON M5T 3H7, Canada. <sup>4</sup>Department of Infection and Immunity, Luxembourg Institute of Health, L-4354 Esch-sur-Alzette, Luxembourg. <sup>5</sup>Odense Research Center for Anaphylaxis (ORCA), Department of Dermatology and Allergy Center, Odense University Hospital, University of Southern Denmark, Odense, Denmark. <sup>6</sup>Ontario Institute for Cancer Research and Department of Medical Biophysics, University of Toronto, Toronto, ON M5G 2C1, Canada. <sup>7</sup>Department of Immunology, University of Toronto, Toronto, ON M5G 2C1, Canada. <sup>8</sup>Laboratory of Biomedical Science, Feinstein Institute for Medical Research, Manhasset, NY 11030, USA. <sup>9</sup>Center for Bioelectronic Medicine, Department of Medicine, Solna, Karolinska Institutet, Karolinska University Hospital, 17176 Stockholm, Sweden. <sup>10</sup>Department of Pathology, University of Hong Kong, Hong Kong.

\*Present address: Trillium Therapeutics Inc., Mississauga, ON L5L 1J9, Canada. †Present address: Department of Anesthesia and Pain Medicine, The Hospital for Sick Children, Toronto, ON M5G 1X8, Canada.

‡Corresponding author. Email: tmak@uhnresearch.ca

**Fig. 1. *Chat* is induced in virus-specific T cells in an IL-21-dependent manner. (A)** *Chat*-GFP<sup>+</sup> and *Chat*-GFP<sup>-</sup> animals were infected with LCMV-Arm, and the expression of *Chat*-GFP in total CD4<sup>+</sup> (top) or CD8<sup>+</sup> (bottom) T cells 8 days postinfection was compared with expression in uninfected *Chat*-GFP<sup>+</sup> cohorts.

Mean ± SEM, representative of two to four experimental cohorts, *n* = 8 to 12 mice for *Chat*-GFP<sup>+</sup>, *n* = 4 for *Chat*-GFP<sup>-</sup>. (B) The fraction of virus-specific CD4<sup>+</sup> (left) or CD8<sup>+</sup> (right) T cells expressing *Chat*-GFP was determined 8, 20, and 30 days postinfection with LCMV-Arm or LCMV-CI13 by evaluating tetramer staining and *Chat*-GFP expression by flow cytometry. Composite data of two (Arm) or four (CI13) experiments. *n* = 7 to 12 (Arm) and *n* = 10 to 27 (CI13) animals per group per time point.

(C) Pooled splenocytes from *n* = 5 *Chat*-GFP mice infected 8 days previously with LCMV-CI13 were sorted to obtain CD4<sup>+</sup> GFP<sup>+</sup>, CD4<sup>+</sup> GFP<sup>-</sup>, CD8<sup>+</sup> GFP<sup>+</sup>, and CD8<sup>+</sup> GFP<sup>-</sup> populations. RNA was isolated from the cells, and expression of *Chat* and *Rsp9* was evaluated by reverse transcription polymerase chain reaction in technical triplicates. *Chat* expression in CD4<sup>+</sup> and CD8<sup>+</sup> populations was normalized to the expression in the relevant sorted GFP<sup>-</sup> population. Mean ± SEM, representative of two experimental cohorts. Ct, cycle threshold. (D) *Chat*-GFP<sup>+</sup> and *Chat*-GFP<sup>-</sup> P14 CD8<sup>+</sup> T cells were stimulated in vitro with GP33 peptide and indicated cytokines for 5 days. The expression of *Chat*-GFP in the P14 cells was determined by flow cytometry. Composite of two experimental cohorts, box plots indicate 25th to 75th percentile, line at median. Whiskers represent range minimum

to maximum, *n* = 5 *Chat*-GFP<sup>+</sup> P14 mice. Significance tested using one-way analysis of variance (ANOVA), *P* < 0.0001, significance between samples determined by *t* test (depicted). (E) *Il21r*<sup>+/+</sup> (dark gray), *Il21r*<sup>+/-</sup> (light gray), and *Il21r*<sup>-/-</sup> (white) mice expressing *Chat*-GFP were infected with LCMV-CI13, and *Chat* expression was determined in splenocyte fractions 8 days postinfection by flow cytometry. Box and whiskers drawn with the Tukey method, line at median. Values outside of 1.5 times the interquartile range are depicted as individual symbols. Two-way ANOVA was performed (*P* < 0.0001), followed by multiple comparisons between groups. (F) Representative flow plots of virus-specific D<sup>b</sup>(GP33)<sup>+</sup> (left) or D<sup>b</sup>(GP276)<sup>+</sup> (right) CD8<sup>+</sup> T cells 8 days postinfection in *Il21r*<sup>+/+</sup> or *Il21r*<sup>-/-</sup> mice. Representative of two to three experimental cohorts, *n* = 8 to 13. Statistical significance determined by unpaired two-tailed *t* test; \**P* < 0.05, \*\**P* < 0.01, \*\*\**P* < 0.001, \*\*\*\**P* < 0.0001.

could affect viral control, as fewer migrated cytotoxic T lymphocytes (CTLs) would result in the poor elimination of infected cells. In vivo CTL activity in the liver was impaired for two epitopes examined 8 days postinfection in T-*Chat*<sup>KO</sup> mice (Fig. 3D), despite equivalent expression of granzyme B and degranulation (Fig.

3E) by noncirculating CTLs. Furthermore, this diminution in CTL activity was observed only for the GP33 epitope in the spleen (Fig. 3D), suggesting that the poor CTL activity in the liver was not due to intrinsic defects in the cells but rather their impaired infiltration of tissues.

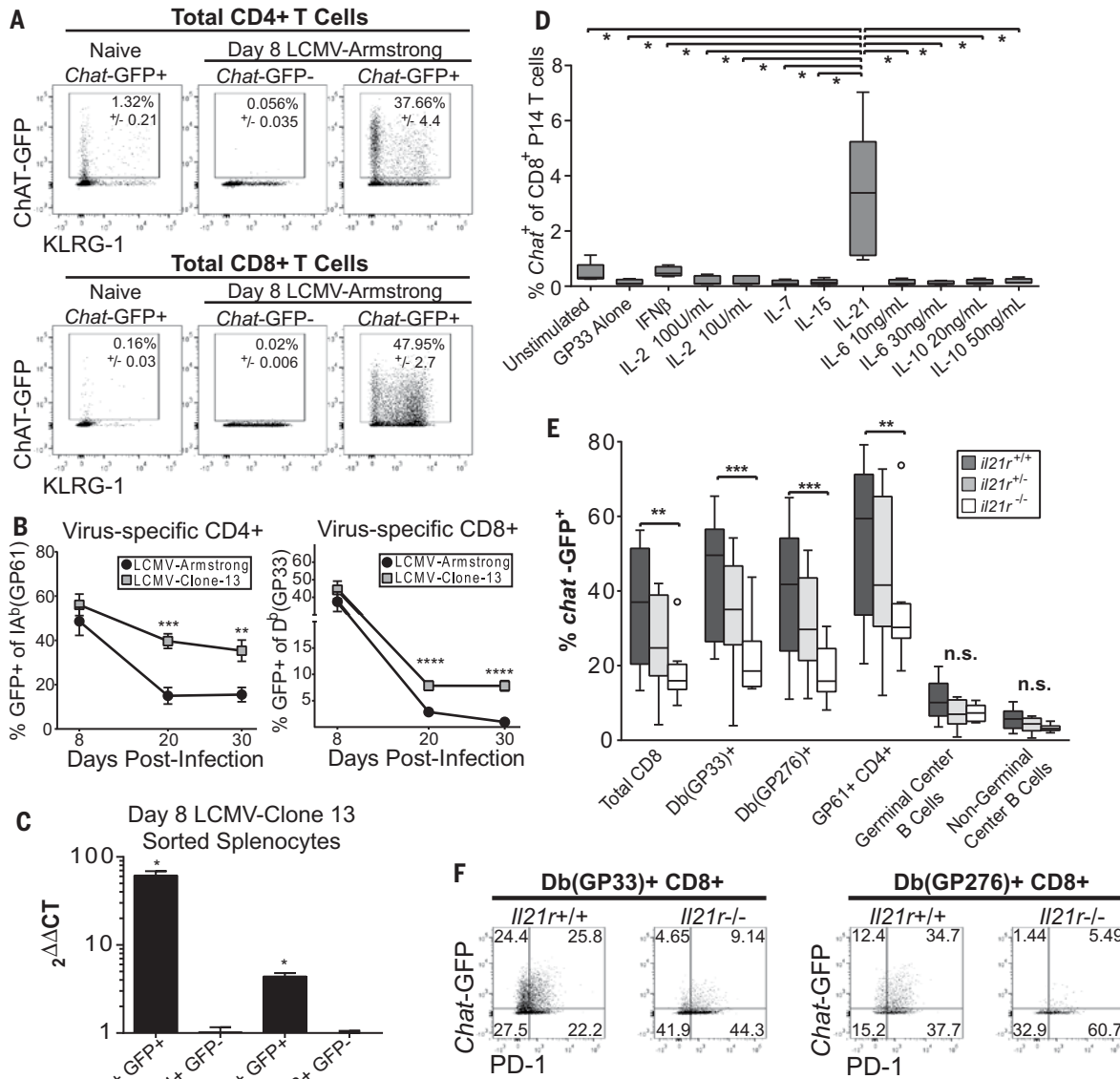


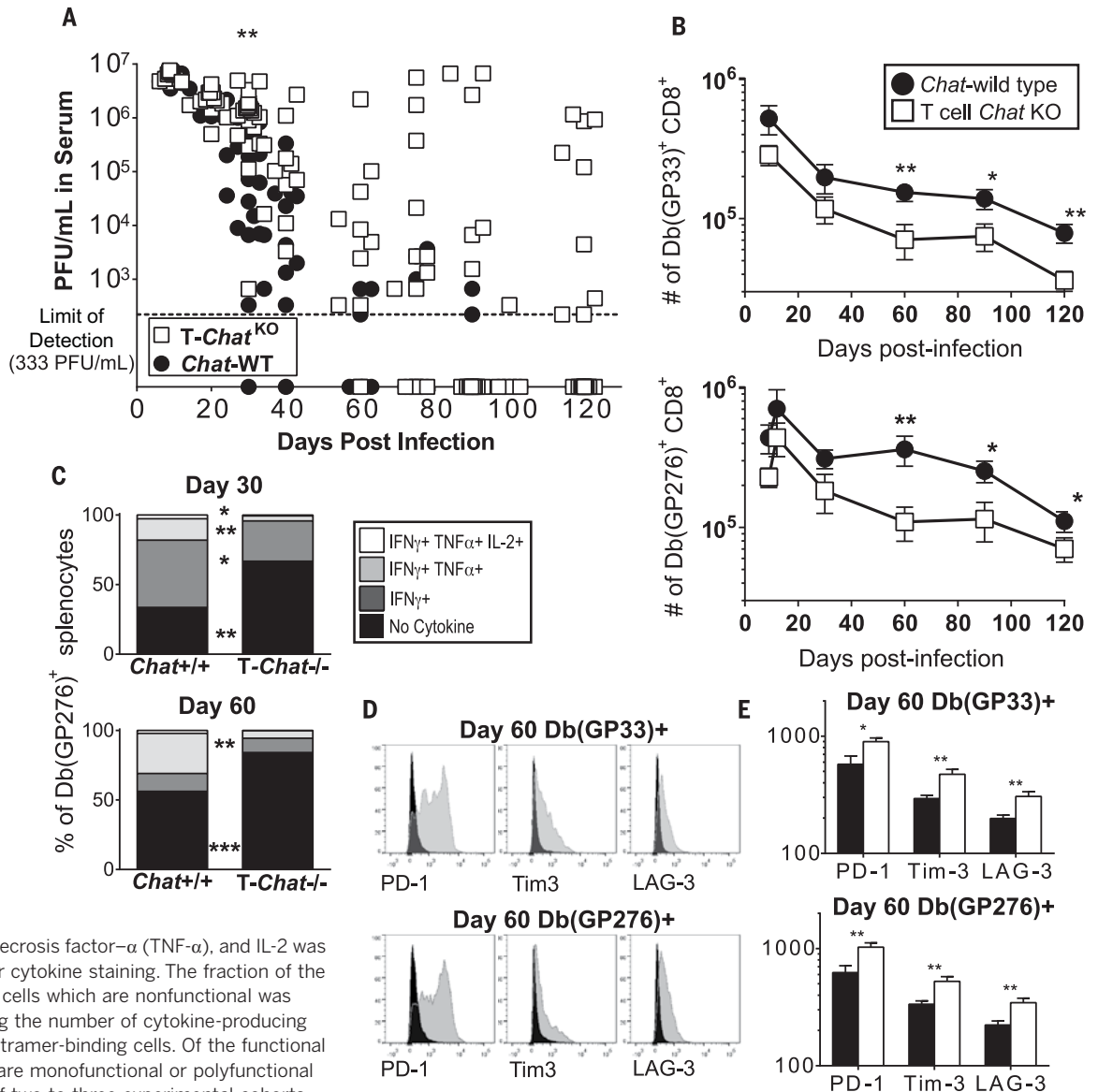
**Fig. 2. Loss of *Chat* in T cells compromises control of viral infection.**

(A) *Chat*<sup>WT</sup> and T-*Chat*<sup>KO</sup> were infected with LCMV-Cl13. Viral titers in the serum of either *Chat*<sup>WT</sup> (black) or T-*Chat*<sup>KO</sup> (white) were determined at indicated time points by plaque assay. Each symbol indicates an individual animal. Composite data of two to three experimental replicates, *n* = 11 to 23. Line at limit of detection, 333 PFU/ml (PFU, plaque-forming units).

(B) The number of D<sup>b</sup>(GP33)<sup>+</sup> or D<sup>b</sup>(GP276)<sup>+</sup> CD8<sup>+</sup> splenocytes was determined over time by tetramer staining. Mean ± SEM, composite of three to four experimental cohorts, *n* = 10 to 16.

(C) Splenocytes from *Chat*<sup>WT</sup> and T-*Chat*<sup>KO</sup> animals were stimulated with the GP276 peptide in vitro, and the number of cells producing IFN-γ, tumor necrosis factor-α (TNF-α), and IL-2 was quantified by intracellular cytokine staining. The fraction of the total D<sup>b</sup>(GP276)-specific cells which are nonfunctional was determined by comparing the number of cytokine-producing cells to the number of tetramer-binding cells. Of the functional cells, the fraction which are monofunctional or polyfunctional was determined. Mean of two to three experimental cohorts, *n* = 9 (day 30), *n* = 8 (day 60).

(D) Representative flow plot of PD-1, Tim3, and LAG-3 expression in virus-specific CD8<sup>+</sup> T cells 60 days postinfection in *Chat*<sup>WT</sup> (black) or T-*Chat*<sup>KO</sup> (gray) mice. (E) MFI for PD-1, Tim3, and LAG-3 in virus-specific CD8<sup>+</sup> T cells 60 days postinfection in *Chat*<sup>WT</sup> (black) or T-*Chat*<sup>KO</sup> (white) mice. Mean ± SEM, composite of three experimental cohorts, *n* = 13 to 15. Statistical significance for all samples determined by unpaired two-tailed *t* test; \**P* < 0.05, \*\**P* < 0.01, \*\*\**P* < 0.001.



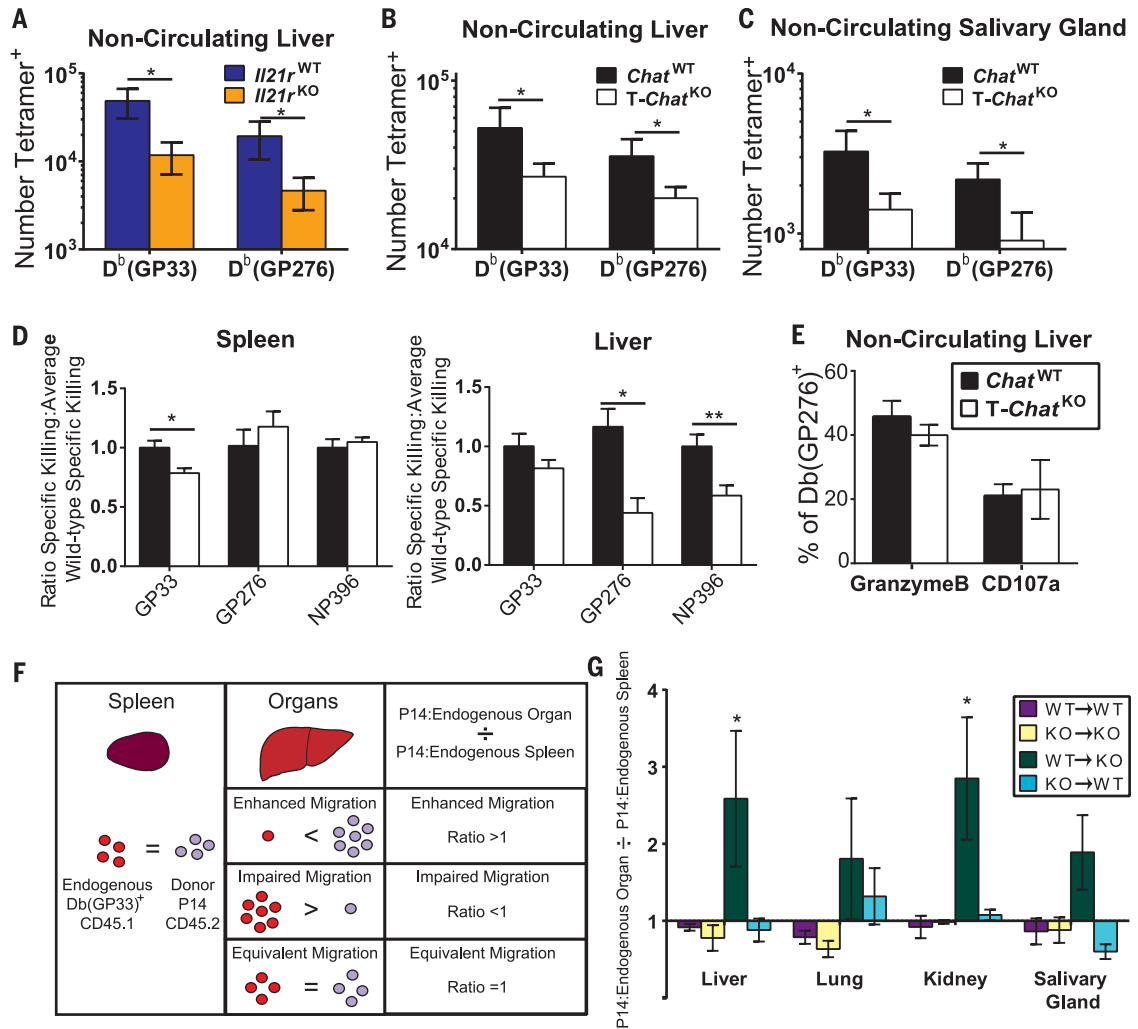
total noncirculating D<sup>b</sup>(GP33)<sup>+</sup> in the spleen and organs and determined what percentage of these D<sup>b</sup>(GP33)<sup>+</sup> cells were donor P14 cells. This percentage in each organ was then compared against the percentage in the spleen of that individual animal to determine whether the P14 cells had migrated in a superior (ratio > 1), inferior (ratio < 1), or equivalent (ratio = 1) manner compared with the endogenous D<sup>b</sup>(GP33)<sup>+</sup> T cells (Fig. 3F). In control mice (WT P14→WT recipients and KO P14→KO recipients), the frequency of P14 cells was similar in the spleen and organs, resulting in a ratio of ~1 (Fig. 3G and fig. S6G). However, in T-*Chat*<sup>KO</sup> mice receiving *Chat*<sup>WT</sup> P14 cells, we observed a greater frequency of *Chat*<sup>WT</sup> P14 cells in the liver and kidney than would be predicted by their rate of occurrence in

the spleen (Fig. 3G and fig. S6G). Thus, *Chat*<sup>WT</sup> cells were more efficient at seeding these peripheral organs than T-*Chat*<sup>KO</sup> cells in the same animal. When T-*Chat*<sup>KO</sup> P14 cells were transplanted into a *Chat*<sup>WT</sup> recipient, they migrated just as well as endogenous *Chat*<sup>WT</sup> cells, indicating that the observed differences were not due to an intrinsic failure of T-*Chat*<sup>KO</sup> cells to adhere or sense chemokines. We postulated that this migratory advantage of *Chat*<sup>WT</sup> cells in a T-*Chat*<sup>KO</sup> host was due to local changes in the vasculature induced by the presence of *Chat*<sup>+</sup> T cells and would still be present in *Chat*<sup>WT</sup> recipients of T-*Chat*<sup>KO</sup> P14 cells.

Vasodilation is critical for immune responses and is one of the hallmarks of inflammation facilitating the entry of immune cells into infected tissues. Not only do *Il21r*<sup>-/-</sup> mice exhibit

smaller arterial connections in the brain (19), T-*Chat*<sup>KO</sup> mice exhibit higher blood pressure than *Chat*<sup>WT</sup> littermates (6), indicating that they also have smaller arteries. ACh signaling has long been known to induce vasodilation (20). We posited that *Chat*<sup>+</sup> T cells induced by infection are the primary mediators of vasodilation via the release of ACh and that loss of *Chat* in T cells would consequently abrogate infection-driven vasodilation. Upon imaging the liver arterial vasculature of naive and LCMV-Cl13-infected *Chat*<sup>WT</sup> and T-*Chat*<sup>KO</sup> mice (movies S1 to S4), we found that infection-induced vasodilation in the liver was completely abrogated in T-*Chat*<sup>KO</sup> mice, in contrast to their *Chat*<sup>WT</sup> counterparts (Fig. 4, A and B), resulting in fewer detectable terminal branches (fig. S7A)

**Fig. 3. IL-21-driven *Chat* expression in T cells facilitates migration into infected tissues.** (A) Day 8 LCMV-CI13 infected *Il21r<sup>+/+</sup>* (blue) or *Il21r<sup>-/-</sup>* (orange) animals were injected intravenously with  $\alpha$ -CD8-FITC (FITC, fluorescein isothiocyanate) 3 min before being euthanized. Livers were then processed, washed, and stained for CD8, tetramer, and inhibitory receptors. FITC<sup>-</sup> liver-infiltrating CD8<sup>+</sup> T cells were enumerated. Composite of three experimental cohorts, *n* = 10 to 11. (B and C) The number of virus-specific CD8 T cells in the tissue of *Chat<sup>WT</sup>* (black) and *T-Chat<sup>KO</sup>* (white) mice was determined in liver (B) and salivary gland (C) by intravascular staining as in (A). Mean  $\pm$  SEM, composite of five experimental cohorts for liver, two experimental cohorts for salivary gland, *n* = 12 to 22. (D) In vivo cytolytic activity was determined in the spleen and liver of *Chat<sup>WT</sup>* or *T-Chat<sup>KO</sup>* mice 8 days post-*LCMV-CI13* infection. Mean  $\pm$  SEM, composite of three to four experimental cohorts, *n* = 15 (GP276 and NP396), *n* = 23 (GP33). (E) The fraction of liver-infiltrating D<sup>b</sup>(GP276)-specific CD8 T cells expressing granzyme B was determined by intravascular staining as in (A). The fraction of liver-infiltrating CD8 T cells expressing CD107a and IFN- $\gamma$  after in vitro stimulation with GP276 was compared with the total number of liver-infiltrating D<sup>b</sup>(GP276)<sup>+</sup> cells to determine the percent of GP276-specific cells capable of degranulation. Mean  $\pm$  SEM, composite of two experimental cohorts, *n* = 11 to 12. (F) Analysis schematic for P14 transfer experiments. *Chat<sup>WT</sup>* P14 or *Chat<sup>KO</sup>* P14 T cells were transferred into either *Chat<sup>WT</sup>* or *T-Chat<sup>KO</sup>* recipient mice, which were subsequently infected with LCMV-CI13. Intravascular cells in



different tissues were marked as in (A), 30 days postinfection. The D<sup>b</sup>(GP33)-specific nonvascular cells were evaluated to determine the relative ratio of endogenous and P14 cells in the spleen and peripheral organs. The relative abundance of P14 cells in the organs was then compared with that in the spleen to determine whether P14 cells migrated better than, as well as, or worse than the endogenous D<sup>b</sup>(GP33)-specific cells. (G) The ratio of migrated P14 cells to endogenous D<sup>b</sup>(GP33)<sup>+</sup> cells was determined as described in (F). Mean  $\pm$  SEM, composite of two experimental cohorts for controls and four experimental cohorts, *n* = 5 to 10 control animals, *n* = 12 to 17 experimental animals. Statistical significance for all samples determined by unpaired two-tailed *t* test; \**P* < 0.05, \*\**P* < 0.01, \*\*\**P* < 0.001, \*\*\*\**P* < 0.0001.

and smaller mean vessel diameter at equivalent branch depths (fig. S7B).

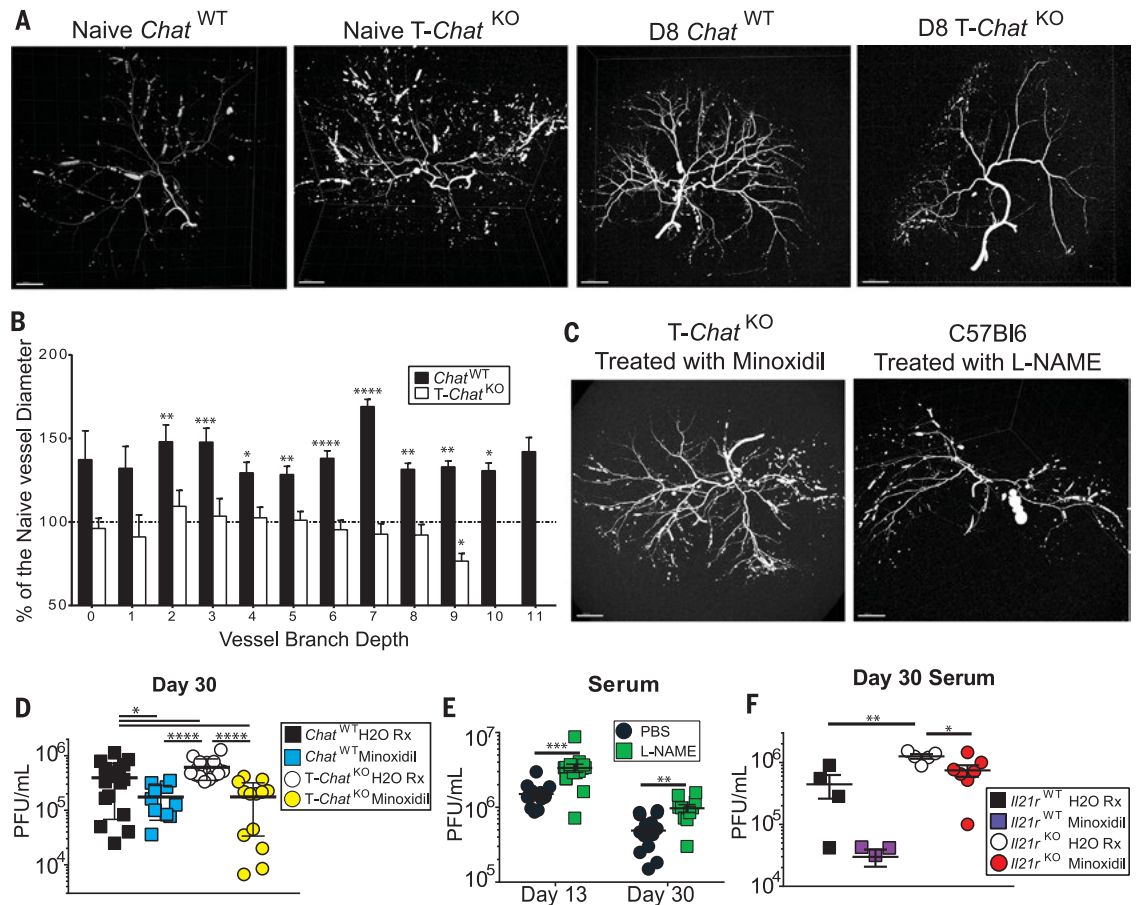
The blood vessel phenotype in *T-Chat<sup>KO</sup>* mice was reversed with short-term treatment with the vasodilator minoxidil (Fig. 4C, fig. S7, and movie S5). Thus, these differences were not developmental but reflective of poor vasodilation in the absence of *T-Chat*. Furthermore, treatment of wild-type mice with the vasoconstrictor L-NAME was sufficient to recapitulate the vascular phenotype observed in *T-Chat<sup>KO</sup>* mice (Fig. 4C, fig. S7, and movie S6). Minoxidil treatment was sufficient to restore viral control in *T-Chat<sup>KO</sup>* mice and also augmented viral con-

trol in *Chat<sup>WT</sup>* animals (Fig. 4D). Moreover, viral titers were significantly higher in wild-type mice treated with L-NAME on days 6 through 12 postinfection when compared with phosphate-buffered saline (PBS)-treated controls (Fig. 4E). Thus, vasodilation mediated by *Chat*-expressing T cells is critical for appropriate viral control.

IL-21 supports antiviral immunity beyond *Chat* induction and vasomodulation (21). Indeed, treatment with minoxidil was not sufficient to fully rescue *Il21r<sup>-/-</sup>* mice, although this treatment did reduce viral titers compared with vehicle-treated *Il21r<sup>-/-</sup>* mice (Fig. 4F). Efficient migration of effector T cells into tissues is crit-

ical for the control of viral infections (22) and is also of great interest for immunotherapy directed at tumors (23). In addition to its other reported roles during infection, IL-21 signaling enhances the efficacy of expanded tumor-infiltrating lymphocytes to combat cancer (24, 25). Here, we report that IL-21, a cytokine critical for control of chronic infection (10–12), drives the expression of *Chat* in T cells to facilitate their migration into infected tissues. These findings underscore the role for IL-21 during the host response to infection and establish a cholinergic mechanism for regulating cellular migration into tissues.

**Fig. 4. Vasodilation during infection is dependent on *Chat*-expressing T cells and is critical for viral control.** (A) Representative liver arterial tree of naïve (left) or day 8 post-LCMV-CI13 infection (right) *Chat*<sup>WT</sup> and *T-Chat*<sup>KO</sup> mice imaged using MICROFIL and micro-computed tomography scan. Representative of two (naïve) or four (day 8) mice. Scale bars, 2000 μm. (B) Mean vessel diameter in day 8 infected *Chat*<sup>WT</sup> (black) or *T-Chat*<sup>KO</sup> (white) mice was normalized to the average vessel diameter of naïve mice at each branch depth. Values above 100% (dashed line) indicate increased blood vessel diameter. Mean + SEM, average of *n* = 2 naïve mice for each genotype used for comparison to values in *n* = 4 day 8 infected samples in each genotype. Statistical significance determined by unpaired two-tailed *t* test between day 8 and naïve mice of the same genotype. (C) Representative liver arterial tree of *T-Chat*<sup>KO</sup> mice treated with minoxidil or B6 mice treated with L-NAME on days 6 to 8 postinfection. MICROFIL injection was performed on day 8 postinfection with LCMV-CI13. Scale bars, 2000 μm. (D) *Chat*<sup>WT</sup> or *T-Chat*<sup>KO</sup> animals were infected with LCMV-CI13 and then gavaged with either water (control) or minoxidil hydrochloride dissolved in water daily on days 6 to 12 postinfection. Serum viral titer was determined 30 days postinfection in *Chat*<sup>WT</sup> control (black), *Chat*<sup>WT</sup> minoxidil-treated (blue), *T-Chat*<sup>KO</sup> control (white), or *T-Chat*<sup>KO</sup> minoxidil-treated (yellow) mice. Composite of three to four experimental cohorts, *n* = 10 to 18.



(E) Serum viral titers of C57Bl/6 mice injected with either PBS (black) or L-NAME (green) on days 6 to 12 post-LCMV-CI13 infection. Composite of three experimental cohorts, *n* = 10 to 15. (F) *Il21r*<sup>+/+</sup> or *Il21r*<sup>-/-</sup> animals were infected with LCMV-CI13 and then gavaged with either water or minoxidil daily on days 6 to 12 postinfection. Serum viral titer was determined 30 days postinfection in *Il21r*<sup>+/+</sup> control (black), *Il21r*<sup>+/+</sup> minoxidil-treated (violet), *Il21r*<sup>-/-</sup> control (white), or *Il21r*<sup>-/-</sup> minoxidil-treated (red) mice. Each symbol represents an individual mouse, *n* = 4 to 7. Statistical significance for all samples determined by unpaired two-tailed *t* test; \**P* < 0.05, \*\**P* < 0.01, \*\*\**P* < 0.001, \*\*\*\**P* < 0.0001.

**REFERENCES AND NOTES**

1. M. C. Fishman, *Yale J. Biol. Med.* **45**, 104–118 (1972).
2. O. Loewi, *J. Mt. Sinai Hosp. N. Y.* **24**, 1014–1016 (1957).
3. R. F. Furchgott, J. V. Zawadzki, *Nature* **288**, 373–376 (1980).
4. M. Rosas-Ballina et al., *Science* **334**, 98–101 (2011).
5. C. Reardon et al., *Proc. Natl. Acad. Sci. U.S.A.* **110**, 1410–1415 (2013).
6. P. S. Olofsson et al., *Nat. Biotechnol.* **34**, 1066–1071 (2016).
7. Y. N. Tallini et al., *Physiol. Genomics* **27**, 391–397 (2006).
8. M. A. Cox, S. M. Kahan, A. J. Zajac, *Virology* **435**, 157–169 (2013).
9. A. Fröhlich et al., *Blood* **109**, 2023–2031 (2007).
10. H. Elsaesser, K. Sauer, D. G. Brooks, *Science* **324**, 1569–1572 (2009).
11. A. Fröhlich et al., *Science* **324**, 1576–1580 (2009).
12. J. S. Yi, M. Du, A. J. Zajac, *Science* **324**, 1572–1576 (2009).
13. T. Misgeld et al., *Neuron* **36**, 635–648 (2002).
14. P. P. Lee et al., *Immunity* **15**, 763–774 (2001).
15. J. S. Yi, J. T. Ingram, A. J. Zajac, *J. Immunol.* **185**, 4835–4845 (2010).

16. Y. Tian et al., *J. Immunol.* **196**, 2153–2166 (2016).
17. A. M. Hanash et al., *Blood* **118**, 446–455 (2011).
18. K. G. Anderson et al., *Nat. Protoc.* **9**, 209–222 (2014).
19. H. K. Lee et al., *J. Clin. Invest.* **126**, 2827–2838 (2016).
20. M. P. Doyle, B. R. Duling, *Am. J. Physiol.* **272**, H1364–H1371 (1997).
21. G. Xin et al., *Cell Rep.* **13**, 1118–1124 (2015).
22. S. N. Mueller, L. K. Mackay, *Nat. Rev. Immunol.* **16**, 79–89 (2016).
23. R. S. Herbst et al., *Nature* **515**, 563–567 (2014).
24. C. L. Hsieh et al., *Immunobiology* **216**, 491–496 (2011).
25. S. J. Santegoets et al., *J. Transl. Med.* **11**, 37 (2013).

**ACKNOWLEDGMENTS**

We thank A. Brustle for scientific advice and helpful discussions, M. Saunders for scientific editing of the manuscript, and R. Flick of the BioZone Mass Spectrometry Facility (University of Toronto) for assisting with the mass spectrometry. We apologize to those authors whose work we were unable to cite because of space constraints. **Funding:** This work was supported by the Cancer Research Institute Irvington Postdoctoral Fellowship (to M.A.C.),

the Knut and Alice Wallenberg Foundation (P.S.O.), and grants from the Canadian Institutes of Health Research (to T.W.M.). D.B. is supported by the FNR-ATTRACT (A14/BM/7632103). **Author contributions:** Conceptualization, M.A.C. and T.W.M.; Methodology, M.A.C., T.W.M., L.X.Y., and B.N.; Investigation, M.A.C., G.S.D., G.H.Y.L., B.E.S., D.B., A.J.E., C.D.-B., S.P.K., T.B., L.N.B., L.X.Y., B.N., and R.F.; Writing—original draft, M.A.C.; Writing—review and editing, M.A.C., T.W.M., K.J.T., and P.S.O.; Resources, P.S.O., A.R.E., K.T.G., and J.H.; Visualization, M.A.C.; Supervision, T.W.M.; Funding acquisition, T.W.M. **Competing interests:** The authors declare no competing interests. **Data and materials availability:** All data supporting the findings of this study are available within the paper and its supplementary materials.

**SUPPLEMENTARY MATERIALS**

www.sciencemag.org/content/363/6427/639/suppl/DC1  
Figs. S1 to S7  
Movies S1 to S6

26 July 2018; accepted 14 December 2018  
10.1126/science.aau9072

## IMMUNOLOGY

# Chimeric camel/human heavy-chain antibodies protect against MERS-CoV infection

V. Stalin Raj<sup>1\*†‡</sup>, Nisreen M. A. Okba<sup>1\*</sup>, Javier Gutierrez-Alvarez<sup>2</sup>, Dubravka Drabek<sup>3</sup>, Brenda van Dieren<sup>4</sup>, W. Widagdo<sup>1</sup>, Mart M. Lamers<sup>1</sup>, Ivy Widjaja<sup>4</sup>, Raul Fernandez-Delgado<sup>2</sup>, Isabel Sola<sup>2</sup>, Albert Bensaid<sup>5</sup>, Marion P. Koopmans<sup>1</sup>, Joaquim Segalés<sup>6,7</sup>, Albert D. M. E. Osterhaus<sup>8,9</sup>, Berend Jan Bosch<sup>4</sup>, Luis Enjuanes<sup>2</sup>, Bart L. Haagmans<sup>1‡</sup>

Middle East respiratory syndrome coronavirus (MERS-CoV) continues to cause outbreaks in humans as a result of spillover events from dromedaries. In contrast to humans, MERS-CoV-exposed dromedaries develop only very mild infections and exceptionally potent virus-neutralizing antibody responses. These strong antibody responses may be caused by affinity maturation as a result of repeated exposure to the virus or by the fact that dromedaries—apart from conventional antibodies—have relatively unique, heavy chain-only antibodies (HCABs). These HCABs are devoid of light chains and have long complementarity-determining regions with unique epitope binding properties, allowing them to recognize and bind with high affinity to epitopes not recognized by conventional antibodies. Through direct cloning and expression of the variable heavy chains (VHHs) of HCABs from the bone marrow of MERS-CoV-infected dromedaries, we identified several MERS-CoV-specific VHHs or nanobodies. In vitro, these VHHs efficiently blocked virus entry at picomolar concentrations. The selected VHHs bind with exceptionally high affinity to the receptor binding domain of the viral spike protein. Furthermore, camel/human chimeric HCABs—composed of the camel VHH linked to a human Fc domain lacking the CH1 exon—had an extended half-life in the serum and protected mice against a lethal MERS-CoV challenge. HCABs represent a promising alternative strategy to develop novel interventions not only for MERS-CoV but also for other emerging pathogens.

## INTRODUCTION

In 2012, a novel virus, termed Middle East respiratory syndrome coronavirus (MERS-CoV), was identified in humans (1). Six years later, more than 2000 laboratory-confirmed MERS cases, including 36% with a fatal outcome, have been reported globally. Most cases thus far originated from the Arabian Peninsula, as a result of hospital outbreaks (2). There is convincing evidence that dromedary camels are the primary source of MERS-CoV infection in humans. The virus isolated from camels is similar to that isolated from humans and also replicates in human cells (3). In addition, epidemiological and phylogenetic analyses suggest multiple introductions of MERS-CoV into the human population (2, 4). This raises a great concern as MERS-CoV could continue to cause outbreaks in the near future. Effective prophylactic and therapeutic intervention strategies are therefore needed to combat this virus.

Monoclonal antibodies (mAbs) are promising candidates for the treatment and prevention of viral infections. Recently, MERS-CoV-

neutralizing mAbs have been identified and characterized by several research groups, using various approaches. These antibodies have been isolated from human naïve B cells (5), memory B cells of MERS-CoV-infected individuals (6), or transgenic mice expressing human antibody variable heavy chains (VHHs) and  $\kappa$  light chains (7). All these mAbs target the receptor binding domain (RBD) of the MERS-CoV spike protein. The MERS-CoV spike protein is a structural viral component that contains the RBD, located in the S1 subunit of the protein, which binds to the MERS-CoV entry receptor dipeptidyl peptidase-4 (DPP4) (8). Antibodies raised against the S1 or RBD block MERS-CoV infection in vitro (9, 10), and the most potent mAbs identified against MERS-CoV thus far recognize the RBD (5, 7, 11–14). However, production of these mAbs at a large scale is costly and requires a long developmental process, and relative large quantities might be needed to protect humans against a viral infection (15). Alternatively, antibody engineering technologies allow the cloning of variable regions of mAbs for expression in *Escherichia coli* or yeast to produce large amounts of recombinant antibody fragments (16). To date, 68 therapeutic mAbs have been licensed, of which 7 are chimeric antibodies (17).

Heavy chain-only antibodies (HCABs) are naturally produced in camelid species (18). These antibodies are dimeric and do not contain a light chain, and their antigen recognition region is solely formed by the VHH region termed single-domain antibody fragment. This fragment is about 14 kDa in size, is relatively stable, and can be produced with high yields in prokaryotic systems (18, 19). Camelid VHHs have long complementarity-determining region 3 (CDR3) loops, capable of binding to unique epitopes not accessible to conventional antibodies (20). Because of these beneficial properties, VHHs have been exploited for a range of biotechnological applications, including diagnostics, therapeutics, and fundamental research (21, 22). The recent preclinical success of a VHH that blocks von Willebrand factor-mediated platelet aggregation (23) shows their

<sup>1</sup>Department of Viroscience, Erasmus Medical Center, Rotterdam, Netherlands. <sup>2</sup>Department of Molecular and Cell Biology, National Center for Biotechnology-Spanish National Research Council (CNB-CSIC), Madrid, Spain. <sup>3</sup>Department of Cell Biology, Erasmus Medical Center, Rotterdam, Netherlands. <sup>4</sup>Virology Division, Department of Infectious Diseases and Immunology, Faculty of Veterinary Medicine, Utrecht University, Utrecht, Netherlands. <sup>5</sup>Institut de Recerca i Tecnologia Agroalimentàries (IRTA), Centre de Recerca en Sanitat Animal [CReSA, IRTA-Universitat Autònoma de Barcelona (UAB)], Campus de la UAB, 08193 Bellaterra, Spain. <sup>6</sup>UAB, CReSA (IRTA-UAB), Campus de la UAB, 08193 Bellaterra, Spain. <sup>7</sup>Departament de Sanitat i Anatomia Animals, Facultat de Veterinària, UAB, 08193 Bellaterra, Spain. <sup>8</sup>Artemis One Health, Utrecht, Netherlands. <sup>9</sup>Center for Infection Medicine and Zoonoses Research, University of Veterinary Medicine, Hannover, Germany.

\*These authors contributed equally to this work.

†Present address: School of Biology, Indian Institute of Science Education and Research Thiruvananthapuram (IISER-TVM), Kerala, India.

‡Corresponding author. Email: stalin@iisertvm.ac.in (V.S.R.); b.haagmans@erasmusmc.nl (B.L.H.)

Copyright © 2018  
The Authors, some  
rights reserved;  
exclusive licensee  
American Association  
for the Advancement  
of Science. No claim to  
original U.S. Government  
Works. Distributed  
under a Creative  
Commons Attribution  
NonCommercial  
License 4.0 (CC BY-NC).

therapeutic potential. VHHs may also efficiently prevent entry of viruses into host cells (24). Chimeric HCABs, which have the camel VHH and the human Fc portion (lacking the CH1 exon as in camel HCABs), allow them to interact with human effector cells and complement cascade factors (15).

Several studies have demonstrated the presence of high levels of MERS-CoV-specific neutralizing antibodies (mean virus neutralization titer  $\approx$  1000) in dromedary camels in the Middle East and Africa (25–27). Therefore, next to human mAbs, characterization of MERS-CoV-neutralizing VHHs from dromedary camels could serve as an alternative strategy to develop neutralizing antibodies. Here, we report the identification and characterization of neutralizing VHHs against MERS-CoV from immunized dromedary camels and demonstrate the prophylactic activity of camel/human chimeric HCABs in a MERS-CoV transgenic mouse model.

**RESULTS**

**Identification of MERS-CoV-specific VHHs from a dromedary camel bone marrow complementary DNA library**

First, we identified MERS-CoV-neutralizing VHHs by direct cloning and screening of VHH complementary DNA (cDNA) libraries derived from bone marrow cells (given the high frequency of specific plasma cells) rather than using B cells from peripheral blood of immunized animals (Fig. 1). Bone marrow was obtained from two dromedary camels immunized with modified vaccinia virus encoding the MERS-CoV spike protein and subsequently challenged with live MERS-CoV (28). At the time of sampling, MERS-CoV-neutralizing antibodies were detected at very high levels (titer > 10,000) in the sera of these dromedaries (Fig. 2A). Subsequently, VHH-specific primers (29) were used to amplify a VHH library from the bone marrow cDNA by nested polymerase chain reaction (PCR) (fig. S1, A to C).

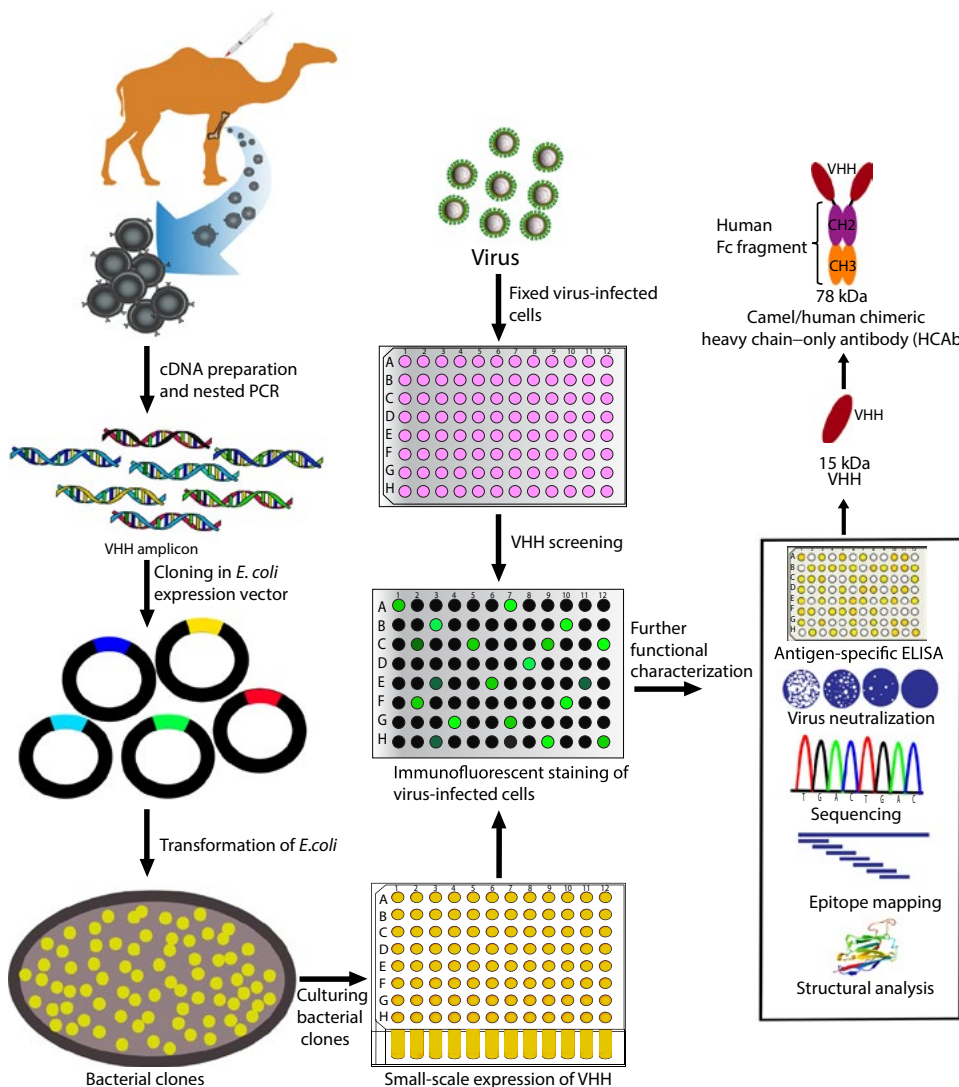


**Fig. 1. Schematic overview of VHH identification by direct cloning using bone marrow from immunized dromedary camels.** Immunized dromedary camels were anesthetized, and bone marrow aspirations were performed. After total RNA isolation and first-strand cDNA synthesis, VHH genes were amplified and cloned into a prokaryotic expression vector (pMES4) and transformed into *E. coli* WK6. Individual clones were grown overnight in 96-deep-well plates, during which they expressed the VHHs in the periplasm. Next, crude VHHs were released from the periplasm by freeze-thawing the bacterial pellet. Crude VHHs were used for immunofluorescent staining on virus-infected cells. Immunofluorescent positive clones were further characterized for their genetic makeup, specificity, and potency by sequencing, antigen-specific enzyme-linked immunosorbent assay (ELISA), virus neutralization assay, epitope mapping, and structural analysis. Finally, potent VHHs were produced as camel/human chimeric single chain-only antibodies.

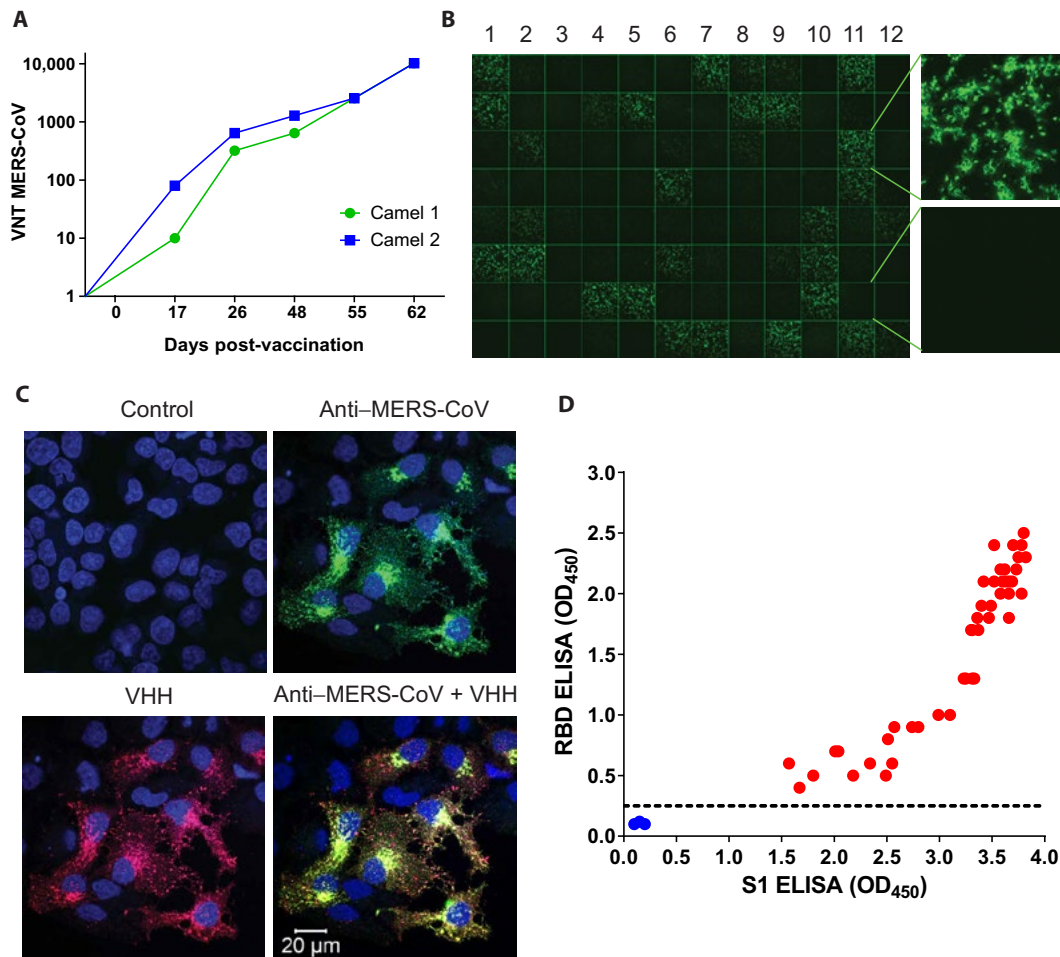


**Fig. 2. Identification of VHHs directed against the spike (S) protein of MERS-CoV.** (A) Virus-neutralizing antibody titers (VNT) of sera from two dromedary camels immunized with MVA expressing the MERS-CoV-S (MVA-S) and challenged with MERS-CoV. (B) Immunofluorescent staining of MERS-CoV-infected Huh-7 cells with crude VHHs. Each square represents staining of an individual VHH. (C) Immunofluorescent staining of MERS-CoV-infected Huh-7 cells with rabbit serum (anti-MERS-CoV) or crude VHHs and overlay. (D) Correlation of the S1-specific ELISA and the RBD-specific ELISA for the 46 MERS-CoV-neutralizing VHHs (red dots) and control VHHs indicated as blue dots (Spearman correlation  $r = 0.9258$ ;  $P < 0.0001$ ; 95% confidence interval, 0.8677 to 0.9589). OD, optical density.

After gel purification, PCR products were directly cloned into the dephosphorylated prokaryotic expression vector pMES4, tagging the VHHs with six histidine amino acids at the C terminus (29). To obtain a high-diversity repertoire of VHHs, we reduced the number of amplification cycles. The ligated VHH plasmid library was transformed into *E. coli* strain WK6 and plated on ampicillin nutrient agar plates without preculturing the bacteria in nutrient medium. A total of 560 VHH clones (225 from camel 1 and 335 from camel 2) were obtained in a single transformation event, and grown individually in 96-deep-well plates. Periplasmic expression of recombinant VHHs was induced by isopropyl- $\beta$ -D-thiogalactopyranoside (Fig. 1). VHHs were purified from the periplasm as a crude extract (30), and expression was verified using SDS-polyacrylamide gel electrophoresis (PAGE) analysis (fig. S1D).

Next, we used formalin-fixed and permeabilized virus-infected cells [either MERS-CoV-infected or severe acute respiratory syndrome coronavirus (SARS-CoV)-infected] to select for MERS-CoV-specific VHHs using immunofluorescent staining. Crude periplasmic VHH extracts were incubated on the infected cells, and VHH cell binding

was visualized with a fluorescently labeled anti-histidine antibody as a secondary antibody. All 560 VHH clones were screened by confocal microscopy (Fig. 2B). We obtained 204 MERS-CoV-reactive VHHs (41.7% from camel 1 and 58.3% from camel 2), of which none reacted to SARS-CoV-infected cells. To confirm the specificity of the VHHs for MERS-CoV, we randomly selected several clones for double staining of MERS-CoV-infected cells using a rabbit anti-MERS-CoV serum, revealing that these VHHs exclusively targeted MERS-CoV-infected cells (Fig. 2C).

#### Blocking of RBD binding to receptor DPP4 by MERS-CoV spike-specific VHHs in vitro

To test whether the VHHs identified in our study recognized the RBD or other parts of the S1, we performed MERS-CoV S1- and MERS-CoV RBD-specific ELISAs. Out of 204 MERS-CoV-reactive VHHs, 188 (92.15%) were directed against the MERS-CoV S1 subunit, of which 46 VHHs (22.5%) blocked the binding of recombinant S1 to the MERS-CoV receptor present on Huh-7 cells (fig. S2). All these in vitro blocking VHHs were directed against the RBD (Fig. 2D).

Next, we selected all blocking VHHs for further characterization. The VHH clone p2E6 (negative for immunofluorescent staining and S1 ELISA) was used as the negative control. Using a MERS-CoV plaque reduction neutralization test (PRNT), we estimated the virus neutralization capacity for each VHH. Except for the control VHH-p2E6, all tested VHHs inhibited MERS-CoV entry at varying concentrations ranging from 100 to 900 pM (PRNT<sub>50</sub>; table S1). VHHs with high neutralizing capacity (VHH-1, VHH-4, VHH-83, and VHH-101) were selected for further characterization.

We obtained sequences from all 46 blocking VHHs. Because CDR3 is known to be of most importance for the interaction with the antigen, the assumption was made that VHHs with the identical CDR3 would recognize the same epitope. Overall, 33 VHHs had different CDR3 sequences ranging in length from 16 to 20 amino acids (fig. S3). Phylogenetic analysis of these sequences revealed considerable diversity among the different VHH clones and showed that the selected VHHs formed 14 different clusters with different CDR3 sequences (fig. S4). All sequences contained the characteristic VHH tetrad, except clone 10 that, at amino acid positions 37, 45, and 47, shows VH characteristics (valine, leucine, and tryptophan). The best MERS-CoV-neutralizing VHHs (VHH-1, VHH-4, VHH-83, and VHH-101) had different CDR3 sequences (fig. S4).

### VHHs bind to MERS-CoV spike protein with high affinity

Subsequently, the best four neutralizing VHHs and the control VHH-p2E6 were selected for large-scale production and purification. We obtained high quantities (5 to 30 mg) of pure (>95%) His-tag affinity-purified VHHs from 1 liter of bacterial culture (fig. S5A). Mixing these VHHs with recombinant MERS-CoV spike S1 protein generated VHH-spike complexes, as observed by nonreducing PAGE analysis (fig. S5B). In addition, the equilibrium dissociation constant ( $K_d$ ) between the VHH and spike protein of these four VHHs was relatively low, with  $K_d$  values ranging from 1 to 0.1 nM, indicating high-affinity binding (fig. S6, A and B).

### Neutralization of MERS-CoV by VHHs and camel/human chimeric HCABs

Next, we tested the neutralizing activities of these VHHs in vitro by PRNT. All four VHHs were confirmed to neutralize MERS-CoV with high efficiency, with PRNT<sub>50</sub> values ranging from 0.0014 to 0.012  $\mu$ g/ml (93 to 800 pM), while no inhibition was observed using the control VHH-p2E6 at high concentration (>1.0  $\mu$ g/ml; 67  $\mu$ M; Fig. 3A). Because of their small size, VHHs are rapidly cleared from the circulation (30, 31). Therefore, we additionally produced the four VHHs as camel/human chimeric HCABs by C-terminal tagging the VHHs with the Fc part of human immunoglobulin G2 (IgG2) (containing the hinge and CH2 and CH3 exons) (Fig. 1, right). These HCABs (HCAB-1, HCAB-4, HCAB-83, and HCAB-101) form homodimers of about 78 kDa in size and exhibit approximately the same neutralizing capacity as the monomeric VHHs in vitro (Fig. 3B). Moreover, using an S1-specific ELISA, we could detect HCAB binding at even lower concentrations, down to 0.00019  $\mu$ g/ml (2.5 pM; Fig. 3C).

### Epitope mapping of four potent MERS-CoV-neutralizing VHHs

To map the VHH binding epitopes, we first tested the binding of the four different VHHs to recombinant S1 protein using ForteBio's Octet system. As shown in fig. S7, all four VHHs competed for a single epitope. Subsequently, we used a set of recombinant S1 proteins that contain single amino acid mutations present in spike proteins of MERS-CoV field isolates, located within the receptor binding subdomain (residues 483 to 566) of the RBD that engages DPP4. MERS-CoV polyclonal antibodies, an irrelevant VHH, and four VHHs were then tested for their ability to bind to these S1 variants. MERS-CoV polyclonal antibodies, but not the control VHH-p2E6, bound to all variants (Fig. 4, A and B), whereas the four MERS-CoV-specific VHHs did not bind to the D539N variant and differed in their binding to the other variants. VHH-1 also did not bind to variant E536K, whereas VHH-4 and VHH-101 showed partial binding to three additional variants (I529T, V534A, and E536K) (Fig. 4, C to F). These data show that all four VHHs bind an epitope in the receptor binding subdomain

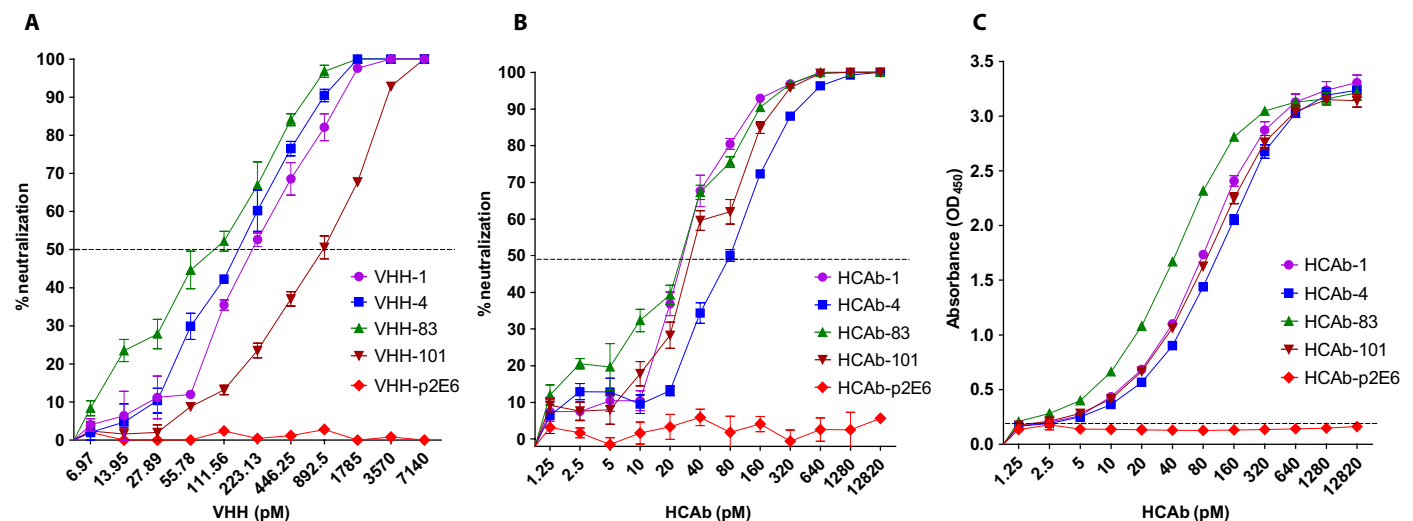


**Fig. 3. MERS-CoV-neutralizing efficacy of monomeric VHHs and chimeric antibodies on Huh-7 cells.** MERS-CoV (EMC isolate) was incubated with either VHHs (monomer), chimeric antibodies, or controls at various concentrations for 1 hour and then the mix was transferred on Huh-7 cells. Cells were fixed 8 hours after infection and stained using rabbit polyclonal antibodies. The PRNT titer was calculated on the basis of a 50% or greater reduction of infected cells (PRNT<sub>50</sub>). (A) PRNT assay for VHH monomer. (B) PRNT for camel/human chimeric heavy-chain antibodies. Experiments were performed at least two times in triplicate, data from an experiment were presented, and error bars show SEM. (C) MERS-CoV S1 ELISA using different HCABs. The optical density at 450 nm was presented in triplicate, with error bars showing SEM.

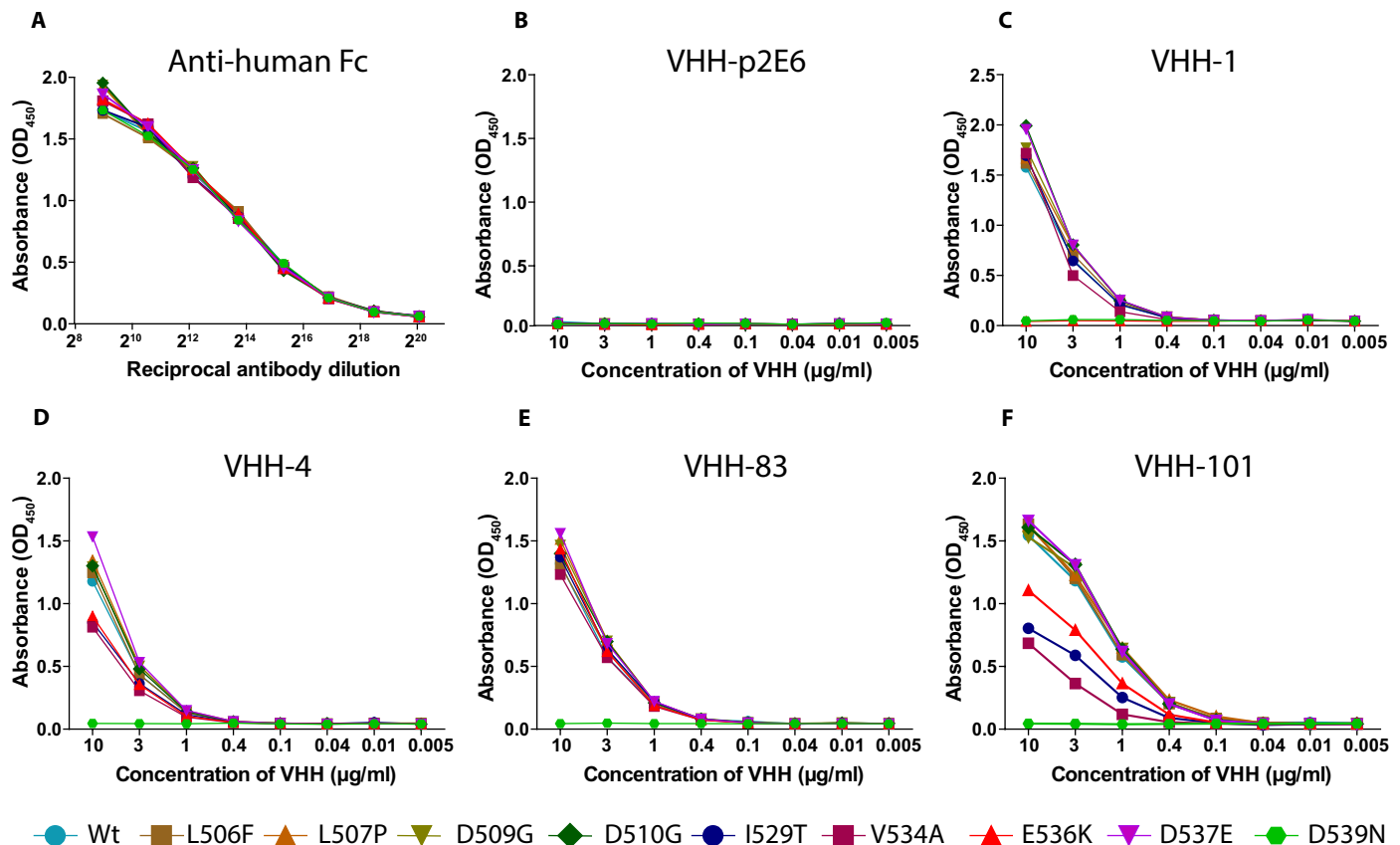


**Fig. 4. Effect of MERS-CoV RBD residue substitution on VHH binding.** Binding efficiency of VHHs to the wild-type and mutant forms of viral spike glycoprotein was analyzed by ELISA. The binding efficiency was calculated on the basis of optical density ( $OD_{450}$ ) of mutant protein versus that of the wild-type spike. (A) Anti-human IgG polyclonal antibodies were used to corroborate equivalent coating of the S1-hFc variants. (B) One irrelevant VHH (VHH-p2E6) lacked binding to wild-type and mutant proteins. (C) VHH-1. (D) VHH-4. (E) VHH-83. (F) VHH-101.

that is partially overlapping, consistent with the binding competition analysis (fig. S7). The RBD residues D537, D539, Y540, and R542 are important for the virus to bind to its cellular receptor DPP4 (32, 33). Because all four VHHs did not bind to the D539N variant, this suggests that these VHHs neutralize MERS-CoV most likely by blocking its binding to its cellular receptor. Despite several attempts, we were not able to identify MERS-CoV escape variants *in vitro*. Because of the best neutralizing capacity and epitope recognition, we selected VHH-83 and HCAb-83 for further *in vivo* testing.

### In vivo efficacy of VHH-83 and HCAb-83

To test the prophylactic efficacy of VHH-83 or HCAb-83 *in vivo*, we used the K18 transgenic mouse model (34). In our first experiment, mice were given VHH-83 or an irrelevant VHH control (p2E6) at 20 or 200  $\mu\text{g}$  per mouse (nine mice per group) by intraperitoneal injection 6 hours before intranasal infection with a lethal dose of MERS-CoV (EMC isolate). Mice that received VHH-83 lost weight and died within 7 days post-inoculation (dpi), as well as those injected with the control VHH (fig. S8).

Next, we tested HCAb-83 or the control HCAb-p2E6 using a similar experimental setup. Mice treated with 200  $\mu\text{g}$  of HCAb-83 gained weight (Fig. 5A), and all mice survived (Fig. 5B). In contrast, control HCAb-p2E6-treated groups lost weight and died within 7 dpi (Fig. 5, A and B). Gross pathological changes (Fig. 5C), mononuclear cell infiltration, and alveolar edema (Fig. 5E) were observed in the lungs of

control HCAb-p2E6-treated mice on day 4 after inoculation. Whereas low doses (20  $\mu\text{g}$ ) of HCAb-83-treated mice were only partially protected on the basis of the observed reduction of pathological abnormalities on 4 dpi (Fig. 5F), the lungs of high-dose HCAb-83-treated mice showed no pathological changes at any time point tested (Fig. 5G). In addition, no infectious virus could be isolated from the lungs of these mice, while high viral titers were observed in the low dose- and control HCAb-treated mice (Fig. 5H).

### Pharmacokinetics of HCAb-83

We also evaluated the pharmacokinetics of VHH and HCAb in the sera of mice treated with either VHH-83 or HCAb-83. First, we estimated the presence of MERS-CoV-neutralizing activity in sera obtained 2 days after treatment. No neutralization of the virus was observed in the sera of VHH-83- or control VHH-p2E6-treated mice (Fig. 6A), consistent with the reported rapid clearance of small VHH domains from the circulation (31). Significant levels of neutralizing antibodies (mean titer, 1024) were observed in the sera of mice treated with 200  $\mu\text{g}$  of HCAb-83 and, to a limited extent, in low dose-treated mice (mean titer, 64; Fig. 6A). Second, we tested the presence of circulating HCAb-83 in the sera obtained at various time points after injection (0, 2, 4, and 8 days after treatment) by ELISA. As shown in Fig. 6B, 200  $\mu\text{g}$  of HCAb-83-treated mice still had high levels of HCAb-83 8 days after treatment, with an apparent serum half-life of approximately 4.5 days.

**DISCUSSION**

VHVs are small in size; have high stability, solubility, and affinity; and efficiently recognize antigens. They have many potential biomedical applications including the treatment of cancer, autoimmune diseases, and virus infections (18, 19, 22, 24, 31). Moreover, VHVs are gaining much attention in the field of diagnostics and therapeutics for viral diseases. They have been used for the detection of viruses, such

as Marburg virus, human immunodeficiency virus (HIV), influenza virus, dengue virus, and norovirus (22, 24). VHVs also block virus attachment to the host cells in respiratory syncytial virus, influenza virus, hepatitis B virus, rotavirus, and HIV infections (22, 24). Some VHVs inhibit viral RNA transcription or nuclear import of viral ribonucleoproteins (35). Here, we have shown that MERS-CoV-neutralizing VHVs can be obtained from immunized dromedary camels that were

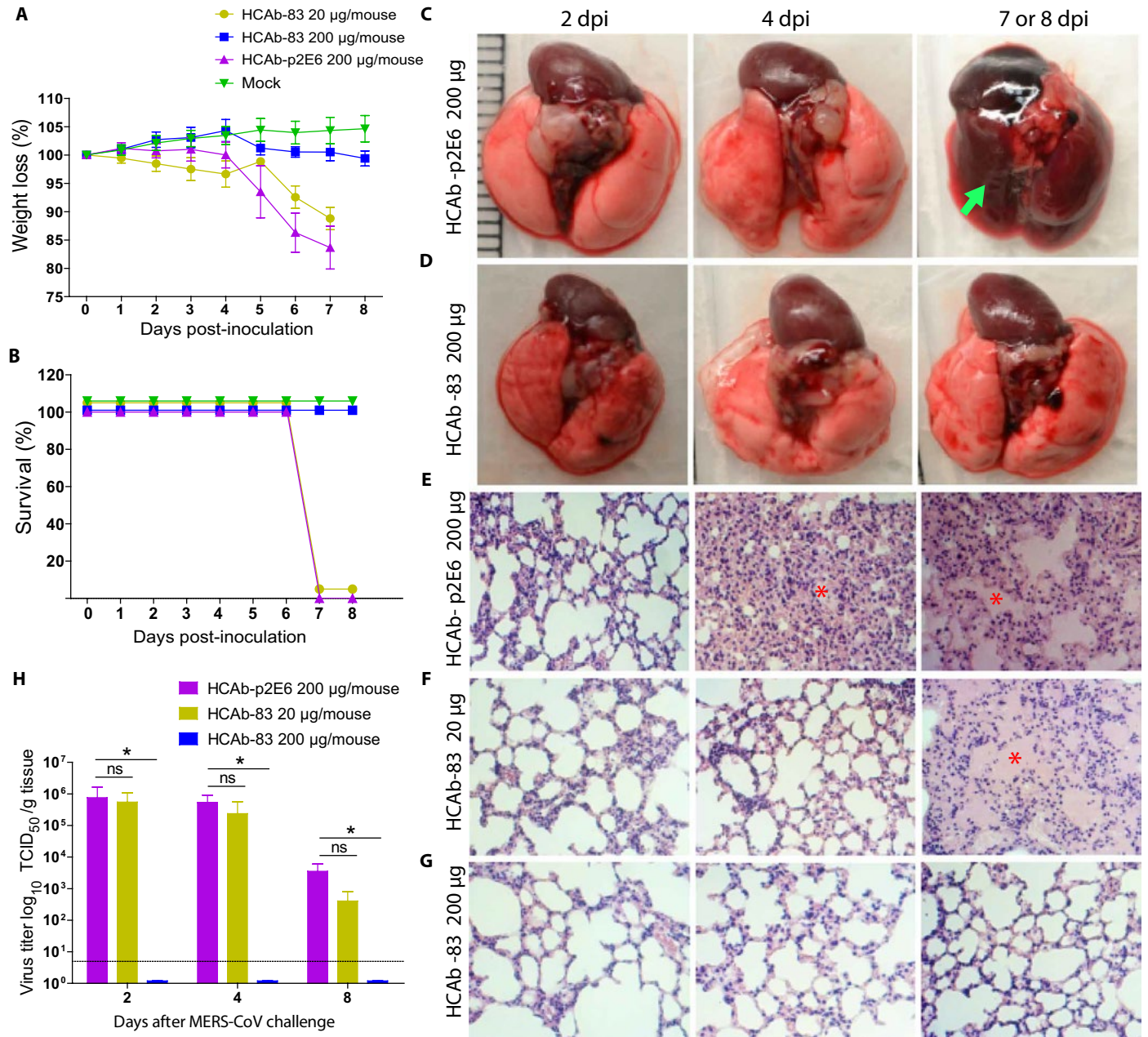


**Fig. 5. Prophylactic efficacy of HCAB-83 in K18 mice challenged with a lethal dose of MERS-CoV.** K18 mice ( $n = 9$  per group) were injected intraperitoneally with HCAB-83 (20 or 200  $\mu\text{g}$  per mouse) 6 hours before challenge with  $10^5$  TCID<sub>50</sub> (median tissue culture infectious dose) of MERS-CoV (EMC isolate). HCAB-p2E6 was injected as a negative control ( $n = 9$ ). Mice were monitored daily for (A) weight loss and (B) mortality. Weight loss is expressed as a percentage of the initial weight. Lungs were collected at days 2, 4, and 8 ( $n = 3$  per time point) or from mice that died in between and were processed to assess gross pathology (C and D) and histopathological changes (E to G). Gross pathology of one representative animal that died at day 7 when treated with HCAB-p2E6 is indicated by a green arrow (C, right). Lung sections were stained with hematoxylin and eosin. Asterisk indicates alveolar edema. (H) MERS-CoV viral titer quantitation of infected lungs at days 2, 4, and 8 ( $n = 3$  per time point) after infection ( $n = 3$  mice per time point); one-way ANOVA. \* $P < 0.05$ . ns, not significant.



studies need to evaluate whether the potency of HCAb-83 may be increased further by replacing the IgG2 Fc with the IgG1 Fc or by combination with other antibodies targeting different epitopes.

In summary, we identified and characterized potent HCABs that neutralized MERS-CoV in vitro and in vivo. Because of their high affinity, in vivo stability, and efficacy, these HCABs may be used as a prophylaxis for MERS-CoV.

## MATERIALS AND METHODS

### Immunization

One female (6-month-old) and one male (8-month-old) healthy dromedary camels (*Camelus dromedarius*), negative for antibodies against MERS-CoV and modified vaccinia virus Ankara (MVA), were obtained from the Canary Islands and housed in biosecurity level 3 (BSL-3) facilities [Centre de Recerca en Sanitat Animal (CRESA)], as described previously (28). Experimental procedures were approved by the local Ethics Committee of the Autonomous University of Barcelona (number 8003). Both animals were immunized twice with a 4-week interval with  $10^8$  plaque-forming units of MVA-S via both nostrils and intramuscularly in the neck of the animals. After the second immunization, both animals were anesthetized with midazolam (5 mg/ml) and inoculated with  $10^7$  TCID<sub>50</sub> MERS-CoV in 3 ml of phosphate-buffered saline (PBS) intranasally in both nostrils using a laryngo-tracheal mucosal atomization device (45). Blood samples were taken at different dpi. On day 14 after inoculation, both animals were anesthetized and femoral bone marrow samples (about 1 cm<sup>3</sup>) were collected next to the epiphysis and placed, each, in tubes containing 3.6 ml of ice-cold fetal calf serum. Specimens were gently crushed with a 1-ml tip and homogenized by slow up and down pipetting. After 10-min incubation on ice, 400  $\mu$ l of dimethyl sulfoxide was mixed into each tube, and the preparation was dispensed into 2-ml cryovials discarding debris and slurs and stored at  $-135^{\circ}\text{C}$ .

### Protein expression

The recombinant S1-Fc fusion proteins were produced as described previously (46). Briefly, plasmids encoding MERS-CoV S1-Fc or MERS-CoV RBD-Fc were generated by ligating a fragment encoding the S1 subunit (GenBank accession number AFS88936; residues 1 to 747) or RBD (residues 358 to 588) 3' terminally to a fragment encoding the Fc domain of human IgG1 into the pCAGGS expression vector. Plasmids encoding S1-Fc variants with single amino acid substitutions were generated by site-directed mutagenesis. S1-Fc fusion proteins were expressed by transfection of the expression plasmids into human embryonic kidney (HEK)-293T (CRL-11268, American Type Culture Collection) cells and affinity-purified from the culture supernatant using Protein A-Sepharose beads (GE Healthcare).

### Estimation of antibody/VHH titers

MERS-CoV-specific antibody titers were measured by ELISA. First, 96-well plates were coated with MERS-CoV S1 or MERS-CoV RBD proteins at 1  $\mu$ g/ml in PBS (pH 7.4) and incubated overnight at 4°C. Wells were then washed three times with PBS, blocked with 10% normal goat serum in PBS, and incubated at 37°C for 30 min. Dromedary camel sera or VHHs were serially diluted in PBS, 100  $\mu$ l was added per well, and plates were incubated at 37°C for 1 hour. Next, plates were washed three times in PBS containing 0.05% Tween 20 (PBST), after which they were incubated with biotin-conjugated goat anti-llama antibodies (1:2000, Abcore) or mouse anti-histidine anti-

bodies (1:2000, Thermo Fisher Scientific) at 37°C for 1 hour. After three washes with PBST, plates were incubated with streptavidin horseradish peroxidase (HRP; 1:10,000, Dako) or goat anti-mouse HRP (1:2000, Dako) at 37°C for 1 hour. After this incubation, plates were washed three times in PBST and incubated at room temperature for 10 min in the presence of 3,3',5,5'-tetramethylbenzidine substrate (eBioscience). Reactions were stopped with 2N H<sub>2</sub>SO<sub>4</sub> (Sigma). The absorbance of each sample was read at 450 nm with an ELISA reader (Tecan Infinite F200).

### RNA isolation and cDNA synthesis

For RNA isolation, cryopreserved bone marrow cells were removed from the  $-135^{\circ}\text{C}$  freezer and transferred to a 37°C water bath. The thawed cell suspension was quickly transferred to 40 ml of ice-cold RPMI 1640 (Lonza) medium. Cells were counted, and  $10^7$  cells were transferred to a new ribonuclease (RNase)-free falcon tube and centrifuged at room temperature at 300g for 10 min. The supernatant was completely removed, and cells were subsequently lysed with 1 ml of TRIzol reagent (Life Technologies) and 0.2 ml of RNase-free chloroform (Life Technologies). The mixture was vortexed for 15 s and incubated for 3 min at room temperature, followed by centrifugation at 13,000 rpm for 15 min at 4°C. The aqueous phase was transferred to a new tube. Subsequently, RNA was isolated using the RNeasy MinElute Cleanup Kit (Qiagen) according to the manufacturer's protocol. Total RNA was quantified at 260 nm using the NanoDrop 2000, and the quality of the isolated RNA sample was determined by measuring the A<sub>260</sub>/A<sub>280</sub> ratio. cDNA was synthesized from 1.5  $\mu$ g of total RNA using a First-Strand cDNA Synthesis kit (Life Technologies). For a 20- $\mu$ l reaction mix, 10  $\mu$ l of RNA, 1  $\mu$ l of deoxy-nucleoside triphosphate (dNTPs; 10 mM each), 1  $\mu$ l of random hexamers (10 mM; Promega), and 1.5  $\mu$ l of distilled water (dH<sub>2</sub>O) were added to a microvial. The mixture was incubated at 65°C for 10 min and then at 4°C for 2 min. Next, 6.5  $\mu$ l of reverse transcriptase mix containing 4  $\mu$ l of 5 $\times$  SuperScript III reaction buffer, 1  $\mu$ l of dithiothreitol (100 mM), 0.5  $\mu$ l of RNase inhibitor (20 U/ $\mu$ l), and 1  $\mu$ l of SuperScript III reverse transcriptase (200 U/ $\mu$ l; Life Technologies) were added to the microvial and incubated at 25°C for 5 min, 50°C for 45 min, and 70°C for 20 min. cDNA was stored at 4°C until PCR amplification.

### PCR amplification and cloning of VHH

The amplification of VHH was performed using a nested PCR approach (29) that was adapted for use with a high-fidelity DNA polymerase (PfuUltra II Fusion HS DNA Polymerase, Stratagene). The first PCR mix (50  $\mu$ l of reaction volume) consisted of 5.0  $\mu$ l of 10 $\times$  PfuUltra II Fusion HS DNA polymerase buffer, 2.5  $\mu$ l of dNTPs (10 mM each), 1.5  $\mu$ l of gene-specific forward primer (CALL001, 5'-GTCCTGGCTGCTCTTCTACAAGG-3'; 10 mM), 1.5  $\mu$ l of gene-specific reverse primer (CALL002, 5'-GGTACGTGCTGTTGAAC-TGTTCC-3'; 10 mM), 1.0  $\mu$ l of PfuUltra II Fusion HS DNA polymerase, 36.5  $\mu$ l of dH<sub>2</sub>O, and 2.0  $\mu$ l of cDNA. PCR amplification was performed in a thermocycler with the following protocol: initial denaturation at 94°C for 3 min, followed by 20 cycles at 94°C for 20 s, 50°C for 30 s, and 72°C for 2 min, and a final extension at 72°C for 10 min. The first PCR generated two amplified products: the heavy chain of conventional antibodies (~1000 bp) and the VHH heavy chain (~700 bp; fig. S1). The amplified VHH amplicon (~700 bp) was purified from the agarose gel using the QIAquick Gel Extraction Kit (Qiagen), according to the manufacturer's instructions. The product

was then subjected to the second round of PCR amplification using VHH inner primers that contained restriction sites for cloning: forward, 5'-CTAGTGGCGCCGCTGGAGACGGTGACCTGGGT-3' (Eco 91I); reverse, 5'-GATGTGCAGCTGCAGGAGTCTGGRG-GAGG-3' (Pst I). PCR amplification continued for 12 to 14 cycles, after which the amplicons were purified with the QIAquick PCR Purification Kit (Qiagen) and digested using Eco 91I and Pst I. The vector pMES4 (GenBank accession number GQ907248) was digested with the same enzymes and dephosphorylated using alkaline phosphatase (New England Biolabs). VHH amplicons were ligated into pMES4 using a ratio of 100 ng of vector to 46 ng of VHH (~1:3 molar ratio). Next, we used *E. coli* strain WK6, prepared using the Mix & Go! *E. coli* Transformation Kit and Buffer Set (Zymo Research), for transformation according to the manufacturer's instructions. After transformation, cells were directly plated onto an ampicillin (100 µg/ml) nutrient agar plates. The following day, the insertion of VHH into the vector was confirmed by randomly picking 25 clones, screening by PCR for the insert, and Sanger sequencing, as described below.

### Sequencing

To sequence the inserts, colony PCR was performed using PfuUltra II Fusion HS DNA Polymerase (Agilent Technologies) and primers (29) 5'-TTATGCTTCCGGCTCGTATG-3' (MP57) and 5'-CCA-CAGACAGCCCTCATAG-3' (GIII) under the following conditions: initial denaturation at 95°C for 3 min, followed by 39 cycles of (95°C for 20 s, 55°C for 30 s, and 72°C for 40 s), and a final extension at 72°C for 5 min. The amplicons were gel-purified and sequenced in both directions using the BigDye Terminator v3.1 Cycle Sequencing Kit and an ABI PRISM 3100 genetic analyzer (Applied Biosystems). The obtained sequences were assembled and aligned using CLC Genomics Workbench (CLC Bio 4.9).

### SUPPLEMENTARY MATERIALS

Supplementary material for this article is available at <http://advances.sciencemag.org/cgi/content/full/4/8/eaas9667/DC1>

Supplementary Materials and Methods

Fig. S1. Direct cloning and expression of VHHs.

Fig. S2. VHHs block the interaction between the S1 protein and the MERS-CoV entry receptor DPP4.

Fig. S3. Amino acid sequences of VHH regions of anti-MERS-CoV spike VHHs.

Fig. S4. Phylogenetic tree of the amino acid sequences of the 46 MERS-CoV-neutralizing VHHs showing the corresponding neutralizing capacity of each VHH.

Fig. S5. Interaction of selected VHHs with recombinant MERS-CoV spike protein.

Fig. S6. Kinetics of VHH-1, VHH-4, VHH-83, and VHH-101 binding to MERS-CoV spike protein.

Fig. S7. Cross-competitive behavior of four different VHH-1, VHH-4, VHH-83, and VHH-101 determined using an Octet biosensor (ForteBio QK).

Fig. S8. Protective efficacy of MERS-CoV-specific VHHs in transgenic mice.

Table S1. Characteristics of MERS-CoV-specific VHHs.

Table S2. List of antibodies used in this study.

References (47–52)

### REFERENCES AND NOTES

1. A. M. Zaki, S. van Boheemen, T. M. Bestebroer, A. D. M. E. Osterhaus, R. A. M. Fouchier, Isolation of a novel coronavirus from a man with pneumonia in Saudi Arabia. *N. Engl. J. Med.* **367**, 1814–1820 (2012).
2. S. Cauchemez, P. Nouvellet, A. Cori, T. Jombart, T. Garske, H. Clapham, S. Moore, H. L. Mills, H. Salje, C. Collins, I. Rodriguez-Barraquer, S. Riley, S. Truelove, H. Algarni, R. Alhakeem, K. AlHarbi, A. Turkistani, R. J. Aguas, D. A. T. Cummings, M. D. Van Kerkhove, C. A. Donnelly, J. Lessler, C. Fraser, A. Al-Barrak, N. M. Ferguson, Unraveling the drivers of MERS-CoV transmission. *Proc. Natl. Acad. Sci. U.S.A.* **113**, 9081–9086 (2016).
3. V. S. Raj, E. A. B. A. Farag, C. B. E. M. Reusken, M. M. Lamers, S. D. Pas, J. Voermans, S. L. Smits, A. D. M. E. Osterhaus, N. Al-Mawlawi, H. E. Al-Romaihi, M. M. AlHajri, A. M. El-Sayed, K. A. Mohran, H. Ghobashy, F. Alhajri, M. Al-Thani, S. A. Al-Marri, M. M. El-Maghraby, M. P. G. Koopmans, Bart L. Haagmans, Isolation of MERS coronavirus from a dromedary camel, Qatar, 2014. *Emerg. Infect. Dis.* **20**, 1339–1342 (2014).
4. M. Cotten, S. J. Watson, P. Kellam, A. A. Al-Rabeah, H. Q. Makhdoom, A. Assiri, J. A. Al-Tawfiq, R. F. Alhakeem, H. Madani, F. A. AlRabiah, S. A. Hajjar, W. N. Al-nassir, A. Albarak, H. Flemban, H. H. Balkhy, S. Alsubaie, A. L. Palsler, A. Gall, Z. A. Memish, Transmission and evolution of the Middle East respiratory syndrome coronavirus in Saudi Arabia: A descriptive genomic study. *Lancet* **382**, 1993–2002 (2013).
5. X.-C. Tang, S. S. Agnihothram, Y. Jiao, J. Stanhope, R. L. Graham, E. C. Peterson, Y. Avnir, A. St. Clair Tallarico, J. Sheehan, Q. Zhu, R. S. Baric, W. A. Marasco, Identification of human neutralizing antibodies against MERS-CoV and their role in virus adaptive evolution. *Proc. Natl. Acad. Sci. U.S.A.* **111**, E2018–E2026 (2014).
6. D. Corti, J. Zhao, M. Pedotti, L. Simonelli, S. Agnihothram, C. Felt, B. Fernandez-Rodriguez, M. Foglierini, G. Agatic, F. Vanzetta, R. Gopal, C. J. Langrish, N. A. Barrett, F. Sallusto, R. S. Baric, L. Varani, M. Zamboni, S. Perlman, A. Lanzavecchia, Prophylactic and postexposure efficacy of a potent human monoclonal antibody against MERS coronavirus. *Proc. Natl. Acad. Sci. U.S.A.* **112**, 10473–10478 (2015).
7. K. E. Pascal, C. M. Coleman, A. O. Mujica, V. Kamat, A. Badithe, J. Fairhurst, C. Hunt, J. Strein, A. Berrebi, J. M. Sisk, K. L. Matthews, R. Babb, G. Chen, K.-M. V. Lai, T. T. Huang, W. Olson, G. D. Yancopoulos, N. Stahl, M. B. Frieman, C. A. Kyratsous, Pre- and postexposure efficacy of fully human antibodies against Spike protein in a novel humanized mouse model of MERS-CoV infection. *Proc. Natl. Acad. Sci. U.S.A.* **112**, 8738–8743 (2015).
8. V. S. Raj, H. Mou, S. L. Smits, D. H. W. Dekkers, M. A. Müller, R. Dijkman, D. Muth, J. A. A. Demmers, A. Zaki, R. A. M. Fouchier, V. Thiel, C. Drosten, P. J. M. Rottier, A. D. M. E. Osterhaus, B. J. Bosch, B. L. Haagmans, Dipeptidyl peptidase 4 is a functional receptor for the emerging human coronavirus-EMC. *Nature* **495**, 251–254 (2013).
9. H. Mou, V. S. Raj, F. J. M. van Kuppeveld, P. J. M. Rottier, B. L. Haagmans, B. J. Bosch, The receptor binding domain of the new Middle East respiratory syndrome coronavirus maps to a 231-residue region in the spike protein that efficiently elicits neutralizing antibodies. *J. Virol.* **87**, 9379–9383 (2013).
10. S. S. Al-amri, A. T. Abbas, L. A. Siddiq, A. Alghamdi, M. A. Sanki, M. K. Al-Muhanna, R. Y. Alhabbab, E. I. Azhar, X. Li, A. M. Hashem, Immunogenicity of candidate MERS-CoV DNA vaccines based on the spike protein. *Sci. Rep.* **7**, 44875 (2017).
11. Y. Li, Y. Wan, P. Liu, J. Zhao, G. Lu, J. Qi, Q. Wang, X. Lu, Y. Wu, W. Liu, B. Zhang, K.-Y. Yuen, S. Perlman, G. F. Gao, J. Yan, A humanized neutralizing antibody against MERS-CoV targeting the receptor-binding domain of the spike protein. *Cell Res.* **25**, 1237–1249 (2015).
12. L. Jiang, N. Wang, T. Zuo, X. Shi, K.-M. V. Poon, Y. Wu, F. Gao, D. Li, R. Wang, J. Guo, L. Fu, K.-Y. Yuen, B.-J. Zheng, X. Wang, L. Zhang, Potent neutralization of MERS-CoV by human neutralizing monoclonal antibodies to the viral spike glycoprotein. *Sci. Transl. Med.* **6**, 234ra59 (2014).
13. A. S. Agrawal, T. Ying, X. Tao, T. Garron, A. Algaissi, Y. Wang, L. Wang, B.-H. Peng, S. Jiang, D. S. Dimitrov, C.-T. K. Tseng, Passive transfer of a germline-like neutralizing human monoclonal antibody protects transgenic mice against lethal Middle East respiratory syndrome coronavirus infection. *Sci. Rep.* **6**, 31629 (2016).
14. X. Yu, S. Zhang, L. Jiang, Y. Cui, D. Li, D. Wang, N. Wang, L. Fu, X. Shi, Z. Li, L. Zhang, X. Wang, Structural basis for the neutralization of MERS-CoV by a human monoclonal antibody MERS-27. *Sci. Rep.* **5**, 13133 (2015).
15. P. Chames, M. Van Regenmortel, E. Weiss, D. Baty, Therapeutic antibodies: Successes, limitations and hopes for the future. *Br. J. Pharmacol.* **157**, 220–233 (2009).
16. O. Spadiut, S. Capone, F. Krainer, A. Glieder, C. Herwig, Microbials for the production of monoclonal antibodies and antibody fragments. *Trends Biotechnol.* **32**, 54–60 (2014).
17. V. Irani, A. J. Guy, D. Andrew, J. G. Beeson, P. A. Ramsland, J. S. Richards, Molecular properties of human IgG subclasses and their implications for designing therapeutic monoclonal antibodies against infectious diseases. *Mol. Immunol.* **67**, 171–182 (2015).
18. C. Hamers-Casterman, T. Atarhouch, S. Muyldermans, G. Robinson, C. Hamers, E. B. Songa, N. Bendahman, R. Hammers, Naturally occurring antibodies devoid of light chains. *Nature* **363**, 446–448 (1993).
19. S. Muyldermans, Nanobodies: Natural single-domain antibodies. *Annu. Rev. Biochem.* **82**, 775–797 (2013).
20. E. De Genst, K. Silence, K. Decanniere, K. Conrath, R. Loris, J. Kinne, S. Muyldermans, L. Wyns, Molecular basis for the preferential cleft recognition by dromedary heavy-chain antibodies. *Proc. Natl. Acad. Sci. U.S.A.* **103**, 4586–4591 (2006).
21. U. Rothbauer, K. Zolghadr, S. Tillib, D. Nowak, L. Schermelleh, A. Gahl, N. Backmann, K. Conrath, S. Muyldermans, M. C. Cardoso, H. Leonhardt, Targeting and tracing antigens in live cells with fluorescent nanobodies. *Nat. Methods* **3**, 887–889 (2006).
22. G. Hassanzadeh-Ghassabeh, N. Devoogdt, P. De Pauw, C. Vincke, S. Muyldermans, Nanobodies and their potential applications. *Nanomedicine* **8**, 1013–1026 (2013).
23. F. Pevyandi, M. Scully, J. A. Kremer Hovinga, S. Caatland, P. Knöbl, H. Wu, A. Artoni, J. P. Westwood, M. Mansouri Taleghani, B. Jilma, F. Callewaert, H. Ulrichts, C. Duby, D. Tersago; TITAN Investigators, Caplacizumab for acquired thrombotic thrombocytopenic purpura. *N. Engl. J. Med.* **374**, 511–522 (2016).

24. P. Vanlandschoot, C. Stortelers, E. Beirnaert, L. I. Ibañez, B. Schepens, E. Depla, X. Saelens, Nanobodies<sup>®</sup>: New ammunition to battle viruses. *Antiviral Res.* **92**, 389–407 (2011).
25. E. A. B. A. Farag, C. B. E. M. Reusken, B. L. Haagmans, K. A. Mohran, V. Stalin Raj, S. D. Pas, J. Voermans, S. L. Smits, G.-J. Godeke, M. M. Al-Hajri, F. H. Alhajri, H. E. Al-Romaihi, H. Ghobashy, M. M. El-Maghraby, A. M. El-Sayed, M. H. J. Al Thani, S. Al-Marri, M. P. G. Koopmans, High proportion of MERS-CoV shedding dromedaries at slaughterhouse with a potential epidemiological link to human cases, Qatar 2014. *Infect. Ecol. Epidemiol.* **5**, 28305 (2015).
26. C. B. E. M. Reusken, B. L. Haagmans, M. A. Müller, C. Gutierrez, G.-J. Godeke, B. Meyer, D. Muth, V. Stalin Raj, L. Smits-De Vries, V. M. Corman, J.-F. Drexler, S. L. Smits, Y. E. El Tahir, R. De Sousa, J. van Beek, N. Nowotny, K. van Maanen, E. Hidalgo-Hermoso, M. P. G. Koopmans, Middle East respiratory syndrome coronavirus neutralising serum antibodies in dromedary camels: A comparative serological study. *Lancet Infect. Dis.* **13**, 859–866 (2013).
27. M. A. Müller, V. M. Corman, J. Jores, B. Meyer, M. Younan, A. M. Lijander, B.-J. Bosch, E. Lattwein, M. Hilali, B. E. Musa, S. Bornstein, S. S. Park, MERS coronavirus neutralizing antibodies in camels, Eastern Africa, 1983–1997. *Emerg. Infect. Dis.* **20**, 2093–2095 (2014).
28. B. L. Haagmans, J. M. A. van den Brand, V. Stalin Raj, A. Volz, P. Wohlsein, S. L. Smits, D. Schipper, T. M. Bestebroer, N. Okba, R. Fux, A. Bensaid, D. S. Foz, T. Kuiken, W. Baumgärtner, J. Segalés, G. Sutter, A. D. M. E. Osterhaus, An orthopoxvirus-based vaccine reduces virus excretion after MERS-CoV infection in dromedary camels. *Science* **351**, 77–81 (2016).
29. E. Pardon, T. Laeremans, S. Triest, S. G. F. Rasmussen, A. Wohlkönig, A. Ruf, S. Muyldermans, W. G. J. Hol, B. K. Koblick, J. Steyaert, A general protocol for the generation of nanobodies for structural biology. *Nat. Protoc.* **9**, 674–693 (2014).
30. G. Hassanzadeh-Ghassabeh, D. Saerens, S. Muyldermans, in *Nanoproteomics*, S. A. Toms, R. J. Weil, Eds. (Humana Press, 2011), vol. 790, pp. 239–259.
31. R. Chakravarty, S. Goel, W. Cai, Nanobody: The “magic bullet” for molecular imaging? *Theranostics* **4**, 386–398 (2014).
32. N. Wang, X. Shi, L. Jiang, S. Zhang, D. Wang, P. Tong, D. Guo, L. Fu, Y. Cui, X. Liu, K. C. Arledge, Y.-H. Chen, L. Zhang, X. Wang, Structure of MERS-CoV spike receptor-binding domain complexed with human receptor DPP4. *Cell Res.* **23**, 986–993 (2013).
33. G. Lu, Y. Hu, Q. Wang, J. Qi, F. Gao, Y. Li, Y. Zhang, W. Zhang, Y. Yuan, J. Bao, B. Zhang, Y. Shi, J. Yan, G. F. Gao, Molecular basis of binding between novel human coronavirus MERS-CoV and its receptor CD26. *Nature* **500**, 227–231 (2013).
34. K. Li, C. Wohlford-Lenane, S. Perlman, J. Zhao, A. K. Jewell, L. R. Reznikov, K. N. Gibson-Corley, D. K. Meyerholz, P. B. McCray Jr., Middle East respiratory syndrome coronavirus causes multiple organ damage and lethal disease in mice transgenic for human dipeptidyl peptidase 4. *J. Infect. Dis.* **213**, 712–722 (2016).
35. F. I. Schmidt, L. Hanke, B. Morin, R. Brewer, V. Brusica, S. P. J. Whelan, H. L. Ploegh, Phenotypic lentivirus screens to identify functional single domain antibodies. *Nat. Microbiol.* **1**, 16080 (2016).
36. B. L. Haagmans, S. H. S. Al Dhahiry, C. B. E. M. Reusken, V. Stalin Raj, M. Galiano, R. Myers, G.-J. Godeke, M. Jonges, B. Farag, A. Diab, H. Ghobashy, F. Alhajri, M. Al-Thani, S. A. Al-Marri, H. E. Al Romaihi, A. A. Khal, A. Bermingham, A. D. M. E. Osterhaus, M. P. G. Koopmans, Middle East respiratory syndrome coronavirus in dromedary camels: An outbreak investigation. *Lancet Infect. Dis.* **14**, 140–145 (2014).
37. A. Radbruch, G. Muehlinghaus, E. O. Luger, A. Inamine, K. G. C. Smith, T. Dörner, F. Hiepe, Competence and competition: The challenge of becoming a long-lived plasma cell. *Nat. Rev. Immunol.* **6**, 741–750 (2006).
38. J. I. Ellyard, D. T. Avery, T. G. Phan, N. J. Hare, P. D. Hodgkin, S. G. Tangye, Antigen-selected, immunoglobulin-secreting cells persist in human spleen and bone marrow. *Blood* **103**, 3805–3812 (2004).
39. E. Paramithiotis, M. D. Cooper, Memory B lymphocytes migrate to bone marrow in humans. *Proc. Natl. Acad. Sci. U.S.A.* **94**, 208–212 (1997).
40. R. A. Manz, A. E. Hauser, F. Hiepe, A. Radbruch, Maintenance of serum antibody levels. *Annu. Rev. Immunol.* **23**, 367–386 (2005).
41. V. K. Nguyen, R. Hamers, L. Wyns, S. Muyldermans, Camel heavy-chain antibodies: Diverse germline *V<sub>H</sub>H* and specific mechanisms enlarge the antigen-binding repertoire. *EMBO J.* **19**, 921–930 (2000).
42. T. Ying, L. Du, T. W. Ju, P. Prabakaran, C. C. Y. Lau, L. Lu, Q. Liu, L. Wang, Y. Feng, Y. Wang, B.-J. Zheng, K.-Y. Yuen, S. Jiang, D. S. Dimitrov, Exceptionally potent neutralization of Middle East respiratory syndrome coronavirus by human monoclonal antibodies. *J. Virol.* **88**, 7796–7805 (2014).
43. D. Sok, K. M. Le, M. Vadnais, K. L. Saye-Francisco, J. G. Jardine, J. L. Torres, Z. T. Berndsen, L. Kong, R. Stanfield, J. Ruiz, A. Ramos, C.-H. Liang, P. L. Chen, M. F. Criscitiello, W. Mwangi, I. A. Wilson, A. B. Ward, V. V. Smider, D. R. Burton, Rapid elicitation of broadly neutralizing antibodies to HIV by immunization in cows. *Nature* **548**, 108–111 (2017).
44. E. A. F. Simões, J. P. DeVincenzo, M. Boeckh, L. Bont, J. E. Crowe Jr., P. Griffiths, F. G. Hayden, R. L. Hodinka, R. L. Smyth, K. Spencer, S. Thirstrup, E. E. Walsh, R. J. Whitley, Challenges and opportunities in developing respiratory syncytial virus therapeutics. *J. Infect. Dis.* **211** (Suppl. 1), S1–S20 (2015).
45. F. Song, R. Fux, L. B. Provacica, A. Volz, M. Eickmann, S. Becker, A. D. M. E. Osterhaus, B. L. Haagmans, G. Sutter, Middle East respiratory syndrome coronavirus spike protein delivered by modified vaccinia virus Ankara efficiently induces virus-neutralizing antibodies. *J. Virol.* **87**, 11950–11954 (2013).
46. V. S. Raj, M. M. Lamers, S. L. Smits, J. A. A. Demmers, H. Mou, B.-J. Bosch, B. L. Haagmans, in *Coronaviruses*, H. J. Maier, E. Bickerton, P. Britton, Eds. (Springer New York, 2015), vol. 1282, pp. 165–182.
47. H. Nakabayashi, K. Taketa, K. Miyano, T. Yamane, J. Sato, Growth of human hepatoma cells lines with differentiated functions in chemically defined medium. *Cancer Res.* **42**, 3858–3863 (1982).
48. S. van Boheemen, M. de Graaf, C. Lauber, T. M. Bestebroer, V. Stalin Raj, A. M. Zaki, A. D. M. E. Osterhaus, B. L. Haagmans, A. E. Gorbalenya, E. J. Snijder, R. A. M. Fouchier, Genomic characterization of a newly discovered coronavirus associated with acute respiratory distress syndrome in humans. *mBio* **3**, e00473-12 (2012).
49. S. L. Smits, A. de Lang, J. M. A. van den Brand, L. M. Leijten, W. F. van Ijcken, M. J. C. Eijkemans, G. vanAmerongen, T. Kuiken, A. C. Andeweg, A. D. M. E. Osterhaus, B. L. Haagmans, Exacerbated innate host response to SARS-CoV in aged non-human primates. *PLOS Pathog.* **6**, e1000756 (2010).
50. F. J. van Kuppeveld, J. T. van der Logt, A. F. Angulo, M. J. van Zoest, W. G. Quint, H. G. Niesters, J. M. Galama, W. J. Melchers, Genus- and species-specific identification of mycoplasmas by 16S rRNA amplification. *Appl. Environ. Microbiol.* **58**, 2606–2615 (1992).
51. B. L. Haagmans, J. M. A. van den Brand, L. B. Provacica, V. Stalin Raj, K. J. Stittelaar, S. Getu, L. de Waal, T. M. Bestebroer, G. van Amerongen, G. M. G. M. Verjans, R. A. M. Fouchier, S. L. Smits, T. Kuiken, A. D. M. E. Osterhaus, Asymptomatic Middle East respiratory syndrome coronavirus infection in rabbits. *J. Virol.* **89**, 6131–6135 (2015).
52. Y. N. Abdiche, D. S. Malashock, A. Pinkerton, J. Pons, Exploring blocking assays using Octet, ProteOn, and Biacore biosensors. *Anal. Biochem.* **386**, 172–180 (2009).

**Acknowledgments:** We thank C. Vincke (Vrije Universiteit Brussel, Belgium) for providing the pMES4 plasmid and *E. coli* strain WK6 used to produce VHHs. We thank G. van Cappellen (Erasmus MC Optical Imaging Centre) for obtaining 96-well confocal pictures. We also thank the technical assistance of D. Solanes, X. Abad, I. Cordón, and all the animal caretakers from the CReSA BSL-3 animal facilities during the dromedary experiment. Evaluation of the protection of K18 mice was performed in CISA-INIA (Centro de Investigación en Sanidad Animal – Instituto de Tecnología Agraria y Alimentaria, Madrid, Spain). **Funding:** This study was financed by a grant from the Zoonotic Anticipation and Preparedness Initiative [ZAPI project; Innovative Medicines Initiative (IMI) grant agreement no. 115760], with the assistance and financial support of IMI and the European Commission, and in-kind contributions from European Federation of Pharmaceutical Industries and Associations partners. A part of the study was supported by the European Virus Archive Goes Global project, which received a grant from the European Union Horizon 2020 Framework Program for Research and Innovation (653316) and grants from the Ministry of Science and Innovation of Spain (Bio2016-75549-R AEI/FEDER, UE) and NIH (2P01AIO60699). **Author contributions:** V.S.R. and B.L.H. designed and coordinated the study. V.S.R., N.M.A.O., J.G.-A., D.D., B.v.D., W.W., M.M.L., I.W., R.F.-D., I.S., B.J.B., L.E., and B.L.H. performed laboratory experiments and analysis. A.B. and J.S. performed the camel experiments and obtained bone marrow samples. M.P.K. and A.D.M.E.O. supervised part of the experiments. V.S.R., N.M.A.O., and B.L.H. wrote the manuscript with comments from all authors. **Competing interests:** V.S.R., B.J.B., A.D.M.E.O., and B.L.H. are inventors on a patent application on MERS-CoV held by Erasmus MC (application no. 61/704,531, filed 23 September 2012, publication no. WO 2014/045254 A2). A.D.M.E.O. is the chief scientific officer of Viroclinics Biosciences BV. A.D.M.E.O. holds certificates of shares in Viroclinics Biosciences B.V. The authors declare no other competing interests. **Data and materials availability:** All data needed to evaluate the conclusions in the paper are present in the paper and/or the Supplementary Materials. The nucleotide sequences of the VHHs reported in this paper have been deposited in GenBank under accession numbers KX278382 to KX278416. The VHH-83 and HCAb-83 can be provided by EVAg pending scientific review and a completed material transfer agreement. Requests should be submitted on the EVAg website ([www.european-virus-archive.com/](http://www.european-virus-archive.com/)).

Submitted 29 January 2018

Accepted 1 July 2018

Published 8 August 2018

10.1126/sciadv.aas9667

**Citation:** V. Stalin Raj, N. M. A. Okba, J. Gutierrez-Alvarez, D. Drabek, B. van Dieren, W. Widagdo, M. M. Lamers, I. Widjaja, R. Fernandez-Delgado, I. Sola, A. Bensaid, M. P. Koopmans, J. Segalés, A. D. M. E. Osterhaus, B. J. Bosch, L. Enjuanes, B. L. Haagmans, Chimeric camel/human heavy-chain antibodies protect against MERS-CoV infection. *Sci. Adv.* **4**, eaas9667 (2018).

## VIROLOGY

# Genetic and structural insights into broad neutralization of hepatitis C virus by human $V_H1-69$ antibodies

Netanel Tzarum<sup>1</sup>, Erick Giang<sup>2</sup>, Leopold Kong<sup>1</sup>, Linling He<sup>2</sup>, Jannick Prentoe<sup>3</sup>, Elias Augestad<sup>3</sup>, Yuanzi Hua<sup>1</sup>, Shaun Castillo<sup>2</sup>, Georg M. Lauer<sup>4</sup>, Jens Bukh<sup>3</sup>, Jiang Zhu<sup>1,2\*</sup>, Ian A. Wilson<sup>1,5\*</sup>, Mansun Law<sup>2\*</sup>

An effective vaccine to the antigenically diverse hepatitis C virus (HCV) must target conserved immune epitopes. Here, we investigate cross-neutralization of HCV genotypes by broadly neutralizing antibodies (bNAbs) encoded by the relatively abundant human gene family  $V_H1-69$ . We have deciphered the molecular requirements for cross-neutralization by this unique class of human antibodies from crystal structures of HCV E2 in complex with bNAbs. An unusually high binding affinity is found for germ line-reverted versions of  $V_H1-69$  precursor antibodies, and neutralization breadth is acquired during affinity maturation. Deep sequencing analysis of an HCV-immune B cell repertoire further demonstrates the importance of the  $V_H1-69$  gene family in the generation of HCV bNAbs. This study therefore provides critical insights into immune recognition of HCV with important implications for rational vaccine design.

## INTRODUCTION

A prophylactic vaccine will be crucial for controlling the worldwide hepatitis C virus (HCV) epidemic. HCV infects an estimated 1 to 2% of the world population, leading to 400,000 deaths annually (1), and is a major cause of liver failure and hepatocellular carcinoma. Recent advances have been made in the treatment of patients with persistent HCV infection using direct-acting antiviral (DAA) therapies (2, 3). However, an effective HCV vaccine is still much needed because of the increase in new infections and the poor awareness of carriers, especially in developing countries and among marginalized populations (4, 5). Despite successful DAA treatment, patients with advanced liver disease remain at risk of liver cancer (6–8).

A major roadblock for HCV vaccine development is the genetic diversity of HCV, as demonstrated by 7 major HCV genotypes and more than 80 subtypes (9, 10). Therefore, an effective vaccine must induce robust immune responses against a wide spectrum of HCV variants. The E2 envelope glycoprotein mediates viral entry by binding the CD81 receptor and other host factors (11–13). The receptor binding site on E2 is likely surface exposed and structurally conserved, thereby presenting a highly desirable target for broadly neutralizing antibodies (bNAbs) known as the neutralizing face of E2. Similar to the HIV-1 envelope glycoprotein, HCV E2 is extensively covered by N-linked glycans (14) and has several variable regions (VRs), particularly hypervariable region 1 (HVR1), which shield conserved epitopes and assist in viral escape from NAbs (Fig. 1A) (9, 15).

Previously, we isolated a panel of human monoclonal Abs (mAbs) that recognize five distinct antigenic regions (ARs; AR1–5) on the HCV E1E2 glycoprotein complex (16, 17). While mAbs targeting AR1 and AR2 showed limited neutralizing activity, mAbs recognizing AR3 (AR3A–D) exhibit cross-genotype neutralization and inhibition of CD81 receptor binding to E1E2 (16, 17). The heavy chains (HCs) of AR3A–D share a similar genetic background and are derived from Ab precursors of the  $V_H1-69$  gene family that have been reported to be associated with cross-neutralization of HCV (16–19), influenza virus (20–24), and HIV-1 (25). Recently, two independent studies reported bNAbs isolated from patients that spontaneously cleared HCV and are also derived from  $V_H1-69$  genes and target AR3 (26, 27). These findings underscore the role of human  $V_H1-69$  Abs in combatting HCV infections and highlight the potential benefits of eliciting  $V_H1-69$ -derived bNAbs by vaccination.

## RESULTS

Here, we investigate how  $V_H1-69$  bNAbs achieve cross-genotype recognition of the E2 neutralizing face and the genetic requirements for the immune system to generate such bNAbs. To overcome the inherent flexibility of E2 (28), we designed an E2 core domain construct (29) of the prototypic genotype 1a isolate, H77, and determined its crystal structure with bNAbs AR3C (Fig. 1B and fig. S1A) (29). In parallel, Khan *et al.* (30) reported the crystal structure of a different E2 core construct derived from a genotype 2a isolate, J6, with nonneutralizing mAb 2A12. Structural analysis of H77 E2c in complex with AR3C Fab and alanine scanning mutagenesis (16, 29, 31) mapped AR3 to the E2 front layer and part of the CD81 binding loop (amino acids 426 to 443 and 529 to 531; Fig. 1A and fig. S1). Most residues in AR3 are highly conserved among HCV genotypes (fig. S1C and table S1). Negative-stain electron microscopy revealed that in soluble E2, AR3 is exposed on the surface and not masked by the glycan shield or by VRs 1 to 3 (VR1–3; Fig. 1B) (29). To examine the accessibility of the AR3 neutralizing epitopes in soluble E2, we investigated binding of four AR3-directed mAbs

<sup>1</sup>Department of Integrative Structural and Computational Biology, The Scripps Research Institute, La Jolla, CA 92037, USA. <sup>2</sup>Department of Immunology and Microbiology, The Scripps Research Institute, La Jolla, CA 92037, USA. <sup>3</sup>Copenhagen Hepatitis C Program (CO-HEP), Department of Infectious Diseases, Hvidovre Hospital, and Department of Immunology and Microbiology, Faculty of Health and Medical Sciences, University of Copenhagen, Copenhagen, Denmark. <sup>4</sup>Gastrointestinal Unit and Liver Center, Massachusetts General Hospital and Harvard Medical School, Boston, MA 02114, USA. <sup>5</sup>Skaggs Institute for Chemical Biology, The Scripps Research Institute, La Jolla, CA 92037, USA.

\*Corresponding author. Email: mlaw@scripps.edu (M.L.); wilson@scripps.edu (I.A.W.); jiang@scripps.edu (J.Z.)



AR3A–D to genotype 1a H77 E2 ectodomain (E2 $\Delta$ TM), E2c, and E2c3 [E2c with VR3 deleted (28)] (fig. S2A). Nanomolar binding ( $K_D$ ) for all three E2 constructs indicates that mAb recognition of AR3 is not dependent on the VRs (Fig. 1C and fig. S2B), whereas a notable reduction was observed in AR1A binding to E2c and E2c3 (Fig. 1C and fig. S2B) (16). Modeling of Man<sub>6</sub>GlcNac<sub>2</sub> N-linked glycans onto the E2 glycosylation sites reveals that AR3 itself is devoid of glycans, although encircled by three glycans (N423, N430, and N532; Fig. 1, A and B, and fig. S1B). Removal of the E2c glycans by EndoH treatment had negligible effect on bNAb binding, confirming that the glycans are not essential for high binding affinity of the AR3 mAbs and, in soluble E2, the AR3 epitopes are not shielded by glycans (Fig. 1C and fig. S2B). In contrast, AR1A binding was reduced by EndoH treatment, suggesting that the glycans are essential for AR1A binding (Fig. 1C and fig. S2B).

Having established AR3 as a key site for HCV neutralization, we extended our structural efforts here to E2c constructs derived from other genotypes (see fig. S3A). The AR3A–D mAbs have cross-genotype binding activity (fig. S3B) that can be used to study the neutralizing face of E2. In addition, AR3A–C mAbs exhibited neutralization breadth among genotypes 1 to 6 strains, whereas AR3D had a more restricted breadth in virus neutralization assays (Fig. 1D and fig. S3C). Crystallization trials of E2c from different genotypes with AR3A–D Fabs resulted in diffraction-quality crystals for E2c3 of the HK6a isolate as complexes with AR3A, AR3B, and AR3D (table S2 and see also Materials and methods). The HK6a E1E2 glycoprotein complex has been shown to be fully functional in vitro [HCV pseudotype particle (HCVpp) and cell culture HCV (HCVcc) systems] and in vivo (chimpanzee and human liver chimeric mouse models). The HK6a E2c3 structures (fig. S4A) revealed that the overall fold is similar to genotypes 1a H77 E2c (29) and 2a J6 E2 core (30), with C $\alpha$  root mean square deviations of 1.09 and 0.86 Å, respectively (for amino acids 491 to 645, using E2c3 from the AR3A complex as representative of the HK6a E2 structures). However, substantial conformational differences were observed in the  $\beta$  sandwich loop connecting  $\beta$ 6 and  $\beta$ 7 (amino acids 540 to 552; fig. S4B) in the VR3 region (fig. S4C) and in the N-terminal part of the back layer (amino acids 564 to 610). Less pronounced differences were seen in the C-terminal part of the back layer (amino acids 629 to 640) and AR3C epitope of H77 E2 (AR3 is absent in the J6 structure; fig. S4B). The  $\beta$ 6– $\beta$ 7 loop of HK6a shows a different conformation compared to H77 and J6, which could result from an N540E substitution that eliminates the seventh N-glycosylation site (N540) that is present in genotypes 1, 2, 4, and 5 but not in genotypes 3 and 6 (figs. S3A and S4, D and E).

Superposition of four E2-AR3 Fab complexes indicates that these Abs bind AR3 with different angles of approach (Fig. 1E) and with their footprints mapped to different but overlapping parts of the antigenic surface (Fig. 1F), consistent with our previous biophysical study indicating flexibility of the E2 front layer and CD81 binding loop (28) (fig. S4F). Analysis of the interactions between the AR3 Fabs and HK6a E2c3, compared to AR3C and H77 E2c (Fig. 1G and fig. S4G), indicates that E2 recognition is mediated mainly by their HCs (29) with few interactions with the LCs. The interaction between HC complementarity-determining regions (CDRs) 1 and 2 with AR3 mainly involves hydrophobic and aromatic side chains, whereas CDRH3 also makes a large number (5 to 8) of main chain—main chain hydrogen bonds with E2 (Fig. 1G and table S3).

It has been shown that V<sub>H</sub>1-69–derived bNAbs against influenza virus and HIV-1 interact with conserved hydrophobic residues in their antigens via hydrophobic residues at the tip of their CDRH2 loops (20–25). Sequence alignment of the V<sub>H</sub>1-69–encoded AR3 mAb HCs indicates a relatively low identity (62 to 73%) for the V<sub>H</sub> region (amino acids 1 to 110; fig. S5A) and even less for the CDR loops (35 to 57%), especially CDRH3 (Fig. 1G). Nevertheless, the CDRH2 tip of AR3A–D mAbs still retains a hydrophobic motif of I/V52-P52a-X53-F54 (X = hydrophobic residue; Fig. 2A), which makes hydrophobic contacts with a highly conserved hydrophobic pocket between the front layer and CD81 binding loop, despite some variations in CDRH2 interactions. The AR3 mAbs have longer than average CDRH3 loops (18 to 22 residues) that interact with a flexible region of the front layer (amino acids 430 to 437; Fig. 1G). Their CDRH3 adopts a  $\beta$  hairpin stabilized by intra-CDR hydrogen bonds and further enhanced by a disulfide between the CDRH3  $\beta$  strands in AR3A and AR3C (fig. S5B). The  $\beta$  hairpin conformations vary depending on CDRH3 length, but the two glycines at its apex contact L427 and W529 (for AR3A–C) of E2 (fig. S5B). Buried surface area (BSA) analysis confirms the indispensable role of the HC (Fig. 2B and fig. S5C). The HC BSA is similar for AR3A, AR3C, and AR3D (648 to 683 Å<sup>2</sup>), but slightly greater for AR3B (797 Å<sup>2</sup>). Structural analysis suggests that the optimal CDRH3 length for the AR3-like bNAbs is 18 to 22 residues, because a shorter loop will likely generate steric clashes with E2, especially with glycans surrounding AR3 (fig. S5D); a longer loop would result in E2 being further away (Fig. 2C), causing a reduction in binding and neutralization breadth, as observed for AR3D mAb (Fig. 1, C and D).

Therefore, we further characterized Abs from an HCV-immune Ab library (16, 17). Within 22 E1E2 HC binding groups, 7 were encoded by the V<sub>H</sub>1-69 germline (GL) gene with CDRH3 loops ranging from 12 to 22 residues (fig. S5E). Abs from groups B (including AR1A) and E have shorter CDRH3s (15 or 12 residues, respectively) and little neutralization activity (16). Notably, CDRH2 of AR1A no longer contains the I/V52-P52a-X53-F54 hydrophobic motif (Fig. 2A). Fabs from group U also target AR3 (17), with a similar CDRH2 hydrophobic motif but a 17-residue CDRH3 (Fig. 2A and fig. S5F); mAb U1 however had limited neutralization breadth (Fig. 1D). A similar reduction was observed when CDRH3 of AR3A was shortened by 1 residue to 17 residues (fig. S5G). Together, the results suggest that a hydrophobic CDRH2 tip and CDRH3 length of 18 to 22 residues capable of forming main-chain hydrogen bonds with the E2 front layer are optimal for broad neutralization by AR3 mAbs (Fig. 2D).

In the HIV field, it is widely acknowledged that maturation of bNAbs from their GL Ab precursors is a long evolutionary process (>2 to 5 years) involving selection for mutations contributing to B cell survival and improved Ab functions. Therefore, an in-depth analysis of how GL precursors recognize their target antigen can provide critical insights into bNAb induction (32). The IMGT V-QUEST program (33) was used to predict GL genes for HC (V<sub>H</sub>, D<sub>H</sub>, and J<sub>H</sub>) and LC (V<sub>L</sub> and J<sub>L</sub>) of AR3A–D mAbs (fig. S6A). The inferred GL precursors (AR3A–D<sub>GL</sub>) and variants with only the V<sub>H</sub> gene reverted (AR3A–D<sub>1-69</sub>) were synthesized. In comparison with anti-HIV bNAbs, AR3 mAbs exhibit relatively low levels of somatic hypermutation (SHM), with identity to the V<sub>H</sub> GL of 84 to 91% and 74 to 84% at the nucleotide and amino acid levels, respectively (Fig. 3A and fig. S6B), similar to that of V<sub>H</sub>1-69 anti-influenza bNAbs (23). Although CDRH2 contains a number of mutations

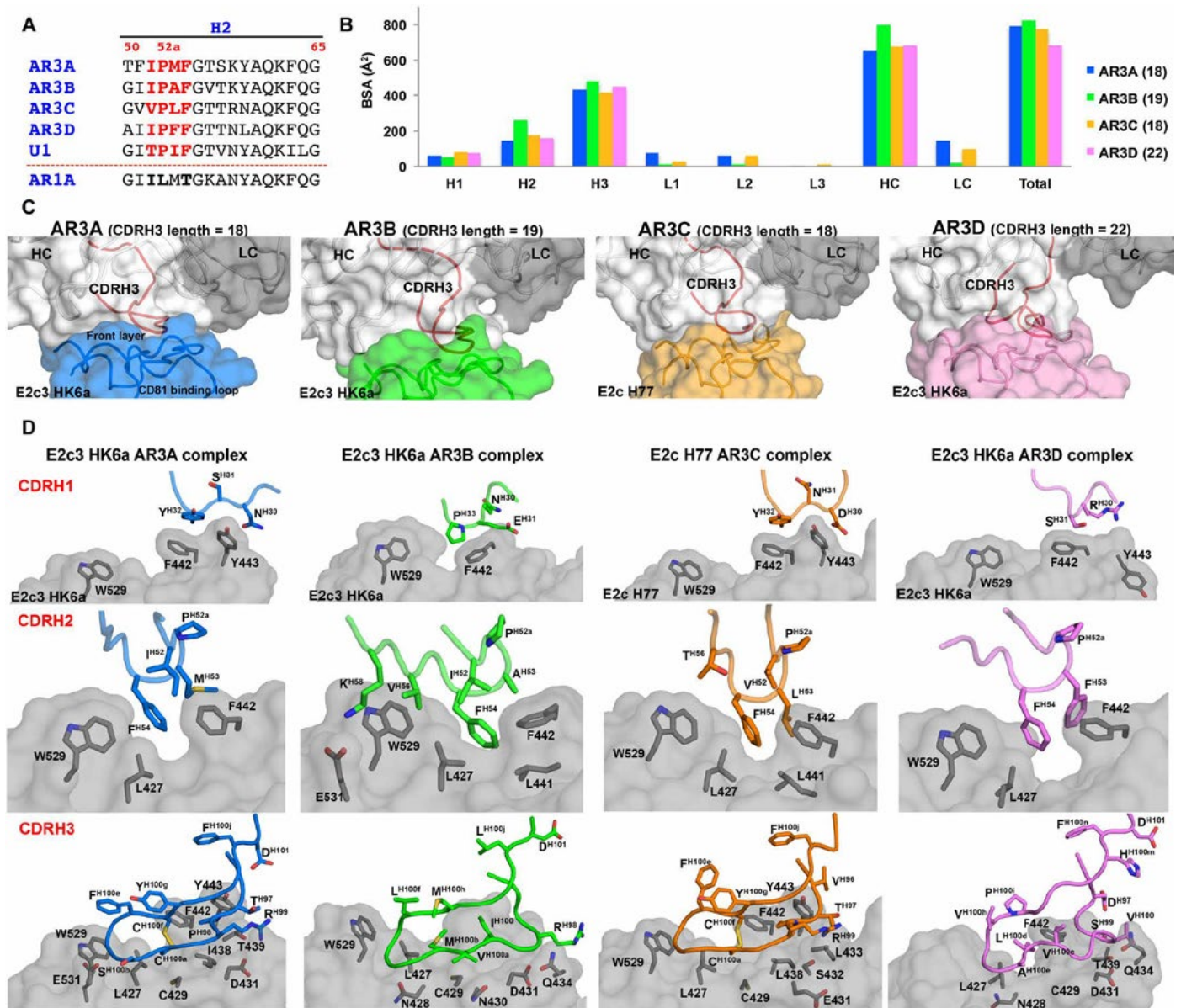


**Fig. 2. Features that enable broad neutralization by AR3 mAbs.** (A) Alignment of the CDRH2 sequences of AR3 bNAbs and mAbs U1 and AR1A. The hydrophobic motif in CDRH2 is highlighted in red. (B) Surface area buried by the CDRs of AR3 mAbs on E2s. CDRH3 length is indicated in brackets. (C) Correlation between CDRH3 length and LC surface area buried. CDRH3 is colored in red. (D) Interactions between E2 and CDRH1-3 of AR3A–D.

(amino acid identity of 64 to 76% with GL), the CDRH2 hydrophobic motif that presumably initiates the interaction with the E2 hydrophobic pocket is conserved from the GL (Fig. 3A). Binding of AR3<sub>GL</sub> and AR3<sub>1-69</sub> IgGs by enzyme-linked immunosorbent assay (ELISA) reveals that AR3A<sub>1-69</sub>, AR3B<sub>1-69</sub>, and AR3C<sub>GL</sub> interact with both H77 E2c and HK6a E2c (fig. S6C). Further quantification using biolayer interferometry for these GL precursors indicated only a 2- to 8-fold decrease in *K<sub>D</sub>* for H77 and 22- to 120-fold for HK6a (Fig. 3B and fig. S6D). AR3A–D<sub>GL</sub> and AR3A–D<sub>1-69</sub> (34) exhibited some neutralization above the 50% level for AR3A<sub>1-69</sub>, AR3A<sub>GL</sub>, and AR3B<sub>1-69</sub>, and more weakly for AR3C<sub>1-69</sub> and AR3C<sub>GL</sub>, mainly against genotypes 5a and 6a (Fig. 3C), suggesting that neutralization breadth was acquired during affinity maturation. Thus,

HCV binding and neutralization can be readily detected in V<sub>H</sub>1-69 precursors.

Our GL reversion analysis and other studies (17, 18, 26) highlight the important role of the V<sub>H</sub>1-69 gene family in E2 recognition and in broad neutralizing responses against HCV. Since the AR3 mAbs were isolated from an HCV-immune phage display Ab library, we used next-generation sequencing (NGS) to characterize enrichment of AR3-like mAbs during panning. The original and three other libraries from panning against native and epitope-masked E1E2 were subjected to NGS, followed by antibodyomics analysis (table S4 and see also Materials and methods). Quantitative library profiles show distinct patterns indicative of rapid enrichment after three panning steps (Pan1 to Pan3) using E1E2 (Fig. 4A). V<sub>H</sub>1 is predominantly

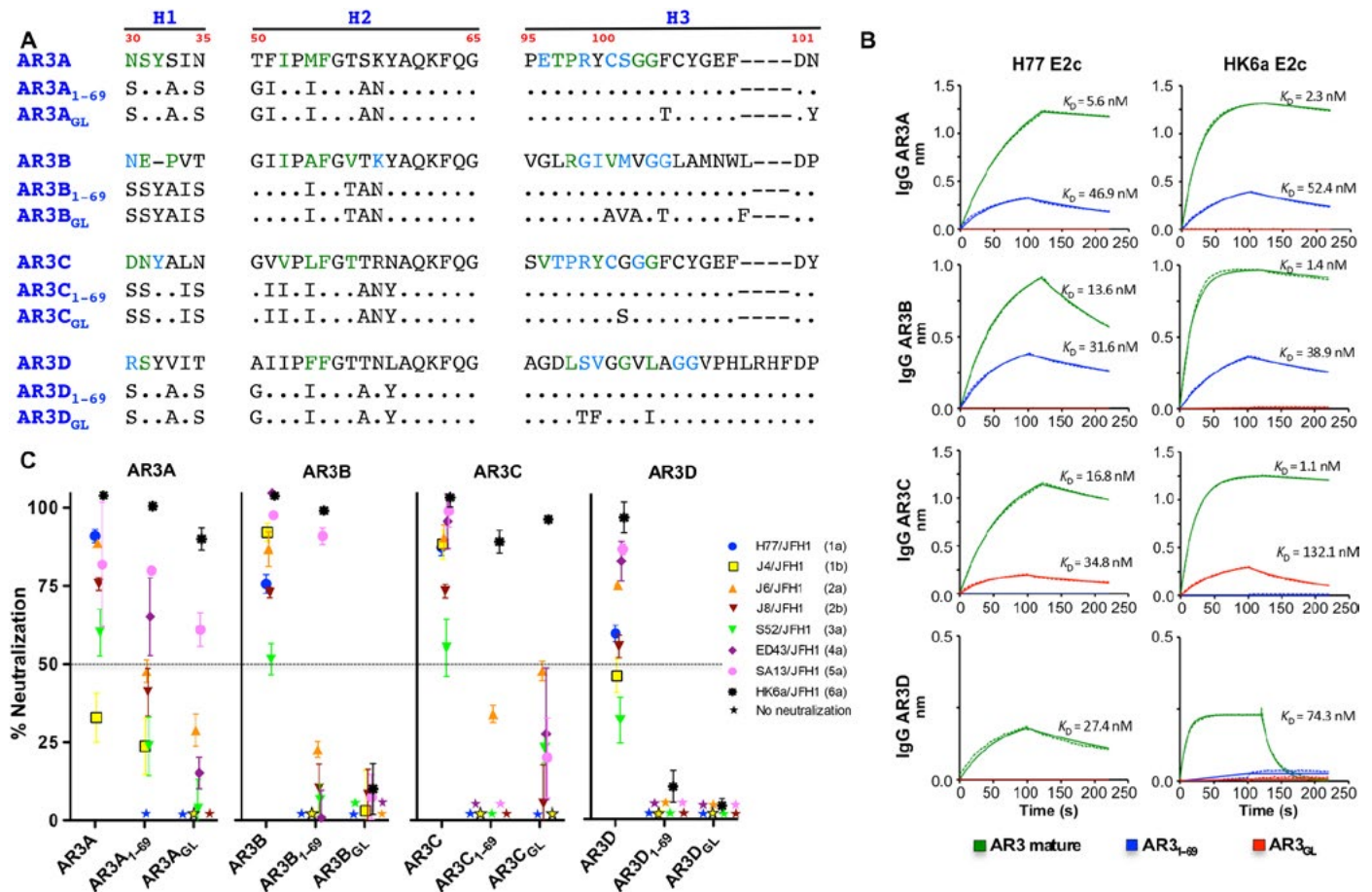


**Fig. 3. The inferred GL of AR3 mAbs. (A)** Alignment of the HC CDRs of AR3, AR3<sub>GL</sub> (inferred GL), and AR3<sub>1-69</sub> (reversion of only the V<sub>H</sub> gene to the V<sub>H</sub>1-69 sequence). The interacting residues in the mature mAbs are colored in blue (hydrogen bonds) and green (hydrophobic interactions). **(B)** Bi-layer interferometry analysis of AR3<sub>1-69</sub> and AR3<sub>GL</sub> IgGs binding to H77 and HK6a E2c. **(C)** Single-dose (50 μg/ml) neutralization assay of AR3<sub>1-69</sub> and AR3<sub>GL</sub> IgGs against the eight HCVcc JFH1-based Core-NS2 recombinants of genotypes 1 to 6. Error bars represent SEM.

selected in the converged Fab library, with V<sub>H</sub>1-69 accounting for 87% of the total V<sub>H</sub> population. A notable shift was observed in SHM, with the peak value increasing from 7–9% to 15–16% in Pan3 (Fig. 4A), and CDRH3 length also increased from 10 to 14 residues to enrichment of 15 to 17 residues (Fig. 4A). Two-dimensional (2D) identity/divergence plots visualize enrichment of AR1–3 mAbs from this Fab library (Fig. 4B and fig. S7A) by showing sequences with CDRH3 identity of 85% or higher (orange dots with number and library percentage labeled). Using AR3C as an example, the 2D plot shows a slow but steady increase of AR3C-like HCs from 0.01% in the prepanning library to 0.5% in the third panning cycle. Similar trends were observed for other AR3 mAbs with long CDRH3s (fig. S7A). By comparison, AR1A shows rapid convergence during antigen selection with a 14,500-fold increase (0.004 to 58%), consistent with the dominant peak of 15-residue CDRH3s (Fig. 4, A and B). In our analysis, HCs with similar CDRH3 loops and low levels of SHM (0 to 10%) that represent intermediate Abs in the library were also identified (Fig. 4B, marked by rectangles, and fig. S7). This provides useful clues as to how these Abs evolved to acquire E1E2 specificity and affinity.

To assess the prevalence of V<sub>H</sub>1-69 AR3 mAbs in comparison to those targeting other E1E2 antigenic sites, we also sequenced the Fab libraries panned with an E1E2 antigen that was masked with AR1

and AR3 Abs (17). HCV-specific mAbs of other GL origins were selected, including the V<sub>H</sub>1-18, V<sub>H</sub>3-30, and V<sub>H</sub>5-51 families, some of which are cross-NABs that recognize AR4 and AR5 on the quaternary E1E2 complex. Other mAb groups include mAbs that bind to epitopes that overlap with AR4 and AR5 (mAbs from groups R1 and S1) and non-cross-NABs that bind to epitopes overlapping with AR1–3 [groups F, I, K, M, and T; for more details, see (17)]. Quantitative library profiles displayed little change in V<sub>H</sub> gene usage, SHM, and CDRH3 length during this epitope-masked panning (fig. S7B), confirming that mAbs AR4A and AR5A, although present in the prepanning library, were only slightly enriched during selection (fig. S7C). Thus, NGS analysis of an HCV-immune Fab library following antigen challenge revealed the prevalence of V<sub>H</sub>1-69-derived Abs targeting AR1 and AR3 of E2, whereas Abs of other GL origins recognize different E1E2 antigenic sites (Fig. 4C).

To investigate whether this V<sub>H</sub>1-69 preference is indeed common to HCV-specific bNABs, we sequenced Ab repertoires of five patients with chronic HCV and compared their repertoires with those from high levels of anti-E1E2 Ab titers and cross-neutralizing activity and compared their repertoires with those from five healthy individuals as controls. Overall, both repertoires displayed similar V<sub>H</sub> gene distributions, with three subjects in each group showing relatively high

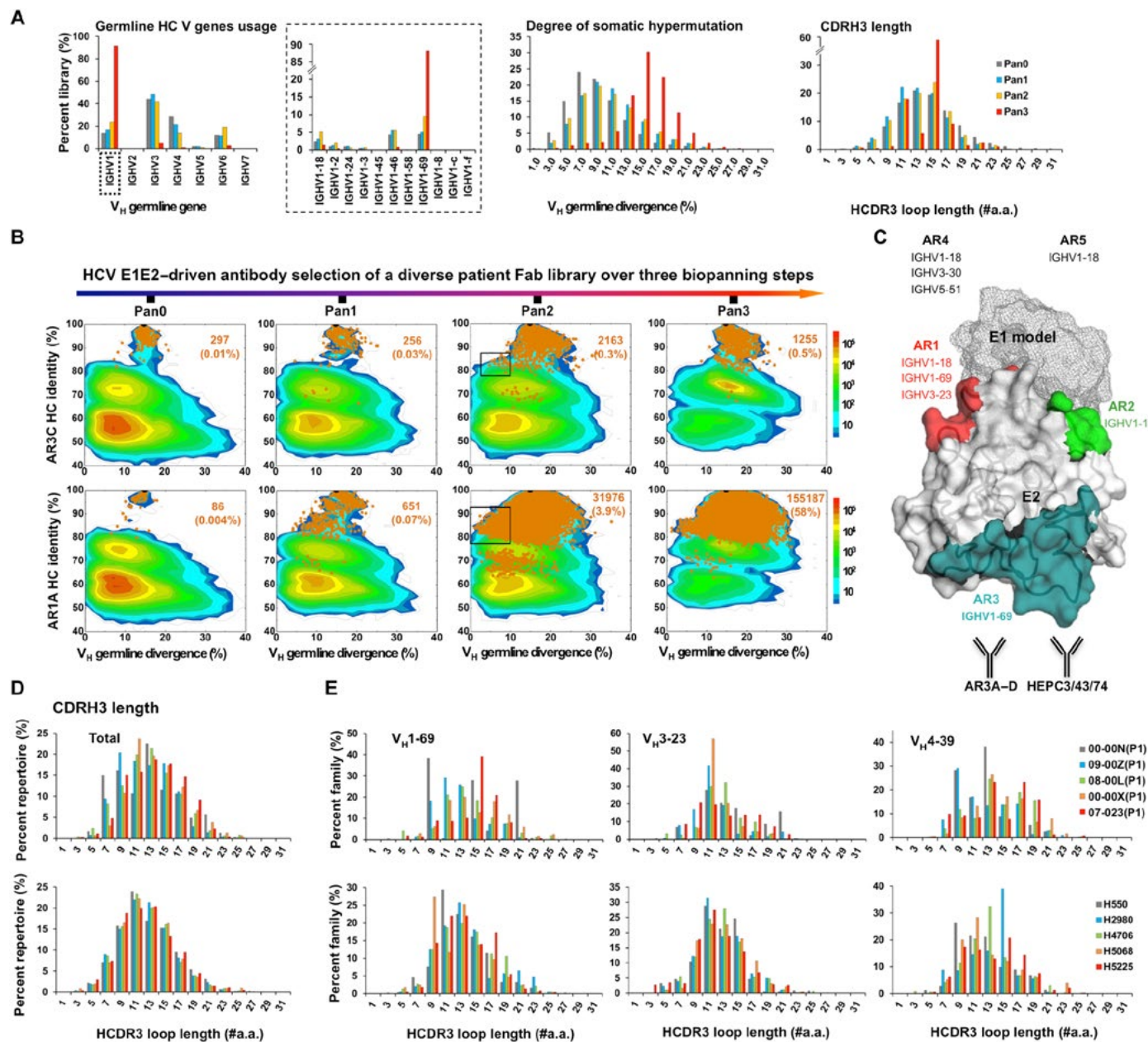


**Fig. 4. Analysis of B cell repertoires of HCV-infected donors.** (A) Quantitative B cell repertoire distribution of HC GL V gene usage, degree of SHM, and CDRH3 length and (B) identity/divergence analysis (to AR mAb/V<sub>H</sub> GL) of the prepanned and panned phage display Ab libraries. #a.a., number of amino acids. The panning experiments were performed using E1E2. (C) Schematic representation of the epitopes and the HC variable genes encoding the AR1–5 mAbs. The AR1–3 epitopes are shown on the E2 structure (16, 17, 31). bNAbs that target the AR3 epitopes are listed. (D) The distribution of CDRH3 length in the total HC GL V genes and (E) the three largest HC GL gene families of five patients with chronic HCV with high anti-E1E2 Ab titers and cross-neutralizing activity (top) and five healthy donors (bottom) as controls.

frequencies of V<sub>H</sub>1-69 (fig. S8A). The HCV-infected donor repertoires exhibit a slightly broader range of CDRH3 lengths than the uninfected controls [normal distribution peaking around 11 to 14 residues (Fig. 4D)], yet with no significant difference for the average length of the HCDR3 loop between the two groups (fig. S10). Further analysis of the three largest V<sub>H</sub> gene families suggests that the distribution of some gene families could be affected by HCV infection (Fig. 4E). In contrast, both HCV-infected and healthy donors exhibit normal CDRH3 length distributions for the V<sub>H</sub>3-23 gene family. Some differences are also observed for other GL gene families (fig. S8B). Comparing the SHM

between the two groups indicates similar distribution of both the HC and LC (fig. S8C). Comparison of the average SHM for the V<sub>H</sub>1-69 gene family and for the overall V<sub>H</sub> repertoire indicates no significant difference between the two groups (fig. S10), although the sample size here is too small for conclusive statistical analysis.

**DISCUSSION**

The Centers for Disease Control and Prevention recently reported an almost threefold increase in the number of new HCV infections

in the United States between 2010 and 2015 (35), a result of the increase in injection drug users caused by the opioid crisis in America (36), underscoring the urgent need for an effective HCV vaccine. The extreme genetic diversity of HCV demands elicitation of cross-genotype immune responses from vaccination. Therefore, structural understanding of bNAb recognition, together with the knowledge on how bNAbs develop from their GL precursors, is essential for the rational design of HCV vaccine immunogens (32, 37). As a main target for bNAbs, AR3 is highly conserved and overlaps with the majority of the E2 neutralizing face (29, 38). It was previously shown that, on native virions, HCV neutralization epitopes are shielded by HVR1 (9, 15) and glycans (39). To overcome the HCV escape by shielding of neutralization epitopes, it is crucial to design an antigen that can elicit a high level of bNAbs to conserved epitopes. Our results indicate that AR3 bNAb recognition of soluble E2 is largely independent of VRs (HVR1, VR2, and VR3) or glycans, highlighting that the AR3 and the neutralizing face are promising targets for inclusion in an HCV vaccine, although a better understanding of the entire E1E2 complex would likely serve to optimize this further.

The E2c structures with bNAbs AR3A–D suggest that flexibility of the front layer facilitates binding of bNAbs encoded by the *V<sub>H1-69</sub>* GL gene family. Other critical features for breadth of AR3-like bNAbs include a hydrophobic CDRH2 tip and CDRH3 of around 18 to 22 residues. The absence of one or more of these features can result in reduced neutralization breadth (as suggested for mAb U1; Fig. 1D). In contrast to HIV-1 (32), some AR3 inferred GL mAbs bind E2 with high affinity, and low to medium SHM is sufficient to neutralize virus, although further somatic mutation can improve breadth. Our results are consistent with a recent study (27), in which AR3-like bNAbs of *V<sub>H1-69</sub>* origin and with similar SHM were isolated from patients with spontaneous viral clearance, suggesting that HCV bNAbs can achieve broad neutralization with rapid lineage development. A possible reason is that the hydrophobic CDRH2 motif that interacts with critical E2 residues for CD81 binding is GL encoded. The tip of the CDRH2 encoded by the *V<sub>H1-69</sub>* gene is the most hydrophobic among the human HC genes (25) and therefore has superiority for targeting the hydrophobic E2 neutralizing face and hydrophobic pockets in the flu hemagglutinin stem region (22, 23). Since most of the interactions of CDRH3 with E2 are main chain—main chain hydrogen bonds, they can tolerate variation in the sequence of the CDRH3 and, therefore, low levels of SHM can be sufficient to optimize the interaction with E2.

While HCV-directed bNAbs can stem from different GL genes, bNAbs encoded by *V<sub>H1-69</sub>* have been reported in multiple studies (16, 18, 26, 27), suggesting an important role of this Ab family in the immune response to HCV. Our analysis revealed that *V<sub>H1-69</sub>* Abs target AR1 and AR3 on E2 when HCV E1E2 was the panning antigen, but significant enrichment of AR1 non-NABs suggests that AR1 may be more accessible in this format. However, other GL gene families are also involved in host Ab response to HCV. For rational vaccine design, a preferable strategy would appear to be developing HCV antigens that present the conserved AR3 neutralizing epitopes to engage the *V<sub>H1-69</sub>* gene family, which is one of the frequent Ab families in the human Ab repertoire. It was recently reported that naïve B cells with high-avidity GL-encoded B cell receptors produce mainly IgM<sup>+</sup> memory B cells following immunization in mice (40). If this is also true in humans, then one may expect that a GL-targeting strategy and E2-based vaccine antigens will trigger the generation of mostly antiviral *V<sub>H1-69</sub>* IgM<sup>+</sup> memory

B cells. Such a strategy should be taken into consideration in HCV vaccine studies. Furthermore, HCV appears to be an excellent model for studying host humoral immunity to viral infection.

## MATERIALS AND METHODS

### Expression and purification of the soluble E2 from genotypes 1 to 6

The DNA constructs of the prototypic isolate H77 (41) for E2c (truncation of N and C termini and VR2 and removal of N448 and N576 glycosylation sites) and E2c3 (additional removal of VR3) were engineered on the basis of the soluble E2 ectodomain (E2ΔTM, amino acids 384 to 717) as previously described (28, 29). On the basis of sequence similarity to H77, E2c constructs of HCV1 (42), CON1 (43), UKN1b12.6 (44), J6 (45), UKN3A1.28c (44), S52 (46), ED43 (47), SA13 (48), and HK6a (34) isolates and the E2c3 constructs of H77, ED43, and HK6a isolates were engineered and synthesized by GeneArt (Invitrogen, USA; fig. S3A). Notably, the E1E2 envelope glycoprotein complex of the HK6a isolate was previously shown to be fully functional in vitro using the HCVpp and HCVcc systems and in vivo in chimpanzee and human liver chimeric mouse models (34, 49, 50). The E2 constructs were expressed and purified as previously described (29).

### Expression and purification of the AR3 IgGs and Fabs

IgGs AR1A, AR3A, AR3B, AR3C, AR3D, and U1 were expressed and purified as previously described (16). The AR3A–D<sub>GL</sub> and AR3A–D<sub>1-69</sub> variable domain genes were synthesized by GeneArt (Invitrogen, USA), cloned into the pIgG vector, and expressed as previously described (16). Fabs AR3C and AR3D were cloned into the phagemid vector pComb3H and transformed into the BL21 (DE3) bacterial strain (Novagen) for expression in the presence of IPTG (isopropyl-β-D-thiogalactopyranoside) overnight at 16°C. The bacterial cells were treated with lysozyme, sonicated, and the Fabs were purified on a protein G affinity column. Fabs AR3A and AR3B were generated from the corresponding IgGs (16) by papain digestion (Sigma-Aldrich). All Fabs were further purified by size exclusion chromatography using a Superdex 200 column (Pharmacia) in 50 mM NaCl, 20 mM tris-HCl (pH 7.2) buffer.

### Crystallization and structural determination of E2c3 HK6a-Fab complexes

From the 10 HCV isolates, only 4 isolates [H77 (1a), J6 (2a), ED43 (4a), and HK6a (6a)] gave high yield and were therefore used for the structural studies. The E2-Fab AR3 complexes were formed by overnight incubation of purified E2 and each AR3 Fab in a molar ratio of 1:1.25 (E2:Fab) at room temperature, followed by size exclusion chromatography (Superdex 200) to remove unbound Fab using 20 mM tris and 50 mM NaCl (pH 7.2) buffer. Crystallization experiments were performed using the vapor diffusion sitting drop method at 20°C. Crystallization experiments of the E2c from the H77, J6, ED43, and HK6a isolates in complex with AR3A–D yielded no crystals. However, further engineering the E2c proteins (E2c3; fig. S2A) resulted in crystals of the HK6a isolate in complexes with AR3A–D (table S2) that diffracted to 2.80, 2.60, and 3.30 Å for the AR3A, AR3B, and AR3D complexes, respectively, and to low resolution (~10 Å) for AR3C complexes. Crystals of the E2c3 HK6a-Fab AR3A complex were obtained using a reservoir solution of 20% (w/v) PEG 3500, 0.2 M sodium citrate (pH 8.2); crystals of E2c3

HK6a-Fab AR3B complex from a reservoir solution of 20% (w/v) PEG 3500, 0.2 M Li chloride (pH 6.7); and crystals of E2c3 HK6a-Fab AR3D complex from a reservoir solution of 20% (w/v) PEG 6000, 0.1 M Hepes (pH 7.0). Prior to data collection, all crystals were cryoprotected with 10% ethylene glycol and flash cooled in liquid nitrogen. Diffraction datasets were collected at the Advanced Photon Source (APS) and the Stanford Synchrotron Radiation Lightsource (SSRL) (table S2). Data were integrated and scaled using HKL2000 (51). The E2c3 HK6a-Fab AR3A structure was solved by molecular replacement method using Phaser (52), with the E2c H77-Fab AR3C (PDB entry 4MWF) as a search model. The E2c3 HK6a-Fab AR3B and E2c3 HK6a-Fab AR3D structures were solved by molecular replacement method using the refined E2c3 HK6a-Fab AR3A structure as a search model. Structure refinement was carried out in Phenix (53), and model building was performed with COOT (54). Final refinement statistics are summarized in table S2.

### Enzyme-linked immunosorbent assay

Purified E2 isolates were coated onto microwells at 5  $\mu\text{g}/\text{ml}$  overnight at 4°C. After blocking with 4% (w/v) nonfat dry milk in dilution buffer (PBS + 0.02% Tween 20) for 30 min, titrated AR3 Abs (purified Ab for fig. S3B and transfected supernatant of Abs from 293T cells for fig. S6C) in dilution buffer with 1% nonfat dry milk were added to the microwells and incubated for 1 hour at room temperature. Titrated Abs were detected with secondary Ab horseradish peroxidase-conjugated goat anti-human IgG Fc (Jackson ImmunoResearch) and developed with 3,3',5,5'-tetramethylbenzidine substrate (Thermo Fisher Pierce). The reaction was stopped with 2 N sulfuric acid, and developed plates were read at absorbance of 450 nm.

### $K_D$ determination

$K_D$  values were determined by biolayer interferometry using an Octet RED instrument (ForteBio Inc.). IgGs at  $\sim 10 \mu\text{g}/\text{ml}$  in a kinetics buffer [1 $\times$  PBS (pH 7.4), 0.01% BSA, and 0.002% Tween 20] were immobilized onto protein G-coated biosensors and incubated with varying concentrations of E2 protein. The  $k_{\text{on}}$  and  $k_{\text{off}}$  values of each E2 protein for each IgG were measured in real time to determine  $K_D$  values. All binding data were collected at 30°C.

### Neutralization assay

In vitro neutralization was carried on Huh7.5 cells using either a single high dose (50  $\mu\text{g}/\text{ml}$ ) or a dilution series of the relevant Ab as previously described (55). Control Ab b6 at the highest dose did not inhibit the viruses. For the dilution series experiments,  $\text{IC}_{50}$  values were calculated in GraphPad Prism 6 using a three-parameter curve fitting.

### Panning of the phage display library

The construction of the phage display Ab library was previously described (16, 17). In summary, RNA of mononuclear cells from the bone marrow of a patient with chronic HCV was extracted, and complementary DNA (cDNA) was synthesized. LC and HC fragments were amplified using gene-specific primers and cloned into phagemid vector with randomized HC and LC pairing. For antigen panning, the Ab Fab fragments were expressed as a fusion protein to the phage coat protein III for surface display. The HCV-immune phage display Ab library was panned for three consecutive rounds with increasing washing stringency in two different panning exper-

iments (16, 17). In the first experiment, recombinant E1E2 proteins captured by *Galanthus nivalis* lectin were used as the panning antigens. In the second experiment, E1E2 antigens captured by mAb AR3A and blocked with mAb AR1B were used (17). In each panning step, antigen was directly coated onto a microtiter plate, followed by blocking with 4% (w/v) milk in PBS. The phage library was added to the wells and incubated for 1 to 2 hours at 37°C, and unbound phages were washed away with PBS/0.5% (v/v) Tween 20. Bound phages were eluted and used to infect freshly grown *Escherichia coli* (XL1-Blue, Stratagene) for titration on LB agar plates with carbenicillin.

### Clinical samples

Normal blood donor samples were procured from the Normal Blood Donor Service (NBDS) of The Scripps Research Institute (TSRI). All healthy donors tested negative for hepatitis B virus, HCV, and HIV (56). Blood samples from patients with HCV with long-term chronic HCV viremia (genotype 1 or genotype 3) were collected at Massachusetts General Hospital. Informed consent was given by all subjects under a protocol approved by the Partners Human Research Committee [Institutional Review Board (IRB) no. 1999P004983]. Peripheral blood mononuclear cells (PBMCs) were extracted by Ficoll-Paque (GE Healthcare Life Sciences) density gradient centrifugation. Plasma samples were evaluated for E1E2-specific Ab by ELISA and for virus neutralizing activity using HCVpp (17). Five HCV<sup>+</sup> donor samples with high cross-neutralizing activity and five random normal blood donor samples were selected for sequencing analysis below.

### NGS and bioinformatics analysis

NGS was performed on the Ion Torrent Personal Genome Machine (PGM) and S5 systems. The HC regions of the Fab phage libraries were amplified from the plasmid stock using PCR with vector-specific primers (tables S4 and S5 and fig. S9). Notably, the forward primer contained a PGM/S5 full-length P1 adaptor, whereas the reverse primer contained a PGM/S5 A adaptor and an Ion Xpress barcode (Life Technologies) to differentiate Fab phage libraries. A total of 25 PCR cycles were performed, and the PCR products with an expected length of 500 to 600 bp were gel purified (Qiagen). The resulting HC libraries were quantitated using the Qubit 2.0 Fluorometer with the Qubit dsDNA HS Assay Kit. The dilution factor required for PGM template preparation was determined such that the final concentration was 50 pM. For the prepanning Fab library (Pan0), template preparation was performed with the Ion PGM Template IA 500 Kit, followed by NGS on the Ion PGM system using the Ion PGM Hi-Q Sequencing Kit and an Ion 316 v2 chip. For the postpanning libraries (Pan1 to Pan3) obtained from two E1E2 panning procedures, template preparation and (Ion 530) chip loading were performed on Ion Chef using the Ion 530 Ext Kit, followed by NGS on the Ion S5 System. For five normal donors and five HCV-infected donors studied here, a previously reported 5'-RACE (rapid amplification of cDNA ends) PCR protocol was used to capture their B cell repertoires in an unbiased manner (table S4) (57). Briefly, total RNA was extracted from 5 to 10 million PBMCs into 30  $\mu\text{l}$  of water with the RNeasy Mini Kit (Qiagen). 5'-RACE was performed with the SMARTer RACE cDNA Amplification Kit (Clontech). The Ig PCRs were set up with the Platinum Taq High-Fidelity DNA Polymerase (Life Technologies) in a total volume of 50  $\mu\text{l}$ , with 5  $\mu\text{l}$  of cDNA as template, 1  $\mu\text{l}$  of 5'-RACE primer, and 1  $\mu\text{l}$

of 10  $\mu$ M reverse primer. The 5'-RACE primer contained a PGM/S5 P1 adaptor, whereas the reverse primer contained a PGM/S5 A adaptor and an Ion Xpress barcode (Life Technologies) to differentiate donor libraries. A similar PCR protocol (25 cycles) was used, and the PCR products with an expected length of 600 bp were gel purified (Qiagen). The Ab HC and LC ( $\kappa$  and  $\lambda$ ) libraries were quantitated using the Qubit 2.0 Fluorometer with the Qubit dsDNA HS Assay Kit and mixed at a ratio of 1:1:1 for each donor. The five donor libraries were further mixed at an equal ratio for template preparation and (Ion 530) chip loading on Ion Chef using the Ion 530 Ext Kit. NGS was performed on the Ion S5 System with default settings. The human antibodyomics pipeline (57–63) was used to process and annotate the NGS data of Fab libraries and Ab repertoires. Notably, a number of methodological modifications have been made to the pipeline to improve data quality (64).

## SUPPLEMENTARY MATERIALS

Supplementary material for this article is available at <http://advances.sciencemag.org/cgi/content/full/5/1/eaav1882/DC1>

Fig. S1. AR3 epitopes.

Fig. S2. Binding of AR3A–D and AR1A IgGs to E2.

Fig. S3. Binding and neutralization of AR3 mAbs to HCV isolates from genotypes 1 to 6.

Fig. S4. Crystal structures of HK6a E2c3 with AR3 Fabs.

Fig. S5. Features that enable broad neutralization by AR3.

Fig. S6. The inferred GL genes of the AR3 mAbs.

Fig. S7. Identity/divergence analysis of the phage display library from an HCV-infected donor.

Fig. S8. B cell repertoire of healthy and HCV-infected donors.

Fig. S9. Primers that were used for amplification of the HC regions of the Fab phage libraries in the different panning steps.

Fig. S10. Summary of the statistic analysis of the NGS of HCV chronically infected and healthy donors.

Table S1. Amino acid sequence variation of the E2 protein of HCV genotypes 1 to 7.

Table S2. Data collection and refinement statistics for HK6a E2c3 AR3 Fab complex structures.

Table S3. Hydrogen bond and hydrophobic interactions between E2 and the HC of AR3 Fabs.

Table S4. NGS of HCV-immune Ab repertoire of an HCV-infected patient.

Table S5. NGS of HCV-immune Ab repertoires.

References (65–68)

## REFERENCES AND NOTES

- Global hepatitis report (2017); [www.who.int/hepatitis/publications/global-hepatitis-report2017/en/](http://www.who.int/hepatitis/publications/global-hepatitis-report2017/en/).
- E. R. Feeney, R. T. Chung, Antiviral treatment of hepatitis C. *BMJ* **348**, g3308 (2014).
- J.-M. Pawlotsky, J. J. Feld, S. Zeuzem, J. H. Hoofnagle, From non-A, non-B hepatitis to hepatitis C virus cure. *J. Hepatol.* **62**, S87–S99 (2015).
- G. L. Armstrong, A. Wasley, E. P. Sismard, G. M. McQuillan, W. L. Kuhnert, M. J. Alter, The prevalence of hepatitis C virus infection in the United States, 1999 through 2002. *Ann. Intern. Med.* **144**, 705–714 (2006).
- M. Thursz, A. Fontanet, HCV transmission in industrialized countries and resource-constrained areas. *Nat. Rev. Gastroenterol. Hepatol.* **11**, 28–35 (2014).
- F. Conti, F. Buonfiglioli, A. Scuteri, C. Crespi, L. Bolondi, P. Caraceni, F. G. Foschi, M. Lenzi, G. Mazzella, G. Verucchi, P. Andreone, S. Brillanti, Early occurrence and recurrence of hepatocellular carcinoma in HCV-related cirrhosis treated with direct-acting antivirals. *J. Hepatol.* **65**, 727–733 (2016).
- M. A. Konerman, A. S. F. Lok, Hepatitis C treatment and barriers to eradication. *Clin. Transl. Gastroenterol.* **7**, e193 (2016).
- S. Pol, Lack of evidence of an effect of direct-acting antivirals on the recurrence of hepatocellular carcinoma: Data from three ANRS cohorts. *J. Hepatol.* **65**, 734–740 (2016).
- J. Prentoe, R. Velázquez-Moctezuma, S. K. H. Fong, M. Law, J. Bukh, Hypervariable region 1 shielding of hepatitis C virus is a main contributor to genotypic differences in neutralization sensitivity. *Hepatology* **64**, 1881–1892 (2016).
- D. B. Smith, P. Becher, J. Bukh, E. A. Gould, G. Meyers, T. Monath, A. S. Muerhoff, A. Pletnev, R. Rico-Hesse, J. T. Stapleton, P. Simmonds, Proposed update to the taxonomy of the genera *Hepacivirus* and *Pegivirus* within the *Flaviviridae* family. *J. Gen. Virol.* **97**, 2894–2907 (2016).
- B. D. Lindenbach, C. M. Rice, The ins and outs of hepatitis C virus entry and assembly. *Nat. Rev. Microbiol.* **11**, 688–700 (2013).
- M. B. Zeisel, D. J. Felmler, T. F. Baumert, Hepatitis C virus entry. *Curr. Top. Microbiol. Immunol.* **369**, 87–112 (2013).
- L. Fénéant, S. Levy, L. Cocquerel, CD81 and hepatitis C virus (HCV) infection. *Viruses* **6**, 535–572 (2014).
- A. Goffard, J. Dubuisson, Glycosylation of hepatitis C virus envelope proteins. *Biochimie* **85**, 295–301 (2003).
- J. Prentoe, L. Verhoye, R. Velázquez-Moctezuma, C. Buysschaert, A. Farhoudi, R. Wang, H. Alter, P. Meuleman, J. Bukh, HVR1-mediated antibody evasion of highly infectious in vivo adapted HCV in humanised mice. *Gut* **65**, 1988–1997 (2016).
- M. Law, T. Maruyama, J. Lewis, E. Giang, A. W. Tarr, Z. Stamatakis, P. Gastaminza, F. V. Chisari, I. M. Jones, R. I. Fox, J. K. Ball, J. A. McKeating, N. M. Kneteman, D. R. Burton, Broadly neutralizing antibodies protect against hepatitis C virus quasispecies challenge. *Nat. Med.* **14**, 25–27 (2008).
- E. Giang, M. Dorner, J. C. Prentoe, M. Dreux, M. J. Evans, J. Bukh, C. M. Rice, A. Ploss, D. R. Burton, M. Law, Human broadly neutralizing antibodies to the envelope glycoprotein complex of hepatitis C virus. *Proc. Natl. Acad. Sci. U.S.A.* **109**, 6205–6210 (2012).
- C. H. Chan, K. G. Hadlock, S. K. H. Fong, S. Levy, *V<sub>H</sub>1-69* gene is preferentially used by hepatitis C virus-associated B cell lymphomas and by normal B cells responding to the E2 viral antigen. *Blood* **97**, 1023–1026 (2001).
- Z.-Y. Keck, J. Xia, Y. Wang, W. Wang, T. Krey, J. Prentoe, T. Carlsen, A. Y.-J. Li, A. H. Patel, S. M. Lemon, J. Bukh, F. A. Rey, S. K. H. Fong, Human monoclonal antibodies to a novel cluster of conformational epitopes on HCV E2 with resistance to neutralization escape in a genotype 2a isolate. *PLOS Pathog.* **8**, e1002653 (2012).
- C. Dreyfus, N. S. Laursen, T. Kwaks, D. Zuijdggeest, R. Khayat, D. C. Ekiert, J. H. Lee, Z. Metlagel, M. V. Bujny, M. Jongeneelen, R. van der Vlugt, M. Lamrani, H. J. W. M. Korse, E. Geelen, Ö. Sahin, M. Sieuwerts, J. P. J. Brakenhoff, R. Vogels, O. T. W. Li, L. M. Poon, M. Peiris, W. Koudstaal, A. B. Ward, I. A. Wilson, J. Goudsmit, R. H. E. Friesen, Highly conserved protective epitopes on influenza B viruses. *Science* **337**, 1343–1348 (2012).
- D. C. Ekiert, G. Bhabha, M.-A. Elsliger, R. H. E. Friesen, M. Jongeneelen, M. Throsby, J. Goudsmit, I. A. Wilson, Antibody recognition of a highly conserved influenza virus epitope. *Science* **324**, 246–251 (2009).
- S. Lang, J. Xie, X. Zhu, N. C. Wu, R. A. Lerner, I. A. Wilson, Antibody 27F3 broadly targets influenza A group 1 and 2 hemagglutinins through a further variation in *V<sub>H</sub>1-69* antibody orientation on the HA stem. *Cell Rep.* **20**, 2935–2943 (2017).
- L. Pappas, M. Foglierini, L. Piccoli, N. L. Kallewaard, F. Turrini, C. Silacci, B. Fernandez-Rodriguez, G. Agatic, I. Giacchetto-Sasselli, G. Pellicciotta, F. Sallusto, Q. Zhu, E. Vicenzi, D. Corti, A. Lanzavecchia, Rapid development of broadly influenza neutralizing antibodies through redundant mutations. *Nature* **516**, 418–422 (2014).
- J. Sui, W. C. Hwang, S. Perez, G. Wei, D. Aird, L.-M. Chen, E. Santelli, B. Stec, G. Cadwell, M. Ali, H. Wan, A. Murakami, A. Yammanuru, T. Han, N. J. Cox, L. A. Bankston, R. O. Donis, R. C. Liddington, W. A. Marasco, Structural and functional bases for broad-spectrum neutralization of avian and human influenza A viruses. *Nat. Struct. Mol. Biol.* **16**, 265–273 (2009).
- C.-C. Huang, M. Venturi, S. Majeed, M. J. Moore, S. Phogat, M.-Y. Zhang, D. S. Dimitrov, W. A. Hendrickson, J. Robinson, J. Sodroski, R. Wyatt, H. Choe, M. Farzan, P. D. Kwong, Structural basis of tyrosine sulfation and *V<sub>H</sub>*-gene usage in antibodies that recognize the HIV type 1 coreceptor-binding site on gp120. *Proc. Natl. Acad. Sci. U.S.A.* **101**, 2706–2711 (2004).
- S. J. Merat, R. Molenkamp, K. Wagner, S. M. Koekkoek, D. van de Berg, E. Yasuda, M. Böhne, Y. B. Claassen, B. P. Grady, M. Prins, A. Q. Bakker, M. D. de Jong, H. Spits, J. Schinkel, T. Beaumont, Hepatitis C virus broadly neutralizing monoclonal antibodies isolated 25 years after spontaneous clearance. *PLOS ONE* **11**, e0165047 (2016).
- J. R. Bailey, A. I. Flyvak, V. J. Cohen, H. Li, L. N. Wasilewski, A. E. Snider, S. Wang, G. H. Learn, N. Kose, L. Loerinc, R. Lampléy, A. L. Cox, J. M. Pfaff, B. J. Doranz, G. M. Shaw, S. C. Ray, J. E. Crowe Jr., Broadly neutralizing antibodies with few somatic mutations and hepatitis C virus clearance. *JCI Insight* **2**, e92872 (2017).
- L. Kong, D. E. Lee, R. U. Kadam, T. Liu, E. Giang, T. Nieuwsma, F. Garces, N. Tzarum, V. L. Woods Jr., A. B. Ward, S. Li, I. A. Wilson, M. Law, Structural flexibility at a major conserved antibody target on hepatitis C virus E2 antigen. *Proc. Natl. Acad. Sci. U.S.A.* **113**, 12768–12773 (2016).
- L. Kong, E. Giang, T. Nieuwsma, R. U. Kadam, K. E. Cogburn, Y. Hua, X. Dai, R. L. Stanfield, D. R. Burton, A. B. Ward, I. A. Wilson, M. Law, Hepatitis C virus E2 envelope glycoprotein core structure. *Science* **342**, 1090–1094 (2013).
- A. G. Khan, J. Whidby, M. T. Miller, H. Scarborough, A. V. Zatorski, A. Cygan, A. A. Price, S. A. Yost, C. D. Bohannon, J. Jacob, A. Grakoui, J. Marcotrigiano, Structure of the core ectodomain of the hepatitis C virus envelope glycoprotein 2. *Nature* **509**, 381–384 (2014).
- R. Gopal, K. Jackson, N. Tzarum, L. Kong, A. Ettenger, J. Guest, J. M. Pfaff, T. Barnes, A. Honda, E. Giang, E. Davidson, I. A. Wilson, B. J. Doranz, M. Law, Probing the antigenicity of hepatitis C virus envelope glycoprotein complex by high-throughput mutagenesis. *PLOS Pathog.* **13**, e1006735 (2017).
- D. R. Burton, L. Hangartner, Broadly neutralizing antibodies to HIV and their role in vaccine design. *Annu. Rev. Immunol.* **34**, 635–659 (2016).

33. M.-P. Lefranc, C. Pommié, M. Ruiz, V. Giudicelli, E. Foulquier, L. Truong, V. Thouvenin-Contet, G. Lefranc, IMGT unique numbering for immunoglobulin and T cell receptor variable domains and Ig superfamily V-like domains. *Dev. Comp. Immunol.* **27**, 55–77 (2003).
34. J. M. Gottwein, T. K. H. Scheel, T. B. Jensen, J. B. Lademann, J. C. Prentoe, M. L. Knudsen, A. M. Hoegh, J. Bukh, Development and characterization of hepatitis C virus genotype 1-7 cell culture systems: Role of CD81 and scavenger receptor class B type I and effect of antiviral drugs. *Hepatology* **49**, 364–377 (2009).
35. Surveillance for Viral Hepatitis – United States 2015 (2017); [www.cdc.gov/hepatitis/statistics/2015surveillance/commentary.htm](http://www.cdc.gov/hepatitis/statistics/2015surveillance/commentary.htm).
36. P. K. Muhuri, J. C. Gfroerer, M. C. Davies, *Associations of Nonmedical Pain Reliever Use and Initiation of Heroin Use in the United States* (Substance Abuse and Mental Health Services Administration, Center for Behavioral Health Statistics and Quality, 2013).
37. G. J. Nabel, Designing tomorrow's vaccines. *N. Engl. J. Med.* **368**, 551–560 (2013).
38. N. Tzarum, I. A. Wilson, M. Law, The neutralizing face of hepatitis C virus E2 envelope glycoprotein. *Front. Immunol.* **9**, 1315 (2018).
39. M. Lavie, X. Hanouille, J. Dubuisson, Glycan shielding and modulation of hepatitis C virus neutralizing antibodies. *Front. Immunol.* **9**, 910 (2018).
40. K. A. Pape, R. W. Maul, T. Dileepan, A. S. Paustian, P. J. Gearhart, M. K. Jenkins, Naive B cells with high-avidity germline-encoded antigen receptors produce persistent IgM<sup>+</sup> and transient IgG<sup>+</sup> memory B cells. *Immunity* **48**, 1135–1143.e4 (2018).
41. A. A. Kolykhalov, E. V. Agapov, K. J. Blight, K. Mihalik, S. M. Feinstone, C. M. Rice, Transmission of hepatitis C by intrahepatic inoculation with transcribed RNA. *Science* **277**, 570–574 (1997).
42. Q. L. Choo, K. H. Richman, J. H. Han, K. Berger, C. Lee, C. Dong, C. Gallegos, D. Coit, R. Medina-Selby, P. J. Barr, Genetic organization and diversity of the hepatitis C virus. *Proc. Natl. Acad. Sci. U.S.A.* **88**, 2451–2455 (1991).
43. V. Lohmann, F. Körner, J.-O. Koch, U. Herian, L. Theilmann, R. Bartenschlager, Replication of subgenomic hepatitis C virus RNAs in a hepatoma cell line. *Science* **285**, 110–113 (1999).
44. D. Lavillette, A. W. Tarr, C. Voisset, P. Donot, B. Bartosch, C. Bain, A. H. Patel, J. Dubuisson, J. K. Ball, F.-L. Cosset, Characterization of host-range and cell entry properties of the major genotypes and subtypes of hepatitis C virus. *Hepatology* **41**, 265–274 (2005).
45. M. Yanagi, R. H. Purcell, S. U. Emerson, J. Bukh, Hepatitis C virus: An infectious molecular clone of a second major genotype (2a) and lack of viability of intertypic 1a and 2a chimeras. *Virology* **262**, 250–263 (1999).
46. J. M. Gottwein, T. K. H. Scheel, B. Callendret, Y.-P. Li, H. B. Eccleston, R. E. Engle, S. Govindarajan, W. Satterfield, R. H. Purcell, C. M. Walker, J. Bukh, Novel infectious cDNA clones of hepatitis C virus genotype 3a (strain 552) and 4a (strain ED43): Genetic analyses and in vivo pathogenesis studies. *J. Virol.* **84**, 5277–5293 (2010).
47. R. W. Chamberlain, N. Adams, A. A. Saeed, P. Simmonds, R. M. Elliott, Complete nucleotide sequence of a type 4 hepatitis C virus variant, the predominant genotype in the Middle East. *J. Gen. Virol.* **78**, 1341–1347 (1997).
48. J. Bukh, C. L. Apgar, R. Engle, S. Govindarajan, P. A. Hegerich, R. Tellier, D. C. Wong, R. Elkins, M. C. Kew, Experimental infection of chimpanzees with hepatitis C virus of genotype 5a: Genetic analysis of the virus and generation of a standardized challenge pool. *J. Infect. Dis.* **178**, 1193–1197 (1998).
49. J. Bukh, P. Meuleman, R. Tellier, R. E. Engle, S. M. Feinstone, G. Eder, W. C. Satterfield, S. Govindarajan, K. Krawczynski, R. H. Miller, G. Leroux-Roels, R. H. Purcell, Challenge pools of hepatitis C virus genotypes 1-6 prototype strains: Replication fitness and pathogenicity in chimpanzees and human liver-chimeric mouse models. *J. Infect. Dis.* **201**, 1381–1389 (2010).
50. J.-C. Meunier, R. E. Engle, K. Faulk, M. Zhao, B. Bartosch, H. Alter, S. U. Emerson, F.-L. Cosset, R. H. Purcell, J. Bukh, Evidence for cross-genotype neutralization of hepatitis C virus pseudo-particles and enhancement of infectivity by apolipoprotein C1. *Proc. Natl. Acad. Sci. U.S.A.* **102**, 4560–4565 (2005).
51. Z. Otwinowski, W. Minor, Processing of X-ray diffraction data collected in oscillation mode. *Methods Enzymol.* **276**, 307–326 (1997).
52. A. J. McCoy, R. W. Grosse-Kunstleve, L. C. Storoni, R. J. Read, Likelihood-enhanced fast translation functions. *Acta Crystallogr. D* **61**, 458–464 (2005).
53. P. D. Adams, R. W. Grosse-Kunstleve, L.-W. Hung, T. R. Ioerger, A. J. McCoy, N. W. Moriarty, R. J. Read, J. C. Sacchettini, N. K. Sauter, T. C. Terwilliger, PHENIX: Building new software for automated crystallographic structure determination. *Acta Crystallogr. D* **58**, 1948–1954 (2002).
54. P. Emsley, K. Cowtan, Coot: Model-building tools for molecular graphics. *Acta Crystallogr. D* **60**, 2126–2132 (2004).
55. R. Velázquez-Moctezuma, M. Law, J. Bukh, J. Prentoe, Applying antibody-sensitive hypervariable region 1-deleted hepatitis C virus to the study of escape pathways of neutralizing human monoclonal antibody AR5A. *PLoS Pathog.* **13**, e1006214 (2017).
56. J. E. Roughan, K. M. Reardon, K. E. Cogburn, H. Quendler, P. J. Pockros, M. Law, Chronic hepatitis C virus infection breaks tolerance and drives polyclonal expansion of autoreactive B cells. *Clin. Vaccine Immunol.* **19**, 1027–1037 (2012).
57. L. He, D. Sok, P. Azadnia, J. Hsueh, E. Landais, M. Simek, W. C. Koff, P. Poignard, D. R. Burton, J. Zhu, Toward a more accurate view of human B-cell repertoire by next-generation sequencing, unbiased repertoire capture and single-molecule barcoding. *Sci. Rep.* **4**, 6778 (2014).
58. L. Kong, B. Ju, Y. Chen, L. He, L. Ren, J. Liu, K. Hong, B. Su, Z. Wang, G. Ozorowski, X. Ji, Y. Hua, Y. Chen, M. C. Deller, Y. Hao, Y. Feng, F. Garces, R. Wilson, K. Dai, S. O'Dell, K. McKee, J. R. Mascola, A. B. Ward, R. T. Wyatt, Y. Li, I. A. Wilson, J. Zhu, Y. Shao, Key gp120 glycans pose roadblocks to the rapid development of VRC01-class antibodies in an HIV-1-infected Chinese donor. *Immunity* **44**, 939–950 (2016).
59. X. Wu, T. Zhou, J. Zhu, B. Zhang, I. Georgiev, C. Wang, X. Chen, N. S. Longo, M. Louder, K. McKee, S. O'Dell, S. Perfetto, S. D. Schmidt, W. Shi, L. Wu, Y. Yang, Z.-Y. Yang, Z. Yang, Z. Zhang, M. Bonsignori, J. A. Crump, S. H. Kapiga, N. E. Sam, B. F. Haynes, M. Simek, D. R. Burton, W. C. Koff, N. A. Doria-Rose, M. Connors, NISC Comparative Sequencing Program, J. C. Mullikin, G. J. Nabel, M. Roederer, L. Shapiro, P. D. Kwong, J. R. Mascola, Focused evolution of HIV-1 neutralizing antibodies revealed by structures and deep sequencing. *Science* **333**, 1593–1602 (2011).
60. T. Zhou, J. Zhu, X. Wu, S. Moquin, B. Zhang, P. Acharya, I. S. Georgiev, H. R. Altae-Tran, G.-Y. Chuang, M. G. Joyce, Y. D. Kwon, N. S. Longo, M. K. Louder, T. Luongo, K. McKee, C. A. Schramm, J. Skinner, Y. Yang, Z. Zhang, Z. Zhang, A. Zheng, M. Bonsignori, B. F. Haynes, J. F. Scheid, M. C. Nussenzweig, M. Simek, D. R. Burton, W. C. Koff; NISC Comparative Sequencing Program, J. C. Mullikin, M. Connors, L. Shapiro, G. J. Nabel, J. R. Mascola, P. D. Kwong, Multidonor analysis reveals structural elements, genetic determinants, and maturation pathway for HIV-1 neutralization by VRC01-class antibodies. *Immunity* **39**, 245–258 (2013).
61. J. Zhu, S. O'Dell, G. Ofek, M. Pancera, X. Wu, B. Zhang, Z. Zhang; NISC Comparative Sequencing Program, J. C. Mullikin, M. Simek, D. R. Burton, W. C. Koff, L. Shapiro, J. R. Mascola, P. D. Kwong, Somatic populations of PGT135–137 HIV-1-neutralizing antibodies identified by 454 pyrosequencing and bioinformatics. *Front. Microbiol.* **3**, 315 (2012).
62. J. Zhu, G. Ofek, Y. Yang, B. Zhang, M. K. Louder, G. Lu, K. McKee, M. Pancera, J. Skinner, Z. Zhang, R. Parks, J. Eudailey, K. E. Lloyd, J. Blinn, S. M. Alam, B. F. Haynes, M. Simek, D. R. Burton, W. C. Koff; NISC Comparative Sequencing Program, J. C. Mullikin, J. R. Mascola, L. Shapiro, P. D. Kwong, Mining the antibodyome for HIV-1-neutralizing antibodies with next-generation sequencing and phylogenetic pairing of heavy/light chains. *Proc. Natl. Acad. Sci. U.S.A.* **110**, 6470–6475 (2013).
63. J. Zhu, X. Wu, B. Zhang, K. McKee, S. O'Dell, C. Soto, T. Zhou, J. P. Casazza; NISC Comparative Sequencing Program, J. C. Mullikin, P. D. Kwong, J. R. Mascola, L. Shapiro, De novo identification of VRC01 class HIV-1-neutralizing antibodies by next-generation sequencing of B-cell transcripts. *Proc. Natl. Acad. Sci. U.S.A.* **110**, E4088–E4097 (2013).
64. L. He, X. Lin, N. de Val, K. L. Saye-Francisco, C. J. Mann, R. Augst, C. D. Morris, P. Azadnia, B. Zhou, D. Sok, G. Ozorowski, A. B. Ward, D. R. Burton, J. Zhu, Hidden lineage complexity of glycan-dependent HIV-1 broadly neutralizing antibodies uncovered by digital panning and native-like gp140 trimer. *Front. Immunol.* **8**, 1025 (2017).
65. E. Krissinel, K. Henrick, Inference of macromolecular assemblies from crystalline state. *J. Mol. Biol.* **372**, 774–797 (2007).
66. I. W. Davis, A. Leaver-Fay, V. B. Chen, J. N. Block, G. J. Kapral, X. Wang, L. W. Murray, W. B. Arendall III, J. Snoeyink, J. S. Richardson, D. C. Richardson, MolProbity: All-atom contacts and structure validation for proteins and nucleic acids. *Nucleic Acids Res.* **35**, W375–W383 (2007).
67. R. A. Laskowski, M. B. Swindells, LigPlot+: Multiple ligand-protein interaction diagrams for drug discovery. *J. Chem. Inf. Model.* **51**, 2778–2786 (2011).
68. A. C. Martin, Accessing the Kabat antibody sequence database by computer. *Proteins* **25**, 130–133 (1996).

**Acknowledgments:** We thank R. Stanfield, X. Dai, and M. Elsliger for crystallographic and computational support; H. Tien in the Wilson lab for automated crystal screening; K. Cogburn, A. Honda, and K. Jackson for HCV donor sample analysis; and J. Ball for the UKN HCV constructs. **Funding:** This work was funded in part by NIH grants R01AI079031 (to M.L.), R01AI123365 and R01AI106005 (to M.L. and I.A.W.), U19AI123861 (to M.L. and J.Z.), U01AI131314 (to G.M.L.), and R01AI129698 (to J.Z.); the HIV Vaccine Research and Design (HIVRAD) program P01AI124337 (to J.Z.); the Danish Council for Independent Research DFF-4004-00598 (to J.B.); the Novo Nordisk Foundation NNF14OC001253 (to J.B.); and the Candys Foundation (to J.P., E.A., and J.B.). NBDS at TSRI was supported by the Clinical Translational Science Award (CTSA) grant UL1 TR001114. X-ray datasets were collected at the APS beamline 23ID-B (GM/CA CAT) and SSRl beamline 12-2. The use of the APS was supported by the U.S. Department of Energy (DOE), Basic Energy Sciences, Office of Science, under contract DE-AC02-06CH11357. The use of the SSRl Structural Molecular Biology Program was supported by the DOE Office of Biological and Environmental Research and by the NIH NIGMS (including P41GM103393) and the National Center for Research Resources (P41RR001209).

**Author contributions:** N.T., J.Z., I.A.W., and M.L. designed the project. N.T., E.G., and Y.H. expressed and purified the E2 proteins and mAbs. N.T. and L.K. determined and analyzed the x-ray structures. N.T., S.C., and E.G. determined  $K_D$ s and assessed binding. J.Z. and L.H.

performed the NGS. J.P., E.A., and J.B. performed the HCVcc neutralization assays. G.M.L. provided the clinical samples and discussion, and N.T., J.B., J.Z., I.A.W., and M.L. wrote the manuscript with support from all the other authors. **Competing interests:** The authors declare that they have no competing interests. **Data and materials availability:** All data and code to understand and assess the conclusions of this research are available in the main text, Supplementary Materials, and the PDB (accession codes 6BKB, 6BKC, and 6BKD). Additional data related to this paper may be requested from the authors. This is manuscript 29614 from The Scripps Research Institute.

Submitted 22 August 2018  
Accepted 27 November 2018  
Published 2 January 2019  
10.1126/sciadv.aav1882

**Citation:** N. Tzarum, E. Giang, L. Kong, L. He, J. Prentoe, E. Augestad, Y. Hua, S. Castillo, G. M. Lauer, J. Bukh, J. Zhu, I. A. Wilson, M. Law, Genetic and structural insights into broad neutralization of hepatitis C virus by human V<sub>H</sub>1-69 antibodies. *Sci. Adv.* **5**, eaav1882 (2019).



Science Webinars help you keep pace with emerging scientific fields!

Stay informed about scientific breakthroughs and discoveries.

Gain insights into current research from top scientists.

Take the opportunity to ask questions during live broadcasts.

 Get alerts about upcoming free webinars.

**Sign up at: [webinar.sciencemag.org/stayinformed](https://webinar.sciencemag.org/stayinformed)**

## TUBERCULOSIS

# Tuberculosis and impaired IL-23–dependent IFN- $\gamma$ immunity in humans homozygous for a common *TYK2* missense variant

Stéphanie Boisson-Dupuis<sup>1,2,3,\*†</sup>, Noe Ramirez-Alejo<sup>1†</sup>, Zhi Li<sup>4,5‡</sup>, Etienne Patin<sup>6,7,8‡</sup>, Geetha Rao<sup>9‡</sup>, Gaspard Kerner<sup>2,3‡</sup>, Che Kang Lim<sup>10,11‡</sup>, Dimitry N. Kremensov<sup>12‡</sup>, Nicholas Hernandez<sup>1</sup>, Cindy S. Ma<sup>9,13</sup>, Qian Zhang<sup>1,14</sup>, Janet Markle<sup>1</sup>, Ruben Martinez-Barricarte<sup>1</sup>, Kathryn Payne<sup>9</sup>, Robert Fisch<sup>1</sup>, Caroline Deswarte<sup>2,3</sup>, Joshua Halpern<sup>1</sup>, Matthieu Bouaziz<sup>2,3</sup>, Jeanette Mulwa<sup>1</sup>, Durga Sivanesan<sup>15,16</sup>, Tomi Lazarov<sup>17</sup>, Rodrigo Naves<sup>18</sup>, Patricia Garcia<sup>19</sup>, Yuval Itan<sup>1,20,21</sup>, Bertrand Boisson<sup>1,2,3</sup>, Alix Checchi<sup>2,3</sup>, Fabienne Jabot-Hanin<sup>2,3</sup>, Aurélie Cobat<sup>2,3</sup>, Andrea Guennoun<sup>14</sup>, Carolyn C. Jackson<sup>1,22</sup>, Sevgi Pekcan<sup>23</sup>, Zafer Caliskaner<sup>24</sup>, Jaime Inostroza<sup>25</sup>, Beatriz Tavares Costa-Carvalho<sup>26</sup>, Jose Antonio Tavares de Albuquerque<sup>27</sup>, Humberto Garcia-Ortiz<sup>28</sup>, Lorena Orozco<sup>28</sup>, Tayfun Ozcelik<sup>29</sup>, Ahmed Abid<sup>30</sup>, Ismail Abderahmani Rhorfi<sup>30,31</sup>, Hicham Souhi<sup>30</sup>, Hicham Naji Amrani<sup>30</sup>, Adil Zegmout<sup>30</sup>, Frédéric Geissmann<sup>17</sup>, Stephen W. Michnick<sup>15</sup>, Ingrid Muller-Fleckenstein<sup>31</sup>, Bernhard Fleckenstein<sup>31</sup>, Anne Puel<sup>1,2,3</sup>, Michael J. Ciancanelli<sup>1</sup>, Nico Marr<sup>14</sup>, Hassan Abolhassani<sup>10,32</sup>, María Elvira Balcells<sup>33</sup>, Antonio Condino-Neto<sup>27</sup>, Alexis Strickler<sup>34</sup>, Katia Abarca<sup>35</sup>, Cory Teuscher<sup>36</sup>, Hans D. Ochs<sup>37</sup>, Ismail Reisli<sup>38</sup>, Esra H. Sayar<sup>38</sup>, Jamila El-Baghdadi<sup>39</sup>, Jacinta Bustamante<sup>1,2,3,40§</sup>, Lennart Hammarström<sup>10,11,41§</sup>, Stuart G. Tangye<sup>9,13§</sup>, Sandra Pellegrini<sup>4,5§</sup>, Lluís Quintana-Murci<sup>6,7,8§</sup>, Laurent Abel<sup>1,2,3||</sup>, Jean-Laurent Casanova<sup>1,2,3,42,43\*||</sup>

Inherited IL-12R $\beta$ 1 and *TYK2* deficiencies impair both IL-12– and IL-23–dependent IFN- $\gamma$  immunity and are rare monogenic causes of tuberculosis, each found in less than 1/600,000 individuals. We show that homozygosity for the common *TYK2* P1104A allele, which is found in about 1/600 Europeans and between 1/1000 and 1/10,000 individuals in regions other than East Asia, is more frequent in a cohort of patients with tuberculosis from endemic areas than in ethnicity-adjusted controls ( $P = 8.37 \times 10^{-8}$ ; odds ratio, 89.31; 95% CI, 14.7 to 1725). Moreover, the frequency of P1104A in Europeans has decreased, from about 9% to 4.2%, over the past 4000 years, consistent with purging of this variant by endemic tuberculosis. Surprisingly, we also show that *TYK2* P1104A impairs cellular responses to IL-23, but not to IFN- $\alpha$ , IL-10, or even IL-12, which, like IL-23, induces IFN- $\gamma$  via activation of *TYK2* and *JAK2*. Moreover, *TYK2* P1104A is properly docked on cytokine receptors and can be phosphorylated by the proximal *JAK*, but lacks catalytic activity. Last, we show that the catalytic activity of *TYK2* is essential for IL-23, but not IL-12, responses in cells expressing wild-type *JAK2*. In contrast, the catalytic activity of *JAK2* is redundant for both IL-12 and IL-23 responses, because the catalytically inactive P1057A *JAK2*, which is also docked and phosphorylated, rescues signaling in cells expressing wild-type *TYK2*. In conclusion, homozygosity for the catalytically inactive P1104A missense variant of *TYK2* selectively disrupts the induction of IFN- $\gamma$  by IL-23 and is a common monogenic etiology of tuberculosis.

## INTRODUCTION

About a quarter of the world's population is infected with *Mycobacterium tuberculosis*, but this bacterium causes tuberculosis in less than 10% of infected individuals, generally within 2 years of infection (a situation referred to here as primary tuberculosis) (1–3). In the countries in which tuberculosis is highly endemic, primary tuberculosis is particularly common in children, who often develop life-threatening disease (4–6). Clinical and epidemiological studies have long suggested that tuberculosis in humans has a strong genetic basis (7–9). Autosomal recessive (AR) complete interleukin-12 receptor  $\beta$ 1 (IL-12R $\beta$ 1) and tyrosine kinase 2 (*TYK2*) deficiencies are the only two inborn errors of immunity reported to date to underlie primary tuberculosis in otherwise healthy patients in two or more kindreds (10–17). Cells from patients with IL-12R $\beta$ 1 deficiency do not respond to IL-12 or IL-23 (12, 18–24). These patients are susceptible to weakly virulent mycobacteria, such as the Bacille Calmette-Guérin (BCG) vaccine and environmental species [Mendelian susceptibility to mycobacterial disease (MSMD)], to the more virulent species *M. tuberculosis*, and

more rarely to *Candida albicans* (20, 25). They are prone to MSMD and tuberculosis because they produce too little interferon- $\gamma$  (IFN- $\gamma$ ) (7, 12, 26, 27) and, in some cases, to chronic mucocutaneous candidiasis (CMC) because they produce too little IL-17A/F (28–32).

In patients with *TYK2* deficiency, cellular responses to IL-12 and IL-23 are severely impaired, but not abolished (10, 33–35). These patients are, thus, also prone to MSMD and tuberculosis, although probably with a lower penetrance than for IL-12R $\beta$ 1 deficiency, because they display residual responses to IL-12 and IL-23. They do not seem to be susceptible to *C. albicans*, which may merely reflect the lower penetrance of candidiasis and smaller number of patients, when compared with IL-12R $\beta$ 1 deficiency. However, unlike patients with IL-12R $\beta$ 1 deficiency, they are susceptible to viral diseases due to the impairment of their responses to IFN- $\alpha/\beta$  (10, 36). In vitro, their cells respond poorly to IL-10, but this defect, which is not observed in patients with IL-12R $\beta$ 1 deficiency, is clinically silent (10, 37, 38). Both IL-12R $\beta$ 1 and *TYK2* deficiencies are caused by rare or private alleles, accounting for each deficiency being found in

Copyright © 2018  
The Authors, some  
rights reserved;  
exclusive licensee  
American Association  
for the Advancement  
of Science. No claim  
to original U.S.  
Government Works

no more than 1/600,000 individuals worldwide. Here, we tested the hypothesis that two common and catalytically inactive missense TYK2 variants, P1104A and I684S (39), might underlie MSMD, tuberculosis, or both.

## RESULTS

### Ten homozygotes for TYK2 P1104A suffered from mycobacterial diseases

The common TYK2 variants P1104A (rs34536443) and I684S (rs12720356) are both catalytically impaired, as shown by *in vitro* kinase assays in reconstituted TYK2-deficient fibrosarcoma cells (U1A cells) (39). Other studies with selective small-molecule kinase inhibitors suggested that the catalytic activity of TYK2 was required for T cell responses to IL-12 and IL-23, but not IFN- $\alpha$  and IL-10 (40). Consistently, the P1104A variant has been reported to impair cellular responses to both IL-12 and IL-23 in human memory T cells, whereas discordant results were obtained for IFN- $\alpha$  (39, 41). The response to IL-10 was normal in human leukocytes (41). On the basis of the gnomAD database (42) (gnomAD: <http://gnomad.broadinstitute.org>), these two missense variants are rare (<0.02%) in East Asian populations, but otherwise common (>0.8%) in the other four main gnomAD populations, reaching their highest frequencies in Europeans (4.2% for P1104A and 9% for I684S) (fig. S1, A and B) (43, 44). On the basis of the 1000 Genomes Project database (45), these two variants are not in linkage disequilibrium. We investigated the possibility that these variants might confer a predisposition to MSMD, tuberculosis, or both. We screened our whole-exome sequencing (WES) data for 463 patients with MSMD and 291 children with tuberculosis, from different geographic locations and ancestries, and for 163 adults of North African ancestry with early-onset pulmonary tuberculosis (table S1). None of these patients carried pathogenic mutations in known MSMD- and tuberculosis-causing genes (12, 46). Our WES data for 2835 other

patients, from various ethnic origins (fig. S1C) and with various genetically unexplained non-mycobacterial infections, were used as a control. Among the 3752 exomes available in total, we identified 366 I684S heterozygotes, 168 P1104A heterozygotes, 18 I684S homozygotes, and 6 I684S/P1104A compound heterozygotes, with no clustering of any of these genotypes within any of the patient cohorts (table S1). By contrast, we identified 11 unrelated P1104A homozygotes, which were confirmed by Sanger sequencing: 7 with tuberculosis (3 children under the age of 15 years and 4 adults under the age of 40 years), 3 with MSMD (all under 3 years of age), and 1 with CMC (aged 1 year) (Fig. 1, A to C; fig. S1D; and Supplementary Materials and Methods). We further Sanger sequenced TYK2 in parents and siblings of these 11 patients. We found that, in kindred K with the CMC patient, homozygosity for P1104A did not segregate with CMC, because one sibling with CMC was heterozygous for P1104A, implying that there is another genetic cause for CMC in this kindred (fig. S1D). We also found only one asymptomatic P1104A homozygote among the relatives of the other 10 patients (kindred G, I.1). In total, we identified 10 unrelated P1104A TYK2 homozygotes with MSMD (3 patients) or primary tuberculosis (7 patients).

### P1104A homozygosity is strongly enriched in patients with tuberculosis

Principal components analysis (PCA) based on the WES data (fig. S1C) (47) confirmed the diverse ancestries of the 10 patients. Eight were living in their countries of origin (Fig. 1C and fig. S1B). The Mexican patient was living in the United States, and the 10th patient, who was living in Brazil, had mixed European and African ancestry. We compared the proportions of individuals with P1104A in each cohort and estimated odds ratios (ORs) by logistic regression, with adjustment for the first three principal components of the PCA to account for ethnic heterogeneity (48). In addition to the 2835 exomes already used as controls, we used all 2504 available

<sup>1</sup>St. Giles Laboratory of Human Genetics of Infectious Diseases, Rockefeller Branch, Rockefeller University, New York, NY, USA. <sup>2</sup>Laboratory of Human Genetics of Infectious Diseases, Necker Branch, INSERM U1163, Paris, France. <sup>3</sup>Paris Descartes University, Imagine Institute, Paris, France. <sup>4</sup>Cytokine Signaling Unit, Pasteur Institute, Paris, France. <sup>5</sup>INSERM U1221, Paris, France. <sup>6</sup>Human Evolutionary Genetics Unit, Pasteur Institute, Paris, France. <sup>7</sup>CNRS UMR2000, Paris, France. <sup>8</sup>Center of Bioinformatics, Biostatistics and Integrative Biology, Pasteur Institute, Paris, France. <sup>9</sup>Immunology Division, Garvan Institute of Medical Research, Darlinghurst, New South Wales, Australia. <sup>10</sup>Division of Clinical Immunology, Department of Laboratory Medicine, Karolinska Institute, Karolinska University Hospital Huddinge, Stockholm, Sweden. <sup>11</sup>Department of Clinical Translational Research, Singapore General Hospital, Singapore, Singapore. <sup>12</sup>Department of Biomedical and Health Sciences, University of Vermont, Burlington, VT, USA. <sup>13</sup>St. Vincent's Clinical School, University of New South Wales, Darlinghurst, New South Wales, Australia. <sup>14</sup>Sidra Medicine, Doha, Qatar. <sup>15</sup>Department of Biochemistry, University of Montreal, Montreal, Quebec, Canada. <sup>16</sup>Department of Biochemistry, Microbiology, and Immunology, University of Ottawa, Ottawa, Ontario, Canada. <sup>17</sup>Immunology Program, Sloan Kettering Institute, Memorial Sloan Kettering Cancer Center, New York, NY, USA. <sup>18</sup>Institute of Biochemical Sciences, Faculty of Medicine, University of Chile, Santiago, Chile. <sup>19</sup>Laboratory of Microbiology, Clinical Laboratory Department School of Medicine, Pontifical Catholic University of Chile, Santiago, Chile. <sup>20</sup>The Charles Bronfman Institute for Personalized Medicine, Icahn School of Medicine at Mount Sinai, New York, NY, USA. <sup>21</sup>Department of Genetics and Genomic Sciences, Icahn School of Medicine at Mount Sinai, New York, NY, USA. <sup>22</sup>Department of Pediatrics, Memorial Sloan Kettering Cancer Center, New York, NY, USA. <sup>23</sup>Department of Pediatric Pulmonology, Necmettin Erbakan University, Meram Medical Faculty, Konya, Turkey. <sup>24</sup>Meram Faculty of Medicine, Department of Internal Medicine, Division of Allergy and Immunology, Necmettin Erbakan University, Konya, Turkey. <sup>25</sup>Jeffrey Modell Center for Diagnosis and Research in Primary Immunodeficiencies, Faculty of Medicine University of La Frontera, Temuco, Chile. <sup>26</sup>Department of Pediatrics, Federal University of São Paulo Medical School, São Paulo, Brazil. <sup>27</sup>Department of Immunology, Institute of Biomedical Sciences, and Institute of Tropical Medicine, University of São Paulo, São Paulo, Brazil. <sup>28</sup>National Institute of Genomic Medicine, Mexico City, Mexico. <sup>29</sup>Department of Molecular Biology and Genetics, Bilkent University, Ankara, Turkey. <sup>30</sup>Department of Pneumology, Military Hospital Mohammed V, Rabat, Morocco. <sup>31</sup>Institute of Clinical and Molecular Virology, University of Erlangen-Nuremberg, Erlangen, Germany. <sup>32</sup>Research Center for Immunodeficiencies, Pediatrics Center of Excellence, Children's Medical Center, Tehran University of Medical Sciences, Tehran, Iran. <sup>33</sup>Department of Infectious Diseases, Medical School, Pontifical Catholic University of Chile, Santiago, Chile. <sup>34</sup>Department of Pediatrics, San Sebastián University, Santiago, Chile. <sup>35</sup>Department of Infectious Diseases and Pediatric Immunology, School of Medicine, Pontifical Catholic University of Chile, Santiago, Chile. <sup>36</sup>Department of Medicine, Immunobiology Program, University of Vermont, Burlington, VT, USA. <sup>37</sup>Seattle Children's Research Institute and Department of Pediatrics, University of Washington, Seattle, WA, USA. <sup>38</sup>Department of Pediatric Immunology and Allergy, Necmettin Erbakan University, Meram Medical Faculty, Konya, Turkey. <sup>39</sup>Genetics Unit, Military Hospital Mohamed V, Hay Riad, Rabat, Morocco. <sup>40</sup>Center for the Study of Primary Immunodeficiencies, AP-HP, Necker Hospital for Sick Children, Paris, France. <sup>41</sup>Beijing Genomics Institute BGI-Shenzhen, Shenzhen, China. <sup>42</sup>Pediatric Hematology-Immunology Unit, Necker Hospital for Sick Children, AP-HP, Paris, France. <sup>43</sup>Howard Hughes Medical Institute, New York, NY, USA.

\*Corresponding author. Email: stbo603@rockefeller.edu (S.B.-D.); jean-laurent.casanova@rockefeller.edu (J.-L.C.)

†These authors contributed equally to this work.

‡These authors contributed equally to this work.

§These authors contributed equally to this work.

||These authors contributed equally to this work.

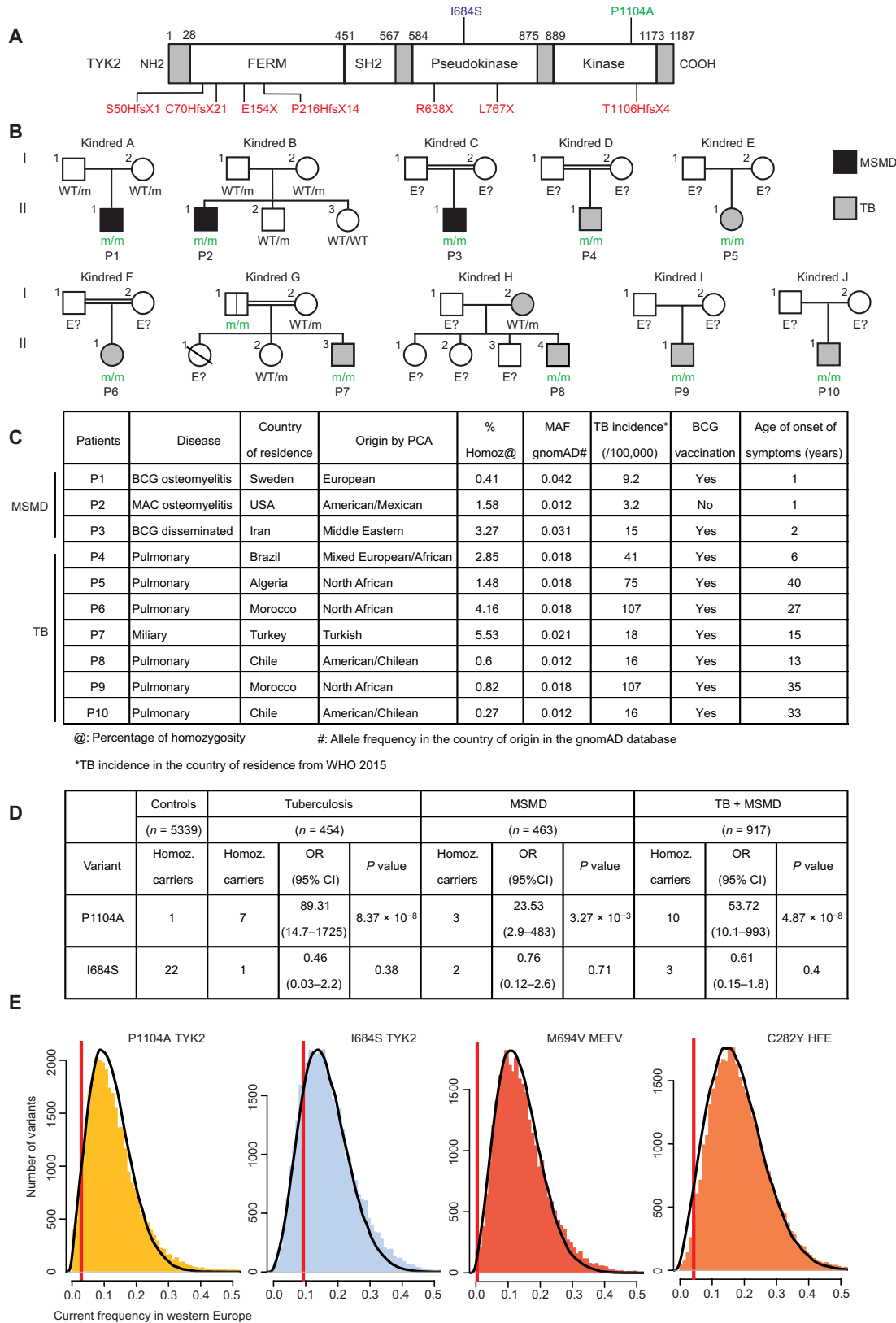


**Fig. 1. Familial segregation and clinical information for patients homozygous for TYK2 P1104A.**

(A) Schematic diagram of the TYK2 protein with its various domains (FERM, SH2, pseudokinase, and tyrosine kinase). The positions of the previously reported TYK2 mutations resulting in premature STOP codons are indicated in red. The positions of the I684S and P1104A polymorphisms are indicated in blue and green, respectively. (B) Pedigrees of the 10 TYK2-deficient families. Each generation is designated by a Roman numeral (I–II), and each individual by an Arabic numeral. The double lines connecting the parents indicate consanguinity based on interview and/or a homozygosity rate of >4% estimated from the exome data. Solid shapes indicate disease status. Individuals whose genetic status could not be determined are indicated by “E?”, and “m” indicates a TYK2 P1104A allele. (C) Summary table of clinical details and origin of the patients associated with the MAF in the country of origin. The incidence of tuberculosis (TB) in the country of residence is also mentioned. MAC indicates *Mycobacterium avium* complex. (D) Summary of WES, indicating the numbers of individuals with tuberculosis or MSMD and of controls carrying the I684S or P1104A variant of TYK2 in the homozygous state, and the associated P value and OR. (E) Distributions of the current allele frequencies of variants that segregated 4000 years ago at frequencies similar to those of the P1104A and I684S TYK2, M694V MEFV, and C282Y HFE variants. The red vertical lines indicate the current frequency of the four variants of interest. Colored bars indicate the distribution of current allele frequency, in the 1000 Genomes Project, for variants with frequencies in ancient European human DNA similar to those of the four candidate variants (52). Black lines indicate the distribution of simulated frequencies, in the present generation, for alleles with a past frequency similar to that of the four candidate variants, with propagation over 160 generations (corresponding to a period of ~4000 years) under the Wright-Fisher neutral model. For instance, for the P1104A allele, which had a frequency of ~9% in ancient Europeans, colored bars indicate the observed distribution of current frequencies for the 31,276 variants with a frequency of 8 to 10% 4000 years ago. The black lines indicate the distribution of frequencies for 100,000 simulated alleles obtained after 160 generations under the Wright-Fisher neutral model.

period of ~4000 years) under the Wright-Fisher neutral model. For instance, for the P1104A allele, which had a frequency of ~9% in ancient Europeans, colored bars indicate the observed distribution of current frequencies for the 31,276 variants with a frequency of 8 to 10% 4000 years ago. The black lines indicate the distribution of frequencies for 100,000 simulated alleles obtained after 160 generations under the Wright-Fisher neutral model.

individuals from the 1000 Genomes Project (45), giving a total of 5339 controls for whom we have complete WES data (Fig. 1D). P1104A homozygosity was more enriched among patients with MSMD than among controls [ $P = 3.27 \times 10^{-3}$ ; OR, 23.53; 95% confidence interval (CI), 2.9 to 483], and an even higher level of enrichment was observed among patients with tuberculosis ( $P = 8.37 \times 10^{-8}$ ; OR, 89.31; 95% CI, 14.7 to 1725). The level of enrichment in homozygosity for this variant was intermediate but more significant when both groups were analyzed together (OR, 53.72; 95% CI, 10.1 to 993;  $P = 4.87 \times 10^{-8}$ ). By contrast, no enrichment in homozygosity for this variant was observed among the patients with other infections studied in the laboratory (table S1) (49, 50). Aside from the 10 MSMD and tuberculosis patients, we identified only one other P1104A homozygote by WES: a CMC patient whose P1104A homozygosity was not CMC-causing, living in the United States, where infants are not inoculated with BCG and *M. tuberculosis* is not endemic (fig. S1D). No homozygotes were observed among the 2504 individuals of the 1000 Genomes Project. No significant enrichment in P1104A heterozygosity was observed in any of the cohorts studied, including patients with MSMD ( $P = 0.57$ ) or tuberculosis ( $P = 0.49$ ), demonstrating the recessive nature of P1104A inheritance for both mycobacterial conditions. Moreover, no significant enrichment in I684S heterozygotes or homozygotes or in P1104A/I684S compound heterozygotes was observed in any of the cohorts studied (table S1). Last, the *TYK2* P1104A allele yielded the highest OR at genome-wide level in an independent enrichment analysis performed under the assumption of a recessive mode of inheritance and considering all common missense or potential loss-of-function (LOF) alleles in our entire cohort of 3752 patients (fig. S1E). These results strongly suggest that homozygosity for P1104A is a genetic etiology of primary tuberculosis and MSMD.

### ***TYK2* P1104A allele frequency has decreased in Europe over the past 4000 years**

The higher risk of life-threatening tuberculosis in P1104A homozygotes suggests that this variant has been subject to negative selection in areas in which this disease has long been endemic, such as Europe (51). We analyzed changes in the frequencies of the P1104A and I684S *TYK2* variants in the European population, from ancient to modern times (52). Only three nonsynonymous *TYK2* variants—P1104A, I684S, and V362F—were found in an available sample of central European individuals who lived during the late Neolithic age ~4000 years ago (52). Over this period, the frequency of *TYK2* P1104A has significantly decreased in Europeans, from about 9% to 4.2% (Fig. 1E). Of the 31,276 variants with frequencies in the 8 to 10% range 4000 years ago, P1104A is among the 5% displaying the largest decrease in frequency (empirical  $P = 0.048$ ; Fig. 1E). Furthermore, the neutral model of evolution was significantly rejected for P1104A in Wright-Fisher simulations (simulation  $P = 0.050$ ; Fig. 1E and Supplementary Materials and Methods), suggesting an absence of bias in the empirical analyses. As a negative control, the frequency of V362F remained stable (from 25% to 26.2%) and that of I684S did not decrease significantly over this period (empirical  $P = 0.181$ ). The frequency of I684S was about 14% 4000 years ago and is now 9%, placing this variant among the 80% of the 36,469 polymorphisms considered with a frequency that was in the 13 to 15% range 4000 years ago and has remained relatively stable.

### ***TYK2* P1104A allele was possibly purged in Europe by tuberculosis**

We subsequently analyzed, as positive controls, two relatively common mutations known to cause life-threatening AR disorders and present in ancient Europeans: the *MEFV* M694V variant underlying Mediterranean fever (MF) (53) and the *HFE* C282Y underlying hemochromatosis (which also decreases male fertility) (54). Both these variants decreased significantly in frequency over the same period, from about 11% to 0.4% for *MEFV* M694V and from 16% to 5.7% for *HFE* C282Y (empirical  $P = 0.016$  for both variants; Fig. 1E). Therefore, our preliminary assessments suggest that *TYK2* P1104A, *MEFV* M694V, and *HFE* C282Y have been subject to negative selection in Europeans, whereas *TYK2* I684S has not. The stronger selection operating on *MEFV* M694V, and to a lesser extent *HFE* C282Y, than on *TYK2* P1104A is consistent with the inevitability of MF and hemochromatosis in patients with these mutations, whereas tuberculosis development also requires exposure to *M. tuberculosis*. These results suggest that, unlike I684S, P1104A has been undergoing a purge in Europe since the Neolithic period due to the continued endemic nature of life-threatening tuberculosis (51). No other intramacrophagic infection, whose control depends on IFN- $\gamma$ , has been endemic for so long in Europe (55, 56). The purging of deleterious mutations is expected to be much less effective in the absence of continued exposure (57, 58), which has been the case for other infections that killed a sizeable proportion of Europeans, albeit for no more than several decades or a few centuries, such as plague (59). The observed decline in P1104A allele frequency is consistent with the purging of a recessive trait that kills in childhood or when the individual is of reproductive age. This decrease would be much steeper for a dominant trait with a similar fitness effect. These results suggest that homozygosity for P1104A, which is still present in about 1/600 Europeans and between 1/10,000 and 1/1000 individuals in other regions of the world, with the exception of East Asia, where the allele is almost absent, has been a major human genetic determinant of primary tuberculosis during the course of human history.

### ***TYK2* P1104A impairs IL-23 but not IFN- $\alpha$ , IL-12, and IL-10 signaling**

We performed a functional characterization of the I684S and P1104A *TYK2* alleles, focusing on the four known human *TYK2*-dependent signaling pathways (10). In reconstituted U1A cells stimulated with IFN- $\alpha$  in vitro, both mutant proteins were previously shown to be catalytically inactive, i.e., unable to autophosphorylate or phosphorylate a substrate such as signal transducer and activator of transcription 3 (STAT3) (39). However, both could be phosphorylated by Janus kinase 1 (JAK1), unlike the prototypical kinase-dead adenosine 5' triphosphate (ATP)-binding mutant K930R (39). Epstein-Barr virus (EBV)-transformed B (EBV-B) cells and herpesvirus saimiri (HVS)-transformed T (HVS-T) cells derived from a *TYK2*-deficient patient without *TYK2* protein expression (10) were stably transduced with a retrovirus generated with an empty vector or a vector containing the wild-type (WT), P1104A, I684S, or K930R *TYK2* complementary DNA (cDNA) (60). Transduction with the WT or any mutant *TYK2* restored both *TYK2* expression, as shown by Western blotting, and the corresponding *TYK2* scaffolding-dependent surface expression of IFN- $\alpha$ R1, IL-10R2, and IL-12R $\beta$ 1, as shown by flow cytometry (Fig. 2, A and B, and fig. S2, A and B). In P1104A-expressing cells, the IFN- $\alpha$ - and IL-12-dependent signaling pathways were normal, as shown by the levels

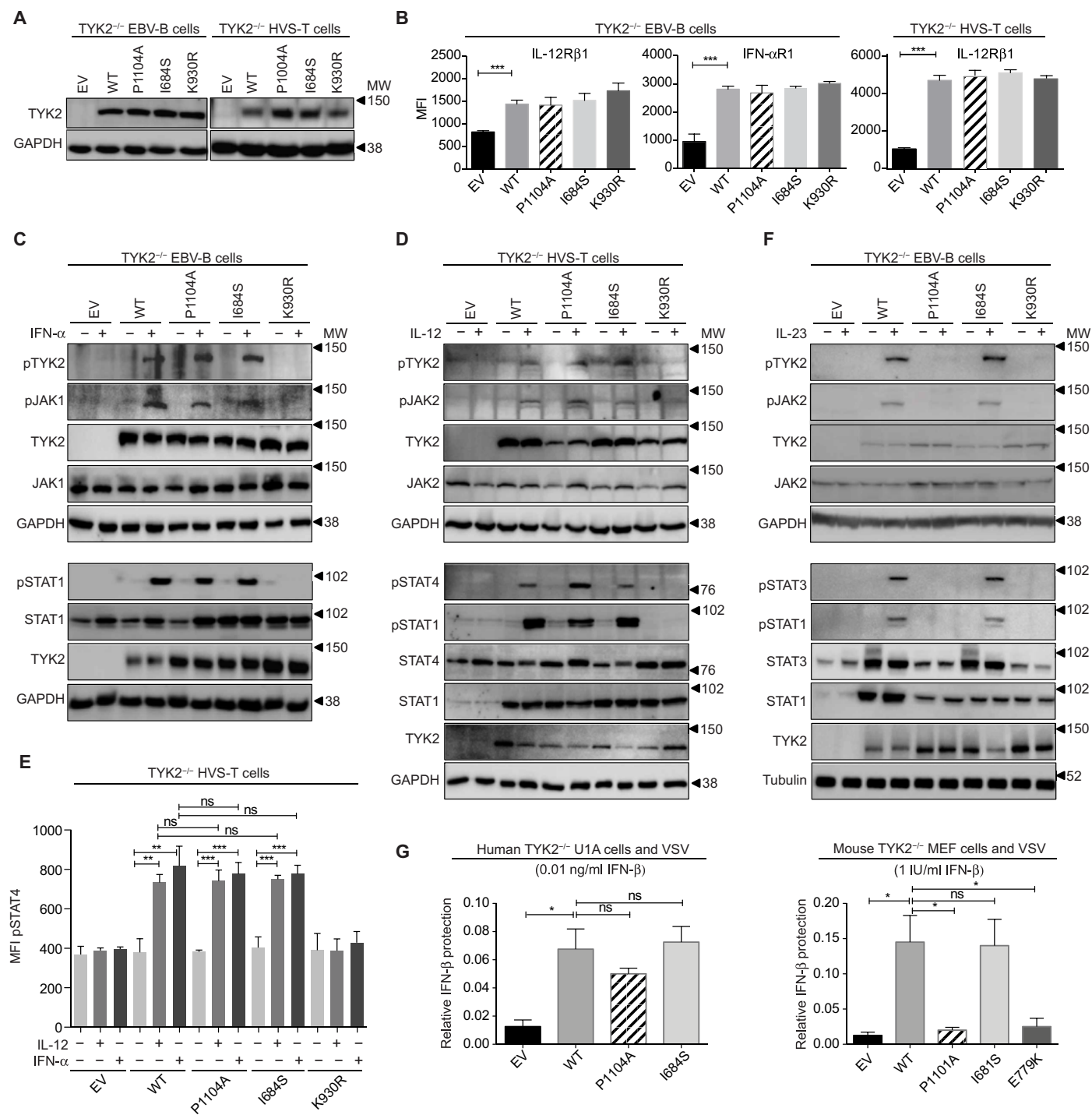


**Fig. 2. Cellular responses to IFN-α, IL-12 and IL-23 in transduced EBV-B and HVS-T cells.** TYK2-deficient EBV-B and HVS-T cells were transduced with a retrovirus generated with an empty vector (EV), or vectors encoding WT TYK2, or the P1104A, I684S, or K930R TYK2 alleles. (A) Levels of TYK2 in transduced EBV-B (left) and HVS-T (right) cells, as determined by Western blotting. (B) Levels of IL-12Rβ1 and IFN-αR1 in transduced EBV-B (left) and HVS-T (right) cells, as determined by flow cytometry. \*\*\**P* < 0.001, two-tailed Student's *t* test. Error bars indicate SEM. (C, D, and F) Phosphorylation of JAKs and STATs in unstimulated (-) transduced EBV-B or HVS-T cells or in these cells after stimulation (+) with IFN-α (C) (pTYK2, pJAK1, and pSTAT1), IL-12 (D) (pTYK2, pJAK2, pSTAT1, and pSTAT4), and IL-23 (F) (pTYK2, pJAK2, pSTAT3, and pSTAT1), as assessed by Western blotting with specific antibodies recognizing phospho-TYK2, phospho-JAK1, phospho-JAK2, phospho-STAT1, phospho-STAT4, and phospho-STAT3. MW, molecular weight. (E) Phosphorylation of STAT4 in response to IFN-α and IL-12, as determined by flow cytometry in HVS-transduced T cells and expression as mean fluorescence intensity (MFI). \*\**P* < 0.01, \*\*\**P* < 0.001, two-tailed Student's *t* test. ns, not significant. (G) IFN-β response of U1A (left) and MEF (right) cells, both lacking TYK2, after transduction with the indicated human and mouse TYK2 alleles, respectively, or with empty vector control, as measured in an IFN-β-induced antiviral activity assay (see Materials and Methods). A unique dose is shown: an IFN-β dose of 0.01 ng/ml for human cells and 1 IU/ml for mouse cells.

of induced phosphorylation of the key components [TYK2, JAK1, STAT1, and STAT3 for IFN- $\alpha$ ; TYK2, JAK2, STAT1, and STAT4 for IL-12] (Fig. 2, C to E, and fig. S2, C, D, and H). All Western blots were quantified, as shown in the supplementary figures. No phosphorylation of TYK2 or JAK1 was detected after stimulation with IL-10, despite only very slight decreases in the phosphorylation of STAT3 and STAT1, as shown by Western blotting and flow cytometry (fig. S2, E to H). In response to IL-23, the phosphorylation of TYK2, JAK2, and STAT3 was as severely impaired as observed in TYK2-deficient and K930R-transduced recipient cells (Fig. 2F and fig. S2, H and I). Stimulation with higher concentrations of IL-23 did not reverse this phenotype, but a residual response was observed in P1104A cells after longer periods of stimulation (fig. S2J). I684S cells responded normally to the four cytokines, whereas K930R cells did not respond at all. Because Pro<sup>1104</sup> and Ile<sup>684</sup> are located in two different domains of TYK2, their substitutions may differentially affect cytokine-induced JAK activation. Our findings indicate that the expression of TYK2 I684S in TYK2-deficient EBV-B and HVS-T cells rescues JAK-STAT activation in response to IFN- $\alpha$ , IL-10, IL-12, and IL-23, whereas TYK2 P1104A expression selectively fails to rescue responses to IL-23.

#### Human TYK2 P1104A, unlike mouse P1101A, rescues antiviral activity

The impact of TYK2 variants on cellular responses to IL-12 and IL-23 is irrelevant in nonhematopoietic cells, because the receptors for these cytokines are expressed only on leukocytes. Yet, TYK2 variants may affect IFN- $\alpha/\beta$  and IL-10 responses in multiple cell types. To study the IFN- $\alpha/\beta$  response pathway, we measured the antiviral response to IFN- $\beta$  of U1A cells (61–63) stably transduced with a retroviral particle generated with an empty vector or a vector encoding the WT, P1104A, or I684S TYK2 cDNA. Cells were treated with increasing concentrations of IFN- $\beta$  and were then challenged with vesicular stomatitis virus (VSV), which is cytopathic. U1A cells transduced with an empty vector displayed almost no response to IFN- $\beta$ , with high proportions of dead cells, whereas cells transduced with WT, P1104A, or I684S TYK2 responded robustly, with diminished proportions of dead cells (Fig. 2G, left, and fig. S2K, left). Both the I684S and P1104A mutant proteins are, therefore, functional for antiviral immunity mediated by IFN- $\beta$  in human fibrosarcoma cells, consistent with the results shown above for lymphocytes. We then expressed the orthologous mouse missense alleles (P1101A and I681S) and a known mouse LOF missense allele (E779K, which impairs TYK2 expression and abolishes its function) in TYK2-deficient mouse embryonic fibroblasts (MEFs) (64). Protection against VSV infection was measured by assessing the response to increasing concentrations of IFN- $\beta$ . P1101A and E779K did not protect, unlike WT and I681S TYK2 (Fig. 2G, right, and fig. S2K, right). Consistently, the P1101A variant did not restore the IFN- $\beta$ -dependent inhibition of IFN- $\gamma$ -induced major histocompatibility complex class II up-regulation in mouse peritoneal macrophages (41). These overexpression data show that mouse TYK2 P1101A does not rescue IFN- $\alpha/\beta$  signaling in mouse fibroblasts, consistent with a previous study on lymphocytes (41), whereas human P1104A can rescue IFN- $\alpha/\beta$  signaling in human cells. The mouse P1101A variant has also been reported to impair cellular responses to IL-12 and IL-23 in lymphocytes (41). Thus, both the two human missense proteins (P1104A versus I684S, for IL-23) and the two orthologs (P1104A versus P1101A, for IFN- $\alpha/\beta$  and IL-12) have qualitatively different

impacts on some TYK2-dependent pathways, at least when overexpressed. The other two orthologs (I684S versus I681S) behaved in a similar manner. Overall, the human P1104A allele did not disrupt responses to IFN- $\alpha/\beta$  in either lymphocytes or fibroblasts.

#### IL-23 signaling is impaired in patients' cells homozygous for TYK2 P1104A

The study of overexpressed mutant allele cDNAs captures different information than the study of cells carrying a biallelic genotype in the context of the patients' entire genome. Hence, we analyzed EBV-B and HVS-T cells from controls and patients homozygous for P1104A or I684S, compound heterozygous for P1104A and I684S, or with complete TYK2 deficiency, in the same experimental conditions. TYK2 levels were similar in cells with any of the three mutant genotypes other than complete TYK2 deficiency (Fig. 3A and fig. S3A). Cell surface expression of IFN- $\alpha$ R1 and IL-10R2 in EBV-B cells and of IL-12R $\beta$ 1 in EBV-B and HVS-T cells was also normal, attesting to the intact scaffolding function of constitutively expressed P1104A and I684S (Fig. 3B and fig. S3B) (10). In P1104A homozygous cells, the response to IFN- $\alpha$  was modestly reduced in terms of JAK1, TYK2, STAT3, and STAT1 phosphorylation (Fig. 3C and fig. S3, C to F), whereas the response to IL-12 was normal, as shown by levels of JAK2, TYK2, and STAT4 phosphorylation (Fig. 3D and fig. S4, A to D). In the same experimental conditions, TYK2-deficient cells had severe phenotypes, in terms of phosphorylation of JAK1, TYK2, STAT1, STAT3 in response to IFN- $\alpha$ , and JAK2, TYK2, and STAT4 in response to IL-12. In contrast, cells homozygous for I684S or compound heterozygous for I684S and P1104A had no detectable phenotype. As in TYK2-deficient cells, the phosphorylation of JAK1 and TYK2 in response to IL-10 was impaired in P1104A homozygous cells, as tested by Western blotting, whereas that of STAT3 was barely affected, as tested by flow cytometry (fig. S4, E to H). The phosphorylation of JAK2, TYK2, and STAT3 in response to IL-23, as assessed by Western blotting, was normal in I684S homozygous and I684S/P1104A compound heterozygous EBV-B cells, but equally and severely impaired in P1104A and TYK2-deficient EBV-B cells, despite the normal levels of IL-23R in these cells, as assessed by flow cytometry (Fig. 4A and fig. S5, A and B). Higher concentrations of IL-23 and longer periods of stimulation with this cytokine did not reverse this phenotype (fig. S5, C and D). Moreover, STAT3 phosphorylation was also impaired in P1104A HVS-T cells stimulated with IL-23, as assessed by flow cytometry (Fig. 4B). Thus, consistent with the results of previous overexpression studies, the constitutive expression of P1104A did not impair JAK-STAT responses to IL-12 and had only a modest effect on responses to IFN- $\alpha/\beta$  and IL-10, whereas it disrupted JAK-STAT responses to IL-23 as severely as complete TYK2 deficiency, in both EBV-B and HVS-T cells.

#### The induction of target genes by IL-23 is impaired in patients' EBV-B cells

We then assessed the more distal induction of target genes in control and patient EBV-B cells after stimulation with IL-10, IFN- $\alpha$ , and IL-23. The induction of *SOCS3* mRNA after stimulation with IL-10 was not significantly weaker in P1104A cells than in control cells, as shown by quantitative reverse transcription polymerase chain reaction (RT-qPCR) (fig. S6A). We also performed RNA-sequencing (RNA-seq) on EBV-B cells stimulated with IFN- $\alpha$  or IL-23. STAT1- and TYK2-deficient cells displayed abnormally low levels of induction

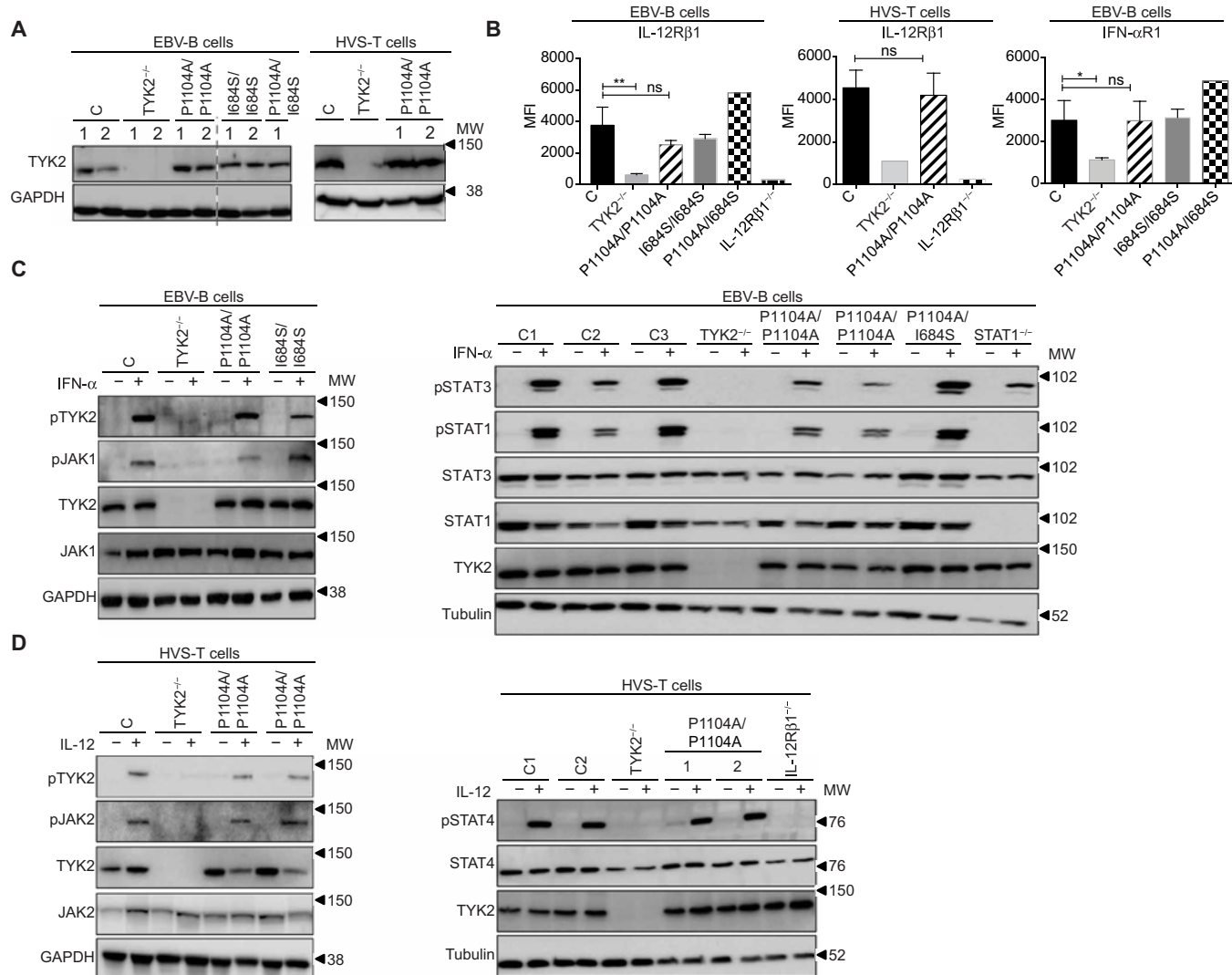


**Fig. 3. Cellular responses to IFN- $\alpha$  and IL-12 in cell lines from patients.** (A) TYK2 levels in EBV-B cells from two controls, two TYK2-deficient patients, two patients homozygous for TYK2 P1104A, two patients homozygous for TYK2 I684S, and a patient compound heterozygous for the P1104A/I684S TYK2 alleles, as assessed by Western blotting. (B) Levels of IL-12R $\beta$ 1 in EBV-B cells and HVS-T cells and of IFN- $\alpha$ 1 in EBV-B cells from controls, TYK2-deficient patients, patients homozygous for TYK2 P1104A, patients homozygous for TYK2 I684S, and a patient compound heterozygous for P1104A/I684S TYK2 alleles, as assessed by flow cytometry. \* $P < 0.05$ , \*\* $P < 0.01$ , two-tailed Student's  $t$  test. (C and D) Phosphorylation of JAKs and STATs in EBV-B or HVS-T cells of the indicated TYK2 genotypes after stimulation with IFN- $\alpha$  (C) (pTYK2, pJAK1, pSTAT1, and pSTAT3) or IL-12 (D) (pTYK2, pJAK2, and pSTAT4), as determined by Western blotting.

for a number of IFN- $\alpha$ -stimulated genes (ISGs), but no major differences were detected between controls and P1104A cells (Fig. 4C). We confirmed these results by RT-qPCR to assess the induction of two ISGs (*MX1* and *ISG15*) in EBV-B cells and HVS-T cells stimulated with IFN- $\alpha$  (fig. S6B). RNA-seq analysis of IL-23-stimulated control EBV-B cells detected the induction of fewer target genes, *SOCS3* being one of the genes most strongly induced in these conditions. IL-12R $\beta$ 1<sup>-/-</sup>, TYK2<sup>-/-</sup>, and TYK2 P1104A cells displayed no response whatsoever to IL-23 (fig. S6C). Cells from a patient suffering from hyper-immunoglobulin E (IgE) syndrome and carrying a heterozygous dominant-negative (DN) mutation of *STAT3* (*STAT3-DN*) had a normal pattern of target gene induction, presumably due to residual *STAT3* activity, and consistent with the absence of mycobacterial infections in these patients (fig. S6C). We confirmed, by RT-qPCR, that *SOCS3* mRNA was induced in control cells, but not in cells from

two P1104A patients, or in TYK2- or IL-12R $\beta$ 1-deficient cells, in response to IL-23 (Fig. 4D). Last, we assessed IFN- $\alpha$ -mediated protection against VSV infection in primary fibroblasts from two patients homozygous for P1104A. The response of fibroblasts to IFN- $\alpha$  was indistinguishable between these patients and healthy controls, in terms of proportions of dead cells (Fig. 4E). Thus, in the cells homozygous for TYK2 P1104A tested, IFN- $\alpha$  did induce ISGs and antiviral immunity, whereas IL-23 did not induce the expression of its target genes, resulting in a phenotype as severe as that of TYK2-deficient cells.

**TYK2 P1104A is catalytically inactive but can be phosphorylated**

We then analyzed the intriguing mechanism by which TYK2 P1104A selectively disrupts the IL-23-responsive pathway. As shown above, this mutant protein is well expressed and has intact scaffolding

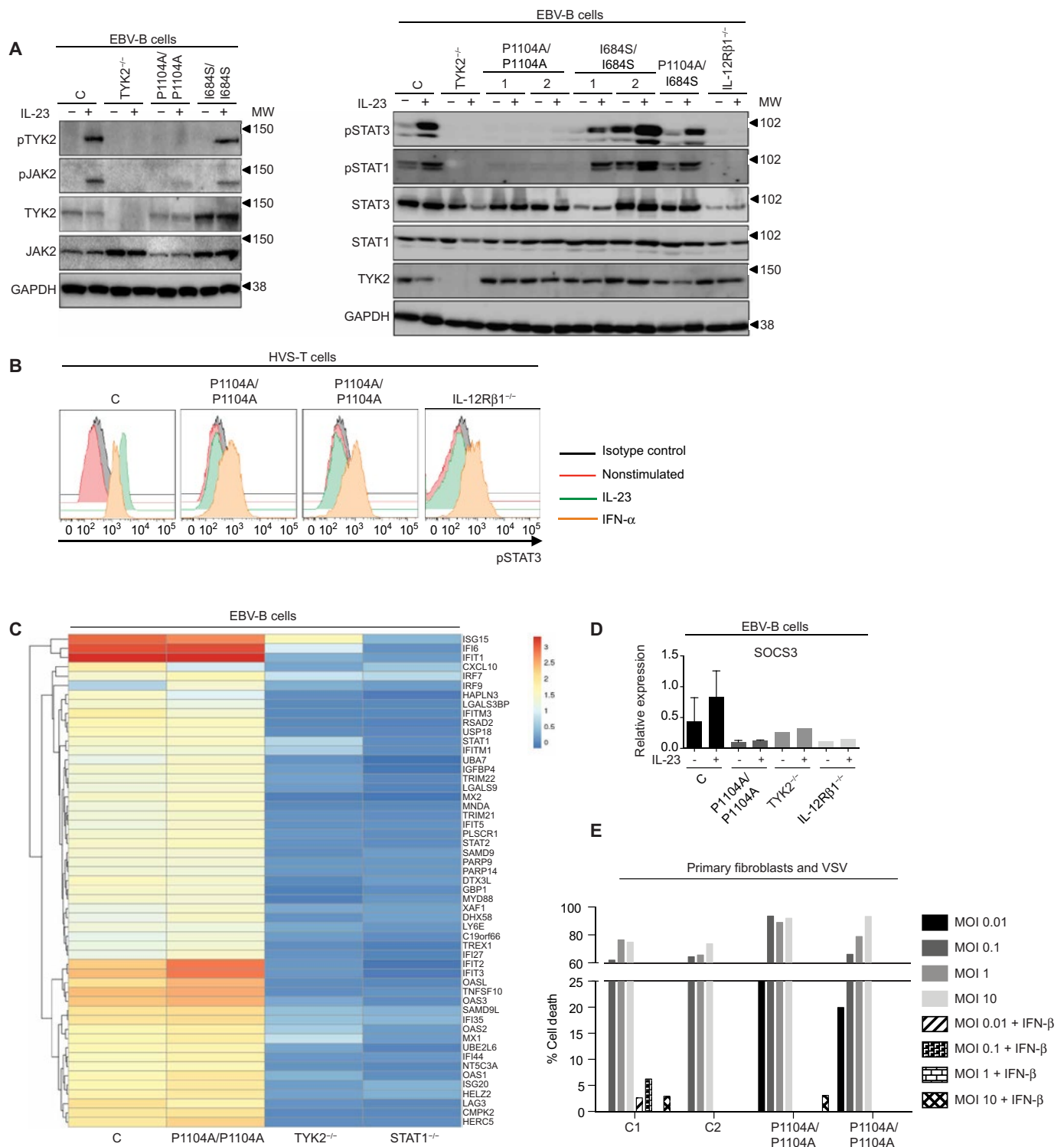


**Fig. 4. Cellular responses to IL-23 and IFN-α in cell lines from patients.** (A) Phosphorylation of JAKs and STATs in EBV-B cells carrying the indicated *TYK2* genotypes after stimulation with IL-23 (pTYK2, pJAK2, pSTAT3, and pSTAT1). (B) Phosphorylation of STAT3 after stimulation with IFN-α or IL-23, in HVS-T cells of the indicated genotypes, as assessed by flow cytometry. (C) Expression patterns on RNA-seq of EBV-B cells stimulated with IFN-α. The heat map represents the fold change (FC) difference in expression before and after stimulation on a log<sub>2</sub> scale. Red blocks represent up-regulated genes, and blue blocks represent down-regulated genes. The genes up-regulated with an FC of ≥2.5, i.e., log<sub>2</sub>(FC) ≥ 1.3, in the group of controls are shown. (D) Relative levels of *SOCS3* expression in EBV-B cells after IL-23 stimulation. (E) Percentage of cell death for primary fibroblasts of the indicated genotype after VSV infection at various MOIs, with and without IFN-β pretreatment.

activity via its docking to cytokine receptors (Figs. 2, A and B, and 3, A and B) (65). We analyzed the capacity of TYK2 P1104A to phosphorylate itself and STATs both in cells and by in vitro kinase assay. TYK2 WT, P1104A, I684S, and K930R were transiently transfected in human embryonic kidney (HEK) 293T cells, and in the absence of cytokine stimulation, baseline phosphorylation of TYK2, STAT1, STAT2, and STAT3 was assessed by Western blotting. Overexpression of TYK2 WT and I684S, unlike that of P1104A, led to phosphorylation of TYK2, STAT1, and STAT3 (fig. S7A). These data confirmed the catalytic impairment of TYK2 P1104A, in terms of both auto- and transphosphorylation (39). We then compared the abilities of TYK2 WT and P1104A to autophosphorylate and transphosphorylate recombinant STAT1 and STAT3 in an in vitro kinase assay. U1A cells were transfected with TYK2 WT or P1104A and left unstimulated or stimulated with IFN- $\beta$ . TYK2 was immunoprecipitated and assayed in vitro for autophosphorylation and transphosphorylation of recombinant STAT1 and STAT3 in the presence of ATP. When purified from IFN- $\beta$ -treated cells, TYK2 WT, but not P1104A, had detectable in vitro kinase activity, phosphorylating itself and recombinant STAT substrates (Fig. 5A). Notably, TYK2 P1104A immunoprecipitated from cells stimulated with IFN- $\beta$  was phosphorylated (Fig. 5A, lane 7). Thus, TYK2 P1104A cannot phosphorylate itself and STAT proteins in vitro, yet it can be phosphorylated in cells most likely by the proximal JAK1. These results render the selective impairment of the IL-23-responsive pathway even more intriguing.

#### **TYK2 P1104A and JAK2 are in proximity after IL-23 stimulation**

Our studies of lymphoid cell lines overexpressing the P1104A allele or derived from patients homozygous for P1104A revealed a normal response to IL-12 and an impaired response to IL-23. We therefore decided to study the proximal molecular events occurring in these two pathways, which have a number of components in common. The IL-12 and IL-23 pathways share a receptor chain (IL-12R $\beta$ 1) and two kinases (TYK2 and JAK2) (66). Little is known about the mode of TYK2 and JAK2 activation after the binding of IL-12 and IL-23 to their heterodimeric receptors (66). The IL-23R/JAK complex has been shown to assemble in a noncanonical manner, with JAK2 binding to IL-23R much farther away from the juxtamembrane region than observed for JAK2 and IL-12R $\beta$ 2 in the IL-12R/JAK complex (67). The impact of the Pro to Ala substitution on the structure of the tyrosine kinase domain of TYK2 is not known (68). We hypothesized that this substitution may perturb TYK2 folding, disrupting its proximity to JAK2 docked on IL-23R, but not IL-12R $\beta$ 2. We used the *Renilla* luciferase protein fragment complementation assay (Rluc PCA) (69, 70) to test this hypothesis (Fig. 5B). Briefly, we used reporter vectors encoding TYK2 fused to the N-terminal fragment of the Rluc protein or JAK2 fused to the C-terminal fragment of Rluc. We transiently cotransfected U1A cells previously engineered to express either IL-12 or IL-23 receptor complexes with vectors encoding both TYK2 (WT or P1104A) and JAK2 fusion proteins. We monitored bioluminescence after stimulation with IL-12 or IL-23 and the addition of benzyl-coelenterazine. JAK2 interacted with both TYK2 WT and P1104A, as shown by measurements of luciferase induction, invalidating our working hypothesis (Fig. 5B). Hence, we conclude that, in this context, the Pro to Ala substitution in TYK2 does not alter the proximity of the two enzymes docked on the IL-23 receptor complex.

#### **TYK2 catalytic activity is required for IL-23 signaling**

We then tested the specific requirement of TYK2 versus JAK2 catalytic activities for cellular responses to IL-12 and IL-23. We engineered JAK2 P1057A carrying the same Pro to Ala mutation as TYK2 P1104A (41) and JAK2 K882E as a kinase-dead negative control (71). HEK293T cells were first transfected with the different alleles. Like TYK2 P1104A, JAK2 P1057A displayed impaired autophosphorylation (fig. S7, A and B). We then used TYK2-deficient U1A cells expressing IL-12R $\beta$ 1, IL-12R $\beta$ 2, and IL-23R and engineered JAK2-deficient fibrosarcoma  $\gamma$ 2A cells to express IL-12R $\beta$ 1, IL-12R $\beta$ 2, and IL-23R. These  $\gamma$ 2A cells were transfected with JAK2 alleles, whereas U1A cells were transfected with TYK2 alleles. All cell lines were stimulated with IL-12 or IL-23. The expression of TYK2 and JAK2 and the phosphorylation of TYK2, JAK2, STAT1, and STAT3 were analyzed by Western blotting. TYK2 P1104A did not rescue phosphorylation of TYK2, JAK2, STAT3, and STAT1 in response to IL-23, but rescued response to IL-12 (Fig. 5C and fig. S7C). The phosphorylation of TYK2 P1104A by WT JAK2 in response to IL-12 was consistent with that previously seen by WT JAK1 in response to IFN- $\beta$  (Fig. 5A). These data indicated that TYK2 P1104A, unlike K930R, was impaired as an enzyme but not as a substrate. In contrast, JAK2 P1057A was phosphorylated by WT TYK2 in response to both IL-12 and IL-23 (Fig. 5C and fig. S7C), unlike JAK2 K882E, thereby leading to STAT1 phosphorylation. Together, these results suggest that IL-12 signaling can occur in the presence of only one active kinase, either JAK2 or TYK2, as long as the juxtaposed JAK can be phosphorylated. In contrast, IL-23 signaling specifically requires a catalytically active TYK2, because in this context TYK2 P1104A cannot be phosphorylated by JAK2. This may result from the different positioning of JAK2 and TYK2 within the IL-12 and IL-23 receptor complexes, which, in turn, determines the mode of activation and the specific role of each enzyme.

#### **IL-23-mediated production of IFN- $\gamma$ is impaired in TYK2 P1104A cells**

We then analyzed the cellular basis of mycobacterial diseases in the patients. Human antimycobacterial immunity is controlled by IFN- $\gamma$  (12). We analyzed the ex vivo responses of leukocytes to IL-12 and IL-23, the two TYK2-dependent cytokines that can induce IFN- $\gamma$  (66, 72–74). We first performed a global analysis of leukocytes, in the form of whole blood or peripheral blood mononuclear cells (PBMCs). Whole blood from healthy travel controls (control samples transported with the patients' blood), and from individuals homozygous for P1104A or I684S, or with complete TYK2 or IL-12R $\beta$ 1 deficiency, were either left nonstimulated or stimulated with BCG alone or with BCG plus IL-12. IFN- $\gamma$  levels in the supernatant were determined by enzyme-linked immunosorbent assay (ELISA) 48 hours later (Fig. 6A). As a control, the blood was stimulated with BCG alone or with BCG plus IFN- $\gamma$ , and the production of IL-12p40 was evaluated (fig. S8A). Blood from all five P1104A homozygous patients tested responded normally to IL-12, as reported for I684S homozygotes, but not TYK2-deficient patients (Fig. 6A). All of these patients also produced normal amounts of IL-12p40 (fig. S8A). Stimulation was also performed with BCG plus IL-23 for three P1104A patients, and IFN- $\gamma$  production was measured. No induction of IFN- $\gamma$  was detected after the addition of IL-23 to whole blood from patients homozygous for P1104A (fig. S8B). The same assay was performed with PBMCs from five P1104A patients. Five patients with DN-STAT3 deficiency, a patient with complete TYK2 deficiency

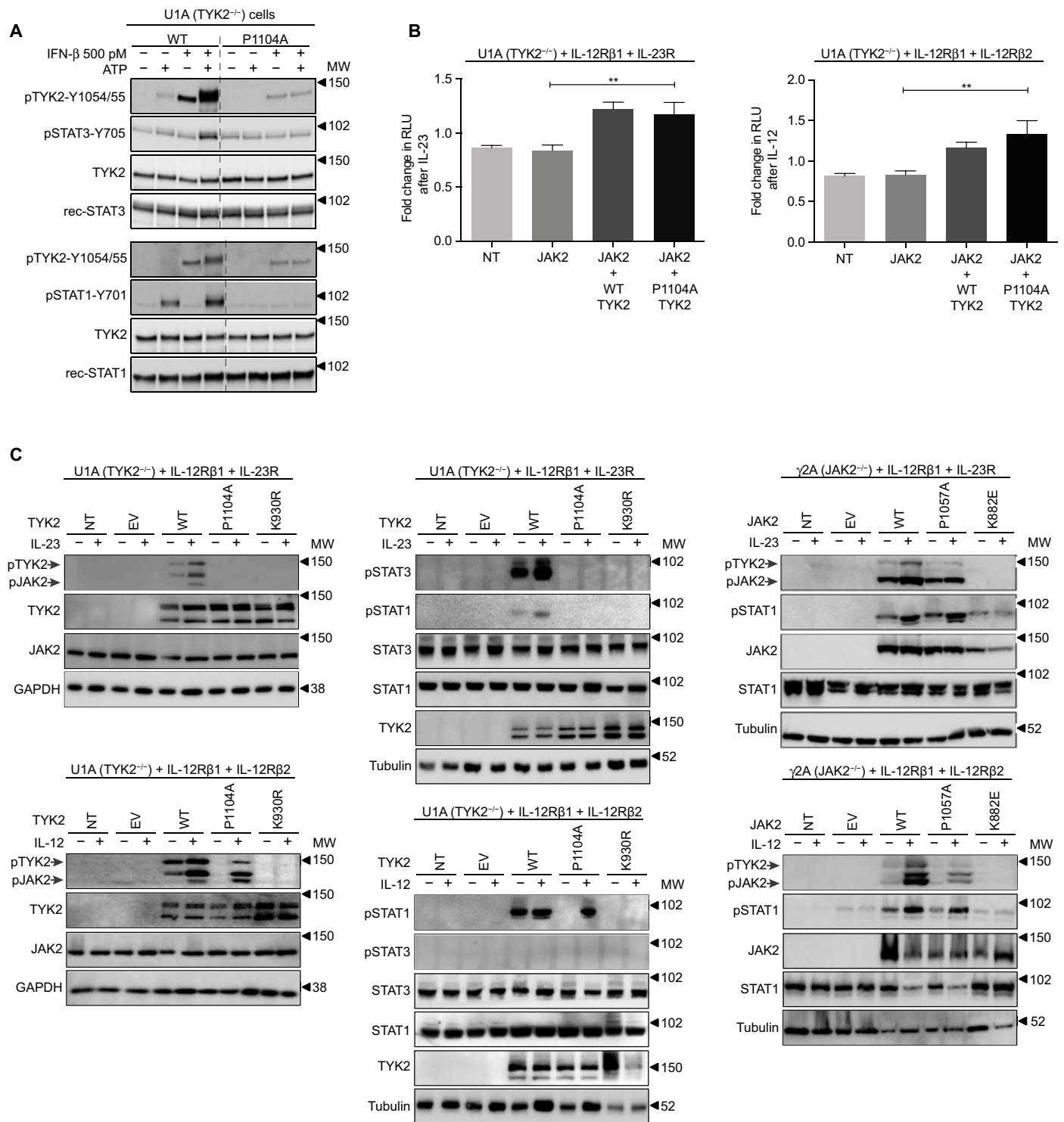


**Fig. 5. Molecular mechanisms of impaired response to IL-23 by TYK2 P1104A.** (A) In vitro kinase assay performed in the presence or absence of added ATP on TYK2 immunopurified from human TYK2-deficient cells (U1A) stably reconstituted with either TYK2 WT or TYK2 P1104A. RecSTAT3 (top) or recSTAT1 (bottom) was added to the reaction mixture. The products of the reaction were analyzed by immunoblotting with antibodies specific to the two activation loop tyrosine residues of TYK2 (Tyr<sup>1054-1055</sup>), phospho-STAT1 (Tyr<sup>701</sup>), or phospho-STAT3 (Tyr<sup>705</sup>). (B) Fold change in Renilla luciferase (RLU) after stimulation with IL-23 (left) or IL-12 (right) in TYK2<sup>-/-</sup> cells stably reconstituted with IL-12R $\beta$ 1 and IL-23R (left) or IL-12R $\beta$ 1 and IL-12R $\beta$ 2 (right). Cells were left untransfected, or were transfected with JAK2 and TYK2 fused to Rluc fragments, for the detection of interactions after stimulation. The TYK2 used was either WT or P1104A. (C) Phosphorylation of JAK2, TYK2, STAT1, and STAT3 after stimulation with IL-12 and IL-23 in TYK2<sup>-/-</sup> and JAK2<sup>-/-</sup> fibrosarcoma cells reconstituted with IL-12R $\beta$ 1, IL-12R $\beta$ 2, and IL-23R. TYK2<sup>-/-</sup> cells were transfected with WT, P1104A, or K930R TYK2, and JAK2<sup>-/-</sup> cells were transfected with WT, P1057A, or K882E JAK2.

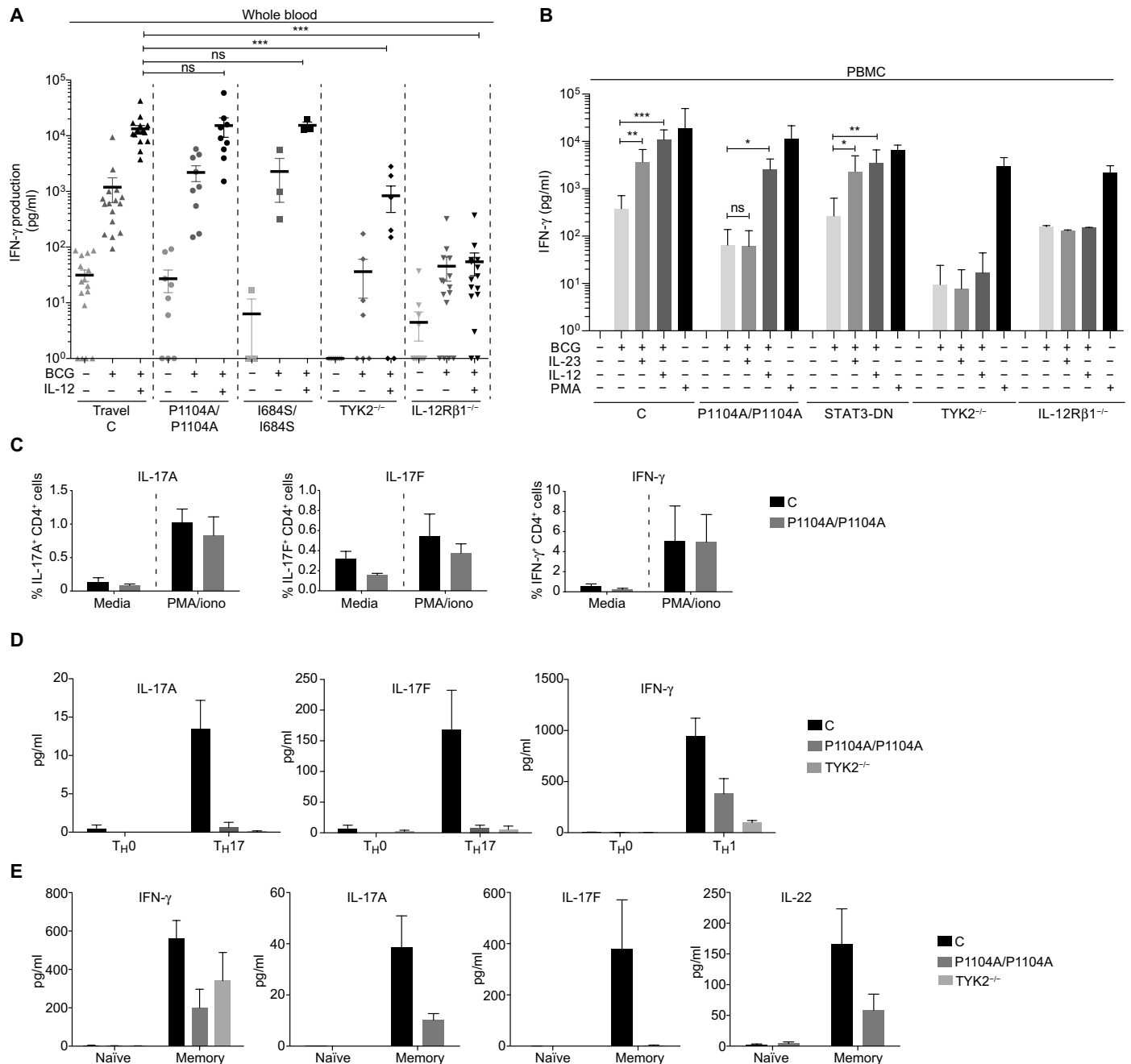


**Fig. 6. Analysis of primary cells from patients.** (A) ELISA analysis of IFN- $\gamma$  levels in whole blood after stimulation with BCG, or BCG plus IL-12, in travel controls, TYK2-deficient and IL-12R $\beta$ 1-deficient patients, and patients homozygous for the P1104A or I684S TYK2 alleles. \* $P$  < 0.05, \*\* $P$  < 0.01, \*\*\* $P$  < 0.001, two-tailed Student's  $t$  tests. (B) Production of IFN- $\gamma$  from PBMCs stimulated with BCG, BCG plus IL-12, BCG plus IL-23, or PMA plus ionomycin (PMA) in healthy controls, homozygous TYK2 P1104A patients, hyper-IgE patients with heterozygous *STAT3* mutations (*STAT3*-DN), and patients with complete TYK2 and IL-12R $\beta$ 1 deficiencies, as determined by ELISA. (C) Percentages of IL-17A<sup>+</sup>, IL-17F<sup>+</sup>, and IFN- $\gamma$ <sup>+</sup> CD4<sup>+</sup> T cells after the stimulation of PBMCs from healthy controls and patients homozygous for TYK2 P1104A with PMA plus ionomycin. (D) In vitro differentiation of naive CD4<sup>+</sup> T cells from healthy controls, patients homozygous for P1104A TYK2 alleles, and patients with TYK2 deficiency, after culture under T<sub>H</sub>17 (with IL-23) or T<sub>H</sub>1 (with IL-12) polarizing conditions, as determined by assessments of the induction of IL-17A/F and IFN- $\gamma$  secretion, respectively. (E) Production of IFN- $\gamma$ , IL-17A, IL-17F, and IL-22 by naive and memory CD4<sup>+</sup> T cells from healthy controls, patients homozygous for P1104A TYK2, and TYK2-deficient patients, stimulated with TAE beads for 5 days.

(tested twice), and two patients with complete IL-12R $\beta$ 1 deficiency were used as controls (Fig. 6B). Like patients with complete TYK2 and IL-12R $\beta$ 1 deficiencies, P1104A homozygotes did not respond to IL-23, in terms of IFN- $\gamma$  production, as shown by comparison

with healthy controls. Cells from DN-*STAT3* patients responded normally, consistent with the absence of susceptibility to mycobacterial disease in these patients (75). This lack of susceptibility may result from residual *STAT3* activity, the involvement of another

STAT, or both. TYK2 P1104A patients thus displayed impaired IL-23-mediated IFN- $\gamma$  immunity.

### The production of IFN- $\gamma$ is impaired in T<sub>H</sub> cells homozygous for P1104A

We analyzed individual T cell subsets. Consistent with the results obtained for IL-12R $\beta$ 1- and IL-23R-deficient patients reported in a companion paper (76), in both of whom the IL-23 response was completely abolished, P1104A homozygotes had higher percentages of naïve T cells than of effector memory T cells. This difference was particularly marked for the CD8<sup>+</sup> T cell compartment (fig. S8C). Given the known role of human IL-23 in the development of IL-17<sup>+</sup> CD4<sup>+</sup> T cells (77), we assessed the ex vivo production of IL-17 cytokines by PBMCs upon stimulation with phorbol 12-myristate 13-acetate (PMA) plus ionomycin by intracellular flow cytometry (Fig. 6C). Patients homozygous for P1104A, like patients with complete TYK2 deficiency (10), had normal proportions of IL-17A<sup>+</sup> and IL-17F<sup>+</sup> CD4<sup>+</sup> T cells, probably because of residual TYK2-independent responses to IL-23 (10, 28), and consistent with the absence of CMC in these patients. In these conditions, the percentages of IFN- $\gamma$ <sup>+</sup> CD4<sup>+</sup> T cells in P1104A patients were also normal (Fig. 6C). We also analyzed the frequencies of the four different CD4<sup>+</sup> memory T helper (T<sub>H</sub>) cell subsets (T<sub>H</sub>1, T<sub>H</sub>2, T<sub>H</sub>17, and T<sub>H</sub>1\*), as determined by the differential expression of CCR6, CCR4, and CXCR3, in only one patient. The frequencies of T<sub>H</sub>1 (CXCR3<sup>+</sup>CCR6<sup>-</sup>) and T<sub>H</sub>1\* (CXCR3<sup>+</sup>CCR6<sup>+</sup>) cells, the main memory subsets involved in antimycobacterial immunity (76, 78), were found to be low (fig. S8E).

### The response to IL-23 is impaired in T cells homozygous for P1104A

We then studied the capacity of naïve CD4<sup>+</sup> T cells from P1104A homozygotes to differentiate into T<sub>H</sub>17 cells in an IL-23-dependent manner, using T cell activation and expansion (TAE) beads (antibodies directed against CD2, CD3, and CD28) in addition to TGF- $\beta$  (transforming growth factor- $\beta$ ), IL-1 $\beta$ , IL-6, IL-21, IL-23, anti-IL-4, and anti-IFN- $\gamma$  (79). These cells were unable to produce IL-17A/IL-17F, consistent with the impairment of IL-23 signaling, as observed in IL-12R $\beta$ 1- and TYK2-deficient patients (Fig. 6D). Conversely, naïve CD4<sup>+</sup> T cells from P1104A homozygotes were able to differentiate into IFN- $\gamma$ -producing T<sub>H</sub>1 cells in an IL-12-dependent manner (TAE beads and IL-12), like control cells and cells from IL-23R-deficient patients, but unlike cells from TYK2-, IL-12R $\beta$ 1-, and IL-12R $\beta$ 2-deficient patients (Fig. 6D and companion paper). We also analyzed the memory CD4<sup>+</sup> T cell compartment of five P1104A patients by stimulating these cells with TAE beads. As expected, incubation with these beads resulted in lower levels of T<sub>H</sub>17 cytokines (IL-17A, IL-17F, and IL-22) being produced by TYK2 P1104A memory CD4<sup>+</sup> T cells than memory CD4<sup>+</sup> T cells from healthy donors (Fig. 6E and fig. S8D). Moreover, P1104A cells had a reduced capacity to produce IFN- $\gamma$ , similar to that of IL-23R- and IL-12R $\beta$ 1-deficient cells. Overall, these data reveal that P1104A homozygosity impairs IL-23, but not IL-12, responses in peripheral CD4<sup>+</sup> T cells, as previously shown in B and T cell lines. They also show that CD4<sup>+</sup> T cells of P1104A homozygotes have impaired IFN- $\gamma$  production, due to their very weak response to IL-23, accounting for the susceptibility to MSMD or primary tuberculosis. Paradoxically, the TYK2-dependent response to IL-23 that is disrupted by P1104A is essential for antimycobacterial IFN- $\gamma$  immunity, but seems to be redundant for anti-

fungal IL-17 immunity, given the absence of *Candida* infection in the patients described here.

### The frequencies of MSMD and tuberculosis differ in P1104A homozygotes

The clinical infectious presentation of the 10 P1104A homozygotes was restricted to mycobacterial disease. The penetrance for infections due to weakly virulent mycobacteria (MSMD) is probably lower than that for primary tuberculosis after exposure to these microbial species, as inferred from (i) the lower ethnicity-adjusted ORs estimated for MSMD (~23) than for primary tuberculosis (~89); (ii) the respective frequencies of MSMD (about 1/50,000 BCG-vaccinated individuals, as inferred from the equal proportions of idiopathic BCG-osis, and severe combined immunodeficiency, the frequency of which has been determined in several human populations) (80) and primary tuberculosis in human populations (about 5 to 7% of infected individuals) (9, 81), reflecting the difference in virulence between the causal mycobacteria; (iii) the higher level of exposure worldwide to BCG and environmental mycobacteria than to *M. tuberculosis*; and (iv) the biological impact of P1104A homozygosity (severely impaired but not abolished response to IL-23 and normal response to IL-12) relative to that of IL-12R $\beta$ 1 deficiency (abolished responses to both IL-12 and IL-23) (20, 25). The vast majority of P1104A homozygotes worldwide would be predicted to be asymptomatic, particularly if living in areas of low endemicity for tuberculosis. Most of the patients with symptoms would be predicted to suffer from tuberculosis, with only a minority presenting MSMD. Our own observation of three patients with MSMD and seven patients with tuberculosis reflects an ascertainment bias, because the proportion of all patients worldwide included in our database is much higher for MSMD than for tuberculosis. The proportions of P1104A homozygotes with these two diseases were similar in our study: MSMD (3/464 = 0.6%) and tuberculosis (7/453 = 1.5%). Because tuberculosis is much more common than MSMD by at least two orders of magnitude (and probably around three orders of magnitude in highly endemic areas), it would be expected to be, by far, the most frequent disease in symptomatic P1104A homozygotes.

### The penetrance of P1104A homozygosity is high for tuberculosis

A more formal estimation of the penetrance of P1104A homozygosity for tuberculosis (or MSMD), denoted  $F_{\text{TYK2TB}}$  (or  $F_{\text{TYK2MSMD}}$  for MSMD), can be calculated from the observed ORs, and the probability of developing tuberculosis (or MSMD) for those infected who are not P1104A homozygotes, denoted  $F_{\text{TB}}$  (or  $F_{\text{MSMD}}$ ), is detailed in Supplementary Materials and Methods. Because P1104A homozygotes account for only a small proportion of tuberculosis (or MSMD) cases (see below),  $F_{\text{TB}}$  (or  $F_{\text{MSMD}}$ ) can reasonably be inferred from the general risk of primary tuberculosis (or MSMD) for an infected individual indicated above [see (ii)]. For P1104A, we used the frequency observed in North Africa (1.8%), which is approximately the same as the mean frequency in the regions in which our tuberculosis and MSMD patients were living. For an  $F_{\text{TB}}$  value of 5% and an OR of 89.31 (14.7 to 1725), the estimated  $F_{\text{TYK2TB}}$  is 82% (44 to 99%) and the proportion of tuberculosis cases due to P1104A homozygotes is 0.5% (0.3 to 0.6%) for a P1104A minor allele frequency (MAF) of 1.8%. For an  $F_{\text{MSMD}}$  value of 0.002% (corresponding to a prevalence of MSMD of 1/50,000) and an OR of

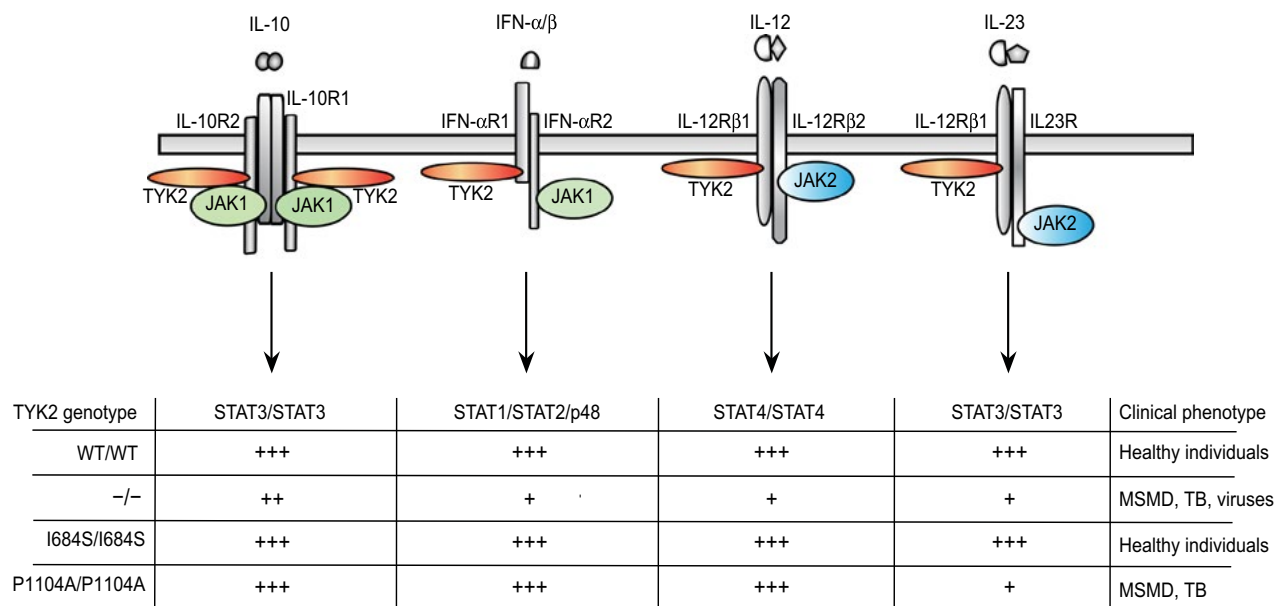


**Fig. 7. Schematic representation of TYK2-dependent signaling pathways.** The cytokines, receptors, and JAK and STAT complexes formed are indicated. A summary of the functionality of each pathway is provided for the various genotypes: TYK2 WT/WT, TYK2<sup>-/-</sup>, TYK2 I684S/I684S, and TYK2 P1104A/P1104A. The main STAT-containing complexes are shown. Other complexes include STAT1/STAT1 in response to IL-10, IL-12, IL-23, and IFN- $\alpha/\beta$  and STAT3/STAT3 and STAT4/STAT4 in response to IFN- $\alpha/\beta$ . The symbol +++ indicates that the pathway is functional and optimal (corresponding to WT TYK2). The symbol ++ indicates that the function of the pathway is decreased without overt clinical implications. The symbol + means that the function of the pathway is impaired, but not completely abolished because of TYK2-independent residual signaling, and can bear clinical consequences (except for IL-10). The clinical phenotypes of individuals homozygous for the WT, P1104A, and I684S TYK2 alleles are indicated on the right.

23.53 (2 to 483), the estimated  $F_{TYK2MSMD}$  is 0.05% (0.004 to 1%) and the proportion of MSMD cases due to P1104A homozygosity is 0.7% (0.06 to 15%) for the same MAF (1.8%). This proportion is close to that estimated for tuberculosis here (0.5%). The CIs associated with these estimates are large, but these findings clearly indicate that the penetrance of P1104A homozygosity is high for tuberculosis in endemic areas (about 80%), certainly much higher than that for MSMD in areas in which BCG vaccination is mandatory (about 0.05%). Conversely, the penetrance of IL-12R $\beta$ 1 deficiency for MSMD is higher, estimated at about 80% in adults (20), consistent with the observation that most of these patients present with MSMD, whereas most patients homozygous for P1104A present with tuberculosis. Consistently, homozygosity for TYK2 P1104A is predicted to account for about 0.5% of cases of primary tuberculosis in areas of endemic disease, such as Morocco, whereas AR TYK2 and IL-12R $\beta$ 1 complete deficiency are much less common genetic etiologies.

**DISCUSSION**

In conclusion, homozygosity for TYK2 P1104A confers a predisposition to severe mycobacterial diseases, including MSMD and, more frequently, primary tuberculosis. Several genome-wide association studies have shown that homozygosity for TYK2 P1104A has a strong protective effect (ORs ranging from 0.1 to 0.3) against various autoinflammatory or autoimmune conditions (41). Our findings suggest a mechanism based on selective or preferential impairment of the IL-23 responsive pathway (Fig. 7). In other experimental conditions, TYK2 P1104A also impaired IL-12 and IFN- $\alpha/\beta$  responses (41). These findings are unlikely to be physiologically relevant, as illustrated by the viral infections seen in TYK2-deficient

but not P1104A-homozygous patients (10). The higher incidence of inflammatory conditions in modern adults than in earlier human populations may result partly from the negative selection of alleles, such as P1104A, that impair protective immunity to primary infection by dampening inflammatory responses (82–84). In this respect, this study should also help to delimit the potential beneficial and adverse effects of pharmaceutical TYK2 inhibitors (85–87).

The P1104A TYK2 variant selectively disrupts IL-23-dependent antimycobacterial IFN- $\gamma$  immunity, accounting for the susceptibility of homozygotes to mycobacteria. The gradual decline of the P1104A allele in the European continent, which requires further investigation using more ancient DNA samples from different geographic locations and epochs, suggests that tuberculosis has been continuously endemic from the Neolithic until the middle of the 20th century (56). Given the current MAF for P1104A of 4.2% in European populations, there are about 1/600 (1.7/1000) homozygotes in Europe and populations of European descent, making P1104A TYK2 homozygosity an AR condition almost as frequent in Europeans as hemochromatosis (3/1000) and more common than cystic fibrosis (0.4/1000) and  $\alpha$ 1 anti-trypsin deficiency (0.4/1000). Our findings are thus important and support a revision of the genetic architecture of human diseases, because tuberculosis is much more common than these three other AR disorders. They suggest that common infections, and more generally common human diseases, may be caused by relatively common AR disorders in a small but not negligible proportion of patients.

The clinical penetrance of P1104A homozygosity for mycobacterial disease in Europe is now particularly low, because few Europeans are exposed to BCG, and even fewer to *M. tuberculosis*. The vast majority of present-day European homozygotes are apparently

healthy (41, 42). Genetic testing before travels into endemic areas may, however, be warranted. Homozygosity for P1104A is more likely to be symptomatic elsewhere, as illustrated by the fact that 9 of our 10 patients are from geographic regions outside Europe, in continents on which BCG vaccination is mandatory and tuberculosis is endemic. Between 1/10,000 and 1/1000 individuals are homozygous in endemic regions of the world (other than East Asia), where P1104A TYK2 is likely to define a strictly recessive but relatively common etiology of severe primary tuberculosis (about 0.5% of cases). This observation has important clinical implications, because injections of recombinant IFN- $\gamma$  would probably be beneficial in these patients, as it is in patients with IL-12R $\beta$ 1 deficiency (12, 19, 88).

## MATERIALS AND METHODS

### Study design

We studied the contributions of two common *TYK2* missense variants, I684S and P1104A, to predisposition to mycobacterial diseases. We screened our WES database including 463 patients with MSMD, 454 with tuberculosis, and 2835 with non-mycobacterial infections used as controls, as well as the WES data of the 2504 from the 1000 Genomes Project (a total of 5339 controls). We tested the association of the two *TYK2* variants with MSMD and tuberculosis using a logistic regression model including the first three principal components of the PCA to account for the ethnic heterogeneity of the cohorts. After adjusting for ethnicity, we found a strong enrichment of P1104A homozygotes in the tuberculosis cohort ( $P = 8.37 \times 10^{-8}$ ; OR, 89.31; 95% CI, 14.7 to 1725) and, to a lesser extent, in the MSMD cohort ( $P = 3.27 \times 10^{-3}$ ; OR, 23.53; 95% CI, 2.9 to 483). We analyzed the occurrence of negative selection acting on the two *TYK2* variants by testing whether their frequency in Europeans has decreased more than other variants that were in the same frequency range 4000 years ago. We tested the impact of both *TYK2* variant in both transduced cell lines and homozygous patients' cell lines in terms of cellular responses to IL-10, IL-12, IL-23, and IFN- $\alpha/\beta$ . We also tested the patient's primary leukocytes.

### Ethics statement

This study was conducted in accordance with the Helsinki Declaration, with written informed consent obtained from the patients' families. Approval for this study was obtained from the French Ethics Committee "Comité de Protection des Personnes," The French National Agency for Medicine and Health Product Safety (ANSM) and the Institut National de la Santé et de la Recherche Médicale in France, and the Rockefeller University Institutional Review Board (IRB), New York, USA.

### Whole-blood activation experiments

Venous blood samples from controls and patients were collected into heparin-containing tubes and processed according to a modified version of the protocol described by Feinberg *et al.* (89). Briefly, they were diluted 1:2 in RPMI 1640 (Gibco BRL) and supplemented with penicillin (100 U/ml) and streptomycin (100  $\mu$ g/ml) (Gibco BRL). We then dispensed 5 ml of each diluted blood sample into each of five wells (1 ml per well) of a 48-well plate (Nunc). These samples were incubated for 48 hours at 37°C under an atmosphere containing 5% CO<sub>2</sub>/95% air, under three different sets of activation conditions:

with medium alone, with live BCG (*Mycobacterium bovis* BCG, Pasteur substrain) at a multiplicity of infection (MOI) of 20 BCG cells per leukocyte, with BCG plus recombinant human (rh) IL-23 (100 ng/ml; R&D Systems), with BCG plus rhIL-12 (20 ng/ml; R&D Systems), and with PMA (40 ng/ml; Sigma-Aldrich) plus ionomycin (10<sup>-5</sup> M; Sigma-Aldrich). ELISA was then performed on the collected supernatants, with the human IFN- $\gamma$  ELISA Kit (Ready-SET-Go! from eBioscience or PeliPair from Sanquin), in accordance with the manufacturer's instructions. All venous blood samples were collected in accordance with the IRB protocols of The Rockefeller University, New York.

### Plasmids and retroviral transduction of T and B cell lines

T cell lines (HVS-T) and EBV-transformed lymphoblastoid cell lines (EBV-B cells) were generated by infecting PBMCs from healthy controls or patients with HVS or EBV, as previously described (10). A retroviral vector expressing WT *TYK2* was generated by inserting the *TYK2* sequence from pMSCVpuro retrovirus (Takara Bio Inc.) into the pLZRS-IRES- $\Delta$ NGFR vector, which contains a puromycin resistance cassette (60). The WT *TYK2* allele used here contains a mutation at position 1016, P1016S. Various alleles of *TYK2* (P1104A, I684S, and K930R) were then generated by site-directed mutagenesis, with specific primers and the PfuUltra II Hotstart PCR Master Mix (Agilent Technologies), according to the manufacturer's instructions. The plasmids were used to transfect Phoenix-A packing cells to generate retroviral particles carrying each allelic variant. Briefly, 10  $\mu$ g of vector was used to transfect Phoenix-A packaging cells in the presence of Opti-MEM + GlutaMAX (Gibco) and X-tremeGENE 9 (Roche), according to the manufacturer's instructions. Positively transfected cells were selected with puromycin (Gibco) at a concentration of 2  $\mu$ g/ml until all the cells were positive for the surface expression of  $\Delta$ NGFR, as assessed by fluorescence-activated cell sorting with Alexa Fluor 647 anti-NGFR staining (BD Pharmingen). The Phoenix-A cell culture was then split in two flasks, to which puromycin-free medium was added. After 24 hours, the supernatant was collected and retroviral particles were concentrated with Retro-X Concentrator (Clontech) according to the manufacturer's instructions. One million HVS-T cells were mixed with retrovirus-containing supernatant in a total volume of 2 ml. After incubation for 24 hours, 200  $\mu$ l of fetal calf serum was added and the cells were allowed to grow for a further 4 days. Transduced cells were positively purified by magnetic-activated cell sorting with an anti-NGFR-biotin antibody and an anti-biotin antibody conjugated with magnetic beads (Miltenyi Biotec) according to the manufacturer's protocol.

### Cell culture and stimulation

EBV-B cells were cultured in RPMI (Gibco) supplemented with 10% fetal bovine serum (FBS) (Invitrogen). HVS-T cells were cultured in a 1:1 mixture (by volume) of RPMI and Panserin 401 (PAN Biotech) supplemented with 10% FBS, GlutaMAX (350  $\mu$ g/ml; Gibco), gentamicin (0.1 mg/ml; Gibco), and rhIL-2 (20 IU/ml; Roche). The cells were then starved for 2 hours by incubation in serum-free RPMI. The cells were then left unstimulated or were stimulated with rhIFN- $\alpha$  2b (3.2  $\times 10^4$  IU/ml; Schering), rhIL-23 (100 ng/ml; R&D Systems), rhIL-12 (20 ng/ml; R&D Systems), or rhIL-10 (50 ng/ml; PeproTech) for 5 min to assess the phosphorylation of TYK2, JAK1, or JAK2 and for 30 min to assess the phosphorylation of STAT1, STAT3, or STAT4. A dose-response experiment was performed on EBV-B cells, with different concentrations of rhIL-23 ranging from

50 to 200 ng/ml and a stimulation time of 30 min. A kinetic analysis of the response to IL-23 was also performed, in which EBV-B cells were stimulated with rhIL-23 (100 µg/ml) for 0, 1, 3, and 5 hours. For RT-qPCR, cells were stimulated for 6 hours with IL-10 (50 ng/ml), IL-23 (100 ng/ml), or IFN- $\alpha$  ( $10^5$  IU/ml). For the RNA-seq experiment, cells were stimulated for 8 hours with IL-23 (100 ng/ml) or IFN- $\alpha$  ( $10^5$  IU/ml).

### Western blotting

Total protein was extracted from EBV-B or HVS-T cells in a lysis buffer containing 1% NP-40, 20 mM Tris-HCl (pH 7.4), 140 mM NaCl, 2 mM EDTA, and 50 nM NaF supplemented with 100 mM orthovanadate, 200 mM phenylmethylsulfonyl fluoride, 1% aprotinin, pepstatin (1 mg/ml), leupeptin (1 mg/ml), and antipain (1 mg/ml). Protein extracts were separated by SDS-polyacrylamide gel electrophoresis, and the resulting bands were electroblotted onto polyvinylidene difluoride membranes. The blots were incubated for 1 hour with a blocking solution consisting of tris-buffered saline (TBS), 0.01% Tween 20 (Sigma-Aldrich), and 5% nonfat milk powder (Bio-Rad). The following primary antibodies were diluted 1:1000 with the blocking solution and incubated overnight with the blots: rabbit anti-phospho-Y1054/1055 TYK2 (Cell Signaling Technology), rabbit anti-phospho-1022/1023 JAK1 (Cell Signaling Technology), rabbit anti-phospho-1007/1008 JAK2 (Cell Signaling Technology), mouse anti-phospho-Y701 STAT1 (BD), rabbit anti-phospho-Y705 STAT3 (Cell Signaling Technology), rabbit anti-phospho-693 STAT4 (Cell Signaling Technology), mouse anti-STAT1 (BD), mouse anti-STAT3 (Cell Signaling Technology), rabbit anti-STAT4 (Cell Signaling Technology), mouse anti-tubulin (Santa Cruz Biotechnology Inc.), and rabbit anti-GAPDH (glyceraldehyde-3-phosphate dehydrogenase) (Santa Cruz Biotechnology Inc.) antibodies. The blots were washed three times, for 10 min per wash, with washing buffer consisting of TBS plus 0.01% Tween 20. An anti-rabbit horseradish peroxidase (HRP) or anti-mouse HRP antibody (GE Healthcare) was then added at a dilution of 1:10,000 or 1:5000, respectively, and the blots were incubated for 1 hour. Last, the blots were washed with washing buffer, and antibody binding was detected with the SuperSignal West Femto System (Thermo Fisher Scientific). The membranes were analyzed with an Amersham Imager 600 instrument (GE Healthcare Life Sciences).

For fig. S3D, immunoblots were revealed using enhanced chemiluminescence detection reagent (Western Lightning, PerkinElmer) and signals were acquired with Fuji ImageQuant LAS 4000. The intensity of bands was quantified with MultiGauge software. In IFN-stimulated samples, for each protein, the intensity of the phosphorylated band was normalized by the corresponding total protein content. The level of phosphorylated band in control cells was set as 100. All the other Western blots were analyzed and quantified using the ImageJ software [National Institutes of Health (NIH)] following the manufacturer's instructions. The phosphorylation of TYK2, JAK2, JAK1, STAT1, STAT3, and STAT4 for each treatment was normalized with the density of total TYK2, JAK2, JAK1, STAT1, STAT3, and STAT4, respectively, and the quantification was expressed in arbitrary units (relative density). Statistical analysis was performed considering technical replicates for the transduced cells with the TYK2 alleles, and technical and biological replicates for EBV-B and HVS-T cell lines derived from controls and patients.

### Population genetic analysis

We investigated the occurrence of strong negative selection acting on the candidate *TYK2* missense variants over the last few hundreds of generations, by comparing the current allele frequency of these variants in Europeans with that estimated from the low-coverage sequenced genomes of 22 individuals from Late Stone Age (LSA) Central Europe (52). For a candidate variant at frequency  $p_t$  in the current generation and  $p_0$  during the LSA, we retrieved all variants with a frequency of  $p_0 \pm 1\%$  during this time period and considered the candidate variant to have been under strong and recent negative selection if its frequency  $p_t$  was among the lowest 5% of values for all the variants retrieved. Only variants that were still segregating in the current European population (CEU, TSI, or FIN from the 1000 Genomes Project) were considered in this analysis.

We checked that these empirical observations were not biased due to sampling or sequencing errors, by performing 100,000 forward simulations under the Wright-Fisher neutral model (R code available upon request). We simulated the fate of a neutral allele at frequency  $p_0$  160 generations ago, in a population of size  $N_e = 4000$ , and retrieved the distribution of its current frequency  $p_t$  (160 generations later) across all simulations. The lower quantiles of the simulated and observed distributions were largely similar (Fig. 1E), suggesting that our analyses were unbiased.

### WES and RNA-seq analyses

WES was performed as previously described (47). For RNA-seq, reads were mapped with STAR v2.5.3a (90). A genome index specific to our data was first created, and single-end reads were then aligned, in a two-pass mode in which novel splicing junctions are first detected, before final mapping. Read counts were obtained for each gene with HTSeq v0.9.1 (91). Homozygosity rates from exome data were estimated as described previously (47). Gene expression levels were estimated with TPM (transcripts per kilobase million). TPM takes into account the size of each sample library and gene lengths to assess expression levels (92).

Statistical analysis was performed with R v3.2.3 (93) (www.R-project.org/). Gene expression profiles are expressed as the fold change in expression between the values obtained before and after stimulation. These profiles were compared between the different groups of individuals: controls ( $n = 2$ ), TYK2 P1104A ( $n = 2$ ), IL12RB1<sup>-/-</sup> ( $n = 1$ ), TYK2<sup>-/-</sup> ( $n = 1$ ), and STAT1<sup>-/-</sup> ( $n = 1$ ).

### Variant enrichment analysis

We performed an enrichment analysis of *TYK2* variants in our two cohorts of 463 MSMD patients and 454 tuberculosis patients. We used as controls 2835 individuals of diverse ethnic origin (as shown in PCA of fig. S1C) from our in-house database who were patients with various genetically unexplained non-mycobacterial infections, as well as the 2504 individuals of the 1000 Genomes Project, leading to a total of 5339 controls. The proportion of individuals with specific *TYK2* variants in each cohort were compared by means of logistic regression using the likelihood ratio test. To account for the ethnic heterogeneity of the cohorts, the first three principal components of the PCA were systematically included in the logistic regression model, as previously described (48). ORs were also estimated by logistic regression and adjusted for ethnic heterogeneity.

## SUPPLEMENTARY MATERIALS

immunology.sciencemag.org/cgi/content/full/3/30/eaau8714/DC1

## Materials and Methods

## Case Reports

Fig. S1. Population and medical genetics.

Fig. S2. Response to IFN- $\alpha/\beta$ , IL-10, IL-12, and IL-23 in TYK2-deficient cell lines transduced with different TYK2 alleles.

Fig. S3. Response to IFN- $\alpha/\beta$  in cell lines with different TYK2 genotypes.

Fig. S4. Response to IL-12 and IL-10 in cell lines with different TYK2 genotypes.

Fig. S5. Response to IL-23 in cell lines with different TYK2 genotypes.

Fig. S6. Induction of target genes after IL-10, IFN- $\alpha$ , and IL-23 stimulation in cell lines with different TYK2 genotypes.

Fig. S7. Auto- and transphosphorylation of P1104A TYK2 and P1057A JAK2.

Fig. S8. Analysis of leukocytes with different TYK2 genotypes.

Table S1. Summary of the TYK2 genotypes among the different cohorts of patients and healthy individuals.

Table S2. Raw data used to generate dot plots and bar graphs.

References (94–96)

## REFERENCES AND NOTES

- R. M. G. J. Houben, P. J. Dodd, The global burden of latent tuberculosis infection: A re-estimation using mathematical modelling. *PLoS Med.* **13**, e1002152 (2016).
- M. W. Borgdorff, M. Sebek, R. B. Geskus, K. Kremer, N. Kalisvaart, D. van Soolingen, The incubation period distribution of tuberculosis estimated with a molecular epidemiological approach. *Int. J. Epidemiol.* **40**, 964–970 (2011).
- H. Esmail, C. E. Barry 3rd, D. B. Young, R. J. Wilkinson, The ongoing challenge of latent tuberculosis. *Philos. Trans. R. Soc. Lond. Ser. B Biol. Sci.* **369**, 20130437 (2014).
- World Health Organization, *Global Tuberculosis Report* (World Health Organization, 2015).
- L. Abel, J. El-Baghdadi, A. A. Bousfiha, J.-L. Casanova, E. Schurr, Human genetics of tuberculosis: A long and winding road. *Philos. Trans. R. Soc. Lond. Ser. B Biol. Sci.* **369**, 20130428 (2014).
- B. J. Marais, R. P. Gie, H. S. Schaaf, N. Beyers, P. R. Donald, J. R. Starke, Childhood pulmonary tuberculosis: Old wisdom and new challenges. *Am. J. Respir. Crit. Care Med.* **173**, 1078–1090 (2006).
- J. L. Casanova, L. Abel, Genetic dissection of immunity to mycobacteria: The human model. *Annu. Rev. Immunol.* **20**, 581–620 (2002).
- A. Alcaïs, C. Fieschi, L. Abel, J.-L. Casanova, Tuberculosis in children and adults: Two distinct genetic diseases. *J. Exp. Med.* **202**, 1617–1621 (2005).
- L. Abel, J. Fellay, D. W. Haas, E. Schurr, G. Srikrishna, M. Urbanowski, N. Chaturvedi, S. Srinivasan, D. H. Johnson, W. R. Bishai, Genetics of human susceptibility to active and latent tuberculosis: Present knowledge and future perspectives. *Lancet Infect. Dis.* **18**, e64–e75 (2018).
- A. Y. Kreins, M. J. Ciancanelli, S. Okada, X.-F. Kong, N. Ramirez-Alejo, S. S. Kilic, J. El Baghdadi, S. Nonoyama, S. A. Mahdaviyani, F. Aïlal, A. Bousfiha, D. Mansouri, E. Nieves, C. S. Ma, G. Rao, A. Bernasconi, H. Sun Kuehn, J. Niemela, J. Stoddard, P. Deveau, A. Cobat, S. El Azbaoui, A. Sabri, C. K. Lim, M. Sundin, D. T. Avery, R. Halwani, A. V. Grant, B. Boisson, D. Bogunovic, Y. Itan, M. Moncada-Velez, R. Martinez-Barricarte, M. Migaud, C. Deswarte, L. Alsina, D. Kotlarz, C. Klein, I. Muller-Fleckenstein, B. Fleckenstein, V. Cormier-Daire, S. Rose-John, C. Picard, L. Hammarstrom, A. Puel, S. Al-Muhsen, L. Abel, D. Chaussabel, S. D. Rosenzweig, Y. Minegishi, S. G. Tangye, J. Bustamante, J.-L. Casanova, S. Boisson-Dupuis, Human TYK2 deficiency: Mycobacterial and viral infections without hyper-IgE syndrome. *J. Exp. Med.* **212**, 1641–1662 (2015).
- S. Boisson-Dupuis, J. Bustamante, J. El-Baghdadi, Y. Camcioglu, N. Parvaneh, S. El Azbaoui, A. Agader, A. Hassani, N. El Hafidi, N. A. Mrani, Z. Jouhadi, F. Aïlal, J. Najib, I. Reisli, A. Zamani, S. Yosunkaya, S. Gulle-Girit, A. Yildiran, F. E. Cipe, S. H. Torun, A. Metin, B. Y. Atikan, N. Hatipoglu, C. Aydogmus, S. S. Kilic, F. Dogu, N. Karaca, G. Aksu, N. Kutukculer, M. Keser-Emiroglu, A. Somer, G. Tanir, C. Aytekin, P. Adimi, S. A. Mahdaviyani, S. Mamishi, A. Bousfiha, O. Sanal, D. Mansouri, J. L. Casanova, L. Abel, Inherited and acquired immunodeficiencies underlying tuberculosis in childhood. *Immunol. Rev.* **264**, 103–120 (2015).
- J. Bustamante, S. Boisson-Dupuis, L. Abel, J. L. Casanova, Mendelian susceptibility to mycobacterial disease: Genetic, immunological, and clinical features of inborn errors of IFN- $\gamma$  immunity. *Semin. Immunol.* **26**, 454–470 (2014).
- S. Boisson-Dupuis, J. El Baghdadi, N. Parvaneh, A. Bousfiha, J. Bustamante, J. Feinberg, A. Samarina, A. V. Grant, L. Janniere, N. El Hafidi, A. Hassani, D. Nolan, J. Najib, Y. Camcioglu, N. Hatipoglu, C. Aydogmus, G. Tanir, C. Aytekin, M. Keser, A. Somer, G. Aksu, N. Kutukculer, D. Mansouri, A. Mahdaviyani, S. Mamishi, A. Alcaïs, L. Abel, J. L. Casanova, IL-12R $\beta$ 1 deficiency in two of fifty children with severe tuberculosis from Iran, Morocco, and Turkey. *PLoS ONE* **6**, e18524 (2011).
- P. Tabarsi, M. Marjani, N. Mansouri, P. Farnia, S. Boisson-Dupuis, J. Bustamante, L. Abel, P. Adimi, J.-L. Casanova, D. Mansouri, Lethal tuberculosis in a previously healthy adult with IL-12 receptor deficiency. *J. Clin. Immunol.* **31**, 537–539 (2011).
- F. Altare, A. Ensser, A. Breiman, J. Reichenbach, J. E. Baghdadi, A. Fischer, J.-F. Emile, J.-L. Gaillard, E. Meini, J.-L. Casanova, Interleukin-12 receptor  $\beta$ 1 deficiency in a patient with abdominal tuberculosis. *J. Infect. Dis.* **184**, 231–236 (2001).
- I. Caragol, M. Raspall, C. Fieschi, J. Feinberg, M. N. Larrosa, M. Hernandez, C. Figueras, J.-M. Bertrán, J. L. Casanova, T. Español, Clinical tuberculosis in 2 of 3 siblings with interleukin-12 receptor  $\beta$ 1 deficiency. *Clin. Infect. Dis.* **37**, 302–306 (2003).
- N. Özbek, C. Fieschi, B. T. Yilmaz, L. De Beaucoudrey, Y. E. Bikmaz, J. Feinberg, J.-L. Casanova, Interleukin-12 receptor beta 1 chain deficiency in a child with disseminated tuberculosis. *Clin. Infect. Dis.* **40**, e55–e58 (2005).
- F. Altare, A. Durandy, D. Lammas, J.-F. Emile, S. Lamhamedi, F. Le Deist, P. Drysdale, E. Jouanguy, R. Döffinger, F. Bernaudin, O. Jeppsson, J. A. Gollob, E. Meini, A. W. Segal, A. Fischer, D. Kumararatne, J.-L. Casanova, Impairment of mycobacterial immunity in human interleukin-12 receptor deficiency. *Science* **280**, 1432–1435 (1998).
- C. Fieschi, S. Dupuis, E. Catherinot, J. Feinberg, J. Bustamante, A. Breiman, F. Altare, N. Özbek, F. Le Deist, S. Kayal, H. Koch, D. Richter, M. Brezina, G. Aksu, P. Wood, S. Al-Jumaah, M. Raspall, A. J. Da Silva Duarte, D. Tuerlinckx, J. L. Virelizier, A. Fischer, A. Enright, J. Bernhöft, A. M. Cleary, C. Vermynen, C. Rodriguez-Gallego, G. Davies, R. Blütters-Sawatzki, C. A. Siegrist, M. S. Ehlayel, V. Novelli, W. H. Haas, J. Levy, J. Freihorst, I. Caragol, D. Nadal, D. De Moraes Vasconcelos, O. Jeppsson, N. Kutukculer, K. Brocra, I. Caragol, D. Lammas, D. S. Kumararatne, L. Abel, J. L. Casanova, Low penetrance, broad resistance, and favorable outcome of interleukin 12 receptor  $\beta$ 1 deficiency: Medical and immunological implications. *J. Exp. Med.* **197**, 527–535 (2003).
- L. de Beaucoudrey, A. Samarina, J. Bustamante, A. Cobat, S. Boisson-Dupuis, J. Feinberg, S. Al-Muhsen, L. Janniere, Y. Rose, M. de Suremain, X. F. Kong, O. Filipe-Santos, A. Chappier, C. Picard, A. Fischer, F. Dogu, A. Ikinciogullari, G. Tanir, S. Al-Hajjar, S. Al-Jumaah, H. H. Frayha, Z. AlSum, S. Al-Ajaji, A. Alangari, A. Al-Ghonaïum, P. Adimi, D. Mansouri, I. Ben-Mustapha, J. Yancoski, B. Z. Garty, C. Rodriguez-Gallego, I. Caragol, N. Kutukculer, D. S. Kumararatne, S. Patel, R. Döffinger, A. Exley, O. Jeppsson, J. Reichenbach, D. Nadal, Y. Boyko, B. Pietrucha, S. Anderson, M. Levin, L. Schandené, K. Schepers, A. Efir, F. Mascar, M. Matsuoka, T. Sakai, C. A. Siegrist, K. Freceirova, R. Blütters-Sawatzki, J. Bernhöft, J. Freihorst, U. Baumann, D. Richter, F. Haerynck, F. De Baets, V. Novelli, D. Lammas, C. Vermynen, D. Tuerlinckx, C. Nieuwhof, M. Pac, W. H. Haas, I. Müller-Fleckenstein, B. Fleckenstein, J. Levy, R. Raj, A. C. Cohen, D. B. Lewis, S. M. Holland, K. D. Yang, X. Wang, L. Jiang, X. Yang, C. Zhu, Y. Xie, P. P. Lee, K. W. Chan, T. X. Chen, G. Castro, I. Natera, A. Codoceo, A. King, L. Bezrodnik, D. Di Giovanni, M. I. Gaillard, D. de Moraes-Vasconcelos, A. S. Grumach, A. J. da Silva Duarte, R. Aldana, F. J. Espinosa-Rosales, M. Bejaoui, A. A. Bousfiha, J. E. Baghdadi, N. Özbek, G. Aksu, M. Keser, A. Somer, N. Hatipoglu, C. Aydogmus, S. Asilsoy, Y. Camcioglu, S. Gulle, T. T. Ozgur, M. Ozen, M. Oleastro, A. Bernasconi, S. Mamishi, N. Parvaneh, S. Rosenzweig, R. Barbouche, S. Pedraza, Y. L. Lau, M. S. Ehlayel, C. Fieschi, L. Abel, O. Sanal, J. L. Casanova, Revisiting human IL-12R $\beta$ 1 deficiency: A survey of 141 patients from 30 countries. *Medicine* **89**, 381–402 (2010).
- C. Fieschi, M. Bosticardo, L. De Beaucoudrey, S. Boisson-Dupuis, J. Feinberg, O. F. Santos, J. Bustamante, J. Levy, F. Candotti, J.-L. Casanova, A novel form of complete IL-12/IL-23 receptor  $\beta$ 1 deficiency with cell surface-expressed nonfunctional receptors. *Blood* **104**, 2095–2101 (2004).
- E. van de Vosse, M. H. Haverkamp, N. Ramirez-Alejo, M. Martinez-Gallo, L. Blancas-Galicia, A. Metin, B. Z. Garty, C. Sun-Tan, A. Broides, R. A. de Paus, Ö. Keskin, D. Çağdaş, I. Tezcan, E. Lopez-Ruzafa, J. I. Arostegui, J. Levy, F. J. Espinosa-Rosales, Ö. Sanal, L. Santos-Argumedo, J. L. Casanova, S. Boisson-Dupuis, J. T. van Dissel, J. Bustamante, IL-12R $\beta$ 1 deficiency: Mutation update and description of the IL12RB1 variation database. *Hum. Mutat.* **34**, 1329–1339 (2013).
- J. Rosain, C. Oleaga-Quintas, C. Deswarte, H. Verdin, S. Marot, G. Syridou, M. Mansouri, S. A. Mahdaviyani, E. Venegas-Montoya, M. Tsoia, M. Mesdaghi, L. Chernyshova, Y. Stepanovskiy, N. Parvaneh, D. Mansouri, S. Pedraza-Sanchez, A. Bondarenko, S. E. Espinosa-Padilla, M. A. Yamazaki-Nakashimada, A. Nieto-Patlán, G. Kerner, N. Lambert, C. Jacques, E. Corvilain, M. Migaud, V. Grandin, M. T. Herrera, F. Jabot-Hanin, S. Boisson-Dupuis, C. Picard, P. Nitschke, A. Puel, F. Tores, L. Abel, L. Blancas Galicia, E. De Baere, C. Bole-Feysot, J. L. Casanova, J. Bustamante, Alu-elements in IL12RB1 locus likely contributing to copy number variations and Mendelian susceptibility to mycobacterial diseases. *J. Clin. Immunol.* **38**, 617–627 (2018).
- R. de Jong, F. Altare, I. A. Haagen, D. G. Elferink, T. Boer, P. J. C. van Breda Vriesman, P. J. Kabel, J. M. Draaisma, J. T. van Dissel, F. P. Kroon, J.-L. Casanova, T. H. M. Ottenhoff, Severe mycobacterial and *Salmonella* infections in interleukin-12 receptor-deficient patients. *Science* **280**, 1435–1438 (1998).
- M. Ouederni, O. Sanal, A. Ikinciogullari, I. Tezcan, F. Dogu, I. Sologuren, S. Pedraza-Sanchez, M. Keser, G. Tanir, C. Nieuwhof, E. Colino, D. Kumararatne, J. Levy, N. Kutukculer, C. Aytekin, E. Herrera-Ramos, M. Bhatti, N. Karaca, R. Barbouche, A. Broides, E. Goudouris, J. L. Franco, N. Parvaneh, I. Reisli, A. Strickler, A. Shcherbina, A. Somer, A. Segal, A. Angel-Moreno, J. L. Lezana-Fernandez, M. Bejaoui, M. B. Valle, S. Kachboura, T. Sentongo, I. Ben-Mustapha, J. Bustamante, C. Picard, A. Puel, S. Boisson-Dupuis, L. Abel, J.-L. Casanova, C. Rodriguez-Gallego, Clinical features of candidiasis in patients with inherited interleukin 12 receptor  $\beta$ 1 deficiency. *Clin. Infect. Dis.* **58**, 204–213 (2014).

26. M. J. Newport, C. M. Huxley, S. Huston, C. M. Hawrylowicz, B. A. Oostra, R. Williamson, M. Levin, A mutation in the interferon- $\gamma$ -receptor gene and susceptibility to mycobacterial infection. *N. Engl. J. Med.* **335**, 1941–1949 (1996).
27. E. Jouanguy, F. Altare, S. Lamhamedi, P. Revy, J.-F. Emile, M. Newport, M. Levin, S. Blanche, E. Seboun, A. Fischer, J.-L. Casanova, Interferon- $\gamma$ -receptor deficiency in an infant with fatal bacille Calmette–Guérin infection. *N. Engl. J. Med.* **335**, 1956–1961 (1996).
28. L. de Beaucoudrey, A. Puel, O. Filipe-Santos, A. Cobat, P. Ghandil, M. Chrabieh, J. Feinberg, H. von Bernuth, A. Samarina, L. Janniere, C. Fieschi, J. L. Stephan, C. Boileau, S. Lyonnet, G. Jondeau, V. Cormier-Daire, M. Le Merrer, C. Hoarau, Y. Lebranchu, O. Lortholary, M. O. Chandesaris, F. Tron, E. Gambineri, L. Bianchi, C. Rodriguez-Gallego, S. E. Zitnik, J. Vasconcelos, M. Guedes, A. B. Vitor, L. Marodi, H. Chapel, B. Reid, C. Roifman, D. Nadal, J. Reichenbach, I. Caragol, B. Z. Garty, F. Dogu, Y. Camcioglu, S. Gulle, O. Sanal, A. Fischer, L. Abel, B. Stockinger, C. Picard, J. L. Casanova, Mutations in *STAT3* and *IL12RB1* impair the development of human IL-17-producing T cells. *J. Exp. Med.* **205**, 1543–1550 (2008).
29. A. Puel, S. Cypowyj, J. Bustamante, J. F. Wright, L. Liu, H. K. Lim, M. Migaud, L. Israel, M. Chrabieh, M. Audry, M. Gumbleton, A. Toulon, C. Bodemer, J. El-Baghdadi, M. Whitters, T. Paradis, J. Brooks, M. Collins, N. M. Wolfman, S. Al-Muhsen, M. Galicchio, L. Abel, C. Picard, J.-L. Casanova, Chronic mucocutaneous candidiasis in humans with inborn errors of interleukin-17 immunity. *Science* **332**, 65–68 (2011).
30. Y. Ling, S. Cypowyj, C. AYTEKIN, M. Galicchio, Y. Camcioglu, S. Nepesov, A. Ikinciogullari, F. Dogu, A. Belkadi, R. Levy, M. Migaud, B. Boisson, A. Bolze, Y. Itan, N. Goudin, J. Cottineau, C. Picard, L. Abel, J. Bustamante, J.-L. Casanova, A. Puel, Inherited IL-17RC deficiency in patients with chronic mucocutaneous candidiasis. *J. Exp. Med.* **212**, 619–631 (2015).
31. B. Boisson, C. Wang, V. Pedergrana, L. Wu, S. Cypowyj, M. Rybojad, A. Belkadi, C. Picard, L. Abel, C. Fieschi, A. Puel, X. Li, J. L. Casanova, An ACT1 mutation selectively abolishes interleukin-17 responses in humans with chronic mucocutaneous candidiasis. *Immunity* **39**, 676–686 (2013).
32. R. Lévy, S. Okada, V. Béziat, K. Moriya, C. Liu, L. Y. A. Chai, M. Migaud, F. Hauck, A. Al Ali, C. Cyrus, C. Vatte, T. Patrioglu, E. Unal, M. Ferneiny, N. Hyakuna, S. Nepesov, M. Oleastro, A. Ikinciogullari, F. Dogu, T. Asano, O. Ohara, L. Yun, E. Della Mina, D. Bronnimann, Y. Itan, F. Gothe, J. Bustamante, S. Boisson-Dupuis, N. Tahuil, C. AYTEKIN, A. Salhi, S. Al Muhsen, M. Kobayashi, J. Toubiana, L. Abel, X. Li, Y. Camcioglu, F. Celmeli, C. Klein, S. A. Alkhatir, J. L. Casanova, A. Puel, Genetic, immunological, and clinical features of patients with bacterial and fungal infections due to inherited IL-17RA deficiency. *Proc. Natl. Acad. Sci. U.S.A.* **113**, E8277–E8285 (2016).
33. S. S. Kilic, M. Hacimustafaoglu, S. Boisson-Dupuis, A. Y. Kreins, A. V. Grant, L. Abel, J.-L. Casanova, A patient with tyrosine kinase 2 deficiency without hyper-IgE syndrome. *J. Pediatr.* **160**, 1055–1057 (2012).
34. Y. Minegishi, M. Saito, T. Morio, K. Watanabe, K. Agematsu, S. Tsuchiya, H. Takada, T. Hara, N. Kawamura, T. Ariga, H. Kaneko, N. Kondo, I. Tsuge, Y. Sakiyama, T. Iwata, F. Bessho, T. Ohishi, K. Joh, K. Imai, K. Kogawa, M. Shinohara, M. Fujieda, H. Wakiguchi, S. Pasic, M. Abinun, H. D. Ochs, E. D. Renner, A. Jansson, B. H. Belohradsky, A. Metin, N. Shimizu, S. Mizutani, T. Miyawaki, S. Nonoyama, H. Karasuyama, Human tyrosine kinase 2 deficiency reveals its requisite roles in multiple cytokine signals involved in innate and acquired immunity. *Immunity* **25**, 745–755 (2006).
35. S. Fuchs, P. Kaiser-Labusch, J. Bank, S. Ammann, A. Kolb-Kokocinski, C. Edelbusch, H. Omran, S. Ehl, Tyrosine kinase 2 is not limiting human antiviral type III interferon responses. *Eur. J. Immunol.* **46**, 2639–2649 (2016).
36. V. Sancho-Shimizu, R. P. de Diego, E. Jouanguy, S.-Y. Zhang, J.-L. Casanova, Inborn errors of anti-viral interferon immunity in humans. *Current Opin. Virol.* **1**, 487–496 (2011).
37. K. R. Engelhardt, B. Grimbacher, IL-10 in humans: Lessons from the gut, IL-10/IL-10 receptor deficiencies, and IL-10 polymorphisms. *Curr. Top. Microbiol. Immunol.* **380**, 1–18 (2014).
38. D. S. Shouval, J. Ouahed, A. Biswas, J. A. Goettel, B. H. Horwitz, C. Klein, A. M. Muise, S. B. Snapper, Interleukin 10 receptor signaling: Master regulator of intestinal mucosal homeostasis in mice and humans. *Adv. Immunol.* **122**, 177–210 (2014).
39. Z. Li, M. Gakovic, J. Ragimbeau, M.-L. Eloranta, L. Rönnblom, F. Michel, S. Pellegrini, Two rare disease-associated TYK2 variants are catalytically impaired but signaling competent. *J. Immunol.* **190**, 2335–2344 (2013).
40. S. J. Sohn, K. Barrett, A. Van Abbema, C. Chang, P. B. Kohli, H. Kanda, J. Smith, Y. Lai, A. Zhou, B. Zhang, W. Yang, K. Williams, C. Macleod, C. A. Hurley, J. J. Kulagowski, N. Lewin-Koh, H. S. Dengler, A. R. Johnson, N. Ghilardi, M. Zak, J. Liang, W. S. Blair, S. Magnuson, L. C. Wu, A restricted role for TYK2 catalytic activity in human cytokine responses revealed by novel TYK2-selective inhibitors. *J. Immunol.* **191**, 2205–2216 (2013).
41. C. A. Dendrou, A. Cortes, L. Shipman, H. G. Evans, K. E. Attfield, L. Jostins, T. Barber, G. Kaur, S. B. Kuttikkatte, O. A. Leach, C. Desel, S. L. Faergeman, J. Cheeseman, M. J. Neville, S. Sawcer, A. Compston, A. R. Johnson, C. Everett, J. I. Bell, F. Karpe, M. Ultsch, C. Eigenbrot, G. McVean, L. Fugger, Resolving TYK2 locus genotype-to-phenotype differences in autoimmunity. *Sci. Transl. Med.* **8**, 363ra149 (2016).
42. M. Lek, K. J. Karczewski, E. V. Minikel, K. E. Samocha, E. Banks, T. Fennell, A. H. O'Donnell-Luria, J. S. Ware, A. J. Hill, B. B. Cummings, T. Tukiainen, D. P. Birnbaum, J. A. Kosmicki, L. E. Duncan, K. Estrada, F. Zhao, J. Zou, E. Pierce-Hoffman, J. Berghout, D. N. Cooper, N. Deflaux, M. DePristo, R. Do, J. Flannick, M. Fromer, L. Gauthier, J. Goldstein, N. Gupta, D. Howrigan, A. Kiezun, M. I. Kurki, A. L. Moonshine, P. Natarajan, L. Orozco, G. M. Peloso, R. Poplin, M. A. Rivas, V. Ruano-Rubio, S. A. Rose, D. M. Ruderfer, K. Shakir, P. D. Stenson, C. Stevens, B. P. Thomas, G. Tiao, M. T. Tusie-Luna, B. Weisburd, H.-H. Won, D. Yu, D. M. Altshuler, D. Ardissino, M. Boehnke, J. Danesh, S. Donnelly, R. Elosua, J. C. Florez, S. B. Gabriel, G. Getz, S. J. Glatt, C. M. Hultman, S. Kathiresan, M. Laakso, S. McCarroll, M. I. McCarthy, D. McGovern, R. McPherson, B. M. Neale, A. Palotie, S. M. Purcell, D. Saleheen, J. M. Scharf, P. Sklar, P. F. Sullivan, J. Tuomilehto, M. T. Tsuang, H. C. Watkins, J. G. Wilson, M. J. Daly, D. G. MacArthur, Exome Aggregation Consortium, Analysis of protein-coding genetic variation in 60,706 humans. *Nature* **536**, 285–291 (2016).
43. Y. Itan, L. Shang, B. Boisson, M. J. Ciancanelli, J. G. Markle, R. Martinez-Barricarte, E. Scott, I. Shah, P. D. Stenson, J. Gleeson, D. N. Cooper, L. Quintana-Murci, S.-Y. Zhang, L. Abel, J.-L. Casanova, The mutation significance cutoff: Gene-level thresholds for variant predictions. *Nat. Methods* **13**, 109–110 (2016).
44. M. Kircher, D. M. Witten, P. Jain, B. J. O'Roak, G. M. Cooper, J. Shendure, A general framework for estimating the relative pathogenicity of human genetic variants. *Nat. Genet.* **46**, 310–315 (2014).
45. 1000 Genomes Project Consortium, A. Auton, L. D. Brooks, R. M. Durbin, E. P. Garrison, H. M. Kang, J. O. Korbel, J. L. Marchini, S. McCarthy, G. A. McVean, G. R. Abecasis, A global reference for human genetic variation. *Nature* **526**, 68–74 (2015).
46. X.-F. Kong, R. Martinez-Barricarte, J. Kennedy, F. Mele, T. Lazarov, E. K. Deenick, C. S. Ma, G. Breton, K. B. Lucero, D. Langlais, A. Bousfiha, C. AYTEKIN, J. Markle, C. Trouillet, F. Jabot-Hanin, C. S. L. Arlehamn, G. Rao, C. Picard, T. Lasseau, D. Latorre, S. Hambleton, C. Deswarte, Y. Itan, K. Abarca, D. Moraes-Vasconcelos, F. Ailal, A. Ikinciogullari, F. Dogu, I. Benhsaien, A. Sette, L. Abel, S. Boisson-Dupuis, B. Schröder, M. C. Nussenzweig, K. Liu, F. Geissmann, S. G. Tangye, P. Gros, F. Sallusto, J. Bustamante, J.-L. Casanova, Disruption of an antimicrobial circuit between dendritic and helper T cells in human SPPL2a deficiency. *Nat. Immunol.* **19**, 973–985 (2018).
47. A. Belkadi, V. Pedergrana, A. Cobat, Y. Itan, Q. B. Vincent, A. Abhyankar, L. Shang, J. El Baghdadi, A. Bousfiha; Exome/Array Consortium, A. Alcais, B. Boisson, J.-L. Casanova, L. Abel, Whole-exome sequencing to analyze population structure, parental inbreeding and familial linkage. *Proc. Natl. Acad. Sci. U.S.A.* **113**, 6713–6718 (2016).
48. S. Belkaya, A. R. Kontorovich, M. Byun, S. Mulero-Navarro, F. Bajolle, A. Cobat, R. Josowitz, Y. Itan, R. Quint, L. Lorenzo, S. Boucherit, C. Stoven, S. Di Filippo, L. Abel, S. Y. Zhang, D. Bonnet, B. D. Gelb, J. L. Casanova, Autosomal recessive cardiomyopathy presenting as acute myocarditis. *J. Am. Coll. Cardiol.* **69**, 1653–1665 (2017).
49. J.-L. Casanova, Severe infectious diseases of childhood as monogenic inborn errors of immunity. *Proc. Natl. Acad. Sci. U.S.A.* **112**, E7128–E7137 (2015).
50. J.-L. Casanova, Human genetic basis of interindividual variability in the course of infection. *Proc. Natl. Acad. Sci. U.S.A.* **112**, E7118–E7127 (2015).
51. A. Posa, F. Maixner, B. G. Mende, K. Kohler, A. Osztas, C. Sola, O. Dutour, M. Masson, E. Molnar, G. Palfi, A. Zink, Tuberculosis in late neolithic-early copper age human skeletal remains from Hungary. *Tuberculosis* **95** (Suppl. 1), S18–S22 (2015).
52. I. Mathieson, I. Lazaridis, N. Rohland, S. Mallick, N. Patterson, S. A. Roodenberg, E. Harney, K. Stewardson, D. Fernandes, M. Novak, K. Sirak, C. Gamba, E. R. Jones, B. Llamas, S. Dryomov, J. Pickrell, J. L. Arsuaga, J. M. de Castro, E. Carbonell, F. Gerritsen, A. Khokhlov, P. Kudyshev, M. Lozano, H. Meller, O. Mochalov, V. Moiseyev, M. A. Guerra, J. Roodenberg, J. M. Vergès, J. Krause, A. Cooper, K. W. Alt, D. Brown, D. Anthony, C. Laluzza-Fox, W. Haak, R. Pinhasi, D. Reich, Genome-wide patterns of selection in 230 ancient Eurasians. *Nature* **528**, 499–503 (2015).
53. D. Rigante, B. Frediani, L. Cantarini, A comprehensive overview of the hereditary periodic fever syndromes. *Clin. Rev. Allergy Immunol.* **54**, 446–453 (2016).
54. L. W. Powell, R. C. Seckington, Y. Deugnier, Haemochromatosis. *Lancet* **388**, 706–716 (2016).
55. J. Cairns, *Matters of Life and Death* (Princeton Univ. Press, 1997), pp. 257.
56. R. J. Dubos, J. Dubos, *The White Plague: Tuberculosis, Man, and Society* (Little Brown, ed. 1, 1952), pp. viii, 277.
57. E. K. Karlsson, D. P. Kwiatkowski, P. C. Sabeti, Natural selection and infectious disease in human populations. *Nat. Rev. Genet.* **15**, 379–393 (2014).
58. I. Cvjovic, B. H. Good, E. R. Jerison, M. M. Desai, Fate of a mutation in a fluctuating environment. *Proc. Natl. Acad. Sci. U.S.A.* **112**, E5021–E5028 (2015).
59. S. K. Cohn Jr., Epidemiology of the Black Death and successive waves of plague. *Med. Hist. Suppl.* 74–100 (2008).
60. R. Martinez-Barricarte, S. J. de Jong, J. Markle, R. de Paus, S. Boisson-Dupuis, J. Bustamante, E. van de Vosse, B. Fleckenstein, J. L. Casanova, Transduction of herpesvirus saimiri-transformed T cells with exogenous genes of interest. *Curr. Protoc. Immunol.* **115**, 7.21C.1–7.21C.12 (2016).
61. R. McKendry, J. John, D. Flavell, M. Müller, I. M. Kerr, G. R. Stark, High-frequency mutagenesis of human cells and characterization of a mutant unresponsive to both alpha and gamma interferons. *Proc. Natl. Acad. Sci. U.S.A.* **88**, 11455–11459 (1991).

62. S. Pellegrini, J. John, M. Shearer, I. M. Kerr, G. R. Stark, Use of a selectable marker regulated by alpha interferon to obtain mutations in the signaling pathway. *Mol. Cell. Biol.* **9**, 4605–4612 (1989).
63. J. John, R. McKendry, S. Pellegrini, D. Flavell, I. M. Kerr, G. R. Stark, Isolation and characterization of a new mutant human cell line unresponsive to alpha and beta interferons. *Mol. Cell. Biol.* **11**, 4189–4195 (1991).
64. M. H. Shaw, V. Boyartchuk, S. Wong, M. Karaghiosoff, J. Ragimbeau, S. Pellegrini, M. Muller, W. F. Dietrich, G. S. Yap, A natural mutation in the Tyk2 pseudokinase domain underlies altered susceptibility of B10.Q/J mice to infection and autoimmunity. *Proc. Natl. Acad. Sci. U.S.A.* **100**, 11594–11599 (2003).
65. J. Ragimbeau, E. Dondi, A. Alcover, P. Eid, G. Uzé, S. Pellegrini, The tyrosine kinase Tyk2 controls IFNAR1 cell surface expression. *EMBO J.* **22**, 537–547 (2003).
66. M. W. L. Teng, E. P. Bowman, J. J. McElwee, M. J. Smyth, J.-L. Casanova, A. M. Cooper, D. J. Cua, IL-12 and IL-23 cytokines: From discovery to targeted therapies for immune-mediated inflammatory diseases. *Nat. Med.* **21**, 719–729 (2015).
67. D. M. Floss, T. Klocker, J. Schroder, L. Lamertz, S. Mrotzek, B. Strobl, H. Hermans, J. Scheller, Defining the functional binding sites of interleukin 12 receptor  $\beta$ 1 and interleukin 23 receptor to Janus kinases. *Mol. Biol. Cell* **27**, 2301–2316 (2016).
68. V. Tsui, P. Gibbons, M. Ultsch, K. Mortara, C. Chang, W. Blair, R. Pulk, M. Stanley, M. Starovasnik, D. Williams, M. Lamers, P. Leonard, S. Magnuson, J. Liang, C. Eigenbrot, A new regulatory switch in a JAK protein kinase. *Proteins* **79**, 393–401 (2011).
69. D. Sivanesan, C. Beauchamp, C. Quinou, J. Lee, S. Lesage, S. Chemtob, J. D. Rioux, S. W. Michnick, IL23R (interleukin 23 receptor) variants protective against inflammatory bowel diseases (IBD) display loss of function due to impaired protein stability and intracellular trafficking. *J. Biol. Chem.* **291**, 8673–8685 (2016).
70. E. Stefan, S. Aquin, N. Berger, C. R. Landry, B. Nyfeler, M. Bouvier, S. W. Michnick, Quantification of dynamic protein complexes using *Renilla* luciferase fragment complementation applied to protein kinase A activities in vivo. *Proc. Natl. Acad. Sci. U.S.A.* **104**, 16916–16921 (2007).
71. J. Briscoe, N. C. Rogers, B. A. Witthuhn, D. Watling, A. G. Harpur, A. F. Wilks, G. R. Stark, J. N. Ihle, I. M. Kerr, Kinase-negative mutants of JAK1 can sustain interferon-gamma-inducible gene expression but not an antiviral state. *EMBO J.* **15**, 799–809 (1996).
72. C. MacLennan, C. Fieschi, D. A. Lamm, C. Picard, S. E. Dorman, O. Sanal, J. M. MacLennan, S. M. Holland, T. H. M. Ottenhoff, J.-L. Casanova, D. S. Kumararatne, Interleukin (IL)-12 and IL-23 are key cytokines for immunity against *Salmonella* in humans. *J. Infect. Dis.* **190**, 1755–1757 (2004).
73. B. Oppmann, R. Lesley, B. Blom, J. C. Timans, Y. Xu, B. Hunte, F. Vega, N. Yu, J. Wang, K. Singh, F. Zonin, E. Vaisberg, T. Churakov, M.-r. Liu, D. Gorman, J. Wagner, S. Zurawski, Y. Liu, J. S. Abrams, K. W. Moore, D. Rennick, R. de Waal-Malefyt, C. Hannum, J. F. Bazan, R. A. Kastelein, Novel p19 protein engages IL-12p40 to form a cytokine, IL-23, with biological activities similar as well as distinct from IL-12. *Immunity* **13**, 715–725 (2000).
74. K. I. Happel, E. A. Lockhart, C. M. Mason, E. Porretta, E. Keoshkerian, A. R. Odden, S. Nelson, A. J. Ramsay, Pulmonary interleukin-23 gene delivery increases local T-cell immunity and controls growth of *Mycobacterium tuberculosis* in the lungs. *Infect. Immun.* **73**, 5782–5788 (2005).
75. L. Moens, H. Schaballie, B. Bosch, A. Voet, X. Bossuyt, J.-L. Casanova, S. Boisson-Dupuis, S. G. Tangye, I. Meyts, AD hyper-IgE syndrome due to a novel loss-of-function mutation in STAT3: A diagnostic pursuit won by clinical acuity. *J. Clin. Immunol.* **37**, 12–17 (2017).
76. R. Martinez-Barricarte, J. G. Markle, C. S. Ma, E. K. Deenick, N. Ramirez-Alejo, F. Mele, D. Latorre, S. A. Mahdavian, C. Aytakin, D. Mansouri, V. Bryant, F. Jabot-Hanin, C. Deswarte, A. Nieto-Patán, L. Surace, G. Kerner, Y. Itan, S. Jovic, D. T. Avery, N. Wong, G. Rao, E. Patin, S. Okada, B. Bigio, B. Boisson, F. Rapaport, Y. Seeleuthner, M. Schmidt, A. Ikinciogullari, F. Dogu, G. Tanir, P. Tabarsi, M. R. Bloursaz, J. K. Joseph, A. Heer, X.-F. Kong, M. Migaud, T. Lazarov, F. Geissmann, B. Fleckenstein, C. L. Arlehamn, A. Sette, A. Puel, J.-F. Emile, E. van de Vosse, L. Quintana-Murci, J. P. Di Santo, L. Abel, S. Boisson-Dupuis, J. Bustamante, S. G. Tangye, F. Sallusto, J.-L. Casanova, Human IFN- $\gamma$  immunity to mycobacteria is governed by both IL-12 and IL-23. *Sci. Immunol.* **3**, eaau6759 (2018).
77. T. Korn, E. Bettelli, M. Oukka, V. K. Kuchroo, IL-17 and Th17 cells. *Annu. Rev. Immunol.* **27**, 485–517 (2009).
78. F. Sallusto, Heterogeneity of human CD4<sup>+</sup> T cells against microbes. *Annu. Rev. Immunol.* **34**, 317–334 (2016).
79. S. Okada, J. G. Markle, E. K. Deenick, F. Mele, D. Averbuch, M. Lagos, M. Alzahran, S. Al-Muhsen, R. Halwani, C. S. Ma, N. Wong, C. Soudais, L. A. Henderson, H. Marzouqa, J. Shamma, M. Gonzalez, R. Martinez-Barricarte, C. Okada, D. T. Avery, D. Latorre, C. Deswarte, F. Jabot-Hanin, E. Torrado, J. Fountain, A. Belkadi, Y. Itan, B. Boisson, M. Migaud, C. S. L. Arlehamn, A. Sette, S. Breston, J. McCluskey, J. Rossjohn, J.-P. de Villartay, D. Moshov, S. Hambleton, S. Latour, P. D. Arkwright, C. Picard, O. Lantz, D. Engelhard, M. Kobayashi, L. Abel, A. M. Cooper, L. D. Notarangelo, S. Boisson-Dupuis, A. Puel, F. Sallusto, J. Bustamante, S. G. Tangye, J.-L. Casanova, Impairment of immunity to *Candida* and *Mycobacterium* in humans with bi-allelic *RORC* mutations. *Science* **349**, 606–613 (2015).
80. J. L. Casanova, E. Jouanguy, S. Lamhamedi, S. Blanche, A. Fischer, Immunological conditions of children with BCG disseminated infection. *Lancet* **346**, 581 (1995).
81. A. O'Garra, P. S. Redford, F. W. McNab, C. I. Bloom, R. J. Wilkinson, M. P. R. Berry, The immune response in tuberculosis. *Annu. Rev. Immunol.* **31**, 475–527 (2013).
82. N. Fodil, D. Langlais, P. Gros, Primary immunodeficiencies and inflammatory disease: A growing genetic intersection. *Trends Immunol.* **37**, 126–140 (2016).
83. J. F. Brinkworth, L. B. Barreiro, The contribution of natural selection to present-day susceptibility to chronic inflammatory and autoimmune disease. *Curr. Opin. Immunol.* **31**, 66–78 (2014).
84. L. B. Barreiro, L. Quintana-Murci, From evolutionary genetics to human immunology: How selection shapes host defence genes. *Nat. Rev. Genet.* **11**, 17–30 (2010).
85. M. Gadina, C. Johnson, D. Schwartz, M. Bonelli, S. Hasni, Y. Kanno, P. Changelian, A. Laurence, J. J. O'Shea, Translational and clinical advances in JAK-STAT biology: The present and future of jakinibs. *J. Leukoc. Biol.* **104**, 499–514 (2018).
86. K. Papp, K. Gordon, D. Thaci, A. Morita, M. Gooderham, P. Foley, I. G. Gergis, S. Kundu, S. Banerjee, Phase 2 trial of selective tyrosine kinase 2 inhibition in Psoriasis. *N. Engl. J. Med.* **379**, 1313–1321 (2018).
87. D. M. Schwartz, Y. Kanno, A. Villarino, M. Ward, M. Gadina, J. J. O'Shea, JAK inhibition as a therapeutic strategy for immune and inflammatory diseases. *Nat. Rev. Drug Discov.* **16**, 843–862 (2017).
88. S. M. Holland, Immunotherapy of mycobacterial infections. *Semin. Respir. Infect.* **16**, 47–59 (2001).
89. J. Feinberg, C. Fieschi, R. Doffinger, M. Feinberg, T. Leclerc, S. Boisson-Dupuis, C. Picard, J. Bustamante, A. Chappier, O. Filipe-Santos, C.-L. Ku, L. de Beaucoudrey, J. Reichenbach, G. Antoni, R. Baldé, A. Alcais, J.-L. Casanova, Bacillus Calmette Guérin triggers the IL-12/IFN- $\gamma$  axis by an IRAK-4- and NEMO-dependent, non-cognate interaction between monocytes, NK, and T lymphocytes. *Eur. J. Immunol.* **34**, 3276–3284 (2004).
90. A. Dobin, C. A. Davis, F. Schlesinger, J. Drenkow, C. Zaleski, S. Jha, P. Batut, M. Chaisson, T. R. Gingeras, STAR: Ultrafast universal RNA-seq aligner. *Bioinformatics* **29**, 15–21 (2013).
91. S. Anders, P. T. Pyl, W. Huber, HTSeq—A Python framework to work with high-throughput sequencing data. *Bioinformatics* **31**, 166–169 (2015).
92. A. Conesa, P. Madrigal, S. Tarazona, D. Gomez-Cabrero, A. Cervera, A. McPherson, M. W. Szczesniak, D. J. Gaffney, L. L. Elo, X. Zhang, A. Mortazavi, A survey of best practices for RNA-seq data analysis. *Genome Biol.* **17**, 13 (2016).
93. R. C. Team, R: A language and environment for statistical computing. R Foundation for Statistical Computing, Vienna, Austria (2015).
94. J. Ragimbeau, E. Dondi, A. Vasserot, P. Romero, G. Uzé, S. Pellegrini, The receptor interaction region of Tyk2 contains a motif required for its nuclear localization. *J. Biol. Chem.* **276**, 30812–30818 (2001).
95. S. N. Vogel, R. M. Friedman, M. M. Hogan, Measurement of antiviral activity induced by interferons  $\alpha$ ,  $\beta$ , and  $\gamma$ . *Curr. Protoc. Immunol.* **Chapter 6**, Unit 6.9 (2001).
96. S. Purcell, B. Neale, K. Todd-Brown, L. Thomas, M. A. R. Ferreira, D. Bender, J. Maller, P. Sklar, P. I. W. de Bakker, M. J. Daly, P. C. Sham, PLINK: A tool set for whole-genome association and population-based linkage analyses. *Am. J. Hum. Genet.* **81**, 559–575 (2007).

**Acknowledgments:** We would like to thank the patients, their relatives, and their physicians. We also thank Y. Nemirovskaya, T. Kochetkov, D. Papandrea, S. O. Lugo Reyes, L. Blancas Galicia, M. Orlova, E. Schurr, A. Boussiha, L. Lorenzo-Diaz, C. Desvallees, C. Pattisier, C. Carvajal, N. Scioscia, F. Zegna-Ratá, and C. Tiznado. **Funding:** The Laboratory of Human Genetics of Infectious Diseases was supported, in part, by grants from the French National Agency for Research (ANR) under the "Investissement d'avenir" program (grant no. ANR-10-IAHU-01), the TBPATGEN project (grant no. ANR-14-CE14-0007-01), the GENMSMD project (grant no. ANR-16-CE17-0005-01), the Integrative Biology of Emerging Infectious Diseases Laboratory of Excellence (grant no. ANR-10-LABX-62-IBEID), the European Research Council (ERC; grant no. ERC-2010-AdG-268777), the SCOR Corporate Foundation for Science, the St. Giles Foundation, the National Center for Research Resources and the National Center for Advancing Sciences (NCATS), NIH (grant no. UL1TR001866), the National Institute of Allergy and Infectious Diseases (NIAID) (grant nos. 5R01AI089970, 5R37AI095983, 5U01AI088685, and 5U19AI111143), and The Rockefeller University. Work at the Cytokine Signaling Unit was supported, in part, by a grant from Fondation de la Recherche Médicale to S. Pellegrini (grant no. DEQ20170336741). J.B. was supported by Support of Clinical Research (grant no. SRC2017). C.S.M. and S.G.T. were supported by fellowships and grants from the National Health and Medical Research Council of Australia and the Office of Health and Medical Research of the Government of New South Wales (Australia). M.E.B. was supported by Fondo Nacional de Desarrollo Científico y Tecnológico (FONDECYT; grant no. 1171570) A.C.-N. was supported by Fundação de Amparo a Pesquisa do Estado de São Paulo (Fapesp) and Conselho Nacional de Desenvolvimento Científico e Tecnológico (CNPq). N.R.-A. was supported by fellowships from Consejo Nacional de Ciencia y Tecnología (CONACYT; grant no. 264011) and the Stony Wold-Herbert Fund. Z.L. was supported by the CNRS. J. Markle was supported by the Charles H. Revson Senior Fellowship in Biomedical Sciences and NIAID grant K99AI27932. C.C.J. was the Damon

Runyon-Richard Lumsden Foundation Physician Scientist supported by the Damon Runyon Cancer Research Foundation (PST-03-15). H.D.O. was supported by the Jeffrey Modell Foundation. N.H. was supported by a Medical Scientist Training Program grant from the National Institute of General Medical Sciences of the NIH under award no. T32GM007739 to the Weill Cornell/Rockefeller/Sloan-Kettering Tri-Institutional MD-PhD Program. The content of this study is the sole responsibility of the authors and does not necessarily represent the official views of the NIH. The Yale Center for Mendelian Genomics (UM1HG006504) is funded by the National Human Genome Research Institute. Funds were also provided by the National Heart, Lung, and Blood Institute. The GSP Coordinating Center (U24 HG008956) contributed to cross-program scientific initiatives and provided logistical and general study coordination.

**Author contributions:** R.N., P.G., C.C.J., S. Pekcan, Z.C., J.I., B.T.C.-C., J.A.T.d.A., H.G.-O., L.O., T.O., A.A., I.A.R., H.S., H.N.A., A.Z., H.A., M.E.B., A.C.-N., A.S., K.A., H.D.O., I.R., E.H.S., J.E.-B., and L.H. took care of the patients, provided clinical samples, and analyzed clinical data. S.B.-D., N.R.-A., E.P., G.K., L.Q.-M., and L.A. performed statistical analysis. S.B.-D., N.R.-A., Z.L., E.P., G.R., G.K., J. Markle, R.M.-B., C.K.L., D.N.K., N.H., C.S.M., Q.Z., K.P., R.F., C.D., J.H., M.B., J. Mulwa, A.G., M.J.C., N.M., C.T., A.P., J.B., S.G.T., S. Pellegrini, L.Q.-M., L.A., and J.-L.C. performed experiments and analyzed the data. D.S., T.L., Y.I., B.B., A. Checchi, F.J.-H., A. Cobat, F.G., S.W.M., I.M.-F., and B.F. provided reagents or computational assistance. S.B.-D., L.A., and J.-L.C. designed and supervised the study and wrote the paper with the assistance of all coauthors. **Competing interests:** The authors declare that they have no competing interests. **Data and materials availability:**

The RNA-seq and WES data are available from the Sequence Read Archive ([www.ncbi.nlm.nih.gov/sra](http://www.ncbi.nlm.nih.gov/sra)) (SRA accession no. PRJNA495387).

Submitted 23 July 2018

Accepted 20 November 2018

Published 21 December 2018

10.1126/sciimmunol.aau8714

**Citation:** S. Boisson-Dupuis, N. Ramirez-Alejo, Z. Li, E. Patin, G. Rao, G. Kerner, C. K. Lim, D. N. Krementsov, N. Hernandez, C. S. Ma, Q. Zhang, J. Markle, R. Martinez-Barricarte, K. Payne, R. Fisch, C. Deswarte, J. Halpern, M. Bouaziz, J. Mulwa, D. Sivanesan, T. Lazarov, R. Naves, P. Garcia, Y. Itan, B. Boisson, A. Checchi, F. Jabot-Hanin, A. Cobat, A. Guennoun, C. C. Jackson, S. Pekcan, Z. Caliskaner, J. Inostroza, B. T. Costa-Carvalho, J. A. Tavares de Albuquerque, H. Garcia-Ortiz, L. Orozco, T. Ozcelik, A. Abid, I. A. Rhorfi, H. Souhi, H. N. Amrani, A. Zegmout, F. Geissmann, S. W. Michnick, I. Muller-Fleckenstein, B. Fleckenstein, A. Puel, M. J. Ciancanelli, N. Marr, H. Abolhassani, M. E. Balcells, A. Condino-Neto, A. Strickler, K. Abarca, C. Teuscher, H. D. Ochs, I. Reisli, E. H. Sayar, J. El-Baghdadi, J. Bustamante, L. Hammarström, S. G. Tangye, S. Pellegrini, L. Quintana-Murci, L. Abel, J.-L. Casanova, Tuberculosis and impaired IL-23-dependent IFN- $\gamma$  immunity in humans homozygous for a common *TYK2* missense variant. *Sci. Immunol.* **3**, eaau8714 (2018).

## TRANSPLANTATION

# Generation and persistence of human tissue-resident memory T cells in lung transplantation

Mark E. Snyder<sup>1,2\*</sup>, Michael O. Finlayson<sup>3</sup>, Thomas J. Connors<sup>2,4</sup>, Pranay Dogra<sup>2,5</sup>, Takashi Senda<sup>2,6</sup>, Erin Bush<sup>3</sup>, Dustin Carpenter<sup>2,6</sup>, Charles Marboe<sup>7</sup>, Luke Benvenuto<sup>1</sup>, Lori Shah<sup>1</sup>, Hilary Robbins<sup>1</sup>, Jaime L. Hook<sup>1</sup>, Megan Sykes<sup>1,2,5</sup>, Frank D'Ovidio<sup>6</sup>, Matthew Bacchetta<sup>6</sup>, Joshua R. Sonett<sup>6</sup>, David J. Lederer<sup>1,8</sup>, Selim Arcasoy<sup>1,4</sup>, Peter A. Sims<sup>3</sup>, Donna L. Farber<sup>2,5,6†</sup>

Tissue-resident memory T cells ( $T_{RM}$ ) maintain immunity in diverse sites as determined in mouse models, whereas their establishment and role in human tissues have been difficult to assess. Here, we investigated human lung  $T_{RM}$  generation, maintenance, and function in airway samples obtained longitudinally from human leukocyte antigen (HLA)-disparate lung transplant recipients, where donor and recipient T cells could be localized and tracked over time. Donor T cells persist specifically in the lungs (and not blood) of transplant recipients and express high levels of  $T_{RM}$  signature markers including CD69, CD103, and CD49a, whereas lung-infiltrating recipient T cells gradually acquire  $T_{RM}$  phenotypes over months in vivo. Single-cell transcriptome profiling of airway T cells reveals that donor T cells comprise two  $T_{RM}$ -like subsets with varying levels of expression of  $T_{RM}$ -associated genes, whereas recipient T cells comprised non- $T_{RM}$  and similar  $T_{RM}$ -like subpopulations, suggesting de novo  $T_{RM}$  generation. Transplant recipients exhibiting higher frequencies of persisting donor  $T_{RM}$  experienced fewer adverse clinical events such as primary graft dysfunction and acute cellular rejection compared with recipients with low donor  $T_{RM}$  persistence, suggesting that monitoring  $T_{RM}$  dynamics could be clinically informative. Together, our results provide spatial and temporal insights into how human  $T_{RM}$  develop, function, persist, and affect tissue integrity within the complexities of lung transplantation.

## INTRODUCTION

Tissue-resident memory T cells ( $T_{RM}$ ) are generated in diverse tissues after site-specific infection or antigen exposure, where they remain as noncirculating subsets with the potential to mediate rapid, in situ immune responses (1–6). Studies in mouse models have revealed important roles for  $T_{RM}$  in tissue-localized immunity. In mucosal and barrier sites such as the lung, skin, and female reproductive tract, protective  $T_{RM}$  can be generated after viral or bacterial infection or to locally administered vaccines (2, 4, 7–15). Conversely, lung  $T_{RM}$  can also be generated after inhaled allergen exposure and mediate hyperresponsiveness in mouse asthma models (16, 17). These findings in mouse models indicate a key role for  $T_{RM}$  in maintaining protection and promoting immunopathology. The generation and persistence of  $T_{RM}$  in human tissues and their role in tissue-localized immune responses remain unclear.

In humans, subsets of memory T cells with phenotypes and transcriptional profiles homologous to mouse  $T_{RM}$  have been identified in multiple tissues, including mucosal and barrier sites (lungs, intestines, and skin) and primary and secondary lymphoid tissues (bone marrow, spleen, and lymph nodes) (18–20). In healthy human lungs,  $T_{RM}$  express markers for retention, adhesion, and migration to tissues (CD69,

CD103, CD49a, and CXCR6); produce proinflammatory cytokines [interferon- $\gamma$  (IFN- $\gamma$ ) and interleukin-17 (IL-17)]; and also exhibit up-regulation of inhibitory molecules (PD-1 and CD101) (18, 20, 21), indicating proinflammatory and immunomodulatory properties. The functional role of human  $T_{RM}$  in vivo has been inferred by correlative studies: The presence of  $T_{RM}$  in tumors of the lung and breast is associated with a better prognosis (22, 23), whereas in skin  $T_{RM}$  are associated with disease pathology in psoriasis (21, 24). However, it is difficult to follow human immune responses in situ, particularly in internal tissues such as lung, and consequently, little is known about the generation, maintenance, and role of human  $T_{RM}$  in health and disease.

Lung transplantation, in which donor lungs are transplanted into human leukocyte antigen (HLA)-mismatched recipients, represents a unique opportunity to study the development and maintenance of human  $T_{RM}$  in vivo. Bronchoalveolar lavage (BAL) sampling of the airway (and blood) is obtained for clinical monitoring at regular intervals during the first year after transplant and at specific intervals thereafter, enabling prospective tracking of donor- and recipient-derived T cells as they persist or develop into  $T_{RM}$ , respectively. It is also possible to correlate findings in patient BAL to critical clinical events such as primary graft dysfunction (PGD) (25), indicative of early lung injury that affects graft survival, and acute cellular rejection (ACR), which can occur at all times after transplantation (26).

Through a longitudinal analysis of blood and BAL samples from >20 lung transplant recipients, we demonstrate here that donor-derived T cells persist for more than 1 year after transplantation specifically in the lung allograft as  $T_{RM}$  that are not detected in blood. In the BAL, donor lung T cells exhibit enhanced expression of multiple  $T_{RM}$  signature markers, whereas recipient-derived T cells gradually express  $T_{RM}$  markers in the months after transplantation. Single-cell transcriptome profiling of BAL T cells reveals three distinct subpopulations—a mature  $T_{RM}$  subset composed of donor T cells, a second  $T_{RM}$ -like subset containing donor and recipient cells, and a third non- $T_{RM}$  subset

<sup>1</sup>Department of Medicine, Columbia University Medical Center, New York, NY 10032, USA. <sup>2</sup>Columbia Center for Translational Immunology, Columbia University Medical Center, New York, NY 10032, USA. <sup>3</sup>Department of Systems Biology, Columbia University Medical Center, New York, NY 10032, USA. <sup>4</sup>Department of Pediatrics, Columbia University Medical Center, New York, NY 10032, USA. <sup>5</sup>Department of Microbiology and Immunology, Columbia University Medical Center, New York, NY 10032, USA. <sup>6</sup>Department of Surgery, Columbia University Medical Center, New York, NY 10032, USA. <sup>7</sup>Department of Pathology, Columbia University Medical Center, New York, NY 10032, USA. <sup>8</sup>Department of Epidemiology, Mailman School of Public Health, Columbia University, New York, NY 10032, USA.

\*Present address: Division of Pulmonary, Allergy, and Critical Care Medicine, University of Pittsburgh, Pittsburgh, PA 15260, USA.

†Corresponding author. Email: df2396@cumc.columbia.edu

comprising recipient T cells—that suggest *in situ* differentiation of  $T_{RM}$  from tissue-infiltrating T cells. We found that long-term persistence of donor lung  $T_{RM}$  is associated with reduced incidence of clinical events that precipitate lung injury, including PGD and ACR. Our findings demonstrate human  $T_{RM}$  maturation and perpetuation in the lung and suggest that  $T_{RM}$  dynamics may be informative for monitoring clinical outcomes after transplantation.

## RESULTS

### Prospective analysis of T cell responses in lung transplant recipients

In this study, we investigated the dynamics of human lung  $T_{RM}$  persistence, migration, and generation in BAL and blood samples obtained longitudinally from 20 HLA-disparate lung transplant recipients (Fig. 1A and table S1). The majority of participants were male (70%) and ranged in age from 27 to 73 years old (median, 63) with a median lung allocation score of 49 (range, 33 to 91) (27); more than one-half of patients (55%) underwent single lung transplantation. The most common indication for transplantation was interstitial lung disease (hypersensitivity pneumonitis, sarcoidosis, and idiopathic pulmonary fibrosis), followed by cystic fibrosis and chronic obstructive pulmonary disease (table S1). All patients received induction therapy with anti-CD25 antibody (basiliximab) and high-dose steroids, and maintenance immunosuppression with tacrolimus and mycophenolate mofetil (see Materials and Methods).

### Donor-derived T cells persist specifically within the lung allograft

We initially assessed the extent of lung allograft and peripheral blood donor T cell chimerism after transplantation in BAL and blood samples collected longitudinally from the transplant recipients. The origin of lymphocytes as donor- or recipient-derived was determined by staining for HLA discrepancies and analyzed by flow cytometry (Fig. 1, B and C, and figs. S1 and S2). Peripheral blood macrochimerism, defined as the presence of  $\geq 4\%$  of donor T cells (28), was observed postoperatively in 3 of 20 patients (15%) (Fig. 1D, left); however, the number of donor T cells in the blood based on cell counts was negligible in all transplant recipients by 2 months after transplantation ( $<0.01$  donor cell/ $\mu$ l; Fig. 1D, right). Compared with blood, BAL samples contained high frequencies of donor-derived  $CD4^+$  and  $CD8^+$  T cells in all recipients (20 of 20), with levels as high as 93% for donor  $CD8^+$  T cells and 81% for donor  $CD4^+$  T cells (Fig. 1E). Of the 17 patients followed for  $>1$  year, the majority of patients (13 of 17) retained substantial donor T cell chimerism in the BAL at 12 months for both  $CD4^+$  T cells (range, 0.5 to 55%) and  $CD8^+$  T cells (0.7 to 85%) (Fig. 1E). Absolute numbers of T cells in BAL samples ranged from 688 to 34,678 cells (average, 8991) due to heterogeneous volume recovery from the procedure and the fact that a portion was used for clinical monitoring. Over time after transplantation, the CD4:CD8 subset composition was stably maintained for recipient T cells but decreased significantly for donor T cells (Fig. 1F), suggesting biased persistence of donor  $CD8^+$  T cells. Together, these results establish that donor T cells persist specifically in the lung tissue allograft.

### T cells in healthy BAL exhibit predominant tissue-resident memory phenotypes similar to lung parenchyma and airways

The biased persistence of donor T cells within the BAL suggested the presence of  $T_{RM}$ , which have been shown in mice and humans to pre-

dominate in mucosal and barrier tissue sites (1, 4, 29, 30). However, it was first important to determine the subset composition and anatomic origin of BAL T cells derived from healthy lungs to establish a baseline control from which to interpret transplant patient BAL. We therefore characterized T cells derived in parallel from the BAL, lung parenchyma, and airways from healthy lungs (Fig. 2A) obtained through an organ donor tissue resource we have extensively validated for immune cell studies (18, 30, 31). BAL T cells contained a CD4:CD8 content similar to that in the lung parenchyma but higher to that derived from the airways (Fig. 2B) and consisted of predominantly effector memory T cells ( $T_{EM}$ ;  $CCR7^- CD45RA^-$ ) similar to lung airways and parenchyma (Fig. 2C). Lung-derived  $CD8^+$  T cells also contained a substantial frequency of terminal effector cells ( $T_{EMRA}$ ;  $CD45RA^+ CCR7^-$ ) (Fig. 2C). These findings establish that BAL T cells are predominantly memory phenotype, similar to T cells in the lung parenchyma and airways.

We examined whether BAL memory T cells exhibited the canonical phenotypic  $T_{RM}$  markers, including the activation/retention marker CD69 (for  $CD4^+$  and  $CD8^+$   $T_{RM}$ ) and the integrin CD103 (for  $CD8^+$   $T_{RM}$ ) (3, 18, 20). The majority (60 to  $>90\%$ ) of  $CD4^+$  and  $CD8^+$   $T_{EM}$  in BAL express CD69 similar to frequencies in the lung and airways (Fig. 2D), suggesting that BAL T cells are predominantly  $T_{RM}$ . CD103 is coexpressed by  $CD69^+ CD8^+$  T cells in BAL, airway, and lung, with the highest frequency of CD103-expressing  $CD8^+$   $T_{RM}$  in the airways followed by BAL and lung (Fig. 2D). CD103 was also expressed by a low frequency of  $CD69^+ CD4^+$   $T_{RM}$  in the airways and at lower frequencies in the lung and BAL (Fig. 2D). Together, these findings indicate that the overwhelming majority of both  $CD4^+$  and  $CD8^+$  T cells obtained from human BAL exhibit  $T_{RM}$  phenotypes.

### Donor and recipient BAL T cells exhibit features of resting memory T cells with effector potential

Examination of the subset composition of donor and recipient BAL T cells over time after transplantation revealed that, similar to control BAL, the  $T_{EM}$  subset predominated for donor and recipient populations, with some variations particularly among recipient  $CD8^+$  T cells (Fig. 3, A and B). Donor  $CD4^+$  and  $CD8^+$  T cells were predominantly  $T_{EM}$  at all times after transplantation, with significant frequencies (10 to 30%) of  $T_{EMRA}$  present among donor  $CD8^+$  T cells (Fig. 3B, left). Recipient T cells similarly contained majority populations of  $T_{EM}$ ; however,  $CD8^+$   $T_{EMRA}$  were present in substantial frequencies (20 to 50%) in the first 6 months after transplantation, and this frequency was reduced to the level found in donor T cells at later times ( $>6$  months) after transplantation (Fig. 3B, right). Given these dynamic changes in the recipient T cell subset composition, we investigated whether donor and/or recipient T cells exhibited markers of activation *in vivo*, such as HLA-DR, which is up-regulated on human T cells after T cell receptor/CD3 stimulation. At early times ( $<1$  month) after transplantation, HLA-DR was expressed by both donor and recipient T cells; however, after 1 month *in vivo*, T cells of both donor and host origin were uniformly HLA-DR negative (Fig. 3C), suggesting that T cells persisting in transplanted lungs were not overtly activated.

Functionally, both donor and recipient BAL T cells exhibited rapid production of multiple cytokines after stimulation that is a hallmark of memory T cells and similar to the functional profiles of memory T cells isolated from healthy human lungs and lymphoid tissues (32–34). High frequencies of donor and recipient  $CD4^+$  and  $CD8^+$  T cells produced IFN- $\gamma$  with higher frequencies produced by donor compared with recipient T cells in many patients (Fig. 3D). IL-17 was

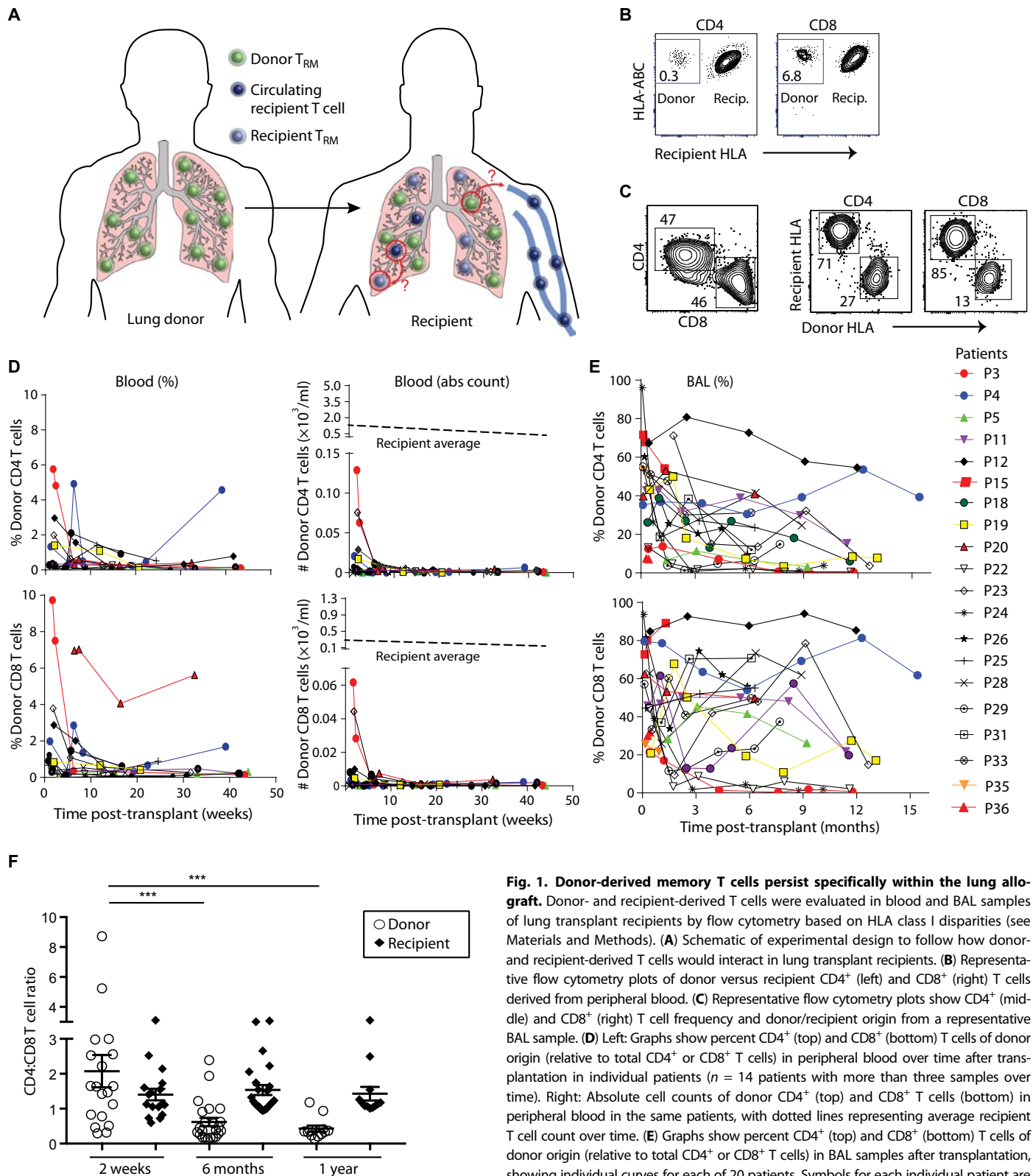


**Fig. 1. Donor-derived memory T cells persist specifically within the lung allograft.** Donor- and recipient-derived T cells were evaluated in blood and BAL samples of lung transplant recipients by flow cytometry based on HLA class I disparities (see Materials and Methods). (A) Schematic of experimental design to follow how donor- and recipient-derived T cells would interact in lung transplant recipients. (B) Representative flow cytometry plots of donor versus recipient CD4<sup>+</sup> (left) and CD8<sup>+</sup> (right) T cells derived from peripheral blood. (C) Representative flow cytometry plots show CD4<sup>+</sup> (middle) and CD8<sup>+</sup> (right) T cell frequency and donor/recipient origin from a representative BAL sample. (D) Left: Graphs show percent CD4<sup>+</sup> (top) and CD8<sup>+</sup> (bottom) T cells of donor origin (relative to total CD4<sup>+</sup> or CD8<sup>+</sup> T cells) in peripheral blood over time after transplantation in individual patients ( $n = 14$  patients with more than three samples over time). Right: Absolute cell counts of donor CD4<sup>+</sup> (top) and CD8<sup>+</sup> T cells (bottom) in peripheral blood in the same patients, with dotted lines representing average recipient T cell count over time. (E) Graphs show percent CD4<sup>+</sup> (top) and CD8<sup>+</sup> (bottom) T cells of donor origin (relative to total CD4<sup>+</sup> or CD8<sup>+</sup> T cells) in BAL samples after transplantation, showing individual curves for each of 20 patients. Symbols for each individual patient are designated in the legend at the right. (F) CD4:CD8 T cell content in the BAL of transplant recipients (total T cell content from donor and recipient) at indicated times after transplantation. Results are shown for 19 patients; \*\*\* $P < 0.01$ ; all other comparisons are nonsignificant.

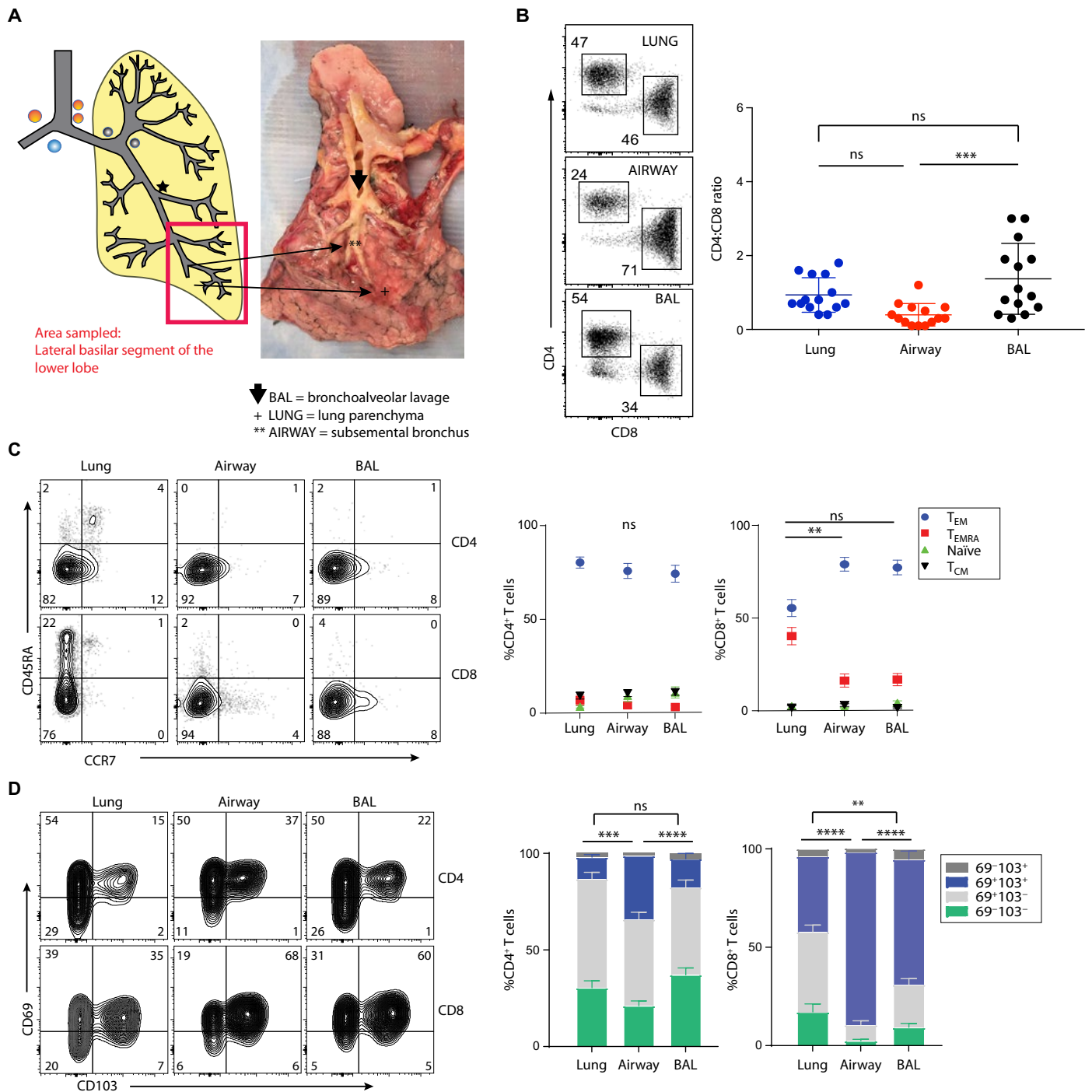


**Fig. 2. BAL of human lungs samples T cells from both the lung parenchyma and airways.** (A) Schematic diagram (left) highlighting the lateral basilar segment of the lower lobe, which is where the BAL was performed and where control lung and airway segments were procured, and photograph (right) of one study lung included in the analysis. (B) Representative flow cytometry plots showing CD4 and CD8 ratio across locations.  $***P = 0.0008$ . (C) T cell subset composition in the BAL, airway, and lung parenchyma showing effector memory ( $T_{EM}$ ;  $CCR7^-CD45RA^-$ ), terminal effector ( $T_{EMRA}$ ;  $CCR7^+CD45RA^+$ ), central memory ( $T_{CM}$ ;  $CCR7^+CD45RA^-$ ), and naïve T cells ( $CCR7^+CD45RA^+$ ) in representative flow cytometry plots (left) and compiled frequencies (means  $\pm$  SEM) from 15 control lungs.  $***P = 0.006$ . (D) Cell surface expression of tissue residency markers CD69 and CD103 by CD4<sup>+</sup> and CD8<sup>+</sup> T cells across locations shown as representative flow cytometry plots (left) and compiled frequencies (right) from 15 donors.  $**P = 0.0013$ ,  $***P = 0.0002$ , and  $****P < 0.0001$ . ns, not significant.

produced at higher frequencies by donor compared with recipient BAL CD4<sup>+</sup> T cells (Fig. 3E), whereas both donor- and recipient-derived T cells produced comparable levels of IL-2 after stimulation

(Fig. 3F). Granzyme B production was higher among recipient-derived compared with donor-derived CD8<sup>+</sup> T cells (Fig. 3G). These results indicate that persisting donor- and recipient-derived T cells in

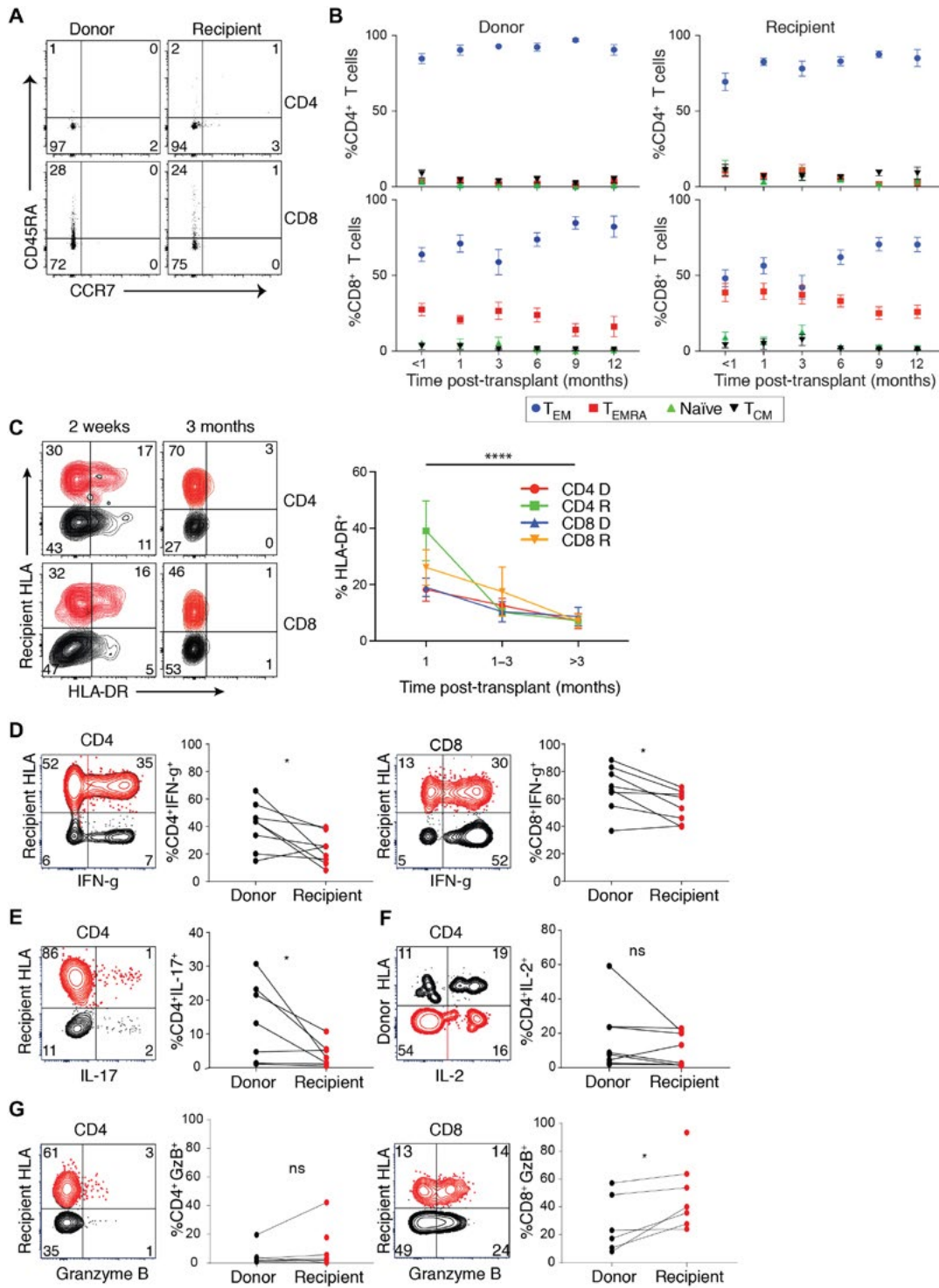
the lung maintain multifunctional profiles associated with mucosal memory T cells.

Regulatory T cells ( $T_{reg}$ ) have been shown to play key roles in allograft acceptance in murine models (35, 36). We therefore assessed

$T_{reg}$  frequency at early and late times after transplantation in blood and BAL from the patients in Fig. 1 and additional patients with long-term transplants (table S2) based on gating for  $CD4^+CD25^+CD127^{lo}Foxp3^+$  T cells (fig. S3) (37). In the blood,  $T_{reg}$  frequency in

**Fig. 3. Donor and recipient BAL T cells are phenotypically and functionally memory T cells.**

(A) Subset composition of donor and recipient  $CD4^+$  and  $CD8^+$  T cells in representative patient BAL based on CD45RA and CCR7 expression as in Fig. 2. (B) Compiled data (means  $\pm$  SEM) of donor (left) and recipient (right) T cell subset composition ( $T_{EM}$ , blue;  $T_{EMRA}$ , red; naïve, green;  $T_{CM}$ , black) over time after transplantation for  $CD4^+$  (top) and  $CD8^+$  T cell (bottom) lineages. Results compiled from 20 patients with one sample per patient per time point. (C) HLA-DR expression by donor and recipient T cells in patient BAL at indicated times after transplantation shown as representative flow cytometry plots (left) and compiled frequencies from 23 samples derived from 11 patients (right). (D to F) T cells from patient BAL samples were stimulated with PMA/ionomycin, and cytokine production was determined by intracellular staining after 5 hours. (D) IFN- $\gamma$  production by donor (black) and recipient (red)  $CD4^+$   $T_{EM}$  (left) and  $CD8^+$   $T_{EM}$  (right) in representative flow cytometry plots and graphs showing paired frequencies (based on percent cytokine $^+$  of donor or recipient T cells) in patient BAL samples ( $n = 8$ ) 1 to 9 months after transplantation (right). \* $P = 0.04$  for  $CD4^+$   $T_{EM}$  and \* $P = 0.01$  for  $CD8^+$   $T_{EM}$ . (E) IL-17 production by donor (black) and recipient (red)  $CD4^+$   $T_{EM}$  in representative flow cytometry plot (left) and graph (right) showing paired frequencies in patient BAL samples ( $n = 7$ ) 1 to 9 months after transplantation. \* $P = 0.05$ . (F) IL-2 production by donor (black) and recipient (red)  $CD4^+$   $T_{EM}$  in representative flow cytometry plot (left) and graph (right) showing paired frequencies in patient BAL samples (right;  $n = 8$ ). (G) Granzyme B (GzB) expression by  $CD4^+$   $T_{EM}$  (left) and  $CD8^+$   $T_{EM}$  (right) from BAL samples obtained >2 months after transplantation in representative flow cytometry plots (left) and cumulative paired data (right) from six transplant recipients of donor (black) and recipient (red). \* $P = 0.04$ .



transplant recipients was lower than in control blood (fig. S3, A and B), consistent with all patients having received basiliximab (anti-CD25 antibody) induction, known to cause peripheral  $T_{reg}$  depletion (38). In the BAL,  $T_{regs}$  were present in much lower frequencies than found in control BAL, and largely derived from recipient T cells with negligible donor-derived  $T_{regs}$ , even in samples with significant T cell chimerism (fig. S3, C and D). These findings establish that  $T_{EM}$  are the predominant functional T cell subset in transplant patient BAL, with donor T cells being exclusively memory.

### Differential expression of $T_{RM}$ markers by donor- and recipient-derived T cells with time

We examined whether the predominant memory T cell population within patient BAL exhibited features of  $T_{RM}$ . In BAL samples from transplant recipients, expression of  $T_{RM}$  markers CD69 and CD103 differed for donor- and recipient-derived T cells, and as a function of time after transplantation as indicated in representative and compiled patient data (Fig. 4, A and B). For donor T cells, the majority of  $CD4^+$  and  $CD8^+$  T cells were  $CD69^+$ , whereas CD103 was coexpressed by 30 to 40% of donor  $CD4^+$  T cells and >80% of donor  $CD8^+$  T cells at >3 months after transplantation (Fig. 4, A and B). The frequency of  $CD69^+/CD103^+$  donor T cells was greater than or at the upper limit compared with that of control BAL T cells (Fig. 4B, compare blue lines with gray shaded rectangles). These results indicate that donor T cells in patient BAL exhibit canonical features of  $T_{RM}$ , consistent with their biased maintenance in the lung but not peripheral blood.

Compared with donor BAL T cells, recipient T cell populations in the BAL expressed much lower frequencies of  $T_{RM}$  markers at early times (2 to 4 weeks) after transplantation (20 to 40%  $CD69^+CD4^+$  and  $CD8^+$  T cells); however, by 6 months after transplantation, >50% of recipient BAL T cells were  $CD69^+$ , with substantial frequencies of recipient  $CD8^+$  T cells coexpressing CD103 (Fig. 4, A and B). By 3 to 6 months after transplantation, recipient BAL T cells expressed CD69 and CD103 at frequencies similar to those observed in control BAL T cells (Fig. 4B). This gradual acquisition of  $T_{RM}$  markers by recipient-derived T cells that infiltrate the lung allograft suggests de novo  $T_{RM}$  generation.

In addition to CD69 and CD103, we and others have identified additional signature markers expressed by human  $T_{RM}$  (18, 21), including the collagen-binding integrin CD49a and negative regulators PD-1 and CD101 (39, 40). We confirmed that these three markers were expressed in high frequencies by T cells obtained from control BAL, airways, and lung parenchyma (Fig. 4, C to E). In the BAL of lung transplant recipients, CD49a was expressed by a significant (>50%) frequency of donor and recipient T cells in all patients, with higher frequencies expressed by donor compared with recipient T cells (Fig. 4F). Expression of PD-1 and CD101 by donor and recipient BAL T cells was more variable between donors, with 20 to 80% of T cells expressing these markers and donor  $CD4^+$  T cells expressing significantly higher levels compared with recipient-derived  $CD4^+$  T cells (Fig. 4, G and H). Together, these results show that transplant BAL T cells express additional  $T_{RM}$  signature markers, with increased expression by donor- compared with recipient-derived T cells.

### Single-cell transcriptome analysis of transplant BAL T cells reveals two $T_{RM}$ -like subsets

To investigate the differentiation state of donor and recipient BAL T cells, we performed single-cell transcriptome profiling from two lung transplant recipients (P19 and P29) at >9 months after transplantation—

a time point in which we could dissect the heterogeneity of recipient T cells in the context of persisting donor  $T_{RM}$  populations. We sorted single  $CD3^+$  T cells from patient BAL into 96-well plates (Fig. 5A and fig. S4A), followed by library preparation, barcoding, and RNA sequencing using PLATE-seq (pooled library amplification for transcriptome expression sequencing) as described (41). The results obtained were referenced to individual cell surface protein expression including donor and recipient HLA and  $T_{RM}$  markers CD69 and CD103 (Fig. 5B). The analysis yielded 492 unique cells from P29 and 185 unique cells from P19; each patient's transcriptome was analyzed separately to minimize batch effects (table S3).

The scRNA-seq (single-cell RNA sequencing) results revealed three distinct clusters of T cells from the BAL of P29, which correlated with phenotypic and cell origin differences determined by the index sorting: Cluster 1 comprised predominantly donor  $CD8^+$  T cells expressing CD69 and CD103 (putative  $T_{RM}$ ); cluster 2 was mainly recipient-derived T cells lacking CD69 and CD103 expression (putative circulating  $T_{EM}$ ); and cluster 3 was a mix of donor and recipient  $CD4^+$  and  $CD8^+$  T cells expressing  $CD69^{\pm}/CD103$  ( $T_{RM}$ -like) (Fig. 5C). The clustering of gene expression based on expression of  $T_{RM}$  markers and donor and recipient origin suggests that distinct differentiation states could be attributed to these populations.

The heat map of gene expression from individual cells in Fig. 5D shows the top differentially expressed genes in each cluster and their level of expression in individual cells from each cluster. Cluster 1 is enriched for cells expressing genes associated with T cell effector function (*GZMA*, *NKG7*, *CCL5*, *KLRD1*, *PFN1*, *CD27*, and *IL32*) and  $T_{RM}$  differentiation including  $T_{RM}$  markers (*ITGA1* and *CXCR6*), and the transcription factors *ZNF683* (Hobit) and *RUNX3* shown to mediate  $CD8^+$   $T_{RM}$  formation in mice (42, 43). Gene expression in cluster 2 differs from that in cluster 1, with greatly reduced expression of  $T_{RM}$  and effector-associated genes and increased expression of genes involved in regulation of transcription/translation (*RPL13*, *PABPC1*, and *MLLT3*), cell cycle (*BTG1*), and cytokine signaling (*IL7R* and *JAK3*) (Fig. 5D). Cells within cluster 3 expressed  $T_{RM}$  genes (*ITGA1*, *CXCR6*, and *RUNX3*), but these were fewer in number compared with cluster 1 (Fig. 5D), and many cluster 3 cells up-regulated a unique set of genes associated with cell differentiation and fate determination (*SOX11* and *CDH6*), cellular transport (*PDZD3* and *TTPAL*), cell cycle regulation (*DOCK7*), and cytokine signaling (*TNFSF13B*).

To determine significant differential gene expression in the clusters, we plotted the average gene expression between clusters onto a new heat map (Fig. 6A). This analysis reveals three distinct T cell subsets, including two subsets with transcriptional features of  $T_{RM}$  and one non- $T_{RM}$  subset: cluster 1, which we designate as “mature  $T_{RM}$ ” based on the high expression of multiple  $T_{RM}$  signature molecules and transcription factors; cluster 3 as “ $T_{RM}$ -like” based on differential expression of  $T_{RM}$ -associated molecules; and cluster 2 as “ $T_{EM}$ ” based on the lack of expression of  $T_{RM}$  signature molecules and biased recipient origin. To assess heterogeneity within each cluster, we further compared gene expression between donor- and recipient-derived T cells within each cluster (Fig. 6B). Volcano plots show a greater concordance of gene expression between donor and recipient T cells within cluster 1 (mature  $T_{RM}$ ) with a low magnitude of differential gene expression compared with higher magnitude of gene expression differences between donor and recipient T cells within clusters 2 and 3 (Fig. 6B). Donor T cells within cluster 3 express significantly higher levels of  $T_{RM}$ -associated genes *ITGA1*, *ZNF683*, and *CXCR6* compared with recipient T cells, whereas recipient cells expressed higher

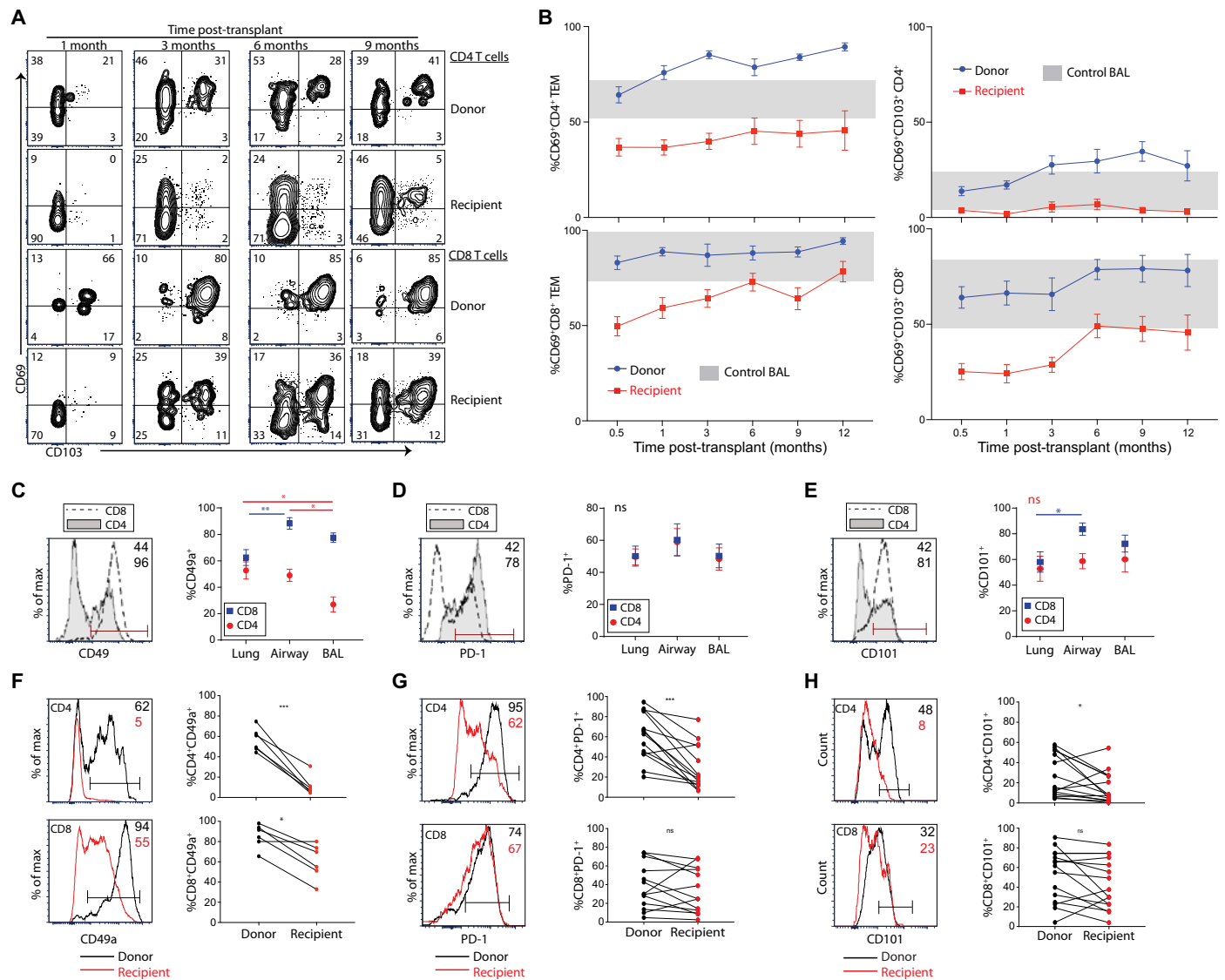


**Fig. 4. Differential expression of T<sub>RM</sub> markers by donor- and recipient-derived T cells with time. (A)** Expression of CD69 and CD103 by CD4<sup>+</sup> (top two rows) and CD8<sup>+</sup> T cells (third and fourth rows) of donor or recipient origin as indicated over time after transplantation for one representative patient, P5. **(B)** Graphs show mean frequency (±SEM) of CD69 expression (left) or CD69/CD103 coexpression (right) by CD4<sup>+</sup> T<sub>EM</sub> (top) or CD8<sup>+</sup> T<sub>EM</sub> (bottom) cells in patient BAL at indicated times after transplantation, compiled from 20 patients. T cell origin designated as donor (blue) and recipient (red) based on HLA disparities (see Fig. 1); gray shaded rectangles denote 1 SD around the average frequency of CD69<sup>+</sup> (left) and CD69<sup>+</sup>CD103<sup>+</sup> (right) expression by control BAL T cells compiled from Fig. 2D. Expression of **(C)** CD49a, **(D)** PD-1, and **(E)** CD101 by BAL, airways, and parenchyma obtained from control lungs shown as representative flow cytometry plots and mean frequencies (±SEM), compiled from 14 lungs. \*P = 0.02 (CD101); \*P < 0.05 and \*\*P = 0.004 (CD49a); ns (PD-1). **(F)** CD49a expression by donor (black) and recipient (red) CD4<sup>+</sup> T<sub>EM</sub> (top) and CD8<sup>+</sup> T<sub>EM</sub> (bottom) cells in patient BAL samples shown as representative flow cytometry plots (left) and in graphs showing paired frequencies from individual patient BAL samples (n = 6) at >1 month after transplantation. \*\*\*P = 0.0003 and \*P = 0.007. **(G)** PD-1 expression by donor (black) and recipient (red) CD4<sup>+</sup> T<sub>EM</sub> (top) and CD8<sup>+</sup> T<sub>EM</sub> (bottom) cells in patient BAL shown as representative flow cytometry plots (left) and graphs showing paired frequencies in patient BAL samples (n = 14) >6 months after transplant. \*\*\*P = 0.0001. **(H)** CD101 expression by donor (black) and recipient (red) CD4<sup>+</sup> T<sub>EM</sub> (top) and CD8<sup>+</sup> T<sub>EM</sub> (bottom) cells in representative flow cytometry plots (left) and paired frequencies in patient BAL samples (n = 15) at >1 month after transplantation. \*P = 0.02.

levels of *RUNX3* and *KLRD1*. These findings suggest that clusters 2 and 3 contain cells with more heterogeneous differentiation states compared with cluster 1 (mature T<sub>RM</sub>) cells, which may represent the most differentiated population.

We also obtained scRNA-seq results from the BAL of P19, which contained predominantly donor-derived cells. The data resolved into two clusters by *t*-distributed stochastic neighbor embedding (tSNE) analysis (Fig. 6C) similar to the T<sub>RM</sub>-like clusters we identified for

P29. Cluster 1 in P19 with high CD69/CD103 expression strongly correlated with P29 cluster 1 (Fig. 6, C and D, and fig. S4B). Similarly, cluster 2 for P19 correlated with cluster 3 for P29, representing a distinct T<sub>RM</sub> population (Fig. 6D). Cluster 2 from P29 representing the tissue-infiltrating T<sub>EM</sub> population was not identified in P19 (Fig. 6D), likely due to the low number of recipient T cells. Together, these results confirm the presence of two T<sub>RM</sub>-like subsets in patient BAL from lung transplantation that are consistent between disparate individuals.

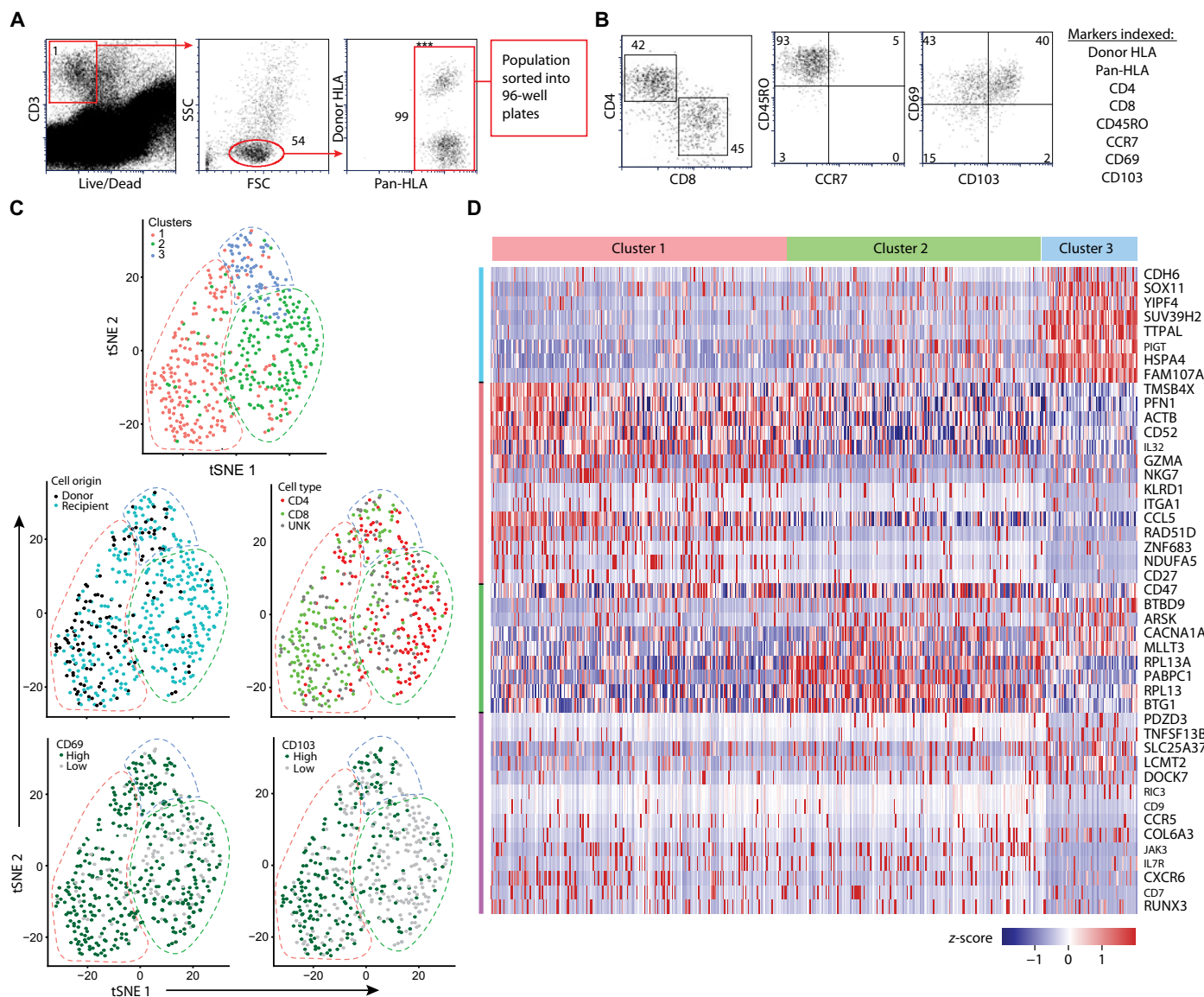


**Fig. 5. Single-cell transcriptome profiling of BAL T cells reveals three distinct subsets with differential expression of  $T_{RM}$ -associated genes.** (A) Representative flow cytometry plots from the BAL of P29 11 months after transplantation showing gating strategy to identify cell populations sorted into 96-well plates for scRNA-seq; “\*\*\*\*” indicates the population sorted: live,  $CD3^+$ , lymphocytes, and pan- $HLA^+$ . (B) Representative flow cytometry plot from influx sorter identifying cell surface markers indexed to individual wells. (C) PC clustering identifying three distinct clusters demarcated by color and tSNE plots visualizing cluster differentiation (see Materials and Methods); indexed cell surface markers identifying cell origin (donor versus recipient) and protein surface expression for CD4, CD8, CD69, and CD103 are indicated within each cluster in separate tSNE plots. (D) Heat map illustrating single-cell analysis for top differentially expressed genes along with select genes of interest, arranged by cluster. Heat map of z-scored expression values, where expression values are defined as  $\log(1 + nUMI_{ij} \frac{\text{median}(nUMI_i)}{nUMI_j})$ , where  $nUMI_{ij}$  is the number of UMI counts for gene  $i$  in cell  $j$ , and  $nUMI_j$  is the total number of UMI counts in cell  $j$ .

**Persisting donor  $T_{RM}$  localize around airways and are associated with decreased PGD and ACR**

To gain insight into potential in vivo functional roles of donor  $T_{RM}$  in the transplanted lung, we assessed their localization and association with clinical outcome. Immunofluorescence imaging of transbronchial biopsies showed large clusters of both donor- and recipient-derived T cells around the small airways of the allograft, described as bronchus-associated lymphoid tissue (Fig. 7). Donor- and recipient-derived T cells were found to colocalize within the peribronchiolar region of the airway of these tissues (Fig. 7, A to I). Whereas donor-derived  $CD4^+$  and  $CD8^+$  T cells were found exclusively within the peri-

bronchiolar region of the airway, recipient-derived T cells were also found in the peribronchiolar, subepithelial, and intraepithelial regions. These findings indicate broader localization of recipient compared with donor T cells.

We investigated whether persistence of donor T cells in the BAL was associated with specific clinical events after transplantation. PGD, characterized by allograft opacification (on chest x-ray) within 72 hours of transplantation not secondary to infection or cardiac dysfunction, has been significantly correlated with increased chronic lung allograft dysfunction and reduced lung allograft survival (25, 44). Among the recipients, patients who did not experience PGD (13 of 20)

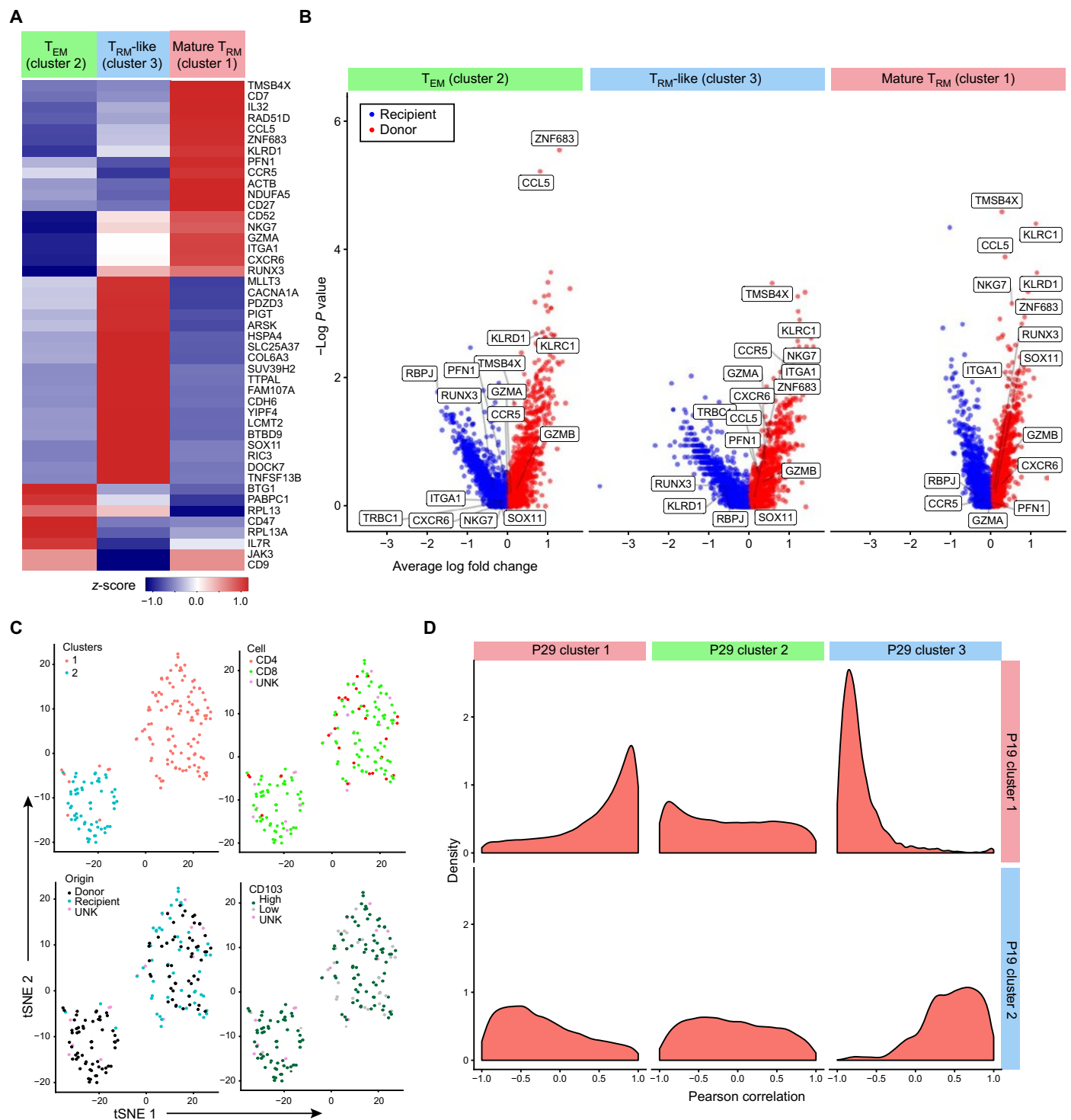


**Fig. 6.  $T_{RM}$ -like subsets exhibit quantitative gene expression differences in donor and recipient T cells and are consistent between patients. (A)** Heat map of the z-scored mean expression values (as defined in Fig. 5D) of select genes based on differential expression analysis in each cluster, with cluster 1 designated as mature  $T_{RM}$ , cluster 2 designated as  $T_{EM}$ , and cluster 3 designated as  $T_{RM}$ -like. **(B)** Volcano plots showing differential gene expression in donor compared with recipient T cells in each cluster. **(C)** PC clustering from scRNA-seq analysis of  $CD3^+$  T cells obtained from the BAL of P19 13 months after transplantation identifies two distinct clusters, demarcated by color; tSNE plots visualizing cluster differentiation. **(D)** Pearson correlation analysis comparing gene expression within clusters 1, 2, and 3 from patient P29 to gene expression within clusters 1 and 2 from patient P19.

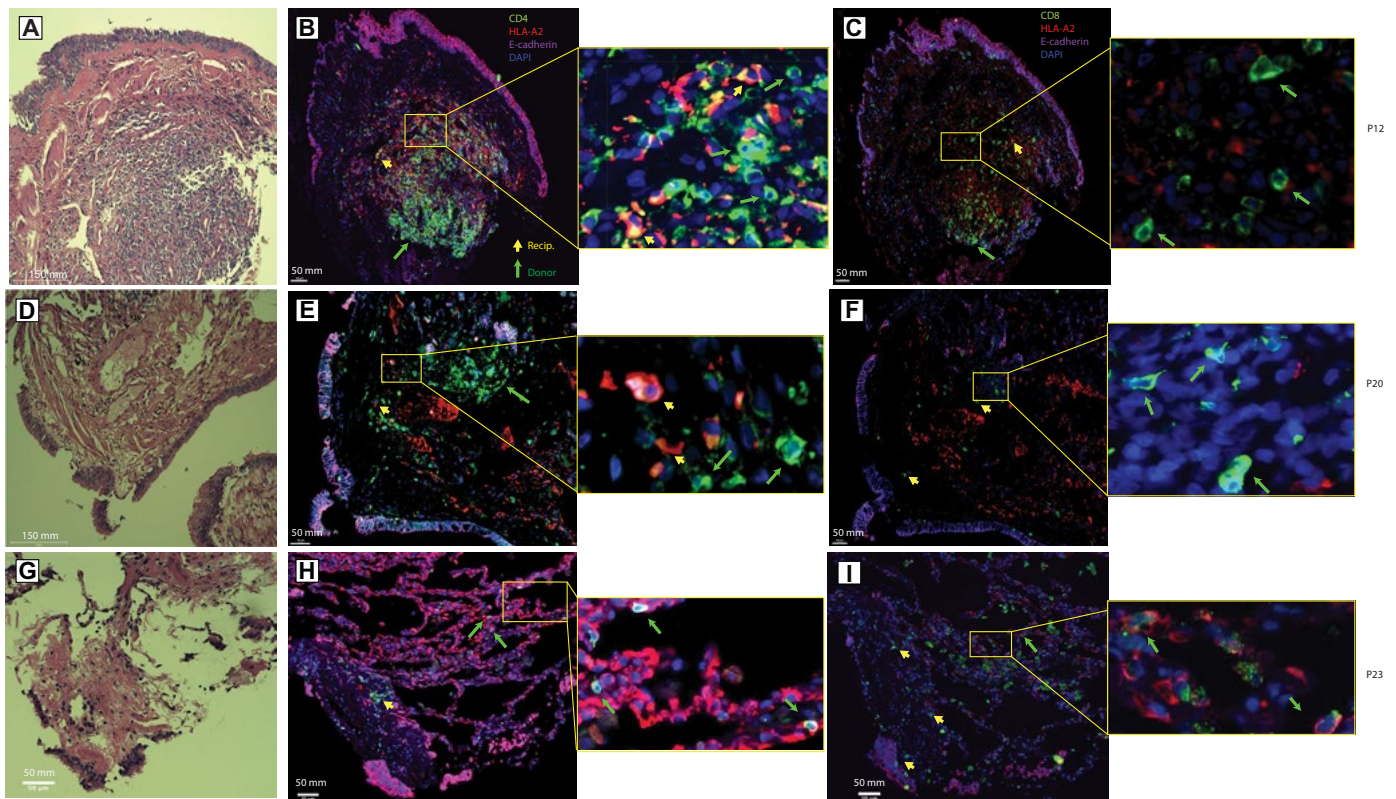


**Fig. 7. Donor- and recipient-derived T cells cluster near airways.** Immunofluorescence imaging of transbronchial biopsies (TBBx) obtained from three transplant recipients (P12, P20, and P23); for P12 and P20, the recipient is HLA-A2<sup>+</sup> and donor is HLA-A2<sup>-</sup>; for P23, the recipient is HLA-A2<sup>-</sup> and donor is HLA-A2<sup>+</sup>. Short yellow arrows point to recipient-derived T cells, and long green arrows point to donor-derived T cells. (A, D, and G) Hematoxylin and eosin (H&E)-stained samples showing small airway with cluster of lymphocytes. (B, E, and H) Expression of E-cadherin (purple), DAPI (blue), CD4 (green), and HLA-A2 (red). (C, F, and I) Expression of E-cadherin (purple), DAPI (blue), CD8 (green), and HLA-A2 (red).

all exhibited higher levels of donor CD4<sup>+</sup> and CD8<sup>+</sup> T cell chimerism in the BAL compared with patients experiencing PGD (7 of 20); this difference persisted throughout the 15-month study (Fig. 8A). These results show a clear association between increased retention of donor lung T<sub>RM</sub> and reduced incidence and severity of PGD.

ACR is another major clinical complication in lung transplantation (26), diagnosed as perivascular infiltrate of T cells found on transbronchial biopsies. Analysis of ACR diagnoses at each time point, where BAL samples were obtained from the 20 patients we followed over the 15-month study period (95 BAL samples in total), showed rejection episodes in 7 of 20 patients with 10 episodes of biopsy-proven ACR, grade A1 or higher, whereas the remaining 13 patients did not show evidence of ACR. At all time points, samples from patients with ACR had significantly lower levels of donor T cell chimerism compared with levels in samples from patients without ACR, which were markedly higher ( $P < 0.01$ , Fig. 8B). Immunofluorescence imaging from a transplant recipient with ACR showed a perivascular infiltration composed of recipient-derived CD4<sup>+</sup> and CD8<sup>+</sup> T cells and a few donor-derived HLA-A2<sup>+</sup> CD4<sup>+</sup> and CD8<sup>+</sup> T cells sparsely distributed in the parenchymal regions (Fig. 8, C to E). These results are consistent with ACR being mediated by recipient-derived T cells infiltrating the perivascular space. We also found a correlation between samples with a positive bacterial culture and low CD4<sup>+</sup> T cell chimerism (Fig. 8F), but no association between BAL T cell chimerism and viral infection (fig. S5). These results show that maintenance of donor T<sub>RM</sub> is associated with improved clin-

ical outcome, with reduced PGD and ACR, and some protective effects to infection.

### DISCUSSION

The identification of T<sub>RM</sub> and their functional roles in vivo have been elucidated in mouse models based, in part, on the ability to monitor T cell tissue infiltration and retention in vivo (19, 42, 43). Two experimental models have been used in mice to verify T cell tissue residency: parabiosis, in which primed mice are surgically conjoined to naïve mice and T<sub>RM</sub> can be identified by specific retention in the host mouse tissues, and in vivo fluorescent antibody labeling to distinguish circulating T cells, which become labeled, from T<sub>RM</sub> that are protected from labeling (4, 29, 45, 46). The dynamics of human T<sub>RM</sub> tissue retention and development, by contrast, have been more challenging to assess.

Here, we studied human lung T<sub>RM</sub> generation, persistence, and function in airway samples obtained prospectively from patients undergoing HLA-disparate lung transplantation. Using in-depth phenotypic, functional, and transcriptome profiling on the single-cell level, we demonstrate that donor T cells persist specifically in the lung of transplant recipients for >1 year after transplant, express multiple T<sub>RM</sub> signature markers, and persist as two transcriptionally distinct T<sub>RM</sub> subpopulations. Recipient T cells infiltrating the lung, by contrast, are heterogeneous consisting of T<sub>RM</sub> and non-T<sub>RM</sub> populations and exhibit increased T<sub>RM</sub> phenotypes over months in vivo. Increased

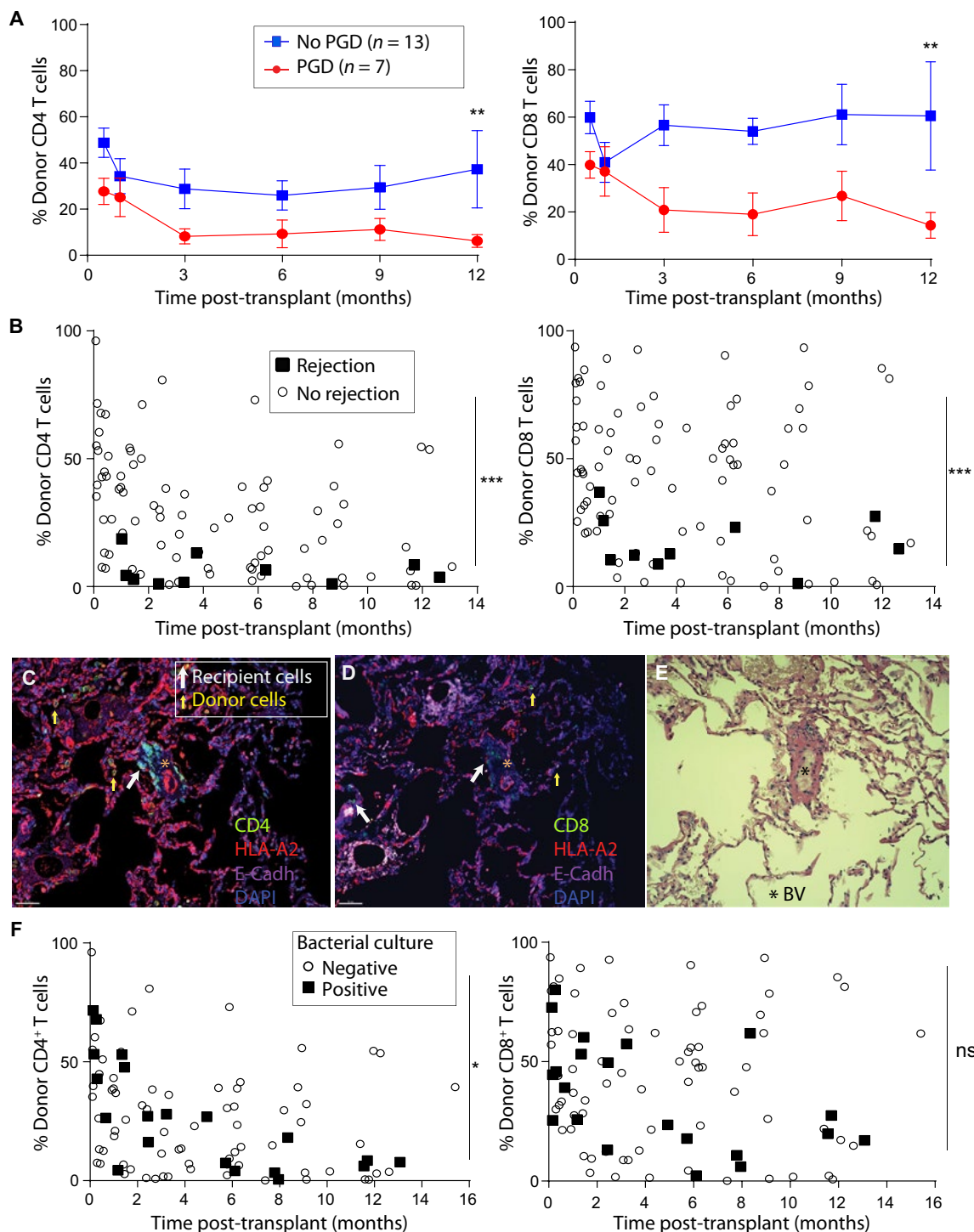


**Fig. 8. Donor T<sub>RM</sub> persistence is associated with reduced clinical complications.** Patient records were examined for clinical complications including PGD and episodes of ACR at all time points of BAL acquisition (see Materials and Methods). (A) Graphs show percentage (mean  $\pm$  SEM) of donor CD4<sup>+</sup> (left) or CD8<sup>+</sup> (right) T cells in the BAL over indicated times after transplantation in patients (n = 20) stratified on the basis of those who experienced PGD (red) or did not (blue). \*\*\*P = 0.003 (left) and \*\*\*P = 0.002 (right). Cumulative data across all time points showed increased proportion of donor CD8<sup>+</sup> (P = 0.008) and trends in increased donor CD4<sup>+</sup> (P = 0.06) T cells in those participants without PGD. (B) Donor CD4<sup>+</sup> (left) and CD8<sup>+</sup> (right) T cell frequencies over indicated times after transplantation in patients (n = 20 total patients; n = 7 patients with 10 discrete episodes of ACR at any time) based on the presence (solid squares) or absence (open circles) of ACR. \*\*\*P < 0.01. (C to E) Serial sections of a TBBx from one patient (P29) who experienced ACR at 1 month after lung transplant (grade 1); donor is HLA-A2<sup>+</sup>, and recipient is HLA-A2<sup>-</sup>. Immunofluorescence imaging stained for E-cadherin (purple), CD4 (green), HLA-A2 (red), and DAPI (blue). Yellow arrows indicate donor cells, and green arrows indicate recipient cells. "\*" identifies a blood vessel (E) H&E stain, and "\*" identifies blood vessel (\*BV). (F) Frequency of donor origin CD4 (left) and CD8 (right) T cells in the BAL stratified on the basis of the presence or absence of a positive bacterial culture. \*P < 0.05.

donor  $T_{RM}$  persistence is correlated with improved clinical outcome. Together, our results provide insights into human  $T_{RM}$  biology in the paradigm of lung transplantation.

$T_{RM}$  constitute a subset of memory  $CD4^+$  and  $CD8^+$  T cells defined by their tissue retention, distinct phenotypes, transcriptional profile, and requirements for generation. Mouse studies have demonstrated a requirement for the transcription factors Hobit (encoded by the gene *ZNF683*) and *Runx3* for  $CD8^+$   $T_{RM}$  generation (42, 43). Human lung  $T_{RM}$  express phenotypes and transcriptional profiles similar to mouse  $T_{RM}$ , including up-regulated expression of *CD69*, *CD103*, *CD49a*, and *CXCR6* (18, 20, 47); expression of *ZNF683* was increased in lung  $CD8^+$  but not  $CD4^+$   $T_{RM}$  (18). Here, we show by phenotypic, functional, and transcriptional analysis with single-cell resolution that donor  $T_{RM}$  persisting in the lung allograft express elevated levels of the major human  $T_{RM}$  signature markers on the cell surface (*CD103*, *CD49a*, and *PD-1*), produce *IFN- $\gamma$*  and *IL-17* when stimulated, and exhibit elevated levels of  $T_{RM}$ -associated genes including *ZNF683* and *RUNX3* and genes related to T cell differentiation and effector function including *NKG7*, the chemokine *CCL5*, and cytotoxic mediators *GRMA* (granzyme A) and *PFN1* (perforin). These findings establish that persisting donor T cells are mature  $T_{RM}$  and suggest that Hobit and *Runx3* may be involved in human  $CD8^+$   $T_{RM}$  generation and/or maintenance, as donor T cells were mostly  $CD8^+$  T cells. The ability of  $T_{RM}$  to persist at least 15 months in the donor lung and retain high functional capacity suggests long-term tissue maintenance in situ. The increased expression of  $T_{RM}$ -associated molecules by donor T cell over time, such as *CD49a* and *CD103*, which mediate interactions with collagen and epithelial cells, respectively, suggests that sustained expression of these molecules is required for  $T_{RM}$  maintenance.

Our findings from both flow cytometry and single-cell RNA sequencing provide evidence that recipient T cells infiltrating the allograft from circulation developed  $T_{RM}$ -like profiles in a stepwise fashion in the lung. Recipient  $T_{RM}$  development occurred over months after transplantation, as assessed by a gradual increase in surface *CD69* and *CD103* expression reaching a steady state after 6 months. The scRNA-seq results reveal two  $T_{RM}$  populations: one with high level expression of  $T_{RM}$  markers that was largely donor derived and designated as mature  $T_{RM}$ , and a second donor- and recipient-derived  $T_{RM}$ -like subset, expressing lower levels of  $T_{RM}$  markers and higher levels of genes controlling cell fate, including the transcription factor *Sox11* involved in fate determination in retinal ganglial cells (48, 49) and osteoclasts (50). A third non- $T_{RM}$  subset (cluster 2) comprising recipient cells may represent tissue-infiltrating  $T_{EM}$  not yet activated. The functional role of recipient-generated  $T_{RM}$  as presented here is not clear; they have the capacity for cytokine production when stimulated but do not exhibit markers of activation in situ, and few recipient cells are represented among mature  $T_{RM}$  with high expression of effector genes.

Persisting, donor-derived, allograft T cells, often referred to as passenger lymphocytes, have been linked to clinical outcomes in liver, heart, and intestinal transplantation (28, 51, 52), although the role of circulating populations versus resident populations in these transplant scenarios is not clear. In heart and liver transplantation, donor T cells have been implicated in vascular pathologies and graft versus host disease, respectively (52, 53). By contrast, in intestinal transplant recipients, donor T cell chimerism in peripheral blood and intestines was linked to reduced rejection rates (28, 54). Here, we show in a cohort of 20 patients that increased persistence of donor lung  $T_{RM}$  specifically within the allograft is associated with reduced lung injury from PGD,

bacterial infections, and ACR. Whether the donor lung  $T_{RM}$  are acting directly to promote reduced lung injury and inflammation or serve as an indicator of a suppressed recipient immune system is not clear and requires further study in larger cohorts. Because donor lung  $T_{RM}$  have presumably adapted to maintain protection and homeostasis in the presence of respiratory insults, they could serve similar protective functions in the transplanted lung. Localization of donor  $T_{RM}$  near airways may facilitate their protective role to inhaled antigens, whereas recipient T cells disseminate throughout the lung with the potential to trigger tissue inflammation.

In summary, our results provide spatial and temporal insights into how human  $T_{RM}$  develop, function, persist, and affect clinical outcome within the complexities of lung transplantation. Monitoring and targeting  $T_{RM}$  persistence and localization can serve as a new strategy for promoting long-term allograft survival in the setting of lung transplantation and beyond.

## MATERIALS AND METHODS

### Study design and subject recruitment

All human studies and procedures were approved by the Columbia University Medical Center Institutional Review Board, and informed consent was obtained from all patients. Hospitalized patients who were actively listed for lung transplantation or had previously undergone lung transplantation were approached for enrollment. A total of 23 patients were recruited, of whom 1 died before transplantation, 1 died after transplantation but before procurement of samples, and 1 participant had HLA similarities to their donor preventing accurate determination of cell origin. BAL and blood samples were obtained from the remaining 20 lung transplant recipients included in this study (table S1). Additional blood and BAL samples from lung transplant recipients with longer follow-up time were used for assessment of  $T_{reg}$  frequencies (table S2). All participants underwent induction immunosuppression with an *IL-2* receptor antagonist (basiliximab), high-dose glucocorticoids (methylprednisolone), mycophenolate mofetil (MMF), and tacrolimus. Maintenance immunosuppression consisted of MMF, tacrolimus, and prednisone. Seven patients experienced PGD, grade 1 or higher, defined as allograft opacification within 72 hours of transplantation not due to heart failure or infection. Seven patients experienced 10 discrete episodes of ACR; the diagnosis and grading of ACR are based on the pathologic finding of perivascular lymphocytic infiltration in transbronchial biopsy specimens.

### Acquisition of control human lungs

Human lungs were obtained from brain-dead, organ donors through a collaboration with our local organ procurement organization for New York City (LiveOnNY), as previously described (30, 31). Donors ranged in age from 20 to 73 years old, and the majority died of a cerebral vascular accident (table S4). BAL was obtained by placing a 25-ml pipette into the lateral basilar segment of the lower lobe of the lung, injecting 60 ml of RPMI followed by suctioning. After obtaining BAL, the same segment of lung was dissected, and cells were isolated after mechanical and enzymatic digestion of the lung and airway as described (18, 30, 31, 55).

### Lymphocyte isolation from BAL and peripheral blood

BAL samples were filtered through a 100- $\mu$ m filter, followed by a 40- $\mu$ m filter, and centrifuged at 1500 rpm for 5 min; the cell pellet was resuspended in flow cytometry staining buffer or in medium

for functional analysis and sorting. Human TruStain FcX receptor blocker (BioLegend) was then applied at room temperature for 10 min before application of antibodies. Lymphocytes were isolated from peripheral blood using lymphocyte separation medium (Cellgro) and ACK lysis buffer.

### Flow cytometry analysis

Total mononuclear cells isolated from BAL and blood were surface and intracellularly stained with fluorochrome-conjugated antibodies (see table S5 for a full list of antibodies). Intracellular staining was performed after fixation and permeabilization with Invitrogen fixation/permeabilization buffer. For cytokine determination, lymphocytes were isolated from BAL and cultured for 5 hours with phorbol 12-myristate 13-acetate (PMA)/ionomycin in the presence of monensin (0.4  $\mu$ l/200  $\mu$ l of medium; GolgiStop BD Biosciences), followed by treatment with fixation/permeabilization buffer and intracellular staining with anti-cytokine antibodies. Stained samples were acquired on an LSRII flow cytometer or sorted with an Influx cell sorter (BD Biosciences), and data were analyzed using FCS Express v6 (De Novo Software, Glendale, CA).

### Immunofluorescence imaging

Transbronchial biopsy specimens were received from pathology in 5- $\mu$ m sections from paraffin. Slides were deparaffinized using Histo-clear and rehydrated with serial dilutions of ethanol. Antigen retrieval was performed at 95°C for 20 min in the presence of Dako Target Retrieval Solution (Agilent) (pH 9). Slides were preincubated with Blocking One buffer (Nacalai Tesque Inc.), followed by staining with primary antibody, washing, and staining with secondary antibody and 4',6-diamidino-2-phenylindole (DAPI; table S5). Slides were imaged using an EVOS FL Auto 2 imaging system (Thermo Fisher Scientific) and analyzed using Imaris image analysis software (Bitplane).

### Single-cell transcriptome profiling by RNA sequencing

Single CD3<sup>+</sup> T cells from patient BAL were sorted directly into wells of 96-well plates; each well contained 7.5  $\mu$ l of lysis buffer [0.2% Triton X-100 (Sigma), SUPERaseIN (1 U/ $\mu$ l) (Thermo Fisher Scientific), 2 mM deoxyribonucleotides (dNTPs) (Thermo Fisher Scientific), and 2  $\mu$ M reverse transcriptase (RT) primer (Integrated DNA Technologies)]. Primer annealing was performed at 72°C for 3 min. Reverse transcription was performed by adding 7.5  $\mu$ l of RT mix to each well [2 M betaine (Affymetrix), 2 $\times$  Protoscript Buffer (New England Biolabs), 12 mM MgCl<sub>2</sub> (Thermo Fisher Scientific), 10 mM dithiothreitol (Thermo Fisher Scientific), 5.3 U of Protoscript II Reverse Transcriptase (New England Biolabs), 0.53 U of SUPERaseIN (Thermo Fisher Scientific), and 2  $\mu$ M Template Switching Oligo (Integrated DNA Technologies; table S6)]. Reverse transcription was performed at 42°C for 90 min, followed by 10 cycles of 50°C for 2 min, 42°C for 2 min, 70°C for 10 min, followed by a 4°C hold. Excess primers were removed by adding 2  $\mu$ l of Exonuclease I (Thermo Fisher Scientific) mix to each well (1.875 U of ExoI in water) and incubating at 37°C for 30 min, 85°C for 15 min, 75°C for 30 s, and 4°C hold.

All wells were pooled into a single 15-ml falcon tubes, and complementary DNA (cDNA) was purified and concentrated using Dynabeads MyOne Silane beads (Thermo Fisher Scientific) according to the manufacturer's instructions. The cDNA was split into duplicate reactions containing 25  $\mu$ l of cDNA, 25  $\mu$ l of 2 $\times$  HIFI HotStart Ready Mix (Kapa Biosystems), and 0.2 M SMART PCR Primer (table S6) and polymerase chain reaction (PCR)-amplified as above, and duplicate

reactions were combined and purified using 0.7 volume of AMPure XP beads (Beckman Coulter). The amplified cDNA was visualized on an Agilent TapeStation and quantified using a Qubit II fluorometer (Thermo Fisher Scientific).

Sequencing libraries were constructed using Nextera XT (Illumina) with modifications. A custom i5 primer was used (Nextera PCR; table S6) with 0.6 ng of input cDNA, and 10 cycles of amplification were performed. Unique i7 indexes were used for each plate. After amplification, the library was purified with two rounds of AMPure XP beads, visualized on the TapeStation, and quantified using the Qubit II fluorometer. Libraries were sequenced on an Illumina NextSeq 500 using the 75-cycle High Output Kit [read lengths 26(R1)  $\times$  8(i)  $\times$  58(R2)]. Custom sequencing primers were used for Read 1 (SMART\_R1seq and ILMN\_R1seq; see table S6). With each plate, we targeted ~70 million reads. Library pools were loaded at 1.8 pM with 30% PhiX (Illumina).

### Analysis of scRNA-seq data

#### Read processing

Reads were aligned to the human genome reference GRCh38 using STAR (version 2.5) (56). During alignment, reads with more than one mapping were recorded as unmapped using the arguments '-outFilterMultimapNmax 1' and '-outSAMunmapped Within'. Alignment counts were generated using Subread's featureCounts (version 1.6) (57) with default parameters. Reads were assigned to cell and unique molecular indicator (UMI) barcodes using UMI-tools (58).

#### Data preparation

Analysis of single-cell RNA-seq data was performed in R (version 3.4.4) (59). Count matrices for both patients P29 and P19 were limited to protein coding genes, based on the datasets. Cells for each patient were filtered by excluding those with extreme values of cell summary metrics: total UMI count (nUMI), number of genes detected (nGene), and proportion of expression from mitochondrial genes (PMT). This was done by modeling the distribution of each metric within each library as a normal distribution, generating probabilities for each cell using the normal distribution function, and applying cutoffs to eliminate outlier cells.

For libraries from P29, the same cutoffs were applied to each library. For nUMI, 0.1 and 0.98 were the low and high cutoffs, respectively. For nGene, 0.1 and 0.98 were the low and high cutoffs, respectively. For PMT, 0.94 was the high cutoff used, and there was no low cutoff applied. Each library from P19 was filtered separately due to the high degree of dissimilarity between the distributions of their cell summary metrics. The cutoffs used for each library are shown in table S7.

### Gene selection and clustering

Genes used as the basis for clustering were selected in a two-step process described in detail in Supplementary Methods. Principal components (PCs) for clustering and visualization were selected by computationally drawing a cutoff at the inflection point in a plot of SD versus PC number. The tSNE projection used in the visualizations was produced by running the t-SNE algorithm (60) as implemented in the R package tsne (61) on a Euclidean distance matrix created from a cell-by-cell Spearman correlation matrix computed with the selected PCs.

Clustering and differential expression analysis were performed using Seurat (62). For both patients, the clustering resolution used was 0.8. Differential expression analysis was performed with Wilcoxon rank sum tests. For each cluster, differential expression analysis was performed between the cells of the cluster and all other cells. Differential expression comparisons were also made between each pair of clusters.

To analyze differences across experimental factors determined during the cell sort, differential expression comparisons were made between factor values within clusters. Also, enrichment of clusters for factor values was assessed by testing the equality of proportions of a cluster for a given factor value versus all cells outside the cluster.

### Comparison of clusters between patients

The clusters identified for P19 and P29 were compared by assessing the similarity of the cells in each cluster from P19 to those in each cluster derived from P29. This was done by first developing a transformation matrix to score each cell's similarity to each cluster of each patient

$$A_i = X_i^T C_i$$

where  $X_i$  is a matrix of normalized expression value (NEV) scaled and centered across genes for patient  $i$ ;  $C_i$  is the cell-by-cluster matrix with dummy variables for each cluster, scaled and centered column wise. After matrices  $A_{19}$  and  $A_{29}$  were created, the columns of each were combined into one matrix,  $A$ . Then, each cell's similarity to each cluster was scored as follows:

$$S = A^T X$$

where  $X$  is a gene-by-cell matrix of NEV scaled and centered across rows. The matrix  $S$  is then a cluster-by-cell matrix containing cluster scores. Pearson correlation coefficients were then computed between all the cells of P19 and all the cells of P29 from the values of  $S$ . The distributions of these correlation coefficients, separated by cluster, were then used to visually determine the relative similarity of clusters across patients. Heat maps illustrating the single-cell analysis were generated in R using heatmap3 (63). Other plots were created with ggplot2 (64) and cowplot (65).

### Statistical analysis and data visualization

All statistics were calculated using GraphPad Prism (GraphPad Software Inc., La Jolla, CA) and R (R Foundation for Statistical Computing, Vienna, Austria). Statistical significance between donor and recipient cell expression of cell surface and intracellular markers was calculated using a paired  $t$  test when occurring at a single time point. Analysis of variance (ANOVA) was used to test for statistically significant differences across T cell populations obtained from different anatomic locations among the control lung population. Unpaired  $t$  test was used to investigate statistical significance of donor CD4<sup>+</sup> and CD8<sup>+</sup> T cells at 12 months between participants who experienced PGD and those who did not. The impact of PGD on T cell chimerism after transplantation for all time points was investigated using repeated-measures ANOVA. Repeated-measures ANOVA was used to test statistical significance between CD4<sup>+</sup> and CD8<sup>+</sup> T cell chimerism and the presence of ACR over time. Adobe Illustrator CC 2017 (Ventura, CA) was used to compile all graphics.

### SUPPLEMENTARY MATERIALS

immunology.sciencemag.org/cgi/content/full/4/33/eaav5581/DC1  
Methods

- Fig. S1. Gating strategy for donor and recipient T cells from BAL samples.
- Fig. S2. Gating strategy for donor and recipient T cells from blood.
- Fig. S3. Lung transplant recipients have low frequencies of CD4<sup>+</sup> T<sub>reg</sub>s in blood and BAL samples.
- Fig. S4. Single-cell RNA sequencing schematic and comparison between patients.
- Fig. S5. Lack of association of donor T cell chimerism in BAL with viral infection.
- Table S1. Patient demographics and transplant characteristics.

- Table S2. Patient demographics for transplant recipients used for CD4<sup>+</sup> T<sub>reg</sub> data.
- Table S3. Summary of scRNA-seq results by a 96-well plate.
- Table S4. Characteristics of the organ donors for control lung samples.
- Table S5. List of antibodies used for flow cytometry and immunofluorescence imaging.
- Table S6. Details of reverse transcriptase primers.
- Table S7. Cell filtration cutoffs for P19.

### REFERENCES AND NOTES

1. R. Watanabe, A. Gehad, C. Yang, L. L. Scott, J. E. Teague, C. Schlapbach, C. P. Elco, V. Huang, T. R. Matos, T. S. Kupper, R. A. Clark, Human skin is protected by four functionally and phenotypically discrete populations of resident and recirculating memory T cells. *Sci. Transl. Med.* **7**, 279ra39 (2015).
2. J. M. Schenkel, K. A. Fraser, L. K. Beura, K. E. Pauken, V. Vezys, D. Masopust, Resident memory CD8 T cells trigger protective innate and adaptive immune responses. *Science* **346**, 98–101 (2014).
3. S. N. Mueller, L. K. Mackay, Tissue-resident memory T cells: Local specialists in immune defence. *Nat. Rev. Immunol.* **16**, 79–89 (2016).
4. J. R. Teijaro, D. Turner, Q. Pham, E. J. Wherry, L. Lefrançois, D. L. Farber, Cutting edge: Tissue-retentive lung memory CD4 T cells mediate optimal protection to respiratory virus infection. *J. Immunol.* **187**, 5510–5514 (2011).
5. D. L. Turner, D. L. Farber, Mucosal resident memory CD4 T cells in protection and immunopathology. *Front. Immunol.* **5**, 331 (2014).
6. J. M. Schenkel, D. Masopust, Tissue-resident memory T cells. *Immunity* **41**, 886–897 (2014).
7. K. D. Zens, J. K. Chen, D. L. Farber, Vaccine-generated lung tissue-resident memory T cells provide heterosubtypic protection to influenza infection. *J. Clin. Invest. Insight* **1**, e85832 (2016).
8. C. Perdomo, U. Zedler, A. A. Kühl, L. Lozza, P. Saikali, L. E. Sander, A. Vogelzang, S. H. E. Kaufmann, A. Kupz, Mucosal BCG vaccination induces protective lung-resident memory T cell populations against tuberculosis. *MBio* **7**, e01686-16 (2016).
9. T. Wu, Y. Hu, Y.-T. Lee, K. R. Bouchard, A. Benechet, K. Khanna, L. S. Cauley, Lung-resident memory CD8 T cells (TRM) are indispensable for optimal cross-protection against pulmonary virus infection. *J. Leukoc. Biol.* **95**, 215–224 (2014).
10. S. Sakai, K. D. Kauffman, J. M. Schenkel, C. C. McBerry, K. D. Mayer-Barber, D. Masopust, D. L. Barber, Cutting edge: Control of *Mycobacterium tuberculosis* infection by a subset of lung parenchyma-homing CD4 T cells. *J. Immunol.* **192**, 2965–2969 (2014).
11. K. M. Morabito, T. R. Ruckwardt, A. J. Redwood, S. M. Moin, D. A. Price, B. S. Graham, Intranasal administration of RSV antigen-expressing MCMV elicits robust tissue-resident effector and effector memory CD8<sup>+</sup> T cells in the lung. *Mucosal Immunol.* **10**, 545–554 (2017).
12. J. M. Schenkel, K. A. Fraser, V. Vezys, D. Masopust, Sensing and alarm function of resident memory CD8<sup>+</sup> T cells. *Nat. Immunol.* **14**, 509–513 (2013).
13. X. Jiang, R. A. Clark, L. Liu, A. J. Wagers, R. C. Fuhlbrigge, T. S. Kupper, Skin infection generates non-migratory memory CD8<sup>+</sup> TRM cells providing global skin immunity. *Nature* **483**, 227–231 (2012).
14. H. Shin, A. Iwasaki, A vaccine strategy that protects against genital herpes by establishing local memory T cells. *Nature* **491**, 463–467 (2012).
15. D. L. Turner, K. L. Bickham, J. J. Thome, C. Y. Kim, F. D'Ovidio, E. J. Wherry, D. L. Farber, Lung niches for the generation and maintenance of tissue-resident memory T cells. *Mucosal Immunol.* **7**, 501–510 (2014).
16. B. D. Hondowicz, D. An, J. M. Schenkel, K. S. Kim, H. R. Steach, A. T. Krishnamurthy, G. J. Keitany, E. N. Garza, K. A. Fraser, J. J. Moon, W. A. Altemeier, D. Masopust, M. Pepper, Interleukin-2-dependent allergen-specific tissue-resident memory cells drive asthma. *Immunity* **44**, 155–166 (2016).
17. D. L. Turner, M. Goldklang, F. Cvetkovski, D. Paik, J. Trischler, J. Barahona, M. Cao, R. Dave, N. Tanna, J. M. D'Armiento, D. L. Farber, Biased generation and in situ activation of lung tissue-resident memory CD4 T cells in the pathogenesis of allergic asthma. *J. Immunol.* **200**, 1561–1569 (2018).
18. B. V. Kumar, W. Ma, M. Miron, T. Granot, R. S. Guyer, D. J. Carpenter, T. Senda, X. Sun, S.-H. Ho, H. Lerner, A. L. Friedman, Y. Shen, D. L. Farber, Human tissue-resident memory T cells are defined by core transcriptional and functional signatures in lymphoid and mucosal sites. *Cell Rep.* **20**, 2921–2934 (2017).
19. L. K. Mackay, A. Kallies, Transcriptional regulation of tissue-resident lymphocytes. *Trends Immunol.* **38**, 94–103 (2017).
20. P. Hombirink, C. Helbig, R. A. Backer, B. Piet, A. E. Oja, R. Stark, G. Brassler, A. Jongejan, R. E. Jonkers, B. Nota, O. Basak, H. C. Clevers, P. D. Moerland, D. Amsen, R. A. W. van Lier, Programs for the persistence, vigilance and control of human CD8<sup>+</sup> lung-resident memory T cells. *Nat. Immunol.* **17**, 1467–1478 (2016).
21. S. Cheuk, H. Schlums, I. Gallais Sérézal, E. Martini, S. C. Chiang, N. Marquardt, A. Gibbs, E. Detlofsson, A. Intraini, M. Forkel, C. Höög, A. Tjernlund, J. Michaëlsson, L. Folkersen,

- J. Mjösberg, L. Blomqvist, M. Ehrström, M. Ståhle, Y. T. Bryceson, L. Eidsmo, CD49a expression defines tissue-resident CD8<sup>+</sup> T cells poised for cytotoxic function in human skin. *Immunity* **46**, 287–300 (2017).
22. A.-P. Ganesan, J. Clarke, O. Wood, E. M. Garrido-Martin, S. J. Chee, T. Mellows, D. Samaniego-Castruita, D. Singh, G. Seumois, A. Alzetani, E. Woo, P. S. Friedmann, E. V. King, G. J. Thomas, T. Sanchez-Elsner, P. Vijayanand, C. H. Ottensmeier, Tissue-resident memory features are linked to the magnitude of cytotoxic T cell responses in human lung cancer. *Nat. Immunol.* **18**, 940–950 (2017).
  23. P. Savas, B. Virassamy, C. Ye, A. Salim, C. P. Mintoff, F. Caramia, R. Salgado, D. J. Byrne, Z. L. Teo, S. Dushyanthen, A. Byrne, L. Wein, S. J. Luen, C. Poliness, S. S. Nightingale, A. S. Skandarajah, D. E. Gyorki, C. M. Thornton, P. A. Beavis, S. B. Fox; Kathleen Cuninghame Foundation Consortium for Research into Familial Breast Cancer, P. K. Darcy, T. P. Speed, L. K. Mackay, P. J. Neeson, S. Loi, Single-cell profiling of breast cancer T cells reveals a tissue-resident memory subset associated with improved prognosis. *Nat. Med.* **24**, 986–993 (2018).
  24. R. A. Clark, Resident memory T cells in human health and disease. *Sci. Transl. Med.* **7**, 269rv1 (2015).
  25. A. Bharat, D. Kreisel, Immunopathogenesis of primary graft dysfunction after lung transplantation. *Ann. Thorac. Surg.* **105**, 671–674 (2018).
  26. J. M. Gauthier, W. Li, H.-M. Hsiao, T. Takahashi, S. Arefanian, A. S. Krupnick, A. E. Gelman, D. Kreisel, Mechanisms of graft rejection and immune regulation after lung transplant. *Ann. Am. Thorac. Soc.* **14**, S216–S219 (2017).
  27. J. Gottlieb, Lung allocation. *J. Thorac. Dis.* **9**, 2670–2674 (2017).
  28. J. Zuber, B. Shonts, S.-P. Lau, A. Obradovic, J. Fu, S. Yang, M. Lambert, S. Coley, J. Weiner, J. Thome, S. DeWolf, D. L. Farber, Y. Shen, S. Caillat-Zucman, G. Bhagat, A. Griesemer, M. Martinez, T. Kato, M. Sykes, Bidirectional intragraft alloreactivity drives the repopulation of human intestinal allografts and correlates with clinical outcome. *Sci. Immunol.* **1**, eaah3732 (2016).
  29. K. G. Anderson, K. Mayer-Barber, H. Sung, L. Beura, B. R. James, J. J. Taylor, L. Qunaj, T. S. Griffith, V. Vezy, D. L. Barber, D. Masopust, Intravascular staining for discrimination of vascular and tissue leukocytes. *Nat. Protoc.* **9**, 209–222 (2014).
  30. J. J. C. Thome, N. A. Yudanin, Y. Ohmura, M. Kubota, B. Grinshpun, T. Sathaliyawala, T. Kato, H. Lerner, Y. Shen, D. L. Farber, Spatial map of human T cell compartmentalization and maintenance over decades of life. *Cell* **159**, 814–828 (2014).
  31. D. J. Carpenter, T. Granot, N. Matsuoka, T. Senda, B. V. Kumar, J. J. C. Thome, C. L. Gordon, M. Miron, J. Weiner, T. Connors, H. Lerner, A. Friedman, T. Kato, A. D. Griesemer, D. L. Farber, Human immunology studies using organ donors: Impact of clinical variations on immune parameters in tissues and circulation. *Am. J. Transplant.* **18**, 74–88 (2018).
  32. B. V. Kumar, R. Kratchmarov, M. Miron, D. J. Carpenter, T. Senda, H. Lerner, A. Friedman, S. L. Reiner, D. L. Farber, Functional heterogeneity of human tissue-resident memory T cells based on dye efflux capacities. *JCI Insight* **3**, e123568 (2018).
  33. T. Sathaliyawala, M. Kubota, N. Yudanin, D. Turner, P. Camp, J. J. C. Thome, K. L. Bickham, H. Lerner, M. Goldstein, M. Sykes, T. Kato, D. L. Farber, Distribution and compartmentalization of human circulating and tissue-resident memory T cell subsets. *Immunity* **38**, 187–197 (2013).
  34. J. J. C. Thome, B. Grinshpun, B. V. Kumar, M. Kubota, Y. Ohmura, H. Lerner, G. D. Sempowski, Y. Shen, D. L. Farber, Long-term maintenance of human naïve T cells through in situ homeostasis in lymphoid tissue sites. *Sci. Immunol.* **1**, eaah6506 (2016).
  35. W. Li, A. C. Bribiesco, R. G. Nava, A. A. Brescia, A. Ibricevic, J. H. Spahn, S. L. Brody, J. H. Ritter, A. E. Gelman, A. S. Krupnick, M. J. Miller, D. Kreisel, Lung transplant acceptance is facilitated by early events in the graft and is associated with lymphoid neogenesis. *Mucosal Immunol.* **5**, 544–554 (2012).
  36. I. R. Ferrer, J. Hester, A. Bushell, K. J. Wood, Induction of transplantation tolerance through regulatory cells: From mice to men. *Immunity Rev.* **258**, 102–116 (2014).
  37. N. Seddiki, B. Santner-Nanan, J. Martinson, J. Zaunders, S. Sasson, A. Landay, M. Solomon, W. Selby, S. I. Alexander, R. Nanan, A. Kelleher, B. Fazekas de St Groth, Expression of interleukin (IL)-2 and IL-7 receptors discriminates between human regulatory and activated T cells. *J. Exp. Med.* **203**, 1693–1700 (2006).
  38. T. Zhao, C. Yang, Y. Xue, Y. Y. Qiu, L. Hu, Y. Qiu, X. Wang, B. Yang, R. Rong, M. Xu, T. Zhu, Impact of basiliximab on the proportion of regulatory T cells and their subsets early after renal transplantation: A preliminary report. *Transplant. Proc.* **44**, 175–178 (2012).
  39. L. R. B. Soares, L. Tsalvaler, A. Rivas, E. G. Engleman, V7 (CD101) ligation inhibits TCR/CD3-induced IL-2 production by blocking Ca<sup>2+</sup> flux and nuclear factor of activated T cell nuclear translocation. *J. Immunol.* **161**, 209–217 (1998).
  40. E. J. Wherry, T cell exhaustion. *Nat. Immunol.* **12**, 492–499 (2011).
  41. E. C. Bush, F. Ray, M. J. Alvarez, R. Realubit, H. Li, C. Karan, A. Califano, P. A. Sims, PLATE-Seq for genome-wide regulatory network analysis of high-throughput screens. *Nat. Commun.* **8**, 105 (2017).
  42. L. K. Mackay, M. Minnich, N. A. M. Kragten, Y. Liao, B. Nota, C. Seillet, A. Zaid, K. Man, S. Preston, D. Freestone, A. Braun, E. Wynne-Jones, F. M. Behr, R. Stark, D. G. Pellicci, D. I. Godfrey, G. T. Belz, M. Pellegrini, T. Gebhardt, M. Busslinger, W. Shi, F. R. Carbone, R. A. W. van Lier, A. Kallies, K. P. J. M. van Gisbergen, Hobit and Blimp1 instruct a universal transcriptional program of tissue residency in lymphocytes. *Science* **352**, 459–463 (2016).
  43. J. J. Milner, C. Toma, B. Yu, K. Zhang, K. Omilusik, A. T. Phan, D. Wang, A. J. Getzler, T. Nguyen, S. Crotty, W. Wang, M. E. Pipkin, A. W. Goldrath, Runx3 programs CD8<sup>+</sup> T cell residency in non-lymphoid tissues and tumours. *Nature* **552**, 253–257 (2017).
  44. D. Kreisel, A. S. Krupnick, V. Puri, T. J. Guthrie, E. P. Trulock, B. F. Meyers, G. A. Patterson, Short- and long-term outcomes of 1000 adult lung transplant recipients at a single center. *J. Thorac. Cardiovasc. Surg.* **141**, 215–222 (2011).
  45. K. G. Anderson, H. Sung, C. N. Skon, L. Lefrançois, A. Deisinger, V. Vezy, D. Masopust, Cutting edge: Intravascular staining redefines lung CD8 T cell responses. *J. Immunol.* **189**, 2702–2706 (2012).
  46. K. D. Klonowski, K. J. Williams, A. L. Marzo, D. A. Blair, E. G. Lingenheld, L. Lefrançois, Dynamics of blood-borne CD8 memory T cell migration in vivo. *Immunity* **20**, 551–562 (2004).
  47. R. Purwar, J. Campbell, G. Murphy, W. G. Richards, R. A. Clark, T. S. Kupper, Resident memory T cells (TRM) are abundant in human lung: Diversity, function, and antigen specificity. *PLOS ONE* **6**, e16245 (2011).
  48. Y. Jiang, Q. Ding, X. Xie, R. T. Libby, V. Lefebvre, L. Gan, Transcription factors SOX4 and SOX11 function redundantly to regulate the development of mouse retinal ganglion cells. *J. Biol. Chem.* **288**, 18429–18438 (2013).
  49. K.-C. Chang, J. Hertz, SoxC transcription factors in retinal development and regeneration. *Neural Regen. Res.* **12**, 1048–1051 (2017).
  50. J. Gadi, S.-H. Jung, M.-J. Lee, A. Jami, K. Ruthala, K.-M. Kim, N.-H. Cho, H.-S. Jung, C.-H. Kim, S.-K. Lim, The transcription factor protein Sox11 enhances early osteoblast differentiation by facilitating proliferation and the survival of mesenchymal and osteoblast progenitors. *J. Biol. Chem.* **288**, 25400–25413 (2013).
  51. H. J. Schlitt, G. Raddatz, G. Steinhoff, K. Wonigeit, R. Pichlmayr, Passenger lymphocytes in human liver allografts and their potential role after transplantation. *Transplantation* **56**, 951–955 (1993).
  52. T. S. Win, S. Rehakova, M. C. Negus, K. Saeb-Parsy, M. Goddard, T. M. Conlon, E. M. Bolton, J. A. Bradley, G. J. Pettigrew, Donor CD4 T cells contribute to cardiac allograft vasculopathy by providing help for autoantibody production. *Circ. Heart Fail.* **2**, 361–369 (2009).
  53. A. R. Murali, S. Chandra, Z. Stewart, B. R. Blazar, U. Farooq, M. N. Ince, J. Dunkelberg, Graft versus host disease after liver transplantation in adults: A case series, review of literature, and an approach to management. *Transplantation* **100**, 2661–2670 (2016).
  54. J. Zuber, S. Rosen, B. Shonts, B. Sprangers, T. M. Savage, S. Richman, S. Yang, S. P. Lau, S. DeWolf, D. Farber, G. Vlad, E. Zorn, W. Wong, J. Emond, B. Levin, M. Martinez, T. Kato, M. Sykes, Macrochimerism in intestinal transplantation: Association with lower rejection rates and multivisceral transplants, without GVHD. *Am. J. Transplant.* **15**, 2691–2703 (2015).
  55. T. Granot, T. Senda, D. J. Carpenter, N. Matsuoka, J. Weiner, C. L. Gordon, M. Miron, B. V. Kumar, A. Griesemer, S.-H. Ho, H. Lerner, J. J. C. Thome, T. Connors, B. Reizis, D. L. Farber, Dendritic cells display subset and tissue-specific maturation dynamics over human life. *Immunity* **46**, 504–515 (2017).
  56. A. Dobin, C. A. Davis, F. Schlesinger, J. Drenkow, C. Zaleski, S. Jha, P. Batut, M. Chaisson, T. R. Gingeras, STAR: Ultrafast universal RNA-seq aligner. *Bioinformatics* **29**, 15–21 (2013).
  57. Y. Liao, G. K. Smyth, W. Shi, featureCounts: An efficient general purpose program for assigning sequence reads to genomic features. *Bioinformatics* **30**, 923–930 (2014).
  58. T. Smith, A. Heger, I. Sudbery, UMI-tools: Modeling sequencing errors in Unique Molecular Identifiers to improve quantification accuracy. *Genome Res.* **27**, 491–499 (2017).
  59. R Core Team, *R: A Language and Environment for Statistical Computing* (R Foundation for Statistical Computing, 2018).
  60. L. van der Matten, G. Hinton, Visualizing data using t-SNE. *Mach. Learn. Res.* **9**, 2579–2605 (2008).
  61. J. Donaldson, tsne: T-distributed stochastic neighbor embedding for R (t-SNE). R package version 0.1-3 (2016); <https://CRAN.R-project.org/package=tsne>.
  62. A. Butler, P. Hoffman, P. Smibert, E. Papalexi, R. Satija, Integrating single-cell transcriptomic data across different conditions, technologies, and species. *Nat. Biotechnol.* **36**, 411–420 (2018).
  63. S. Zhao, Y. Guo, Q. Sheng, Y. Shyr, heatmap3: An improved heatmap package. R package version 1.1.1 (2015); <https://CRAN.R-project.org/package=heatmap3>.
  64. H. Wickham, *ggplot2: Elegant Graphics for Data Analysis* (Springer-Verlag, 2009).
  65. C. O. Wilke, cowplot: Streamlined plot theme and plot annotations for 'ggplot2'. R package version 0.9.3 (2018); <https://CRAN.R-project.org/package=cowplot>.
- Acknowledgments:** We would like to thank all of our study participants, the staff and transplant coordinators of LiveOnNY for their collaboration in acquisition of tissues from organ donors, and the families of the organ donors for their generosity in advancing the study of human immunology. **Funding:** This work was supported by NIH grants A1106697 and

HL116136 awarded to D.L.F., HL114626 awarded to D.J.L., and K24 HL131937 awarded to D.J.L. M.E.S. was supported by NIH T32 HL105323, the American Society of Transplantation TIRN award, and a Parker B. Francis Foundation fellowship. P.A.S. was supported by NIH R33 CA202827. P.D. was supported by a CRI Irvington Postdoctoral Fellowship. Research reported in this publication was performed in the CCTI Flow Cytometry Core, supported, in part, by award S10RR027050. The content is solely the responsibility of the authors and does not necessarily represent the official views of the NIH. **Author contributions:** M.E.S. and D.L.F. conceived and designed the study and wrote and edited the paper. M.O.F., E.B., and P.A.S. helped design scRNA-seq experiments and performed gene library construction, read alignment, and analysis. M.E.S. and T.J.C. procured transplant samples and performed flow cytometry and imaging analysis. P.D. processed donor tissues and extraction of airway lymphocytes. T.S. and D.C. performed donor lung procurements. C.M. analyzed pathology specimens and guidance with imaging techniques. L.B., L.S., H.R., J.L.H., F.D., M.B., J.R.S., and S.A. assisted in participant recruitment and tissue procurement. M.S. assisted with study design. D.J.L. assisted with analytic

approach and clinical interpretations. **Competing interests:** The authors declare that they have no competing interests. **Data and materials availability:** The scRNA-seq data have been deposited in the Gene Expression Omnibus database (accession number GSE124675).

Submitted 27 September 2018

Accepted 28 January 2019

Published 8 March 2019

10.1126/sciimmunol.aav5581

**Citation:** M. E. Snyder, M. O. Finlayson, T. J. Connors, P. Dogra, T. Senda, E. Bush, D. Carpenter, C. Marboe, L. Benvenuto, L. Shah, H. Robbins, J. L. Hook, M. Sykes, F. D'Ovidio, M. Bacchetta, J. R. Sonett, D. J. Lederer, S. Arcasoy, P. A. Sims, D. L. Farber, Generation and persistence of human tissue-resident memory T cells in lung transplantation. *Sci. Immunol.* **4**, eaav5581 (2019).

# Transforming the **Future** of **Robotics**



As a multidisciplinary online-only journal, *Science Robotics* publishes original, peer-reviewed, research articles that advance the field of robotics. The journal provides a central forum for communication of new ideas, general principles, and original developments in research and applications of robotics for all environments.

Learn more at: [ScienceRobotics.org](http://ScienceRobotics.org)

**Science  
Robotics**  
AAAS

## IMMUNOLOGY

# Desynchronization of the molecular clock contributes to the heterogeneity of the inflammatory response

Nancy C. Allen<sup>1\*</sup>, Naomi H. Philip<sup>1</sup>, Lucy Hui<sup>1</sup>, Xu Zhou<sup>1</sup>, Ruth A. Franklin<sup>1</sup>,  
Yong Kong<sup>1,2</sup>, Ruslan Medzhitov<sup>3†</sup>

Copyright © 2019  
The Authors, some  
rights reserved;  
exclusive licensee  
American Association  
for the Advancement  
of Science. No claim  
to original U.S.  
Government Works

Heterogeneity in the behavior of genetically and developmentally equivalent cells is becoming increasingly appreciated. There are several sources of cellular heterogeneity, including both intrinsic and extrinsic noise. We found that some aspects of heterogeneity in the response of macrophages to bacterial lipopolysaccharide (LPS) were due to intercellular desynchronization of the molecular clock, a cell-intrinsic oscillator. We found that the ratio of the relative expression of two clock genes, *Nfil3* and *Dbp*, expressed in opposite phases of the clock, determined the fraction of cells that produced the cytokine IL-12p40 in response to LPS. The clock can be entrained by various environmental stimuli, making it a mechanism by which population-level heterogeneity and the inflammatory response can be regulated.

## INTRODUCTION

From prokaryotes to complex multicellular organisms, cells from seemingly homogeneous or even clonal populations have diverse responses to the same stimulus (1, 2). This functional heterogeneity plays critical roles in processes as different as the generation of population fitness in cyanobacteria, developmental patterning in *Drosophila melanogaster*, and even differentiation of the vertebrate hematopoietic system (1–4). Given the multitude and diversity of scenarios in which such heterogeneity has been observed, it is not unexpected that cells of the innate immune system, which includes macrophages and dendritic cells (DCs), also demonstrate highly heterogeneous behavior (5–7). Much of the described heterogeneity among innate immune cells is fixed through differentiation or influenced by environmental signals (8–10), leading to phenotypically distinct cellular populations. Here, we sought to identify heterogeneity in the innate immune response among a phenotypically homogeneous population.

Heterogeneity among developmentally and phenotypically equivalent cells is often attributable to noise. Noise can be characterized as either “intrinsic” or “extrinsic” (11). Intrinsic noise refers to the noise inherent in gene transcription and can be demonstrated as differential expression from two identical alleles within a genome. Extrinsic noise encompasses all other cell-intrinsic variables that lead to intercellular variability in behavior. Some examples of extrinsic noise include heterogeneity in ribosome number or the abundance of a pathway-specific transcription factor (11, 12). One specific type of extrinsic noise is heterogeneity due to the desynchronization of cell-intrinsic oscillators (12, 13). This type of noise is unique, because cell-to-cell variability can be modulated by the degree of oscillator synchronization between cells.

One well-recognized cell-intrinsic oscillator is the circadian clock, which is present in organisms from cyanobacteria to humans and regulates various aspects of physiology and behavior, from sleep-wake

cycles to nutrient and xenobiotic metabolism (14–16). In mammals, the clock is controlled by transcriptional-translational feedback loops. The core components of the circadian clock include the transcriptional activators brain and muscle ARNT-like (BMAL) and circadian locomotor output cycles protein kaput (CLOCK), which form a heterodimeric complex and drive the expression of genes encoding the transcriptional repressors period circadian protein homolog (PER) and cryptochrome (CRY). PER and CRY, in return, negatively regulate CLOCK-BMAL complexes by associating with them and preventing the histone acetylation that is required for gene transcription (15). In addition to the core loop, there are additional loops that interact with the core loop. One of these secondary loops involves transcriptional activators of the proline and acidic amino acid-rich basic leucine zipper (PAR-bZIP) family, including albumin D box-binding protein (DBP), thyrotroph embryonic factor (TEF), and hepatic leukemia factor (HLF), all of which function in opposition to the transcriptional repressor NFIL3 (nuclear factor, interleukin-3-regulated) (16, 17).

We found that cells of a phenotypically homogeneous population of mouse bone marrow (BM)-derived macrophages (BMDMs) exhibited a heterogeneous cytokine response to bacterial lipopolysaccharide (LPS). The response to LPS was not a fixed property of the cells. Instead, the response of an individual cell depended on the phase of the circadian oscillation. The phase of the circadian clock can be modulated by various environmental stimuli (18, 19); therefore, it is likely that both the phase of the clock and the degree to which populations are synchronized with respect to the phase of the clock are important mechanisms by which responses are controlled at the population level.

## RESULTS

### The macrophage response to LPS is heterogeneous and unstable

To initially characterize heterogeneity in the response of mouse BMDMs to LPS stimulation in vitro, we analyzed cytokine production by flow cytometry. Both of the cytokines tumor necrosis factor (TNF) and interleukin-12 p40 (IL-12p40) were produced in a bimodal manner, meaning that within the cell population, there were distinct groups of cells with respect to the amount of cytokine produced

<sup>1</sup>Department of Immunobiology, Yale University School of Medicine, New Haven, CT 06510, USA. <sup>2</sup>Department of Molecular Biophysics and Biochemistry, Yale University School of Medicine, New Haven, CT 06510, USA. <sup>3</sup>Howard Hughes Medical Institute, Department of Immunobiology, Yale University School of Medicine, New Haven, CT 06510, USA.

\*Present address: Division of Pulmonary, Critical Care, Allergy and Sleep Medicine, Department of Medicine, University of California, San Francisco, San Francisco, CA 94143, USA.

†Corresponding author. Email: ruslan.medzhitov@yale.edu

(Fig. 1, A and B). This was in contrast to inducible nitric oxide synthase (iNOS), which was produced in an analog fashion, referring to a continuous spectrum of iNOS production among the population (Fig. 1C). Whereas all BMDMs produced TNF when exposed to a large enough concentration of LPS, there always remained a fraction of BMDMs that did not produce IL-12p40 regardless of the concentration of LPS or the length of stimulation (Fig. 1B). To determine whether heterogeneity in the IL-12p40 response was due to macrophage preprogramming during differentiation, we tested the stability of IL-12p40 production. To do this, we stimulated BMDMs from mice carrying a fluorescent IL-12p40 reporter (*yet40*) (20) with LPS and sorted them by flow cytometry based on the abundance of yellow

fluorescent protein (YFP). These sorted populations were then rested in culture for 4 days to enable the reversal of LPS tolerance and subsequently restimulated with LPS. LPS tolerance describes a macrophage state that develops after initial macrophage activation in the presence of persistent LPS. It is characterized by a dampened inflammatory response to LPS, preventing excessive inflammation, whereas other less destructive antimicrobial processes are continuously expressed (21). Upon restimulation, bimodal IL-12p40 production was reproduced in both the previously IL-12p40-negative and IL-12p40-positive populations, suggesting that heterogeneity in IL-12p40 production is largely controlled by nonstable cellular variables rather than differences in cell differentiation or identity (Fig. 1D).

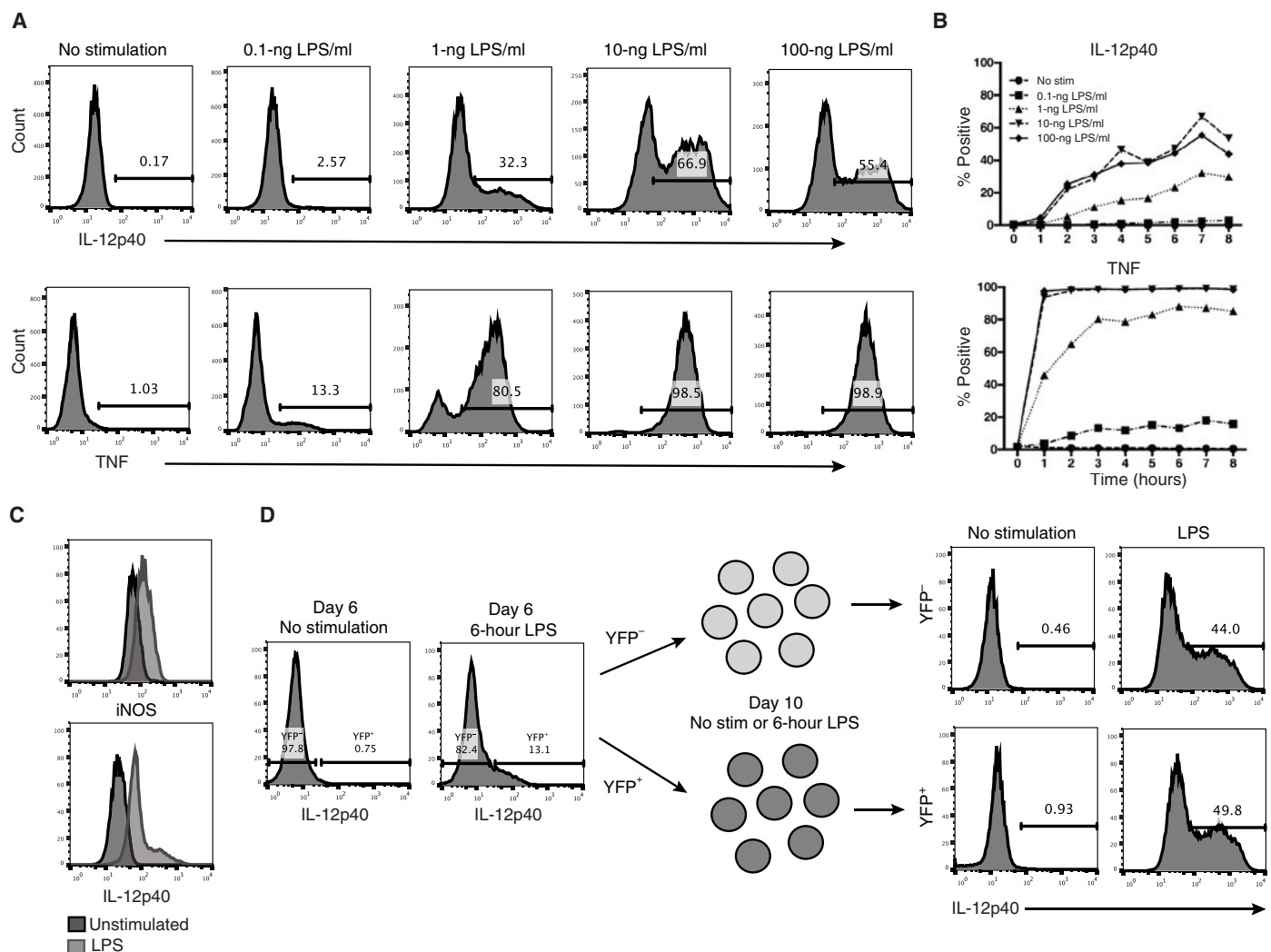


**Fig. 1. Heterogeneity in BMDM cytokine production is bimodal and unstable.** (A) BMDMs were stimulated with the indicated concentrations of LPS for 7 hours (top) or 3 hours (bottom) in the presence of brefeldin A (BFA) and then analyzed by intracellular flow cytometry for IL-12p40 (top) or TNF (bottom). Numbers within flow cytometry plots indicate the percentages of cytokine-positive cells. Count (y axis) refers to the number of cells with a given amount of cytokine measured by fluorescence (x axis). (B) Concentration-time response curves for BMDMs stimulated with LPS for the indicated times and then analyzed by intracellular flow cytometry for IL-12p40 or TNF. Graphs indicate the percentage of the total population of cells that were positive for the indicated cytokine at each time point. Data in (A) and (B) are representative of two independent experiments. (C) BMDMs were stimulated with 10-ng LPS/ml for 10 hours. BFA was added after 4 hours of stimulation. Cells were then analyzed by flow cytometry for iNOS and IL-12p40. Data are representative of three independent experiments. (D) Day 6 BMDMs from IL-12p40 (*yet40*) YFP reporter mice were stimulated with 10-ng LPS/ml for 6 hours and subsequently sorted by flow cytometry into YFP<sup>+</sup> and YFP<sup>-</sup> populations. Cells were returned to culture for 4 days and on day 10 were left unstimulated or were restimulated with 10-ng LPS/ml for 6 hours in the presence of BFA before being subjected to intracellular staining for IL-12p40. Data are representative of two independent experiments.

### Molecular clock components control the macrophage response to LPS

Desynchronization of cell-intrinsic oscillators is one mechanism by which unstable heterogeneity can be generated within a population of cells (Fig. 2A) (13). This was an appealing model for control of the inflammatory response, because modulation of heterogeneity through cell-intrinsic oscillators would enable increased control relative to other noise-mediated mechanisms. The molecular clock is a cell-intrinsic oscillator present nearly ubiquitously in mammalian cells, and it is composed of a transcription-translation feedback loop with an about 24-hour period (Fig. 2B) (16). The clock protein NFIL3 inhibits *Il12b* transcription (22), and we therefore suspected that desynchronization of the clock could contribute to the observed heterogeneity in IL-12p40 production.

Consistent with NFIL3 being a negative regulator of *Il12b* expression, we observed that with the loss of *Nfil3* through genetic deletion in *Nfil3*<sup>+/-</sup> and *Nfil3*<sup>-/-</sup> mice, the fraction of BMDMs producing IL-12p40 in response to LPS increased (Fig. 2C). This finding was also observed in BM-derived DCs (BMDCs), demonstrating a more generalizable contribution of NFIL3 to *Il12b* gene regulation (fig. S1). NFIL3 inhibition of *Il12b* transcription is thought to be mediated through binding to a D-box within the *Il12b* enhancer (22, 23). PAR-bZIP proteins share the ability to bind D-boxes and function as transcriptional activators. DBP is a member of the PAR-bZIP family and is produced in the opposite phase of the clock as NFIL3 (24). To test whether DBP functions in the opposite manner as NFIL3, we overexpressed either *Nfil3* or *Dbp* in BMDMs using retroviral transduction of overexpression vectors (fig. S2, A to C). Whereas *Nfil3* overexpression decreased the fraction of BMDMs that were IL-12p40<sup>+</sup>, *Dbp* overexpression increased this fraction. Additionally, within transduced BMDMs, the degree to which *Dbp* or *Nfil3* was overexpressed correlated with the extent to which the IL-12p40<sup>+</sup> fraction was increased or decreased, respectively (Fig. 2, D and E). Because NFIL3 and DBP are both capable of binding to D-boxes, we predicted that NFIL3 and DBP competitively bind at the *Il12b* enhancer. Consistent with this hypothesis, chromatin immunoprecipitation (ChIP) of Flag in BMDMs transduced with a retrovirus overexpressing Flag-tagged *Dbp* revealed enrichment of DBP at the *Il12b* enhancer at the time of peak *Il12b* transcription, whereas enrichment of NFIL3 was observed later at times of *Il12b* repression (Fig. 2, F to H, and fig. S3, A and B). This late enrichment of NFIL3 at the *Il12b* enhancer also correlated with LPS-induced *Nfil3* expression and *Dbp* repression (fig. S3, C and D).

Given the opposing roles of DBP and NFIL3 in the regulation of *Il12b*, we suspected that there might be other genes that can be similarly regulated by these two factors. To investigate this, we performed RNA sequencing (RNA-seq) on BMDMs from wild-type and *Nfil3*<sup>-/-</sup> mice that were either unstimulated or stimulated with LPS for 4 or 24 hours. We noted that even before LPS stimulation *Nfil3*<sup>-/-</sup> BMDMs had statistically significantly higher expression of the gene encoding the chemokine receptor CCR2, which is found predominately on inflammatory monocytes (25). After LPS stimulation, *Nfil3*<sup>-/-</sup> BMDMs had enrichment for a subset of genes involved in the proinflammatory antibacterial response and decreased expression of a subset of genes involved in inhibition of the LPS inflammatory response (26–28) (Fig. 3A). Consistent with our hypothesis that DBP and NFIL3 can play opposing roles in the LPS inflammatory response, gene expression analysis of *Dbp*-overexpressing BMDMs revealed that for several genes, *Dbp* overexpression phenocopied the loss of *Nfil3* (Fig. 3, B and C).

Our data suggest that CCR2 might serve as an indicator of the clock phase given that expression of *Ccr2* is affected by the abundances of DBP and NFIL3. If that was the case, macrophages with greater CCR2 abundance should have a higher LPS-induced IL-12<sup>+</sup> fraction than those with low CCR2 abundance. To test this hypothesis, macrophages were sorted on CCR2 abundance and immediately stimulated with LPS. As expected, CCR2-high macrophages had larger fraction of IL-12<sup>+</sup> cells than did CCR2-low macrophages (Fig. 3, D and E). Of note, in all the CCR2 sorting experiments, the total fraction of IL-12<sup>+</sup> BMDMs was low, which we suspect is due to the immediate stimulation of the cells after sorting without allowing time for the cells to rest.

### The molecular clock controls heterogeneity in the macrophage response to LPS in vivo

We sought to determine whether the phase of the clock controls fractional heterogeneity in vivo. Consistent with a previous report (29), we confirmed that peritoneal macrophages exhibited circadian oscillation of clock gene expression (Fig. 4A and fig. S4, A to C). Given that the *Nfil3/Dbp* ratio was highest in macrophages harvested at zeitgeber time (ZT) 0, the time at which the lights came on in the animal facility, and lowest in macrophages harvested at ZT 12, the time at which the lights switched off, we predicted that the fraction of macrophages producing IL-12p40 in response to LPS would be smaller at ZT 0 relative to that at ZT 12. As predicted, peritoneal macrophages isolated and stimulated in vitro at ZT 0 or ZT 1 had a significantly smaller IL-12p40<sup>+</sup> fraction than those isolated at ZT 12 (Fig. 4, B and C). We then examined the response to LPS in peritoneal macrophages from *Bmal1*<sup>fl/fl</sup>*LysM-cre* mice, in which the core clock gene *Bmal1* is deleted specifically in macrophages. Expression analysis of peritoneal macrophages from ZT 1 and ZT 12 in these mice revealed that they had lost their circadian regulation of *Nfil3* and *Dbp*. Additionally, loss of *Bmal1* led to persistently high *Nfil3* and low *Dbp* expression, mimicking ZT 0, throughout the ZT 0 to ZT 12 light phase of the circadian cycle (Fig. 4, D and E). When peritoneal macrophages from *Bmal1*<sup>fl/fl</sup>-*LysM-cre*<sup>+</sup> mice were stimulated with LPS, they demonstrated a loss of circadian variation in IL-12<sup>+</sup> fraction. As predicted by the high *Nfil3/Dbp* ratio in these cells, they behaved as if they were at ZT 0 regardless of the time of stimulation (Fig. 4C).

### DISCUSSION

We showed that the heterogeneity in IL-12p40 production by macrophages in response to LPS was not stable and that this instability was, at least in part, attributable to the phase of the molecular clock. We focused on the heterogeneity in IL-12 production because it is a key cytokine in the T helper 1 inflammatory response. Although NFIL3 was previously identified as a negative regulator of *Il12b* expression (22), our studies demonstrate the importance of NFIL3 as a clock protein in the regulation of IL-12 production. Additionally, we showed that in combination with NFIL3, the clock protein DBP modulated the inflammatory response. The molecular clock as a functional regulator of heterogeneity in the inflammatory response is logical for several reasons. First, other noise-mediated mechanisms of heterogeneity are inherently difficult to control. Oscillator-driven mechanisms have the benefit of being able to regulate a response through both the phase of oscillation and the degree to which populations are synchronized. Because the molecular clock can be entrained to various environmental

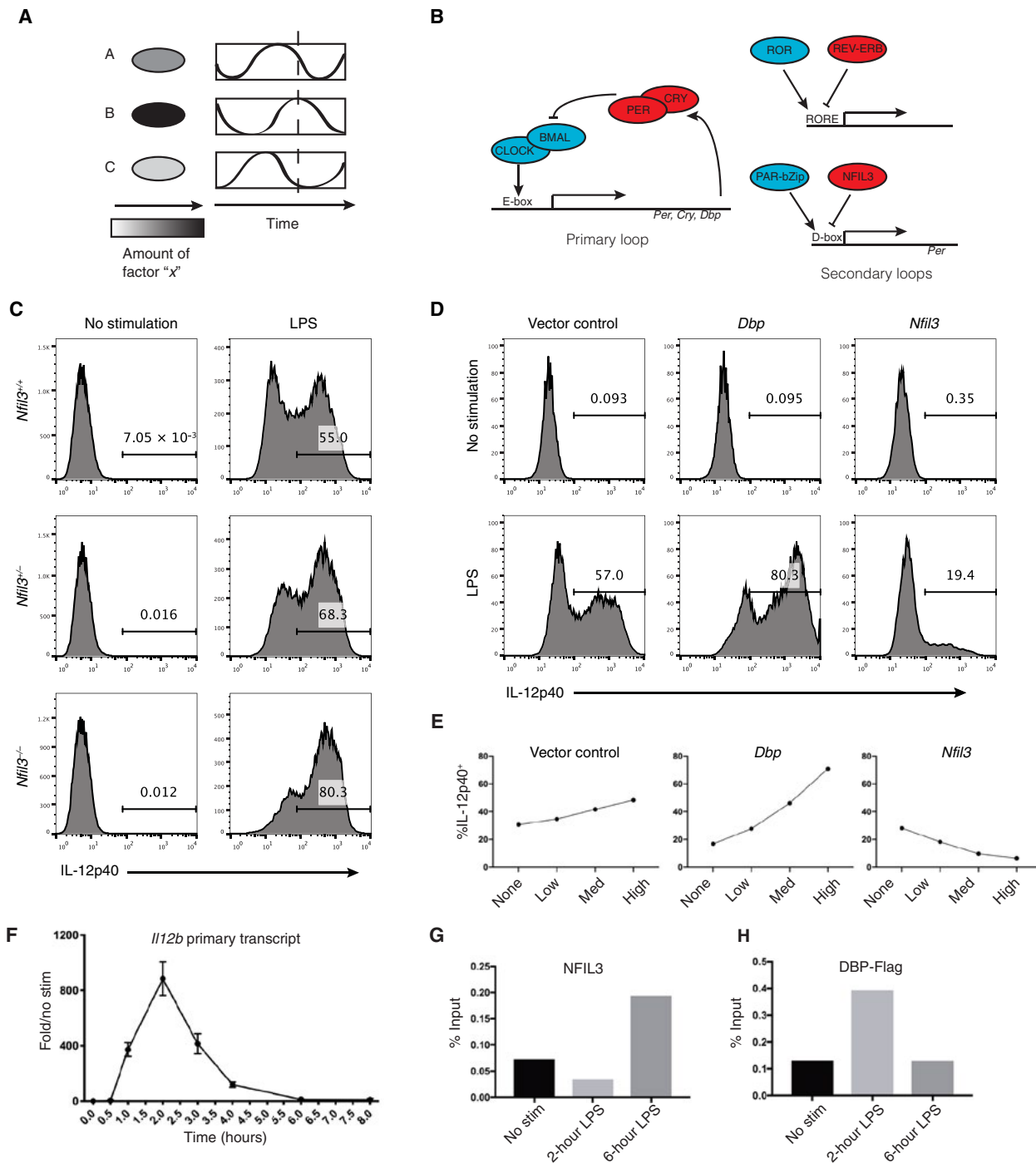


**Fig. 2. Clock genes *Nfil3* and *Dbp* oppositely control the fraction of LPS-induced BMDMs that are IL-12p40<sup>+</sup>.** (A) Intercellular heterogeneity can be generated through desynchronization of cell-intrinsic oscillators. (B) Schematic representation of the primary and secondary loops of the molecular clock. (C) Flow cytometry plots of IL-12p40 in BMDMs of the indicated genotype unstimulated or stimulated with 10-ng LPS/ml for 6 hours. Data are representative of two independent experiments. The numbers within the flow cytometry plots indicate fraction of cells positive for IL-12p40. (D) BMDMs retrovirally transduced with *Nfil3*, *Dbp*, or empty expression vectors containing an IRES-hCD2 to allow for identification of successfully transduced cells. BMDMs were either unstimulated or stimulated with 10-ng LPS/ml for 6 hours. Flow cytometry plots for IL-12p40 in transduced BMDMs are shown. Data are representative of three independent experiments. (E) Relationship between the amount of gene overexpression and the fraction of LPS-induced cells that were IL-12p40<sup>+</sup>. Data are representative of two independent experiments. (F) Reverse transcription–quantitative polymerase chain reaction (RT-qPCR) for *Il12b* primary transcripts in BMDMs stimulated with 10-ng LPS/ml for the indicated times. Error bars represent mean with SD. Graph is representative of two independent experiments. (G) ChIP for NFIL3 at the *Il12b* enhancer at time 0 (no stim), 2 hours, and 6 hours after BMDM stimulation with 10-ng LPS/ml. (H) ChIP for FLAG at the *Il12b* enhancer at the indicated times in *Dbp*-Flag retrovirally transduced BMDMs after stimulation with 10-ng LPS/ml. For (G) and (H), the percent input represents enrichment of *Il12b* enhancer DNA relative to DNA immunoprecipitated from an unrelated region of the genome (negative control). Data are representative of three independent experiments (fig. S3, A and B).

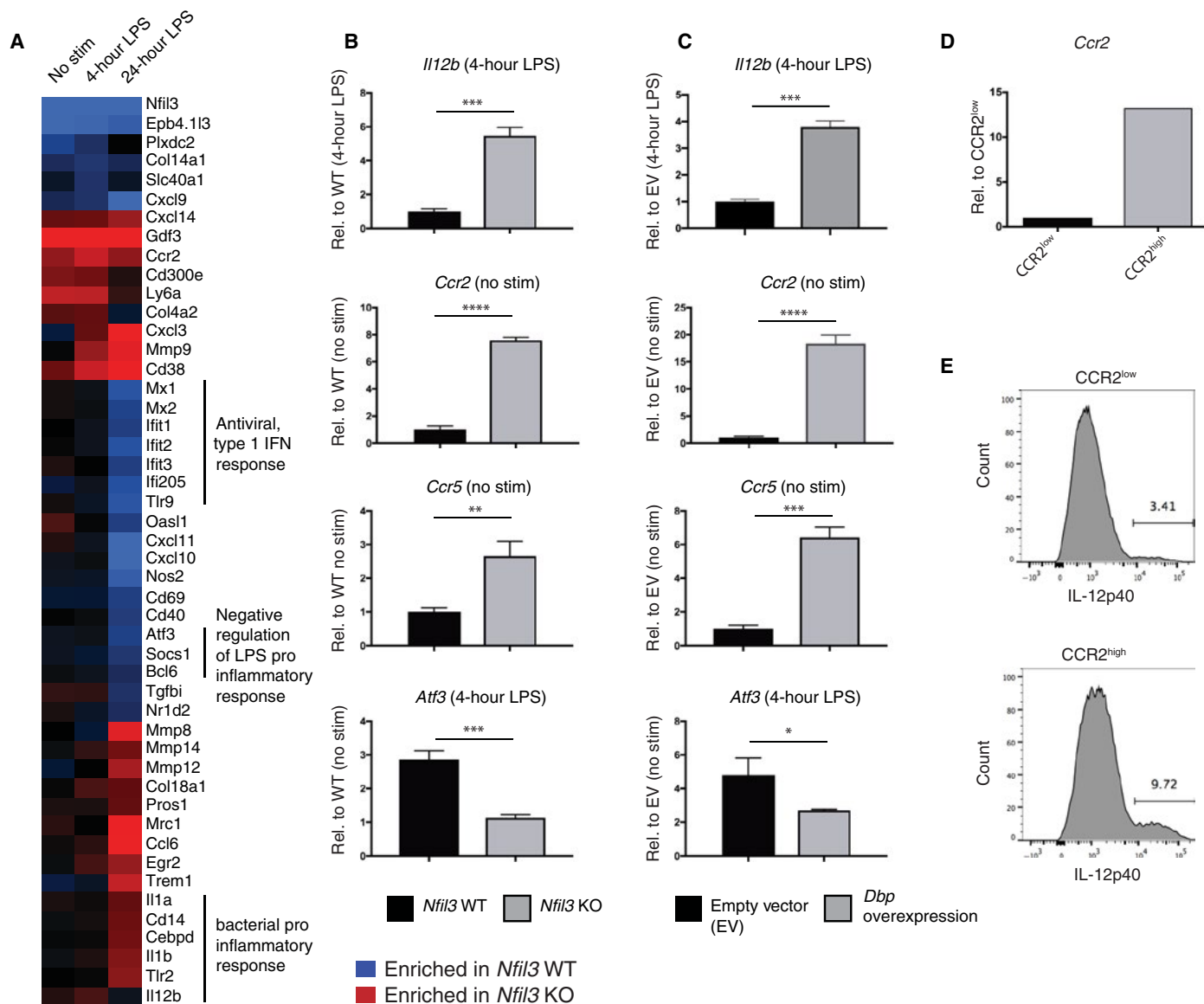


**Fig. 3. *Nfil3* and *Dbp* regulate BMDM inflammatory response to LPS.** (A) RNA-seq of wild-type (WT) and *Nfil3* knockout (KO) BMDMs stimulated with 10-ng LPS/ml for 0 (no stim), 4, or 24 hours. Two independent samples for each condition were sequenced. Genes differentially expressed greater than twofold ( $P_{adj} < 0.01$ ) in WT or *Nfil3* KO BMDMs during at least one of the assayed times are shown. Differential expression is plotted in  $\log_2$ . Blue indicates enriched in WT BMDMs; red indicates enriched in *Nfil3* KO BMDMs. *Il12b* is shown but was only 1.8 $\times$  enriched in *Nfil3* KO at 4-hour LPS. IFN, interferon. (B) RT-qPCR for selected transcripts in WT and *Nfil3* KO BMDMs under the indicated conditions (expressed as relative to WT for the indicated conditions). Error bars represent mean with SD from three technical replicates. Data are representative of three independent experiments. (C) RT-qPCR for selected transcripts in BMDMs either transduced with a *Dbp*-overexpressing or empty vector (EV) under the indicated conditions. Expressed as relative to empty vector for the indicated conditions. Error bars represent mean with SD from three technical replicates. Data are representative of two independent experiments. (D) *Ccr2* expression in BMDMs sorted by CCR2 abundance (normalized to *Ccr2* expression in CCR2-low cells). Data are representative of three independent experiments. (E) IL-12p40 production in BMDMs sorted by CCR2 abundance and immediately stimulated with LPS (10 ng/ml) with BFA for 6 hours. Data are representative of three independent experiments. \* $P < 0.05$ , \*\* $P < 0.01$ , \*\*\* $P < 0.001$ , \*\*\*\* $P < 0.0001$  by Student's *t* test.

stimuli (18, 19, 30), the population-level response can be tuned to environmental demands. This is an intuitively effective way to control the inflammatory response because it enables an adequate strength of response for pathogen clearance while minimizing immunopathology.

A remaining question is the degree to which the molecular clock is synchronized in vivo. It is generally considered that our cellular (peripheral) clocks in vivo are synchronized by daily entrainment signals from the central (master) clock in the hypothalamus. This

viewpoint is, at least in part, supported by our data demonstrating the time-of-day difference in macrophage IL-12 production in addition to the circadian oscillation of clock gene expression at the population level. If macrophages are synchronized in vivo, there needs to be an explanation as to why we did not see 100% of peritoneal macrophages responding at ZT 12. One explanation for this would be that because of other noncircadian factors, individual cells have different activation barriers that need to be overcome to sustain

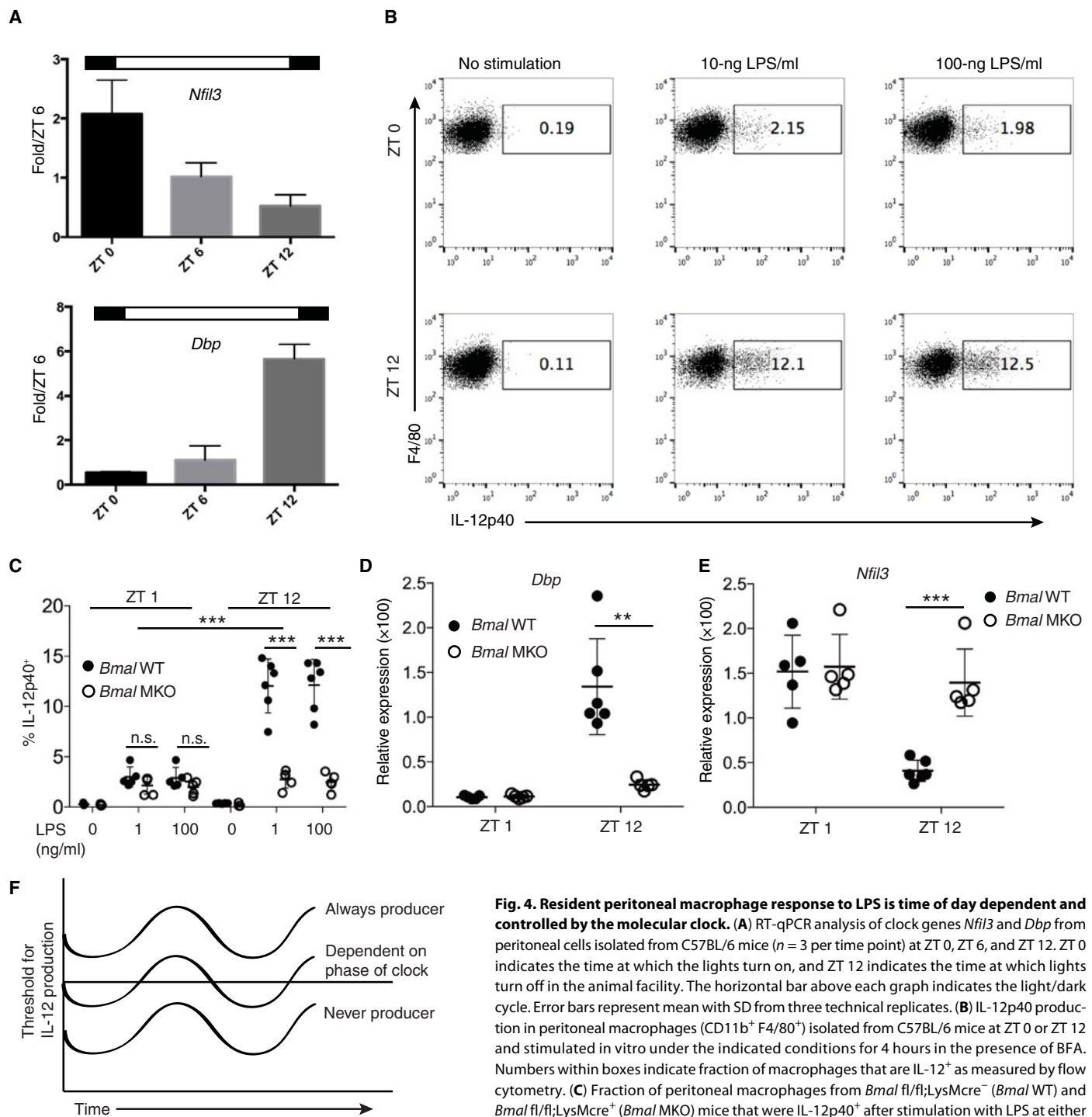


**Fig. 4. Resident peritoneal macrophage response to LPS is time of day dependent and controlled by the molecular clock.** (A) RT-qPCR analysis of clock genes *Nfil3* and *Dbp* from peritoneal cells isolated from C57BL/6 mice ( $n = 3$  per time point) at ZT 0, ZT 6, and ZT 12. ZT 0 indicates the time at which the lights turn on, and ZT 12 indicates the time at which lights turn off in the animal facility. The horizontal bar above each graph indicates the light/dark cycle. Error bars represent mean with SD from three technical replicates. (B) IL-12p40 production in peritoneal macrophages ( $CD11b^+ F4/80^+$ ) isolated from C57BL/6 mice at ZT 0 or ZT 12 and stimulated *in vitro* under the indicated conditions for 4 hours in the presence of BFA. Numbers within boxes indicate fraction of macrophages that are IL-12<sup>+</sup> as measured by flow cytometry. (C) Fraction of peritoneal macrophages from *Bmal fl/fl*;LysMcre<sup>-</sup> (*Bmal* WT) and *Bmal fl/fl*;LysMcre<sup>+</sup> (*Bmal* MKO) mice that were IL-12p40<sup>+</sup> after stimulation with LPS at either ZT 1 or ZT 12. Cells were stimulated as described in (B). Each circle represents one mouse.

Error bars represent mean with SD. (D) *Dbp* and (E) *Nfil3* expression in *Bmal fl/fl*;LysMcre<sup>-</sup> (*Bmal* WT) and *Bmal fl/fl*;LysMcre<sup>+</sup> (*Bmal* MKO) mice at either ZT 1 or ZT 12. Error bars represent mean with SD. (F) Proposed mechanism of why clock phase may control IL-12 production only in a fraction of cells. Each oscillation represents the molecular clock in an individual cell with respect to a “threshold” for IL-12 production. All data are representative of at least three independent experiments. \*\*\* $P < 0.001$ , \*\* $P < 0.01$ . n.s., not significant by Student’s *t* test.

*Il12b* transcription and that only cells fluctuating near the activation threshold will show circadian variation in response (Fig. 4F). However, it is also possible that not all macrophages are synchronized *in vivo*, as was shown to be the case among epidermal stem cells within

individual hair follicles. This desynchronization is biologically important and ensures that not all stem cells have the same responsiveness to activating signals (31). With currently available tools, we were unfortunately unable to answer this question in our system.

An additional finding from this study is that the LPS-induced cytokines IL-12 and TNF exhibited bimodal production, as compared to iNOS, which was produced in an analog manner. This raises the interesting question of why some genes are expressed digitally, whereas others are analog. One difference between cytokines and iNOS is that cytokines are secreted, whereas iNOS functions intracellularly to produce reactive nitrogen species that can both directly and indirectly promote intracellular bacterial killing (32). These data raise the possibility that the cell-intrinsic function versus cell-extrinsic function of gene products determines whether genes are regulated in a digital or analog fashion. This hypothesis is supported by another study demonstrating bimodal production of the cytokine IL-6 in macrophages (5). Logically, all cells need to express genes that are required for their intrinsic functions, whereas production of secreted factors can be delegated to a fraction of the population. Additionally, the partitioning of responses may enable the segregation of incompatible processes. Given that several of the LPS-induced cytokines are produced digitally, heterogeneity in the population-level response is particularly important, because a homogeneous “all-or-none” inflammatory response risks either failure to respond to an infection or a hyperinflammatory response with resultant immunopathology.

In sum, our data demonstrate that the phase of the molecular clock is an important determinant in the macrophage response to LPS. Furthermore, this interaction between the clock and the environment is bidirectional, enabling changing functional demands to control cellular responses through manipulation of the clock phase. Although we examined the role of cell-intrinsic oscillators in the control of the macrophage inflammatory response, we suspect that these findings are generalizable as a mechanism by which many other cell decisions are made.

## MATERIALS AND METHODS

### Animals

All mice were housed in the Yale Animal Resources Center in a specific pathogen-free environment. All management and handling of animals were in accordance with approved guidelines by the Institutional Animal Care and Use Committee at Yale. Mice were kept on a strict 12-hour light/12-hour dark (LD) cycle, and for circadian experiments, mice were kept on the LD cycle for a minimum of 2 weeks before use. C57BL/6J mice were purchased from National Cancer Institute or the Jackson Laboratory for experiments. Yet40 (B6.129-*Il12btm1Lky/J*), *Bmal* flox (B6.129S4-*Arntlmt1Weit/J*), and *LysM-cre* [B6.129P2-*Lyz2tm1(cre)Ifo/J*] mice were purchased from the Jackson Laboratory and maintained within our animal facility. *Nfil3* KO mice were provided by P. B. Rothman at the University of Iowa (USA). *Nfil3* genotyping primers are NFscreen28809anti (common 3') CGATGTCCAGTGTCTTCCTTA, NFWT5' (wild type 5') GGAGATGGATGCCTCAGTTGGGGT, and PTEN Neo (KO 5') ACGAGACTAGTGAGACGTGC. Cycling conditions are as follows: 94°C, 30 s; 58°C, 30 s; 72°C, 45 s.

### BMDM differentiation and stimulation

BMDMs were generated by plating mouse BM cells in non-tissue culture (TC) dishes in macrophage growth medium (MGM) composed of 30% L929 supernatant/70% RPMI 1640 with L-glutamine (Corning). RPMI 1640 was supplemented with 10% heat-inactivated fetal bovine serum (FBS) (Gibco), penicillin/streptomycin, sodium pyruvate, HEPES, and 2-mercaptoethanol. BM was prepared by crushing mouse femurs and tibias to release marrow, followed by ACK (ammonium-chloride-

potassium) lysis and passage through a 70- $\mu$ m cell strainer. BM was plated on day of isolation (day 0) at  $7 \times 10^6$  cells/20 ml of MGM in a 15-cm non-TC dish. On day 4 of differentiation, cells were supplemented with 10 ml of MGM. Unless otherwise stated, on day 6, adherent cells were lifted with cold phosphate-buffered saline (PBS) containing 5 mM EDTA and were replated at  $0.75 \times 10^6$  cells per well of 12-well non-TC dish or  $1.5 \times 10^6$  cells per well of six-well non-TC dish in MGM for stimulation on day 7 of differentiation. All cell culture was done at 37°C with 5% CO<sub>2</sub>. LPS stimulation was performed with Ultrapure LPS, *Escherichia coli* 0111:B4 (Invivogen, catalog no. tlr1-3pelps). Concentrations and length of stimulations are indicated in the figure legends and/or the results section of the main text. If intracellular cytokine staining was to be performed, GolgiPlug (BD Biosciences, catalog no. 555029), a BFA-containing reagent, was added at the time of stimulation.

### BMDC differentiation

To generate BMDCs, murine BM was cultured in DC growth medium, which consisted of Dulbecco's modified Eagle's medium (DMEM) containing 10% FBS, sodium pyruvate, L-glutamine, HEPES, penicillin/streptomycin,  $\beta$ -mercaptoethanol, and granulocyte-macrophage colony-stimulating factor for 6 days (33). BM cells ( $1 \times 10^6$ ) were plated in 1 ml of DC growth medium, and 500  $\mu$ l of medium was replaced every 2 days. BMDCs were gated on live, singlets CD11c<sup>+</sup> MHC II<sup>hi</sup>, CD11b<sup>-</sup>.

### Flow cytometry staining and analysis

BMDMs were collected for flow cytometry from non-TC dishes with cold PBS with 5 mM EDTA. All staining steps and washes were done in staining buffer (PBS with 2% FBS, 2.5 mM EDTA) unless otherwise indicated. Cells were Fc blocked with anti-CD16/CD32 (clone 93, eBioscience) at 1:200 for 15 min on ice before staining with labeled antibodies. Cells were stained with extracellular antibodies for 30 min. Antibodies include anti-CD11b-fluorescein isothiocyanate at 1:250 (clone M1/70, eBioscience, catalog no. 11-0112-82), anti-F4/80-allophycocyanin (APC) at 1:500 (clone BM8, eBioscience, catalog no. 17-4801-82), anti-hCD2 at 1:50 (clone RPA-2.10, eBioscience, catalog no. 12-0029-42), and anti-CCR2-APC at 1:10 (clone no. 475301, R&D Systems, catalog no. FAB5538A). After extracellular staining, cells were washed and fixed with 4% paraformaldehyde in PBS for 15 min on ice. For intracellular staining, cells were subsequently permeabilized with BD Perm/Wash buffer (catalog no. 554723), and intracellular staining was performed in BD Perm/Wash buffer for 45 min. Antibodies included anti-TNF $\alpha$ -phycoerythrin (PE) at 1:100 (clone MP6-XT22-PE, eBioscience, catalog no. 12-7321-81) and anti-IL-12/IL-23 p40 at 1:100 (clone C17.8, eBioscience, catalog no. 12-7123-82 or 50-7123-82). After intracellular staining, cells were washed with BD Perm/Wash buffer followed by staining buffer. Samples were run on a BD FACScalibur or LSR II followed by analysis with FlowJo software.

### Cell sorting

BMDMs were stimulated as described in the figure legends and main text and subsequently lifted with cold PBS containing 5 mM EDTA. Cells were spun at 1350 rpm at 4°C and washed once with sterile staining buffer (PBS with 2% FBS, 2.5 mM EDTA). If needed, extracellular staining was performed as described earlier. Cells were then filtered and sorted on a Beckman Coulter MoFlo or BD FACSAria in the Yale fluorescence-activated cell sorting (FACS) Facility. Peritoneal cells were collected as described under the section “Peritoneal cell isolation and stimulation.” They were then stained with anti-CD11b and

anti-F4/80 as described under the section “Flow cytometry staining and analysis.” Stained cells were washed with sterile staining buffer and filtered (as described above), followed by sorting on a BD FACSAria in the Yale FACS Facility.

### RNA isolation, reverse transcription, and RT-qPCR

BMDM RNA was collected with RNA Bee (Amsbio). Phase separation was performed with chloroform, followed by isopropanol precipitation of RNA and ethanol wash according to the manufacturer's protocol. For peritoneal cells and sorted cells, RNA was isolated using the RNeasy Mini Kit including On-Column DNase Digestion with the RNase-Free DNase Set (Qiagen). Purified RNA was resuspended in nuclease-free water and quantitated using a NanoDrop 8000 Spectrophotometer before reverse transcription (RT). Oligo(dT) (Sigma-Aldrich) or random hexamer (Sigma-Aldrich) primers were used for mRNA or primary transcript analysis, respectively. Primers were annealed to RNA by adding 1  $\mu$ l of oligo(dT) (0.5  $\mu$ g/ $\mu$ l) or random hexamer to 10  $\mu$ l (1  $\mu$ g) of RNA, followed by 70°C for 3 min and 4°C for 5 min in a thermocycler. Subsequent RT was performed using SMART MMLV Reverse Transcriptase (Clontech) in a 20- $\mu$ l total reaction volume according to the manufacturer's protocol. Upon completion of RT, complementary DNA (cDNA) volume was brought to 100  $\mu$ l with nuclease-free water. RT-qPCR was performed with PerfeCTa SYBR Green SuperMix, Low ROX (Quanta Biosciences) in a 10- $\mu$ l reaction volume according to the manufacturer's protocol. Bio-Rad CFX96 was used for thermocycling. Primers for RT-qPCR are listed in table S1.

### Retroviral transduction

Human embryonic kidney (HEK) 293 T (293 T) cells were grown in DMEM with 10% FBS at 37°C, 5% CO<sub>2</sub>. 293 T cells (0.75  $\times$  10<sup>6</sup>/6-cm dish/3-ml medium) were transfected with 4  $\mu$ g of retroviral vector (MIGR2.IRES-hCD2) and 4  $\mu$ g of pCL-Eco packaging vector with Lipofectamine 2000 (Life Technologies) as a transfection reagent. Twenty-four hours after transfection, medium was removed and replaced with MGM. Twenty-four hours later, HEK 293 T viral supernatant was collected and passed through a 0.45- $\mu$ m filter. Fresh MGM (3 ml) was added to 293 T cultures. Lipofectamine 2000 was added to viral supernatant at 1/250 and incubated at room temperature for 10 min. BM from one mouse was isolated as described under “BMDM differentiation and stimulation” and resuspended in 200  $\mu$ l of MGM. Fifty microliters of BM was mixed with 3 ml of viral supernatant and spininfected by centrifuging at 2500 rpm, 90' at 32°C in a six-well non-TC plate. After spininfection, 1.5 ml of fresh MGM was added to each well, and cells were incubated overnight at 37°C. The following day, fresh viral supernatant was filtered and incubated with Lipofectamine 2000 as described above. BM cells were collected, spun down, and resuspended in freshly prepared viral supernatant. Spininfection was repeated. After spininfection, BM was collected and washed once with MGM, and cells were counted. D1 BM cells were plated at  $\sim$ 7  $\times$  10<sup>6</sup> cells per 15-cm petri dish in 20 ml of MGM. From this point, BMDMs were differentiated as described under “BMDM culture.”

### Cloning

Murine *Dbp* was cloned from BMDM cDNA, and murine *Nfil3* was cloned from pcDNA3.1-mNFIL-3, a gift from P. Murray (Addgene plasmid no. 34572). Inserts were subcloned into the multiple cloning site of the modified pMSCV.IRES-hCD2 retroviral overexpression vector, MIGR2 (provided by D. Stetson, University of Washington, Seattle,

WA). Q5 Site-Directed Mutagenesis kit (New England Biolabs, catalog no. E0554) was used to add a FLAG sequence to the 5' end of *Dbp*.

### Chromatin immunoprecipitation

About 40  $\times$  10<sup>6</sup> BMDMs were used per condition. After simulation with LPS, cells were directly fixed with 1% formaldehyde and incubated at room temperature for 10 min. Cross-linking was quenched by adding freshly prepared glycine in PBS to a final concentration of 0.125 M and let sit for 5 min at room temperature. Plates were washed twice with cold PBS and were scraped into a 50-ml conical tube using cell scrapers. Collected cells were spun and resuspended in 0.5 ml of SDS lysis buffer [1% SDS, 10 mM EDTA, and 50 mM tris (pH 8.0)] with 1 $\times$  protease inhibitors (Sigma-Aldrich, catalog no. S8830). Cells were sonicated using a Virtis Virsonic 600 with a microtip and the following settings: total process time, 5 min; pulse on, 0.5 s; pulse off, 0.5 s; output, 1. Chromatin was stored overnight (O/N) at  $-80^{\circ}$ C and thawed the following day on ice. Samples were centrifuged for 15 min, with a maximum speed at 4°C in a tabletop centrifuge, and supernatant was taken for quantification on a NanoDrop 8000. Chromatin (100  $\mu$ g) was used per immunoprecipitation (IP) in a total volume of 300  $\mu$ l in ChIP dilution buffer (16.7 mM tris-HCl, 167 mM NaCl, 1.2 mM EDTA, 0.01% SDS, and 1.1% Triton X-100) with protease inhibitors. After this, the appropriate antibodies were added to each IP, 10  $\mu$ g of anti-NFIL3 (Santa Cruz Biotechnology, catalog no. sc-9550x), 8  $\mu$ g of anti-FLAG (Sigma-Aldrich, catalog no. F7425), and samples were rotated overnight at 4°C. To pull down immune complexes, 50  $\mu$ l of Protein G Agarose/Salmon Sperm DNA (EMD Millipore) was added per IP and rotated 2 hours at 4°C. Fifteen microliters of supernatant from no-antibody control samples was saved as 5% input. Samples were washed in the following sequence: 1 $\times$  with 1 ml of low-salt wash buffer [0.1% SDS, 1% Triton X-100, 2 mM EDTA, 20 mM tris-HCl (pH 8.1), and 150 mM NaCl], 1 $\times$  with 1 ml of high-salt wash buffer [0.1% SDS, 1% Triton X-100, 2 mM EDTA, 20 mM tris-HCl (pH 8.1), and 500 mM NaCl], 1 $\times$  with LiCl wash buffer [0.25 M LiCl, 1% IGEPAL CA-630, 1% deoxycholic acid (sodium salt), 1 mM EDTA, 10 mM tris (pH 8.1)], and 2 $\times$  with 1-ml tris-EDTA (TE) (pH 8.0). All washes were done with ice-cold buffer at 4°C with rotation, except TE washes that were done at room temperature. After washes, samples and inputs were resuspended in 300- $\mu$ l SDS lysis buffer with 1- $\mu$ l Proteinase K (20  $\mu$ g/ $\mu$ l) and incubated for 2 hours at 55°C to digest proteins. Samples were reverse-cross-linked by incubating overnight at 65°C. Immunoprecipitated DNA was purified with the Qiagen PCR purification kit, and samples were eluted in 200  $\mu$ l of water. RT-qPCR was performed as described in the section “RNA isolation, reverse transcription, and RT-qPCR.” ChIP primers were as follows: *Il12b* enhancer, TTCAC-CAGTGACTCCAGCAG (forward) and AGGACCATGGCTGGTACAAC (reverse); *Il12b* promoter, GGGGAGGGAGGAACTTCTTA (forward) and CTTTCTGATGGAAACCCAAAG (reverse); and negative control, AGCTGTGTAGGGACACATATTGAG (forward) and CACACAACTCTTAGTCCAGTTCC (reverse).

### RNA-seq and sample preparation

RNA for next-generation sequencing was isolated using the RNeasy Mini Kit (Qiagen), including QIAshredder (Qiagen) sample homogenization and On-Column DNase Digestion with the RNase-Free DNase Set (Qiagen). RNA purity and quality were analyzed on an Agilent Bioanalyzer 2100 before library preparation. Libraries were prepared by the Yale Center for Genome Analysis and run on a HiSeq

2000 (eight samples per lane) at 1 × 75 base pairs. Raw data were analyzed as follows: The raw sequence reads of RNA-seq experiments from Illumina were trimmed off sequencing adaptors and low-quality regions by btrim (34). The trimmed reads were mapped to mouse genome (mm10) by TopHat2 (35). The gene definitions of mouse genome were based on University of California, Santa Cruz annotation and downloaded from iGenomes ([http://support.illumina.com/sequencing/sequencing\\_software/igenome.html](http://support.illumina.com/sequencing/sequencing_software/igenome.html)). After the counts were collected, the differential expression analysis was carried out by DESeq2 (36) using the default setting to normalize the read counts and calculate the adjusted *P* values.

**Peritoneal cell isolation and stimulation**

Mice were euthanized by CO<sub>2</sub> asphyxiation. Abdominal skin was removed, and peritoneum was flushed with 8 ml of RPMI 1640 with 10% FBS and 1× penicillin/streptomycin (supplemented RPMI 1640) using a 20-gauge needle. Medium was prewarmed to 37°C if cells were to be used for culture; otherwise, medium was at 4°C. For subsequent RNA isolation, cells were spun at 1350 rpm, 5 min at 4°C, and cell pellet was resuspended in 350 µl of Buffer RLT supplemented with 2-mercaptoethanol as directed by RNeasy Mini Protocol (Qiagen). For subsequent cell culture, peritoneal cells were spun at 1350 rpm, 5 min at room temperature, and were resuspended in supplemented RPMI 1640 with GolgiPlug (BD Biosciences, catalog no. 555029). Cells were transferred to a 96-well round-bottom plate for subsequent stimulation. Cells were stimulated with Ultrapure LPS, *E. coli* 0111:B4 (Invivogen, catalog no. tlr-3pelps) as described in the figure legends and main text.

**Statistical analysis**

When comparing two groups with three or more technical replicates per group, a two-tailed unpaired Student’s *t* test was performed to determine statistical significance. Error bars indicate SD. For experiments with only two samples for group, error bars represent mean with range.

**SUPPLEMENTARY MATERIALS**

[www.sciencesignaling.org/cgi/content/full/12/571/eaau1851/DC1](http://www.sciencesignaling.org/cgi/content/full/12/571/eaau1851/DC1)

Fig. S1. IL-12p40 production by BMDCs depends on *Nfil3*.

Fig. S2. The surface abundance of hCD2 correlates with the extent of retroviral gene overexpression.

Fig. S3. NFIL3 and DBP dynamically interact with the *Il12b* enhancer after LPS stimulation.

Fig. S4. Peritoneal macrophages exhibit circadian oscillation of clock gene expression.

Table S1. RT-qPCR primers used in this study.

**REFERENCES AND NOTES**

1. G. Balázs, A. van Oudenaarden, J. J. Collins, Cellular decision making and biological noise: From microbes to mammals. *Cell* **144**, 910–925 (2011).
2. R. J. Johnston Jr., C. Desplan, Stochastic mechanisms of cell fate specification that yield random or robust outcomes. *Annu. Rev. Cell Dev. Biol.* **26**, 689–719 (2010).
3. H. H. Chang, M. Hemberg, M. Barahona, D. E. Ingber, S. Huang, Transcriptome-wide noise controls lineage choice in mammalian progenitor cells. *Nature* **453**, 544–547 (2008).
4. S. L. Spencer, S. Gaudet, J. G. Albeck, J. M. Burke, P. K. Sorger, Non-genetic origins of cell-to-cell variability in TRAIL-induced apoptosis. *Nature* **459**, 428–432 (2009).
5. A. K. Shalek, R. Satija, X. Adiconis, R. S. Gertner, J. T. Gaublotomme, R. Raychowdhury, S. Schwartz, N. Yosef, C. Malboeuf, D. Lu, J. J. Trombetta, D. Gennert, A. Gnirke, A. Goren, N. Hacohen, J. Z. Levin, H. Park, A. Regev, Single-cell transcriptomics reveals bimodality in expression and splicing in immune cells. *Nature* **498**, 236–240 (2013).
6. A. K. Shalek, R. Satija, J. Shuga, J. J. Trombetta, D. Gennert, D. Lu, P. Chen, R. S. Gertner, J. T. Gaublotomme, N. Yosef, S. Schwartz, B. Fowler, S. Weaver, J. Wang, X. Wang, R. Ding, R. Raychowdhury, N. Friedman, N. Hacohen, H. Park, A. P. May, A. Regev, Single-cell RNA-seq reveals dynamic paracrine control of cellular variation. *Nature* **510**, 363–369 (2014).

7. I. Amit, D. R. Winter, S. Jung, The role of the local environment and epigenetics in shaping macrophage identity and their effect on tissue homeostasis. *Nat. Immunol.* **17**, 18–25 (2016).
8. S. Epelman, K. J. Lavine, G. J. Randolph, Origin and functions of tissue macrophages. *Immunity* **41**, 21–35 (2014).
9. Y. Okabe, R. Medzhitov, Tissue-specific signals control reversible program of localization and functional polarization of macrophages. *Cell* **157**, 832–844 (2014).
10. M. Haldar, M. Kohyama, A. Y.-L. So, K. C. Wumes, X. Wu, C. G. Briseno, A. T. Satpathy, N. M. Kretzer, H. Arase, N. S. Rajasekaran, L. Wang, T. Egawa, K. Igarashi, D. Baltimore, T. L. Murphy, K. M. Murphy, Heme-mediated SPI-C induction promotes monocyte differentiation into iron-recycling macrophages. *Cell* **156**, 1223–1234 (2014).
11. M. B. Elowitz, A. J. Levine, E. D. Siggia, P. S. Swain, Stochastic gene expression in a single cell. *Science* **297**, 1183–1186 (2002).
12. J. M. Raser, E. K. O’Shea, Noise in gene expression: Origins, consequences, and control. *Science* **309**, 2010–2013 (2005).
13. S. Huang, Non-genetic heterogeneity of cells in development: More than just noise. *Development* **136**, 3853–3862 (2009).
14. C. Dibner, U. Schibler, U. Albrecht, The mammalian circadian timing system: Organization and coordination of central and peripheral clocks. *Annu. Rev. Physiol.* **72**, 517–549 (2010).
15. M. H. Hastings, A. B. Reddy, E. S. Maywood, A clockwork web: Circadian timing in brain and periphery, in health and disease. *Nat. Rev. Neurosci.* **4**, 649–661 (2003).
16. J. A. Mohawk, C. B. Green, J. S. Takahashi, Central and peripheral circadian clocks in mammals. *Annu. Rev. Neurosci.* **35**, 445–462 (2012).
17. A. M. Curtis, M. M. Bellet, P. Sassone-Corsi, L. A. O’Neill, Circadian clock proteins and immunity. *Immunity* **40**, 178–186 (2014).
18. A. Balsalobre, S. A. Brown, L. Marcacci, F. Tronche, C. Kellendonk, H. M. Reichardt, G. Schütz, U. Schibler, Resetting of circadian time in peripheral tissues by glucocorticoid signaling. *Science* **289**, 2344–2347 (2000).
19. E. D. Buhr, S.-H. Yoo, J. S. Takahashi, Temperature as a universal resetting cue for mammalian circadian oscillators. *Science* **330**, 379–385 (2010).
20. R. L. Reinhardt, S. Hong, S.-J. Kang, Z.-e. Wang, R. M. Locksley, Visualization of IL-12/23p40 in vivo reveals immunostimulatory dendritic cell migrants that promote Th1 differentiation. *J. Immunol.* **177**, 1618–1627 (2006).
21. S. L. Foster, D. C. Hargreaves, R. Medzhitov, Gene-specific control of inflammation by TLR-induced chromatin modifications. *Nature* **447**, 972–978 (2007).
22. T. Kobayashi, K. Matsuoka, S. Z. Sheikh, H. Elloumi, N. Kamada, T. Hisamatsu, J. Hansen, K. R. Doty, S. D. Pope, S. T. Smale, T. Hibi, P. Rothman, M. Kashiwada, S. E. Plevy, NFIL3 is a regulator of IL-12 p40 in macrophages and mucosal immunity. *J. Immunol.* **186**, 4649–4655 (2011).
23. A. M. Smith, J. E. Qualls, K. O’Brien, L. Balouzian, P. F. Johnson, S. Schultz-Cherry, S. T. Smale, P. J. Murray, A distal enhancer in *Il12b* is the target of transcriptional repression by the STAT3 pathway and requires the basic leucine zipper (B-ZIP) protein NFIL3. *J. Biol. Chem.* **286**, 23582–23590 (2011).
24. S. Mitsui, S. Yamaguchi, T. Matsuo, Y. Ishida, H. Okamura, Antagonistic role of E4BP4 and PAR proteins in the circadian oscillatory mechanism. *Genes Dev.* **15**, 995–1006 (2001).
25. C. Auffray, D. Fogg, M. Garfa, G. Elaine, O. Join-Lambert, S. Kayal, S. Sarnacki, A. Cumano, G. Lauvau, F. Geissmann, Monitoring of blood vessels and tissues by a population of monocytes with patrolling behavior. *Science* **317**, 666–670 (2007).
26. M. Gilchrist, V. Thorsson, B. Li, A. G. Rust, M. Korb, J. C. Roach, K. Kennedy, T. Hai, H. Bolouri, A. Aderem, Systems biology approaches identify ATF3 as a negative regulator of toll-like receptor 4. *Nature* **441**, 173–178 (2006).
27. V. Litvak, S. A. Ramsey, A. G. Rust, D. E. Zak, K. A. Kennedy, A. E. Lampano, M. Nykter, I. Shmulevich, A. Aderem, Function of C/EBP $\delta$  in a regulatory circuit that discriminates between transient and persistent TLR4-induced signals. *Nat. Immunol.* **10**, 437–443 (2009).
28. G. D. Barish, R. T. Yu, M. Karunasiri, C. B. Ocampo, J. Dixon, C. Benner, A. L. Dent, R. K. Tangirala, R. M. Evans, Bcl-6 and NF- $\kappa$ B cistromes mediate opposing regulation of the innate immune response. *Genes Dev.* **24**, 2760–2765 (2010).
29. M. Keller, J. Mazuch, U. Abraham, G. D. Eom, E. D. Herzog, H.-D. Volk, A. Kramer, B. Maier, A circadian clock in macrophages controls inflammatory immune responses. *Proc. Natl. Acad. Sci. U.S.A.* **106**, 21407–21412 (2009).
30. F. Damiola, N. Le Minh, N. Preitner, B. Kornmann, F. Fleury-Olela, U. Schibler, Restricted feeding uncouples circadian oscillators in peripheral tissues from the central pacemaker in the suprachiasmatic nucleus. *Genes Dev.* **14**, 2950–2961 (2000).
31. P. Janich, G. Pascual, A. Merlos-Suárez, E. Batlle, J. Ripperger, U. Albrecht, H.-Y. M. Cheng, K. Obrietan, L. Di Croce, S. A. Benitah, The circadian molecular clock creates epidermal stem cell heterogeneity. *Nature* **480**, 209–214 (2011).
32. C. Bogdan, Nitric oxide synthase in innate and adaptive immunity: An update. *Trends Immunol.* **36**, 161–178 (2015).
33. K. Inaba, M. Inaba, N. Romani, H. Aya, M. Deguchi, S. Ikehara, S. Muramatsu, R. M. Steinman, Generation of large numbers of dendritic cells from mouse bone marrow

- cultures supplemented with granulocyte/macrophage colony-stimulating factor. *J. Exp. Med.* **176**, 1693–1702 (1992).
34. Y. Kong, Btrim: A fast, lightweight adapter and quality trimming program for next-generation sequencing technologies. *Genomics* **98**, 152–153 (2011).
35. D. Kim, G. Pertea, C. Trapnell, H. Pimentel, R. Kelley, S. L. Salzberg, TopHat2: Accurate alignment of transcriptomes in the presence of insertions, deletions and gene fusions. *Genome Biol.* **14**, R36 (2013).
36. M. I. Love, W. Huber, S. Anders, Moderated estimation of fold change and dispersion for RNA-seq data with DESeq2. *Genome Biol.* **15**, 550 (2014).

**Acknowledgments:** We thank P. B. Rothman for the *Nfil3*<sup>-/-</sup> mice, P. Murray for the Nfil3 cDNA containing plasmid, and D. Stetson for the MIGR2 retroviral overexpression vector. We would also like to thank Y. Okabe for intellectual contributions to the work. **Funding:** This work was supported by the Howard Hughes Medical Institute, Else Kröner Fresenius Foundation, the Blavatnik Family Foundation, and the Trudeau Fellowship from Yale University. **Author**

**contributions:** R.M. and N.C.A. conceived and designed the project. N.C.A., N.H.P., L.H., X.Z., and R.A.F. designed and performed the experiments. N.C.A., N.H.P., and Y.K. performed the computational and statistical analysis. N.C.A. wrote the manuscript, and all authors were involved in the interpretation, discussion, and preparation of the final manuscript. **Competing interests:** The authors declare that they have no competing interests. **Data and materials availability:** All data needed to evaluate the conclusions in the paper are present in the paper or the Supplementary Materials.

Submitted 15 May 2018  
Accepted 11 February 2019  
Published 5 March 2019  
10.1126/scisignal.aau1851

**Citation:** N. C. Allen, N. H. Philip, L. Hui, X. Zhou, R. A. Franklin, Y. Kong, R. Medzhitov, Desynchronization of the molecular clock contributes to the heterogeneity of the inflammatory response. *Sci. Signal.* **12**, eaau1851 (2019).

## CAR T CELLS

# Phosphoproteomic analysis of chimeric antigen receptor signaling reveals kinetic and quantitative differences that affect cell function

Alexander I. Salter<sup>1,2</sup>, Richard G. Ivey<sup>2</sup>, Jacob J. Kennedy<sup>2</sup>, Valentin Voillet<sup>3</sup>, Anusha Rajan<sup>1,2</sup>, Eva J. Alderman<sup>1,2\*</sup>, Uliana J. Voytovich<sup>2</sup>, Chenwei Lin<sup>2</sup>, Daniel Sommermeyer<sup>1,2†</sup>, Lingfeng Liu<sup>1,2‡</sup>, Jeffrey R. Whiteaker<sup>2</sup>, Raphael Gottardo<sup>3</sup>, Amanda G. Paulovich<sup>2</sup>, Stanley R. Riddell<sup>1,2,4§</sup>

Chimeric antigen receptors (CARs) link an antigen recognition domain to intracellular signaling domains to redirect T cell specificity and function. T cells expressing CARs with CD28/CD3 $\zeta$  or 4-1BB/CD3 $\zeta$  signaling domains are effective at treating refractory B cell malignancies but exhibit differences in effector function, clinical efficacy, and toxicity that are assumed to result from the activation of divergent signaling cascades. We analyzed stimulation-induced phosphorylation events in primary human CD8<sup>+</sup> CD28/CD3 $\zeta$  and 4-1BB/CD3 $\zeta$  CAR T cells by mass spectrometry and found that both CAR constructs activated similar signaling intermediates. Stimulation of CD28/CD3 $\zeta$  CARs activated faster and larger-magnitude changes in protein phosphorylation, which correlated with an effector T cell–like phenotype and function. In contrast, 4-1BB/CD3 $\zeta$  CAR T cells preferentially expressed T cell memory–associated genes and exhibited sustained antitumor activity against established tumors *in vivo*. Mutagenesis of the CAR CD28 signaling domain demonstrated that the increased CD28/CD3 $\zeta$  CAR signal intensity was partly related to constitutive association of Lck with this domain in CAR complexes. Our data show that CAR signaling pathways cannot be predicted solely by the domains used to construct the receptor and that signal strength is a key determinant of T cell fate. Thus, tailoring CAR design based on signal strength may lead to improved clinical efficacy and reduced toxicity.

## INTRODUCTION

Synthetic receptors that mimic natural T cell signaling cascades are being developed as immunotherapeutic reagents for cancer, autoimmunity, and infections. Chimeric antigen receptors (CARs), chimeric costimulatory receptors, and engineered T cell receptors (TCRs) can be introduced into T cells by gene transfer to redirect specificity and promote signaling pathways that initiate effector T cell functions (1). The most successful of these novel therapeutics to date are CARs, which are composed of an extracellular antigen-specific single-chain variable immunoglobulin fragment (scFv) fused to intracellular signaling domains that activate T cells upon ligand binding (2). Although treatment with CAR T cells can result in the complete remission of relapsed or refractory B cell malignancies, it can also cause life-threatening toxicities including cytokine release syndrome (CRS) and neurotoxicity (3–12). Both efficacy and toxicity result from activation of intracellular signaling pathways mediated by CAR engagement.

T cell activation occurs after TCR engagement with antigen-specific peptide bound within the major histocompatibility complex (MHC). TCR binding stimulates intracellular phosphorylation of immunoreceptor tyrosine-based activating motifs (ITAMs) on the CD3 $\delta$ ,  $\epsilon$ ,  $\gamma$ , and  $\zeta$  chains of the TCR (13). Combined with protein

phosphorylation signals delivered *in trans* from costimulatory molecules and cytokines, these events alter T cell transcriptional programs, induce proliferation, promote cytotoxic functions, and stimulate cytokine release. Most CARs use a simplified format to recapitulate the signals necessary for T cell effector function and proliferation. CAR constructs combine the CD3 $\zeta$  endodomain in a single chain with a costimulatory domain from CD28 or 4-1BB. Both CD28/CD3 $\zeta$  and 4-1BB/CD3 $\zeta$  CAR T cells are effective for treating patients with B cell malignancies but may behave differently *in vivo*. CD28/CD3 $\zeta$  CAR T cells generally undergo intense proliferation within 7 days of adoptive transfer and seldom persist more than 60 days after infusion (7, 14). In contrast, 4-1BB/CD3 $\zeta$  CAR T cells reach peak number by 7 to 14 days after transfer and can persist for several months (8, 15). However, variability in patient cohorts, CAR structures, and clinical trial designs impede robust comparisons across trials. Studies comparing CD28/CD3 $\zeta$  and 4-1BB/CD3 $\zeta$  CAR T cells *in vitro* and in animal models partially explain these clinical differences by demonstrating that 4-1BB/CD3 $\zeta$  CAR T cells have greater mitochondrial mass and a more memory T cell–like surface phenotype, and better retain effector functions in settings of chronic antigen stimulation (16, 17).

It is widely assumed that the differences in phenotype and function of CD28/CD3 $\zeta$  and 4-1BB/CD3 $\zeta$  CAR T cells are conferred by activation of divergent signaling pathways through the distinct CAR costimulatory molecule domains. Analyses of signaling pathways stimulated by 4-1BB/CD3 $\zeta$  or third-generation CD28/4-1BB/CD3 $\zeta$  CARs performed using phospho–flow cytometry, Western blot, or blot array do not identify differences between CD28/CD3 $\zeta$  and 4-1BB/CD3 $\zeta$  CAR signaling modules and only profile a small number of known signaling events to which there are experimentally validated antibodies (18, 19). A more comprehensive, unbiased

<sup>1</sup>Program in Immunology, Fred Hutchinson Cancer Research Center, Seattle, WA 98109, USA. <sup>2</sup>Clinical Research Division, Fred Hutchinson Cancer Research Center, Seattle, WA 98109, USA. <sup>3</sup>Vaccine and Infectious Disease Division, Fred Hutchinson Cancer Research Center, Seattle, WA 98109, USA. <sup>4</sup>Department of Medicine, University of Washington School of Medicine, Seattle, WA 98195, USA.

\*Present address: Juno Therapeutics, Seattle, WA 98109, USA.

†Present address: Medigene Immunotherapies GmbH, Planegg/Martinsried 82152, Germany.

‡Present address: Fudan University, Shanghai 200433, China.

§Corresponding author. Email: sriddell@fhcrc.org

and quantitative approach to examine CAR signaling would be to use liquid chromatography–tandem mass spectrometry (LC-MS/MS). When applied to study TCR signaling, LC-MS/MS uncovered hundreds of novel phosphoprotein signaling events that were missed by antibody-based techniques (20–24).

Here, we used LC-MS/MS to analyze CAR stimulation–induced signaling events in primary human CD8<sup>+</sup> T cells that express clinically relevant CD28/CD3 $\zeta$  or 4-1BB/CD3 $\zeta$  CARs specific for CD19 or ROR1. We found that stimulation through CD28/CD3 $\zeta$  and 4-1BB/CD3 $\zeta$  CARs produced nearly identical protein phosphorylation events. Instead, stimulation of CD28/CD3 $\zeta$  CAR T cells prompted more rapid and intense phosphorylation of signaling intermediates and a more effector cell–like phenotype than stimulation of 4-1BB/CD3 $\zeta$  CAR T cells. CD28/CD3 $\zeta$  CAR T cells were less potent at eradicating disseminated lymphoma in a xenograft mouse model than 4-1BB/CD3 $\zeta$  CAR T cells. Increased basal phosphorylation of the CAR CD3 $\zeta$  chain and CAR-associated Lck contributed to the rapid kinetics and stronger signal strength of CD28/CD3 $\zeta$  CARs. Thus, the major distinction between CD28/CD3 $\zeta$  and 4-1BB/CD3 $\zeta$  CARs related not to divergent phosphoprotein signaling pathways but rather signaling strength and kinetics, which, in turn, affect T cell function and fate. These results may inform the design of new therapeutic receptors.

## RESULTS

### CAR designs containing a Strep-tag II sequence enable selective activation of CAR signaling in primary T cells

TCR signaling has been studied using LC-MS/MS analysis of transfected Jurkat T cells stimulated with anti-CD3 monoclonal antibodies (mAbs) (20, 21, 24). Jurkat cells were selected for signaling studies because of the ease at which they can be grown and manipulated with common molecular biology techniques. Primary T cells from human subjects are more appropriate for studying CAR signaling, and we previously developed a method to activate CAR signaling in T cells without the need for ligand-expressing stimulator cells (25). We modified two lentiviral vectors encoding CD19- and ROR1-specific 4-1BB/CD3 $\zeta$  CARs that are currently being tested in clinical trials by adding a nine–amino acid Strep-tag II (STII) sequence to the extracellular CAR hinge. For comparison, we cloned structurally identical CD19- and ROR1-specific CD28/CD3 $\zeta$  CARs containing the STII tag (Fig. 1A). All constructs contained a truncated epidermal growth factor receptor (EGFRt) marker downstream of a T2A ribosomal skip element for purification of CAR-expressing T cells (26). Inclusion of the STII sequence does not interfere with CAR T cell recognition or function, and STII CD28/CD3 $\zeta$  or 4-1BB/CD3 $\zeta$  CAR T cells are efficiently activated and expanded *in vitro* by stimulation with STII microbeads (Fig. 1B) (25). Primary CD8<sup>+</sup> T cells were transduced with each lentiviral vector, sorted for EGFRt expression, and expanded to  $>1.6 \times 10^6$  cells with a single cycle of stimulation before subsequent analysis (Fig. 1C). The abundance of CD28/CD3 $\zeta$  and 4-1BB/CD3 $\zeta$  CARs of each scFv specificity was similar on the cell surface as measured by staining with STII mAb (Fig. 1D). CAR T cells also expressed similar amounts of CD45RO, CD62L, CD27, and CD28 (Fig. 1E), indicating that CAR T cells retained markers associated with memory and proliferative potential. We only detected small frequencies of PD-1– or Tim-3–positive CAR T cells, suggesting that the cells were not activated or exhausted after cell culture (Fig. 1E). Accordingly,  $>85\%$  of CD28/CD3 $\zeta$  and

4-1BB/CD3 $\zeta$  CAR T cells were in the G<sub>0</sub>–G<sub>1</sub> cell cycle phase, indicating that the cells were resting (Fig. 1F).

We evaluated canonical T cell signaling events induced by STII ligation and found that cell-free STII microbead stimulation of CARs was similar to CAR antigen–expressing tumor cells. ROR1-specific 4-1BB/CD3 $\zeta$  CAR T cells were incubated for 45 min with increasing amounts of STII microbeads or with ROR1-transduced K562 (K562/ROR1) tumor cells, and CD3 $\zeta$  Tyr<sup>142</sup> and SLP-76 Ser<sup>376</sup> were measured by Western blot. At the highest bead to CAR T cell ratio, the phosphorylation of CD3 $\zeta$  and SLP-76 was grossly similar to that observed in lysates from CAR T cells stimulated with K562/ROR1 cells (Fig. 1G and fig. S1A). This bead-to-cell ratio was used for all subsequent experiments. Thus, STII microbead stimulation provided a precise method to selectively activate CAR signaling in primary T cells.

### MS identifies common protein phosphorylation events after stimulation of CD28/CD3 $\zeta$ or 4-1BB/CD3 $\zeta$ CAR T cells

We performed LC-MS/MS analysis to interrogate the signaling pathways activated in CD28/CD3 $\zeta$  or 4-1BB/CD3 $\zeta$  CARs in an unbiased manner. Human T cells expressing CD28/CD3 $\zeta$  or 4-1BB/CD3 $\zeta$  CARs were incubated with STII or uncoated (control) microbeads for 10 or 45 min (Fig. 2A). CD19-specific CAR T cells generated from two different donors were used in two independent experiments, and a third independent experiment used ROR1-specific CAR T cells derived from one of the two donors (Fig. 2B). Given that ROR1- and CD19-specific CARs displayed similar phenotypes across the two donors and were stimulated identically in a ligand-independent manner, the corresponding measurements were considered biological replicates. To provide relative quantitation of phosphopeptides within each experiment, we labeled each trypsin-digested lysate with a unique isobaric tandem mass tag (TMT) and globally enriched for phosphopeptides by both phosphorylated tyrosine (pTyr) immunoprecipitation and immobilized metal affinity chromatography (IMAC) (27) (fig. S1B). We identified a total of 26,804 phosphorylation sites across the three experiments corresponding to 4849 proteins. Among phosphorylation sites, 571 (2.13%) were pTyr, 4647 (17.33%) were phosphorylated threonine (pThr), and 21,586 (80.53%) were phosphorylated serine (pSer). (Fig. 2C). Considering the stochastic limitations inherent in data-dependent acquisition shotgun proteomics (28), we found considerable overlap in the captured phosphoproteome between replicate experiments (Fig. 2D). As previously described in murine T cells, 99% of phosphorylation sites detected in each experiment were present in both unstimulated and stimulated T cell lysates, enabling quantitation of changes induced by CAR activation (22, 29).

We analyzed well-described TCR phosphorylation events within the MS data set to identify sites that were modified by CAR engagement (13). We calculated the log<sub>2</sub> of the fold-change (log<sub>2</sub>FC) value for all phosphorylation sites within each experiment by comparing stimulated samples to appropriate controls (that is, CD28/CD3 $\zeta$  CAR 10-min stimulation versus CD28/CD3 $\zeta$  CAR 10-min control). At 10 min, phosphorylation of CD3 $\zeta$  at Tyr<sup>83</sup>, Tyr<sup>111</sup>, and Tyr<sup>142</sup>, was increased in stimulated CAR T cells (Fig. 2E). All CAR T cells displayed increased phosphorylation of CD28 at Tyr<sup>209</sup> after 10 min, which demonstrated that 4-1BB/CD3 $\zeta$  CAR activation stimulates phosphorylation of endogenous CD28. After 45 min of stimulation, phosphoprotein signaling spread to downstream TCR nodes, and we measured increased phosphorylation of phospholipase C- $\gamma$ 1 (PLC- $\gamma$ 1) at Ser<sup>1248</sup> and BCL10 at Ser<sup>138</sup> (Fig. 2E) (30, 31). We did not observe

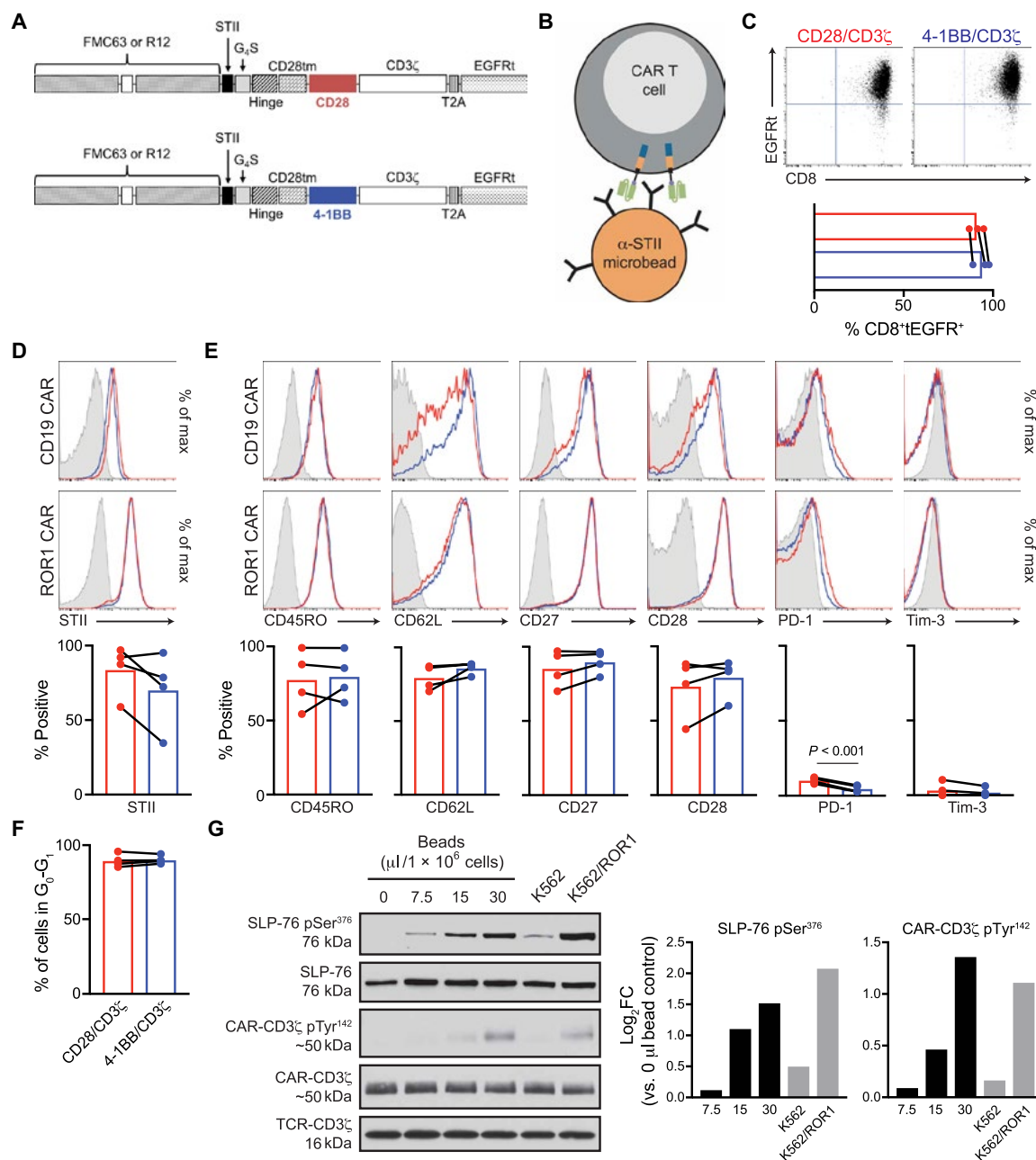


**Fig. 1. Both CD28/CD3 $\zeta$  and 4-1BB/CD3 $\zeta$  CAR T cells can be activated through an engineered STII hinge.** (A) Schematic of CARs incorporating an STII sequence in the extracellular hinge. CARs contained either the CD19-specific FMC63 scFv or the ROR1-specific R12 scFv. (B) Schematic of CAR T cell activation through the STII hinge using magnetic beads coated with antibody against STII. (C) Flow cytometry analysis of CD8 and EGFRt staining on singlet CD19 CAR T cells after expansion. Dot plots are representative of three independent experiments. The frequency values of positive cells are means from all experiments. (D and E) Flow cytometry analysis of cell surface CAR (D) or CD45RO, CD62L, CD27, CD28, PD-1, and Tim-3 phenotypic marker staining (E) on sort-purified CD19- or ROR1-specific singlet CD8<sup>+</sup> CAR T cells after expansion. Histogram plots of CD28/CD3 $\zeta$  CAR T cells (red), 4-1BB/CD3 $\zeta$  CAR T cells (blue), or isotype control staining (gray) are representative of four independent experiments. The frequency values of positive cells are means from all experiments. (F) Flow cytometry analysis of the DNA content of CAR T cells after expansion. Histograms are representative of four independent experiments. The frequency values of cells in G<sub>0</sub>-G<sub>1</sub> gate are means from all experiments. (G) Western blot analysis for CD3 $\zeta$ , CD3 $\zeta$  pTyr<sup>142</sup>, SLP-76, and SLP-76 pSer<sup>376</sup> in lysates of ROR1 4-1BB/CD3 $\zeta$  CAR T cells after 45 min of coculture with varying quantities of STII microbeads, K562 cells, or K562/ROR1 cells. Blots and fold change (log<sub>2</sub>FC) of normalized band intensity values are representative of two independent experiments. The indicated *P* values were calculated by paired two-tailed *t* test (E).

reproducible changes at either time point in the phosphorylation of CD3 $\delta$ ,  $\epsilon$ , or  $\gamma$  ITAMs. Because these sites are phosphorylated after TCR stimulation (13), our data indicated that CAR signaling only partially mimics endogenous TCR activation.

The MS data suggested that CD28/CD3 $\zeta$  CAR stimulation may initiate a greater magnitude log<sub>2</sub>FC than 4-1BB/CD3 $\zeta$  CARs at both 10 and 45 min, and we confirmed this finding by Western blot. Evaluation of cell lysates for CD3 $\zeta$  pTyr<sup>142</sup>, ZAP-70 pTyr<sup>319</sup>, and

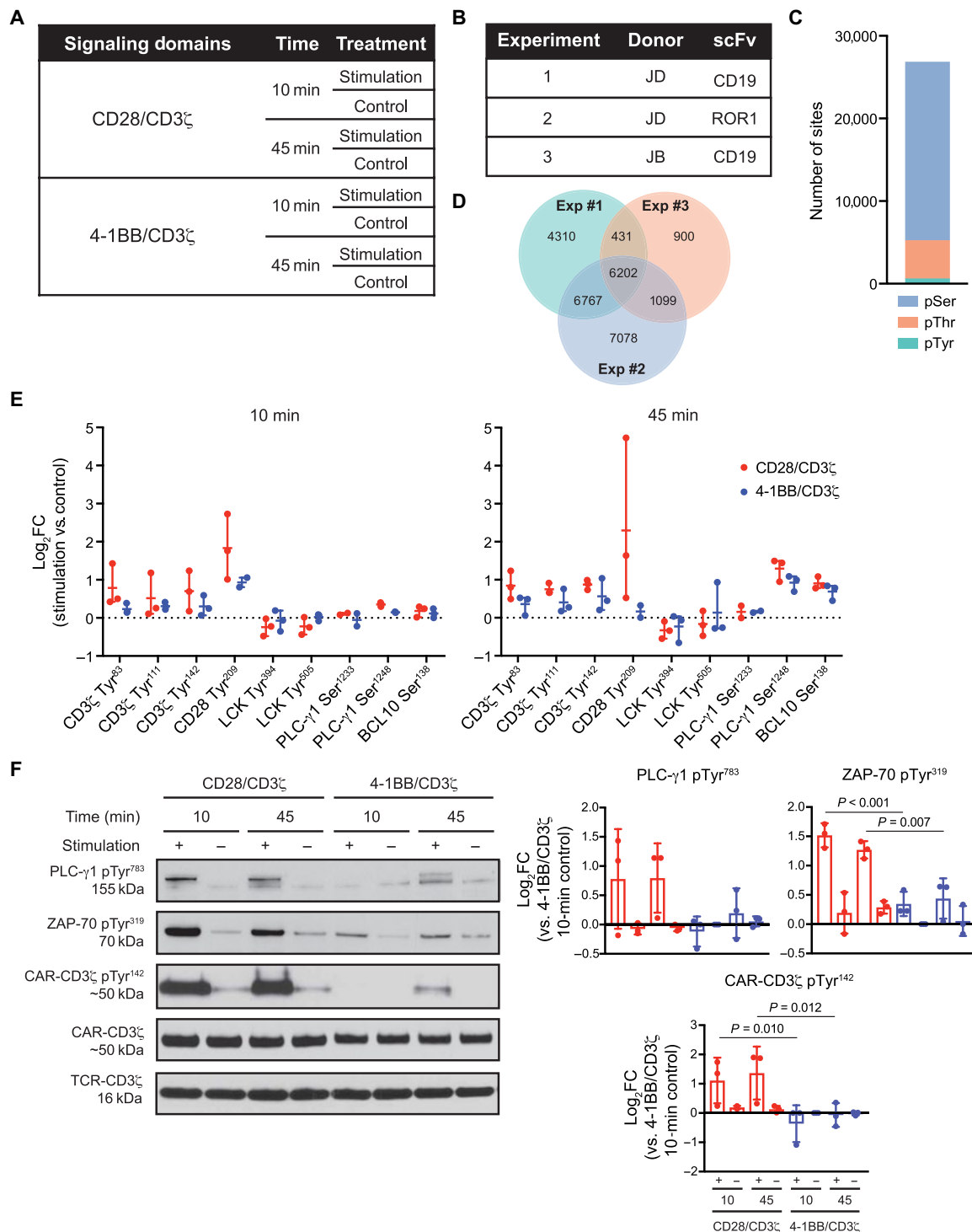


**Fig. 2. CAR T cells signal through endogenous T cell signaling proteins.** (A and B) Human CAR T cell treatment conditions and experimental groups. (C to E) MS/MS analysis of phosphorylated peptides from lysates of CAR T cells stimulated as in (A). The total number of pSer, pThr, and pTyr peptides identified (C) and the Venn diagram of the overlap among phosphorylation sites (D) are pooled from three independent experiments. The fold change ( $\log_2$ FC) data in phosphorylation at the indicated times at sites involved in canonical TCR signaling (E) are means  $\pm$  range from two or three independent experiments. (F) Western blot analysis for CD3 $\zeta$ , CD3 $\zeta$  pTyr<sup>142</sup>, ZAP-70 pTyr<sup>319</sup>, and PLC- $\gamma$ 1 pTyr<sup>783</sup> in lysates from CD19-specific CD28/CD3 $\zeta$  or 4-1BB/CD3 $\zeta$  CAR T cells at the indicated times after stimulation. Blots are representative of three independent experiments. Fold change ( $\log_2$ FC) data of normalized band intensity are means  $\pm$  SD from all experiments. The indicated *P* values were calculated by repeated-measures one-way analysis of variance (ANOVA) with Tukey's multiple comparisons test comparing CD28/CD3 $\zeta$  and 4-1BB/CD3 $\zeta$  CAR samples (F).

PLC- $\gamma$ 1 pTyr<sup>783</sup> demonstrated that both CD28/CD3 $\zeta$  and 4-1BB/CD3 $\zeta$  CAR stimulation increased phosphorylation of these sites, but we observed more intense ZAP-70 and CAR CD3 $\zeta$  phosphorylation in stimulated CD28/CD3 $\zeta$  CAR T cells compared to 4-1BB/CD3 $\zeta$  CAR T cells (Fig. 2F). We also detected a low level of basal CAR CD3 $\zeta$  phosphorylation in unstimulated CD28/CD3 $\zeta$  CD19 and ROR1 CAR T cells that was not present in 4-1BB/CD3 $\zeta$  CAR T cells. Western blot analysis of lysates from primary CD4<sup>+</sup> T cells transduced with CD19 CARs and stimulated with STII microbeads also demonstrated similar patterns of basal CAR CD3 $\zeta$  phosphorylation as well as more rapid and robust phosphorylation of CD3 $\zeta$  and SLP-76 within CD28/CD3 $\zeta$  CAR T cells (fig. S2A). Constitutive phosphorylation of the CAR CD3 $\zeta$  domain or tonic signaling has been shown to occur with some CARs, including a CD19-specific CD28/CD3 $\zeta$  CAR that is being used in the clinic (32). Strong tonic signaling has been linked to sequences in the scFv that promote clustering of CAR molecules at the cell surface and results in the up-regulation of T cell exhaustion markers (33, 34). Because we did not observe differences in PD-1 or Tim-3 expression, or evidence of CAR clustering in unstimulated CD28/CD3 $\zeta$  or 4-1BB/CD3 $\zeta$  CAR T cells (Fig. 1, E and F, and fig. S2B), the low level of basal CAR CD3 $\zeta$  domain phosphorylation detected here may be distinct from more extreme tonic signaling observed in some CARs with different scFv specificities.

### Phosphorylation events mediated by CD28/CD3 $\zeta$ or 4-1BB/CD3 $\zeta$ CARs differ in kinetics and magnitude

An advantage of shotgun MS is that it can quantitatively and temporally measure thousands of phosphorylation events outside of the canonical TCR signaling pathway to which there are no experimentally validated antibodies. We leveraged the *limma* statistical framework and associated R package to identify phosphorylation sites that were increased or decreased in abundance after CD28/CD3 $\zeta$  and 4-1BB/CD3 $\zeta$  CAR ligation (35). We assigned a phosphorylation site to be CAR stimulation-responsive if it was detected in at least two of the three experiments, displayed an average  $|\log_2\text{FC}| \geq 0.7$  between stimulated and unstimulated conditions at 10 or 45 min, and met a 5% false discovery rate (FDR) cutoff. A  $\log_2\text{FC}$  cutoff of 0.7 was chosen because this represents approximately 2 SDs of the distribution of  $\log_2\text{FC}$  values (fig. S3).

Using these cutoffs, 26 phosphorylation sites were identified as stimulation-responsive at 10 min after activation of CD28/CD3 $\zeta$  CAR T cells. These sites were enriched for proteins in the Kyoto Encyclopedia of Genes and Genomes (KEGG) TCR signaling pathway including increased phosphorylation of p21-activated kinase 2 (PAK2) at Ser<sup>64</sup>, CD8 $\alpha$  (CD8A) at Ser<sup>231</sup>, protein kinase C  $\theta$  (PKCT) at Ser<sup>370</sup>, and proto-oncogene *vav* (VAV1) at Ser<sup>748</sup> and Thr<sup>749</sup> (Fig. 3A and table S1). We also detected increased phosphorylation of neuroblast differentiation-associated protein (AHNAK) at Ser<sup>5857</sup>, which activates PLC- $\gamma$ 1 and is required for T cell calcium (Ca<sup>2+</sup>) mobilization and effector functions (36, 37). In contrast, no sites met  $\log_2\text{FC}$  and FDR criteria at 10 min after stimulation of 4-1BB/CD3 $\zeta$  CAR T cells (Fig. 3A and table S1). The lack of robust alterations in early protein phosphorylation in 4-1BB/CD3 $\zeta$  CAR T cells was consistent with Western blot data showing a very low level of phosphorylation of CAR CD3 $\zeta$ , ZAP-70, and PLC- $\gamma$ 1 at 10 min after stimulation (Fig. 2F).

After 45 min of stimulation, more intense changes in protein phosphorylation had occurred, and we detected phosphorylation at

1289 sites that met the  $\log_2\text{FC}$  and FDR cutoffs in either CD28/CD3 $\zeta$  or 4-1BB/CD3 $\zeta$  CAR T cell samples. These included 1279 phosphorylation sites from 743 gene products in CD28/CD3 $\zeta$  CAR T cells and 522 sites from 346 gene products in 4-1BB/CD3 $\zeta$  CAR T cells (Fig. 3A and tables S2 and S3). These data indicated that stimulation of CD28/CD3 $\zeta$  CAR T cells increased phosphorylation at a greater number of sites than did stimulation of 4-1BB/CD3 $\zeta$  CAR T cells. However, both CD28/CD3 $\zeta$  and 4-1BB/CD3 $\zeta$  CAR activation stimulated highly similar changes in the phosphorylation of activation-responsive sites (Fig. 3B). Only 12 (0.93%) of the 1289 phosphorylation sites that met the cutoffs in CD28/CD3 $\zeta$  CAR samples exhibited an opposite response after 4-1BB/CD3 $\zeta$  CAR stimulation, and only 43 (3.3%) sites exhibited a greater magnitude  $\log_2\text{FC}$  after 4-1BB/CD3 $\zeta$  CAR stimulation. These observations were consistent with our earlier data suggesting that signaling downstream of CD28/CD3 $\zeta$  CAR activation was more intense than downstream of 4-1BB/CD3 $\zeta$  CAR activation. Furthermore, these subsets of 12 and 43 phosphorylation sites did not map to currently defined 4-1BB signaling networks (38).

Finding relatively few differences in the phosphorylation events stimulated after activation of CD28/CD3 $\zeta$  and 4-1BB/CD3 $\zeta$  CARs was unexpected. When we questioned how proteins involved in the canonical T cell costimulatory signaling pathways were affected, we found that the phosphorylation of CD28 signaling intermediates VAV1, PIK3C2A, and PKCT was also increased after stimulation of both CD28/CD3 $\zeta$  and 4-1BB/CD3 $\zeta$  CAR T cells (Fig. 3C) (39). This result appeared to agree with our earlier observations that endogenous CD28 was phosphorylated after activation of 4-1BB/CD3 $\zeta$  CAR T cells (Fig. 2E). Within the 4-1BB signaling pathway, phosphorylation of lymphocyte-specific protein 1 (LSP1), a direct target of 4-1BB and TRAF2 signaling, was altered by stimulation of both CD28/CD3 $\zeta$  and 4-1BB/CD3 $\zeta$  CAR T cells (40). Thus, rather than activating divergent costimulatory pathways, as might be predicted from the distinct costimulatory domains encoded by the receptors, activation of CD28/CD3 $\zeta$  and 4-1BB/CD3 $\zeta$  CARs induced highly similar changes in intracellular protein phosphorylation that encompassed both canonical CD28 and 4-1BB signaling intermediates.

A map illustrating the major pathways and individual protein phosphorylation events affected by CD28/CD3 $\zeta$  and 4-1BB/CD3 $\zeta$  CAR stimulation includes proteins involved in canonical TCR signaling and mitogen-activated protein kinase (MAPK) signaling pathways (Fig. 4 and table S3). In addition, stimulation of either CD28/CD3 $\zeta$  or 4-1BB/CD3 $\zeta$  CAR T cells affected phosphorylation of actin-cytoskeletal regulatory proteins, RNA processing proteins, nuclear pore proteins, and mitochondrial fission regulators such as DRP1 (41, 42). A list of CAR stimulation-responsive phosphorylation sites is provided in tables S1 and S2. Many of these proteins have not been previously associated with TCR or CAR signaling.

### Differences in the magnitude of CD28/CD3 $\zeta$ and 4-1BB/CD3 $\zeta$ CAR signaling persist across time

Phosphorylation events activated by CD28/CD3 $\zeta$  and 4-1BB/CD3 $\zeta$  CAR T cell stimulation were highly similar but differed in intensity at the vast majority of sites. Signaling strength during T cell activation, measured as a composite of TCR affinity, costimulation, and cytokine signals, dictates clonal expansion and the effector capacities of a T cell response (43–45). To provide a holistic measure of CAR signal strength, we sorted stimulation-responsive phosphorylation sites at 45 min from CD28/CD3 $\zeta$  and 4-1BB/CD3 $\zeta$  CAR samples by

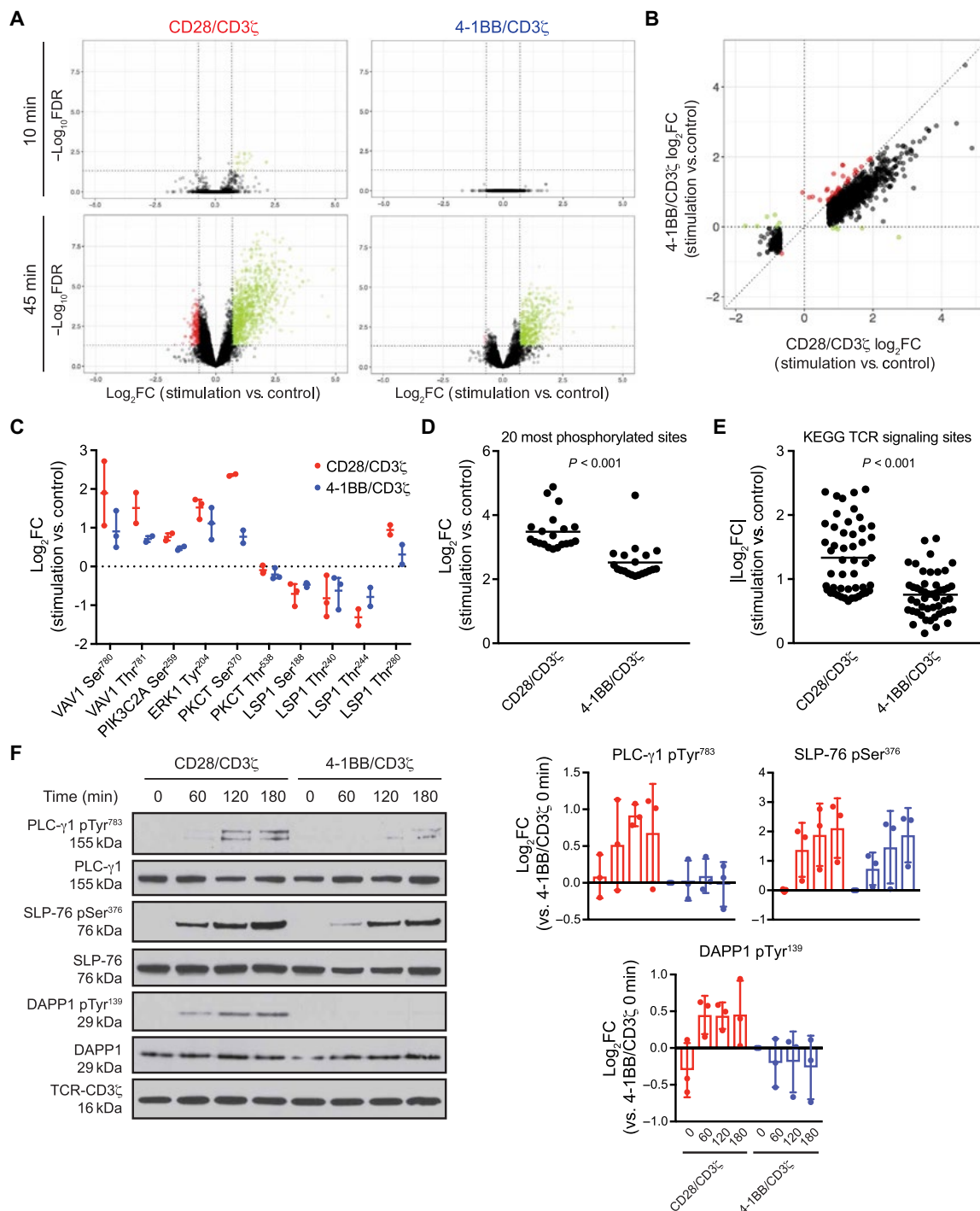


**Fig. 3. The kinetics and strength of signaling vary after stimulation of CD28/CD3 $\zeta$  or 4-1BB/CD3 $\zeta$  CAR T cells. (A)** Volcano plots of fold change ( $\text{log}_2\text{FC}$ ) and FDR for phosphorylation sites identified by MS/MS in Fig. 2. Green dots indicate sites with increased phosphorylation, and red dots indicate sites with decreased phosphorylation after CAR stimulation in at least two experiments. **(B)** Comparison of stimulation-responsive phosphorylation sites identified by MS/MS at 45 min after activation in either CD28/CD3 $\zeta$  or 4-1BB/CD3 $\zeta$  CAR samples. Green dots specify sites that exhibited opposite responses after CD28/CD3 $\zeta$  or 4-1BB/CD3 $\zeta$  CAR activation, whereas red dots indicate sites phosphorylated to a greater extent after stimulation of 4-1BB/CD3 $\zeta$  CAR T cells in at least two MS/MS experiments in Fig. 2. **(C)** Fold change in phosphorylation sites on known CD28 and 4-1BB signaling pathway members at 45 min after CAR T cell stimulation. Data are means  $\pm$  range from two or three MS/MS experiments in Fig. 2. **(D)** Fold change in the 20 most phosphorylated sites identified by MS/MS in Fig. 2. Data are means from all experiments. **(E)** Absolute fold change of phosphorylation sites on known KEGG TCR signaling pathway proteins identified by MS/MS in Fig. 2. Data are means from all experiments. **(F)** Western blot analysis for CD3 $\zeta$ , DAPP1, DAPP1 pTyr<sup>139</sup>, SLP-76, SLP-76 pSer<sup>376</sup>, PLC- $\gamma$ 1, and PLC- $\gamma$ 1 pTyr<sup>783</sup> in lysates from ROR1 CAR T cells stimulated with STII microbeads for the indicated times. Blots are representative of three independent experiments. Fold change data of normalized band intensity are means  $\pm$  SD from all experiments. The indicated  $P$  values were calculated by unpaired two-tailed  $t$  test (D and E).

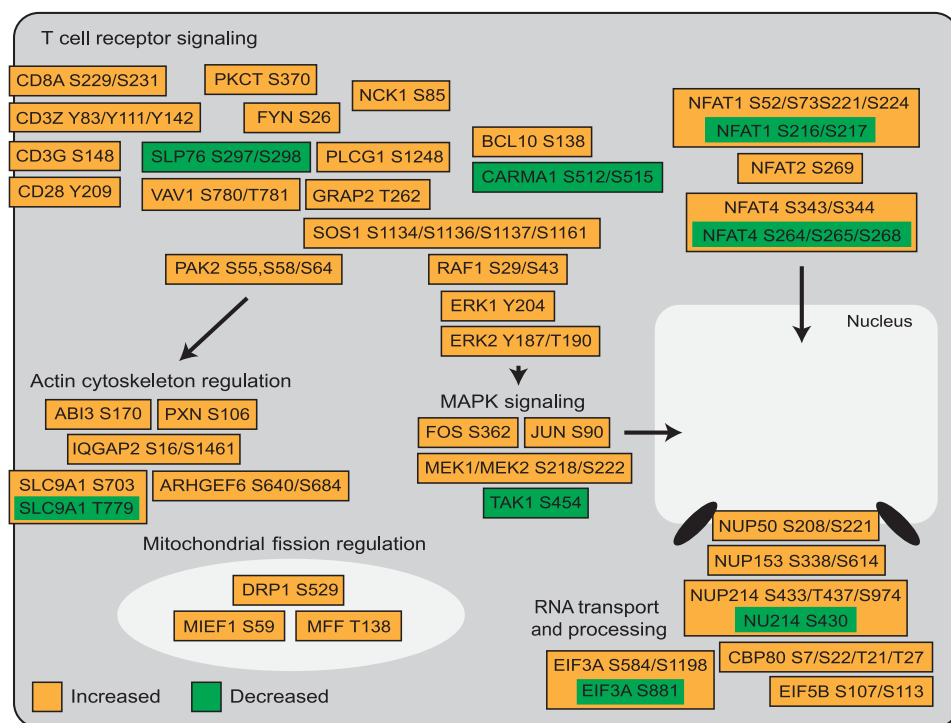


**Fig. 4. Stimulation of CD28/CD3 $\zeta$  or 4-1BB/CD3 $\zeta$  CAR T cells alters protein phosphorylation across similar signaling pathways and cellular compartments.** Map of select proteins differentially phosphorylated after 45 min of CAR T cell stimulation from analysis of all MS/MS experiments in Fig. 2.

decreasing log<sub>2</sub>FC. In line with results showing that stimulation of both CARs altered similar phosphorylation sites, 15 of the 20 most phosphorylated sites after stimulation were shared between CD28/CD3 $\zeta$  and 4-1BB/CD3 $\zeta$  CAR T cells (table S4). However, phosphorylation of the top 20 sites increased from control samples by 11.15-fold on average in CD28/CD3 $\zeta$  CAR samples but only by 5.8-fold on average in 4-1BB/CD3 $\zeta$  CAR samples (Fig. 3D). Stratifying CAR stimulation-responsive phosphorylation sites by signaling pathway further indicated that the average phosphorylation site within the KEGG TCR signaling pathway was modulated by 2.52-fold in CD28/CD3 $\zeta$  CAR samples but only by 1.69-fold in 4-1BB/CD3 $\zeta$  CAR samples (Fig. 3E). To determine whether 4-1BB/CD3 $\zeta$  CAR signals reached a similar intensity to those of CD28/CD3 $\zeta$  CARs at later times, we stimulated identically prepared CD8<sup>+</sup> CAR T cells for 60, 120, or 180 min and measured phosphorylation of canonical and newly identified signaling intermediates (table S4). Phosphorylation of PLC- $\gamma$ 1 Tyr<sup>783</sup> and DAPP1 Tyr<sup>139</sup> was apparent after stimulation of CD28/CD3 $\zeta$  but not 4-1BB/CD3 $\zeta$  CAR T cells (Fig. 3F). These data suggest that 4-1BB/CD3 $\zeta$  CAR stimulation may not achieve the same signal intensity as CD28/CD3 $\zeta$  CAR T cells during this time frame.

**Increased CAR signal intensity is associated with an effector cell-like phenotype and reduced in vivo antitumor activity**

The strength of T cell activation and signal transduction influences transcriptional programs that regulate effector cell differentiation and memory formation (44). We used RNA sequencing (RNA-seq) to analyze changes in transcription within CD28/CD3 $\zeta$  or 4-1BB/CD3 $\zeta$  CD8<sup>+</sup> CAR T cells at 6 hours after STII microbead stimulation.

Consistent with the faster and more intense phosphoprotein signal, CD28/CD3 $\zeta$  CAR stimulation initiated more marked transcriptional changes. A comparison of stimulated to unstimulated CD28/CD3 $\zeta$  CAR T cells identified 4894 differentially expressed genes at 6 hours, whereas 4-1BB/CD3 $\zeta$  CAR stimulation resulted in 197 differentially expressed genes. CD28/CD3 $\zeta$  or 4-1BB/CD3 $\zeta$  CAR stimulation increased expression of the canonical T cell activation marker CD69 to a similar degree (Fig. 5A), but greater fold increases in expression of the effector molecules granzyme B (*GZMB*), interferon- $\gamma$  (*IFNG*), interleukin-2 (*IL2*), tumor necrosis factor- $\alpha$  (*TNF*), macrophage inflammatory protein 1 $\alpha$  (*CCL3*), and macrophage inflammatory protein 1 $\beta$  (*CCL4*) were observed in CD28/CD3 $\zeta$  CAR T cells (Fig. 5B). Direct comparison of CD28/CD3 $\zeta$  and 4-1BB/CD3 $\zeta$  CAR T cells identified 1673 differentially expressed genes after stimulation (table S5). Of these, Krüppel-like factor 2 (*KLF2*), IL-7 receptor (*IL7R*), and Rho family-interacting cell polarization regulator 2 (*RIPOR2*; previously known as *FAM65B*) expression was decreased in CD28/CD3 $\zeta$  CAR T cells when compared to 4-1BB/CD3 $\zeta$  CAR T cells (Fig. 5C).

*KLF2* and *IL7R* are associated with memory T cell formation and are targets of the FOXO family of transcription factors (46–48). Consistent with this observation, *FOXO4* expression was reduced in stimulated CD28/CD3 $\zeta$  CAR T cells when compared to 4-1BB/CD3 $\zeta$  CAR T cells. Quantitative polymerase chain reaction (qPCR) confirmed that some of these T cell memory-associated genes were only differentially expressed in stimulated and not unstimulated CD28/CD3 $\zeta$  or 4-1BB/CD3 $\zeta$  CAR T cells (Fig. 5D).

Because differences in TCR signal quantity affect T cell functions (44, 45), we measured CD28/CD3 $\zeta$  and 4-1BB/CD3 $\zeta$  CAR T cell effector functions in vitro. We activated CD28/CD3 $\zeta$  and 4-1BB/CD3 $\zeta$  CAR T cells with ROR1- and CD19-expressing K562 cells or STII microbeads and measured cytokine production and proliferation. After 24 hours of coculture, CD28/CD3 $\zeta$  CAR T cells secreted markedly more IFN- $\gamma$ , IL-2, and TNF- $\alpha$  than 4-1BB/CD3 $\zeta$  CAR T cells (Fig. 5E). By 72 hours, both CD28/CD3 $\zeta$  and 4-1BB/CD3 $\zeta$  CAR T cells proliferated (Fig. 5F). These data suggested that stronger signaling by CD28/CD3 $\zeta$  CAR T cells correlated with increased short-term effector responses.

We also investigated the function of CD28/CD3 $\zeta$  and 4-1BB/CD3 $\zeta$  CAR T cells in vivo. For these studies, we used a defined 1:1 CD4/CD8 ratio CAR T cell product that displays superior control of xenograft Raji lymphoma in NOD/SCID/ $\gamma$ c<sup>-/-</sup> (NSG) mice (49). Adoptive transfer of 3  $\times$  10<sup>6</sup> CD28/CD3 $\zeta$  or 4-1BB/CD3 $\zeta$  CAR T cells into tumor-bearing mice mediated complete tumor regression (Fig. 5G). However, when fewer (7.5–8  $\times$  10<sup>5</sup>) cells were transferred, CD28/CD3 $\zeta$  CAR T cells were much less potent at eliminating Raji lymphoma cells than 4-1BB/CD3 $\zeta$  CAR T cells, and all CD28/CD3 $\zeta$  CAR T cell-treated mice died of tumor progression within 40 days

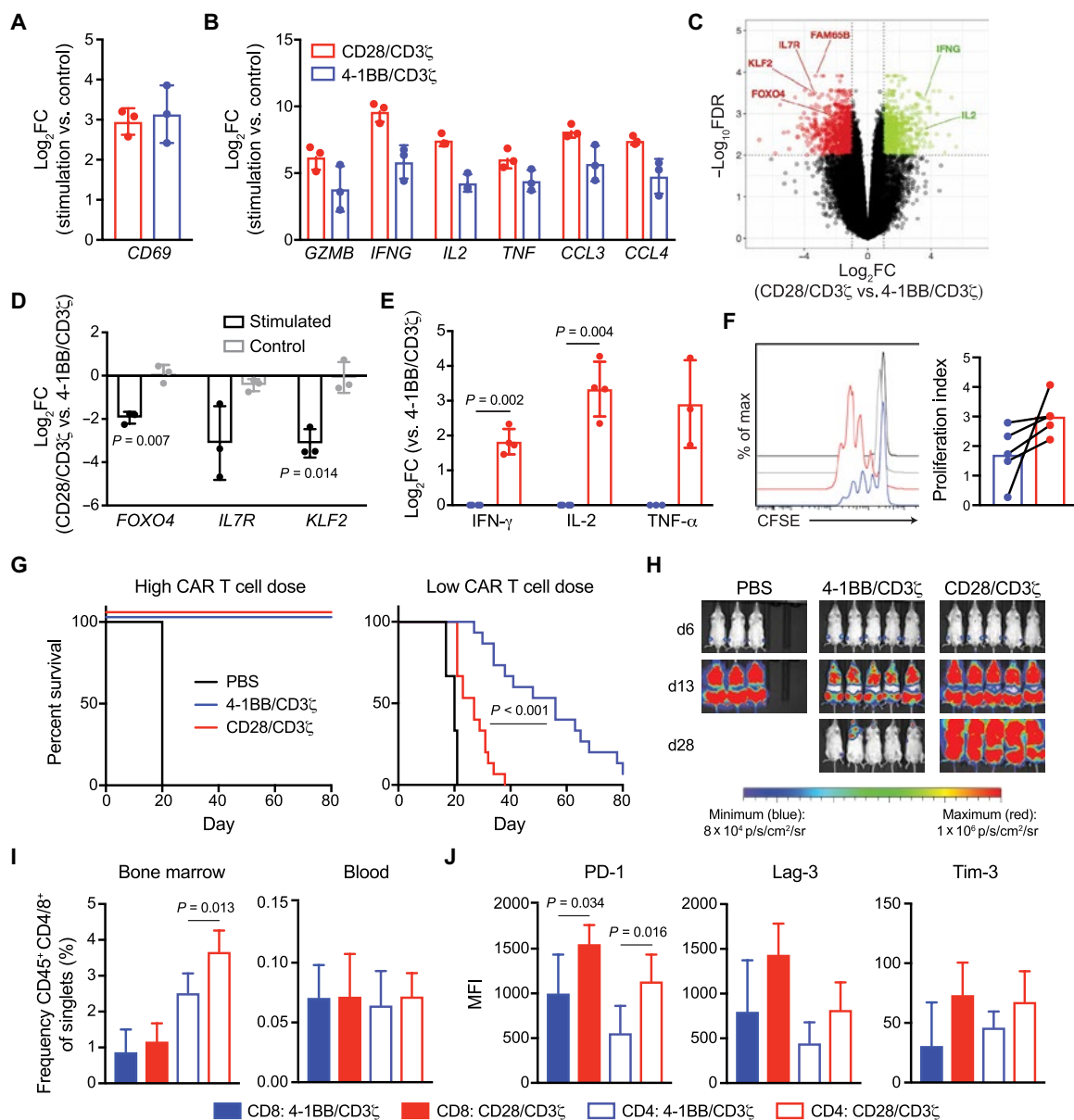


**Fig. 5. Increased CD28/CD3 $\zeta$  CAR signal intensity is associated with an effector cell-like phenotype and reduced in vivo antitumor activity.** (A to C) RNA-seq analysis of total RNA expression in CD28/CD3 $\zeta$  or 4-1BB/CD3 $\zeta$  CAR T cells with and without stimulation. The fold change values of the indicated transcripts (A and B) are means  $\pm$  SD from three independent experiments. Transcripts in (B) met an FDR of 1% for differential expression between CD28/CD3 $\zeta$  and 4-1BB/CD3 $\zeta$  CAR T cells. Volcano plot analysis (C) indicates genes with increased expression in CD28/CD3 $\zeta$  CAR T cells (green) or increased expression in 4-1BB/CD3 $\zeta$  CAR T cells (red). (D) Quantitative PCR analysis of *IL7R*, *KLF2*, and *FOXO4* expression in CD28/CD3 $\zeta$  and 4-1BB/CD3 $\zeta$  CAR T cells. Fold change data are means  $\pm$  SD from three biological replicates. (E) Enzyme-linked immunosorbent assay (ELISA) analysis of cytokine production 24 hours after coculture of ROR1-specific CAR T cells with K562/ROR1 cells. Data are means  $\pm$  SD of three to four independent experiments. (F) Flow cytometry analysis of T cell proliferation as measured by carboxyfluorescein diacetate succinimidyl ester (CFSE) dye dilution at 72 hours after STIL microbead stimulation. Histogram plot of unstimulated CD28/CD3 $\zeta$  CAR T cells (gray), unstimulated 4-1BB/CD3 $\zeta$  CAR T cells (black), stimulated CD28/CD3 $\zeta$  CAR T cells (red), and stimulated 4-1BB/CD3 $\zeta$  CAR T cells (blue). The proliferation index values of cells are means from five independent experiments ( $P = 0.0747$ ). (G to J) At 7 days after Raji/ffluc engraftment, NSG mice were treated with a single infusion of the indicated dose of CAR T cells. Survival analyses (G) of 6, 9, or 15 mice per group are pooled from two to three independent experiments. Bioluminescence images of Raji/ffluc tumor burden in mice at the indicated time points (H) are representative of all experiments. PBS, phosphate-buffered saline. (I and J) Flow cytometry analysis of CAR T cell frequency in bone marrow or peripheral blood (I) or abundance of PD-1, Lag-3, or Tim-3 on CAR T cells in the bone marrow (J) on day 20. Frequency and mean fluorescence intensity (MFI) data are means  $\pm$  SD of 10 mice per group from two independent experiments. The indicated  $P$  values were calculated by one-sample  $t$  test with null hypothesis  $H_0 = 0$  (D), paired two-tailed  $t$  test (E and F), log-rank (Mantel-Cox) test (G), or unpaired two-tailed  $t$  test (I and J).

(Fig. 5, G and H). Tumor progression occurred in mice treated at the lower CD28/CD3 $\zeta$  CAR T cell dose despite accumulation of CAR T cells to higher frequencies in tumor-involved bone marrow (Fig. 5I). CD28/CD3 $\zeta$  CAR T cells in the bone marrow expressed higher levels of PD-1,

Lag-3, and Tim-3 (Fig. 5J), consistent with the acquisition of an exhausted phenotype. In summary, the rapid and intense signaling mediated by CD28/CD3 $\zeta$  CAR activation correlated with an exhausted phenotype in CD8 $^+$  and CD4 $^+$  CAR T cells and reduced antitumor activity.

### CD28/CD3 $\zeta$ and 4-1BB/CD3 $\zeta$ CARs differentially associate with endogenous CD28 and Lck

To interrogate possible causes of increased CD28/CD3 $\zeta$  CAR signaling kinetics and strength, we immunoprecipitated CAR complexes from unstimulated CD8<sup>+</sup> T cells and probed for differences among associated T cell signaling proteins in the basal state. Western blot confirmed efficient CAR pull-down and showed association of endogenous CD28 and Lck with the CD28/CD3 $\zeta$  CAR but only minimal CD28 and Lck association with the 4-1BB/CD3 $\zeta$  CAR (Fig. 6A). Because basal CAR phosphorylation was conferred by the presence of the CD28 costimulatory domain and Tyr<sup>206</sup>, Tyr<sup>209</sup>, and Tyr<sup>218</sup> were intensely phosphorylated after CAR stimulation, we constructed CD28/CD3 $\zeta$  CARs with tyrosine to phenylalanine mutations at these residues (Fig. 6B). CD19 and ROR1 CARs with mutations of Y218F (Y1) or all three tyrosines (Y3) were efficiently expressed in T cells and led to vigorous IFN- $\gamma$  production and proliferation in response to coculture with ROR1<sup>+</sup> or CD19<sup>+</sup> tumor cells (Fig. 6, C and D). We observed partial (Y1) or complete (Y3) abrogation of basal CAR CD3 $\zeta$  phosphorylation in CARs containing Y to F mutations as compared to CD28/CD3 $\zeta$  CARs; however, Y1 and Y3 CARs still phosphorylated SLP-76 and PLC- $\gamma$ 1 with similar kinetics and intensity as the wild-type CD28/CD3 $\zeta$  CAR after STII microbead stimulation (Fig. 6E). Immunoprecipitation of each CAR indicated that Lck association was not abrogated by the Y1 and Y3 mutations, although endogenous CD28 did not associate with the Y3 CAR (Fig. 6F). Together, these results suggested that neither basal CAR CD3 $\zeta$  phosphorylation nor endogenous CD28 association was responsible for the increased signal kinetics and strength of CD28/CD3 $\zeta$  CARs.

Constitutive Lck activation promotes T cell effector functions (50, 51). Therefore, we tested whether association of Lck with CD28/CD3 $\zeta$  CARs mediated rapid and robust phosphorylation of signaling intermediates after CAR activation. We generated proline to alanine mutations at the Lck binding site of CD28 (Fig. 7A) (52, 53). Immunoprecipitation of the wild-type and mutant CD28/CD3 $\zeta$  CARs showed that Lck association was absent in CARs with proline to alanine mutations (Fig. 7 and fig. S4). Signaling analyses of these constructs demonstrated that mutation of proline residues alone in CD28P CARs partially abrogated basal CAR CD3 $\zeta$  phosphorylation but did not reduce signal intensity (Fig. 7C). However, simultaneous mutation of proline and tyrosine residues in Y3P CARs fully abrogated basal CAR phosphorylation and reduced the magnitude of SLP-76 and PLC- $\gamma$ 1 phosphorylation after stimulation (Fig. 7C). Thus, differences in CAR signal intensity between CD28/CD3 $\zeta$  CARs and 4-1BB/CD3 $\zeta$  CARs were, in part, related to greater Lck association with CD28/CD3 $\zeta$  CARs. These data suggest that CAR signal intensity could be altered by mutating tyrosine and proline residues in the CD28 signaling domain.

### DISCUSSION

The adoptive transfer of CD28/CD3 $\zeta$  or 4-1BB/CD3 $\zeta$  CD19 CAR T cells is an effective therapy for patients with certain B cell malignancies but can cause serious toxicities that originate from CAR signaling after tumor recognition (1). However, CD28/CD3 $\zeta$  or 4-1BB/CD3 $\zeta$  CAR signaling modules confer differences in effector functions and metabolic profiles, and both types of CAR T cells can cause serious toxicities that originate from CAR signaling after T cell activation (16, 17). Crafting safer and more effective CAR

T cells might be accomplished by modifying CAR design, but optimization is hindered by the rudimentary understanding of how signaling by synthetic CARs directs T cell functional outputs and cell fate decisions.

We used MS to study changes in the phosphoproteome of T cells after CAR ligation and captured 26,804 unique phosphorylation sites that describe changes induced by CD28/CD3 $\zeta$  and 4-1BB/CD3 $\zeta$  CARs in detail. Our experiments used structurally identical CARs specific for two target antigens being pursued in clinical trials. In contrast to the current perception of how costimulatory domains function in CARs, our data show that, in the space of this data set, CD28/CD3 $\zeta$  and 4-1BB/CD3 $\zeta$  CAR activation initiated nearly identical directional changes in protein phosphorylation. Notably, both CARs altered phosphorylation of proteins involved in canonical TCR, CD28, and 4-1BB signaling pathways. Only 12 of 1289 (0.93%) phosphorylation sites exhibited opposite responses to stimulation when comparing CAR constructs at 45 min after activation, and these few sites are not directly linked to either CD28 or 4-1BB signaling pathways. Therefore, our data refute the notion that CD28/CD3 $\zeta$  and 4-1BB/CD3 $\zeta$  CARs activate divergent signaling cascades and indicate that one cannot predict the signaling cascades initiated by synthetic CARs by focusing solely on the domains encoded by the receptor polypeptide. Rather, synthetic CARs initiate a plethora of signals that both encompass and surpass those of the natural molecules on which the synthetic receptors are based.

Instead, our data demonstrate that a major difference between CD28/CD3 $\zeta$  and 4-1BB/CD3 $\zeta$  CARs is that CD28/CD3 $\zeta$  receptors signal with markedly increased kinetics and intensity. Within 45 min, CD28/CD3 $\zeta$  CAR stimulation altered the phosphorylation state of hundreds of proteins involved in TCR signaling, MAPK signaling, actin-cytoskeleton rearrangement, and RNA processing pathways. Alterations in protein phosphorylation after 4-1BB/CD3 $\zeta$  CAR stimulation affected identical proteins as CD28/CD3 $\zeta$  CAR stimulation but proceeded more slowly and with reduced intensity. Subsequent analysis of CAR binding partners demonstrated more Lck in immunoprecipitates from unstimulated CD28/CD3 $\zeta$  CAR T cells than from 4-1BB/CD3 $\zeta$  CAR T cells. Mutational analysis of the CAR CD28 signaling domain identified residues responsible for basal CAR CD3 $\zeta$  phosphorylation as well as Lck association, and showed that abrogation of these features reduced CAR signal intensity. Thus, future analyses of novel CAR designs should consider how interactions with potential binding partners might affect signaling.

Our data also showed that the more rapid and intense phosphoprotein signaling in CD28/CD3 $\zeta$  CAR T cells induced an effector cell-like transcriptional profile and more robust T cell cytokine production early after CAR ligation, but less potent antitumor function in an *in vivo* tumor model of disseminated lymphoma. These data are consistent with previous findings that intense TCR signaling and IL-2 production promote differentiation of short-lived effector CD8<sup>+</sup> T cells (54, 55), and also support a model by which TCR and costimulatory signals sum linearly to affect cell fate (45). Some amount of CD28 signaling is beneficial for T cell memory formation (56), and we found that the 4-1BB/CD3 $\zeta$  CARs used in this study phosphorylated endogenous CD28 and activated the CD28 signaling pathway. However, encoding a fully functional CD28 signaling domain on a CAR polypeptide chain may yield excessive stimulation that increases the incidence of CRS, promotes T cell exhaustion, and reduces persistence. Indeed, analyses of acute lymphoblastic leukemia patients who were in morphologic relapse at the time of treatment with

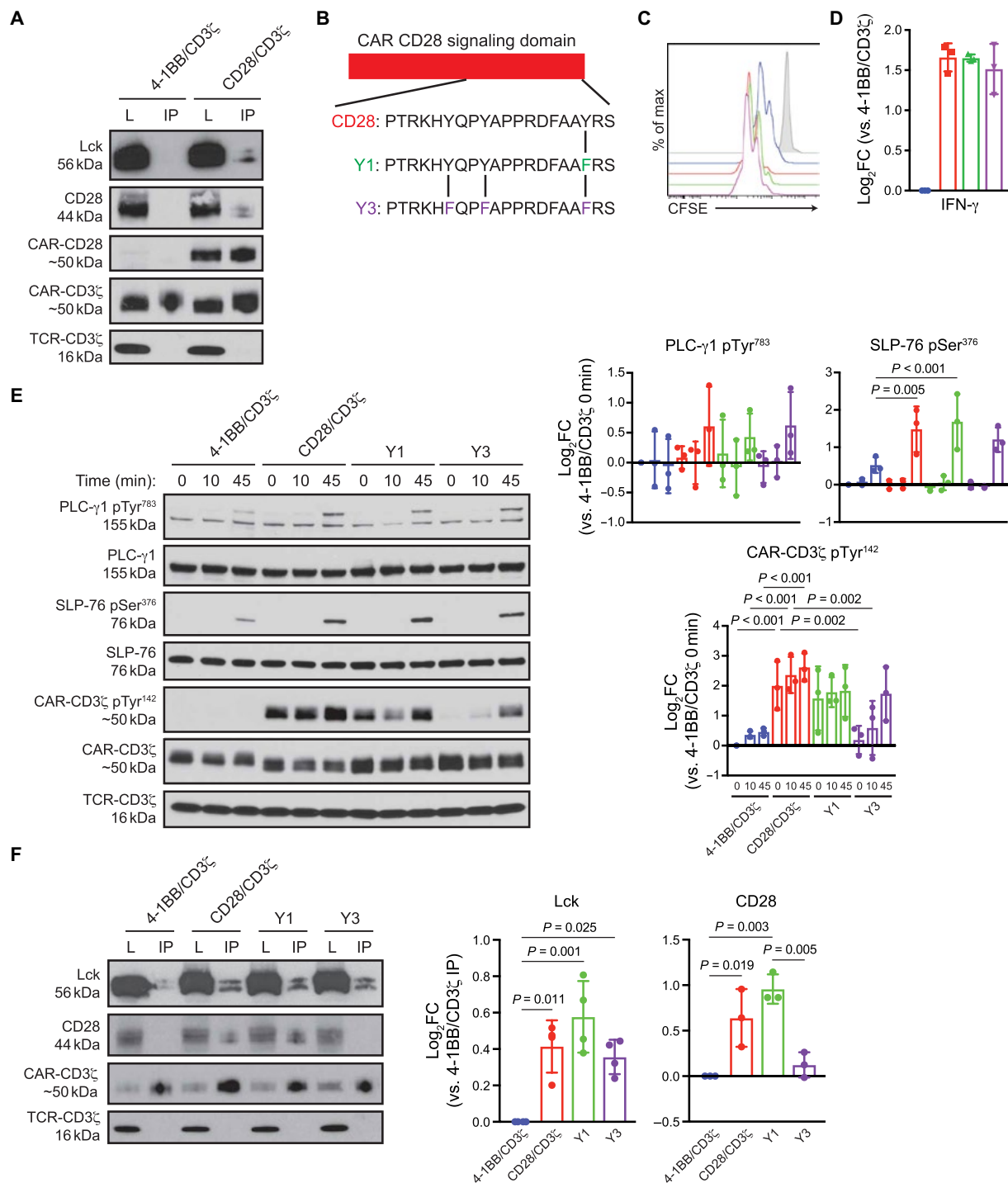


**Fig. 6. CD28/CD3 $\zeta$  and 4-1BB/CD3 $\zeta$  CARs differentially associate with endogenous Lck and CD28.** (A) Western blot analysis for Lck, CD28, and CD3 $\zeta$  in whole-cell lysates (L) and STII immunoprecipitated fractions (IP) from unstimulated ROR1-specific CAR T cells. Blots are representative of three to four independent experiments. (B) Schematic of mutations made to the CAR CD28 signaling domain. (C) Flow cytometry analysis of ROR1-specific CAR T cell proliferation as measured by CFSE dye dilution at 72 hours after coculture with K562/ROR1 cells. Histograms of untransduced T cells (gray) or 4-1BB/CD3 $\zeta$  (blue), CD28/CD3 $\zeta$  (red), Y1 (green), and Y3 CAR T cells (purple) after stimulation are representative of three independent experiments. (D) ELISA analysis of IFN- $\gamma$  production by ROR1-specific 4-1BB/CD3 $\zeta$  (blue), CD28/CD3 $\zeta$  (red), Y1 (green), or Y3 CAR T cells (purple) after coculture with K562/ROR1 cells for 24 hours. Fold change data are means  $\pm$  SD of three independent experiments. (E) Western blot analysis for CD3 $\zeta$ , CD3 $\zeta$  pTyr<sup>142</sup>, SLP-76, SLP-76 pSer<sup>376</sup>, PLC- $\gamma$ 1, and PLC- $\gamma$ 1 pTyr<sup>783</sup> in lysates from ROR1-specific CAR T cells stimulated for the indicated times with STII microbeads. Blots are representative of three independent experiments. Fold change data of normalized band intensity are means  $\pm$  SD from all experiments. (F) Western blot analysis for Lck, CD28, and CD3 $\zeta$  in whole-cell lysates (L) and STII immunoprecipitated fractions (IP) from resting CAR T cells. Blots are representative of at least three independent experiments. Fold change data of normalized band intensity are means  $\pm$  SD from three (CD28) or four (Lck) independent experiments. The indicated *P* values were calculated by repeated-measures one-way ANOVA with Tukey's multiple comparisons test comparing samples at equivalent time points (E and F).

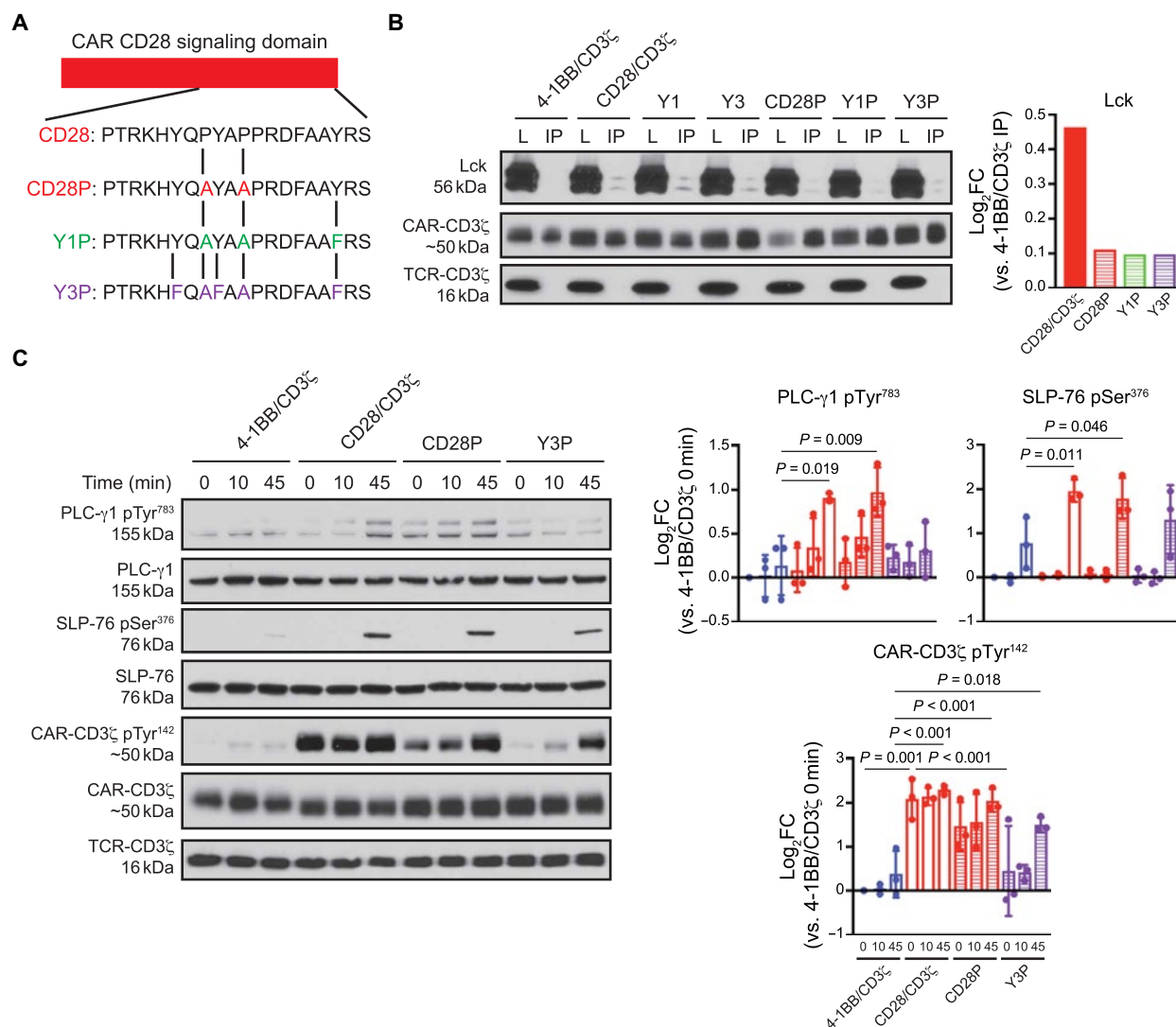


**Fig. 7. Mutations that reduce Lck binding diminish CD28/CD3 $\zeta$  CAR signal intensity.** (A) Schematic of mutations made to the CAR CD28 signaling domain. (B) Western blot analysis for Lck and CD3 $\zeta$  within whole-cell lysates (L) and STII immunoprecipitated fractions (IP) from resting CAR T cells. Blots and fold change in the normalized band intensity values are representative of two independent experiments. (C) Western blot analysis for CD3 $\zeta$ , CD3 $\zeta$  pTyr<sup>142</sup>, SLP-76, SLP-76 pSer<sup>376</sup>, PLC- $\gamma$ 1, and PLC- $\gamma$ 1 pTyr<sup>783</sup> within lysates from CAR T cells stimulated for the indicated times with STII microbeads. Blots are representative of three independent experiments. Fold change data in the normalized band intensity values are means  $\pm$  SD from all experiments. The indicated *P* values were calculated by repeated-measures one-way ANOVA with Tukey's multiple comparisons test comparing samples at equivalent time points (C).

CD28/CD3 $\zeta$  CAR T cells showed poor long-term CAR T cell persistence and low overall survival due to frequent relapse with CD19<sup>+</sup> disease (57).

CARs are often currently selected to maximize measures of in vitro T cell effector functions and proliferation, and our findings indicate that these selection criteria may not be optimal for predicting in vivo efficacy. Future optimizations to CAR design should consider both the signaling domains contained within the receptor, interactions with potential binding partners, and how modifications of costimulatory domains might tailor overall signal strength for downstream T cell functional outputs. Mutating the CAR CD28 signaling domain is a logical approach for reducing excessive signal strength, and further studies of mutated CAR signaling domains are warranted. However, variability in CAR structural features outside of the costimulatory CD28 or 4-1BB and CD3 $\zeta$  signaling do-

ains may limit the universality of this approach. Most CARs have a unique combination of scFv, hinge, and transmembrane domain, and this structural variation can affect CAR signaling and may alter association with endogenous T cell signaling molecules. For instance, the CAR CD28 transmembrane domain used in this study may have influenced association with endogenous CD28 and Lck. Further immunoprecipitation analysis of CARs with CD8 $\alpha$  transmembrane domains and other structural features could answer this question (3).

Our approach evaluating CD28/CD3 $\zeta$  and 4-1BB/CD3 $\zeta$  CAR signaling using a cell-free stimulation method has the advantage of identifying phosphorylation events induced by the synthetic receptors in isolation. Although this approach did not integrate the multitude of other events that may occur when CAR T cells encounter tumor cells in vivo (58), it could be extended to interrogate cross-talk between

CAR signaling and costimulatory or inhibitory pathways by immobilizing various ligands onto the magnetic beads. Our approach was also not designed to compare TCR and CAR signaling. A direct comparison of TCR and CAR ligation-induced phosphoprotein signaling is likely to be valuable and is a focus of ongoing research. Thus, MS analysis can provide important insights into CAR signaling that will affect next-generation CAR designs.

## MATERIALS AND METHODS

### Acquisition of peripheral blood T cells from healthy donors

Healthy adults (>18 years old) were enrolled in an institutional review board–approved study for peripheral blood collection. Informed consent was obtained from all enrollees. Researchers were blinded to all personally identifiable information about study participants and were provided only donor age and a nondescript donor ID number. Peripheral blood (400 cm<sup>3</sup>) was collected by venipuncture, and mononuclear cells [peripheral blood mononuclear cells (PBMCs)] were isolated by density gradient using Lymphocyte Separation Media (Corning). CD4<sup>+</sup> and CD8<sup>+</sup> T cells were isolated using the EasySep Human CD4<sup>+</sup> and CD8<sup>+</sup> T Cell Isolation Kits (STEMCELL Technologies). For the three shotgun MS experiments, CD8<sup>+</sup>CD62L<sup>+</sup> T cells were further enriched by staining with CD62L-PE (DREG-56, Thermo Fisher Scientific) followed by the EasySep Human PE Selection Kit (STEMCELL Technologies). Isolations were performed in accordance with the manufacturer's instructions.

### Cell culture

293T Lenti-X cells (Clontech) were cultured in Dulbecco's modified Eagle's medium (Gibco) supplemented with 10% fetal bovine serum, 1 mM L-glutamine (Gibco), 25 mM HEPES (Gibco), and penicillin/streptomycin (100 U/ml; Gibco). K562 (CCL-243) and Raji (CCL-86) cells were obtained from the American Type Culture Collection and cultured in RPMI 1640 (Gibco) supplemented with 5% fetal bovine serum, 1 mM L-glutamine, 25 mM HEPES, and penicillin/streptomycin (100 U/ml). Primary human T cells were cultured in CTL medium consisting of RPMI 1640 supplemented with 10% human serum, 2 mM L-glutamine, 25 mM HEPES, penicillin/streptomycin (100 U/ml), 50 μM β-mercaptoethanol (Sigma), and human IL-2 (50 U/ml; Prometheus). All cells were cultured at 37°C and 5% CO<sub>2</sub> and tested bimonthly for the absence of mycoplasma using the MycoAlert Mycoplasma Detection Kit (Lonza).

### Generation of CARs and recombinant lentiviral vectors

CD19- and ROR1-specific CAR constructs have been previously described (49, 59). For work in this study, a single STII sequence and two G<sub>4</sub>S linkers were inserted between the FMC63 or R12 scFv and immunoglobulin G<sub>4</sub> (IgG<sub>4</sub>) hinge (25). These were linked to the 27–amino acid transmembrane domain of human CD28 (UniProt: P10747) and to a signaling module comprising either (i) the 41–amino acid cytoplasmic domain of human CD28 with an LL→GG substitution located at positions 186 to 187 of the native CD28 protein (60) or (ii) the 42–amino acid cytoplasmic domain of human 4-1BB (UniProt: Q07011), each of which was linked to the 112–amino acid cytoplasmic domain of isoform 3 of human CD3ζ (UniProt: P20963-3). Mutant CD28/CD3ζ CARs with tyrosine to phenylalanine substitutions at CD28 UniProt positions 206, 209, and 218 and/or with proline to alanine substitutions at CD28 UniProt positions 208 and 211 were generated by site-directed mutagenesis. All CAR constructs were

linked by T2A sequence to EGFRt, codon-optimized, and cloned into an HIV7 lentiviral vector. For fluorescence microscopy, the CD3ζ endodomain was directly fused to enhanced green fluorescent protein (eGFP). To make CAR antigen-expressing K562 cells, amino acids 1 to 325 of human CD19 (UniProt: P15391) were cloned into an HIV7 lentiviral vector, and amino acids 1 to 937 of human ROR1 (UniProt: Q01973) were cloned into an mp71 retroviral vector, which was a gift of W. Uckert (Max Delbrück Center for Molecular Medicine). All cloning was performed by PCR, enzyme digest, and/or Gibson assembly. Plasmids were verified by capillary sequencing and restriction digest.

### Lentivirus preparation and transduction

To prepare CAR T cells, Lenti-X cells were transiently transfected with the HIV7 CAR vector, as well as psPAX2 (Addgene plasmid no. 12260) and pMD2.G (Addgene plasmid no. 12259) packaging plasmids. One day later (day 1), primary T cells were activated using Dynabeads Human T-Activator CD3/CD28 (Thermo Fisher Scientific) and cultured in CTL supplemented with IL-2 (50 U/ml). On the next day (day 2), lentiviral supernatant was harvested from Lenti-X cells, filtered using 0.45-μm polyethersulfone (PES) syringe filters (Millipore), and added to activated T cells. Polybrene (Millipore) was added to reach a final concentration of 4.4 μg/ml, and cells were spinoculated at 800g and 32°C for 90 min. Viral supernatant was replaced 8 hours later with fresh CTL supplemented with IL-2 (50 IU/ml). Half-media changes were then performed every 48 hours using CTL supplemented with IL-2 (50 U/ml). Dynabeads were removed on day 6; CD8<sup>+</sup>EGFRt<sup>+</sup>-transduced T cells were FACS (fluorescence-activated cell sorting)–purified on a FACSARIAII (BD Biosciences) on day 9.

To prepare K562/CD19 cells, Lenti-X cells were transiently transfected with psPAX2, pMD2.G, and an HIV7 lentiviral vector encoding CD19. To prepare K562/ROR1 cells, Lenti-X cells were transiently transfected with MLV g/p, 10A1, and an mp71 retroviral vector encoding ROR1. To prepare Raji/ffluc cells, Lenti-X cells were transiently transfected with psPAX2, pMD2.G, and an HIV7 lentiviral vector encoding GFP and firefly luciferase. Two days later, viral supernatant was filtered using a 0.45-μm PES syringe filter and added to K562 or Raji cells. Five days later, transduced cells were stained with mAbs specific for CD19 (HIB19, BioLegend) or ROR1 (2A2, Miltenyi Biotec) and FACS-purified on a FACSARIA II to greater than 97% purity.

### T cell expansion for MS and functional analyses

FACS-purified CD8<sup>+</sup>EGFRt<sup>+</sup> cells were expanded over a single stimulation cycle before MS and/or functional analyses. CD19-specific CAR T cells were expanded by coculture with irradiated CD19<sup>+</sup> lymphoblastoid cell lines (LCLs) in a 1:7 (T cell/LCL) ratio and assayed 8 days after stimulation. ROR1-specific CAR T cells were expanded using a rapid expansion protocol containing purified OKT3, irradiated LCL, and irradiated PBMCs and were assayed 11 days after stimulation. During expansion, cultures were fed with fresh CTL media containing IL-2 (50 IU/ml) every 2 to 3 days.

### Flow cytometry and cell phenotyping

T cells were stained with a 1:100 dilution of fluorophore-conjugated mAbs specific for human CD4 (RPA-T4), CD8 (SK1), CD27 (M-T271), CD28 (CD28.2), CD45 (HI30), CD45RO (UCHL1), CD62L (DREG-56), CD223 (3DS223H), CD279 (eBioJ105), or CD366 (F38-2E2) purchased from BD Biosciences, Thermo Fisher Scientific, or BioLegend. T cells

were also stained with isotype control fluorophore-conjugated antibodies when appropriate. Cetuximab (anti-EGFR, Bristol-Myers Squibb) and 3E8 [anti-STII, Fred Hutchinson Cancer Research Center (FHCRC)] were biotinylated using the EZ-Link Sulfo-NHS-Biotin Kit (Thermo Fisher Scientific) followed by cleanup with the Zeba Spin Desalting Column (Thermo Fisher Scientific) and used to stain T cells in conjunction with streptavidin-allophycocyanin (Thermo Fisher Scientific). DNA content staining was performed by fixing T cells with 70% ice-cold ethanol, permeabilizing cells with 1% Triton X-100 (Sigma), degrading RNA with ribonuclease A (100  $\mu\text{g}/\text{ml}$ ; Thermo Fisher Scientific), and staining DNA with propidium iodide (20  $\mu\text{g}/\text{ml}$ ; Thermo Fisher Scientific). All data were collected on a FACSCanto II or FACSAria II (BD Biosciences).

### STII and control microbead preparation

Streptavidin-coated magnetic particles (1 ml; Spherotech) were washed once in excess  $1\times$  PBS supplemented with penicillin/streptomycin (100 U/ml) (PBS + P/S) using a benchtop magnet. STII microbeads were prepared by resuspending beads in PBS + P/S (1 ml) and then slowly adding 16.67  $\mu\text{g}$  of STII biotin mAb (GenScript) while vortexing. Beads were incubated overnight at 4°C on a three-dimensional orbital shaker, washed three times with excess PBS + P/S using a benchtop magnet, and resuspended in PBS + P/S (4 ml). To make control beads, streptavidin-coated magnetic particles (1 ml) were washed once using a benchtop magnet and resuspended in PBS + P/S (4 ml). Beads were stored at 4°C.

### Cell stimulations, protein lysates, and RNA isolation

CAR T cells were washed and resuspended in warm CTL medium at a concentration of  $2 \times 10^7$  cells/ml. Cells were then incubated with STII or control microbeads at a ratio of 30  $\mu\text{l}$  of beads per  $1 \times 10^6$  cells in a 37°C water bath. After the allotted time, cells were quickly washed twice using ice-cold PBS and lysed in a 6 M urea, 25 mM tris (pH 8.0), 1 mM EDTA, 1 mM EGTA solution supplemented with protease (Sigma) and phosphatase inhibitors (Sigma) at a 1:100 dilution, hereon referred to as lysis buffer. Lysates were sonicated for 15 s before centrifuging at 10,000g and 4°C for 10 min. Beads were removed during lysate clearing. After 6 hours of stimulation, RNA isolations were performed using a NucleoSpin RNA kit (Macherey-Nagel) according to the manufacturer's instructions. Beads were removed using a benchtop magnet before cell lysis and RNA extraction.

### Protein digestion, TMT labeling, and pTyr peptide immunoprecipitation

Protein was quantified in lysates by Micro BCA Assay (Thermo Fisher Scientific), and lysates were diluted to 2 mg/ml using lysis buffer. Lysates were reduced in 24 mM TCEP [tris(2-carboxyethyl) phosphine hydrochloride] (Thermo Fisher Scientific) for 30 min at 37°C with shaking, followed by alkylation with 48 mM iodoacetamide (Sigma) in the dark at room temperature for 30 min. Lysates were then diluted with 200 mM tris (pH 8.0) to a urea concentration of 2 M. Lys-C (Wako) was dissolved in 25 mM tris (pH 8.0) at 200  $\mu\text{g}/\text{ml}$  and added to lysates at 1:100 (enzyme/protein) ratio by mass and incubated for 2 hours at 37°C with shaking. Samples were further diluted with 200 mM tris (pH 8.0) to a urea concentration of 1 M before adding trypsin at a 1:50 trypsin/protein ratio. After 2 hours, a second trypsin aliquot was added at a 1:100 trypsin/protein ratio. Digestion was carried out overnight at 37°C with shaking. After 16 hours, the reaction was quenched with formic acid (FA) to a final concentration of 1% by

volume. Samples were desalted using Oasis HLB 96-well plates (Waters) and a positive pressure manifold (Waters). The plate wells were washed with  $3 \times 400 \mu\text{l}$  of 50% MeCN/0.1% FA and then equilibrated with  $4 \times 400 \mu\text{l}$  of 0.1% FA. The digests were applied to the wells and then washed with  $4 \times 400 \mu\text{l}$  of 0.1% FA before being eluted drop by drop with  $3 \times 400 \mu\text{l}$  of 50% MeCN/0.1% FA. The eluates were lyophilized, followed by storage at  $-80^\circ\text{C}$  until use. For TMT labeling (Thermo Fisher Scientific), desalted peptides were resuspended in 50 mM Hepes at 1 mg/ml based on starting protein mass. TMT reagents were resuspended in 257  $\mu\text{l}$  of MeCN and transferred to the peptide sample. Samples were incubated at room temperature for 1 hour with mixing. Labeling reactions were quenched by the addition of 50  $\mu\text{l}$  of 5% hydroxyl amine (Sigma) and incubated for 15 min at room temperature with mixing. The independent labeling reactions were then pooled together and lyophilized. The labeled peptides were desalted as above and then lyophilized and stored at  $-80^\circ\text{C}$ . Immunoprecipitation of pTyr peptides was performed using the PTMScan P-Tyr-1000 Kit (Cell Signaling Technology). The enriched pTyr peptide fraction was purified using a C18 Spin Tip (Thermo Fisher Scientific), lyophilized, and stored at  $-80^\circ\text{C}$  until analysis. The flow-through fraction was desalted, lyophilized, and stored at  $-80^\circ\text{C}$ .

### Basic (high-pH) reversed-phase LC

The desalted and pTyr peptide-depleted flow-through was fractionated by high-pH reversed-phase (RP) LC. Protein digest (4 mg) was loaded onto an LC system consisting of an Agilent 1200 high-performance LC with mobile phases of 5 mM  $\text{NH}_4\text{HCO}_3$  (pH 10) (A) and 5 mM  $\text{NH}_4\text{HCO}_3$  in 90% MeCN (pH 10) (B). The peptides were separated by a 4.6 mm  $\times$  250 mm Zorbax Extend-C18, 3.5  $\mu\text{m}$ , column (Agilent) over 96 min at a flow rate of 1.0 ml/min by the following timetable: hold 0% B for 9 min, gradient from 0 to 10% B for 4 min, 10 to 28.5% B for 50 min, 28.5 to 34% B for 5.5 min, 34 to 60% B for 13 min, hold at 60% B for 8.5 min, 60 to 0% B for 1 min, reequilibrate at 0% B for 5 min. Fractions were collected at 1-min intervals from 0 to 96 min by the shortest path by row in a 1-ml deep well plate (Thermo Fisher Scientific). The high-pH RP fractions were concatenated into 24 samples by every other plate column starting at 15 min (for example, sample 1 contained fractions from wells B10, D10, F10, etc.). The remaining fractions were combined such that fractions from 12 to 14 min were added to sample 1, all fractions after 86 min were added to sample 24, and all fractions from 0 to 11 min were combined into sample "A." Ninety-five percent of every 12th fraction of the 24 samples was combined (1,13; 2,14;...) to generate 12 more samples, which were dried down and stored at  $-80^\circ\text{C}$  before phosphopeptide enrichment by IMAC.

### Immobilized metal affinity chromatography

IMAC enrichment was performed using Ni-NTA agarose beads (Qiagen) stripped with EDTA and incubated in a 10 mM  $\text{FeCl}_3$  solution to prepare  $\text{Fe}^{3+}$ -NTA agarose beads. Fractionated lysate was reconstituted in 200  $\mu\text{l}$  of 0.1% trifluoroacetic acid (TFA) in 80% MeCN and incubated for 30 min with 100  $\mu\text{l}$  of the 5% bead suspension while mixing at room temperature. After incubation, beads were washed three times with 300  $\mu\text{l}$  of 0.1% TFA in 80% MeCN. Phosphorylated peptides were eluted from the beads using 200  $\mu\text{l}$  of 70% acetonitrile, 1% ammonium hydroxide for 1 min with agitation at room temperature. Samples were transferred into a fresh tube containing 60  $\mu\text{l}$  of 10% FA, dried down, and resuspended in 0.1% FA and 3% MeCN. Samples were frozen at  $-80^\circ\text{C}$  until analysis.

### Nano-LC-MS/MS

Phosphopeptide-enriched samples were analyzed by LC-MS/MS on an Easy-nLC 1000 (Thermo Fisher Scientific) coupled to an LTQ-Orbitrap Fusion mass spectrometer (Thermo Fisher Scientific) operated in positive ion mode. The LC system, configured in a vented format, consisted of a fused-silica nanospray needle [PicoTip emitter, 50  $\mu$ m inside diameter (ID)  $\times$  20 cm, New Objective] packed in-house with ReproSil-Pur C18-AQ, 3  $\mu$ m, and a trap (IntegraFrit Capillary, 100  $\mu$ m ID  $\times$  2 cm, New Objective) containing the same resin as in the analytical column with mobile phases of 0.1% FA in water (A) and 0.1% FA in MeCN (B). The peptide sample was diluted in 20  $\mu$ l of 0.1% FA, 3% MeCN, and 8.5  $\mu$ l was loaded onto the column and separated over 210 min at a flow rate of 300 nl/min with a gradient from 5 to 7% B for 2 min, 7 to 35% B for 150 min, and 35 to 50% B for 1 min, hold 50% B for 9 min, 50 to 95% B for 2 min, hold 95% B for 7 min, 95 to 5% B for 1 min, reequilibrate at 5% B for 38 min. A spray voltage of 2000 V was applied to the nanospray tip. MS/MS analysis occurred over a 3-s cycle time consisting of one full-scan MS from 350 to 1500 mass/charge ratio ( $m/z$ ) at a resolution of 120,000, followed by data-dependent MS/MS scans using high-energy collision dissociation activation with 27% normalized collision energy of the most abundant ions. Selected ions were dynamically excluded for 45 s after a repeat count of 1.

### Immunoprecipitation

Protein G Dynabeads (Thermo Fisher Scientific) were incubated with anti-STII antibody (GenScript) for 60 min, cross-linked for 30 min using 20 mM dimethyl pimelimidate (Thermo Fisher Scientific) diluted in 200 mM triethanolamine (Thermo Fisher Scientific), quenched with 150 mM monoethanolamine (Thermo Fisher Scientific), and washed three times with 1 $\times$  PBS. T cells were lysed in NP40 Cell Lysis Buffer (Thermo Fisher Scientific) supplemented with protease and phosphatase inhibitors. Lysates were incubated on ice for 15 min and then centrifuged at 10,000g and 4°C for 10 min. Immunoprecipitations were performed according to the manufacturer's instructions, where Dynabeads were incubated with equal masses of cleared lysates for 90 min at room temperature.

### Western blotting

Equal masses of protein lysate or equal volumes of immunoprecipitation eluents were loaded into NuPAGE gels (Thermo Fisher Scientific). After protein transfer onto nitrocellulose membranes (Thermo Fisher Scientific), membranes were blocked with Western Blocking Reagent (Sigma). Membranes were stained with primary and secondary antibodies diluted in SuperBlock (Thermo Fisher Scientific) supplemented with 0.1% Tween. The following antibodies were used: anti-human CD247 (8D3, BD Biosciences), anti-human CD247 pTyr<sup>142</sup> (K25-407.69, BD Biosciences), anti-ZAP-70 pTyr<sup>319</sup> (65E4, Cell Signaling Technology), anti-SLP-76 (polyclonal, Cell Signaling Technology), anti-SLP-76 pSer<sup>376</sup> (D9D6E, Cell Signaling Technology), anti-PLC- $\gamma$ 1 (D9H10, Cell Signaling Technology), anti-PLC- $\gamma$ 1 pTyr<sup>783</sup> (D6M9S, Cell Signaling Technology), anti-DAPP1 (D9K4O, Cell Signaling Technology), anti-DAPP1 pTyr<sup>139</sup> (D7G4G, Cell Signaling Technology), anti-Lck (D88, Cell Signaling Technology), anti-CD28 (D2Z4E, Cell Signaling Technology), anti-mouse horseradish peroxidase (HRP) (polyclonal, Cell Signaling Technology), and anti-rabbit HRP (polyclonal, Cell Signaling Technology). Typical antibody dilutions ranged from 1:10,000 to 1:2500. Band intensities were quantified using ImageJ [National Institutes of Health (NIH)]; normalized to total protein, loading control, or immunoprecipitation input; and then renormalized to a control sample.

### RNA sequencing

RNA was extracted from 24 samples from three donors. Total RNA integrity was checked using an Agilent 4200 TapeStation (Agilent Technologies) and quantified using a Trinean DropSense96 spectrophotometer (Caliper Life Sciences). RNA-seq libraries were prepared from total RNA using the TruSeq RNA Sample Prep Kit v2 (Illumina) and a Sciclone NGSx Workstation (PerkinElmer). Library size distributions were validated using an Agilent 4200 TapeStation. Additional library quality control, blending of pooled indexed libraries, and cluster optimization were performed using a Qubit 2.0 Fluorometer (Thermo Fisher Scientific). RNA-seq libraries were pooled (6- to 8-plex) and clustered onto a flow cell lane. Sequencing was performed using an Illumina HiSeq 2500 in rapid mode using a paired-end, 50-base read length sequencing strategy.

### Quantitative polymerase chain reaction

RNA was extracted, and total RNA integrity was verified using an Agilent 4200 TapeStation (Agilent Technologies). RNA (500 ng) was used to prepare complementary DNA (cDNA) with SuperScript III (Thermo Fisher Scientific). cDNA (15 ng) was added to a reaction with TaqMan Universal Master Mix II with uracil N-glycosylase (Thermo Fisher Scientific) and one of the following Thermo Fisher Scientific TaqMan assay probes: Hs00172973\_m1 (*FOXO4*), Hs00902234\_m1 (*IL7R*), Hs00360439\_g1 (*KLF2*), or Hs99999907\_m1 (*B2M*). Reactions were run in duplicate or triplicate on one 384-well plate.  $\Delta C_t$  values were calculated by dividing mean  $C_t$  of technical replicates from *FOXO4*, *IL7R*, and *KLF2* probes by the mean  $C_t$  of the housekeeping gene  $\beta$ 2 microglobulin (*B2M*). CD28/CD3 $\zeta$  versus 4-1BB/CD3 $\zeta$  ratios for each donor were calculated and subjected to a log<sub>2</sub> transformation.

### In vitro functional assays

CAR T cells were cocultured with K562, K562/CD19, or K562/ROR1 cells at a T cell-to-tumor cell ratio of 2:1. In some experiments, CAR T cells were also incubated with control or STII microbeads at a ratio of 30  $\mu$ l of beads per 1  $\times$  10<sup>6</sup> cells. Cytokine concentrations in cellular supernatant were quantified by ELISA (Thermo Fisher Scientific) 24 hours after stimulation. T cell proliferation was quantified by staining CAR T cells with a 0.2  $\mu$ M solution of CFSE dye (Thermo Fisher Scientific) and incubating CAR T cells with K562/CD19 cells, K562/ROR1 cells, control beads, or STII microbeads for 72 hours.

### Transfer of T cells in NSG mice

Six- to 8-week-old male or female NSG mice were obtained from the Jackson Laboratory or bred in-house. Mice were engrafted via tail vein with 5  $\times$  10<sup>5</sup> CD19<sup>+</sup> Raji/ffluc cells and, 7 days later, injected intravenously with PBS or a defined product of purified CD8<sup>+</sup> and CD4<sup>+</sup> CD19-specific CAR T cells mixed together in a 1:1 ratio. Bioluminescence imaging was performed as described (49). Mice were either followed for survival or sacrificed on day 20 for analysis of T cell frequencies and phenotypes by flow cytometry. Peripheral blood was extracted, red blood cells were lysed using ACK Lysing Buffer (Thermo Fisher Scientific), and remaining cells were stained with fluorochrome-labeled mAbs. Bone marrow was isolated from hindlimbs by mechanical disruption, followed by red blood cell lysis, and staining with fluorochrome-labeled mAbs. Mice handlers were blinded to group allocation. The FHCRC Institutional Animal Care and Use Committee approved all experimental procedures.

### Fluorescence microscopy

CD8<sup>+</sup> T cells from healthy donors were transduced as previously described. Instead of FACS purification on day 9, cells were imaged on a DeltaVision Elite microscope (GE Healthcare). At least eight cells were visualized per condition. Raw images were subjected to a linear adjustment of brightness and contrast using ImageJ (NIH).

### Shotgun MS data analysis

Raw MS/MS spectra from each replicate experiment were searched together against the reviewed Human Universal Protein Resource (UniProt) sequence database (release 2016\_01) with common laboratory contaminants using the MaxQuant/Andromeda search engine version 1.6.0.1 (61). The search was performed with a tryptic enzyme constraint for up to two missed cleavages. Variable modifications were oxidized methionine, pSer, pThr, and pTyr. Carbamidomethylated cysteine was set as a static modification. Peptide MH<sup>+</sup> mass tolerances were set at 20 parts per million (ppm). The overall FDR was set at ≤1% using a reverse database target decoy approach.

For the three TMT experiments, phosphopeptide site localization was determined by MaxQuant and converted to phosphorylation sites using Perseus version 1.6.0.7 (62). At this step, reverse hits and potential contaminants were excluded from further analysis. Data normalization was performed by scaling each TMT channel to the channel median, followed by a log<sub>2</sub> transformation. Stimulation versus control ratios were calculated by subtracting the appropriate control channels from stimulated channels. Because of incomplete MS sampling, some phosphorylation sites (features) were only found in one or two replicate experiments, and a much smaller minority (<1%) of sites were not found in every TMT channel.

Differential expression analyses over phosphorylation sites were performed using the limma statistical framework and associated R package (35, 63). For these analyses, we chose to keep only features that had values in at least two experiments and all TMT channels, leaving us with 14,490 quantified phosphorylation sites. A linear model was fitted to each phosphorylation site, and empirical Bayes moderated *t* statistics were used to assess differences in expression/abundance. Contrasts comparing stimulation versus control treatments were tested. Intraclass correlations were estimated using the duplicate correlation function of the limma package to account for measures originating from the same patients and the same antigens (64). An absolute log<sub>2</sub>FC cutoff (stimulation versus control) of 0.7 and an FDR cutoff of 5% were used to determine differentially expressed phosphorylation sites. Analyses of signaling networks and KEGG pathways were performed using StringDB.

### RNA-seq data analysis

Image analysis and base calling were performed using Illumina's Real Time Analysis v1.18 software, followed by "demultiplexing" of indexed reads and generation of FASTQ files, using Illumina's bcl2fastq Conversion Software v1.8.4. The RNA-seq data were aligned to the human genome (University of California, Santa Cruz Human Genome Assembly GRCh38 reference) using STAR (Spliced Transcripts Alignment to a Reference), and gene quantification was performed using RSEM (RNA-Seq by Expectation Maximization) (65, 66). Genes with less than 10 nonzero read counts (taking into account technical replicates) were discarded, leaving 18,498 expressed genes. All libraries passed the quality control criteria (libraries with more than 200,000 reads, 12,000 detected genes, and an exon range > 60%). Raw count data were imported into R. edgeR was used to calculate the normaliza-

tion factors to scale the raw library sizes, followed by a voom transformation from the limma Bioconductor package (67, 68). It transforms count data to log<sub>2</sub> counts per million and estimates the mean-variance relationship to compute appropriate observation-level weights. Linear models with subject random effects were again used for differential gene expression analysis as described in the "Shotgun MS data analysis" section. Contrasts comparing treatments (control versus stimulation) or CARs (CD28/CD3ζ versus 4-1BB/CD3ζ) were tested. An absolute log<sub>2</sub>FC cutoff of 1 and an FDR cutoff of 1% were used to determine differentially expressed genes.

### Analysis of T cell phenotype, function, and in vivo experiments

FlowJo version 9 (Tree Star) was used to analyze flow cytometry files and calculate proliferation indices. Prism version 7 (GraphPad Software) was used to plot data and calculate statistics. *P* values meeting an  $\alpha = 0.05$  level of statistical significance are indicated in the figures. The precise statistical tests used are indicated in the figure legends.

### SUPPLEMENTARY MATERIALS

www.sciencesignaling.org/cgi/content/full/11/544/eaat6753/DC1

Fig. S1. CAR designs containing an STII sequence enable selective activation of CAR signaling in primary T cells.

Fig. S2. CD19- and ROR1-specific CD28/CD3ζ and 4-1BB/CD3ζ CARs signal similarly in CD4<sup>+</sup> T cells and are uniformly expressed on the cell surface.

Fig. S3. Log<sub>2</sub>FC summary statistics.

Fig. S4. Mutations to the CAR CD28 domain abrogate Lck binding.

Table S1. CAR stimulation-responsive phosphorylation sites after 10 min.

Table S2. CAR stimulation-responsive phosphorylation sites after 45 min.

Table S3. KEGG pathways identified by StringDB after 45 min of CAR stimulation.

Table S4. Phosphorylation sites increased by CAR stimulation at 45 min.

Table S5. Differentially expressed genes between stimulated CD28/CD3ζ and 4-1BB/CD3ζ CAR T cells.

### REFERENCES AND NOTES

- M. Sadelain, I. Rivière, S. Riddell, Therapeutic T cell engineering. *Nature* **545**, 423–431 (2017).
- S. Srivastava, S. R. Riddell, Engineering CAR-T cells: Design concepts. *Trends Immunol.* **36**, 494–502 (2015).
- M. Kalos, B. L. Levine, D. L. Porter, S. Katz, S. A. Grupp, A. Bagg, C. H. June, T cells with chimeric antigen receptors have potent antitumor effects and can establish memory in patients with advanced leukemia. *Sci. Transl. Med.* **3**, 95ra73 (2011).
- S. L. Maude, N. Frey, P. A. Shaw, R. Aplenc, D. M. Barrett, N. J. Bunin, A. Chew, V. E. Gonzalez, Z. Zheng, S. F. Lacey, Y. D. Mahnke, J. J. Melenhorst, S. R. Rheingold, A. Shen, D. T. Teachey, B. L. Levine, C. H. June, D. L. Porter, S. A. Grupp, Chimeric antigen receptor T cells for sustained remissions in leukemia. *N. Engl. J. Med.* **371**, 1507–1517 (2014).
- M. L. Davila, I. Rivière, X. Wang, S. Bartido, J. Park, K. Curran, S. S. Chung, J. Stefanski, O. Borquez-Ojeda, M. Olszewska, J. Qu, T. Wasielewska, Q. He, M. Fink, H. Shinglot, M. Youssif, M. Satter, Y. Wang, J. Hosey, H. Quintanilla, E. Halton, Y. Bernal, D. C. G. Bouhassira, M. E. Arcila, M. Gonen, G. J. Roboz, P. Maslak, D. Douer, M. G. Frattini, S. Giral, M. Sadelain, R. Brentjens, Efficacy and toxicity management of 19-28z CAR T cell therapy in B cell acute lymphoblastic leukemia. *Sci. Transl. Med.* **6**, 224ra25 (2014).
- D. W. Lee, J. N. Kochenderfer, M. Stetler-Stevenson, Y. K. Cui, C. Delbrook, S. A. Feldman, T. J. Fry, R. Orentas, M. Sabatino, N. N. Shah, S. M. Steinberg, D. Stroncek, N. Tschernia, C. Yuan, H. Zhang, L. Zhang, S. A. Rosenberg, A. S. Wayne, C. L. Mackall, T cells expressing CD19 chimeric antigen receptors for acute lymphoblastic leukaemia in children and young adults: A phase 1 dose-escalation trial. *Lancet* **385**, 517–528 (2015).
- J. N. Kochenderfer, M. E. Dudley, S. H. Kassim, R. P. T. Somerville, R. O. Carpenter, M. Stetler-Stevenson, J. C. Yang, G. Q. Phan, M. S. Hughes, R. M. Sherry, M. Raffeld, S. Feldman, L. Lu, Y. F. Li, L. T. Ngo, A. Goy, T. Feldman, D. E. Spaner, M. L. Wang, C. C. Chen, S. M. Kranick, A. Nath, D.-A. N. Nathan, K. E. Morton, M. A. Toomey, S. A. Rosenberg, Chemotherapy-refractory diffuse large B-cell lymphoma and indolent B-cell malignancies can be effectively treated with autologous T cells expressing an anti-CD19 chimeric antigen receptor. *J. Clin. Oncol.* **33**, 540–549 (2015).
- C. J. Turtle, L.-A. Hanafi, C. Berger, T. A. Gooley, S. Cheria, M. Hudecek, D. Sommermeyer, K. Melville, B. Pender, T. M. Budiarto, E. Robinson, N. N. Steevens, C. Chaney, L. Soma,

- X. Chen, C. Yeung, B. Wood, D. Li, J. Cao, S. Heimfeld, M. C. Jensen, S. R. Riddell, D. G. Maloney, CD19 CAR-T cells of defined CD4<sup>+</sup>:CD8<sup>+</sup> composition in adult B cell ALL patients. *J. Clin. Invest.* **126**, 2123–2138 (2016).
9. C. J. Turtle, L.-A. Hanafi, C. Berger, M. Hudecek, B. Pender, E. Robinson, R. Hawkins, C. Chaney, S. Cherian, X. Chen, L. Soma, B. Wood, D. Li, S. Heimfeld, S. R. Riddell, D. G. Maloney, Immunotherapy of non-Hodgkin's lymphoma with a defined ratio of CD8<sup>+</sup> and CD4<sup>+</sup> CD19-specific chimeric antigen receptor-modified T cells. *Sci. Transl. Med.* **8**, 355ra116 (2016).
  10. C. J. Turtle, K. A. Hay, L.-A. Hanafi, D. Li, S. Cherian, X. Chen, B. Wood, A. Lozanski, J. C. Byrd, S. Heimfeld, D. G. Maloney, Durable molecular remissions in chronic lymphocytic leukemia treated with CD19-specific chimeric antigen receptor-modified T cells after failure of ibrutinib. *J. Clin. Oncol.* **35**, 3010–3020 (2017).
  11. K. A. Hay, L.-A. Hanafi, D. Li, J. Gust, W. C. Liles, M. M. Wurfel, J. A. López, J. Chen, D. Chung, S. Harju-Baker, S. Cherian, X. Chen, S. R. Riddell, D. G. Maloney, C. J. Turtle, Kinetics and biomarkers of severe cytokine release syndrome after CD19 chimeric antigen receptor-modified T-cell therapy. *Blood* **130**, 2295–2306 (2017).
  12. J. Gust, K. A. Hay, L.-A. Hanafi, D. Li, D. Myerson, L. F. Gonzalez-Cuyar, C. Yeung, W. C. Liles, M. Wurfel, J. A. Lopez, J. Chen, D. Chung, S. Harju-Baker, T. Özpolat, K. R. Fink, S. R. Riddell, D. G. Maloney, C. J. Turtle, Endothelial activation and blood-brain barrier disruption in neurotoxicity after adoptive immunotherapy with CD19 CAR-T cells. *Cancer Discov.* **7**, 1404–1419 (2017).
  13. R. J. Brownlie, R. Zamojska, T cell receptor signalling networks: Branched, diversified and bounded. *Nat. Rev. Immunol.* **13**, 257–269 (2013).
  14. S. S. Neelapu, F. L. Locke, N. L. Bartlett, L. J. Lekakis, D. B. Miklos, C. A. Jacobson, I. Braunschweig, O. O. Oluwole, T. Siddiqi, Y. Lin, J. M. Timmerman, P. J. Stiff, J. W. Friedberg, I. W. Flinn, A. Goy, B. T. Hill, M. R. Smith, A. Deol, U. Farooq, P. McSweeney, J. Munoz, I. Avivi, J. E. Castro, J. R. Westin, J. C. Chavez, A. Ghobadi, K. V. Komanduri, R. Levy, E. D. Jacobsen, T. E. Witzig, P. Reagan, A. Bot, J. Rossi, L. Navale, Y. Jiang, J. Aycock, M. Elias, D. Chang, J. Wieszorek, W. Y. Go, Axicabtagene ciloleucel CAR T-cell therapy in refractory large B-cell lymphoma. *N. Engl. J. Med.* **377**, 2531–2544 (2017).
  15. S. L. Maude, T. W. Laetsch, J. Buechner, S. Rives, M. Boyer, H. Bittencourt, P. Bader, M. R. Verneris, H. E. Stefanski, G. D. Myers, M. Qayed, B. De Moerloose, H. Hiramatsu, K. Schlis, K. L. Davis, P. L. Martin, E. R. Nemecek, G. A. Yanik, C. Peters, A. Baruchel, N. Boissel, F. Mechinaud, A. Balduzzi, J. Krueger, C. H. June, B. L. Levine, P. Wood, T. Taran, M. Leung, K. T. Mueller, Y. Zhang, K. Sen, D. Leibold, M. A. Pulsipher, S. A. Grupp, Tisagenlecleucel in children and young adults with B-cell lymphoblastic leukemia. *N. Engl. J. Med.* **378**, 439–448 (2018).
  16. L. Cherkassky, A. Morello, J. Villena-Vargas, Y. Feng, D. S. Dimitrov, D. R. Jones, M. Sadelain, P. S. Adusumilli, Human CAR T cells with cell-intrinsic PD-1 checkpoint blockade resist tumor-mediated inhibition. *J. Clin. Invest.* **126**, 3130–3144 (2016).
  17. O. U. Kawalekar, R. S. O'Connor, J. A. Fraietta, L. Guo, S. E. McGettigan, A. D. Posey Jr., P. R. Patel, S. Guedan, J. Scholler, B. Keith, N. W. Snyder, I. A. Blair, M. C. Milone, C. H. June, Distinct signaling of coreceptors regulates specific metabolism pathways and impacts memory development in CAR T Cells. *Immunity* **44**, 380–390 (2016).
  18. S. Terakura, T. N. Yamamoto, R. A. Gardner, C. J. Turtle, M. C. Jensen, S. R. Riddell, Generation of CD19-chimeric antigen receptor modified CD8<sup>+</sup> T cells derived from virus-specific central memory T cells. *Blood* **119**, 72–82 (2012).
  19. H. Karlsson, E. Svensson, C. Gigg, M. Jarvius, U. Olsson-Strömberg, B. Savoldo, G. Dotti, A. Loskog, Evaluation of intracellular signaling downstream chimeric antigen receptors. *PLoS ONE* **10**, e0144787 (2015).
  20. V. Mayya, D. H. Lundgren, S.-I. Hwang, K. Rezaul, L. Wu, J. K. Eng, V. Rodionov, D. K. Han, Quantitative phosphoproteomic analysis of T cell receptor signaling reveals system-wide modulation of protein-protein interactions. *Sci. Signal.* **2**, ra46 (2009).
  21. V. Nguyen, L. Cao, J. T. Lin, N. Hung, A. Ritz, K. Yu, R. Jianu, S. P. Ulin, B. J. Raphael, D. H. Laidlaw, L. Brossay, A. R. Salomon, A new approach for quantitative phosphoproteomic dissection of signaling pathways applied to T cell receptor activation. *Mol. Cell. Proteomics* **8**, 2418–2431 (2009).
  22. M. N. Navarro, J. Goebel, C. Feijoo-Carnero, N. Morrice, D. A. Cantrell, Phosphoproteomic analysis reveals an intrinsic pathway for the regulation of histone deacetylase 7 that controls the function of cytotoxic T lymphocytes. *Nat. Immunol.* **12**, 352–361 (2011).
  23. P. Ruperez, A. Gago-Martinez, A. L. Burlingame, J. A. Osés-Prieto, Quantitative phosphoproteomic analysis reveals a role for serine and threonine kinases in the cytoskeletal reorganization in early T cell receptor activation in human primary T cells. *Mol. Cell. Proteomics* **11**, 171–186 (2012).
  24. M. Salek, S. McGowan, D. C. Trudgian, O. Dushek, B. de Wet, G. Efsthathiou, O. Acuto, Quantitative phosphoproteome analysis unveils LAT as a modulator of CD3ζ and ZAP-70 tyrosine phosphorylation. *PLoS ONE* **8**, e77423 (2013).
  25. L. Liu, D. Sommermeyer, A. Cabanov, P. Kosasih, T. Hill, S. R. Riddell, Inclusion of Strep-tag II in design of antigen receptors for T-cell immunotherapy. *Nat. Biotechnol.* **34**, 430–434 (2016).
  26. X. Wang, W.-C. Chang, C. W. Wong, D. Colcher, M. Sherman, J. R. Ostberg, S. J. Forman, S. R. Riddell, M. C. Jensen, A transgene-encoded cell surface polypeptide for selection, in vivo tracking, and ablation of engineered cells. *Blood* **118**, 1255–1263 (2011).
  27. A. Thompson, J. Schäfer, K. Kuhn, S. Kienle, J. Schwarz, G. Schmidt, T. Neumann, R. Johnstone, A. K. A. Mohammed, C. Hamon, Tandem mass tags: A novel quantification strategy for comparative analysis of complex protein mixtures by MS/MS. *Anal. Chem.* **75**, 1895–1904 (2003).
  28. A. Michalski, J. Cox, M. Mann, More than 100,000 detectable peptide species elute in single shotgun proteomics runs but the majority is inaccessible to data-dependent LC-MS/MS. *J. Proteome Res.* **10**, 1785–1793 (2011).
  29. N. S. van Oers, W. Tao, J. D. Watts, P. Johnson, R. Aebbersold, H. S. Teh, Constitutive tyrosine phosphorylation of the T-cell receptor (TCR) ζ subunit: Regulation of TCR-associated protein tyrosine kinase activity by TCR ζ. *Mol. Cell. Biol.* **13**, 5771–5780 (1993).
  30. D. Rueda, O. Gaide, L. Ho, E. Lewkowicz, F. Niedergang, S. Haifinger, F. Rebeaud, M. Guezardi, B. Conne, M. Thelen, J. Delon, U. Ferch, T. W. Mak, J. Ruland, J. Schwaller, M. Thome, Bcl10 controls TCR- and FcγR-induced actin polymerization. *J. Immunol.* **178**, 4373–4384 (2007).
  31. K. Ishiguro, T. Ando, H. Goto, R. Xavier, Bcl10 is phosphorylated on Ser138 by Ca<sup>2+</sup>/calmodulin-dependent protein kinase II. *Mol. Immunol.* **44**, 2095–2100 (2007).
  32. J. Eyquem, J. Mansilla-Soto, T. Giavridis, S. J. C. van der Stegen, M. Hamieh, K. M. Cunanan, A. Odak, M. Gönen, M. Sadelain, Targeting a CAR to the TRAC locus with CRISPR/Cas9 enhances tumour rejection. *Nature* **543**, 113–117 (2017).
  33. M. J. Frigault, J. Lee, M. C. Basil, C. Carpenito, S. Motoshashi, J. Scholler, O. U. Kawalekar, S. Guedan, S. E. McGettigan, A. D. Posey Jr., S. Ang, L. J. N. Cooper, J. M. Platt, F. B. Johnson, C. M. Paulos, Y. Zhao, M. Kalos, M. C. Milone, C. H. June, Identification of chimeric antigen receptors that mediate constitutive or inducible proliferation of T cells. *Cancer Immunol. Res.* **3**, 356–367 (2015).
  34. A. H. Long, W. M. Haso, J. F. Shern, K. M. Wanhainen, M. Murgai, M. Ingaramo, J. P. Smith, A. J. Walker, M. E. Kohler, V. R. Venkateshwarra, R. N. Kaplan, G. H. Patterson, T. J. Fry, R. J. Orentas, C. L. Mackall, 4-1BB costimulation ameliorates T cell exhaustion induced by tonic signaling of chimeric antigen receptors. *Nat. Med.* **21**, 581–590 (2015).
  35. G. K. Smyth, Linear models and empirical Bayes methods for assessing differential expression in microarray experiments. *Stat. Appl. Genet. Mol. Biol.* **3**, Article3 (2004).
  36. F. Sekiya, Y. S. Bae, D. Y. Jhon, S. C. Hwang, S. G. Rhee, AHNK1, a protein that binds and activates phospholipase C-γ1 in the presence of archidonic acid. *J. Biol. Chem.* **274**, 13900–13907 (1999).
  37. D. Matza, A. Badou, K. S. Kobayashi, K. Goldsmith-Pestana, Y. Masuda, A. Komuro, D. McMahon-Pratt, V. T. Marchesi, R. A. Flavell, A scaffold protein, AHNK1, is required for calcium signaling during T cell activation. *Immunity* **28**, 64–74 (2008).
  38. A. R. Sanchez-Paulete, S. Labiano, M. E. Rodriguez-Ruiz, A. Azpilikueta, I. Etxeberria, E. Bolaños, V. Lang, M. Rodriguez, M. A. Aznar, M. Jure-Kunkel, I. Melero, Deciphering CD137 (4-1BB) signaling in T-cell costimulation for translation into successful cancer immunotherapy. *Eur. J. Immunol.* **46**, 513–522 (2016).
  39. J. S. Boomer, J. M. Green, An enigmatic tail of CD28 signaling. *Cold Spring Harb. Perspect. Biol.* **2**, a002436 (2010).
  40. L. Sabbagh, D. Andreeva, G. D. Laramée, N. A. E. Oussa, D. Lew, N. Bisson, Y. Soumounou, T. Pawson, T. H. Watts, Leukocyte-specific protein 1 links TNF receptor-associated factor 1 to survival signaling downstream of 4-1BB in T cells. *J. Leukoc. Biol.* **93**, 713–721 (2013).
  41. F. Baixauli, N. B. Martín-Cófreces, G. Morlino, Y. R. Carrasco, C. Calabia-Linares, E. Veiga, J. M. Serrador, F. Sánchez-Madrid, The mitochondrial fission factor dynamin-related protein 1 modulates T-cell receptor signalling at the immune synapse. *EMBO J.* **30**, 1238–1250 (2011).
  42. D. Röth, P. H. Krammer, K. Gülow, Dynamin related protein 1-dependent mitochondrial fission regulates oxidative signalling in T cells. *FEBS Lett.* **588**, 1749–1754 (2014).
  43. M. A. Daniels, E. Teixeira, TCR signaling in T cell memory. *Front. Immunol.* **6**, 617 (2015).
  44. S. M. Kaech, W. Cui, Transcriptional control of effector and memory CD8<sup>+</sup> T cell differentiation. *Nat. Rev. Immunol.* **12**, 749–761 (2012).
  45. J. M. Marchingo, A. Kan, R. M. Sutherland, K. R. Duffy, C. J. Wellard, G. T. Belz, A. M. Lew, M. R. Dowling, S. Heinzl, P. D. Hodgkin, Antigen affinity, costimulation, and cytokine inputs sum linearly to amplify T cell expansion. *Science* **346**, 1123–1127 (2014).
  46. P. Rougerie, Q. Largeteau, L. Megrelis, F. Carrette, T. Lejeune, L. Toffali, B. Rossi, M. Zeghouf, J. Cherfils, G. Constantin, C. Laudanna, G. Bismuth, M. Mangeney, J. Delon, Fam65b is a new transcriptional target of FOXO1 that regulates RhoA signaling for T lymphocyte migration. *J. Immunol.* **190**, 748–755 (2013).
  47. S. M. Kaech, J. T. Tan, E. J. Wherry, B. T. Konieczny, C. D. Surh, R. Ahmed, Selective expression of the interleukin 7 receptor identifies effector CD8 T cells that give rise to long-lived memory cells. *Nat. Immunol.* **4**, 1191–1198 (2003).
  48. Y. M. Kerdiles, D. R. Beisner, R. Tinoco, A. S. Dejean, D. H. Castrillon, R. A. DePinho, S. M. Hedrick, Foxo1 links homing and survival of naive T cells by regulating L-selectin, CCR7 and interleukin 7 receptor. *Nat. Immunol.* **10**, 176–184 (2009).

49. D. Sommermeyer, M. Hudecek, P. L. Kosasih, T. Gogishvili, D. G. Maloney, C. J. Turtle, S. R. Riddell, Chimeric antigen receptor-modified T cells derived from defined CD8<sup>+</sup> and CD4<sup>+</sup> subsets confer superior antitumor reactivity in vivo. *Leukemia* **30**, 492–500 (2016).
50. D. Moogk, S. Zhong, Z. Yu, I. Liadi, W. Rittase, V. Fang, J. Dougherty, A. Perez-Garcia, I. Osman, C. Zhu, N. Varadarajan, N. P. Restifo, A. B. Frey, M. Krogsgaard, Constitutive Lck activity drives sensitivity differences between CD8<sup>+</sup> memory T cell subsets. *J. Immunol.* **197**, 644–654 (2016).
51. K. Nika, C. Soldani, M. Salek, W. Paster, A. Gray, R. Etzensperger, L. Fugger, P. Polzella, V. Cerundolo, O. Dushek, T. Höfer, A. Viola, O. Acuto, Constitutively active Lck kinase in T cells drives antigen receptor signal transduction. *Immunity* **32**, 766–777 (2010).
52. J. Dobbins, E. Gagnon, J. Godec, J. Pyrdol, D. A. A. Vignali, A. H. Sharpe, K. W. Wucherpfennig, Binding of the cytoplasmic domain of CD28 to the plasma membrane inhibits Lck recruitment and signaling. *Sci. Signal.* **9**, ra75 (2016).
53. R. Tavano, G. Gri, B. Molon, B. Marinari, C. E. Rudd, L. Tuosto, A. Viola, CD28 and lipid rafts coordinate recruitment of Lck to the immunological synapse of human T lymphocytes. *J. Immunol.* **173**, 5392–5397 (2004).
54. V. Kalia, S. Sarkar, S. Subramaniam, W. N. Haining, K. A. Smith, R. Ahmed, Prolonged interleukin-2Ralpha expression on virus-specific CD8<sup>+</sup> T cells favors terminal-effector differentiation in vivo. *Immunity* **32**, 91–103 (2010).
55. M. E. Pipkin, J. A. Sacks, F. Cruz-Guilloty, M. G. Lichtenheld, M. J. Bevan, A. Rao, Interleukin-2 and inflammation induce distinct transcriptional programs that promote the differentiation of effector cytolytic T cells. *Immunity* **32**, 79–90 (2010).
56. R. I. Klein Geltink, D. O'Sullivan, M. Corrado, A. Bremser, M. D. Buck, J. M. Buescher, E. Firat, X. Zhu, G. Niedermann, G. Caputa, B. Kelly, U. Warthorst, A. Rensing-Ehl, R. L. Kyle, L. Vandersarren, J. D. Curtis, A. E. Patterson, S. Lawless, K. Grzes, J. Qiu, D. E. Sanin, O. Kretz, T. B. Huber, S. Janssens, B. N. Lambrecht, A. S. Rambold, E. J. Pearce, E. L. Pearce, Mitochondrial priming by CD28. *Cell* **171**, 385–397.e11 (2017).
57. J. H. Park, I. Rivière, M. Gonen, X. Wang, B. Sénéchal, K. J. Curran, C. Sauter, Y. Wang, B. Santomasso, E. Mead, M. Roshal, P. Maslak, M. Davila, R. J. Brentjens, M. Sadelain, Long-term follow-up of CD19 CAR therapy in acute lymphoblastic leukemia. *N. Engl. J. Med.* **378**, 449–459 (2018).
58. M. E. Keir, M. J. Butte, G. J. Freeman, A. H. Sharpe, PD-1 and its ligands in tolerance and immunity. *Annu. Rev. Immunol.* **26**, 677–704 (2008).
59. M. Hudecek, M.-T. Lupo-Stanghellini, P. L. Kosasih, D. Sommermeyer, M. C. Jensen, C. Rader, S. R. Riddell, Receptor affinity and extracellular domain modifications affect tumor recognition by ROR1-specific chimeric antigen receptor T cells. *Clin. Cancer Res.* **19**, 3153–3164 (2013).
60. P. Nguyen, I. Moisini, T. L. Geiger, Identification of a murine CD28 dileucine motif that suppresses single-chain chimeric T-cell receptor expression and function. *Blood* **102**, 4320–4325 (2003).
61. J. Cox, M. Mann, MaxQuant enables high peptide identification rates, individualized p.p.b.-range mass accuracies and proteome-wide protein quantification. *Nat. Biotechnol.* **26**, 1367–1372 (2008).
62. S. Tyanova, T. Temu, P. Sinitcyn, A. Carlson, M. Y. Hein, T. Geiger, M. Mann, J. Cox, The Perseus computational platform for comprehensive analysis of (prote)omics data. *Nat. Methods* **13**, 731–740 (2016).
63. M. E. Ritchie, B. Phipson, D. Wu, Y. Hu, C. W. Law, W. Shi, G. K. Smyth, limma powers differential expression analyses for RNA-sequencing and microarray studies. *Nucleic Acids Res.* **43**, e47 (2015).
64. G. K. Smyth, J. Michaud, H. S. Scott, Use of within-array replicate spots for assessing differential expression in microarray experiments. *Bioinformatics* **21**, 2067–2075 (2005).
65. A. Dobin, C. A. Davis, F. Schlesinger, J. Drenkow, C. Zaleski, S. Jha, P. Batut, M. Chaisson, T. R. Gingeras, STAR: Ultrafast universal RNA-seq aligner. *Bioinformatics* **29**, 15–21 (2013).
66. B. Li, C. N. Dewey, RSEM: Accurate transcript quantification from RNA-seq data with or without a reference genome. *BMC Bioinformatics* **12**, 323 (2011).
67. M. D. Robinson, A. Oshlack, A scaling normalization method for differential expression analysis of RNA-seq data. *Genome Biol.* **11**, R25 (2010).
68. C. W. Law, Y. Chen, W. Shi, G. K. Smyth, voom: Precision weights unlock linear model analysis tools for RNA-seq read counts. *Genome Biol.* **15**, R29 (2014).

**Acknowledgments:** We thank the M.J. Murdock Charitable Trust and members of the FHCRC Proteomics Shared Resource for help in data acquisition. We also thank D. E. S. Parrilla and M. Jess for performing mouse husbandry and tumor xenograft experiments. **Funding:** This research was supported by NIH (R01 #CA136551 and R01 #CA114536 to S.R.R., U01 #CA214114 to A.G.P., and R50 #CA211499 to J.R.W.) and FHCRC (Bezos Immunotherapy Pilot Award to A.G.P. and S.R.R. and Interdisciplinary Training in Cancer Research Training Grant support to A.I.S.). **Author contributions:** A.I.S., R.G.I., D.S., A.G.P., and S.R.R. designed the experiments. A.I.S., R.G.I., J.J.K., A.R., E.J.A., and U.J.V. conducted the experiments. V.V., C.L., J.R.W., J.J.K., and R.G. processed the data and wrote accompanying software. L.L. developed STII CAR technology and provided reagents. A.I.S. and R.G.I. performed formal data analysis. A.I.S. and S.R.R. wrote the manuscript. A.I.S., R.G.I., V.V., R.G., A.G.P., and S.R.R. edited the manuscript. A.G.P. and S.R.R. supervised all work. **Competing interests:** S.R.R. is a founder, shareholder, and scientific advisor of Juno Therapeutics. R.G. is a consultant for Juno Therapeutics. STII CAR technology used in this study is licensed to Juno Therapeutics. A.I.S. and S.R.R. have filed a provisional patent application number 62/635,450 covering applications of mutant CD28 CARs for cellular therapy. The other authors declare that they have no competing interests. **Data and materials availability:** LC-MS/MS proteomics data have been deposited to the ProteomeXchange Consortium via the PRIDE partner repository with the data set identifier PXD007921. RNA-seq data have been deposited in the National Center for Biotechnology Information Gene Expression Omnibus (GEO) under accession number 109161. All other data needed to evaluate the conclusions in the paper are present in the paper or the Supplementary Materials.

Submitted 12 December 2017  
 Resubmitted 23 March 2018  
 Accepted 1 August 2018  
 Published 21 August 2018  
 10.1126/scisignal.aat6753

**Citation:** A. I. Salter, R. G. Ivey, J. J. Kennedy, V. Voillet, A. Rajan, E. J. Alderman, U. J. Voytovich, C. Lin, D. Sommermeyer, L. Liu, J. R. Whiteaker, R. Gottardo, A. G. Paulovich, S. R. Riddell, Phosphoproteomic analysis of chimeric antigen receptor signaling reveals kinetic and quantitative differences that affect cell function. *Sci. Signal.* **11**, eaat6753 (2018).

## PEDIATRICS

# Recurrent group A *Streptococcus* tonsillitis is an immunosusceptibility disease involving antibody deficiency and aberrant T<sub>FH</sub> cells

Jennifer M. Dan<sup>1,2</sup>, Colin Havenar-Daughton<sup>1,3</sup>, Kayla Kendric<sup>1</sup>, Rita Al-kolla<sup>1</sup>, Kirti Kaushik<sup>1</sup>, Sandy L. Rosales<sup>1</sup>, Ericka L. Anderson<sup>4,5,6</sup>, Christopher N. LaRock<sup>4,5,7</sup>, Pandurangan Vijayanand<sup>1</sup>, Grégory Seumois<sup>1</sup>, David Layfield<sup>8</sup>, Ramsey I. Cutress<sup>8</sup>, Christian H. Ottensmeier<sup>8</sup>, Cecilia S. Lindestam Arlehamn<sup>1</sup>, Alessandro Sette<sup>1,2</sup>, Victor Nizet<sup>4,5</sup>, Marcella Bothwell<sup>9,10,11</sup>, Matthew Brigger<sup>9,10,11</sup>, Shane Crotty<sup>1,2,3\*</sup>

“Strep throat” is highly prevalent among children, yet it is unknown why only some children develop recurrent tonsillitis (RT), a common indication for tonsillectomy. To gain insights into this classic childhood disease, we performed phenotypic, genotypic, and functional studies on pediatric group A *Streptococcus* (GAS) RT and non-RT tonsils from two independent cohorts. GAS RT tonsils had smaller germinal centers, with an underrepresentation of GAS-specific CD4<sup>+</sup> germinal center T follicular helper (GC-T<sub>FH</sub>) cells. RT children exhibited reduced antibody responses to an important GAS virulence factor, streptococcal pyrogenic exotoxin A (SpeA). Risk and protective human leukocyte antigen (HLA) class II alleles for RT were identified. Lastly, SpeA induced granzyme B production in GC-T<sub>FH</sub> cells from RT tonsils with the capacity to kill B cells and the potential to hobble the germinal center response. These observations suggest that RT is a multifactorial disease and that contributors to RT susceptibility include HLA class II differences, aberrant SpeA-activated GC-T<sub>FH</sub> cells, and lower SpeA antibody titers.

## INTRODUCTION

“Strep throat” is one of the most prevalent human infections, with an estimated 600 million cases worldwide each year (1). Clinical features of fever, tonsillar swelling or exudates, enlarged cervical lymph nodes (LNs), and absence of cough warrant testing for group A *Streptococcus* (GAS, also known as *Streptococcus pyogenes*) (2, 3). Prompt antibiotic treatment can rapidly clear the infection (4), reducing the risk of GAS-associated syndromes such as acute rheumatic fever and rheumatic heart disease (3, 5–7). Some children, however, develop recurrent tonsillitis (RT) because of GAS (8, 9). Tonsillitis is a substantial health care burden and cause of repeated antibiotic usage. RT can be a severe disease, resulting in substantial morbidity and school absences in hundreds of thousands of children per year. There are more than 750,000 tonsillectomies performed annually in the United States, with RT being a common indication (2, 8, 10). Tonsils are LN-like structures with open crypts evolved for sampling oropharyngeal microbes. As tonsils are a nidus for GAS infection, these lymphoid tissues are anatomically poised to mount a protective immune response to the pathogen (11, 12). It remains a long-standing mystery why some children get GAS RT and others do not.

<sup>1</sup>Division of Vaccine Discovery, La Jolla Institute for Immunology (LJI), La Jolla, CA 92037, USA. <sup>2</sup>Department of Medicine, Division of Infectious Diseases, University of California, San Diego (UCSD), La Jolla, CA 92037, USA. <sup>3</sup>Scripps Center for HIV/AIDS Vaccine Immunology and Immunogen Discovery (CHAVI-ID), La Jolla, CA 92037, USA. <sup>4</sup>Department of Pediatrics, School of Medicine, UCSD, La Jolla, CA 92037, USA. <sup>5</sup>Skaggs School of Pharmacy and Pharmaceutical Sciences, UCSD, La Jolla, CA 92037, USA. <sup>6</sup>Human Longevity Inc., San Diego, CA 92121, USA. <sup>7</sup>Department of Microbiology and Immunology, Emory School of Medicine, Atlanta, GA 30322, USA. <sup>8</sup>Cancer Sciences Division, Faculty of Medicine, University of Southampton, UK. <sup>9</sup>Division of Pediatric Otolaryngology, Rady Children's Hospital, San Diego, CA 92123, USA. <sup>10</sup>Department of Surgery, UCSD, La Jolla, CA 92037, USA. <sup>11</sup>Department of Otolaryngology, Head and Neck Surgery, Naval Medical Center San Diego, San Diego, CA 92134, USA.

\*Corresponding author. Email: shane@lji.org

Copyright © 2019  
The Authors, some  
rights reserved;  
exclusive licensee  
American Association  
for the Advancement  
of Science. No claim  
to original U.S.  
Government Works

To attempt to answer this question of why some children are predisposed to RT, we examined immunological characteristics of children (ages 5 to 18 years) from the San Diego (SD) area undergoing tonsillectomies for GAS RT or for noninfectious reasons, e.g., sleep apnea (non-RT). We hypothesized that differences in the GAS-specific tonsillar immune responses may explain a predilection for some children to selectively develop GAS RT.

## RESULTS

## Germinal center T follicular helper cells and B cells are reduced in RT disease

By clinical history, RT children in our first SD cohort had a mean of 12 tonsillitis episodes in total compared to 0.4 episodes among non-RT children ( $P = 0.0001$ ; Fig. 1A). Multiple epidemiological studies have reported similar asymptomatic GAS carriage rates between RT and non-RT children (18 to 30%) (9, 13, 14). This suggests that RT may not be due to differences in GAS exposure. We therefore examined the tonsillar immune response in children with RT. We systematically phenotyped tonsillar immune cells from a cohort of children consisting of 26 RT and 39 non-RT children, ages 5 to 18 years (cohort 1; Table 1). Tonsils contain germinal centers (GCs), composed of germinal center T follicular helper (GC-T<sub>FH</sub>) cells, follicular dendritic cells, and germinal center B (B<sub>GC</sub>) cells (15). T<sub>FH</sub> cells are a distinct type of CD4<sup>+</sup> T cells that provide help to B cells (16, 17). T<sub>FH</sub> cells are required for GCs and thus almost all affinity-matured antibody responses to pathogens (18). GC-T<sub>FH</sub> cells instruct the survival, proliferation, and somatic hypermutation of B<sub>GC</sub> cells. RT tonsils contained a significantly reduced frequency of GC-T<sub>FH</sub> cells (CD4<sup>+</sup>CD45RO<sup>+</sup>CXCR5<sup>hi</sup>PD-1<sup>hi</sup>) compared to non-RT tonsils ( $P = 0.0001$ ; Fig. 1, B and C, and fig. S1A). Mantle T<sub>FH</sub> cell frequencies (mT<sub>FH</sub>; CXCR5<sup>+</sup>PD-1<sup>+</sup>, T<sub>FH</sub> cells outside of GCs) were not significantly different ( $P = 0.076$ ; fig. S1B). There was no difference in

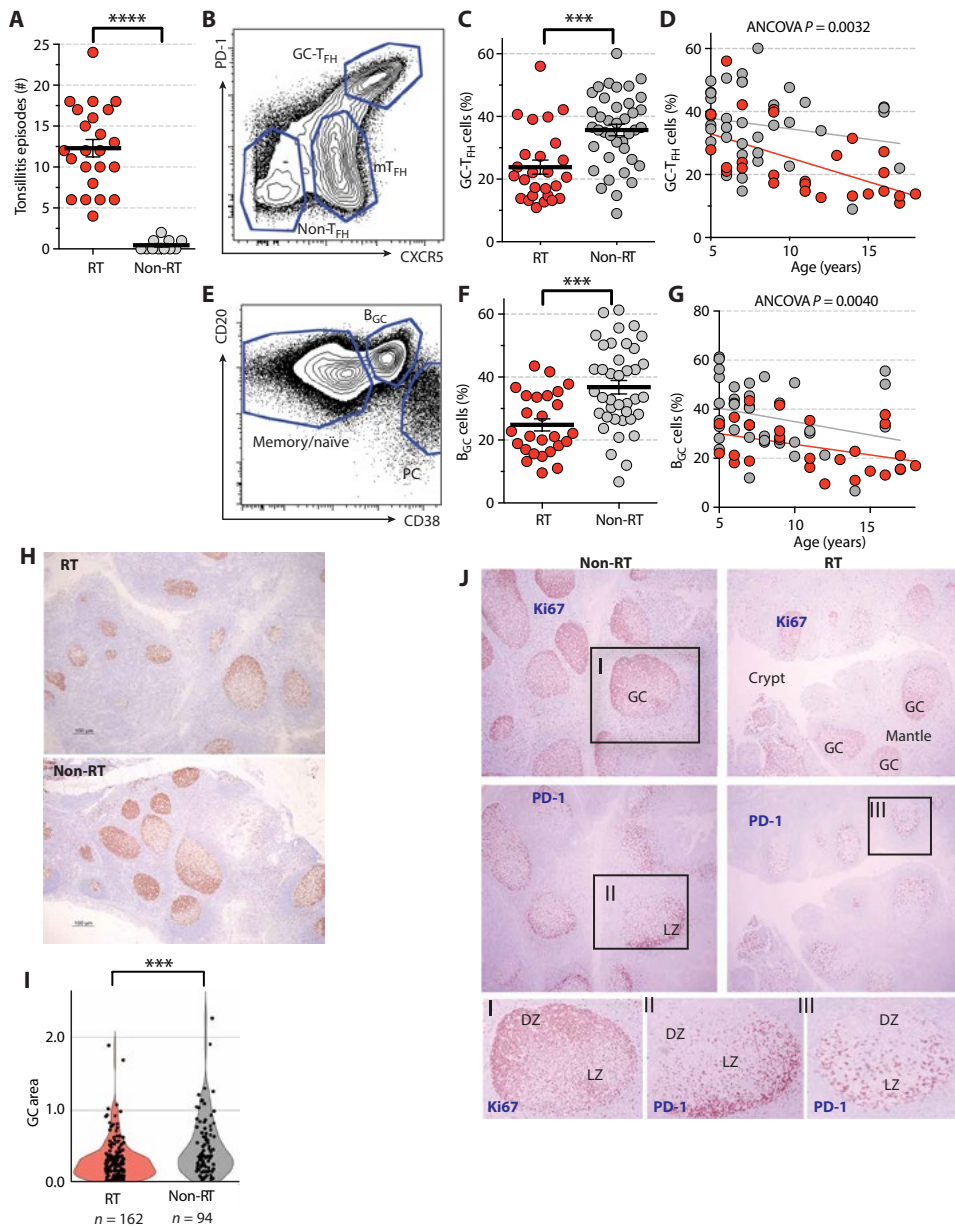


**Fig. 1. RT children have fewer GC-T<sub>FH</sub> cells in their tonsils.** Immunophenotyping analysis of cohort 1 of patients with and without RT. (A) Number of RT episodes in RT children (*n* = 23) and non-RT children (*n* = 11). (B) Flow cytometry of GC-T<sub>FH</sub> (CXCR5<sup>hi</sup>PD-1<sup>hi</sup>CD45RO<sup>+</sup>CD4<sup>+</sup>), mT<sub>FH</sub> (CXCR5<sup>+</sup>PD-1<sup>+</sup>CD45RO<sup>+</sup>CD4<sup>+</sup>), and non-T<sub>FH</sub> (CXCR5<sup>-</sup>CD45RO<sup>+</sup>CD4<sup>+</sup>) cells. (C) GC-T<sub>FH</sub> cell frequencies in RT tonsils (*n* = 26) and non-RT tonsils (*n* = 39), quantified as percentage of total CD4<sup>+</sup> T cells. (D) GC-T<sub>FH</sub> cells by age. (E) Flow cytometry of B<sub>GC</sub> cells (CD38<sup>+</sup>CD20<sup>+</sup>CD19<sup>+</sup>), plasma cells (PC; CD38<sup>hi</sup>CD20<sup>+</sup>CD19<sup>+</sup>), and memory (CD27<sup>hi</sup>CD20<sup>+</sup>CD19<sup>+</sup>)/naïve (CD27<sup>-</sup>CD20<sup>+</sup>CD19<sup>+</sup>) B cells. (F) B<sub>GC</sub> cell frequencies in RT and non-RT tonsils, quantified as percentage of total B cells. (G) B<sub>GC</sub> cells by age. (H) Representative Ki67-stained sections from RT and non-RT tonsils. (I) Quantitation of GC areas (in µm<sup>2</sup>) in RT tonsils (*n* = 21) and non-RT tonsils (*n* = 16). Each data point represents an individual GC. (J) Staining of B<sub>GC</sub> cells (Ki67) and GC-T<sub>FH</sub> cells [programmed cell death protein 1 (PD-1)]. Insets: Enlarged versions of representative GCs stained for Ki67 or PD-1. II and III show PD-1<sup>+</sup> GC-T<sub>FH</sub> cells in representative GCs from a non-RT tonsil and an RT tonsil, respectively. \*\*\*\**P* < 0.0001, \*\*\**P* < 0.001. Statistical significance was determined by Mann-Whitney tests (A to C, E, F, and I) and multivariate analysis of covariance (ANCOVA; D and G). DZ, dark zone; LZ, light zone.

B cell lymphoma 6 (BCL6) expression by GC-T<sub>FH</sub> and mT<sub>FH</sub> cells between RT and non-RT samples (fig. S1C). RT tonsils had higher non-T<sub>FH</sub> cell frequencies (CXCR5<sup>-</sup>) (*P* = 0.013; fig. S1D) and com-

parable naïve CD4<sup>+</sup> T cell frequencies (*P* = 0.183; fig. S1E). Multivariate analysis demonstrated that the GC-T<sub>FH</sub> frequencies in RT children were highly significant with or without age (*P* = 0.0032; Fig. 1D) or gender (*P* = 0.0034; fig. S1F) as a covariate.

Paralleling the significant reduction in GC-T<sub>FH</sub> cells in RT children, RT tonsils exhibited fewer B<sub>GC</sub> cells compared to non-RT tonsils (*P* = 0.0005; Fig. 1, E and F, and fig. S1A). This reduction remained statistically significant with or without age (*P* = 0.0040; Fig. 1G) or gender (*P* = 0.0064; fig. S1G) as a covariate. Memory B cell frequencies were comparable (*P* = 0.16; fig. S1H), plasma cell frequencies were lower (*P* = 0.006; fig. S1I), and naïve B cell frequencies were higher in RT tonsils (*P* = 0.0002; fig. S1J).

Histological examination revealed that RT tonsils had smaller GCs compared to non-RT tonsils (*P* < 0.002; Fig. 1, H and I). GC light and dark zones were well defined (Fig. 1J). There were no differences in the frequencies of B<sub>GC</sub> cells in the light (*P* = 0.33; fig. S1K) and dark zones (*P* = 0.90; fig. S1L). Smaller GCs suggested a potential CD4<sup>+</sup> T cell defect in RT disease, consistent with the flow cytometry data. However, differences in GC-T<sub>FH</sub> cell frequencies and GC sizes could not be directly ascribed as RT associated without additional information; thus, we explored additional parameters to establish whether the GC differences were associated with RT disease.

**RT disease is associated with impaired development of anti-SpeA antibodies**  
Diminished GC activity could potentially result in impaired circulating antibody responses to GAS. Examining antibodies was necessary to test this possibility; however, blood samples are not normally taken during tonsillectomies. Thus, a second cohort of children, from whom blood samples were obtained, was recruited using the same enrollment criteria, i.e., children ages 5 to 18 years undergoing tonsillectomies for either RT or non-RT, e.g., sleep apnea (cohort 2; Table 2). Antibody titers were examined against two GAS proteins: streptolysin O (SLO; the standard GAS serodiagnostic

**Table 1. Study participant demographics for cohort 1.**

	RT (n = 26)	Non-RT (n = 39)	P value
Gender (%)			0.21*
Female	65.4%	48.7%	
Male	34.6%	51.2%	
Age (mean years)	11	8.31	0.0092 <sup>†</sup>

\*P value determined by Fisher's exact test using *R*. †P value determined by Mann-Whitney *U* test.

antibodies than non-RT children because the former group had multiple bouts of tonsillitis, including experiencing a tonsillitis episode within a few months before surgery. However, anti-SLO immunoglobulin G (IgG) titers were not elevated in RT children compared to non-RT children ( $P = 0.51$ ; Fig. 2A). Detectable and comparable levels of anti-SLO IgG indicated that both RT and non-RT children had all been exposed to GAS. RT children had significantly lower anti-SpeA IgG titers than non-RT children ( $P = 0.024$ ; Fig. 2B). The anti-SpeA IgG titers of RT children were subsequently compared to healthy adult volunteers; average anti-SpeA IgG titers in RT children were less than 10% that of healthy adult volunteers ( $P = 0.0008$ ; Fig. 2B). Anti-SpeA antibodies have been implicated epidemiologically in immunity against severe systemic GAS infections in adults (19, 20). SpeA antibodies have been shown to be protective in a mouse GAS infection model (21). Therefore, impaired production of circulating anti-SpeA IgG in RT children may be associated with RT children's lack of protective immunity against recurrent GAS infections.

The tonsillar cells of cohort 2 were examined by multiparameter flow cytometry (Fig. 2, C to F, and fig. S2). RT tonsils of cohort 2 had significantly lower frequencies of GC-T<sub>FH</sub> cells than non-RT tonsils ( $P < 0.0001$ ; Fig. 2C), which were independent of age ( $P = 0.00026$ ; Fig. 2D) and gender ( $P = 0.0002$ ; fig. S2G). Those results confirmed the observations made in cohort 1. Significant differences in B<sub>GC</sub> cell frequencies were not observed ( $P = 0.24$ ; Fig. 2, E and F), suggesting that an RT immunological defect may be directly related to GC-T<sub>FH</sub> cells.

### RT CD4<sup>+</sup> T cells are skewed away from GAS-specific GC-T<sub>FH</sub> cells differentiation

Phenotypic and histologic analyses of RT tonsils suggested an impairment of CD4<sup>+</sup> T cell help to B cells in RT disease. For all subsequent experiments (Figs. 3 to 6 and figs. S3 to S8), samples from both cohorts 1 and 2 were used. We next assessed the frequencies of GAS-specific GC-T<sub>FH</sub> cells in the entire cohort of RT and non-RT children. Antigen-specific GC-T<sub>FH</sub> cells are difficult to identify by intracellular cytokine staining. The main function of a GC-T<sub>FH</sub> cell is to provide help to nearby B cells, resulting in stingy cytokine secretion by GC-T<sub>FH</sub> cells. We therefore used our previously developed cytokine-independent approach to identify antigen-specific GC-T<sub>FH</sub> cells by T cell receptor-dependent activation-induced markers (AIMs), expressed upon recognition of antigen (22–24). We applied the AIM technique to quantify tonsillar GAS-specific CD4<sup>+</sup> T cells (Fig. 3A). The nonpathogenic Gram-positive bacterium *Lactococcus lactis* was used as a negative control antigen (Fig. 3, A and B). Because children with RT experienced 12 times more tonsillitis episodes than non-RT

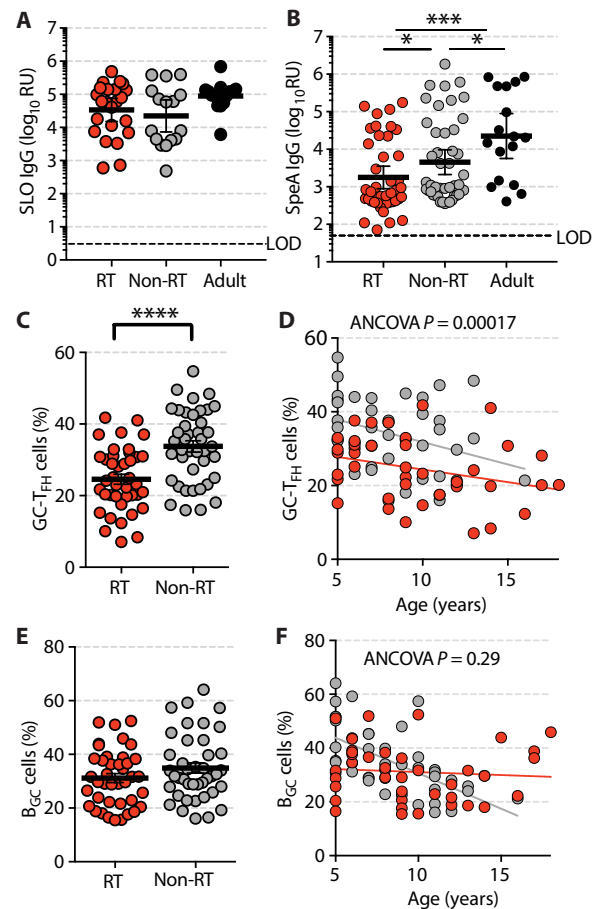


**Fig. 2. RT children have lower circulating anti-SpeA IgG titers.** Serological and immunophenotyping analysis of cohort 2 of patients with and without RT. (A) Plasma anti-SLO IgG titers in RT children ( $n = 23$ ), non-RT children ( $n = 16$ ), and normal healthy adults ( $n = 14$ ). LOD, limit of detection; RU, relative units. (B) Plasma anti-SpeA IgG titers in RT children ( $n = 42$ ), non-RT children ( $n = 45$ ), and normal healthy adults ( $n = 17$ ). (C) GC-T<sub>FH</sub> cell frequencies in RT tonsils ( $n = 40$ ) and non-RT tonsils ( $n = 41$ ), quantified as percentage of total CD4<sup>+</sup> T cells. (D) GC-T<sub>FH</sub> cells by age. (E) B<sub>GC</sub> cell frequencies in RT and non-RT tonsils, quantified as percentage of total B cells. (F) B<sub>GC</sub> cells by age. \* $P < 0.05$ , \*\*\* $P < 0.001$ , \*\*\*\* $P < 0.0001$ . Statistical significance was determined by Mann-Whitney test.

children (Fig. 1A), a simple expectation was that RT tonsils would contain substantially more GAS-specific CD4<sup>+</sup> T cells than non-RT tonsils. Instead, GAS-specific antigen-experienced CD4<sup>+</sup> T cells (CD45RA<sup>+</sup>; Fig. 3C), GAS-specific non-T<sub>FH</sub> cells (fig. S3A), and GAS-specific GC-T<sub>FH</sub> cells (fig. S3B) were not significantly elevated in RT tonsils compared to non-RT tonsils. Rather, GAS-specific CD4<sup>+</sup> T cells from RT tonsils were skewed away from GAS-specific GC-T<sub>FH</sub> cell differentiation, with a lower ratio of GAS-specific GC-T<sub>FH</sub> cells to total GAS-specific CD4<sup>+</sup> T cells ( $P = 0.023$ ; Fig. 3D). Together, these data suggested that GAS-specific GC-T<sub>FH</sub> cell responses were deficient in RT disease.

Using the AIM assay, we performed RNA sequencing (RNA-seq) on sorted GAS-specific and unstimulated (CD25<sup>+</sup>OX40<sup>-</sup>) GC-T<sub>FH</sub> cells (fig. S3C) to assess whether there were functional differences in the GC-T<sub>FH</sub> cells. There were no notable differences between RT and non-RT GC-T<sub>FH</sub> cells. More *IL4* mRNA was observed in GAS-specific GC-T<sub>FH</sub> cells from RT donors (fig. S3C), but the overall

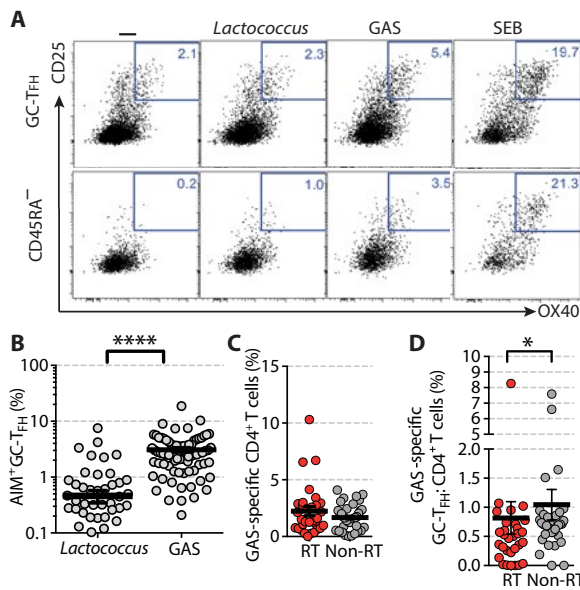


**Fig. 3. RT tonsils have reduced GAS-specific GC-T<sub>FH</sub> cells.** (A) Identification of GAS-specific CD4<sup>+</sup> T cells (CD45RA<sup>-</sup>) and GAS-specific GC-T<sub>FH</sub> cells (CD45RA<sup>-</sup> CXCR5<sup>hi</sup> PD-1<sup>hi</sup>) using OX40<sup>+</sup> CD25<sup>+</sup> AIM (AIM<sub>25</sub>). Tonsil cells were left unstimulated or stimulated with antibiotic-killed *L. lactis* (a nonpathogenic Gram-positive bacteria that served as a negative control; 10 µg/ml), heat-inactivated, antibiotic-killed GAS (10 µg/ml), or staphylococcal enterotoxin B [SEB (positive control); 1 µg/ml] for 18 hours. (B) GAS-specific GC-T<sub>FH</sub> cell frequencies, quantified as percentage of total CD4<sup>+</sup> T cells, in RT tonsils (*n* = 31) and non-RT tonsils (*n* = 35). (C) GAS-specific CD45RA<sup>-</sup> CD4<sup>+</sup> T cell frequencies, quantified as percentage of total CD4<sup>+</sup> T cells, in RT tonsils (*n* = 31) and non-RT tonsils (*n* = 35). (D) Fraction of GAS-specific GC-T<sub>FH</sub> cells (CXCR5<sup>hi</sup> PD-1<sup>hi</sup>) among total GAS-specific CD4<sup>+</sup> T cell (AIM<sub>25</sub><sup>+</sup> CD45RA<sup>-</sup>) in RT tonsils (*n* = 31) and non-RT tonsils (*n* = 35). \*\*\*\**P* < 0.0001, \**P* < 0.05. Statistical significance was determined by paired *t* test (B) and Mann-Whitney tests (C and D).

mRNA abundance was low, and interleukin-4 (IL-4) protein was below the limit of detection (22). The data suggested that the RT and non-RT GC-T<sub>FH</sub> cells were functionally similar by assessment of conventional cytokines of interest.

**RT disease is associated with human leukocyte antigen class II alleles**

Essentially, all children are exposed to GAS during childhood (25). Among children enrolled in this study, RT children were likely to have a significant family history of tonsillectomy (*P* = 0.0004; Fig. 4A), suggesting a potential genetic predisposition. GC responses depend on human leukocyte antigen (HLA) class II antigen presentation by B cells to GC-T<sub>FH</sub> cells. Susceptibility to toxic shock syndrome and invasive forms of GAS infection have been inversely associated with HLA DQB1\*06:02 (26). The DQB1\*06:02 has also been associated with protection from the development of rheumatic heart disease (27, 28), the most severe sequela of long-term untreated GAS RT and the leading cause of heart failure in children worldwide (1, 29). We performed HLA typing on the entire tonsillar cohort to test whether HLA associations previously associated with other GAS-related diseases may have relevant associations with RT disease. HLA class II associations frequently require large sample sizes. To increase the sample size, we generated an HLA-typed cohort of ethnically matched healthy adults from the SD general population (GP) (fig. S4A). HLA DQB1\*06:02 was significantly less frequent in RT children than in the GP (*P* = 0.042; Fig. 4B and fig.

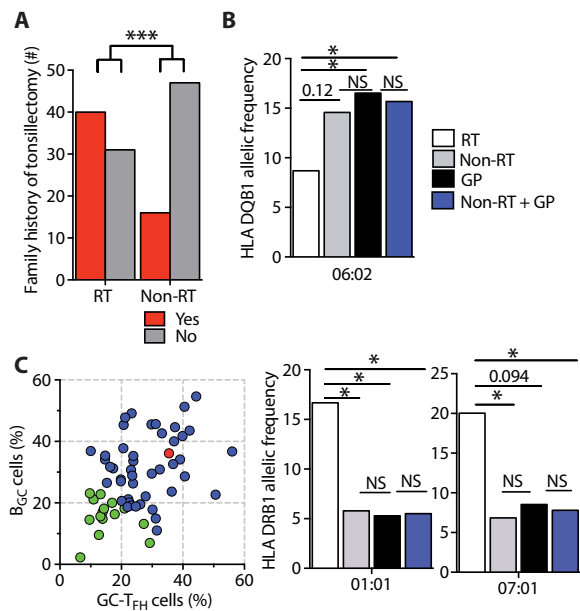


**Fig. 4. HLA class II associations identified in RT children.** (A) Family history of tonsillectomy (RT = 71 and non-RT = 63). (B) HLA DQB1\*06:02 allelic frequency in non-RT children (gray bar, *n* = 192), RT children (white bar, *n* = 138), ethnically matched adults from the SD GP (black bar, *n* = 242), and non-RT children and GP (blue bar, *n* = 434). NS, not significant. (C) Left: HLA DRB1\*01:01 and HLA DRB1\*07:01 allelic frequencies in RT tonsils with the lowest quartile of GC activity, defined as the lowest combined frequencies of GC-T<sub>FH</sub> and B<sub>GC</sub> cells [green dots, *n* = 15 (GC<sup>lo</sup> samples); blue dots, *n* = 46 (GC<sup>lo</sup> samples); red dot, mean of non-RT GC activity]. Right: HLA DRB1\*01:01 and HLA DRB1\*07:01 allelic frequencies in non-RT tonsils (gray bar, *n* = 190), GP (black bar, *n* = 246), and GP and non-RT tonsils (blue bar, *n* = 436). RT children HLA allele counts (white bar, *n* = 30). \*\*\**P* < 0.001, \**P* < 0.05. Statistical significance was determined by Fisher's exact test (A to C).

S4B). HLA DQB1\*06:02 was also significantly less frequent in RT children than the combined groups of non-RT children and GP (*P* = 0.048; Fig. 4B and fig. S4B). There was no difference in the HLA DQB1\*06:02 allelic frequency between non-RT children and ethnically matched SD GP (*P* = 0.89; Fig. 4B and fig. S4B). Overall, these data suggest that DQB1\*06:02 is a protective HLA allele from RT disease, potentially similar to the protective role of DQB1\*06:02 against toxic shock syndrome and invasive forms of GAS infection.

HLA alleles DRB1\*01:01 and DRB1\*07:01 (28, 30) have been linked to increased risk for rheumatic heart disease. No significant DRB1\*01:01 and DRB1\*07:01 allelic associations were observed among all children enrolled in this study (fig. S4B). However, given that RT is a multifactorial disease, we considered that a genetic association with disease susceptibility may be more evident in RT children exhibiting the largest GC deficits. HLA allelic frequencies were thus examined among children with RT with the lowest quartile of GC-T<sub>FH</sub> and B<sub>GC</sub> cells [Fig. 4C and fig. S4, B (GC<sup>lo</sup>) and C]. These children had significantly higher frequencies of HLA DRB1\*01:01 compared to the GP (*P* = 0.03), non-RT children (*P* = 0.049), and the combined control groups (*P* = 0.03; Fig. 4C and fig. S4B). Frequencies of HLA DRB1\*07:01 were also elevated compared to non-RT children and the combined control groups (*P* = 0.03 and *P* = 0.03, respectively; Fig. 4C and fig. S4B). In contrast, no differences were identified between the non-RT and GP cohorts for HLA DRB1\*01:01 (*P* = 0.85) or HLA DRB1\*07:01 (*P* = 0.74; Fig. 4C and fig. S4B). We additionally

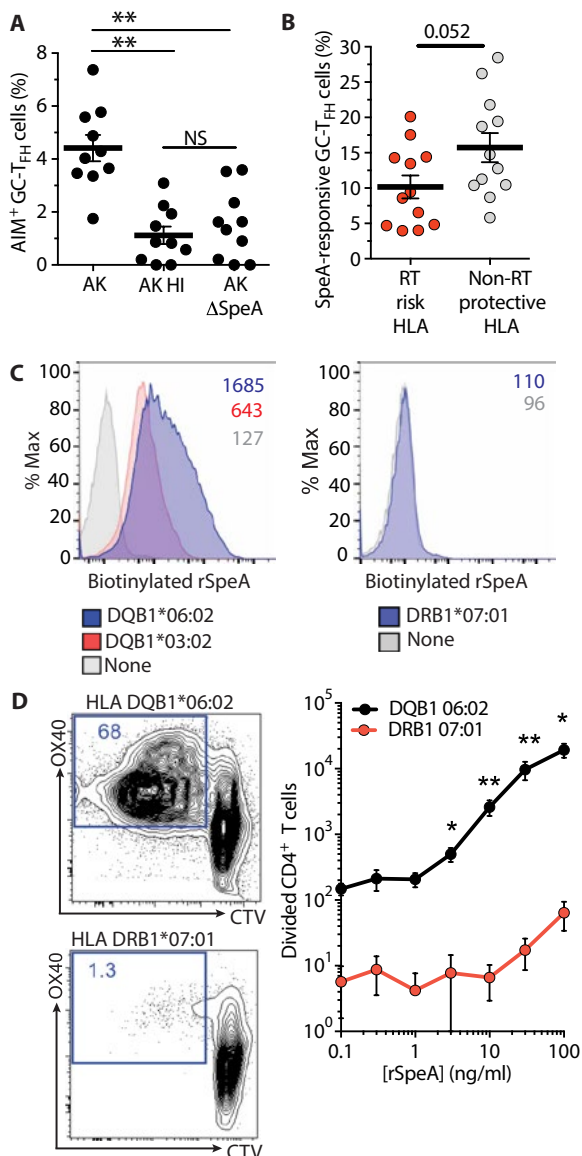


**Fig. 5. HLA class II associations identified in RT and non-RT children segregate on the basis of preferential GAS superantigen SpeA binding.** (A) Comparison of AIM<sup>+</sup> GC-T<sub>FH</sub> cells after stimulation with either antibiotic-killed (AK) GAS (10 μg/ml), antibiotic-killed, heat-inactivated (AK HI) GAS (10 μg/ml), or antibiotic-killed SpeA-deficient (AK ΔSpeA) GAS (10 μg/ml); *n* = 10, including RT and non-RT donors. Heat-inactivation of antibiotic-killed GAS inactivates GAS superantigens. (B) SpeA-responsive GC-T<sub>FH</sub> cells in tonsils from patients with RT with risk HLA alleles (*n* = 12) compared to non-RT patients with protective HLA alleles (*n* = 12). Tonsils were stimulated with SpeA (1 μg/ml) for 18 hours and background-subtracted as determined with unstimulated cells. (C) Histogram flow cytometric quantitation of SpeA binding by HLA allele using HLA cell lines. *n* = 3 experiments. (D) Proliferation of total CD4<sup>+</sup> T cells from peripheral blood mononuclear cells (PBMCs) of HLA DQB1\*06:02<sup>+</sup> donors cocultured with recombinant SpeA (rSpeA) and a cell line expressing HLA DQB1\*06:02 and of CD4<sup>+</sup> T cells from PBMCs of HLA DRB1\*07:01<sup>+</sup> donors cocultured with rSpeA and a cell line expressing HLA DRB1\*07:01. *n* = 4 experiments. \*\**P* < 0.01, \**P* < 0.05 (D). Statistical significance was determined by Mann-Whitney test. CTV, cell trace violet.

compared the lowest quartile of GC-T<sub>FH</sub> and B<sub>GC</sub> cells from non-RT children to all RT children and the GP and observed no difference in HLA DRB1\*01:01 or HLA DRB1\*07:01 frequencies, as expected

(fig. S4D). These data indicate that HLA DRB1\*01:01 and DRB1\*07:01 are risk alleles for RT. Overall, integration of HLA typing and immunophenotyping data revealed relationships between RT disease, GAS, and GC responses.

### RT-associated HLA alleles differentially affect CD4<sup>+</sup> T cell responses to GAS and the GAS superantigen SpeA

SpeA superantigen is an important GAS virulence factor. Comparison of CD4<sup>+</sup> T cell reactivity using an antibiotic-killed wild-type GAS strain MIT1 5448, with or without heat inactivation, or an antibiotic-killed isogenic SpeA-deficient mutant GAS strain (ΔspeA), demonstrated that SpeA superantigen-mediated stimulation of CD4<sup>+</sup> T cells constituted a major fraction of CD4<sup>+</sup> T cell reactivity to in vitro-cultured GAS (*P* = 0.002; Fig. 5A and fig. S5A). SpeA has provided certain GAS strains with an evolutionary advantage (21, 31, 32), associated with the global persistence and dominance of the M1 serotype among throat cultures. GC-T<sub>FH</sub> cells from RT tonsils bearing a risk HLA class II allele were potentially less responsive to SpeA stimulation than non-RT tonsils bearing the protective HLA DQB1\*06:02 allele (*P* = 0.052; Fig. 5B and fig. S5B). Although not reaching statistical significance, in light of the small *N* value, we found the results intriguing enough to examine SpeA interactions with human CD4<sup>+</sup> T cells in greater detail.

Mechanistic relationships between HLA class II alleles and GAS disease manifestations are unclear (29), but a potential role has been suggested for SpeA (26, 33, 34). We tested binding of SpeA to 19 well-defined single-allele HLA class II-expressing cell lines. The highest affinity binding interaction was between SpeA and HLA DQB1\*06:02 (Fig. 5C and fig. S5C), whereas moderate binding was observed to cells expressing another DQ allele DQB1\*03:02. Rapid and robust proliferation of HLA DQB1\*06:02<sup>+</sup> CD4<sup>+</sup> T cells was observed in the presence of the superantigen (*P* = 0.0079; Fig. 5D and fig. S5D). In contrast, minimal proliferation was observed for HLA DQB1\*06:02<sup>-</sup> CD4<sup>+</sup> T cells, including HLA DRB1\*01:01<sup>+</sup> or DRB1\*07:01<sup>+</sup> CD4<sup>+</sup> T cells (Fig. 5D and fig. S5E) with minimal cell death (fig. S5F). High-affinity interaction of SpeA with the protective allele HLA DQB1\*06:02 resulted in robust CD4<sup>+</sup> T cell proliferation (Fig. 5, C and D). Thus, CD4<sup>+</sup> T cells from HLA DQB1\*06:02<sup>+</sup> individuals exhibit differential interaction with SpeA compared to HLA DQB1\*06:02<sup>-</sup> individuals.

### Granzyme B<sup>+</sup> GC-T<sub>FH</sub> cells are found in RT disease

Although we observed that GC-T<sub>FH</sub> cell frequencies were significantly lower in RT compared to non-RT tonsils, BCL6 expression by GC-T<sub>FH</sub> cells was equivalent on a per-cell basis. To identify CD4<sup>+</sup> T cell factors potentially involved in SpeA superantigen-associated GC abnormalities in RT disease, we performed RNA-seq on SpeA-responsive GC-T<sub>FH</sub> cells from RT and non-RT tonsils. We observed no difference in T<sub>FH</sub> and immunomodulatory T helper 1 (T<sub>H</sub>1), T<sub>H</sub>2, or T<sub>H</sub>17 cytokine mRNA expression (fig. S6). *GZMB* mRNA, encoding the cytotoxic effector protein granzyme B (GzmB), was up-regulated in RT GC-T<sub>FH</sub> cells (*P* = 0.0079; Fig. 6A, fig. S7A, and table S1). GzmB is typically secreted by cytotoxic CD8<sup>+</sup> T cells and natural killer cells for killing of target cells. Expression of GzmB by GC-T<sub>FH</sub> cells could be counterproductive to the B cell help function of GC-T<sub>FH</sub> cells. A potential mechanism by which GAS disrupts antibody responses could be aberrant GzmB expression by GC-T<sub>FH</sub> cells, converting a GC-T<sub>FH</sub> cell from one that helps B<sub>GC</sub> cells to one that kills B<sub>GC</sub> cells.

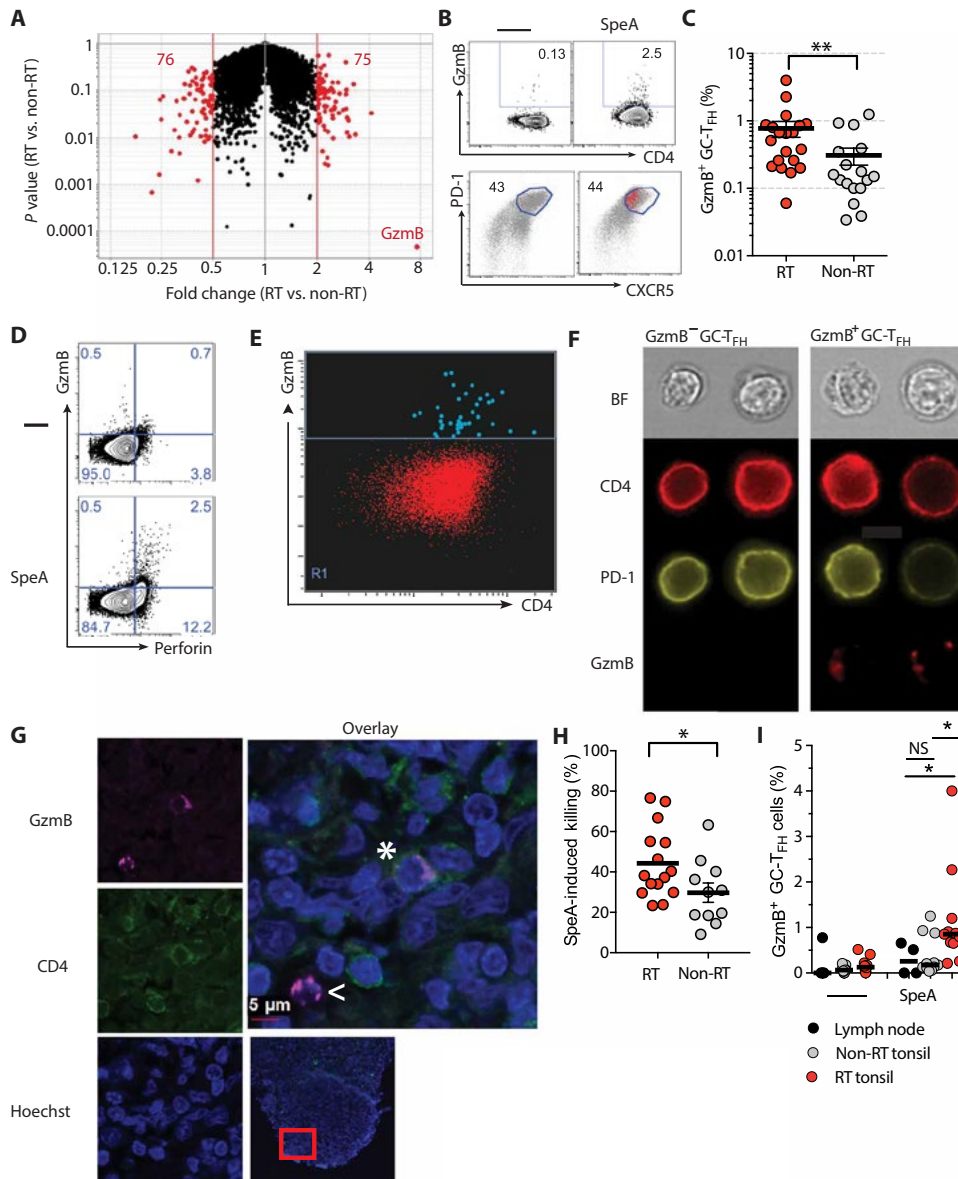


**Fig. 6. SpeA stimulation of GC-T<sub>FH</sub> cells from RT tonsils induces Gzmb.** (A) Volcano plot showing fold change of genes in SpeA-stimulated GC-T<sub>FH</sub> cells from RT tonsils (*n* = 5) compared to SpeA-stimulated GC-T<sub>FH</sub> cells from non-RT tonsils (*n* = 5). Red dots denote genes with a fold change of <0.5 or >2. (B) Frequency of intracellular Gzmb expression in GC-T<sub>FH</sub> cells by flow cytometry. Tonsil cells were stimulated with SpeA (1 μg/ml) for 24 hours (top). Background of the Gzmb<sup>+</sup> GC-T<sub>FH</sub> cells among total CD45RA<sup>-</sup> CD4<sup>+</sup> T cells (bottom). (C) Gzmb<sup>+</sup> GC-T<sub>FH</sub> cells in RT tonsils (*n* = 20) and non-RT tonsils (*n* = 17) after SpeA stimulation. (D) Fluorescence-activated cell-sorted GC-T<sub>FH</sub> cells and autologous B cells were cultured ± SpeA for 5 days and stained for Gzmb and perforin expression. *n* = 3 donors. (E) ImageStream cytometry plot of Gzmb<sup>+</sup> GC-T<sub>FH</sub> cells after SpeA stimulation. GC-T<sub>FH</sub> cells were gated as CXCR5<sup>hi</sup>PD-1<sup>hi</sup> of live CD45RA<sup>-</sup>CD4<sup>+</sup> T cells. *n* = 1 donor. (F) ImageStream imaging of GC-T<sub>FH</sub> cells after SpeA stimulation, showing representative Gzmb<sup>-</sup> and Gzmb<sup>+</sup> cells. (G) Confocal microscopy of a Gzmb<sup>+</sup> CD4<sup>+</sup> T cell in a GC in an RT tonsil (\*). A Gzmb<sup>+</sup> CD8<sup>+</sup> T cell is also shown for reference (<). *m.n* = 8 donors. (H) GC-T<sub>FH</sub> cells (CXCR5<sup>hi</sup>PD-1<sup>hi</sup>CD45RA<sup>-</sup>CD4<sup>+</sup>) were cocultured with autologous CTV-labeled B cells (CD19<sup>+</sup>CD38<sup>-</sup>). Killing was quantified as outlined in Materials and Methods, with controls shown in fig. S7 (J to L). *n* = 15 and 11 (RT and non-RT donors, respectively). (I) Gzmb expression (percentage) by GC-T<sub>FH</sub> cells from healthy LNs and from RT and non-RT tonsils. Gzmb expression after SpeA stimulation of GC-T<sub>FH</sub> cells from RT tonsils (*n* = 11), non-RT tonsils (*n* = 11), or healthy LNs (*n* = 4). \*\**P* < 0.01, \**P* < 0.05. Statistical significance was determined by Mann-Whitney test (C, H, and I).

To determine whether RT GC-T<sub>FH</sub> cells were capable of Gzmb protein expression, four independent approaches were used as follows: (i) flow cytometry of intracellular-stained SpeA-stimulated GC-

SpeA is capable of deviating GC-T<sub>FH</sub> cells into Gzmb<sup>+</sup> perforin<sup>+</sup> killer T<sub>FH</sub> cells, and these killer T<sub>FH</sub> cells are a pathological feature of RT disease.

T<sub>FH</sub> cells, (ii) ImageStream imaging cytometry of SpeA-stimulated GC-T<sub>FH</sub> cells, (iii) immunofluorescence microscopy of human tonsillar tissue, and (iv) killing of target cells. GC-T<sub>FH</sub> cell intracellular protein staining confirmed SpeA-induced Gzmb expression (*P* = 0.006; Fig. 6, B and C), with no difference based on age (fig. S7B) or gender (fig. S7C). Perforin expression was also induced by SpeA stimulation (Fig. 6D). Consistent with these findings, punctate cytoplasmic Gzmb was observed in SpeA-stimulated GC-T<sub>FH</sub> cells from a patient with RT by ImageStream (Fig. 6, E and F). These changes were specific to GC-T<sub>FH</sub> cells because there were no differences in the frequencies of Gzmb<sup>+</sup> mT<sub>FH</sub> cells (fig. S7, D and G), non-T<sub>FH</sub> cells (fig. S7, E and G), or CD8<sup>+</sup> T cells (fig. S7, F and H) between RT and non-RT tonsils. These Gzmb<sup>+</sup> GC-T<sub>FH</sub> cells were not regulatory T cells, because they did not express FoxP3 or Helios (fig. S7I). Gzmb was also observed histologically in some GC-T<sub>FH</sub> cells (Fig. 6G).

We assessed whether SpeA-stimulated GC-T<sub>FH</sub> cells were capable of killing B cells. Killing by cytotoxic CD4<sup>+</sup> T cells is typically difficult to demonstrate in vitro; nevertheless, killing of B cells by GC-T<sub>FH</sub> cells was observed in the presence of SpeA (Fig. 6H and fig. S7, J and K). This killing was more profound by RT GC-T<sub>FH</sub> cells compared to non-RT GC-T<sub>FH</sub> cells. Bystander cell death was not observed (fig. S7L). Phytohemagglutinin did not stimulate Gzmb expression (fig. S7M). B cell killing by RT GC-T<sub>FH</sub> cells in the presence of GAS SpeA was independent of Fas and Fas ligand (fig. S7, N and O) and was associated with perforin expression by the Gzmb<sup>+</sup> GC-T<sub>FH</sub> cells (Fig. 6D).

Lastly, we assessed whether Gzmb<sup>+</sup> GC-T<sub>FH</sub> cells were unique to RT. GC-T<sub>FH</sub> cells from healthy LNs from adult patients undergoing a staging LN biopsy were compared to RT and non-RT tonsils. Gzmb<sup>+</sup> GC-T<sub>FH</sub> cells were sporadically detected in healthy LNs. Significantly more Gzmb<sup>+</sup> GC-T<sub>FH</sub> cells were observed in RT tonsils than healthy LNs, and Gzmb expression was induced upon SpeA stimulation (*P* = 0.025; Fig. 6I). GC-T<sub>FH</sub> cells from non-RT tonsils and healthy LNs were comparable (Fig. 6I).

Collectively, these data suggest that

**Table 2. Study participant demographics for cohort 2.**

	RT (n = 40)	Non-RT (n = 41)	P value
Gender (%)			0.0058*
Female	77.5%	46.3%	
Male	22.5%	53.7%	
Age (mean years)	9.65	8.39	0.21 <sup>†</sup>

\*P value determined by Fisher's exact test using *R*. †P value determined by Mann-Whitney *U* test.

**Table 3. Study participant demographics for entire combined cohort.**

	RT (n = 66)	Non-RT (n = 80)	P value
Gender (%)			0.0055*
Female	72.7%	47.5%	
Male	27.3%	52.5%	
Age (mean years)	10.18	8.35	0.0024 <sup>†</sup>

\*P value determined by Fisher's exact test using *R*. †P value determined by Mann-Whitney *U* test.

## DISCUSSION

By integrating immune profiling and clinical data with transcriptomic and functional analyses, we revealed immunologic features of GAS RT that provide evidence that RT is an immunosusceptibility disease. We observed that (i) RT tonsils have significantly lower GC-T<sub>FH</sub> cell frequencies; (ii) RT children have impaired anti-SpeA antibody titers, which have been associated with protective immunity to GAS; (iii) specific HLA class II alleles were associated with RT; and (iv) SpeA can induce GzmB expression in GC-T<sub>FH</sub> cells. Although RT is surely a multifactorial disease, these findings suggest that the sporadic nature of RT is linked to HLA-associated genetic susceptibility differences with HLA class II allelic variants affecting GAS superantigen binding. SpeA perturbation of GC-T<sub>FH</sub> cells with GC-T<sub>FH</sub> killing of B<sub>GC</sub> cells is a parsimonious model to explain key immunological and pathological aspects of RT. Inability to develop protective anti-SpeA immunity may render a child more susceptible to pharyngitis and reinfection because of disruption of GC-T<sub>FH</sub> cells.

It has been a long-standing mystery why some children get recurrent strep throat. Specific strains of GAS have been proposed as a cause of RT (2, 35, 36). However, previous studies have observed that RT and non-RT children have similar asymptomatic GAS carriage rates (9, 13, 14). Our pediatric cohorts were recruited from the same geographic area to control for circulating GAS serotypes. Globally, GAS disease burden is high and, in recent decades, the M1 serotype has remained one of the dominant strains (37, 38). It is notable that the M1 serotype has a bacteriophage encoding SpeA, and the acquisition of SpeA has been implicated in the dominance of the M1 pandemic strain in the United States (39, 40). Here, we observed that SpeA contributed substantially to GAS superantigen activity on GC-T<sub>FH</sub> cells.

SpeA superantigen actively skewed GC-T<sub>FH</sub> cell function, resulting in cytolytic GC-T<sub>FH</sub> cells. This represents a previously unidentified immune evasion mechanism of a pathogen. The ability of SpeA to convert a conventional GC-T<sub>FH</sub> cell into to a “killer T<sub>FH</sub>” in vitro occurred regardless of whether the GC-T<sub>FH</sub> cells were from an RT or non-RT tonsil. However, conversion to GzmB<sup>+</sup> perforin<sup>+</sup> GC-T<sub>FH</sub> cells, and cytotoxicity, was more extensive with GC-T<sub>FH</sub> cells from RT tonsils, and RT children had much lower anti-SpeA antibody responses. Even a small frequency of GzmB<sup>+</sup> perforin<sup>+</sup> GC-T<sub>FH</sub> cells may potentially have devastating effects within the confines of a GC. We contend that the cytotoxicity scenario is fundamentally different for GzmB<sup>+</sup> GC-T<sub>FH</sub> cell disruption of GCs than it is for cytolytic control of a viral infection. B<sub>GC</sub> cells are probably among the most

proapoptotic cells in the body. Each B<sub>GC</sub> cell requires stimulation by a T<sub>FH</sub> cell every few hours or it will die (41–43). In addition, unlike most cell types, the B<sub>GC</sub> cells are all confined to a densely packed space, the GC. GC-T<sub>FH</sub> cells are constantly making short (~5 min) cognate interactions with B<sub>GC</sub> cells (44–46). Thus, in a 24-hour period, 10 GC-T<sub>FH</sub> cells can make cognate interactions with 2880 B<sub>GC</sub> cells, and an average GC contains only ~1000 total B<sub>GC</sub> cells (47). In contrast, cytolytic killing of virally infected cells takes much longer cognate interactions, with more resistant cells, over a much greater three-dimensional space (48). Hence, we consider it a reasonable model that it may take relatively little GzmB to kill a B<sub>GC</sub> cell and that GzmB<sup>+</sup> T<sub>FH</sub> could serially poison many B<sub>GC</sub> cells each day.

Our finding of SpeA-induced GzmB<sup>+</sup> perforin<sup>+</sup> GC-T<sub>FH</sub> cells within tonsils also highlights the plasticity of T<sub>FH</sub> cells. Granzyme A-expressing GC-T<sub>FH</sub> cells have been described recently in human LNs and tonsils (49, 50). In this study, we observed no RNA expression of granzyme A and no differences in CD57, signal transducer and activator of transcription 3 (STAT3), or cytotoxic and regulatory T cell molecule (CRTAM) between RT and non-RT tonsils (fig. S8, A to D). However, we did observe similarities between GzmB<sup>+</sup> GC-T<sub>FH</sub> and recent reports of CD8<sup>+</sup> T cells acquiring T<sub>FH</sub> phenotypic features (51, 52). CXCR5<sup>+</sup> CD8<sup>+</sup> T cells have been identified in the context of HIV, simian immunodeficiency virus, and lymphocytic choriomeningitis virus chronic infections and have the capacity to migrate into B cell follicles and exhibit cytotoxicity (53–56). Anti-PD1 immunotherapy predominantly rescues exhausted CD8<sup>+</sup> T cells via outgrowth of CXCR5<sup>+</sup> CD8<sup>+</sup> T cells (56). Development of CXCR5<sup>+</sup> CD8<sup>+</sup> T cells is associated with up-regulation of key T<sub>FH</sub> transcription factors T cell factor 1 (TCF1) and BCL6 (57) and a substantial reduction in the expression of GzmB by the CXCR5<sup>+</sup> CD8<sup>+</sup> T cells (56, 58). In this study of RT GC-T<sub>FH</sub> cells, the opposite was observed; down-regulation of *TCF1* and its homolog *LEF1* occurred in SpeA-stimulated GC-T<sub>FH</sub> cells commensurate with GzmB up-regulation, suggesting that the TCF1/lymphoid enhancer factor (LEF1) axis may be required for separation of T<sub>FH</sub> and cytolytic transcriptional programs in both CD4<sup>+</sup> and CD8<sup>+</sup> T cells. Together, the data from this study suggest that conversion of GC-T<sub>FH</sub> cells to GzmB<sup>+</sup> perforin<sup>+</sup> T<sub>FH</sub> cells represents a reciprocal process to the recently described conversion of CXCR5<sup>+</sup> GzmB<sup>hi</sup> CD8<sup>+</sup> T cells to CXCR5<sup>+</sup> GzmB<sup>lo</sup> CD8<sup>+</sup> T cells.

This study identified risk and protective alleles for GAS RT, alleles which have previously been implicated in other clinical presentations of GAS infection. RT disease is associated with a lower frequency of HLA alleles observed to be protective against GAS

invasive infection and toxic shock syndrome and with a higher frequency of HLA risk alleles shared with severe autoimmune rheumatic heart disease. Screening for these HLA alleles in children with strep throat may provide a valuable prognostic indicator for susceptibility to recurrent GAS pharyngeal infections.

There are limitations to this study. Tonsillectomy indication was determined by the otolaryngologist at a tertiary referral hospital on the basis of history provided by the referring pediatrician or parent, with the tonsils analyzed in an unblinded fashion. There were no culture data for the RT group to determine which GAS serotype was the etiologic agent of strep throat. Tonsils were acquired at hospitals specifically in the SD area, and thus, some of the findings here may be specific to certain geographical limitations. In addition, robust statistical associations with HLA class II alleles frequently require cohorts of 1000 or more individuals. Future studies will clearly be of value to address these limitations.

In a murine HLA class II model of GAS infection, establishment of GAS infection was dependent on SpeA, and immunization with an SpeA toxoid elicited anti-SpeA IgG that was protective against GAS infection (21, 31). Our data indicate that differential binding of SpeA to HLA class II alleles may predict susceptibility of individuals to GAS infection. More broadly, these data support central roles for SpeA and anti-SpeA IgG in tonsillitis pathogenesis and GAS protective immunity, respectively. Strong binding of SpeA to HLA DQB1\*06:02 may facilitate the development of SpeA-specific GC-T<sub>FH</sub> cells to provide help to B<sub>GC</sub> cells to generate anti-SpeA IgG to neutralize SpeA upon reexposure. An understanding of this immune evasion strategy may now allow for rational design of countermeasures. An inactivated SpeA toxoid vaccine may be a simple and reasonable candidate for consideration as a strep throat and RT vaccine and as a means to reduce costly RT antibiotics treatments and surgeries per year and to reduce childhood strep throat disease burden generally.

In conclusion, we provide evidence that RT is a genetic immunosusceptibility disease with a role for SpeA and GC-T<sub>FH</sub> cells. We have identified correlates of disease both on the side of the pathogen and on the side of the immune system. These findings have several implications, including the plausibility of SpeA as a potential vaccine target for RT and strep throat generally. Lastly, the finding of GzmB<sup>+</sup> perforin<sup>+</sup> GC-T<sub>FH</sub> cells points to a pathological mechanism of GC control.

## MATERIALS AND METHODS

### Study design

The goal of the study was to understand why only some children get recurrent GAS-associated tonsillitis. On the basis of discussions with pediatricians and pediatric otolaryngologists, we restricted recruitment to children ages 5 to 18 years undergoing tonsillectomies as GAS RT afflicts school-aged children. Tonsils were obtained from children at Rady Children's Hospital or the Naval Medical Center, undergoing tonsillectomies for either GAS-associated RT or sleep apnea. Sleep apnea was chosen as the comparator group because (i) tonsils are never removed from healthy children; (ii) partial tonsil biopsies are not feasible because of the small risk of life-threatening oropharyngeal hemorrhage; (iii) cadaveric tonsils are not adequate for GC research purposes because there are few live cells to perform functional assays, and the quality of the cells is uncertain because of the highly apoptotic nature of GCs; (iv) pedi-

atric whole-body organ donors are extremely rare, and those with tonsils harvested are even rarer; and (v) sleep apnea is another common indication for tonsillectomy but is not associated with a known infectious etiology. Enrollment of children from the same geographic area controlled for circulating GAS strains within the community. Otolaryngologists performing the tonsillectomies determined indication for tonsillectomy (RT or sleep apnea) based on clinical history and laboratory data from referring pediatricians. Inclusion criteria were age and indication for tonsillectomy. Exclusion criteria included active infection, malignancy, autoimmunity, mixed indication (RT/apnea), and age < 5 years. Substantial effort was made to control for age in enrolling RT and non-RT children. Gender was documented and reported but was not an inclusion criterion.

Cohort 1 (Table 1) consisted of children enrolled at the Naval Medical Center and Rady Children's Hospital. Cohort 2 (Table 2) consisted of children enrolled at Rady Children's Hospital by the same pediatric otolaryngologists as cohort 1. Cohort 2 consists of children enrolled after amendment of the institutional review board (IRB) to include a blood specimen at the time of tonsillectomy. Characteristics of the total cohort (cohorts 1 and 2) are in Table 3. Informed consent was obtained from all donors under protocols approved by the IRBs of the University of California, San Diego (UCSD; 131099), Rady Children's Hospital (RCHD 2847), Naval Medical Center (NCRADA-NMCSD-11-378), and La Jolla Institute for Immunology (LJI; VD-108-1113). Antibody panels are described in tables S2 to S8. Primary data are reported in data file S1.

### Statistical analysis

All statistical analyses were performed using two-tailed Mann-Whitney test in GraphPad 7.0, unless otherwise specified. ANCOVA was performed to evaluate age or gender as a covariable. Two-tailed Fisher's exact test was used to evaluate HLA associations, using GraphPad software or R software version 3.3.1.

### SUPPLEMENTARY MATERIALS

[www.sciencetranslationalmedicine.org/cgi/content/full/11/478/eaau3776/DC1](http://www.sciencetranslationalmedicine.org/cgi/content/full/11/478/eaau3776/DC1)

Materials and Methods

Fig. S1. RT and non-RT tonsillar immunophenotyping of cohort 1.

Fig. S2. RT and non-RT tonsillar immunophenotyping of cohort 2.

Fig. S3. GAS-specific CD4<sup>+</sup> T cells by AIM assay.

Fig. S4. HLA typing of entire tonsillar cohort.

Fig. S5. SpeA-responsive GC-T<sub>FH</sub> cells.

Fig. S6. SpeA-responsive GC-T<sub>FH</sub> cells by AIM assay.

Fig. S7. SpeA induced GzmB production.

Fig. S8. SpeA-responsive GC-T<sub>FH</sub> cells by AIM assay.

Table S1. RNA-seq analysis.

Table S2. Flow cytometry antibodies for fresh tonsil stain.

Table S3. Flow cytometry antibodies for AIM assay.

Table S4. Flow cytometry antibodies for PBMC proliferation assay.

Table S5. Flow cytometry antibodies for GzmB detection.

Table S6. Flow cytometry antibodies used for sorting GC-T<sub>FH</sub> and non-B<sub>GC</sub> cells for GzmB expression after 5-day in vitro culture.

Table S7. Flow cytometry antibodies for GzmB detection from sorted GC-T<sub>FH</sub> cells.

Table S8. Flow cytometry antibodies used for sorting for cytotoxicity assay.

Data file S1. Primary data.

References (59–70)

### REFERENCES AND NOTES

- J. R. Carapetis, A. C. Steer, E. K. Mulholland, M. Weber, The global burden of group A streptococcal diseases. *Lancet Infect. Dis.* **5**, 685–694 (2005).
- S. T. Shulman, A. L. Bisno, H. W. Clegg, M. A. Gerber, E. L. Kaplan, G. Lee, J. M. Martin, C. Van Beneden, Clinical practice guideline for the diagnosis and management of group A streptococcal pharyngitis: 2012 update by the Infectious Diseases Society of America. *Clin. Infect. Dis.* **55**, 1279–1282 (2012).

3. M. H. Ebell, M. A. Smith, H. C. Barry, K. Ives, M. Carey, The rational clinical examination. Does this patient have strep throat? *JAMA* **284**, 2912–2918 (2000).
4. R. H. Schwartz, D. Kim, M. Martin, M. E. Pichichero, A reappraisal of the minimum duration of antibiotic treatment before approval of return to school for children with streptococcal pharyngitis. *Pediatr. Infect. Dis. J.* **34**, 1302–1304 (2015).
5. D. Van Brusselen, E. Vlieghe, P. Schelstraete, F. De Meulder, C. Vandeputte, K. Garmyn, W. Laffut, P. Van de Voorde, Streptococcal pharyngitis in children: To treat or not to treat? *Eur. J. Pediatr.* **173**, 1275–1283 (2014).
6. M. J. Walker, T. C. Barnett, J. D. McArthur, J. N. Cole, C. M. Gillen, A. Henningham, K. S. Sriprakash, M. L. Sanderson-Smith, V. Nizet, Disease manifestations and pathogenic mechanisms of group A *Streptococcus*. *Clin. Microbiol. Rev.* **27**, 264–301 (2014).
7. M. W. Cunningham, Pathogenesis of group A streptococcal infections. *Clin. Microbiol. Rev.* **13**, 470–511 (2000).
8. R. F. Baugh, S. M. Archer, R. B. Mitchell, R. M. Rosenfeld, R. Amin, J. J. Burns, D. H. Darrow, T. Giordano, R. S. Litman, K. K. Li, M. E. Mannix, R. H. Schwartz, G. Setzen, E. R. Wald, E. Wall, G. Sandberg, M. M. Patel; American Academy of Otolaryngology-Head and Neck Surgery Foundation, Clinical practice guideline: Tonsillectomy in children. *Otolaryngol. Head Neck Surg.* **144**, S1–S30 (2011).
9. A. L. Roberts, K. L. Connolly, D. J. Kirse, A. K. Evans, K. A. Poehling, T. R. Peters, S. D. Reid, Detection of group A *Streptococcus* in tonsils from pediatric patients reveals high rate of asymptomatic streptococcal carriage. *BMC Pediatr.* **12**, 3 (2012).
10. R. Mandavia, A. G. M. Schilder, P. A. Dimitriadis, E. Mossialos, Addressing the challenges in tonsillectomy research to inform health care policy: A review. *JAMA Otolaryngol. Head Neck Surg.* **143**, 943–947 (2017).
11. E. L. Abbot, W. D. Smith, G. P. S. Siou, C. Chiriboga, R. J. Smith, J. A. Wilson, B. H. Hirst, M. A. Kehoe, Pili mediate specific adhesion of *Streptococcus pyogenes* to human tonsil and skin. *Cell. Microbiol.* **9**, 1822–1833 (2007).
12. S. Bell, A. Howard, J. A. Wilson, E. L. Abbot, W. D. Smith, C. L. Townes, B. H. Hirst, J. Hall, *Streptococcus pyogenes* infection of tonsil explants is associated with a human  $\beta$ -defensin 1 response from control but not recurrent acute tonsillitis patients. *Mol. Oral Microbiol.* **27**, 160–171 (2012).
13. I. P. O. Pontin, D. C. J. Sanchez, R. Di Francesco, Asymptomatic group A *Streptococcus* carriage in children with recurrent tonsillitis and tonsillar hypertrophy. *Int. J. Pediatr. Otorhinolaryngol.* **86**, 57–59 (2016).
14. J. H. Jeong, D. W. Lee, R. A. Ryu, Y. S. Lee, S. H. Lee, J. O. Kang, K. Tae, Bacteriologic comparison of tonsil core in recurrent tonsillitis and tonsillar hypertrophy. *Laryngoscope* **117**, 2146–2151 (2007).
15. G. D. Victora, M. C. Nussenzweig, Germinal centers. *Annu. Rev. Immunol.* **30**, 429–457 (2012).
16. C. G. Vinuesa, M. A. Linterman, D. Yu, I. C. M. MacLennan, Follicular helper T cells. *Annu. Rev. Immunol.* **34**, 335–368 (2016).
17. S. Crotty, Follicular helper CD4 T cells (TFH). *Annu. Rev. Immunol.* **29**, 621–663 (2011).
18. S. Crotty, T follicular helper cell differentiation, function, and roles in disease. *Immunity* **41**, 529–542 (2014).
19. E. M. Mascini, M. Jansze, J. F. P. Schellekens, J. M. Musser, J. A. J. Faber, L. A. E. Verhoef-Verhage, L. Schouls, W. J. van Leeuwen, J. Verhoef, H. van Dijk, Invasive group A streptococcal disease in the Netherlands: Evidence for a protective role of anti-exotoxin A antibodies. *J. Infect. Dis.* **181**, 631–638 (2000).
20. H. Basma, A. Norrby-Teglund, Y. Guédez, A. McGeer, D. E. Low, O. El-Ahmedy, B. Schwartz, M. Kotb, Risk factors in the pathogenesis of invasive group A streptococcal infections: Role of protective humoral immunity. *Infect. Immun.* **67**, 1871–1877 (1999).
21. J. J. Zeppa, K. J. Kasper, I. Mohorovic, D. M. Mazzuca, S. M. M. Haeryfar, J. K. McCormick, Nasopharyngeal infection by *Streptococcus pyogenes* requires superantigen-responsive V $\beta$ -specific T cells. *Proc. Natl. Acad. Sci. U.S.A.* **114**, 10226–10231 (2017).
22. J. M. Dan, C. S. Lindestam Arlehamn, D. Weiskopf, R. da Silva Antunes, C. Haverar-Daughton, S. M. Reiss, M. Brigger, M. Bothwell, A. Sette, S. Crotty, A cytokine-independent approach to identify antigen-specific human germinal center T follicular helper cells and rare antigen-specific CD4<sup>+</sup>T cells in blood. *J. Immunol.* **197**, 983–993 (2016).
23. C. Haverar-Daughton, S. M. Reiss, D. G. Carnathan, J. E. Wu, K. Kendrick, A. Torrents de la Peña, S. P. Kasturi, J. M. Dan, M. Bothwell, R. W. Sanders, B. Pulendran, G. Silvestri, S. Crotty, Cytokine-independent detection of antigen-specific germinal center T follicular helper cells in immunized nonhuman primates using a live cell activation-induced marker technique. *J. Immunol.* **197**, 994–1002 (2016).
24. S. Reiss, A. E. Baxter, K. M. Cirelli, J. M. Dan, A. Morou, A. Daigneault, N. Brassard, G. Silvestri, J.-P. Routy, C. Haverar-Daughton, S. Crotty, D. E. Kaufmann, Comparative analysis of activation induced marker (AIM) assays for sensitive identification of antigen-specific CD4 T cells. *PLoS ONE* **12**, e0186998 (2017).
25. A. C. Steer, S. Vidmar, R. Ritika, J. Kado, M. Batzloff, A. W. J. Jenney, J. B. Carlin, J. R. Carapetis, Normal ranges of streptococcal antibody titers are similar whether streptococci are endemic to the setting or not. *Clin. Vaccine Immunol.* **16**, 172–175 (2009).
26. M. Kotb, A. Norrby-Teglund, A. McGeer, H. El-Sherbini, M. T. Dorak, A. Khurshid, K. Green, J. Peeples, J. Wade, G. Thomson, B. Schwartz, D. E. Low, An immunogenetic and molecular basis for differences in outcomes of invasive group A streptococcal infections. *Nat. Med.* **8**, 1398–1404 (2002).
27. V. Stanevicha, J. Eglite, A. Sochnevs, D. Gardovska, D. Zavadska, R. Shantere, HLA class II associations with rheumatic heart disease among clinically homogeneous patients in children in Latvia. *Arthritis Res. Ther.* **5**, R340–R346 (2003).
28. V. Stanevicha, J. Eglite, D. Zavadska, A. Sochnevs, R. Shantere, D. Gardovska, HLA class II DR and DQ genotypes and haplotypes associated with rheumatic fever among a clinically homogeneous patient population of Latvian children. *Arthritis Res. Ther.* **9**, R58 (2007).
29. E. Marijon, M. Mirabel, D. S. Celermajer, X. Jouven, Rheumatic heart disease. *Lancet* **379**, 953–964 (2012).
30. H. Kudat, G. Telci, A. B. Sozen, F. Oguz, V. Akkaya, M. Ozcan, D. Atilgan, M. Carin, O. Guven, The role of HLA molecules in susceptibility to chronic rheumatic heart disease. *Int. J. Immunogenet.* **33**, 41–44 (2006).
31. K. J. Kasper, J. J. Zeppa, A. T. Wakabayashi, S. X. Xu, D. M. Mazzuca, I. Welch, M. L. Baroja, M. Kotb, E. Cairns, P. P. Cleary, S. M. M. Haeryfar, J. K. McCormick, Bacterial superantigens promote acute nasopharyngeal infection by *Streptococcus pyogenes* in a human MHC class II-dependent manner. *PLOS Pathog.* **10**, e1004155 (2014).
32. S. U. Kazmi, R. Kansal, R. K. Aziz, M. Hooshdaran, A. Norrby-Teglund, D. E. Low, A. B. Halim, M. Kotb, Reciprocal, temporal expression of SpeA and SpeB by invasive M1T1 group A streptococcal isolates in vivo. *Infect. Immun.* **69**, 4988–4995 (2001).
33. G. Rajagopalan, G. Polich, M. M. Sen, M. Singh, B. E. Epstein, A. K. Lytle, M. S. Rouse, R. Patel, C. S. David, Evaluating the role of HLA-DQ polymorphisms on immune response to bacterial superantigens using transgenic mice. *Tissue Antigens* **71**, 135–145 (2008).
34. A. Norrby-Teglund, G. T. Nepom, M. Kotb, Differential presentation of group A streptococcal superantigens by HLA class II DQ and DR alleles. *Eur. J. Immunol.* **32**, 2570–2577 (2002).
35. P. R. Shea, A. L. Ewbank, J. H. Gonzalez-Lugo, A. J. Martagon-Rosado, J. C. Martinez-Gutierrez, H. A. Rehman, M. Serrano-Gonzalez, N. Fittipaldi, S. B. Beres, A. R. Flores, D. E. Low, B. M. Willey, J. M. Musser, Group A *Streptococcus emm* gene types in pharyngeal isolates, Ontario, Canada, 2002–2010. *Emerg. Infect. Dis.* **17**, 2010–2017 (2011).
36. H. A. Haukness, R. R. Tanz, R. B. Thomson Jr, D. K. Piery, E. L. Kaplan, B. Beall, D. Johnson, N. P. Hoe, J. M. Musser, S. T. Shulman, The heterogeneity of endemic community pediatric group A streptococcal pharyngeal isolates and their relationship to invasive isolates. *J. Infect. Dis.* **185**, 915–920 (2002).
37. E. L. Kaplan, J. T. Wotton, D. R. Johnson, Dynamic epidemiology of group A streptococcal serotypes associated with pharyngitis. *Lancet* **358**, 1334–1337 (2001).
38. A. H. Tart, M. J. Walker, J. M. Musser, New understanding of the group A *Streptococcus* pathogenesis cycle. *Trends Microbiol.* **15**, 318–325 (2007).
39. R. K. Aziz, M. J. Pabst, A. Jeng, R. Kansal, D. E. Low, V. Nizet, M. Kotb, Invasive M1T1 group A *Streptococcus* undergoes a phase-shift in vivo to prevent proteolytic degradation of multiple virulence factors by SpeB. *Mol. Microbiol.* **51**, 123–134 (2004).
40. R. K. Aziz, M. Kotb, Rise and persistence of global M1T1 clone of *Streptococcus pyogenes*. *Emerg. Infect. Dis.* **14**, 1511–1517 (2008).
41. C. D. C. Allen, T. Okada, H. L. Tang, J. G. Cyster, Imaging of germinal center selection events during affinity maturation. *Science* **315**, 528–531 (2007).
42. G. D. Victora, T. A. Schwickert, D. R. Fooksman, A. O. Kamphorst, M. Meyer-Hermann, M. L. Dustin, M. C. Nussenzweig, Germinal center dynamics revealed by multiphoton microscopy with a photoactivatable fluorescent reporter. *Cell* **143**, 592–605 (2010).
43. A. D. Gitlin, Z. Shulman, M. C. Nussenzweig, Clonal selection in the germinal centre by regulated proliferation and hypermutation. *Nature* **509**, 637–640 (2014).
44. Z. Shulman, A. D. Gitlin, S. Targ, M. Jankovic, G. Pasqual, M. C. Nussenzweig, G. D. Victora, T follicular helper cell dynamics in germinal centers. *Science* **341**, 673–677 (2013).
45. D. Liu, H. Xu, C. Shih, Z. Wan, X. Ma, W. Ma, D. Luo, H. Qi, T-B-cell entanglement and ICOSL-driven feed-forward regulation of germinal centre reaction. *Nature* **517**, 214–218 (2015).
46. Z. Shulman, A. D. Gitlin, J. S. Weinstein, B. Lainez, E. Esplugues, R. A. Flavell, J. E. Craft, M. C. Nussenzweig, Dynamic signaling by T follicular helper cells during germinal center B cell selection. *Science* **345**, 1058–1062 (2014).
47. J. Jacob, R. Kassir, G. Kelseo, In situ studies of the primary immune response to (4-hydroxy-3-nitrophenyl)acetyl. I. The architecture and dynamics of responding cell populations. *J. Exp. Med.* **173**, 1165–1175 (1991).
48. Q. Li, P. J. Skinner, S.-J. Ha, L. Duan, T. L. Mattila, A. Hage, C. White, D. L. Barber, L. O'Mara, P. J. Southern, C. S. Reilly, J. V. Carls, C. J. Miller, R. Ahmed, A. T. Haase, Visualizing antigen-specific and infected cells in situ predicts outcomes in early viral infection. *Science* **323**, 1726–1729 (2009).
49. B. S. Wendel, D. Del Alcazar, C. He, P. M. Del Rio-Estrada, B. Aiamkitsumrit, Y. Ablanedo-Terrazas, S. M. Hernandez, K.-Y. Ma, M. R. Betts, L. Pulido, J. Huang,

- P. A. Gimotty, G. Reyes-Terán, N. Jiang, L. F. Su, The receptor repertoire and functional profile of follicular T cells in HIV-infected lymph nodes. *Sci. Immunol.* **3**, eaan8884 (2018).
50. J. Alshekaili, R. Chand, C. E. Lee, S. Corley, K. Kwong, I. Papa, D. A. Fulcher, K. L. Randall, J. W. Leiding, C. S. Ma, M. R. Wilkins, G. Uzel, C. C. Goodnow, C. G. Vinuesa, S. G. Tangye, M. C. Cook, STAT3 regulates cytotoxicity of human CD57<sup>+</sup> CD4<sup>+</sup> T cells in blood and lymphoid follicles. *Sci. Rep.* **8**, 3529 (2018).
  51. C. S. Ma, S. G. Tangye, Immunology: Cytotoxic T cells that escape exhaustion. *Nature* **537**, 312–314 (2016).
  52. M. Buggert, S. Nguyen, L. M. McLane, M. Steblyanko, N. Anikeeva, D. Paquin-Proulx, P. M. Del Rio-Estrada, Y. Ablanedo-Terrazas, K. Noyan, M. A. Reuter, K. Demers, J. K. Sandberg, M. A. Eller, H. Streeck, M. Jansson, P. Nowak, A. Sönnnerborg, D. H. Canaday, A. Naji, E. J. Wherry, M. L. Robb, S. G. Deeks, G. Reyes-Terán, Y. Sykulev, A. C. Karlsson, M. R. Betts, D. C. Douek, Limited immune surveillance in lymphoid tissue by cytolytic CD4<sup>+</sup> T cells during health and HIV disease. *PLoS Pathog.* **14**, e1006973 (2018).
  53. C. Petrovas, S. Ferrando-Martinez, M. Y. Gerner, J. P. Casazza, A. Pegu, C. Deleage, A. Cooper, J. Hataye, S. Andrews, D. Ambrozak, P. M. Del Rio-Estrada, E. Boritz, R. Paris, E. Moysi, K. L. Boswell, E. Ruiz-Mateos, I. Vagios, M. Leal, Y. Ablanedo-Terrazas, A. Rivero, L. A. Gonzalez-Hernandez, A. B. McDermott, S. Moir, G. Reyes-Terán, F. Docobo, G. Pantaleo, D. C. Douek, M. R. Betts, J. D. Estes, R. N. Germain, J. R. Mascola, R. A. Koup, Follicular CD8 T cells accumulate in HIV infection and can kill infected cells in vitro via bispecific antibodies. *Sci. Transl. Med.* **9**, eaag2285 (2017).
  54. Y. Fukazawa, R. Lum, A. A. Okoye, H. Park, K. Matsuda, J. Y. Bae, S. I. Hagen, R. Shoemaker, C. Deleage, C. Lucero, D. Morcock, T. Swanson, A. W. Legasse, M. K. Axthelm, J. Hesselgesser, R. Gelezianus, V. M. Hirsch, P. T. Edlfsen, M. Piatak, J. D. Estes, J. D. Lifson, L. J. Picker, B cell follicle sanctuary permits persistent productive simian immunodeficiency virus infection in elite controllers. *Nat. Med.* **21**, 132–139 (2015).
  55. G. H. Mylvaganam, D. Rios, H. M. Abdelaal, S. Iyer, G. Tharp, M. Mavigner, S. Hicks, A. Chahroudi, R. Ahmed, S. E. Bosinger, I. R. Williams, P. J. Skinner, V. Velu, R. R. Amara, Dynamics of SIV-specific CXCR5<sup>+</sup> CD8 T cells during chronic SIV infection. *Proc. Natl. Acad. Sci. U.S.A.* **114**, 1976–1981 (2017).
  56. S. J. Im, M. Hashimoto, M. Y. Gerner, J. Lee, H. T. Kissick, M. C. Burger, Q. Shan, J. S. Hale, J. Lee, T. H. Nasti, A. H. Sharpe, G. J. Freeman, R. N. Germain, H. I. Nakaya, H.-H. Xue, R. Ahmed, Defining CD8<sup>+</sup> T cells that provide the proliferative burst after PD-1 therapy. *Nature* **537**, 417–421 (2016).
  57. Y. S. Choi, J. A. Gullicksrud, S. Xing, Z. Zeng, Q. Shan, F. Li, P. E. Love, W. Peng, H.-H. Xue, S. Crotty, LEF-1 and TCF-1 orchestrate T<sub>FH</sub> differentiation by regulating differentiation circuits upstream of the transcriptional repressor Bcl6. *Nat. Immunol.* **16**, 980–990 (2015).
  58. Y. A. Leong, Y. Chen, H. S. Ong, D. Wu, K. Man, C. Deleage, M. Minnich, B. J. Meckiff, Y. Wei, Z. Hou, D. Zotos, K. A. Fenix, A. Atnerkar, S. Preston, J. G. Chipman, G. J. Beilman, C. C. Allison, L. Sun, P. Wang, J. Xu, J. G. Toe, H. K. Lu, Y. Tao, U. Palendira, A. L. Dent, A. L. Landay, M. Pellegrini, I. Comerford, S. R. McColl, T. W. Schacker, H. M. Long, J. D. Estes, M. Busslinger, G. T. Belz, S. R. Lewin, A. Kallies, D. Yu, CXCR5<sup>+</sup> follicular cytotoxic T cells control viral infection in B cell follicles. *Nat. Immunol.* **17**, 1187–1196 (2016).
  59. M. A. Angelo, A. Grifoni, P. H. O'Rourke, J. Sidney, S. Paul, B. Peters, A. D. de Silva, E. Phillips, S. Mallal, S. A. Diehl, B. D. Kirkpatrick, S. S. Whitehead, A. P. Durbin, A. Sette, D. Weiskopf, Human CD4<sup>+</sup> T cell responses to an attenuated tetravalent dengue vaccine parallel those induced by natural infection in magnitude, HLA restriction, and antigen specificity. *J. Virol.* **91**, e02147–16 (2017).
  60. R. da Silva Antunes, S. Paul, J. Sidney, D. Weiskopf, J. M. Dan, E. Phillips, S. Mallal, S. Crotty, A. Sette, C. S. Lindestam Arlehamn, Definition of human epitopes recognized in tetanus toxoid and development of an assay strategy to detect ex vivo tetanus CD4<sup>+</sup> T cell responses. *PLoS ONE* **12**, e0169086 (2017).
  61. T. Bancroft, M. B. C. Dillon, R. da Silva Antunes, S. Paul, B. Peters, S. Crotty, C. S. Lindestam Arlehamn, A. Sette, Th1 versus Th2 T cell polarization by whole-cell and acellular childhood pertussis vaccines persists upon re-immunization in adolescence and adulthood. *Cell. Immunol.* **304–305**, 35–43 (2016).
  62. D. M. McKinney, S. Southwood, D. Hinz, C. Oseroff, C. S. L. Arlehamn, V. Schulten, R. Taplitz, D. Broide, W. A. Hanekom, T. J. Scriba, R. Wood, R. Alam, B. Peters, J. Sidney, A. Sette, A strategy to determine HLA class II restriction broadly covering the DR, DP, and DQ allelic variants most commonly expressed in the general population. *Immunogenetics* **65**, 357–370 (2013).
  63. C. Oseroff, J. Sidney, R. Vita, V. Tripple, D. M. McKinney, S. Southwood, T. M. Brodie, F. Sallusto, H. Grey, R. Alam, D. Broide, J. A. Greenbaum, R. Kolla, B. Peters, A. Sette, T cell responses to known allergen proteins are differently polarized and account for a variable fraction of total response to allergen extracts. *J. Immunol.* **189**, 1800–1811 (2012).
  64. S. Chatellier, N. Ihendyane, R. G. Kansal, F. Khambaty, H. Basma, A. Norrby-Teglund, D. E. Low, A. McGeer, M. Kotb, Genetic relatedness and superantigen expression in group A *Streptococcus* serotype M1 isolates from patients with severe and nonsevere invasive diseases. *Infect. Immun.* **68**, 3523–3534 (2000).
  65. O. P. Kuipers, P. G. G. A. de Ruyter, M. Kleerebezem, W. M. de Vos, Controlled overproduction of proteins by lactic acid bacteria. *Trends Biotechnol.* **15**, 135–140 (1997).
  66. C. N. LaRock, S. Döhrmann, J. Todd, R. Corriden, J. Olson, T. Johannssen, B. Lepenies, R. L. Gallo, P. Ghosh, V. Nizet, Group A streptococcal M1 protein sequesters cathelicidin to evade innate immune killing. *Cell Host Microbe* **18**, 471–477 (2015).
  67. G. Seumois, L. Chavez, A. Gerasimova, M. Lienhard, N. Omran, L. Kalinke, M. Vedanayagam, A. P. V. Ganesan, A. Chawla, R. Djukanović, K. M. Ansel, B. Peters, A. Rao, P. Vijayanand, Epigenomic analysis of primary human T cells reveals enhancers associated with T<sub>H</sub>2 memory cell differentiation and asthma susceptibility. *Nat. Immunol.* **15**, 777–788 (2014).
  68. C. Trapnell, L. Pachter, S. L. Salzberg, TopHat: Discovering splice junctions with RNA-seq. *Bioinformatics* **25**, 1105–1111 (2009).
  69. D. Weiskopf, D. J. Bangs, J. Sidney, R. V. Kolla, A. D. de Silva, A. M. de Silva, S. Crotty, B. Peters, A. Sette, Dengue virus infection elicits highly polarized CX3CR1<sup>+</sup> cytotoxic CD4<sup>+</sup> T cells associated with protective immunity. *Proc. Natl. Acad. Sci. U.S.A.* **112**, E4256–E4263 (2015).
  70. F.-M. Mbitikon-Kobo, M. Bonneville, R.-P. Sekaly, L. Trautmann, Ex vivo measurement of the cytotoxic capacity of human primary antigen-specific CD8 T cells. *J. Immunol. Methods* **375**, 252–257 (2012).
- Acknowledgments:** We thank S. D. Boyd, K. J. L. Jackson, and J. Oak at Stanford University Medical Center for assistance with histology; C. Kim, L. Nosworthy, D. Hinz, and R. Simmons at LJI for assistance with flow cytometry sorting; Z. Mikulski, A. Lamberth, and the LJI Microscopy Core for assistance with confocal imaging; Y. Altman, the Sanford Burnham Prebys Flow Cytometry Shared Resource, and the James B. Pendleton Charitable Trust for assistance with ImageStream; A. Mittal (UCSD) for assistance with clinical data and N. Bundogji (Rady Children's Hospital) for study enrollment; the LJI Bioinformatics Core and M. Locci for assistance with bioinformatics analysis; A. Frazier and J. Sidney for assistance with HLA typing and analyses; and the donors for participating. **Funding:** This work was supported by a Thrasher Research Fund for an Early Career Award 12969 (to J.M.D.), Pediatric Extramural NIH Loan Repayment Program L40 AI126497 (to J.M.D.), NIH NIAID K08 AI35078 (to J.M.D.), NIH NIAID R01 AI135193 (to S.C.), NIH Center for HIV/AIDS Vaccine Immunology and Immunogen Discovery Grant 1UM1AI100663 (to S.C.), internal funding from the La Jolla Institute (to S.C.) and the UCSD Department of Medicine, Division of Infectious Diseases NIH Training Grants (T32 AI007036 and T32 AI007384 to J.M.D.), NIAID grant R01 AI077780 (to V.N.), Clinical Research Fellowship Grant UK Charity no. 1089464 (to D.L., R.I.C., and C.H.O.), NIH S10 ODD016262 (LJI), and NIH S10 RR027366 (LJI). **Author contributions:** S.C., V.N., C.H.-D., and J.M.D. designed the study. M. Bothwell and M. Brigger enrolled patients and provided clinical specimens. K. Kendrick, K. Kaushik, and R.A.-k. assisted with tonsillar cell isolation. K. Kendrick measured GC areas and performed immunohistochemistry. J.M.D. designed the AIM assay; performed flow cytometry, confocal microscopy experiments, cell culture assays, and enzyme-linked immunosorbent assays; and analyzed immunophenotyping, HLA-typing, and RNA-seq data. C.S.L.A. enrolled patients and provided HLA-typed PBMCs. A.S. facilitated HLA-typing and provided HLA-expressing cell lines and cells for pilot experiments. E.L.A., C.N.L., and V.N. provided antibiotic-killed GAS, antibiotic-killed *L. lactis*, and SpeA-deficient GAS. J.M.D. S.L.R., P.V., and G.S. performed RNA-seq. D.L., R.I.C., and C.H.O. provided healthy LNs. S.C. and J.M.D. wrote the manuscript with input from all authors. **Competing interests:** The authors declare that they have no competing financial interests. S.C. and J.M.D. have an International Patent Application no. PCT/US18/30948, Diagnosis and treatment of infection involving killer T follicular helper cells, methods of preparation, and uses thereof. **Data and materials availability:** All data associated with this study are in the paper and/or the Supplementary Materials. The RNA-seq data are available in the Gene Expression Omnibus (GEO) database under the accession number GSE123977.
- Submitted 4 June 2018  
Resubmitted 29 September 2018  
Accepted 11 January 2019  
Published 6 February 2019  
10.1126/scitranslmed.aau3776
- Citation:** J. M. Dan, C. Havenar-Daughton, K. Kendrick, R. Al-kolla, K. Kaushik, S. L. Rosales, E. L. Anderson, C. N. LaRock, P. Vijayanand, G. Seumois, D. Layfield, R. I. Cutress, C. H. Ottensmeier, C. S. Lindestam Arlehamn, A. Sette, V. Nizet, M. Bothwell, M. Brigger, S. Crotty, Recurrent group A *Streptococcus* tonsillitis is an immunosusceptibility disease involving antibody deficiency and aberrant T<sub>FH</sub> cells. *Sci. Transl. Med.* **11**, eaau3776 (2019).

## AUTOIMMUNITY

## Sustained B cell depletion by CD19-targeted CAR T cells is a highly effective treatment for murine lupus

Rita Kansal<sup>1</sup>, Noah Richardson<sup>1</sup>, Indira Neeli<sup>1</sup>, Saleem Khawaja<sup>1</sup>, Damian Chamberlain<sup>1</sup>, Marium Ghani<sup>1</sup>, Qurat-ul-ain Ghani<sup>1</sup>, Louisa Balazs<sup>2</sup>, Sarka Beranova-Giorgianni<sup>3</sup>, Francesco Giorgianni<sup>3</sup>, James N. Kochenderfer<sup>4</sup>, Tony Marion<sup>1</sup>, Lorraine M. Albritton<sup>1</sup>, Marko Radic<sup>1\*</sup>

The failure of anti-CD20 antibody (Rituximab) as therapy for lupus may be attributed to the transient and incomplete B cell depletion achieved in clinical trials. Here, using an alternative approach, we report that complete and sustained CD19<sup>+</sup> B cell depletion is a highly effective therapy in lupus models. CD8<sup>+</sup> T cells expressing CD19-targeted chimeric antigen receptors (CARs) persistently depleted CD19<sup>+</sup> B cells, eliminated autoantibody production, reversed disease manifestations in target organs, and extended life spans well beyond normal in the (NZB × NZW) F<sub>1</sub> and MRL<sup>fas/fas</sup> mouse models of lupus. CAR T cells were active for 1 year in vivo and were enriched in the CD44<sup>+</sup>CD62L<sup>+</sup> T cell subset. Adoptively transferred splenic T cells from CAR T cell-treated mice depleted CD19<sup>+</sup> B cells and reduced disease in naive autoimmune mice, indicating that disease control was cell-mediated. Sustained B cell depletion with CD19-targeted CAR T cell immunotherapy is a stable and effective strategy to treat murine lupus, and its effectiveness should be explored in clinical trials for lupus.

## INTRODUCTION

Systemic lupus erythematosus (SLE) is an autoimmune disease that is difficult to diagnose and treat because of the episodic nature of flare-ups, the involvement of multiple organ systems and variable presentation, and severity (1). Autoantibodies to DNA and nuclear protein autoantigens are consistently present in lupus and contribute to pathogenesis by forming immune complex deposits in various tissues (2, 3). Additional B cell contributions to lupus include antigen presentation to self-reactive T cells and the secretion of inflammatory cytokines. Approaches that inactivate or deplete B cells offer attractive therapies for lupus, and efforts to identify promising targets on B cells merit continued attention (4–6).

B cell depletion with a monoclonal antibody against the B cell surface marker CD20, Rituximab, has shown therapeutic promise in rheumatoid arthritis (7) and multiple sclerosis (8) but was unsuccessful in two separate clinical trials for SLE (9, 10). Patients whose B cell depletion in peripheral blood occurred faster, was more complete, or lasted longer experienced the most notable improvements in disease presentation in the Lupus Nephritis Assessment with Rituximab (LUNAR) trial (10). However, disease scores and lupus flares did not distinguish between treatment and placebo groups, such that neither the Exploratory Phase II/III SLE Evaluation of Rituximab (EXPLORER) (9) nor LUNAR (10) clinical trials met predetermined end points for clinical efficacy. Studies in lupus-prone mice showed that high concentrations of endogenous immune complexes blocked macrophage function and required a higher dose of anti-CD20 antibody to achieve B cell depletion (11–13). Incomplete B cell depletion of tissue-resident B cells (10), or the transient nature of the treat-

ment, may have contributed to the failure of the initial Rituximab trials to attain satisfactory outcomes.

Administration of anti-CD20 antibodies has additional limitations as treatment for lupus. Upon injection, monoclonal antibodies follow drug-like pharmacokinetics with exponential decay that requires repeated administrations to achieve and maintain a therapeutic dose (14). Over time, resistance to the treatment arises in the host and further limits use (15). Cancer immunotherapy to target malignant transformed B cells has led to an alternative approach that can deplete B cells. Cytotoxic T cells, which express transduced genes for surface receptors against CD19, kill the targeted cells upon binding (16, 17). Autologous T cells with such CD19-targeted chimeric antigen receptors (CARs) have shown remarkable efficacy in a growing number of B cell malignancies because they retain potency over time and can lead to lasting remission (18). Cell-based therapies provide further advantages over antibodies because CAR T cells require only a single administration, migrate to multiple lymphoid tissues and organs in the recipient, and develop into both effector and memory cell populations.

Here, we test whether permanent and profound B cell depletion by CD19-targeted CAR T cells can lead to lasting remission of experimental lupus. In two mouse strains that are reliable models of SLE and that differ in the underlying genetic mechanisms leading to autoimmunity (19), sustained CD19<sup>+</sup> B cell depletion prevented autoantibody production, alleviated manifestations of lupus pathogenesis, and lengthened life spans. In addition, B cell depletion affected the distribution of T cell populations, preventing the disease-associated bias toward CD4<sup>+</sup> lymphocytes (20).

## RESULTS

## Experimental design and implementation

The experimental design for testing of CD19-targeted CAR T cells in mouse models of lupus was closely related to a standard CAR approach, except that we used purified CD8<sup>+</sup> T cells because of concern with the potential disease-enhancing effect of autoreactive CD4<sup>+</sup> T cells (Fig. 1, A to D). We used the 1D3 CD19-targeted CAR (21), which consists of the 1D3 extracellular single-chain Fv (heterodimer

<sup>1</sup>Department of Microbiology, Immunology and Biochemistry, University of Tennessee Health Science Center, Memphis, TN 38163, USA. <sup>2</sup>Department of Pathology, University of Tennessee Health Science Center, Memphis, TN 38163, USA. <sup>3</sup>Department of Pharmaceutical Sciences, University of Tennessee Health Science Center, Memphis, TN 38163, USA. <sup>4</sup>Experimental Transplantation and Immunology Branch, Center for Cancer Research, National Cancer Institute, Bethesda, MD, 20892, USA.

\*Corresponding author. Email: mradic@uthsc.edu

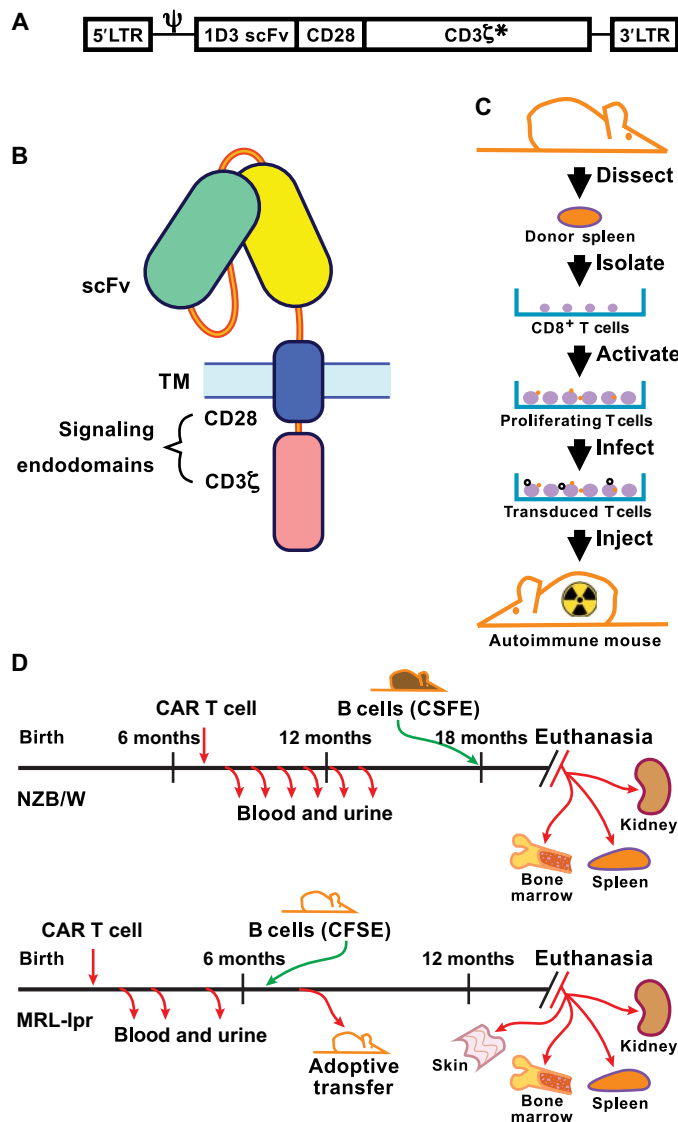


**Fig. 1. CAR design and transduction.** (A) The structural gene for 1D3-28Z.1-3 is shown downstream of the MSGV 5' long terminal repeat (LTR) and splice acceptor ( $\Psi$ ). The asterisk indicates that the first and third ITAMs in CD3 $\zeta$  have tyrosine to alanine replacement mutations. (B) Diagram of CAR protein in the cell membrane showing the extracellular single-chain Fv (scFv) domain and the transmembrane (TM) and signaling domains that combine CD28 and CD3 $\zeta$  C termini. (C) Steps involved in the isolation, activation, and transduction of CD8<sup>+</sup> splenocytes with virus before infusion into a recipient mouse that was irradiated ahead of T cell transfer to achieve transient myeloablation. (D) Timeline of CAR T cell treatment and sample collection in NZB/W and MRL-lpr mice. CFSE, carboxyfluorescein diacetate succinimidyl ester.

of the variable region of the light and heavy chains) domain linked to the CD28 transmembrane and cytoplasmic signaling domains and a variant CD3 $\zeta$  C terminus (Fig. 1A). This CD3 $\zeta$  variant contains alanine residues in place of the conserved tyrosine residues in two of the three cytoplasmic immunoreceptor tyrosine-based activation motif (ITAM) domains. These mutations reduce activation and mitigate the subsequent exhaustion of the CAR T cells, thus contributing to increased persistence of the engineered T cells in vivo (21, 22). Recipient mice were conditioned by irradiation to facilitate engraft-

ment of the transferred T cells by transiently depleting the rapidly dividing endogenous lymphoid and myeloid cell populations.

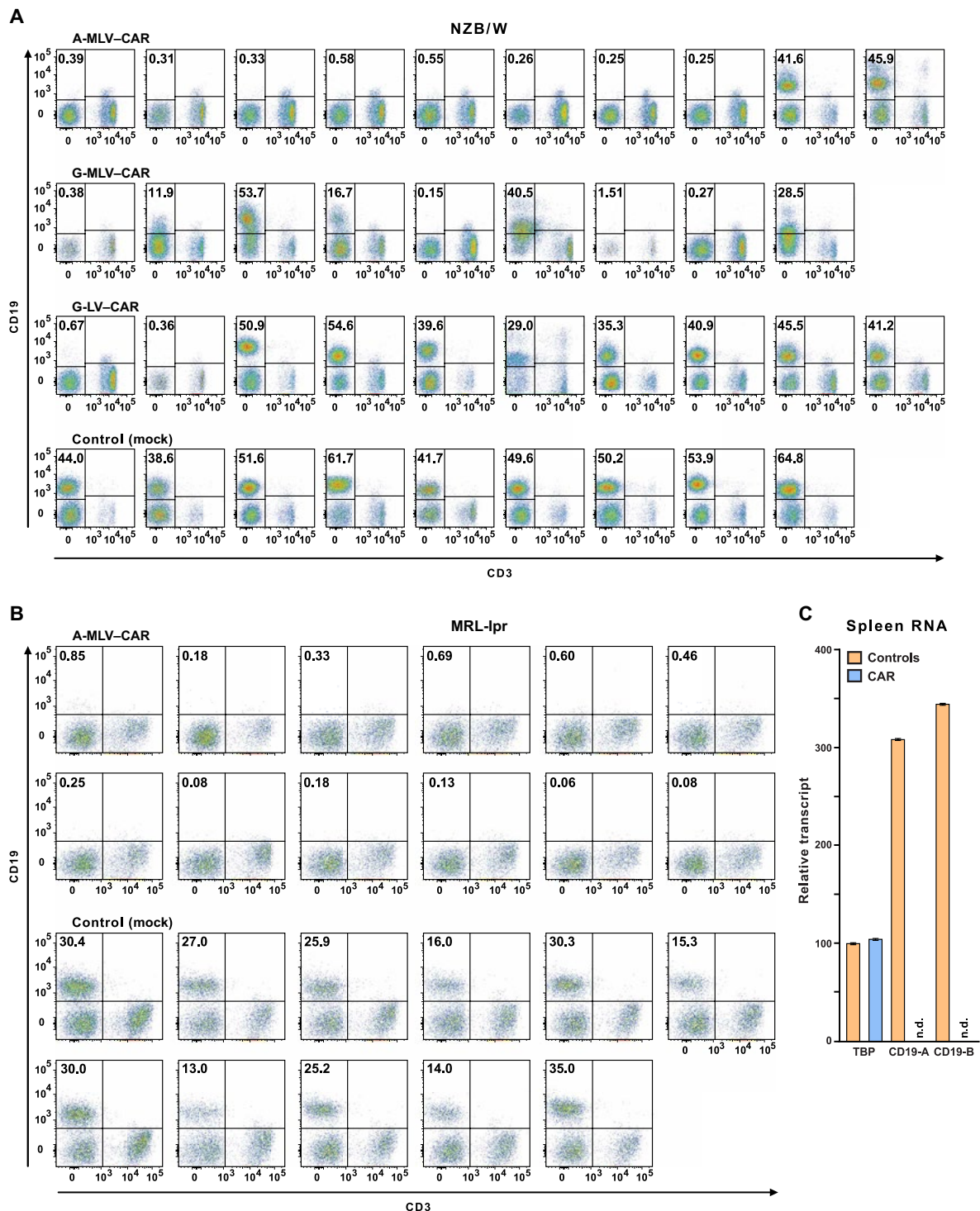
To evaluate gene delivery methods, we transduced the CD19-targeted CAR into splenic CD8<sup>+</sup> T cells via different virus transduction methods. In the (NZB  $\times$  NZW) F<sub>1</sub> (NZB/W) lupus model, 7-month-old female mice were used as donors of CD8<sup>+</sup> T cells for transduction and as recipients of the CD19-targeted CAR T cells. We chose female mice of that age because they manifest overt signs of autoimmune disease (19). The three virus transductions achieved between 5 and 15% expression in primary T cells and more than 90% expression in cells from the human Jurkat T cell line (fig. S1). After 5 days of cell culture, we injected  $1.2 \times 10^6$  transduced CD8<sup>+</sup> T cells per mouse from one of the three tested viral vector groups (table S1) and an equal number of mock-transduced T cells into control mice.

The different viral vectors achieved different efficiencies of B cell depletion (Fig. 2A and table S1). CD19<sup>+</sup> B cells were depleted in 8 of 10 NZB/W mice receiving CD8<sup>+</sup> T cells transduced with the amphotropic murine leukemia virus (A-MLV) retrovirus, in 4 of 9 mice receiving CD8<sup>+</sup> T cells transduced with vesicular stomatitis virus G glycoprotein (VSV-G)-pseudotyped MLV, and in only 2 of 10 mice that received CD8<sup>+</sup> T cells transduced with VSV-G-pseudotyped lentivirus (G-LV). These results defined two comparison groups for follow-up studies, those that were CD19<sup>+</sup> B cell depleted (CD19-d) and those in which CD19<sup>+</sup> B cells recovered within 3 weeks after the transient myeloablation. The CD19<sup>+</sup> B cell depletion phenotypes were stable thereafter because only one mouse that showed CD19<sup>+</sup> B cell depletion at 4 weeks after CAR T cell infusion regained CD19<sup>+</sup> B cells by 8 weeks after treatment (fig. S2). All other CAR T cell-treated mice, in which the CAR T cell infusion depleted CD19<sup>+</sup> B cells, exhibited CD19<sup>+</sup> B cell aplasia throughout the course of the experiments, more than 1 year from the administration of transduced T cells.

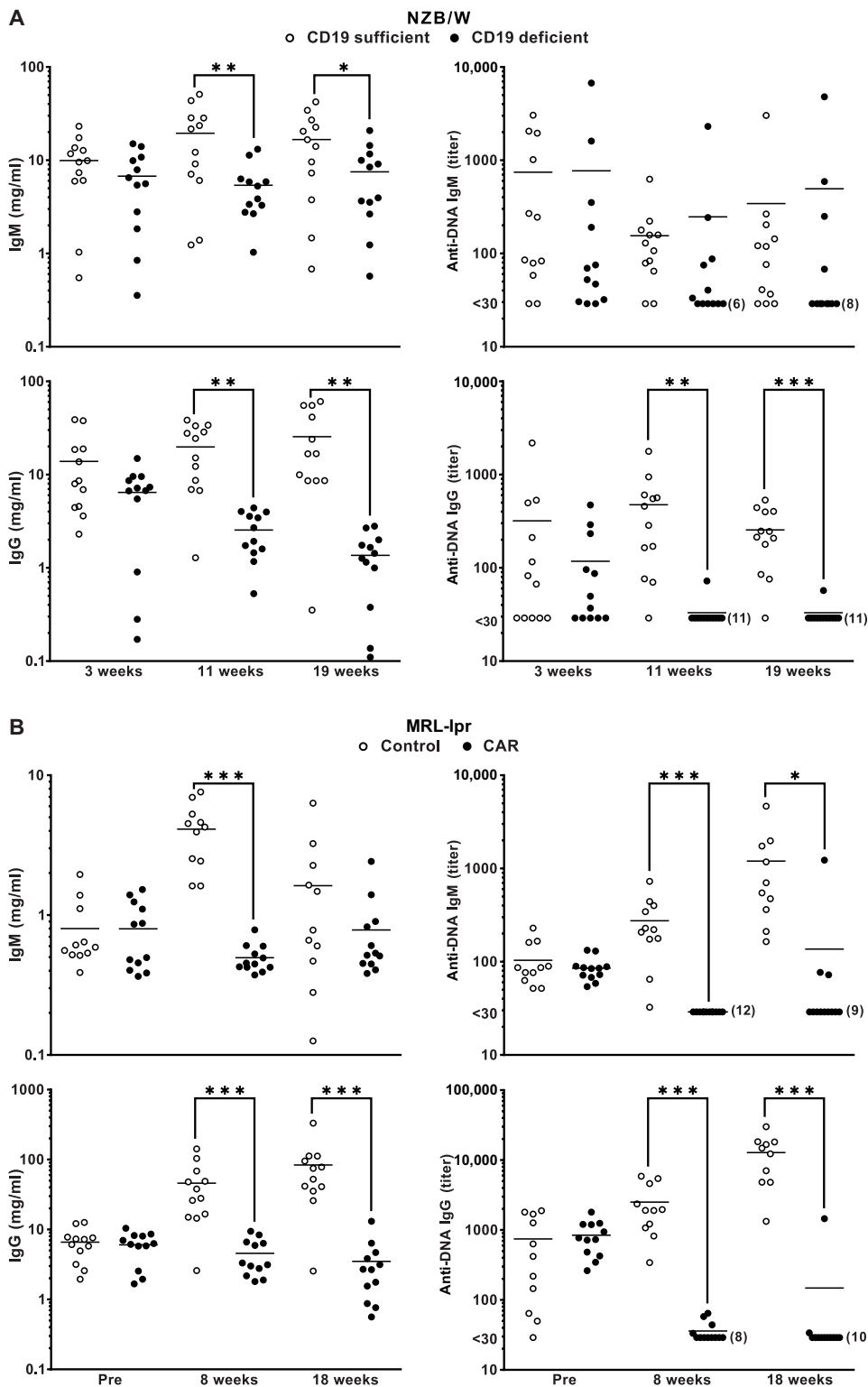
Encouraged by the initial success of the CD19-targeted CAR approach in NZB/W female mice, we expanded the study to include MRL<sup>fas/fas</sup> (MRL-lpr) mice. These mice develop a lupus-like disease that is T cell-driven and manifests more quickly than the disease of NZB/W mice (19). Two-month-old MRL-lpr female mice received CD19-targeted CD8<sup>+</sup> T cells from same-age donor mice after transduction with the A-MLV retrovirus. This virus, along with an improvement of injection procedures (see Materials and Methods), led to the depletion of CD19<sup>+</sup> B cells from 12 of 12 MRL-lpr mice (Fig. 2B). As controls, we used MRL-lpr female mice infused with mock-transduced syngeneic CD8<sup>+</sup> T cells. To test whether CD19-targeted CAR T cells select for structural variants of CD19 that would not be detected by flow cytometry, we quantified CD19 message in splenic RNA from CAR T cell-treated and control mice (Fig. 2C). Probes for exons 5 and 6 and exons 14 and 15 of CD19 confirmed absence of CD19 gene expression in splens of treated mice 1 year after CAR T cell transfer.

**Serology of CAR T cell-treated mice**

We determined total plasma IgM (immunoglobulin M), IgG, and anti-DNA autoantibody titers using enzyme-linked immunosorbent assay (ELISA) in CAR T cell-treated and control mice (Fig. 3). The results revealed statistically significant differences between CAR T cell-treated mice that were CD19-d versus treated but CD19 sufficient (CD19-s) mice and control mice. Total serum IgM and IgG were decreased in CD19-d mice from 8 to 11 weeks to 18 to 19 weeks after CAR T cell injections (for NZB/W and MRL-lpr, respectively;



**Fig. 2. Flow cytometry of blood lymphocytes from CAR T cell-treated mice and controls.** Mice were administered CD19-targeted CAR CD8<sup>+</sup> T cells transduced by one of three different viruses, as indicated above the plots. CD19<sup>+</sup> B cell depletion was assessed 2 months after treatment. Pseudocolor plots indicate CD19 and CD3 expression on lymphocytes, as defined by forward and side scatter in blood from individual mice. Frequencies of CD19<sup>+</sup> B cells are shown in the top left quadrant. **(A)** Fourteen NZB/W mice in the three transduction groups that had less than 1% CD19<sup>+</sup> lymphocytes were designated as CD19-d, whereas control mice and 15 of the CAR T cell-treated mice that had 12 to 60% CD19<sup>+</sup> B cells were combined into the CD19-sufficient (CD19-s) experimental group. **(B)** MRL-lpr mice were injected with A-MLV-CAR-transduced CD8<sup>+</sup> T cells or with nontransduced CD8<sup>+</sup> T cells (control), and frequencies of CD19<sup>+</sup> lymphocytes were determined. **(C)** Total RNA from the spleens of four control and four CAR T cell-treated mice was purified to measure transcripts coding for CD19 and TATA binding protein (TBP). CD19 message, as measured by reverse transcription polymerase chain reaction (RT-PCR) at two exon-intron boundaries (CD19-A or CD19-B; see table S2 for details), was determined in CAR T cell-treated mice and controls. n.d., nondetectable.



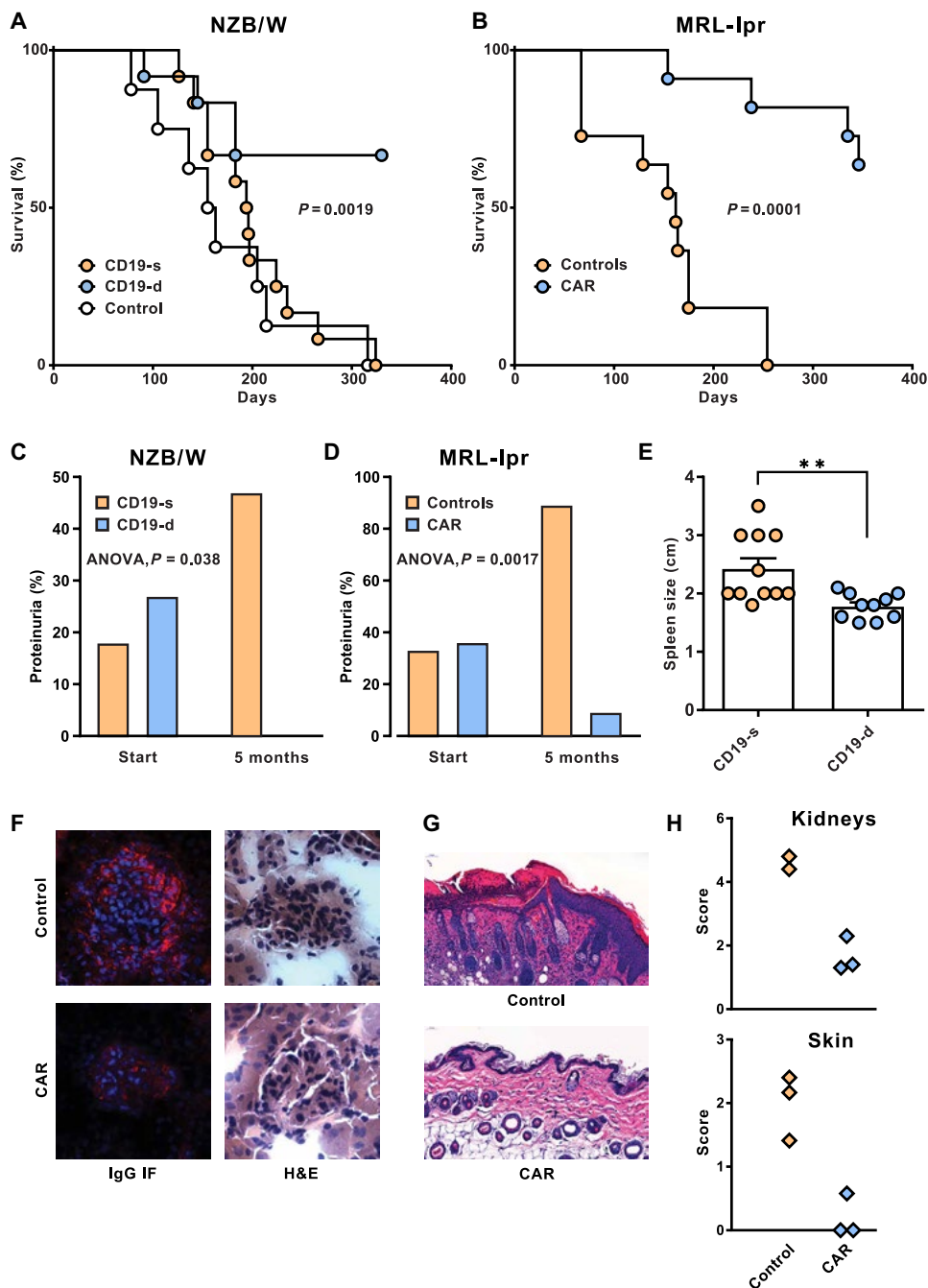
**Fig. 3. Serologic analysis of IgM and IgG concentrations and anti-DNA reactivities at different times after CAR T cell infusion.** (A) NZB/W and (B) MRL-lpr plasma were tested using ELISA for total IgM and IgG concentration and IgM and IgG anti-DNA titers. Values for CD19-d and CD19-s and control mice are indicated. IgM and IgG standards were used to generate standard curves for estimating IgM and IgG concentrations. Times of plasma collection for the relevant groups are indicated. Horizontal lines are means. Differences between measurements taken at the indicated time points were compared by one-tailed t test, and significance is indicated by \* $P < 0.05$ , \*\* $P < 0.01$ , and \*\*\* $P < 0.001$ .

Fig. 3, A and B). Anti-DNA IgG and IgM that were detectable before CAR T cell injections in both NZB/W and MRL-lpr mice were decreased to below the detection limit and remained low to undetectable in most of the CD19-d NZB/W and CAR T cell-treated MRL-lpr mice and CAR T cell-treated MRL-lpr mice (Fig. 3, A and B). In contrast, anti-DNA IgG and IgM autoantibodies remained elevated or increased in CD19-s and control mice, consistent with the progression of autoimmunity in both strains.

**Effects of CAR T cell treatment on lupus pathogenesis and survival**

The most notable effect of CD19-targeted CAR treatment on disease pathogenesis was the increase in life spans of both NZB/W (Fig. 4A) and MRL-lpr mice (Fig. 4B). Most CD19-d NZB/W mice lived about 1 year after CAR T cell injection, attaining 18 months of age. This was a highly significant extension of life spans ( $P = 0.0019$ ) when compared to CD19-s NZB/W mice, all of which had been euthanized because of advanced disease by that time. Similarly, 8 of 12 CAR T cell-treated MRL-lpr mice lived for 1 year after treatment, outliving control MRL-lpr mice and attaining 14 months of age at the termination of the experiment. The CD19-targeted CAR T cell treatment considerably extended life spans, as treated mice reached an age that is quite unusual for these lupus-prone strains of mice (19). This result provided unambiguous confirmation that CAR T cell therapy profoundly affects autoimmune disease progression in both NZB/W and MRL-lpr mice.

To elucidate the extended survival, we evaluated the effects of B cell depletion on disease manifestations. Because anti-DNA autoantibodies are linked to glomerulonephritis in lupus mice, we measured proteinuria as an indication of kidney function. At 7 months of age, before administration of CAR T cells, 6 of 28 NZB/W mice had high-grade proteinuria. Five months after CAR T cell administration, 0 of 11 CD19-d mice had high-grade proteinuria, compared to 8 of 17 CD19-s mice (Fig. 4C). Although 2-month-old MRL-lpr mice are generally considered prediseased, 7 of 20 MRL-lpr mice in our experiment had high-grade proteinuria before CAR T cell treatment. Five months after treatment, high-grade proteinuria was detected in only 1 of



**Fig. 4. Impact of CD19-targeted CAR T cell treatment on lupus pathogenesis and survival.** (A) Survival curves of NZB/W mice after CAR T cell infusion into 7-month-old recipients. Survival of CD19-d mice ( $n = 12$ ) was compared relative to CD19-s mice ( $n = 12$ ), and significance was determined by log rank (Mantel-Cox;  $P = 0.0019$ ). For comparison, the survival of control mice ( $n = 8$ ) is plotted. (B) Survival curves of CAR T cell-treated and control MRL-lpr mice. CAR T cell-treated mice ( $n = 11$ ) were compared to control MRL-lpr mice ( $n = 11$ ), and survival of mice in the two groups was evaluated by long rank (Mantel-Cox;  $P = 0.0001$ ). (C and D) High-grade proteinuria (1 mg/ml and higher) was determined before treatment (start) and at 5 months after CAR T cell treatment. (C) Proteinuria in CD19-s ( $n = 12$ ) and CD19-d ( $n = 11$ ) NZB/W mice was analyzed by single-factor analysis of variance (ANOVA) ( $P = 0.038$ ). (D) High-grade proteinuria in CAR T cell-treated MRL-lpr mice ( $n = 11$ ) and controls ( $n = 9$ ) was similarly compared ( $P = 0.0017$ ). (E) Lengths of spleens in CD19-d and CD19-s NZB/W mice were measured at euthanasia ( $P < 0.005$ ). Bars are means, and horizontal lines are SEMs. (F) Kidneys from NZB/W mice were sectioned and analyzed for cellularity and morphology by H&E staining and for mouse IgG deposits by immunofluorescence (IF). (G) MRL-lpr skin sections were stained by H&E to compare the epidermis of control and CAR T cell-treated mice. (H) Pathology scores of MRL-lpr kidney and skin sections were determined as described in Materials and Methods.

11 CAR T cell-treated mice but was manifested in 8 of 9 control mice (Fig. 4D).

The CD19<sup>+</sup> B cell depletion significantly reduced splenomegaly in CAR T cell-treated NZB/W mice relative to untreated control mice ( $P < 0.005$ ; Fig. 4E). Histopathology of NZB/W kidney sections confirmed that CAR T cell treatment reduced the size and cellular infiltrate in glomeruli and largely prevented IgG deposits in both autoimmune strains of mice (Fig. 4F and fig. S3). In MRL-lpr mice, autoimmune disease also manifests as a skin disorder that begins with alopecia and progresses to skin lesions and scarring (23). To examine the skin pathology in CAR T cell-treated and control mice, we compared hematoxylin and eosin (H&E)-stained skin sections by microscopy. At 8 months, when the control mice had cell infiltrates and inflammation progressing to acanthosis and hyperkeratosis, the CD19-d MRL-lpr mice had nearly normal skin architecture (Fig. 4G) and minimal alopecia (fig. S4). The notable differences in pathology scores between CAR T cell-treated and control MRL-lpr mice (Fig. 4H) confirmed that CD19-targeted CAR T cells alleviate diverse lupus manifestations.

#### Effects of CAR T cell treatment on B and T lymphocyte populations

To investigate a possible source of the persistent plasma IgM in mice that had a near-complete depletion of circulating CD19<sup>+</sup> B cells, we evaluated blood of CD19-d mice for the presence of surface IgM<sup>+</sup> B cells. Control mice of both strains had IgM<sup>hi</sup> and IgM<sup>lo</sup> subpopulations of surface IgM<sup>+</sup> B cells (Fig. 5A). The IgM<sup>lo</sup>, but not the IgM<sup>hi</sup>, subpopulation of B cells was also present in CAR T cell-treated NZB/W and MRL-lpr mice, although these B cells had undetectable CD19. This persisting IgM<sup>lo</sup>, CD19<sup>-</sup> population may contribute to the continued IgM production.

We next considered whether the severe depletion of CD19 B cells may delay the progression of disease, in part, by modulating the T cell contribution to pathogenesis. In MRL-lpr mice, CD4<sup>+</sup> T cells accumulate with age. The CAR T cell treatment prevented the twofold increase in CD4-to-CD8 T cell ratio that was evident in control mice by 7 months of age (Fig. 5B). As consequence of the lpr mutation, the MRL-lpr strain also accumulates

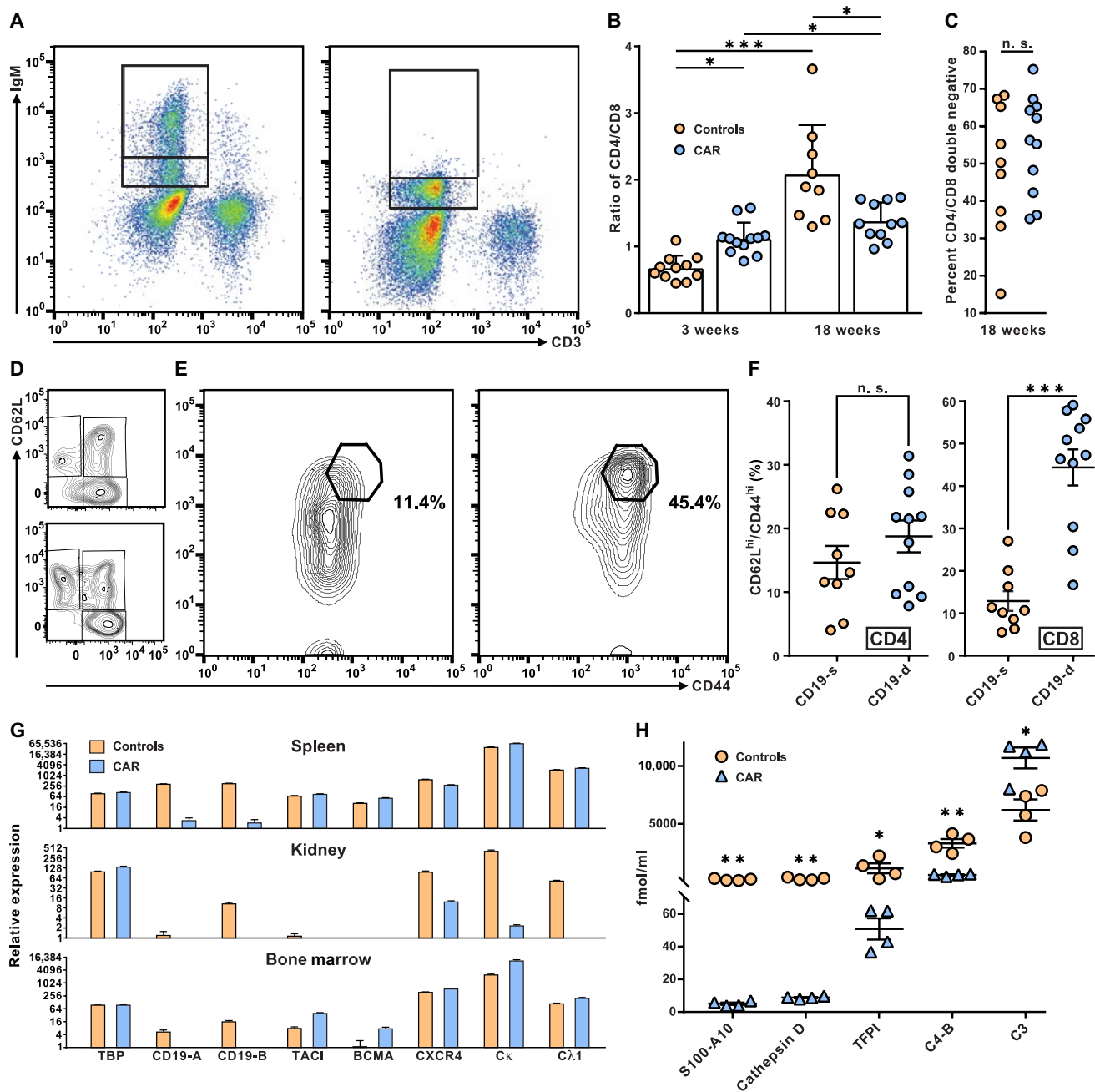


**Fig. 5. Effect of CD19-targeted CAR T cell treatment on lymphocyte phenotype and plasma proteome.** (A) The expression of surface IgM on peripheral blood B lymphocytes from control MRL-lpr mice (left) was used to define an intermediate and a high IgM<sup>+</sup> population (indicated by stacked gates). These gates were used to assess expression of IgM on B cells from CAR T cell–treated MRL-lpr mice (right). (B) The ratio of CD4 to CD8 T cells was determined in 18-week-old MRL-lpr mice treated with CAR T cells and controls. Each symbol represents data from a single mouse, bars are means, and horizontal lines are SDs. Differences between CAR T cell–treated and control mice were examined by two-tailed *t* test and noted by \**P* < 0.05 and \*\*\**P* < 0.001. (C) Proportions of CD4<sup>+</sup>CD8<sup>−</sup>DN T cells as the percentage of CD3<sup>+</sup> cells from CAR T cell–treated and control MRL-lpr mice were plotted (n. s., no significant differences). (D) Effector memory (CD62L<sup>lo</sup>CD44<sup>hi</sup>), central memory (CD62L<sup>hi</sup>CD44<sup>hi</sup>), and naïve (CD62L<sup>hi</sup>CD44<sup>lo</sup>) CD4<sup>+</sup> T cells from representative control (top) and CAR T cell–treated MRL-lpr mice (bottom) were determined (for complete CD4<sup>+</sup> T cell phenotype assessment, see table S3). (E) The CD62L<sup>hi</sup>CD44<sup>hi</sup> population of CD8<sup>+</sup> T cells from a representative control mouse (left) and CAR T cell–treated MRL-lpr mouse (right) are shown, and the percentage of CD8<sup>+</sup> T cells in the CD62L<sup>hi</sup>CD44<sup>hi</sup> gates was displayed. (F) Overall proportions of CD62L<sup>hi</sup>CD44<sup>hi</sup> cells among CD8<sup>+</sup> or CD4<sup>+</sup> T cells in CAR T cell–treated and control mice were determined and plotted. Each symbol represents data from a single mouse, horizontal lines are means, and offset lines are SDs. Differences between CAR T cell–treated and control mice were examined by two-tailed *t* test and marked by \*\*\**P* < 0.001. (G) Relative RNA expression in spleens, kidneys, and bone marrow from four CAR T cell–treated and four control NZB/W mice were measured by RT-PCR for transcripts originating from TBP, a house keeping gene, two regions of CD19, TACI, BCMA, CXCR4, and the light-chain constant regions of Igκ and λ1 (see Materials and Methods and table S2). Values were plotted using ln2. Means and SE are displayed. (H) Plasma was prepared from CAR T cell–treated and control MRL-lpr mice, and plasma proteins were analyzed by mass spectrometry. Horizontal lines are means, and offset lines are SDs. Concentrations were compared by two-tailed *t* test, and significance was indicated by \**P* < 0.05, \*\**P* < 0.01.

CD4<sup>-</sup>CD8<sup>-</sup> double-negative (DN) T cells that do not directly contribute to disease (24); as expected from a T cell-intrinsic genetic defect, we observed no differences between DN T cells from CAR T cell-treated versus control MRL-lpr mice (Fig. 5C). Treatment with CD19-targeted CAR T cells did not appreciably affect the relative proportions of CD62L<sup>lo</sup>CD44<sup>hi</sup> effector memory CD4<sup>+</sup> T cells or CD62L<sup>hi</sup>CD44<sup>hi</sup> central memory CD4<sup>+</sup> T cells (Fig. 5D), although CD62L<sup>hi</sup>CD44<sup>lo</sup> naïve CD4<sup>+</sup> were more abundant in CAR T cell-treated MRL-lpr mice (table S4). CD62L<sup>hi</sup>CD44<sup>hi</sup> central memory CD8<sup>+</sup> T cells constituted nearly half of the CD8<sup>+</sup> T cells in most CAR T cell-treated MRL-lpr mice (Fig. 5E), thus indicating a highly significant ( $P < 0.001$ ) increase in central memory CD8<sup>+</sup> T cells relative to age-matched controls and suggesting that this cell population may harbor the CAR.

To test for the presence and functional status of B cells that may remain in the spleen, kidneys, or bone marrow of CAR T cell-treated mice, we used quantitative PCR (qPCR) to determine relative RNA expression for genes that are implicated in the migration and growth factor response of B cells and plasma cells (Fig. 5G). Although CD19 expression was present in spleens, kidneys, and bone marrow samples from control mice, CD19 expression was not detected in any of the three tissues from treated mice, presumably reflecting the efficacy of CD19-targeted CAR T cells. Despite the strong reduction in CD19 expression, RNA coding for Ig light chains and two growth factor receptors found on B cells, transmembrane activator and CAM1 interactor (TACI) and B cell maturation antigen (BCMA), differed by only twofold or less in spleens from CAR T cell-treated mice versus controls (Fig. 5G). In the bone marrow of treated mice, transcripts for light chains, TACI, and BCMA were expressed at comparable or higher amounts relative to controls, indicating the continued presence of antibody-producing cells in that lymphoid tissue. In contrast, transcripts for Ig light chains were greatly reduced in kidneys from CAR T cell-treated mice relative to control mouse kidneys, suggesting the effective depletion of antibody-producing cells from kidneys of the treated NZB/W mice.

To assess systemic markers of inflammation and autoimmunity in CAR T cell-treated and control MRL-lpr mice, we analyzed the plasma proteome by mass spectrometry. CAR T cell-treated mice had a distinct proteome, in which S100-A10, cathepsin D, tissue factor pathway inhibitor, and complement C4-B were reduced in comparison to control MRL-lpr mice (Fig. 5H). Complement protein C3 was increased in the plasma of CAR T cell-treated mice. The S100-A10 protein is a marker for chronic inflammation (25), and the remaining proteins correlate with

lupus pathogenesis in both mice and humans (26–28). The fact that CAR T cell treatment altered the abundance of these five plasma proteins provides further evidence for the amelioration of disease in CAR T cell-treated mice.

### Functional tests of CD19-targeted CAR T cells

Because we were surprised at the apparent year-long persistence of CAR T cells in mice, we sought to find evidence of their continued cytotoxic efficacy. To test whether CD19-targeted CAR T cells continue to deplete B cells, we adoptively transferred syngeneic, CFSE-labeled B cells into MRL-lpr mice that had received CAR T cells 4 months earlier. Whereas labeled B cells were present in the blood of control mice 6 days after transfer, they were depleted from circulation in the CAR T cell-treated MRL-lpr mice (Fig. 6A). Active depletion of B cells continued at 11 months after infusion of CAR T cells into NZB/W mice. Syngeneic, CFSE-labeled B cells were undetectable 5 days after transfer to CD19-d NZB/W mice, yet they were present in the blood of CD19-s mice (fig. S5). A third test of CD19-targeted CAR T cell function was carried out by transferring

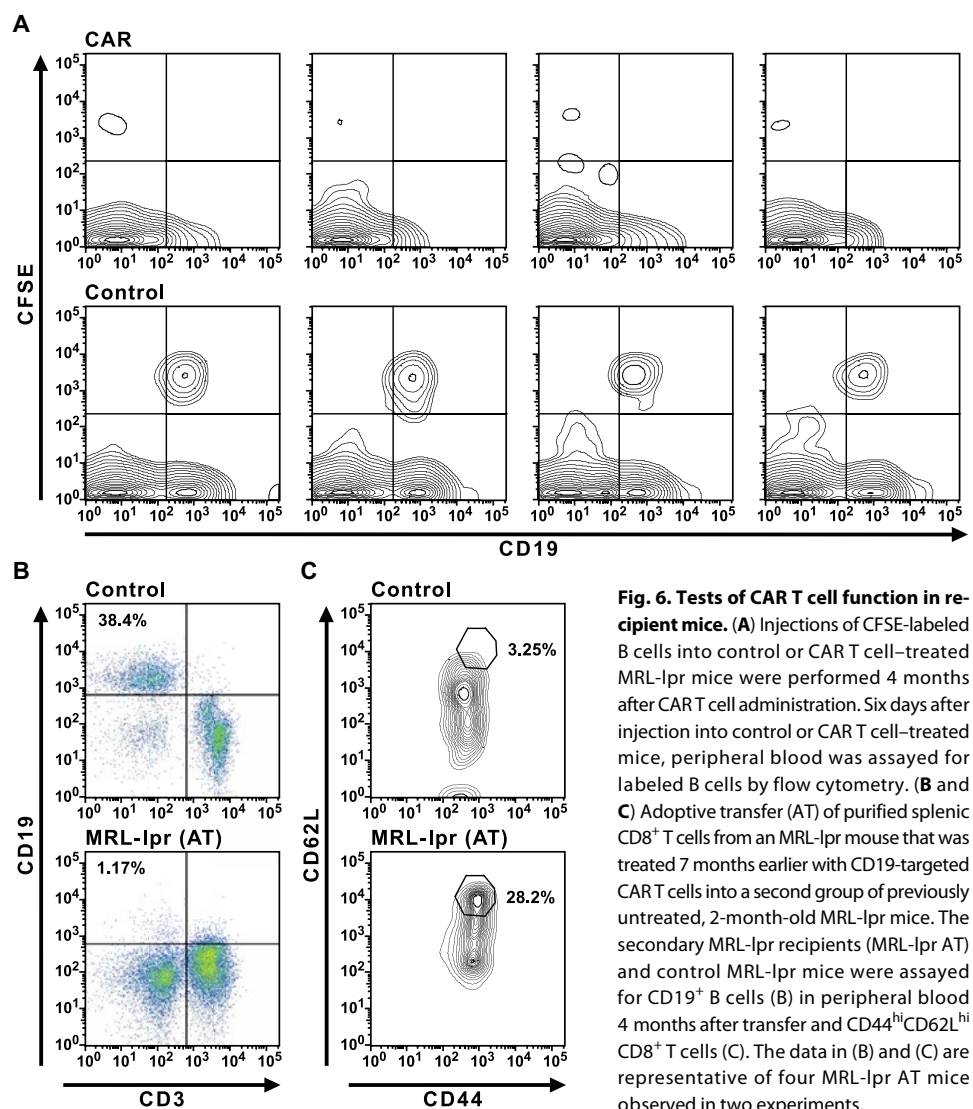


**Fig. 6. Tests of CAR T cell function in recipient mice.** (A) Injections of CFSE-labeled B cells into control or CAR T cell-treated MRL-lpr mice were performed 4 months after CAR T cell administration. Six days after injection into control or CAR T cell-treated mice, peripheral blood was assayed for labeled B cells by flow cytometry. (B and C) Adoptive transfer (AT) of purified splenic CD8<sup>+</sup> T cells from an MRL-lpr mouse that was treated 7 months earlier with CD19-targeted CAR T cells into a second group of previously untreated, 2-month-old MRL-lpr mice. The secondary MRL-lpr recipients (MRL-lpr AT) and control MRL-lpr mice were assayed for CD19<sup>+</sup> B cells (B) in peripheral blood 4 months after transfer and CD44<sup>hi</sup>CD62L<sup>hi</sup> CD8<sup>+</sup> T cells (C). The data in (B) and (C) are representative of four MRL-lpr AT mice observed in two experiments.

purified CD8<sup>+</sup> T cells from CAR T cell–treated MRL-lpr mice to a new cohort of untreated MRL-lpr recipients. An MRL-lpr mouse that had received CAR T cells 7 months earlier served as a donor of splenic CD8<sup>+</sup> T cells that were purified and injected into four recipients. Four months later, the MRL-lpr recipients lacked CD19<sup>+</sup> B cells (Fig. 6B), and they had acquired a prominent CD62L/CD44 double-positive CD8<sup>+</sup> T cell population (Fig. 6C). The CD62L<sup>+</sup>CD44<sup>+</sup> double-positive CD8<sup>+</sup> T cells from the spleen of one secondary recipient mouse were enriched by fluorescence-activated cell sorting and were determined to express CD19-targeted CAR transcripts to about fourfold higher concentrations than the CD62L<sup>lo</sup>CD44<sup>lo</sup> CD8<sup>+</sup> T cells (fig. S6). These data firmly established that the CD19-targeted CAR T cells remained viable and functional for several months after injection into NZB/W or MRL-lpr recipients.

## DISCUSSION

The depletion of CD19<sup>+</sup> B cells by CD19-targeted CAR CD8<sup>+</sup> T cells effectively eliminated autoantibody production and deferred or reversed disease manifestations of experimental lupus in two mouse models. These results contrast with previous results in the same mouse models, which showed resistance to anti-CD20 antibody-mediated B cell depletion (11–13). We propose that CD19-targeted CAR T cells have superior efficacy because cytotoxic T cells induce target cell death by a direct mechanism, whereas antibody-mediated cytotoxicity requires the buildup of bound antibody for complement-dependent target cell lysis, antibody-dependent cellular cytotoxicity, or clearance by phagocytes. Previous studies indicated that in models of lupus, the increased abundance of endogenous antibodies and immune complexes impairs B cell depletion by macrophages (12). Thus, anti-CD20 antibody was only effective if given repeatedly and at high doses to autoimmune mice. CD19-targeted CAR T cells, in contrast, kill B cells without the need for an accessory cell type and, thus, deplete B cells more effectively.

In addition, CD19-targeted CAR T cells may have achieved a more sustained B cell depletion due to the specificity and type of treatment used here. CD19 is a B cell surface marker that is intimately involved in B cell signaling and contributes to marginal zone B cell development in the spleen (29). CD19 is critical for B-1 (30) and B-2 (31) B cell signaling, proliferation, and differentiation in germinal centers (32). Moreover, CD19 is expressed on activated B cells, including dividing plasmablasts and early plasma cells (33). Hence, CD19-targeted CAR T cells may target B cells that are stimulated by autoantigens and that are directly responsible for autoantibody production. The depletion of CD19<sup>+</sup> B cells did not eliminate all IgM<sup>+</sup> B cells, and CAR T cell–treated MRL-lpr mice retained pretreatment expression of plasma IgM and IgG. CAR T cell–treated NZB/W likewise retained plasma IgM and substantial, albeit reduced, IgG.

Potential parallels exist with patients with cancer treated with CD19-targeted CTL019 CAR T cells, who often demonstrate persistence of IgM and IgG in serum, despite the continued presence of CTL019 (34, 35). Patients maintained production of IgM and IgG, including protective antibodies to vaccine antigens (35). The absence of IgM and IgG anti-DNA in CD19-targeted CAR T cell–treated mice was notable and somewhat unexpected. Both B-1 (36) and B-2 (37, 38) cells produce anti-DNA antibodies.

In lupus, autoantibody-secreting cells may arise as short-lived plasmablasts in the spleen and develop into long-lived plasma cells that survive in the bone marrow (39–41). In addition, plasma cells

that are linked to the severity of lupus symptoms may accumulate in the kidneys (42). Our RNA analysis indicates the continued expression of Ig light chains in spleens and bone marrow of CAR T cell–treated NZB/W mice, suggesting that CD19-targeted CAR T cells do not deplete all splenic B cell populations or long-lived plasma cells in the bone marrow. The marked reduction of Ig light-chain message in kidneys and the depletion of circulating anti-DNA antibodies in treated mice support the potential of CD19-targeted CAR T cell treatment to mitigate one particular type of disease-related plasma cell yet spare other long-lived plasma cells in the bone marrow.

Limitations of our study include the incomplete characterization of the plasma cell populations and the limited analysis of the specificity and functions of the residual IgM<sup>lo</sup> B cells in the CAR T cell–treated mice. Similarly, the long-term potential of CD19-targeted CAR T cells may not yet have been fully revealed, in part, because of the short life span of the host species used here. However, the results of the current study provide a blueprint to address most of these limitations.

CD19-targeted CAR T cells may alleviate lupus manifestations over an extended period of time because CAR T cells proliferate in the host and thus offer the potential for a permanent suppression of CD19 B cell production (43). In addition, cell-based therapies ensure that CD19 B cells are depleted from different tissues to which CAR T cells have access, such as the spleen and bone marrow of treated mice. Thus, we presume that B cell depletion starts as soon as CD19-positive, pro-B cells arise in the bone marrow and extend to more mature CD19<sup>+</sup> B cells present in the spleen or the blood. This complete and sustained eradication of all CD19<sup>+</sup> cells may lead to a more effective B cell depletion than that obtained with monoclonal antibody therapy. We confirmed that the CAR T cells remained functional for several months because CAR T cell–treated mice rapidly depleted transferred autologous CD19<sup>+</sup> B cells, whereas such cells persisted in control animals. Moreover, we were able to transfer splenic CD8<sup>+</sup> T cells from a CAR T cell–treated MRL-lpr mouse to a second cohort of recipient mice and determine that the transferred T cells depleted CD19<sup>+</sup> B cells in the recipients. Together, these results validated the anti-CD19 CAR T cell approach, which ensured a stringent and complete CD19<sup>+</sup> B cell depletion and decreased anti-DNA antibodies by one to two orders of magnitude relative to control mice.

The sustained suppression of autoantibody production may have contributed to the observed recovery in kidney function because proteinuria that was initially present in recipient mice returned to baseline. Although experiments with TLR-9<sup>-/-</sup> MRL-lpr mice implicate autoantibody specificities other than for DNA or chromatin in glomerulonephritis (44), anti-DNA antibodies that bind directly to glomerular basement membrane initiate glomerulonephritis in the absence of other autoimmune specificities (45). Therefore, it is likely—albeit unproven—that elimination of anti-DNA antibody-producing cells contributed to the reduction of proteinuria and mitigated lupus pathogenesis in both MRL-lpr and NZB/W mice.

Before this study, it was unclear whether a CAR transgene could function appropriately in T cells from an autoreactive mouse strain. The long-term efficacy of B cell depletion in our study may have benefited from the use of a second-generation CAR in which the CD3 $\zeta$  signaling domain was attenuated. Previous studies had demonstrated that dampened CAR signaling extended *in vivo* persistence of CAR T cells (21, 22). In addition, we also determined that A-MLV retrovirus is a preferable means of CAR gene delivery to mouse CD8<sup>+</sup>

T cells as compared to VSV-G–pseudotyped MLV or LV. The two features, in combination, may have resulted in stable CD19<sup>+</sup> B cell depletion that continued for more than 1 year in both NZB/W and MRL-lpr mice. Using these approaches, we established that CD8<sup>+</sup> T cells from NZB/W and MRL-lpr mice correctly carry out the cytotoxic function of the CD19-directed CAR.

Over time, the CAR T cell–treated mice accumulated a CD62L<sup>hi</sup>CD44<sup>hi</sup> double-positive CD8<sup>+</sup> T cell population, which we observed in the initial and in the secondary recipients of the transduced T cells. In humans, this combination of markers serves to identify a stem cell–like T cell memory population, which has the capacity for self-renewal and differentiation into effector T cells (46, 47). Because central memory CD8<sup>+</sup> T cells maintain cytotoxic activity over an extended time, we predict that the CD62L<sup>+</sup>CD44<sup>+</sup> double-positive cells identified here are particularly relevant for the efficacy of our treatment. In support, we showed that CD62L<sup>hi</sup>CD44<sup>hi</sup> double-positive CD8<sup>+</sup> T cells express the CD19-targeted CAR, which argues for their contribution to sustained B cell depletion.

In summary, advances in CAR T cell technology promise new and more effective treatment options for autoimmune diseases. An antigen-directed CAR that depleted desmoglein-specific B cells in a mouse model of pemphigus was recently described (48). The efficacy of the CD19-targeted CAR T cell approach used here illustrates the potential of CAR therapies in polyantigenic diseases such as lupus. Therapeutic B cell depletion by CD19-targeted CAR T cells for lupus does carry risks: Patients will potentially be susceptible to humoral immunosuppression. Yet, current therapies also suppress the immune system and yield an increased risk of infections. On the basis of 8 years of clinical trial experience with CAR T cells in humans, however, many of the risks associated with CAR T therapy may be manageable. Cancer survivors treated with CD19-targeted CAR T cells retain circulating, protective antibodies and B cells (35). In addition, strategies are available to mitigate toxicity and serious side effects of CD19-targeted CAR T cells. Applications of CD19-targeted CAR T cells to lupus may take advantage of methods for T cell transfer that do not require aggressive patient conditioning (49) that treat excessive cytokine release (50) and that use self-inactivating versions of CAR T cells (51). Confounding risks that are particular to lupus include the potential for autoreactive T cells to be carriers of the activating CAR gene. For the lifetime of recipient mice in our experiments, CAR T cells remained effective without overt side effects. We suggest that CD19-targeted CAR T cells represent a viable strategy for treatment of lupus that may overcome current limitations inherent in the use of monoclonal antibodies. Although caution in extending observations from animal models to humans is essential, our data encourage initial application of CD19-targeted CAR T cells in the most difficult to treat patients with lupus.

## MATERIALS AND METHODS

### Study design

The goal of this study was to test CD19-targeted CAR T cell treatment in two autoimmune mouse models. Figure 1 shows the CAR protocols. The efficiencies of the treatments are compared in table S1. Mice were followed over time to compare the efficacy of treatments by flow cytometry for CD19<sup>+</sup> B cells in blood and by isotype and anti-DNA serology. The effects of the treatment on lupus manifestations were evaluated by overall survival, circulating lymphocyte populations, proteinuria at the beginning and after 5 months of

treatment, splenomegaly and kidney immunofluorescence in NZB/W F<sub>1</sub> mice, and skin pathology in MRL-lpr mice. At the termination of the experiment, kidney pathology in both strains and gene transcripts in target organs of NZB/W mice were analyzed, and plasma proteomics of MRL-lpr mice was performed. The long-term potential for CAR T cells to deplete CD19<sup>+</sup> B cells was tested by transfer of fluorophore-labeled CD19<sup>+</sup> B cells into previously CAR T cell–treated recipients and by adoptive transfer of CD8<sup>+</sup> T cells from CAR T cell–treated MRL-lpr mice into naïve MRL-lpr mice. Primary data are reported in data file S1.

### Animals

Animal welfare was monitored, and euthanasia was induced in strict accordance with University of Tennessee Health Science Center (UTHSC) Institutional Animal Care and Use Committee–approved protocol (15-007). Female NZB/W (at 7 months of age; the Jackson Laboratory) or MRL-lpr mice (7 to 10 weeks old; the Jackson Laboratory) were used in all studies. Two days before the injection of CAR virus injected or control T cells, mice were irradiated with 5 grays to achieve transient myeloablation.

### Antibodies

To phenotype mouse lymphocytes in blood or tissues, we used phycoerythrin (PE)–conjugated anti-mouse CD3ε (no. 50-0031, Tonbo Biosciences), anaphase-promoting complex (APC) anti-mouse CD8α (no. 20-0081, Tonbo Biosciences), PE-Cy7 anti-mouse CD4 (no. 60-0041, Tonbo Biosciences), redFluor 710 anti-mouse CD19 (no. 80-0193, Tonbo Biosciences), PE-CF594 anti-mouse CD197 (no. 563596, BD Horizon), BV605 anti-mouse CD62L (no. 563252, BD Horizon), anti-mouse IgM (no. 1021-01, SouthernBiotech), and APC-Cy7 anti-mouse CD44 (no. 560568, BD Horizon). To detect CD19-targeted CAR, we used Alexa Fluor 488–conjugated AffiniPure mouse anti-rat Fab-fragment specific reagent (no. 121-545-106, Jackson ImmunoResearch).

### Construction and use of retrovirus and lentivirus transfer vectors

All recombinant DNA protocols were approved by the UTHSC Institutional Biosafety Committee. All plasmid constructs were grown in recombination-deficient *Escherichia coli* (K12 derivative strains) using standard molecular biology techniques. The MSGV-1D3-28Z.1-3 retroviral transfer plasmid (GenBank account no. HM754222) was constructed, as previously described (21). Briefly, this transfer genome contains a CAR consisting of the anti-mouse CD19 scFv derived from the 1D3 IgG2a/κ rat hybridoma linked in frame to a transmembrane domain of mouse CD28 and to two intracellular signaling domains, one derived from CD28, the other, an optimized version of the CD3ζ signaling domain. The FEW 1D3-28Z.1-3 lentiviral transfer plasmid was constructed for this study as follows. The FUWG plasmid was obtained from Addgene and its PacI–AgeI restriction fragment containing a ubiquitin C promoter was replaced by a PacI–AgeI fragment containing a human elongation factor 1α (EF-1α) promoter to create the FEWG plasmid. The sequences downstream of the EF-1α promoter were then replaced with the entire anti-mouse CD19 CAR to create the lentiviral transfer plasmid FEW 1D3-28Z.1-3.

MLV-based retroviral vectors were produced by cotransfection of 293FT cells (Invitrogen) with the MSGV-1D3-28Z.1-3 retroviral transfer plasmid and two additional plasmids that complement in trans the assembly of the virus. One plasmid, the pCAGGS-Gag-Pol,

encoded a codon-optimized *gag-pol* gene from the retrovirus Moloney MLV, the second encoded either the surface glycoprotein of amphotropic 4070A MLV (gift of M. Eiden, National Institutes of Health) or the glycoprotein G of vesicular stomatitis virus. Lentiviral vectors were produced by cotransfection of the FEW 1D3-28Z.1-3 transfer plasmid and the ViraPower packaging mix (Invitrogen). Transfections of 293FT cells were carried out using Lipofectamine 2000 (Invitrogen). Virus was collected at 24, 48, and 72 hours after transfection, and cell supernatants were passed through a 0.45- $\mu$ m sterile filter units and then further concentrated to yield high-titer stocks. Retroviral stocks were prepared using sterilized Centricon Plus-70 concentration devices as recommended by the manufacturer. Aliquots of concentrated virus were stored at  $-80^{\circ}\text{C}$ , and all retroviral stocks tested negative for replication-competent virus. Lentivirus were centrifuged at 28,000 rpm at  $4^{\circ}\text{C}$  for 90 min and resuspended in sterile phosphate-buffered saline (PBS) at 1/200 of the original volume, and aliquots were stored at  $-80^{\circ}\text{C}$  until used for transductions.

### Purification of CD8<sup>+</sup> T cells from spleen

Spleens were harvested from age- and strain-matched donor mice, minced, and dispersed into single cells in RPMI-10 (RPMI-1640 with 10% fetal bovine serum) by pressing between sterile frosted glass slides. Cells were filtered through a 40- $\mu$ m pore-size cell strainer and washed in RPMI-10, and red blood cells (RBCs) were lysed using the mouse erythrocyte lysis kit (catalog no. WL2000, R&D Systems). CD8<sup>+</sup> T cells were enriched by negative selection on a MagCelect mouse CD8<sup>+</sup> T cell isolation kit (catalog no. MAGM203, R&D Systems) as instructed by the manufacturer. The yield of CD8<sup>+</sup> T cells was about  $10^7$  per spleen, and 95% of the isolated cells expressed CD8 $\alpha$ . The cells were cultured at 1 million/ml of RPMI-10 medium with recombinant mouse interleukin-2 (IL-2) (no. 402-ML, R&D Systems) at 30 IU/ml and CD28/CD3 beads (Mouse T-activator anti-CD3/CD28 Dynabeads, Gibco) that were added at a 1:1 ratio with the CD8<sup>+</sup> T cells.

### Transduction of CAR transgenes

The T cells were exposed to two consecutive virus infections. The first infection was carried out at 6 hours after plating of cells with activator beads, and the second infection was at 24 hours. Six-well tissue culture plates were coated with 2.5 ml per well of RetroNectin (no. T100B, Clontech) in sterile PBS, without Ca and Mg, at a final concentration of 9  $\mu\text{g}/\text{ml}$ . After coating, plates were washed with sterile PBS and blocked with 2% bovine serum albumin (BSA) in PBS for 30 min. After another wash, plates were incubated with 1.5 ml of RPMI-10 per well to which 40  $\mu\text{l}$  of  $200\times$  concentrated virus were added just before dispensing into wells. The plate was centrifuged at 2000 rpm at room temperature for 2 hours.

After centrifugation, about 0.5 ml of the media was left in the well, and 1 ml of the activated T cells along with the activator beads was added. The second infection was performed exactly as the first, with freshly prepared tissue culture plates. Cells were fed fresh media containing 30 IU of IL-2 every other day and reached a fivefold expansion from the initial cell numbers on the 5th day of culture. At that time, remaining activator beads were magnetically removed and discarded, and CD8<sup>+</sup> T cells were washed, counted, and suspended at  $1.2 \times 10^7/\text{ml}$  in RPMI-1640 containing 10% syngeneic mouse serum just before injections into recipients. An aliquot of the cells was assayed for CAR expression by anti-rat Fab antibody, and

5 to 15% of cells were stained positive (fig. S1). About 100  $\mu\text{l}$  of cell suspension was injected into the retro-orbital sinus of each mouse with appropriate sedation and administration of analgesics. Immediately after the injection, the mice were administered 45,000 IU of IL-2 into the scruff of their neck.

### Flow cytometry

After the injection of CD8<sup>+</sup> T cells, mice were bled at periodic intervals from the retro-orbital plexus, starting at about 3 weeks after T cell injection, and blood was collected into heparinized tubes. Seventy microliters of blood was used to phenotype circulating lymphocytes using antibodies for CD3e, CD4, CD8 $\alpha$ , and CD19, following standard procedures. Cells were incubated with 2  $\mu\text{l}$  of mouse Fc block (no. 14-0161, Affymetrix), before addition of antibody cocktail. After labeling, RBCs were lysed with 750  $\mu\text{l}$  of high-yield lyse solution (no. HYL250, Life Technologies). Cytometry was performed on a Bio-Rad ZE5. CAR expression on primary T cells was determined by staining with Alexa Fluor 488-conjugated mouse anti-rat Fab fragment-specific antibodies (catalog no. 121-545-106, Jackson ImmunoResearch). Ghost Dye Red 710 (no. 13-0871, Tonbo Biosciences) was used to differentiate between live and dead cells.

### Serology and ELISA

Plasma was prepared by centrifugation of blood for 10 min at 2000g and used to determine total IgG, IgM, and anti-DNA antibodies. Total amounts of immunoglobulins in the mouse plasma were determined using ELISA in 96-well plates coated with AffiniPure goat anti-mouse IgG (H + L) (no. 115-005-003, Jackson ImmunoResearch) or, alternatively, with goat anti-mouse IgM (H + L) (SouthernBiotech) in coating buffer [0.1 M  $\text{NaHCO}_3$  (pH 9.6)] at  $4^{\circ}\text{C}$  overnight. Coated plates were washed and incubated for 1 hour at room temperature in blocking buffer (1% BSA in PBS with 0.02%  $\text{NaN}_3$ ).

For mouse IgG and IgM detection, 10-fold serial dilutions of the plasma were prepared in blocking buffer (range  $10^{-2}$  to  $10^{-7}$ ), added to the plates, and incubated at room temperature for 3 hours. The plate was washed four times with PBS containing 0.05% Tween 20 (PBS-T). The detection antibody (alkaline phosphatase-labeled goat anti-mouse IgG, or anti-mouse IgM, at 1:1000 dilution in blocking buffer) was added and incubated for 1 hour at room temperature. The plates were washed four times with PBS-T. Phosphatase detection substrate (no. S0942, Sigma-Aldrich) at 1 mg/ml was added for color development. Absorption in plates was read at 405 nm. With each ELISA, a positive standard mouse IgG (no. 015-000-0030, the Jackson Laboratory), or mouse IgM was used to control for inter-experimental variation. Anti-DNA IgG and IgM antibody titers were determined using ELISA plates coated with calf thymus DNA (no. D3664, Sigma-Aldrich) at 10  $\mu\text{g}/\text{ml}$  of PBS, supplemented with 1 mM EDTA. Titters were calculated as the inverse of dilutions at which optical density equaled twice background readings. The detection of bound antibodies was performed as for isotype ELISAs except that threefold serial dilutions were prepared starting at a 1:30 initial dilution (range, 1:30 to 1:7290).

### Plasma proteome analysis

Plasma was collected from CAR T cell-treated and control MRL-lpr mice and depleted of the most abundant mouse plasma proteins by chromatography on mouse ProSep 10 columns (Sigma-Aldrich), as instructed by the manufacturer. After depletion, 50  $\mu\text{l}$  of plasma samples were mixed with 10  $\mu\text{l}$  of 50 mM  $\text{NH}_4\text{HCO}_3$  and 25  $\mu\text{l}$  of

0.2% RapiGest SF (no. 186001861, Waters). The samples were heated at 80°C for 15 min, 2.5 µl of 100 mM dithiothreitol solution was added, and the samples were incubated at 60°C for 30 min. After cooling to room temperature, 2.5 µl of 300 mM iodoacetamide solution was added and incubated for 30 min in the dark. After protein denaturation and alkylation, the samples were mixed with 10 µl of sequencing-grade trypsin solution (0.05 µg/µl; no. V511A, Promega). Trypsin digestion was carried out overnight at 37°C. The digested samples were acidified by addition of 1 µl of concentrated trifluoroacetic acid (TFA) and dried in a speed vacuum centrifuge. The dried peptide digests were reconstituted with a solution of H<sub>2</sub>O/ACN (acetonitrile)/TFA (98:2:0.1) and desalted with a C18 micro tip column (ZipTip, Millipore). The peptides were diluted 2:1 (v/v) with an internal standard solution containing 37.5 fmol/µl of yeast alcohol dehydrogenase (ADH) tryptic digest (Waters). All peptide separations were performed on a nanoUPLC liquid chromatography system (Waters ACQUITY M-Class UPLC System). Mobile phase A was H<sub>2</sub>O containing 0.1% formic acid; mobile phase B was ACN containing 0.1% formic acid. Peptide samples were injected, 2 µl of partial loop injection onto a Symmetry C18 (5 µm, 180 µm × 20 mm trap column; Waters). After preconcentration, the peptides were eluted from the trap column to the analytical column, HSS T3 C18 (1.8 µm, 75 µm × 250 mm; Waters), and separated with a gradient of 2 to 40% mobile phase B over 90 min at a flow rate of 0.3 µl/min. The column temperature was maintained at 45°C. The eluted peptides were analyzed online on a Synapt G2-Si (Waters) high-resolution ion mobility mass spectrometer (IMS). The lock mass peptide, [Glu<sup>1</sup>]-fibrinopeptide B, was delivered by infusion through the instrument fluidics system. The quadrupole radio frequency was set for efficient transmission of ions with mass/charge ratio of 300 to 2000. Data were acquired in a data-independent acquisition mode with ion mobility separation and optimized transfer collision energy, ultra-definition MS [UDMS(E)] (52). The time-of-flight analyzer was operated in resolution mode (resolution of ≥20,000 full width at half maximum, with average mass error of 5 parts per million or less), a scan time of 0.6 ms, MS(E) range of 50 to 2000 Da, and IMS separation. Protein identification and label-free quantification was performed with Progenesis QI (Nonlinear Dynamics/Waters) (53). The MS(E) data were searched against a mouse protein database (no. UP000000589, UniProt) with static modification on cysteine (carbamidomethylation), variable modification on methionine (oxidation), and allowing up to one missed cleavage per peptide. Label-free quantification was performed using the top three Hi-N method (54) with ADH as internal standard.

### Tissue preparation and pathology

Kidneys and spleens were flash-frozen in optimal cutting temperature (OCT) compound (no. 23-730-571, Fisher Biotec) and sectioned at 5-µm thickness on a cryotome. Frozen sections were thawed, blocked in blocking buffer, and incubated with goat anti-mouse IgG isotype antibodies for fluorescence microscopy. Skin sections were formalin-fixed, paraffin-embedded, sectioned, and stained with H&E stain to evaluate skin pathology. Renal pathology was assessed as described by Singh *et al.* (55) based on the histology of kidneys fixed in 4% paraformaldehyde and embedded in paraffin. Sections were stained with H&E and scored on a 0 to 3 scale, indicating no to severe manifestations. Separate scores were assigned to glomerular hypercellularity, necrosis, karyorrhexis, cellular crescents, and hyaline deposits to indicate acute lesions in glomeruli. Similarly, interstitial

inflammation, tubular cell necrosis, and tubular cell casts were scored to determine acute tubule-interstitial disease. Chronic kidney lesions were scored for glomerulosclerosis, glomerular scars, fibrous crescents, tubular atrophy, and interstitial fibrosis. The scores were averaged to obtain a mean score for glomerular, tubule-interstitial, and chronic components, and the three subscores were added to generate an overall kidney biopsy score. Skin sections were evaluated for acanthosis, hyperkeratosis, cellular infiltration, vascular dilation, ulceration, and scar formation, scored on a scale from 0 to 3 for severity; scores were averaged over all categories, expressed for head versus body; and average scores were computed. Proteinuria was measured by placing a 5-µl drop of freshly collected urine onto an Albustix indicator strip (no. 2191, Siemens) and comparing the observed color to a standard color scale provided by the manufacturer. The classification proposed by Adelman *et al.* (56) was used to define high-grade proteinuria.

### RT-PCR and qPCR

To detect CAR T cell expression in various tissues, we isolated total RNA from spleen, bone marrow, kidney, and blood using TRIzol reagent (no. 15596018, Invitrogen). Kidney and spleen RNA were also prepared from kidneys and spleens of four CD19-d and CD19-s NZB/W mice that were stored frozen in OCT. Those samples were obtained by sectioning tissues into 50-µm-thick sections with a cryotome, removing the OCT by a quick rinse in ice-cold PBS and transferring the slices to tubes containing TRIzol reagent. Contaminating DNA was removed by deoxyribonuclease treatment, and total RNA was quantified using spectrophotometry. The RNA was converted to complementary DNA (cDNA) using transcriptor first-strand cDNA kit (no. 04379012001, Roche), and qPCR was performed on a Lightcycler 480 instrument (Roche) using gene-specific primers and probes designed using Roche's Universal ProbeLibrary Assay Design Center. For details of primers and probes used in this study, see table S2.

### Statistical analysis

Data for the CAR T cell-treated and control experimental groups were analyzed by one or two-tailed *t* test, as appropriate for pairwise comparison of groups with divergent sample distributions. Proteinuria was measured between treated and control mice by one-way ANOVA, and survival curves were compared by Mantel-Cox log-rank test. The statistics features of Microsoft Excel and GraphPad Prism data analysis software suites were used.

### SUPPLEMENTARY MATERIALS

[www.sciencetranslationalmedicine.org/cgi/content/full/11/482/eaav1648/DC1](http://www.sciencetranslationalmedicine.org/cgi/content/full/11/482/eaav1648/DC1)

Fig. S1. Analysis of CAR expression at the cell surface.

Fig. S2. Transient depletion of CD19<sup>+</sup> B cells from one NZB/W mouse.

Fig. S3. Immunofluorescence images of representative glomeruli from CAR T cell-treated and control MRL-lpr mice.

Fig. S4. Comparison of alopecia and skin lesions between CAR T cell-treated and negative control MRL-lpr mice.

Fig. S5. Analysis of CAR T cell cytotoxicity in vivo.

Fig. S6. qPCR of transcripts expressed in sorted CD8<sup>+</sup> T cells.

Fig. S7. Reverse transcription qPCR of CAR RNA in bone marrow and spleen of CD19<sup>+</sup> depleted and CD19<sup>+</sup> intact NZB/W mice.

Fig. S8. Typical gating strategy.

Table S1. Comparison of viral vectors used to transduce T cells.

Table S2. List of oligonucleotide primers used for RT-PCR.

Table S3. CD4<sup>+</sup> T cell subsets.

Data file S1. Primary data.

## REFERENCES AND NOTES

- A. Rahman, D. A. Isenberg, Systemic lupus erythematosus. *N. Engl. J. Med.* **358**, 929–939 (2008).
- M. J. Shlomchik, Activating systemic autoimmunity: B's, T's, and tolls. *Curr. Opin. Immunol.* **21**, 626–633 (2009).
- A. Sang, Y.-Y. Zheng, L. Morel, Contributions of B cells to lupus pathogenesis. *Mol. Immunol.* **62**, 329–338 (2014).
- Y. Li, F. Chen, M. Putt, Y. K. Koo, M. Madaio, J. C. Cambier, P. L. Cohen, R. A. Eisenberg, B cell depletion with anti-CD79 mAbs ameliorates autoimmune disease in MRL/lpr mice. *J. Immunol.* **181**, 2961–2972 (2008).
- S. Gallagher, I. Yusuf, T. M. McCaughy, S. Turman, H. Sun, R. Kolbeck, R. Herbst, Y. Wang, MEDI-551 treatment effectively depletes B cells and reduces serum titers of autoantibodies in mice transgenic for *Sle1* and human CD19. *Arthritis Rheumatol.* **68**, 965–976 (2016).
- Z. Touma, D. D. Gladman, Current and future therapies for SLE: Obstacles and recommendations for the development of novel treatments. *Lupus Sci. Med.* **4**, e000239 (2017).
- S. B. Cohen, P. Emery, M. W. Greenwald, M. Dougados, R. A. Furie, M. C. Genovese, E. C. Keystone, J. E. Loveless, G. R. Burmester, M. W. Cravets, E. W. Hesse, T. Shaw, M. C. Tootitris; REFLEX Trial Group, Rituximab for rheumatoid arthritis refractory to anti-tumor necrosis factor therapy: Results of a multicenter, randomized, double-blind, placebo-controlled, phase III trial evaluating primary efficacy and safety at twenty-four weeks. *Arthritis Rheum.* **54**, 2793–2806 (2006).
- P. A. Calabresi, B-cell depletion — A frontier in monoclonal antibodies for multiple sclerosis. *N. Engl. J. Med.* **376**, 280–282 (2017).
- J. T. Merrill, C. M. Neuwelt, D. J. Wallace, J. C. Shanahan, K. M. Latinis, J. C. Oates, T. O. Utset, C. Gordon, D. A. Isenberg, H.-J. Hsieh, D. Zhang, P. G. Brunetta, Efficacy and safety of rituximab in moderately-to-severely active systemic lupus erythematosus: The randomized, double-blind, phase III/II systemic lupus erythematosus evaluation of rituximab trial. *Arthritis Rheum.* **62**, 222–233 (2010).
- L. M. Gomez Mendez, M. D. Cascino, J. Garg, T. R. Katsumoto, P. Brakeman, M. Dall'Era, R. J. Looney, B. Rovin, L. Dragone, P. Brunetta, Peripheral blood B cell depletion after rituximab and complete response in lupus nephritis. *Clin. J. Am. Soc. Nephrol.* **13**, 1502–1509 (2018).
- K. W. Bekar, T. Owen, R. Dunn, T. Ichikawa, W. Wang, R. Wang, J. Barnard, S. Brady, S. Nevarez, B. I. Goldman, M. Kehry, J. H. Anolik, Prolonged effects of short-term anti-CD20 B cell depletion therapy in murine systemic lupus erythematosus. *Arthritis Rheum.* **62**, 2443–2457 (2010).
- A. Ahuja, L. L. Teichmann, H. Wang, R. Dunn, M. R. Kehry, M. J. Shlomchik, An acquired defect in IgG-dependent phagocytosis explains the impairment in antibody-mediated cellular depletion in lupus. *J. Immunol.* **187**, 3888–3894 (2011).
- A. Ahuja, J. Shupe, R. Dunn, M. Kashgarian, M. R. Kehry, M. J. Shlomchik, Depletion of B cells in murine lupus: Efficacy and resistance. *J. Immunol.* **179**, 3351–3361 (2007).
- V. Reddy, G. Cambridge, D. A. Isenberg, M. J. Glennie, M. S. Cragg, M. Leandro, Internalization of rituximab and the efficiency of B cell depletion in rheumatoid arthritis and systemic lupus erythematosus. *Arthritis Rheumatol.* **67**, 2046–2055 (2015).
- R. J. Looney, J. H. Anolik, D. Campbell, R. E. Felgar, F. Young, L. J. Arend, J. A. Sloan, J. Rosenblatt, I. Sanz, B cell depletion as a novel treatment for systemic lupus erythematosus: A phase I/II dose-escalation trial of rituximab. *Arthritis Rheum.* **50**, 2580–2589 (2004).
- L. J. N. Cooper, M. S. Topp, L. M. Serrano, S. Gonzalez, W.-C. Chang, A. Naranjo, C. Wright, L. Popplewell, A. Raubitschek, S. J. Forman, M. C. Jensen, T-cell clones can be rendered specific for CD19: Toward the selective augmentation of the graft-versus-B-lineage leukemia effect. *Blood* **101**, 1637–1644 (2003).
- R. J. Brentjens, J.-B. Latouche, E. Santos, F. Marti, M. C. Gong, C. Lyddane, P. D. King, S. Larson, M. Weiss, I. Rivière, M. Sadelain, Eradication of systemic B-cell tumors by genetically targeted human T lymphocytes co-stimulated by CD80 and interleukin-15. *Nat. Med.* **9**, 279–286 (2003).
- W. A. Lim, C. H. June, The principles of engineering immune cells to treat cancer. *Cell* **168**, 724–740 (2017).
- A. N. Theofilopoulos, F. J. Dixon, Murine models of systemic lupus erythematosus. *Adv. Immunol.* **37**, 269–390 (1985).
- D.-R. Koh, A. Ho, A. Rahemtulla, W.-P. Fung-Leung, H. Griesser, T.-W. Mak, Murine lupus in MRL/lpr mice lacking CD4 or CD8 T cells. *Eur. J. Immunol.* **25**, 2558–2562 (1995).
- J. N. Kochenderfer, Z. Yu, D. Frasher, N. P. Restifo, S. A. Rosenberg, Adoptive transfer of syngeneic T cells transduced with a chimeric antigen receptor that recognizes murine CD19 can eradicate lymphoma and normal B cells. *Blood* **116**, 3875–3886 (2010).
- Y. Zhao, Q. J. Wang, S. Yang, J. N. Kochenderfer, Z. Zheng, X. Zhong, M. Sadelain, Z. Eshhar, S. A. Rosenberg, R. A. Morgan, A herceptin-based chimeric antigen receptor with modified signaling domains leads to enhanced survival of transduced T lymphocytes and antitumor activity. *J. Immunol.* **183**, 5563–5574 (2009).
- E. Bribes, S. Galiege, B. Bourrie, P. Casellas, Involvement of the peripheral benzodiazepine receptor in the development of cutaneous pathology in Mrl/lpr mice. *Immunol. Lett.* **85**, 13–18 (2003).
- A. M. Jevnikar, M. J. Grusby, L. H. Glimcher, Prevention of nephritis in major histocompatibility complex class II-deficient MRL-lpr mice. *J. Exp. Med.* **179**, 1137–1143 (1994).
- V. Salle, C. Cordonnier, J. Schmidt, C. Mazière, A. Smail, C. Attencourt, M. P. Mabile, J. C. Mazière, R. Makdassi, G. Choukroun, M. Diouf, P. Duhaut, J. P. Ducroix, Vascular expression of annexin A2 in lupus nephritis. *J. Clin. Pathol.* **69**, 533–536 (2016).
- N. C. Phi, D. K. Chien, V. V. Binh, P. Gergely, Cathepsin D-like activity in serum of patients with systemic lupus erythematosus. *J. Clin. Lab. Immunol.* **29**, 185–188 (1989).
- V. Roldan, P. Marco, C. Fernandez, E. Pascual, Levels of tissue factor pathway inhibitor in lupus patients correlate with lupus activity and endothelial damage markers. *Haematologica* **87**, 1231–1232 (2002).
- L. Bao, M. Haas, R. J. Quigg, Complement factor H deficiency accelerates development of lupus nephritis. *J. Am. Soc. Nephrol.* **22**, 285–295 (2011).
- Y. You, H. Zhao, Y. Wang, R. H. Carter, Cutting edge: Primary and secondary effects of CD19 deficiency on cells of the marginal zone. *J. Immunol.* **182**, 7343–7347 (2009).
- S. Sato, A. S. Miller, M. C. Howard, T. F. Tedder, Regulation of B lymphocyte development and activation by the CD19/CD21/CD81/Leu 13 complex requires the cytoplasmic domain of CD19. *J. Immunol.* **159**, 3278–3287 (1997).
- Y. Wang, S. R. Brooks, X. Li, A. N. Anzelon, R. C. Rickert, R. H. Carter, The physiologic role of CD19 cytoplasmic tyrosines. *Immunity* **17**, 501–514 (2002).
- Y. Wang, R. H. Carter, CD19 regulates B cell maturation, proliferation, and positive selection in the FDC zone of murine splenic germinal centers. *Immunity* **22**, 749–761 (2005).
- K. Pracht, J. Meinzinger, P. Daum, S. R. Schulz, D. Reimer, M. Hauke, E. Roth, D. Mielenz, C. Bereik, J. Córte-Real, H. M. Jäck, W. Schu, A new staining protocol for detection of murine antibody-secreting plasma cell subsets by flow cytometry. *Eur. J. Immunol.* **47**, 1389–1392 (2017).
- S. J. Schuster, J. Svoboda, E. A. Chong, S. D. Nasta, A. R. Mato, Ö. Anak, J. L. Brogdon, I. Pruteanu-Malinici, V. Bhoj, D. Landsburg, M. Wasik, B. L. Levine, S. F. Lacey, J. J. Melenhorst, D. L. Porter, C. H. June, Chimeric antigen receptor T cells in refractory B-cell lymphomas. *N. Engl. J. Med.* **377**, 2545–2554 (2017).
- V. G. Bhoj, D. Arhontoulis, G. Wertheim, J. Capobianchi, C. A. Callahan, C. T. Ellebrecht, A. E. Obstfeld, S. F. Lacey, J. J. Melenhorst, F. Nazimuddin, W.-T. Hwang, S. L. Maude, M. A. Wasik, A. Bagg, S. Schuster, M. D. Feldman, D. L. Porter, S. A. Grupp, C. H. June, M. C. Milone, Persistence of long-lived plasma cells and humoral immunity in individuals responding to CD19-directed CAR T-cell therapy. *Blood* **128**, 360–370 (2016).
- K. Hayakawa, R. R. Hardy, M. Honda, L. A. Herzenberg, A. D. Steinberg, L. A. Herzenberg, Ly-1 B cells: Functionally distinct lymphocytes that secrete IgM autoantibodies. *Proc. Natl. Acad. Sci. U.S.A.* **81**, 2494–2498 (1984).
- T. N. Marion, A. L. Bothwell, D. E. Briles, C. A. Janeway Jr., IgG anti-DNA autoantibodies within an individual autoimmune mouse are the products of clonal selection. *J. Immunol.* **142**, 4269–4274 (1989).
- M. Shlomchik, M. Mascelli, H. Shan, M. Z. Radic, D. Pisetsky, A. Marshak-Rothstein, M. Weigert, Anti-DNA antibodies from autoimmune mice arise by clonal expansion and somatic mutation. *J. Exp. Med.* **171**, 265–292 (1990).
- F. Hiepe, T. Alexander, R. E. Voll, Plasma cells. *Z. Rheumatol.* **74**, 20–25 (2015).
- M. Hale, D. J. Rawlings, S. W. Jackson, The long and the short of it: Insights into the cellular source of autoantibodies as revealed by B cell depletion therapy. *Curr. Opin. Immunol.* **55**, 81–88 (2018).
- M. Mahévas, M. Michel, J.-C. Weill, C.-A. Reynaud, Long-lived plasma cells in autoimmunity: Lessons from B-cell depleting therapy. *Front. Immunol.* **4**, 494 (2013).
- M. Espeli, S. Bokors, G. Giannico, H. A. Dickinson, V. Bardsley, A. B. Fogo, K. G. C. Smith, Local renal autoantibody production in lupus nephritis. *J. Am. Soc. Nephrol.* **22**, 296–305 (2011).
- M. L. Davila, C. C. Kloss, G. Gunset, M. Sadelain, CD19 CAR-targeted T cells induce long-term remission and B cell aplasia in an immunocompetent mouse model of B cell acute lymphoblastic leukemia. *PLOS ONE* **8**, e61338 (2013).
- S. R. Christensen, J. Shupe, K. Nickerson, M. Kashgarian, R. A. Flavell, M. J. Shlomchik, Toll-like receptor 7 and TLR9 dictate autoantibody specificity and have opposing inflammatory and regulatory roles in a murine model of lupus. *Immunity* **25**, 417–428 (2006).
- M. R. Krishnan, C. Wang, T. N. Marion, Anti-DNA autoantibodies initiate experimental lupus nephritis by binding directly to the glomerular basement membrane in mice. *Kidney Int.* **82**, 184–192 (2012).
- F. Wu, W. Zhang, H. Shao, H. Bo, H. Shen, J. Li, Y. Liu, T. Wang, W. Ma, S. Huang, Human effector T cells derived from central memory cells rather than CD8<sup>+</sup> T cells modified by tumor-specific TCR gene transfer possess superior traits for adoptive immunotherapy. *Cancer Lett.* **339**, 195–207 (2013).

47. L. Gattinoni, D. E. Speiser, M. Lichterfeld, C. Bonini, T memory stem cells in health and disease. *Nat. Med.* **23**, 18–27 (2017).
48. C. T. Ellebrecht, V. G. Bhoj, A. Nace, E. J. Choi, X. Mao, M. J. Cho, G. Di Zenzo, A. Lanzavecchia, J. T. Seykora, G. Cotsarelis, M. C. Milone, A. S. Payne, Reengineering chimeric antigen receptor T cells for targeted therapy of autoimmune disease. *Science* **353**, 179–184 (2016).
49. H. J. Pegram, J. C. Lee, E. G. Hayman, G. H. Imperato, T. F. Tedder, M. Sadelain, R. J. Brentjens, Tumor-targeted T cells modified to secrete IL-12 eradicate systemic tumors without need for prior conditioning. *Blood* **119**, 4133–4141 (2012).
50. R. Q. Le, L. Li, W. Yuan, S. S. Shord, L. Nie, B. A. Habtemariam, D. Przepiorka, A. T. Farrell, R. Pazdur, FDA approval summary: Tocilizumab for treatment of chimeric antigen receptor T cell-induced severe or life-threatening cytokine release syndrome. *Oncologist* **23**, 943–947 (2018).
51. P. J. Paszkiewicz, S. P. Fräßle, S. Srivastava, D. Sommermeyer, M. Hudecek, I. Drexler, M. Sadelain, L. Liu, M. C. Jensen, S. R. Riddell, D. H. Busch, Targeted antibody-mediated depletion of murine CD19 CAR T cells permanently reverses B cell aplasia. *J. Clin. Invest.* **126**, 4262–4272 (2016).
52. U. Distler, J. Kuharev, P. Navarro, Y. Levin, H. Schild, S. Tenzer, Drift time-specific collision energies enable deep-coverage data-independent acquisition proteomics. *Nat. Methods* **11**, 167–170 (2014).
53. M. Sedic, L. A. Gethings, J. P. C. Vissers, J. P. Shockcor, S. McDonald, O. Vasieva, M. Lemac, J. I. Langridge, D. Batinić, S. K. Pavelić, Label-free mass spectrometric profiling of urinary proteins and metabolites from paediatric idiopathic nephrotic syndrome. *Biochem. Biophys. Res. Commun.* **452**, 21–26 (2014).
54. J. C. Silva, M. V. Gorenstein, G.-Z. Li, J. P. C. Vissers, S. J. Geromanos, Absolute quantification of proteins by LCMSE: A virtue of parallel MS acquisition. *Mol. Cell. Proteomics* **5**, 144–156 (2006).
55. R. R. Singh, V. Saxena, S. Zang, L. Li, F. D. Finkelman, D. P. Witte, C. O. Jacob, Differential contribution of IL-4 and STAT6 vs STAT4 to the development of lupus nephritis. *J. Immunol.* **170**, 4818–4825 (2003).
56. N. E. Adelman, D. L. Watling, H. O. McDevitt, Treatment of (NZB x NZW)F1 disease with anti-I-A monoclonal antibodies. *J. Exp. Med.* **158**, 1350–1355 (1983).

**Acknowledgments:** We thank H. Haecker (St. Jude's Children's Research Hospital), M. Shlomchik (University of Pittsburgh), and D. Pattanaik (UTHSC) for constructive comments on the manuscript. The technical assistance of S. Barnett and T. Costello with animal care, D. Daria with flow cytometry, T. J. Hollingsworth with tissue imaging, and T. Higgins with

graphics are appreciated. **Funding:** This work was supported by the Lupus Research Alliance of New York, NY to M.R. Funding was also provided by the CORNET mechanism (UTHSC) and by the ORR fund to M.R. Portions of the work were supported by PHS NIH award R01CA081171 to L.M.A. **Author contributions:** R.K. performed most aspects of viral infections, cell culture, animal husbandry, flow cytometry, and immunochemistry, organized data, and wrote sections of the manuscript. N.R. performed virus production and purification and tested virus infections and protein expression. I.N. performed aspects of immunochemistry, cell purification, cDNA construction, and quantitation and wrote sections of the manuscript. S.K. and D.C. performed recombinant DNA techniques and cell culture work. M.G. performed immunochemistry, data analysis, and data representation. Q.-u.-a.G. performed data analysis and statistical evaluations and contributed to data representation. L.B. evaluated pathology of mouse kidney and skin specimens and advised on tissue preparation. S.B.-G. advised on mass spectrometry and wrote sections of the manuscript. F.G. performed mass spectrometry, evaluated plasma proteome analysis, and wrote sections of the manuscript. J.N.K. provided the MSGV retroviral genome and advised on virus expression. T.M. advised and consulted on all experiments, guided flow cytometry, immunochemistry and mouse pathogenesis evaluations, and wrote sections of the manuscript. L.M.A. guided and participated in all experiments involving the construction and use of viral vectors and wrote sections of the manuscript. M.R. was responsible for all aspects of the study, including the conception and design of the experimental approach, planning and coordinating experimental procedures, collecting and approving data, and composing and revising the final text. All authors participated in the editing and approval of the final text of the manuscript. **Competing interests:** UTHSC filed a patent application, no. 65022-274929, titled "Use of Anti-CD19 CAR T Cells in Lupus." (M.R., inventor). J.N.K. has patent applications for CARs targeting human CD19. **Data and materials availability:** All data associated with this study are present in the paper or the Supplementary Materials.

Submitted 14 September 2018  
 Resubmitted 21 November 2018  
 Accepted 30 January 2019  
 Published 6 March 2019  
 10.1126/scitranslmed.aav1648

**Citation:** R. Kansal, N. Richardson, I. Neeli, S. Khawaja, D. Chamberlain, M. Ghani, Q.-u.-a. Ghani, L. Balazs, S. Beranova-Giorgianni, F. Giorgianni, J. N. Kochenderfer, T. Marion, L. M. Albritton, M. Radic, Sustained B cell depletion by CD19-targeted CAR T cells is a highly effective treatment for murine lupus. *Sci. Transl. Med.* **11**, eaav1648 (2019).

# SOMETIMES THE GRASS REALLY IS GREENER SOMEPLACE NEW.



Find your next job at [ScienceCareers.org](https://www.sciencecareers.org)

There's scientific proof that when you're happy with what you do, you're better at what you do. Access career opportunities, see who's hiring and take advantage of our proprietary career-search tools. Get tailored job alerts, post your resume and manage your applications all in one place. Start here: [sciencecareers.org](https://www.sciencecareers.org)

**ScienceCareers**

FROM THE JOURNAL SCIENCE  MAAAS

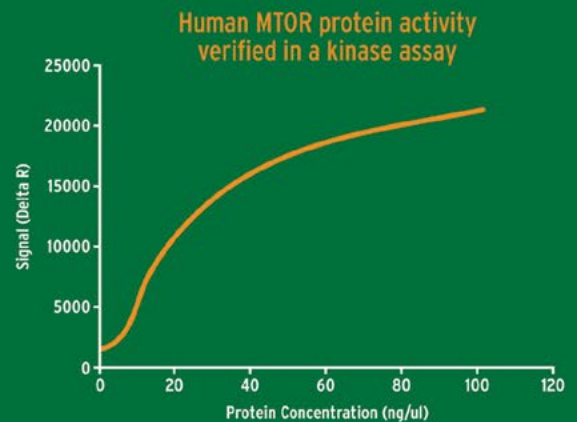
# 10,000 Human Proteins Made from Human Cells

Better Preservation  
of PTMs and  
Functions



## The Largest Collection of Mammalian Cell-Derived Proteins

- Protein functional studies
- Compound screening
- Protein microarrays
- Immunogens for antibody production
- Assay standards: ELISA, Mass Spec, and more



 **ORIGENE**

[origene.com/protein](https://origene.com/protein)

© 2019 OriGene Technologies, Inc. All Rights Reserved.